
18th IEEE Workshop on Nonlinear Dynamics of Electronic Systems

- Proceedings -



**Dresden University of Technology
Dresden, Germany**

26 – 28 May 2010

www.ndes2010.org

organized by:

Dresden University of Technology

in cooperation with:

University of Applied Sciences Dresden
CMD Congress Management GmbH Dresden
IEEE

Welcome Address to NDES 2010 in Dresden

Dear colleagues and friends,

we would like to extend a warm welcome to all the participants of the International Workshop NDES 2010, and we thank you very much for your participation.

NDES 2010 is the eighteenth in a series of workshops, and some of the NDES family might remember the way it took almost around the world:

Dresden (1993) – Krakow (1994) – Dublin (1995) – Seville (1996) – Moscow (1997) -
Budapest (1998) - Rønne (1999) – Catania (2000) - Delft (2001) – Izmir (2002) –
Scuol (2003) – Évora (2004) - Potsdam (2005) – Dijon (2006) – Tokushima (2007) -
Nizhniy Novgorod (2008) - Rapperswil (2009).



– Participants of the first NDES in 1993-

Now it will be held again in the place where it started, and we expect that the workshop will not only be an interesting event in nonlinear science, but that it will also provide all of you with the best of science and education. All program components of NDES, such as invited

talks given by well-known lecturers, presentations of research results and a special session devoted to neural networks will hopefully attract as many participants as in previous years.

We also hope that you will enjoy your stay here in our beautiful city of Dresden.

The workshop was sponsored by the German Research Foundation (DFG), technically co-sponsored by the Circuit and Systems Society (CASS) of the Institute of Electrical and Electronic Engineers (IEEE) Inc., and supported by the Dresden University of Technology. We would like to express our appreciation and sincere thanks to all sponsoring organizations.

Furthermore, we thank all who contributed with their efforts and their engagement to make our workshop possible.

Welcome to Dresden!

Welcome to NDES 2010!

We wish you a very pleasant stay!



Prof. Ronald Tetzlaff

General Chair



Prof. Wolfgang Schwarz

Program Chair



Prof. Kristina Kelber

Publication Chair

Table of Contents

Welcome Address	Page I
Table of Contents	Page III
Symposium Committees	Page IV
Special Thanks	Page V
Conference program (incl. page numbers of papers)	Page VI
Conference papers	
Invited talks.....	Page 1
Regular Papers	Page 14
Wednesday, May 26 th , 2010	Page 15
Thursday, May 27 th , 2010	Page 110
Friday, May 28 th , 2010	Page 210
Author index	Page XIII

Symposium Committees

Scientific Committee

Leon Chua, Berkeley
Alexander Dmitriev, Moscow
Martin Hasler, Lausanne
Hans Hermann, Zurich
Kristina Kelber, Dresden
Jürgen Kurths, Potsdam
Erik Lindberg, Lyngby
Wolfgang Mathis, Hannover
Vladimir Nekorkin, Nizhny Novgorod
Yoshifumi Nishio, Tokushima
Maciej Ogorzalek, Krakow
Toshimichi Saito, Tokyo
Wolfgang Schwarz, Dresden
Ruedi Stoop, Zurich
Ronald Tetzlaff, Dresden

Organisation Committee

General Chair

Ronald Tetzlaff
TU Dresden
chair@ndes2010.org

Technical Program Chair

Wolfgang Schwarz
TU Dresden
program@ndes2010.org

Local Arrangements & Finances

Andreas Mögel
Torsten Schmidt
finance@ndes2010.org

Publication Chair

Kristina Kelber
HTW Dresden
pub@ndes2010.org

Conference Office

Roswitha Weber
Michele Lempke
Technische Universität Dresden
ETIT / IEE / GE
01062 Dresden, F. R. Germany
office@ndes2010.org

Special Thanks

The NDES2010 Organizing Committee would like to acknowledge the technical support of the
Technische Universität Dresden, Professur für Grundlagen der Elektrotechnik
(Dresden University Of Technology, Chair Of Fundamentals Of Electrical Engineering)
and the

Circuit And Systems Society (CASS) of the Institute Of Electrical And Electronics Engineers (IEEE).

They greatly contributed to the success of the event.

We would like to express our appreciation and sincere thanks to the

Deutsche Forschungsgemeinschaft (DFG, German Research Foundation)

which financially supported the Symposium and greatly contributed to make it a memorable event.

Finally, special thanks go to the reviewers, who devoted their valuable time to NDES2010:

Anthony C. Davies,

Martin Hasler,

Jörg Krupar,

Jan Lunze,

Yoshifumi Nishio,

Wolfgang Schwarz,

Hiroiyuki Torikai,

Ute Feldmann,

Kristina Kelber,

Erik Lindberg,

Andreas Mögel,

Toshimichi Saito,

Ronald Tetzlaff,

Michael Tse.

Conference program

May 25, 2010 (Tuesday)

<i>Time slot</i>	<i>Schedule / Room</i>
16:00-20:00	Registration at Görges-Bau (conference venue), Wednesday: 8-17 Thursday: 8-17 Friday: 8-12
18:00-20:00	Welcome and Get-Together / Görges-Bau (conference venue)

May 26, 2010 (Wednesday)

<i>Time slot</i>	<i>Time</i>	<i>Schedule</i>	Room Page
08:15-08:30		Welcome Note <i>Ronald Tetzlaff</i>	226
08:30-10:00		Invited lectures 1: <i>Chairman: Wolfgang Schwarz</i>	226
	08:30	Guanrong (Ron) Chen (City University of Hong Kong, China) Pinning Control of Nonlinear Network Synchronization	Page 1
	09:15	Maciej Ogorzalek (Jagiellonian University, Krakow, Poland) Fractal Techniques Boost Performance of Microelectronic Circuits	Page 1
10:00-10:30		Coffee break	
10:30-11:50		Session 1.1: Nonlinear circuits & systems 1	127
	10:30	The Barkhausen Criterion (Observation ?) <i>Erik Lindberg.</i>	Page 15
	10:50	Asymptotic and Numerical Analysis of Equation with Large Delay <i>Ilya S. Kashchenko.</i>	Page 19
	11:10	A New Quality Factor for the Comparison of Multiplier Architectures <i>Ahmed Darrat and Wolfgang Mathis.</i>	Page 22
	11:30	Design of coupling for arbitrary lag synchronization in chaotic oscillators <i>Prodyot Kumar Roy, Sourav Kumar Bhowmick, Ioan Grosu and Syamal Kumar Dana.</i>	Page 26

<i>Time slot</i>	<i>Time</i>	<i>Schedule</i>	Room Page
10:30-11:50		Session 1.2: Control & Synchronisation 1	229
	10:30	Desynchronization of Mean-Field Coupled Oscillators by Remote Virtual Grounding <i>Arunas Tamasevicius, Skaidra Bumeliene, Elena Tamaseviciute, Gytis Mykolaitis and Raimundas Kirvaitis.</i>	Page 30
	10:50	Nonlinear Observer Based Control of a Chaotic Phase Locked Loop <i>Mohamed Mchiri and Karim Trabelsi.</i>	Page 34
	11:10	Observer approach for synchronization of chaotic time delay Chua circuit: application to secure communication <i>Karim Trabelsi and Mohamed Mchiri.</i>	Page 38
	11:30	Communication system with chaotic radiopulses in the real channels <i>Lev Kuzmin.</i>	Page 42
11:50-12:00		break	
12:00-13:20		Session 2.1: Nonlinear circuits & systems 2	127
	12:00	Generation of the microwave dynamic chaos in ring self-oscillatory system on CMOS structure <i>Alexander Dmitriev, Elena Efremova and Artem Nikishov.</i>	Page 46
	12:20	Influence of electron velocity dispersion on dynamics of electron beam with virtual cathode <i>Semen Kurkin, Alexander Hramov and Alexey Koronovskii.</i>	Page 50
	12:40	Observer Based Measurement of the Adenosine Diphosphate Concentration in Multimodal Oscillatory Pancreatic Beta Cells <i>Klaus Röbenack.</i>	Page 54
	13:00	Spiking in Delay-Coupled FitzHugh-Nagumo Systems with Feedback <i>Anastasiia Panchuk.</i>	Page 58
12:00-13:20		Session 2.2: Control & Synchronisation 2	229
	12:00	Synchronization in Two Polygonal Oscillatory Networks Sharing a Branch <i>Yoko Uwate, Yoshifumi Nishio and Ruedi Stoop.</i>	Page 62
	12:20	Chaos Control of the Chaotic Colpitts Oscillator <i>Arturo Buscarino, Luigi Fortuna, Mattia Frasca and Gregorio Sciuto.</i>	Page 66
	12:40	Generalized synchronization in mutually coupled dynamical systems <i>Olga Moskalenko, Alexey Koronovskiy, Alexander Hramov and Svetlana Shurygina.</i>	Page 70
	13:00	Chaotic Behavior of Hysteresis Cellular Nonlinear Networks and its Control <i>Angela Slavova.</i>	Page 74

<i>Time slot</i>	<i>Time</i>	<i>Schedule</i>	Room Page
13:20-14:30		Lunch	
14:35-15:20		Invited lecture 2: <i>Chairman: Vladimir Nekorkin</i>	226
		Michael Tse (Hong Kong Polytechnic University, China) Composing Music by Complex Networks	<i>Page 2</i>
15:20-15:30		Coffee break	
15:50-17:10		Session 3.1: Chaos phenomena & control	127
	15:50	Focusing Time--Dependent Billiards as Maxwell's Demon <i>Alexander Loskutov and Alexei Ryabov</i>	<i>Page 78</i>
	16:10	Noise-induced Phenomena in a Bio-inspired Chemical Sensor Array <i>Kazuki Nakada, Katsumi Tateno, Hatsuo Hayashi and Kiyonori Yoshii.</i>	<i>Page 82</i>
	16:30	Explicit model predictive control for the start-up and orbital stabilization of a boost converter <i>Axel Schild, Jan Lunze and Wolfgang Schwarz.</i>	<i>Page 86</i>
	16:50	Chaos based networking systems sharing a common nonlinearity <i>M. Santhiah and P. Philominathan.</i>	<i>Page 90</i>
15:50-17:10		Session 3.2: Signal processing	229
	15:50	Music Score Recognition System for a Robot controlling a Theremin <i>Kristina Kelber, Nils Wabnik and Carlos Hernandez Franco.</i>	<i>Page 94</i>
	16:10	A Cochlear Active Transmission-Line Model without Wave Reflection <i>Tohru Kohda, Takao Une and Kazuyuki Aihara</i>	<i>Page 98</i>
	16:30	Automatic Discovery of Subgoals in Reinforcement Learning using Betweenness Centrality Measures <i>Ali Ajdari Rad, Parham Moradi, Alireza Kahdivi and Martin Hasler.</i>	<i>Page 102</i>
	16:50	Prediction of Time-Series Data using PSpice and Runge-Kutta Method <i>Kazuhisa Yoshimatsu, Masayuki Yamauchi and Yoshifumi Nishio.</i>	<i>Page 106</i>

May 27, 2010 (Thursday)

<i>Time slot</i>	<i>Time</i>	<i>Schedule</i>	Room Page
08:30-10:00		Invited lecture 3: <i>Chairman: Ronald Tetzlaff</i>	226
		Leon Chua (University of California at Berkley, USA) From G-clef to 137	Page 2
10:00-10:30		Coffee break	
10:30-11:50		Session 4.1: Nonlinear circuits & systems 3	127
	10:30	Circuit Implementation of an A/D Converter Based on the Scale-Adjusted β -Map Using a Discrete-Time Integrator <i>Yoshihiko Horio, Kenya Jin'no, Tohru Kohda and Kazuyuki Aihara.</i>	Page 110
	10:50	Peak Search Algorithm of Frequency Characteristics with Unstable Region <i>Hiroshige Kataoka, Yoshihiro Yamagami and Yoshifumi Nishio.</i>	Page 114
	11:10	An Experimental Investigation of PWM-1 Controlled Circuit with Time Delay <i>Kenichi Tasaki, Hiroyuki Asahara and Takuji Kousaka.</i>	Page 118
	11:30	Qualitative Mechanism of DC/DC Converter containing Spike Noise <i>Hiroyuki Asahara and Takuji Kousaka.</i>	Page 122
10:30-11:50		Session 4.2: Neural networks, neurodynamics, robots 1	229
	10:30	Two-Compartment Phenomenological Model of Dopaminergic Neuron <i>Denis Zakharov, Alexey Kuznetsov and Vladimir Nekorkin.</i>	Page 126
	10:50	An adaptive coupling scheme for the Kuramoto model of complex networks <i>Ning Bo, Hou Jian-Li, Ren Quansheng and Zhao Jianye.</i>	Page 130
	11:10	Improved Divided Chaotic Associative Memory for Successive Learning <i>Yohei Takamori and Yuko Osana.</i>	Page 134
	11:30	Network motifs in STDP-driven neuronal networks <i>Quansheng Ren, Kiran M. Kolwankar, Areejit Samal and Juergen Jost.</i>	Page 138
11:50-12:00		break	

<i>Time slot</i>	<i>Time</i>	<i>Schedule</i>	Room Page
12:00-13:20		Session 5.1: Nonlinear circuits & systems 4	127
	12:00	An Exactly Solvable Chaotic Circuit <i>Ned Corron, Mark Stahl and Jonathan Blakely.</i>	Page 142
	12:20	Complex dynamics in a new PWL chaotic circuit <i>Arturo Buscarino, Luigi Fortuna and Mattia Frasca.</i>	Page 146
	12:40	Shil'nikov Chaos and Mixed-mode Oscillation in asymmetry-induced Chua circuit <i>Satyabrata Chakraborty and Syamal Kumar Dana.</i>	Page 150
	13:00	Penetration and Reflection Mechanisms of Phase-Inversion Waves in Lattice Oscillators <i>Hitoshi Aburatani, Suguru Yamane, Masayuki Yamauchi and Yoshifumi Nishio.</i>	Page 154
12:00-13:20		Session 5.2: Neural networks, neurodynamics, robots 2	229
	12:00	Data Clustering based on Hebbian Learning in Inhomogeneous Coupled Map Lattices <i>Thomas Ott and Urs Mürset</i>	Page 158
	12:20	Transient Dynamics and Metastable States in an Ensemble of Synaptically Coupled Morris-Lecar Neurons <i>Vladimir Nekorkin, Dmitry Kasatkin and Aleksey Dmitrichev.</i>	Page 162
	12:40	Bifurcations in memristive oscillators <i>Fernando Corinto, Alon Ascoli and Marco Gilli</i>	Page 166
	13:00	On the Chaos Associative Memory with Tchebycheff Activation Function <i>Masahiro Nakagawa.</i>	Page 170
13:20-14:30		Lunch	
14:35-15:20		Invited lecture 4: <i>Chairman: Syamal Dana</i>	226
		Vladimir I. Nekorkin (Institute of Applied Physics, RAS Nizhny Novgorod, Russia) Nonlinear Dynamical Approach for Study of Neural Networks Activity	Page 3
15:20-15:30		Coffee break	

<i>Time slot</i>	<i>Time</i>	<i>Schedule</i>	Room Page
15:50-17:30		Session 6.1: Bifurcation & Chaos 1	127
	15:50	Detecting unstable periodic spatio-temporal states of spatial extended chaotic systems <i>Alexander Hramov and Alexey Koronovskii.</i>	Page 174
	16:10	Phase-flip bifurcation in a system of time-delay coupled oscillators <i>Vladimir Klinshov and Vladimir Nekorkin.</i>	Page 178
	16:30	T-point-Hopf bifurcation in electronic circuits <i>Antonio Algaba, Fernando Fernández, Manuel Merino and Alejandro Rodríguez.</i>	Page 182
	16:50	Global bifurcations in a family of coupled systems <i>Antonio Algaba, Cristobal Garcia, Manuel Merino and Manuel Reyes.</i>	Page 186
	17:10	Generalizations of Blakesley's Voltage Source Shift Theorem <i>Albrecht Reibiger (invited lecture)</i>	Page 10
15:50-17:30		Special Session: Neural networks for cognitive agents	229
	15:50	Multiobjective optimization of Echo State Networks for multiple motor pattern learning <i>A. F. Krause, B. Blasing, T. Schack</i>	Page 190
	16:10	Parallel Central Pattern Generators for locomotion control in a humanoid robot model <i>I. Aleo, P. Arena, L. Patane</i>	Page 194
	16:30	Reaction-diffusion-like Systems for event representation and beyond <i>J.A. Villacorta-Atienza, V. A. Makarov, M. G. Velarde</i>	Page 198
	16:50	Chunking by naming: A nonlinear recurrent network for storing hierarchical memory contents <i>H. Cruse, M Schilling</i>	Page 202
	17:10	Tribot: a hybrid robot for cognitive algorithm implementation <i>P. Arena, L. Patane', M. Pollino, C. Ventura</i>	Page 206
19:00		Visit to the Dresden cathedral (Catholic Church of the Royal Court of Saxony), introduction to the SILBERMANN organ & short concert	
20:00		Conference dinner at Sophienkeller	

May 28, 2010 (Friday)

<i>Time slot</i>	<i>Time</i>	<i>Schedule</i>	Room Page
08:30-10:00		Invited lectures 5: <i>Chairman: Martin Hasler</i>	226
	08:30	Syamal Dana (Central Instrumentation Indian Institute of Chemical Biology, Kolkata, India) Engineering Synchronization in Chaotic Oscillators by Design of Coupling	Page 4
	09:15	Ruedi Stoop (University and ETH Zürich, Switzerland) Global real-world shrimp hierarchies	Page 6
10:00-10:30		Coffee break	
10:30-11:50		Session 7.1: Bifurcation & Chaos 2	226
	10:30	Comparison of Eyelet Intermittency and Type-I Intermittency with Noise <i>Alexander Hramov, Alexey Koronovskiy, Maria Kurovskaya and Olga Moskalenko.</i>	Page 210
	10:50	Bifurcation of a simplified model of the boost converter with solar cell input <i>Toshimichi Saito and Daisuke Kimura.</i>	Page 214
	11:10	Self-Generation of Chaotic Dissipative Soliton Trains in Active Ring Resonators with Ferromagnetic Films <i>Sergey Grishin and Yurii Sharaevskii.</i>	Page 218
10:30-11:50		Session 7.2: Nonlinear network analysis	229
	10:30	Exponential Transient Oscillations and Their Stabilization in a Bistable Ring of Unidirectionally Coupled Maps <i>Yo Horikawa and Hiroyuki Kitajima.</i>	Page 226
	10:50	Bistability and supratransmission in a nonlinear electronic Klein-Gordon network <i>B. Bodo, S. Morfu, P. Marquie and M. Rossé.</i>	Page 230
	11:10	Memristive effect in the model of superconductive-normal transition <i>Linda Ponta, Anna Carbone, Marco Gilli and Piero Mazzetti.</i>	Page 234
	11:30	Studying Circuit Disturbances of MOS LC-Tank Oscillators based on Order Reduction Techniques <i>Jan Bremer, Marco Reit and Wolfgang Mathis</i>	Page 238
11:50-12:00		break	
12:00-12:15		Closing remarks <i>Wolfgang Schwarz</i>	226
12:15-13:30		Lunch	
		end of workshop	

Invited Talks





Guanrong (Ron) Chen
City University of Hong Kong, China

Pining Control of Nonlinear Network Synchronization

Abstract - In this talk, topics on complex nonlinear network synchronization and its pinning control are presented. First, the concept of synchronization and some criteria are briefly introduced for various dynamical networks, including fully-connected, ring-shaped and star-shaped regular networks, as well as small-world and scale-free complex networks. Then, the issue of pinning-controlled synchronization is discussed, for nonlinear networks that do not satisfy self-synchronized conditions. Furthermore, some commonly concerned questions are addressed, such as what kind of controllers to deploy, how many to use, and where to apply them on the network, so as to achieve effective network synchronization. Finally, a simple method is described for designing the state-feedback pinning controller gains, verified and visualized by numerical simulation examples.



Maciej Ogorzalek
Jagiellonian University, Krakow, Poland

Fractal Techniques Boost Performance of Microelectronic Circuits

Abstract - The concepts of fractals and space-filling curves have drawn attention of electrical and electronic engineers during the last decade enabling many interesting developments such as building super-capacitors, multi-band miniature antennas, fractal sensors or new array search algorithms.

With the recent advances in technologies entering the nano-scale electronics, ultra-high frequencies and 3D circuit topologies it seemed that fractal techniques have come to its limit of scalability. This has been confirmed not to be true! In the last three-mentioned areas fractal approaches find even more spectacular applications. The functionality of nano-transistors, bio-nano probes can be efficiently analyzed using fractal transformations, new types of fractal THz antennas can be built and also fractal channel cooling structures could be designed for 3D-stacked ICs. This lecture provides an overview of cutting-edge techniques and most spectacular recent developments.



Michael Tse
Hong Kong Polytechnic University, China

Composing Music by Complex Networks

Abstract - Across cultures, and between individuals, certain musical pieces are consistently rated more favourably than others. We find that musical scores which are widely perceived to be “good” generate complex networks with certain invariant properties: scale-free networks with strong clustering of nodes within the network. We describe a method to generate random musical compositions from these networks (essentially, as a weighted random walk on the network) and find that scores generated in this manner are also perceived to be reasonably “good” and are similar (in the network statistical sense) to the specific score from which the generating network was produced. We will also introduce the concept of “motifs” in music and in networks. Creating and incorporating motifs in our network-based computer composition has shown to produce “appealing” music. We will construct networks for selected works from the late Chinese pop singer Teresa Teng, and use the constructed networks for recomposing music that mimicks the classic Teng’s style.



Leon Chua
University of California at Berkley, USA

From G-clef to 137

Abstract - The *G-clef* and the *prime number 137* will be defined and immortalized for their fundamental significance in chaos and computation.



Vladimir I. Nekorkin
Institute of Applied Physics, RAS Nizhny Novgorod, Russia

Nonlinear Dynamical Approach for Study of Neural Networks Activity

Abstract – In recent years nonlinear wave processes are attracting growing interest in the studies of neuronal network dynamics and information processes in the brain. Waves of excitation, localized activity patterns, their propagation and interactions represent are the key processes in the problem of inter-neuron communication, guiding the information flow and information processing in the neuronal networks of the brain. The mathematical images of such processes are attractors. On the other hand, many neurophysiologic experiments have indicated that some neural processes (for example, processes related with performing of different cognitive tasks – memory, attention, psychomotor coordination, etc.) are accompanied only by transient activity on the level of individual neurons or small enough groups of neurons. As a result of such processes a certain sequence of transitional activity phases appears in neural network. It is clear that such activity of neural networks cannot be understood within the framework of classical models of nonlinear dynamics which are based on concept of attractor because here the main effect is achieved long before the system reaches its neighborhood. My talk is devoted to applying nonlinear dynamics approach to both problems mentioned above.



Ruedi Stoop
University and ETH Zürich, Switzerland

Global real-world shrimp hierarchies

(full paper -> page 6)



Syamal Dana

Central Instrumentation Indian Institute of Chemical Biology, Kolkata, India

Engineering Synchronization in Chaotic Oscillators by Design of Coupling

Abstract— Synchronization is as a process of evolving common rhythm in oscillatory systems. It is true for periodic as well as chaotic oscillators. Most of the studies of synchronization so far assume the unidirectional and mutual coupling mode due to their common existence in many natural systems, physical, chemical and biological and even ecological. Different synchronization regimes, namely, complete synchronization, lag synchronization and phase synchronization and also antiphase synchronization is identified under varying coupling strength. However, there is strict rule how to achieve or to target a particular type of synchronization in any given oscillatory system. However, for engineering purposes, we need robust methods for targeting such synchronization.

In this talk, two different methods, one open-plus-closed-loop coupling and another lyapunov function definition of coupling are proposed to target any of the above-mentioned synchronization regimes in two or more coupled oscillators. We present mathematical foundations of the design of the coupling function for targeting several regimes, synchronization, anti-synchronization and arbitrary lag synchronization. We provide experimental evidences of all the regimes in electronic circuits.



Albrecht Reibiger

Dresden University of Technology, Germany

Generalizations of Blakesley's Voltage Source Shift Theorem

(full paper -> page 10)

Global real-world shrimp hierarchies

Ruedi Stoop, Philipp Benner, Yoko Uwate

Institute of Neuroinformatics,

University of Zürich and Swiss Federal Institute of Technology Zürich, Irchel Campus, 8057 Zurich, Switzerland

Email: ruedi@ini.phys.ethz.ch

Abstract—As a recent result on dynamical invariants in two-dimensional parameter space, islands of periodicities of characteristic shapes ('shrimps') have been shown to exist that are connected by means of spirals, emanating from a joint focal point, offering ways to wander around in parameter space without ever having to cross the chaotic sea. In this paper, we confirm the experimental existence of the shrimp phenomenon, by probing the parameter space of a hardware nonlinear electronic system family and comparing it to the corresponding numerical simulations.

I. INTRODUCTION

The theory of dynamical systems, being developed since Poincaré in the 19th century, can be characterized as the search for dynamical invariants, with respect to variations of the system at hand with respect to its parameters or with respect to the initial conditions used. From the practical viewpoint, knowing the underlying principles spatial extensions and further properties of these invariants provides experimentalists and modelers with strong universal guidelines for their work. One particular important aspect of such properties, for example, is the possibility to maintain a certain given dynamical behavior of the system (e.g., the periodicity of the device) while navigating through the parameter space. For systems depending on one parameter, the system behavior from this respect is fairly well understood in terms of the bifurcation diagrams that tell us what dynamical behavior in physical space is to be expected. In this case, the main parameter intervals pertaining to a fixed periodic behavior are generically of small size and follow a simple scaling behavior. The typical situation in systems having a parameter space of co-dimension two or higher, is less well understood. Here, the fundamental class of such invariants are the so-called 'shrimps' [5]. They owe their name to their peculiar form, which is preserved among a large variety of systems. Similarly to the parameter intervals associated with a certain periodicity in dimension one, the sizes of the shrimps associated with different periodicities follow a simple

scaling behavior, and their geometric shapes remain essentially invariant. More explicitly, the appearance of one such shrimp implies the appearance of an infinite number of self-similar shrimps that are aligned side by side along a particular direction. Moreover, each shrimp occupies an extended region of the parameter space, meaning that one can still stay in the same periodic window even when large variations in two control parameters are being made. In this way, an arbitrary change in only one accessible parameter can replace chaos by periodic behavior, or vice versa. Therefore, a better understanding of the global properties of shrimps is useful in particular in the experimental context, when nonlinearly reacting devices are to be switched from chaotic into periodic behavior just by a minimal application of a change in one (or a combination) of the parameters, or if robust chaotic behavior of a device is needed, e.g. if the periodicity is to be established by means of chaos control, or for chaos-based communication [1], [2].

II. EARLIER APPROACHES AND PREVIOUS RESULTS

A program of investigation of the behavior of nonlinear systems, including the determination of their invariants, was already very early pointed out in the context of electronic systems [3]. One of the first remarkable theoretical results in understanding two-dimensional invariants in parameter space were obtained for time-continuous, near-to-homoclinic systems, in the context of Shilnikov chaos [4].

Later on, the topic was taken up by Gallas, who analyzed the internal structures of the shrimps in a more abstract way [5], [6], building directly upon iterated nonlinear maps. Shrimps were found and discussed in a large number of discrete-time map based systems approach [5], [6], [7], [8], [9], [10], [11], [12]. The simulation of continuous-time systems require more technicalities for ordinary differential equation systems [13], [14], [15], [16], [17], [18]. Their experimental corroboration, however, is even more involved, as, due to the complex

shrimp boundaries, a high experimental resolution is needed in order to pin the object down. In Ref. [13], one of the first examples of a shrimp from a real-world system was reported, for Chua's circuit. Results that concentrate on the internal structure of a period-4 shrimp of an electronic circuit, were recently obtained in Ref. [19]. This work verified in a real-world experiment the theoretical predictions made in [4], [5] on the internal mechanisms responsible for shrimps generation.

To some extent or even more important than the internal structure of shrimps, is the global aspect of their occurrence. In a recent computational effort, Gallas and Bonatto explored the global parameter space aspects associated with a model of a related nonlinear electronic circuit [17]. They demonstrated the existence of a hierarchical structure ('hub'), binding all shrimps in a large portion of the parameter space, and allowing for to change from periodicity to periodicity without ever having to cross the chaotic sea. Such an observation is, as discussed above, at the heart of the whole invariant investigation; in direct simulations, the theoretical predictions of Ref. [4] were corroborated. However, to fulfill the program, also the corroboration from real-world systems is desired, as global properties of differential equations of electronic circuits reflect only the behavior and properties of the latter to a certain extent: They refer to idealized electronic components, which when observed over extended regions of the parameter space, might not be valid everywhere, and so a direct correspondence is questionable.

Here we provide evidence for the first time hinting at the structural stability of these invariants also in the real-world paradigm, by showing that the identical invariant objects exist in the real-parameter world of circuits and that their global organization matches that one predicted by the theoretical, idealized, analysis.

III. ON THE EMERGENCE OF THE SHRIMP PHENOMENON

For an introduction into the shrimp phenomenon, we consider first the prototype of dissipative nonlinear systems, Hénon's map [20] $f : \{x, y\} \rightarrow \{1 - ax^2 + y, bx\}$ (the corresponding prototype for conservative systems, the circle or standard map [21], [22] $f : \{x, y\} \rightarrow \{x_n := x + \Omega - \frac{K}{2\pi} \sin(2\pi x), y_n := y + x_n \mod 1\}$, gives rise to similar observations). In this map, a is the nonlinearity parameter; b characterizes the dissipation. Evaluating this system, we observe that the sets on which simple periodic behavior emerges, are bounded by

complicated geometric boundaries (and have a 'shrimp'-like appearance). Moreover, they have interesting scaling properties, in the phase space as well as in the parameter space, see Fig. 1. Phase-space shrimps are bound by

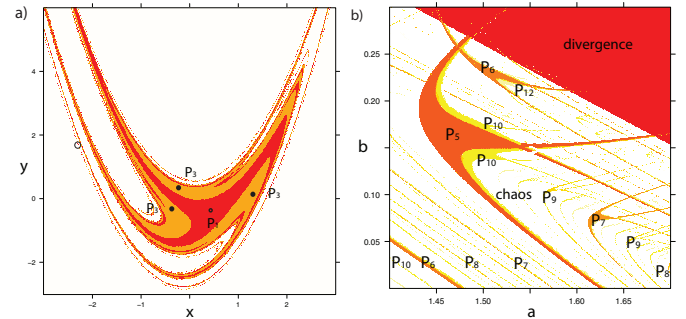


Fig. 1. a) Phase-space shrimp of the dissipative Hénon's map (standard parameters $a = 1.4$, $b = 0.3$). All points that converge to the central period-1 attractor are displayed in red, those that converge to a period-3 attractor in orange. Open dot: unstable period 1. b) Shrimps of different periodicities P_i in parameter space, separated by a chaotic sea (white). Crossing tails reflect non-ergodicity.

nonlinear manifolds that co-operate for their generation: An attracting basin towards fixed periodicity (central point of low periodicity) is bounded by a heteroclinic connection of saddle points of higher periodicity; beyond the separatrix, there are attractive points of higher periodicity (heteroclinic saddle connection [23]). As we will see below, this picture translates in a simple way into the parameter domain. Similarly (and strongly related) to the Feigenbaum period doubling, the emergence of shrimps is a universal feature. Shrimp islands are embedded within a surrounding (possibly hyper-[24]) chaotic sea, characterized by $k \geq 1$ positive Lyapunov exponents, that generally are reached over a series of period doublings. Each shrimp is organized along so-called spines of codimension k . Inside the shrimps, there is at least one point for which the determinant and the trace of the linearization are both zero, around which the shrimp structure is organized [11]. Periodic attractors with close to zero Lyapunov exponents are generated for parameter values on the tails of the shrimp. For dissipative systems, the tails of the shrimps can be seen as a codimension-one curve of nilpotent points. As a consequence, always large parameter changes can be made without breaking an orbit's stability. Shrimps are thus extended and have large scale dimensions in the parameter space. The situation for conservative systems is very similar [11].

IV. SHRIMP RELATIONS

Before demonstrating the existence of the salient shrimp phenomena in real systems, we will exemplarily demonstrate the close relationship between shrimps of the phase- and parameter-space. The observation that phase- and parameter-space shrimps are intimately connected was, among with other fundamental features of shrimps, first outlined in one of the pioneering works by Gallas [6], which we recall here in a condensed form. For simplicity of the argument, instead of the two-dimensional Hénon map, it is sufficient to consider the one-dimensional map $f : x \rightarrow (a - x^2)^2 - b$ [6]. This map can be seen as the nonlinear component of the second iterate of the Hénon map, where various terms involving pre-images of x can be thought of being absorbed in the parameters a and b . Stable k -isoperiodic islands (shrimps) arise whenever $x_k = f^k(x_k)$, $|m_k| = |f^k(x_k)| < 1$ holds, where f^k denotes the k -fold iterated map f and the prime the derivative with respect to x . A superstable locus requires that $m_k = 0$, i.e.

$$f^{k'}(x_k) = -4 \prod_{i=1}^k x_i \prod_{i=1}^k (a - x_i^2) = 0. \quad (1)$$

First, this implies that all k -superstable solutions need to pass either through $x_k = 0$ or $x_k = \pm\sqrt{a}$. By differentiability, this defines three families in parameter and in phase-space. Specifically for the $k = 1$ -isoperiodic islands, we arrive at the two conditions

$$\{a^2 - b - x - 2ax^2 + x^4 = 0, -m - 4ax + 4x^3 = 0\}. \quad (2)$$

From these conditions, the phase-space variable x can be eliminated and the problem can be examined in the parameter space. We end up with $m^4 - 12m^3 + (48 - 32ab)m^2 + 64(ab - 1)m - 256(a - b^2)(a^2 - b) = 0$. The parameter space area of the period-1 shrimp is now obtained by restricting m to values $|m| \leq 1$. As the locus of superstable solutions ($m = 0$), the four parabola $a = \pm\sqrt{b}$, $b = \pm\sqrt{a}$ emerge, which define the legs of the shrimp. Higher order islands are obtained analogously, requiring, however, increased computational efforts. Due to the symmetry and the differentiability of the underlying equation, the centers of the hearts of the islands are obtained for $m = 0$; they are connected by Eq. 2 with the corresponding $\{x, y\}$ -coordinates. $k > 1$ -superstable orbits must similarly pass either through $x = 0$ or $x = \pm\sqrt{a}$, so that the procedure can be repeated for higher periodicities. For the family that passes through $x = 0$, we finally obtain the conditions $k = 1 : a^2 - b = 0$, $k = 2 : (a - (a^2 - b)^2)^2 - b = 0, \dots$

whereas for the families that pass through $x = \pm\sqrt{a}$, the corresponding expressions are $k = 1 : -b = 0$, $k = 2 : (a - b^2)^2 - b = 0$, $k = 3 : (a - ((a - b^2)^2 - b)^2)^2 - b = 0 \dots$. For $k = 1$, this implies the solution $\{a_1, b_1\} = \{0, 0\}$, which is the intersection point of the four parabolas, defining the center, or head, of the shrimp. Similarly, the corresponding solutions for higher k 's define the heads of shrimps of higher periods. These points of intersections can be cast in the form of the pair of equations [6] $\{a = \pm\sqrt{b \pm \sqrt{a \pm \sqrt{b \pm \dots}}}, b = \pm\sqrt{a \pm \sqrt{b \pm \sqrt{a \pm \dots}}}\}$, where the continued formula needs to be cut off according to k . Cutting off after the first radical yields the equation for $k = 1$, with sole solution $\{a_1, b_1\}$. Cutting off after the third radical yields the solutions associated with $k = 2$, and so on. For both equations, identical sequences of signs must be selected, which consequently leads to 2^k islands of period k . The locations of the shrimp heads are then easily derived from equations corresponding to Eq. 2.

V. REAL-WORLD SHRIMPS

Here, we advance these efforts, by providing evidence for the hierarchical shrimp phenomenon from idealized ordinary differential equations of a nonlinear electronic circuit and by providing the corresponding directly real-world experimental evidence. Our experimental system is an asymmetric variant of the Nishio-Inaba circuit family, which we found to be experimentally much more stable than the symmetric two-diode version used in Refs. [25]. In Fig. 2 a), we provide the diagrammatic description of this circuit family and its model equations (note the changed expression of the diode representation f). In Fig. 2 b) we characterize the emergent behavior across the parameter space in terms of Lyapunov exponents (we plot here the largest exponent, constraining ourselves thus to non-negative values) and in c) by means of periodicity. For these figures, as well as for the experimental counterpart in Fig. 2 d), we chose $C = 0.0066 \mu F$ and L_1 was fixed to $L_1 = 634 mH$ and probed the systems by sampling their parameter space $\alpha \times \beta$, exploiting the relationships $\alpha = r\sqrt{C/L_1}$, $\beta = L_1/L_2$ and $\gamma = r_d/L_2\sqrt{L_1C}$ [25]. For the simulated samples, the emergent behavior was observed after a transient and recorded. For the experimental results, we similarly probed the space of systems, however, at a coarser step-size of $\Delta_\beta = 0.025$ and of $\Delta_r = 0.01$, respectively, rendering the value of L_2 to vary across the interval $[105, 507] mH$. For each data point, the periodicity was

observed on the oscilloscope and recorded. In the obtained results, the rich emergence of shrimp structures is obvious. It will be noted that our experimental results do not completely coincide with the simulation results. For this difference, we hold the internal resistance of the inductance (that are not accounted for in the circuit equations) and the precise characteristics of the diode responsible. The stunning similarity between the model and the experimental data is, nonetheless, evident. With the high experimental resolution achievable, a zoom-in also confirms the characteristic details of the recently observed 'periodicity hub' formed by the shrimps [17] (dashed boxes).

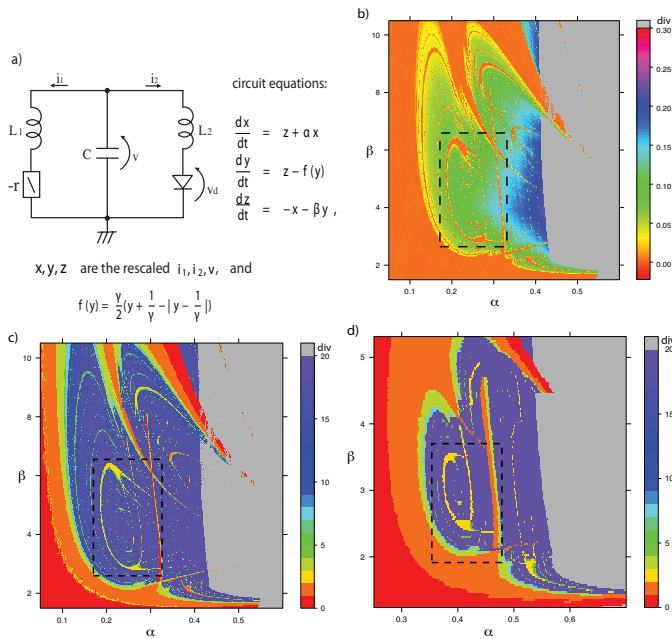


Fig. 2. a) Asymmetric variant of Nishio's circuit with corresponding equations. b) shrimps from simulations expressed in terms of Lyapunov exponents, c) by periodicity, d) experimental shrimps characterized by periodicity (dashed box: location of the 'periodicity hub' [17]).

VI. CONCLUSION

The shrimp phenomenon as the locus of a distinguished periodic behavior may be of particular relevance for bioinformatics. When dealing with experimental high throughput data in biochemistry or genetics, often the question is relevant, what initial conditions or parameter values will give rise to similar behaviors. Chemical substance generation, and, similarly, biological organisms, often require certain physical conditions to be fixed in a certain band-width.

The division of a set of observations into subsets so that observations follow the same behavior in some sense, is termed clustering. If the clusters have a form close to a spatially Gaussian probability distribution, two classical approaches that will solve this problem are k -means [26] and hierarchical clustering [27], [28], if we provide the correct number of clusters to be found. The shrimp phenomenon with its characteristic convex-concave geometric boundaries, however, suggests that in carefully prepared data, Gaussian noise clouds will rather be the exception than the rule. We suspect that this is why in bioinformatics, despite a plethora of standard algorithms, clustering works less well than expected.

REFERENCES

- [1] S. Hayes, C. Grebogi, E. Ott, Phys. Rev. Lett. **70**, 3031(1993).
- [2] S. Hayes, C. Grebogi, E. Ott, A. Mark, Phys. Rev. Lett. **73**, 1781 (1994).
- [3] A. Pikovski and M. Rabinovich, Physica **20**, 8 (1981).
- [4] P. Gaspard, R. Kaprai, G. Nicolis, J. Stat. Phys. **35**, 697 (1984).
- [5] J.A.C. Gallas, Phys. Rev. Lett. **70**, 2714 (1993).
- [6] J.A.C. Gallas, Appl. Phys. B **60**, 203 (1995).
- [7] M.S. Baptista and I.L. Caldas, Chaos, Solitons Fractals **7**, 325 (1996).
- [8] B. Hunt and E. Ott, J. Phys. A **30**, 7067 (1997).
- [9] E. Barreto, B. Hunt, C. Grebogi, J.A. Yorke, Phys. Rev. Lett. **78**, 4561 (1997).
- [10] M. Baptista and I. Caldas, Int. J. Bif. & Chaos **7**, 447 (1997).
- [11] M.S. Baptista, C. Grebogi, E. Barreto, Int. J. Bif. & Chaos **13**, 26812688 (2003).
- [12] Z. Zhushubaliyev, V. Rudakov, E. Soukhoterlin, E. Mosekilde, Discrete Dynamics in Nature and Society **5**, 203 (2006).
- [13] M.S. Baptista, Ph.D thesis, University of Sao Paulo (1996).
- [14] C. Bonatto, J.-C. Garreau, J.A.C. Gallas, Phys. Rev. Lett. **95**, 143905 (2005).
- [15] Y. Zou, M. Thiel, M. C. Romano, Q. Bi, J. Kurths, Int. J. Bif. & Chaos **16**, 3567 (2006).
- [16] V. Castro, M. Monti, W.B. Pardo, J.A. Walkenstein, E. Rosa, Int. J. Bif. & Chaos **17**, 965 (2007).
- [17] C. Bonatto and J. A. C. Gallas, Phys. Rev. Lett. **101**, 054101 (2008).
- [18] J. Cardoso, H. Albuquerque, R. Rubinger, Phys. Lett. A **373**, 2050 (2009).
- [19] D.M. Maranho, M.S. Baptista, J.C. Sartorelli, I.L. Caldas, Phys. Rev. E **77**, 037202 (2008).
- [20] M. Hénon, Comm. Math. Phys. **50**, 69 (1976).
- [21] B. Chirikov, Phys. Rep. **52**, 264 (1979).
- [22] J.M. Greene, J. Math. Phys. **20**, 1183 (1979).
- [23] A. Kusnetzov, Elements of Applied Bifurcation Theory, Springer (Berlin, 2004).
- [24] O.E. Rössler, Phys. Lett. A **71**, 155 (1979).
- [25] Y. Nishio, N. Inaba, S. Mori, T. Saito, IEEE Trans. Circuit Syst. **37**, 473 (1990).
- [26] H. Steinhaus, Bull. Acad. Polon. Sci. **4**, 801 (1956).
- [27] S.C. Johnson, Psychometrika **2**, 241 (1967).
- [28] R. D'Andrade, Psychometrika **4**, 58 (1978).

Generalizations of Blakesley's Voltage Source Shift Theorem

Albrecht Reibiger,

Faculty of Electrical Eng. & Information Technology,
Dresden University of Technology,
D-01062 Dresden, Germany
Email: albrecht.reibiger(at)mailbox.tu-dresden.de

Abstract—It is shown that the well-known Voltage Source Shift Theorem due to Blakesley and its dual version, the Current Source Shift Theorem as well as the rules for the transformation of networks with loops of capacitors or cut sets of inductors into networks without such loops or cutsets, resp., and the relationships between capacitance coefficients and partial capacitors are special cases of general theorems on the terminal behavior of networks. The proof of these theorems is based on the theory of terminal behavior of networks. For these proofs we do not need the substitution theorem with its strong uniqueness assumptions. This fact is an essential advantage in comparison to the original proof given by Chua and Green.

I. INTRODUCTION

The Voltage Source Shift Theorem [5], [3] goes back to the paper [1] of T. H. BLAKESLEY in 1894.

BLAKESLEY considers two cases. In the first one a voltage source is shifted from one branch of an incidence cut into the complementary subset of branches of this cut. In the second one a voltage source is shifted from one branch of an arbitrary cutset into the complementary subset of branches of this cutset.

The Current Source Shift Theorem [5], [3] is the dual form of the Voltage Source Shift Theorem. While the latter is definitely connected with the name of BLAKESLEY, we were unable to identify the originator of the Current Source Shift Theorem.

CHUA and LIN consider in [2], Problem 10-9 and 10-11, examples for the elimination of a single capacitor-loop or inductor-cutset from some network. CHUA and GREEN generalize in [4] these equivalences to nonlinear RLCM-networks including multiple capacitor voltage-source loops or inductor current-source cutsets.

In almost all of today's circuit simulators the network models to be analyzed are described by means of differential-algebraic equations. The so called index

[7], [19] describes an essential property of this class of equations. The equivalences considered in [4] can be used to reduce the index of the corresponding differential algebraic equation. This is an important feature for the development of circuit simulation software since index reduction improves the convergence properties of numerical integration procedures for this special type of equations.

CHUA and GREEN use mathematical induction to prove these equivalences. To verify the corresponding base step they rely on the Substitution Theorem of network theory [5], [3]. This fact is the Achilles heel of their proof since the Substitution Theorem can be used only, if both the original network and the network modified by means of this theorem have the same finite number of solutions (cf. [6]) or, in the standard version [5], [3], only unique solutions. Take into account, for nonlinear networks it is impossible to ensure that this assumption is always fulfilled.

The examples of equivalent networks mentioned above are special cases of more general theorems on the terminal behavior of networks. Here we present only the central results and the ideas behind their proofs; a paper with complete proofs is in preparation [16].

For network theoretical notations used in the following we refer to [15]. As there we define a network as an ordered pair $(\mathcal{C}, \mathcal{V})$ of a skeleton \mathcal{C} and a constitutive relation \mathcal{V} . The skeleton is itself an ordered pair of two oriented graphs with the same branch and node set differing at most with respect to their orientations. The constitutive relation is a binary relation, it is a subset of the universal signal set of the network. Its elements are denoted as signal pairs. Especially we make use here from the notions of constitutive and behavioral equations of a network, of matrix representations of the elements of its universal signal set, of the projections of its solution set defined by subsets of its branch set and

of the canonical representatives of its terminal behavior with respect to a prescribed terminal class family.

The constitutive relation of a network $(\mathcal{C}, \mathcal{V})$ is denoted as *voltage controlled* if it is a right-unique relation, i.e. a mapping which assigns to each element u of $\text{dom } \mathcal{V}$ a unique $i = \mathcal{V}(u)$. Similarly we refer to \mathcal{V} as *current controlled* if \mathcal{V} is a left-unique relation. Then \mathcal{V}^{-1} is a mapping which assigns to each element i of its domain a unique $u = \mathcal{V}^{-1}(i)$.

II. GENERALIZED CURRENT SOURCE SHIFT THEOREMS

In this section we consider a connected network $\mathcal{N} = (\mathcal{C}, \mathcal{V})$ with associated reference directions, with at least one loop, and without self-loops. We assume that \mathcal{N} consists of two complementary subnetworks \mathcal{N}^{vs} and \mathcal{N}^{vc} . The subnetwork \mathcal{N}^{vs} has the branch set \mathcal{Z}^{vs} and consists of independent voltage sources only, of course, without voltage-source loops. The subnetwork \mathcal{N}^{vc} has the branch set \mathcal{Z}^{vc} and a voltage controlled constitutive relation, e.g. it may consist of independent current sources or nonlinear capacitors. Branch and node set of \mathcal{N} are denoted by \mathcal{Z} and \mathcal{K} , resp. Clearly, it holds $\mathcal{Z} = \mathcal{Z}^{\text{vs}} \cup \mathcal{Z}^{\text{vc}}$.

Since \mathcal{N} does not include self-loops, each of its loops consists of at least two branches.

Because \mathcal{N} has associated reference directions there exists an oriented graph \mathcal{G} such that $\mathcal{C} = (\mathcal{G}, \mathcal{G})$.

Since \mathcal{N}^{vs} is loopless, there exists in \mathcal{G} a spanning tree \mathcal{G}_{tr} with a branch set \mathcal{Z}_{tr} consisting of all branches of \mathcal{Z}^{vs} and a minimal subset $\mathcal{Z}_{\text{tr}}^{\text{vc}} \subset \mathcal{Z}^{\text{vc}}$, i.e., $\mathcal{Z}_{\text{tr}} = \mathcal{Z}^{\text{vs}} \cup \mathcal{Z}_{\text{tr}}^{\text{vc}}$. Because \mathcal{N} includes at least one loop, the corresponding set $\mathcal{Z}_{\text{lk}} := \mathcal{Z}^{\text{vc}} \setminus \mathcal{Z}_{\text{tr}}^{\text{vc}}$ of links is nonvoid and consists merely of branches of \mathcal{Z}^{vc} .

A suitable numbering of the branches of \mathcal{N} presupposed the fundamental cutset matrix of \mathcal{N} defined by \mathcal{G}_{tr} can be partitioned as follows

$$S = \begin{pmatrix} E^{\text{vs}} & 0 & F^{\text{vs}} \\ 0 & E^{\text{vc}} & F^{\text{vc}} \end{pmatrix}, \quad (1)$$

where E^{vs} and E^{vc} are $|\mathcal{Z}^{\text{vs}}| \times |\mathcal{Z}^{\text{vs}}|$ or $|\mathcal{Z}_{\text{tr}}^{\text{vc}}| \times |\mathcal{Z}_{\text{tr}}^{\text{vc}}|$ unit matrices, resp.

Using numberings of the branch sets \mathcal{Z}^{vs} , \mathcal{Z}^{vc} , $\mathcal{Z}_{\text{tr}}^{\text{vc}}$, and $\mathcal{Z}_{\text{lk}}^{\text{vc}}$, preserving the arrangement of the corresponding branches introduced by the numbering of \mathcal{Z} to fix the matrix S in equation (1) we assign to each signal pair (u, i) of the universal signal set of \mathcal{N} matrix representations of the quantities u , $u_{\mathcal{Z}^{\text{vs}}}$, $u_{\mathcal{Z}^{\text{vc}}}$, $u_{\mathcal{Z}_{\text{tr}}^{\text{vc}}}$, $u_{\mathcal{Z}_{\text{lk}}^{\text{vc}}}$, and i , $i_{\mathcal{Z}^{\text{vs}}}$, $i_{\mathcal{Z}^{\text{vc}}}$, $i_{\mathcal{Z}_{\text{tr}}^{\text{vc}}}$, $i_{\mathcal{Z}_{\text{lk}}^{\text{vc}}}$. These matrix representations

are now in the same order denoted by u , u^{vs} , u^{vc} , $u_{\text{tr}}^{\text{vc}}$, $u_{\text{lk}}^{\text{vc}}$ and i , i^{vs} , i^{vc} , $i_{\text{tr}}^{\text{vc}}$, $i_{\text{lk}}^{\text{vc}}$, resp.

Because the subnetwork \mathcal{N}^{vs} consists of independent voltage sources only and the constitutive relation of its complementary subnetwork \mathcal{N}^{vc} is voltage controlled, there exists a column matrix u^{pv} and a column-matrix valued mapping G such that

$$u^{\text{vs}} = u^{\text{pv}}|_{\text{dom } u^{\text{vs}}} \quad \text{and} \quad i^{\text{vc}} = G(u^{\text{vc}}) \quad (2)$$

are constitutive equations of \mathcal{N}^{vs} or \mathcal{N}^{vc} , resp. The elements of u^{pv} are the prescribed voltages of \mathcal{N}^{vs} and $i^{\text{vc}} = G(u^{\text{vc}})$ is a representation of the constitutive relation of \mathcal{N}^{vc} in conductance form.

The restriction of u^{pv} to the domain of u^{vs} on the right hand side of (2) is necessary since in the general case the signal pairs $(u, i) \in \mathcal{V}$ have domains which are proper subintervals¹ of $\text{dom } u^{\text{pv}}$. But to simplify the notation we skip the appendix “ $|_{\text{dom } u^{\text{vs}}}$ ” in the following.

To determine the terminal behavior of \mathcal{N} with respect to \mathcal{K} we connect \mathcal{N} with a norator network $\tilde{\mathcal{N}}$ with skeleton $\tilde{\mathcal{C}} = (\tilde{\mathcal{G}}, -\tilde{\mathcal{G}})$ where $\tilde{\mathcal{G}}$ is a tree with node set $\tilde{\mathcal{K}} := \mathcal{K}$ and a branch set $\tilde{\mathcal{Z}}$ with $|\tilde{\mathcal{Z}}| = |\mathcal{Z}_{\text{tr}}|$ branches. The branches of this tree are connected parallel to that of \mathcal{G}_{tr} .

Let $\tilde{\mathcal{N}}$ denote this interconnection. For the analysis of $\tilde{\mathcal{N}}$ then an appropriate system of behavioral equations is set up. Elimination of the branch voltages and currents of its subnetwork \mathcal{N} results in a system of constitutive equations of a canonical representative of the terminal behavior of \mathcal{N} defined by the skeleton $(\tilde{\mathcal{G}}, \tilde{\mathcal{G}})$. After an exchange of variables we obtain the following theorem.

Theorem 2.1: *Let $\hat{\mathcal{N}} = (\hat{\mathcal{C}}, \hat{\mathcal{V}})$ denote that canonical representative of the terminal behavior of \mathcal{N} defined by the skeleton $\hat{\mathcal{C}} := (\mathcal{G}_{\text{tr}}, \mathcal{G}_{\text{tr}})$.*

Then the constitutive relation of $\hat{\mathcal{N}}$ can be represented with

$$S^{\text{vs}} := (0 \quad F^{\text{vs}}), \quad S^{\text{vc}} := (E^{\text{vc}} \quad F^{\text{vc}}), \quad (3)$$

by means of the system

$$u^{\text{vs}} = u^{\text{pv}}, \quad i^{\text{vc}} = S^{\text{vc}} G(S^{\text{vc}} u^{\text{vc}} + S^{\text{vs}} u^{\text{pv}}) \quad (4)$$

of constitutive equations in hybrid form.

As a canonical representative of the terminal behavior of \mathcal{N} the network $\hat{\mathcal{N}}$ does not include any loops.

¹Typical examples for such situations are networks with finite escape times, cf. e.g. [2], p. 442.

III. GENERALIZED VOLTAGE SOURCE SHIFT THEOREMS

In this section we consider a network $\mathcal{N} = (\mathcal{C}, \mathcal{V})$ with associated reference directions, branch set \mathcal{Z} , node set \mathcal{K} , and a current controlled constitutive relation, e.g. it may consist of independent voltage sources or nonlinear inductors. Because \mathcal{N} has associated reference directions, there exists an oriented graph \mathcal{G} such that $\mathcal{C} = (\mathcal{G}, \mathcal{G})$.

In difference to Section II we consider here the terminal behavior of \mathcal{N} with respect to a prescribed terminal class family $(\mathcal{K}_l)_{l \in L}$ which includes in the general case more than one terminal class. Especially we are here interested in that cutsets of the corresponding interconnections consisting only of branches of \mathcal{Z} and do not partition anyone of the terminal classes \mathcal{K}_l ($l \in L$). We assume that each such cutset consists of at least two branches. Also in difference to Section II our prior aim is here not the determination of some canonical representatives of the terminal behavior of \mathcal{N} but rather the determination of a network $\bar{\mathcal{N}}$ with the same skeleton and the same terminal behavior as the given network \mathcal{N} whereas additionally some branches of \mathcal{Z} are realized in $\bar{\mathcal{N}}$ by a short-circuit.

To determine the terminal behavior of \mathcal{N} , and later on that of $\bar{\mathcal{N}}$, with respect to $(\mathcal{K}_l)_{l \in L}$ we connect their terminal classes with a norator network $\tilde{\mathcal{N}}$ with skeleton $\tilde{\mathcal{C}} = (\tilde{\mathcal{G}}, -\tilde{\mathcal{G}})$ and branch set $\tilde{\mathcal{Z}}$. The graph $\tilde{\mathcal{G}}$ is a forest. The node set of each tree of this forest is equal to exactly one of the terminal classes \mathcal{K}_l ($l \in L$). The interconnection of \mathcal{N} with $\tilde{\mathcal{N}}$ may be denoted by $\bar{\mathcal{N}} = (\bar{\mathcal{C}}, \bar{\mathcal{V}})$. Let $\bar{\mathcal{G}}_v$ and $\bar{\mathcal{G}}_c$ denote its voltage and current graph and $\tilde{\mathcal{Z}}$ its branch set.

There exists a minimal subset $\mathcal{Z}_{fo} \subset \mathcal{Z}$ such that the subgraphs of the voltage and the current graph of $\bar{\mathcal{N}}$ generated by $\tilde{\mathcal{Z}}_{fo} := \tilde{\mathcal{Z}} \cup \mathcal{Z}_{fo}$ are spanning forests of these graphs. Let $\mathcal{Z}_{lk} := \mathcal{Z} \setminus \mathcal{Z}_{fo}$ denote the corresponding set of links. Using an appropriate numbering of the branches of $\bar{\mathcal{N}}$ there exist a $|\mathcal{Z}_{lk}| \times |\tilde{\mathcal{Z}}|$ matrix \tilde{F} , a $|\mathcal{Z}_{lk}| \times |\mathcal{Z}_{fo}|$ matrix F , and a $|\mathcal{Z}_{lk}| \times |\mathcal{Z}_{lk}|$ unit matrix E such that the matrices

$$\bar{M}_v = (-\tilde{F} \quad F \quad E) \quad , \quad \bar{M}_c = (\tilde{F} \quad F \quad E) \quad (5)$$

are the fundamental loop matrices of the voltage and current graph of $\bar{\mathcal{N}}$, resp., defined by these spanning forests.

The branches of \mathcal{Z}_{fo} are that branches realized in $\bar{\mathcal{N}}$ by short-circuits.

By means of the same numbering of the branches of $\tilde{\mathcal{Z}}$ used for the determination of the matrices \bar{M}_v and

\bar{M}_c we assign to each signal pair (\bar{u}, \bar{i}) of the universal signal set of $\bar{\mathcal{N}}$ a matrix representation. For simplicity this matrix representation is denoted again by (\bar{u}, \bar{i}) .

Using numberings preserving the arrangements of the branches of the subsets $\mathcal{Z}, \tilde{\mathcal{Z}}, \mathcal{Z}_{fo}, \mathcal{Z}_{lk} \subset \tilde{\mathcal{Z}}$ defined by the numbering of the branches of $\tilde{\mathcal{Z}}$ we assign to $\bar{u}_{\mathcal{Z}}, \bar{u}_{\tilde{\mathcal{Z}}}, \bar{u}_{\mathcal{Z}_{fo}}, \bar{u}_{\mathcal{Z}_{lk}}$ and to $\bar{i}_{\mathcal{Z}}, \bar{i}_{\tilde{\mathcal{Z}}}, \bar{i}_{\mathcal{Z}_{fo}}, \bar{i}_{\mathcal{Z}_{lk}}$ the corresponding matrix representations. These matrix representations are denoted in the same order by $u, \tilde{u}, u_{fo}, u_{lk}$ and $i, \tilde{i}, i_{fo}, i_{lk}$.

Because the constitutive relation of \mathcal{N} current controlled, there exists a column-matrix valued mapping R such that the constitutive relation of \mathcal{N} can be represented by the following constitutive equation

$$u = R(i) \quad (6)$$

in resistance form.

For the representation of the constitutive relation of $\bar{\mathcal{N}}$ by means of a system of constitutive equations we introduce the ansatz

$$u_{fo} = 0, \quad u_{lk} = MR({}^t R i_{lk}). \quad (7)$$

Let $\hat{\mathcal{N}} = (\hat{\mathcal{C}}, \hat{\mathcal{V}})$ and $\check{\mathcal{N}} = (\check{\mathcal{C}}, \check{\mathcal{V}})$ denote the canonical representatives of the terminal behavior of \mathcal{N} or $\bar{\mathcal{N}}$, resp., defined by the skeleton $\hat{\mathcal{C}} := \check{\mathcal{C}} := (\tilde{\mathcal{G}}, \tilde{\mathcal{G}})$.

The proof that the networks \mathcal{N} and $\bar{\mathcal{N}}$ have the same terminal behavior with respect to $(\mathcal{K}_l)_{l \in L}$ is a little bit more involved than that of the proof of Theorem 2.1 in Section II. This is owed the fact that it is now in the general case impossible to derive for the canonical representatives of these networks constitutive equations in closed form. Nevertheless it can be shown, for details see [16], that the canonical representatives $\hat{\mathcal{N}}$ and $\check{\mathcal{N}}$ are identical. Their skeletons are identical by definition. Their constitutive relations are both equal to the set of all pairs (\tilde{u}, \tilde{i}) fulfilling for some value of the variable i_{lk} the equations

$$\tilde{F} \tilde{u} = M R({}^t M i_{lk}), \quad (8)$$

$$\tilde{i} = {}^t \tilde{F} i_{lk}. \quad (9)$$

What implies, they are identical, too.

In that manner it is possible to obtain a proof for the following theorem.

Theorem 3.1: *The networks \mathcal{N} and $\bar{\mathcal{N}}$ have the same terminal behavior with respect to the terminal class family $(\mathcal{K}_l)_{l \in L}$.*

In the terminology introduced in [11] the system of equations (8) and (9) is an example for the representation of a constitutive relation by means of a constitutive

equation with a latent variable. The idea to represent the constitutive relation of the network $\tilde{\mathcal{N}}$ in that manner goes back to the author's former collaborator T. Nähring [10]. It is essential for the proof of Theorem 3.1.

If the branch set $\tilde{\mathcal{Z}}$ of the interconnection of \mathcal{N} with the norator network $\tilde{\mathcal{N}}$ includes a spanning coforest, then the rank of the submatrix \tilde{F} of the matrices \tilde{M}_v and \tilde{M}_c is equal to $|\mathcal{Z}_{lk}|$. Under this assumption it is without additional assumptions on the properties of the column-matrix valued mapping R possible to eliminate the latent variable i_{lk} included in equation (8). This elimination results in a constitutive equation for $\tilde{\mathcal{N}}$ in hybrid form, cf. [16].

In [16] a generalization of Theorem 3.1 is proved wherein for \mathcal{N} networks are admitted which include additionally subnetworks consisting of independent current sources.

IV. CONCLUDING REMARKS

We have presented generalizations of the Source Shift Theorems. Our proofs are based on a theory of terminal behavior of networks developed in [12], [13]. The interconnection of the networks under consideration with trees or forests of norators are substantial parts of these proofs. Other applications of this method are to find in [13], [14], [15], [18]. By the way, these results show that norators (and nullators, too) are by no means "pathological" objects in network theory since their introduction simplifies and unifies the representation of network theory and delivers even starting points for developing important analysis methods.

The most essential applications of the Theorems 2.1 and 3.1 are their use for the reduction of the index of differential-algebraic equations [19] for the analysis of RLCM networks by the elimination of voltage source-capacitor loops and current source-inductor cutsets.

If \mathcal{N} is a capacitor network with n nodes whose voltage graph is a complete graph with $(n+1) \times n/2$ branches, then by Theorem 2.1 it is possible to replace this network by a canonical representative $\tilde{\mathcal{N}}$ consisting of n coupled capacitors whose voltage graph is a star-like tree. This transformation is the inverse of a classical transformation [9], [8] which assigns a network to the matrix of capacitance coefficients describing a physical multi-electrode capacitor, where this network consists of uncoupled capacitors, known as MAXWELL's partial capacitors, arranged on a complete graph. From the point of view of the theory of differential-algebraic equations as well as the theory of state-space equations it follows that for modeling of a physical multi-electrode capacitor

there are generally network models based on a tree of coupled capacitors to prefer over that based on a complete graph of uncoupled capacitors.

The proof of Theorems 3.1 is not a dualization of the proof of Theorem 2.1, resp. It seems to be of interest whether in the theory of graphoidale networks [17] such a dualization is possible. However for this purpose it would be first necessary to develop for this class of generalized networks a theory of multiport behavior as a counterpart to the theory of terminal behavior considered in [12], [13].

REFERENCES

- [1] T.H. BLAKESLEY, A New Electrical Theorem. Proc. Phys. Soc. London, 13(1894), pp. 65 - 67
- [2] L.O. CHUA, P.M. LIN, Computer-Aided Analysis of Electronic Circuits – Algorithms and Computational Techniques, Prentice-Hall, Englewood Cliffs, 1975
- [3] L.O. CHUA, CH.A. DESOER, E.S. KUH, Linear and Nonlinear Circuits, McGraw-Hill, New York, 1987
- [4] L.O. CHUA, D.N. GREEN, Graph-Theoretic Properties of Dynamic Nonlinear Networks. IEEE Trans. Circuits and Systems, 23(1976), pp. 292-312
- [5] CH.A. DESOER, E.S. KUH, Basic Circuit Theory, McGraw-Hill, New York 1969;
- [6] J. HAASE, On generalizations and Applications of the Substitution Theorem. Proc. ECCTD 85, pp. 220-223, Prague 1985
- [7] E. HAIRER, G. WANNER, Solving Ordinary Differential Equations II, Stiff and Differential-Algebraic Problems, 2nd rev. ed., Springer, Berlin 1996
- [8] P. LEUCHTMANN, Einführung in die elektromagnetische Feldtheorie, Pearson Studium, München, 2005
- [9] K. MEETZ, W.L. ENGL, Elektromagnetische Felder, Springer, Berlin, 1980
- [10] T. NÄHRING, Private Communication.
- [11] J.W. POLDERMAN, J.C. WILLEMS, Introduction to Mathematical Systems Theory – A Behavioral Approach, Springer, 1998
- [12] A. REIBIGER, On the Terminal Behaviour of Networks, Proc. ECCTD'85, pp. 224-227, Prague 1985
- [13] A. REIBIGER, Über das Klemmenverhalten von Netzwerken, Wiss. Z. TU Dresden, Vol. 35(1986), pp. 165-173
- [14] A. REIBIGER, Geometrical Proof of the Thévenin-Norton Theorem, Proc. ECCTD'97, Vol. 1, pp. 24-28, Budapest, 1997
- [15] A. REIBIGER, Auxiliary branch method and modified nodal voltage equations, Advances in Radio Sciences, Vol. 6, pp. 157, 2008 (available on: www.adv-radio-sc.net/6/157/2008/)
- [16] A. REIBIGER, Generalizations of Blakesley's Voltage Source Shift Theorem (in preparation)
- [17] A. REIBIGER, H. LOOSE, Bond Graphs and Matroids, Mathematics and Computers in Simulation, 53(2000), pp. 323-332, (cf. also Proc. 3rd MATHMOD, Vienna, 2000)
- [18] A. REIBIGER, W. MATHIS, T. NÄHRING, L.J. TRAJKOVIĆ, Mathematical Foundations of the TC-Method for Computing Multiple DC-Operating Points, Int. Journal of Applied Electromagnetics and Mechanics, Vol. 17, 2003, pp. 169-191
- [19] S. REICH, Differential-Algebraic Equations and Applications in Circuit Theory, AEÜ 46(1992), pp. 298-304

Regular Papers



The Barkhausen Criterion (Observation ?)

Erik Lindberg, IEEE Life member
Faculty of Electrical Eng. & Electronics,
348 Technical University of Denmark,
DK-2800 Kongens Lyngby, Denmark
Email: el@elektro.dtu.dk

Abstract—A discussion of the Barkhausen Criterion which is a necessary but NOT sufficient criterion for steady state oscillations of an electronic circuit. An attempt to classify oscillators based on the topology of the circuit. Investigation of the steady state behavior by means of the time-varying linear approach ("frozen eigenvalues").

I. INTRODUCTION

Oscillators occur all over in nature and in man-made systems. Their behavior is characterized by size (amplitude) and period (frequency). They are controlled by the basic principle of nature which says that a system always try to go to a minimum energy state. We observe oscillators varying in size from $1e^{+31}$ for the galaxies in space to $1e^{-31}$ for the super-strings proposed in physics. Steady state oscillations may be limit cycle oscillations or chaotic oscillations.

Autonomous oscillators are non-linear oscillating systems which are only influenced by a constant energy source. When two oscillating systems are coupled they try to synchronize in order to obtain the minimum energy state.

Electronic oscillators are man-made non-linear circuits which show steady state oscillating behavior when powered only by dc power supplies. The behavior may be limit cycle behavior or chaotic behavior. The order of the circuit is the number of independent memory elements (capacitive, inductive or hysteric).

For many years we have seen that some basic circuit theory textbooks introduce the **Barkhausen Criterion** as the *necessary and sufficient criterion* for an electronic circuit to be an oscillator. Also the concept of *linear steady state oscillators* is introduced. The aim of this discussion is to point out that steady state oscillators must be non-linear circuits and linear oscillators are mathematical fictions.

In some textbooks you may also find statements like: "*an oscillator is an unstable amplifier for which the nonlinearities are bringing back the initial poles in the right*

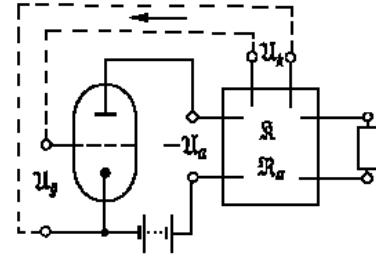


Bild 1. Allgemeines Schema einer Rückkopplung

- (1) $u_a = -\mathfrak{B} u_i$; $\mathfrak{B} = -\frac{u_a}{u_i}$ „Verstärkungsfaktor“
- (2) $\mathfrak{R} = -\frac{u_k}{u_a}$ „Rückkopplungsfaktor“
- (3) $\mathfrak{R} = \frac{1}{\mathfrak{B}}$ oder $\mathfrak{R}\mathfrak{B} = 1$
(Allgemeine Selbsterregungsformel.)

Fig. 1. Barkhausen's original observation

half plane of the complex frequency plane, RHP, to the imaginary axis". This statement is not true [1]. When you solve the implicit non-linear differential equations modeling an electronic circuit the kernel of the numerical method is the solution of a linear circuit. By means of Taylor evaluation the nonlinear components are replaced with linear approximations and iteration is performed until a solution is obtained. The iteration is based on Picard (static) or Newton-Raphson (dynamic) methods. In each integration step a small-signal model is found for the circuit corresponding to a linearization of the Jacobian of the differential equations.

Non-linear circuits may be treated as time-varying linear circuits so it make sense to study the eigenvalues as function of time in order to better understand the mechanisms behind the behavior of an oscillator.

II. BARKHAUSEN'S OBSERVATION

In 1934 H. Barkhausen (1881-1956) [2] pointed out that an oscillator may be described as an inverting ampli-

fier (a vacuum tube) with a linear frequency determining feedback circuit (fig. 1). The non-linear amplifier is a two-port with a static gain-factor equal to the ratio between the signals at the ports. The linear feedback circuit is a two-port with a feed-back-factor equal to the ratio between the port signals. It is obvious that the product of the two factors becomes equal to one. The product is called the Barkhausen Criterion or the *Allgemeine Selbsterregungsformel* in German language.

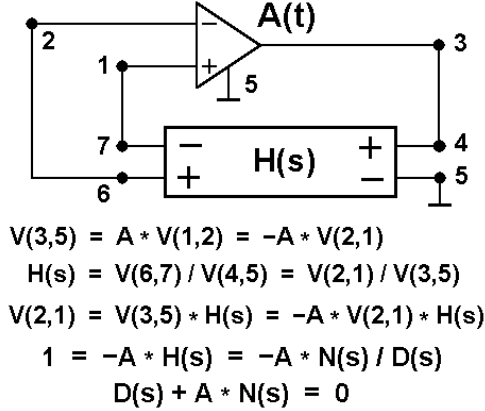


Fig. 2. Barkhausen's Criterion. Characteristic polynomial

Barkhausens figure may be redrawn as shown in fig. 2 where the non-linear amplifier is assumed to be a perfect amplifier with infinite input impedance, zero output impedance and *linear time-varying gain A*. The feedback circuit is assumed to be a linear, lumped element, time-invariant passive two-port with a rational transfer function $H(s)$. It is obvious that the closed-loop gain is always equal to one (1) and the phase-shift is equal to a multiple of 360° (2π). Furthermore it is seen that the Barkhausen Criterion is just an expression for the characteristic polynomial of the circuit as function of the amplifier gain. For zero gain the characteristic polynomial becomes equal to the denominator of $H(s)$. For infinite gain the characteristic polynomial becomes equal to the numerator of $H(s)$.

You may open the loop and study another circuit closely related to the oscillator circuit. This circuit has a time independent bias-point. You may perform the normal linear small-signal analysis (ac analysis) and study the natural frequencies (poles, eigenvalues). You may design the open-loop gain to be one ($1 \angle 360^\circ$) and you may also make the closed-loop circuit unstable with poles in the right half of the frequency plane, RHP, in the hope that the circuit will start to oscillate. However when you close the loop the bias-point of the amplifier will change and you have no guarantee that oscillations start

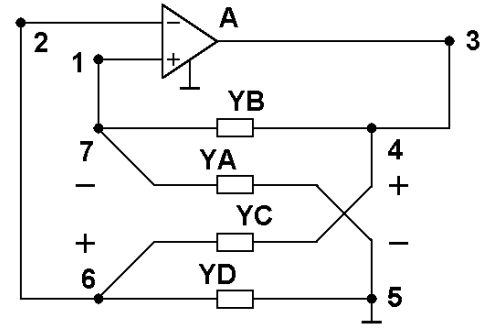


Fig. 3. Proper Barkhausen topology with $H(s)$ as a modified full graph admittance circuit

up. The conclusion is that *you must base your design on the characteristic polynomial of the closed-loop circuit*.

Figure 3 shows a realization of the closed-loop circuit where the feed-back circuit is represented with a modified full graph admittance circuit. The admittance Y_E between node 6 and node 7 is deleted and the admittance Y_F between node 4 and node 5 is deleted.

The characteristic polynomial with a full graph feedback admittance circuit may be found from

$$\begin{aligned} & Y_E \times (Y_A + Y_D + Y_C + Y_B) + \\ & (Y_A + Y_B) \times (Y_D + Y_C) + \\ & A \times (Y_A \times Y_C - Y_B \times Y_D) = 0 \end{aligned} \quad (1)$$

where the admittances are functions of the complex frequency s . The admittance Y_F does not occur because it is in parallel with the output voltage source of the amplifier.

The amplifier is a voltage controlled voltage source (VCVS) and the output signal is returned to the input by positive (Y_A , Y_B) and negative (Y_C , Y_D) voltage division. This structure has been used to investigate various oscillator families [3], [4], [5].

When you study the poles (eigenvalues) of the linearized Jacobian of the non-linear differential equations you may observe that they move around in the complex frequency plane as function of time. The signals are increasing when the poles are in RHP (the right half plane). The signals are decreasing when the poles are in LHP (the left half plane). You may observe how a complex pole pair in RHP goes to the real axis and splits-up into two real poles of which one goes towards zero and the other towards infinity. The two real poles meet again in LHP and leave the real axis as a complex pole pair [6].

The basic mechanism behind the behavior of the oscillator is a balance of the energy received from the power source when the poles are in RHP with the energy lost when the poles are in the LHP. The real part of the poles may go between $+\infty$ and $-\infty$. At a certain instant the frequency is determined by the imaginary part of the complex pole pair. The phase noise observed corresponds to the part of the period where the instantaneous frequency deviates from the dominant frequency, the oscillator frequency [7].

III. CLASSIFICATION OF OSCILLATORS

So far classification of oscillators is not found in the basic electronics textbooks in a proper way. You may classify with respect to *waveform* as relaxation, sinusoidal, multi-frequency or chaotic. You may classify with respect to *application* as e.g. used to synchronize systems (clock of computers), used to communication (carrier of waveforms, audio) or used to test of systems (instrumentation). You may classify with respect to *implementation* as e.g. voltage controlled (VCO), integrated or lumped element. However a given oscillator may fall into several of these classes. Classification based on structure (topology) seems to be the only proper way, see e.g. [8] where oscillators are classified according to number of memory elements.

Based on the topology of the circuit oscillators may be classified as belonging to one of the following classes.

Class I: Proper Barkhausen Topology.

Proper Barkhausen topology is a loop of an amplitude determining inverting *non-linear* amplifier and a passive frequency determining *linear* feed-back circuit.

The two circuits in the loop are 4-terminal or 3-terminal two-ports (fig. 1 and fig. 2). The bias point of the amplifier vary with time.

It is obvious that the power source limits the amplitude of the oscillator. The following question should be discussed: Can you separate the design of the non-linearity from the design of the gain and the linear frequency determining sub-circuit when designing an oscillator ?

Class II: Modified Barkhausen Topology.

Modified Barkhausen topology is a loop of an inverting *linear* amplifier and a passive amplitude and frequency determining two-port *non-linear* feed-back circuit.

From mathematical point of view a linear amplifier with constant gain is easy to implement for analysis and design purposes but a number of questions should be discussed. Is it possible to create a linear real world amplifier which does not influence frequency and amplitude

? Is the dc bias point of the amplifier time-invariant ? What kind of passive non-linearity should be introduced in the feed-back circuit ?

Class III: A topology different from I and II, i.e. *non-linear* amplifier and *non-linear* feed-back circuit.

An example of a circuit belonging to this class is the classic multi-vibrator with two capacitors and two cross-coupled transistors (3-terminal amplifiers) [4].

In [7] an oscillator based on the differential equations which have sine and cosine as solutions is investigated. The oscillator is based on a loop of two active RC integrators and an inverter. By choosing different time constants for the two RC integrators phase noise in the output of one of the amplifiers could be minimized.

IV. AN EXAMPLE TO BE DISCUSSED - WIEN BRIDGE OSCILLATOR

Figure 4 shows a Wien Bridge oscillator with proper Barkhausen topology (Class I) in the case where resistor R_{CL} is ∞ . The circuit is investigated in [9] where the operational amplifier is assumed a perfect linear amplifier with gain $A = 100k$. The components cor-

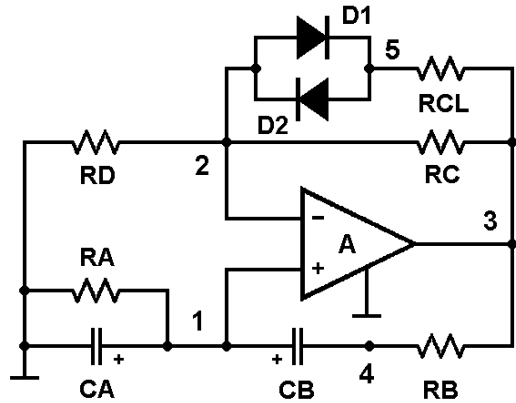


Fig. 4. Wien Bridge Oscillator

responding to a complex pole pair on the imaginary axis are: $C_A = C_B = C = 10nF$, $R_A = R_B = R = 20k\Omega$, $R_D = 3k\Omega$ and $R_C = 6k\Omega$. The frequency becomes 795.8 Hz and $\omega_0 = 5k$ rad/sec. The poles of the linear Wien Bridge oscillator are found as function of resistor R_C . If R_C is amended with a large resistor R_{CL} in series with a non-linear element made from two diodes in antiparallel as shown in fig. 4 you have a mechanism for controlling the movement of the poles between RHP and LHP so you can avoid making use of the non-linear gain. The circuit becomes a Class II oscillator with modified Barkhausen topology. For $R_C = 7k\Omega$ ($> 6k\Omega$), $D_1 = D_2 = D1N4148$ and three values of

R_{CL} : $R_{CL} = \infty$, $R_{CL} = 38k\Omega$ and $R_{CL} = 17.5k\Omega$ it is demonstrated that you may control both frequency and amplitude of the oscillator. When you change the perfect linear $A = 100k$ amplifier to an AD712 operational amplifier with a dominant pole at 12Hz and a high-frequency pole at 15MHz the non-linear control in the feed-back circuit is overruled by the non-linearities of the amplifier and the circuit becomes a Class III oscillator.

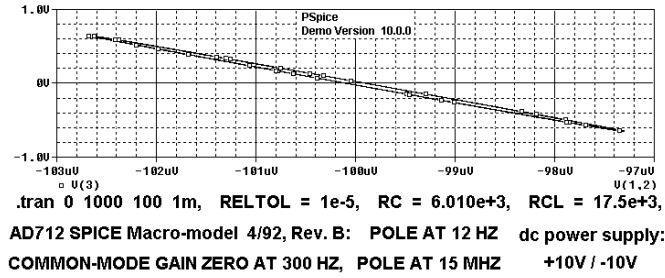


Fig. 5. Dynamic transfer characteristic of the amplifier with almost constant bias point

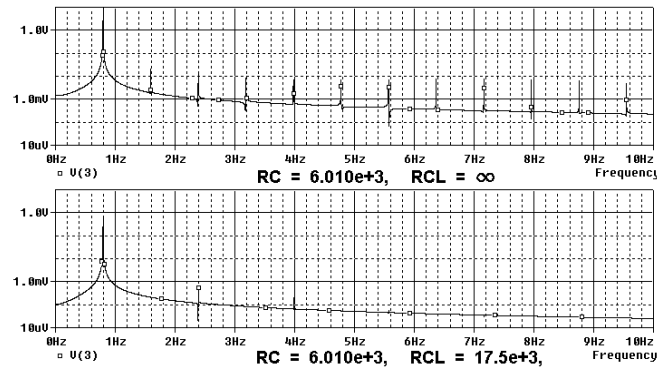


Fig. 6. Frequency spectrum of amplifier output

The circuit is now scaled to low frequencies by means of new capacitor values $C_A = C_B = C = 10\mu F$ and a new value $R_C = 6.010k\Omega$ ($> 6k\Omega$). Figure 5 shows that it is possible to adjust the circuit into a Class II oscillator with an almost linear amplifier. In order to start-up oscillations the initial conditions for the capacitors were chosen as $V(C_A) = -0.17406342924$ V and $V(C_B) = +0.044747527689$ V i.e. values close to an instant time of the steady state. Figure 6 shows how the harmonics are reduced. Figure 7 shows the dynamic and the static gain as functions of time. It is seen how the dynamic gain is almost constant in a large part of the period.

V. CONCLUSION

It is demonstrated that the Barkhausen Criterion is a necessary but not sufficient criterion for steady state

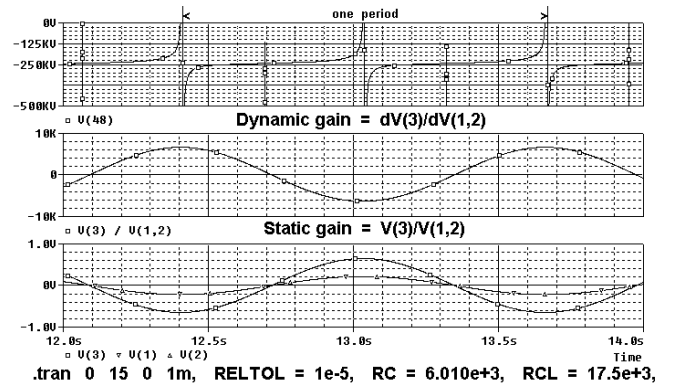


Fig. 7. Dynamic and static gain

oscillations of an electronic circuit. Barkhausen did not "open the loop" ! Oscillators may be classified into three groups based on the Barkhausen Observation. A Wien bridge oscillator with an almost linear inverting amplifier and a nonlinear passive amplitude and frequency determining feed-back circuit is investigated by means of the time-varying linear approach ("frozen eigenvalues").

REFERENCES

- [1] E. Lindberg, "Is the quadrature oscillator a multivibrator ?", IEEE Circuits & Devices Magazine, November/December 2004, Vol.20, Issue.6, Page no. 23–28, 2004.
- [2] H. Barkhausen, Lehrbuch der Elektronen-Röhren, 3. Band., "Rückkopplung", Verlag S. Hirzel, 1935, Achte Auflage, pp. 4–5, 1960.
- [3] E. Lindberg, "The Wien bridge oscillator family", In *Proc. IC-SES06* - International Conference on Signals and Electronic Systems, Technical University of Lodz, September 17-20, vol.1, pp. 189-192, 2006.
- [4] E. Lindberg, K. Murali and A. Tamasevicius, "The Common Multi-Vibrator Family", In *Proc. NDES'07* - The 15th IEEE International Workshop on Non-linear Dynamics of Electronic Systems, Tokushima, Japan, July 23-26, pp.180-183, 2007.
- [5] E. Lindberg, K. Murali and A. Tamasevicius, "The Colpitts Oscillator Family", In *Proc. NDES'08* - NWP-2008, International Symposium: Topical Problems of Non-linear Wave Physics, Nizhny Novgorod, July 20-26, NWP-1: Non-linear Dynamics of Electronic Systems, pp. 47-48, 2008.
- [6] L. Strauss, Wave Generation and Shaping, pp. 1-520, McGraw-Hill, 1960.
- [7] E. Lindberg, K. Murali, A. Tamasevicius and L. von Wangenheim, "An eigenvalue study of a double integrator oscillator", In *Proc. ECCTD'09* - European Conference on Circuit Theory and Design, pp.217-220, 2009.
- [8] J.R. Westra, C.J.M. Verhoeven and A.H.M. van Roermund, Oscillators and Oscillator Systems - Classification, Analysis and Synthesis, pp. 1-282, Kluwer 1999.
- [9] E. Lindberg, "Oscillators - an approach for a better understanding", Invited tutorial in *Proc. ECCTD'03* - European Conference on Circuit Theory and Design 2003, Cracow, Poland, September 1-4, 2003. <http://ecctd03.zet.agh.edu.pl/> erik.lindberg@ieee.org

Asymptotic and Numerical Analysis of Equation with Large Delay

Ilya S. Kashchenko
Faculty of Mathematic,
Yaroslavl State University,
Yaroslavl, Russia
Email: iliyask@uniyar.ac.ru

Abstract—The local dynamics of a differential equation with large delay is analyzed using the normal forms technique. It is shown that, in the critical cases, families of parabolic equations play the role of infinite-dimensional normal forms. It is demonstrated analytically and numerically that even a very simple first-order delay equation can have a complicated dynamical behavior. Methods for constructing classes of stable modes for such equations are described.

I. INTRODUCTION

Differential equations with delay are mathematical models for many applied problems [1, 2]. Among them, an important role is played by systems in which time delay is relatively large. Equations with delay are characterized by the presence of many specific effects and phenomena, which are caused by the infinite-dimensionality of the phase space. Importantly, problems concerning the local (i.e., observed in a small neighborhood of a stationary point) dynamics of singularly perturbed systems with delay may be complicated and specific. In this paper, we develop the method for studying local dynamics in a neighborhood of an equilibrium state suggested in [3 - 6].

II. ASYMPTOTIC ANALYSIS

We study the behavior in a neighborhood of the zero equilibrium state of the solutions to the differential-difference equation

$$\varepsilon \frac{dx}{dt} + x = F(x(t - T))$$

under the assumption that the delay time is sufficiently large, i.e., $T \gg 1$. The change of time $t \rightarrow Tt$ in the initial equation yields the equation

$$\varepsilon \frac{dx}{dt} + x = F(x(t - 1)). \quad (1)$$

(where $\varepsilon = T^{-1} \ll 1$).

We assume that, in a neighborhood of zero, the function $F(x)$ is smooth enough to be represented in the form

$$F(x) = ax + f_2x^2 + f_3x^3 + \dots \quad (2)$$

We study the behavior of all solutions of Eq. (1) at all $t \geq 0$ in a sufficiently small (but not depending on ε) neighborhood of the zero equilibrium state.

The local dynamics of Eq. (1) is largely determined by the linearized (at the zero equilibrium state) equation

$$\varepsilon \frac{dx}{dt} + x = ax(t - 1), \quad (3)$$

and the behavior of solutions to Eq. (3), in turn, depends on the location of the roots of the characteristic quasipolynomial

$$\varepsilon\lambda + 1 = ae^{-\lambda}. \quad (4)$$

For $|a| < 1$, the real parts of all roots of (4) are negative, and for $|a| > 1$, they are positive. Thus, the behavior of the solutions to Eq. (1) needs additional considerations only when the parameter a is close to 1 in absolute value. In this case, the characteristic quasipolynomial (4) has a root $\lambda(\varepsilon)$ such that $\operatorname{Re} \lambda(x) \rightarrow 0$ (as $\varepsilon \rightarrow 0$), and it has no roots in the right complex half-plane bounded away from the imaginary axis for all sufficiently small ε .

The case of a close to 1 is less interesting. We dwell on the situation in which a is close to -1 . Let

$$a = -1 - \mu a_1, \quad 0 < \mu \ll 1. \quad (5)$$

Then, obviously, the quasipolynomial (4) has infinitely many roots of the form

$$\lambda_k(\varepsilon) = \pi(2k - 1)(1 - \varepsilon + \varepsilon^2)i + \mu a_1 - \frac{1}{2}\varepsilon^2\pi^2(2k - 1)^2 + o(\varepsilon^2 + \mu), \quad k \in \mathbb{Z}. \quad (6)$$

Formula (6) gives an asymptotic representation for roots continuously depending on the small parameter. Removing the continuity requirement, we can write roots (4) as follows.

Take an arbitrary number $0 < \gamma < 1$ and positive number ω . Let $\theta(\omega, \varepsilon)$ denote a number from the half-open interval $[0, 2\pi)$ for which $\omega\varepsilon^{-\gamma} + \theta(\omega, \varepsilon)$ is an odd integer multiple of π . Then, formula (7) gives the following asymptotic dependence on ε of the roots with real parts tending to zero:

$$\lambda_k(\omega, \varepsilon) = \frac{\omega(2k+1)}{\varepsilon^\gamma}i + \theta(2k+1)i - \varepsilon^{1-\gamma}\omega(2k+1)i + o(\varepsilon^{1-\gamma} + \mu)i - \varepsilon^{2-2\gamma}\frac{\omega^2(2k+1)^2}{2} + \mu a_1 + o(\varepsilon^{2-2\gamma} + \mu). \quad (7)$$

Note that, although formula (7) depends on the continuous parameters ω , Eq. (4) has only countably many roots. As $\varepsilon \rightarrow 0$, the solution “skips” from one root to another because of the function θ . Thus, the absolute value of each λ_k increases unboundedly as $\varepsilon \rightarrow 0$. The choice of ω affects only the rate of skipping between roots.

Consider the dynamics of (1). First, suppose that $\mu = \varepsilon^2$, i.e.,

$$a = -1 - \varepsilon^2 a_1.$$

It was shown in [3] that, in this case, the local dynamics of Eq. (1) essentially determines the behavior of the solutions of the parabolic-type boundary value problem

$$\frac{\partial u}{\partial \tau} = \frac{1}{2} \frac{\partial^2 u}{\partial r^2} + a_1 u + (f_2^2 - f_3)u^3 \quad (8)$$

with antiperiodic boundary conditions

$$u(\tau, r) = -u(\tau, r+1). \quad (9)$$

Theorem 1. *If the boundary value problem (8), (9) has a bounded solution $u_*(\tau, r)$, then, for sufficiently small ε , Eq. (1) has the following solution asymptotic in discrepancy on the ray $t \geq 0$:*

$$x_*(t, \varepsilon) = \varepsilon u_*(\varepsilon^2 t, (1 - \varepsilon + \varepsilon^2)t) + o(\varepsilon).$$

Note that this assertion does not answer the question of whether Eq. (1) has an exact solution with above asymptotics. It only implies that if u_* is unstable, then the exact solution (if it exists) is surely unstable. Thus, it suffices to consider only stable solutions of (8), (9). Moreover, if u_* has a certain form, then (1) does have an exact solution of the corresponding form.

Theorem 2. *If problem (8), (9) has a solution $u_*(\tau, r)$ periodic in τ and only one multiplier of the problem*

linearized at u_ has absolute value 1, then, for small ε , Eq. (1) has the periodic solution*

$$x_*(t, \varepsilon) = \varepsilon u_*(\varepsilon^2(1 + o(1))t, (1 - \varepsilon + \varepsilon^2 + o(\varepsilon^2))t) + o(\varepsilon)$$

with the same stability properties.

The case where $\mu = o(\varepsilon^2)$ in (5) is trivial. A more complicated situation arises when $\mu = \varepsilon^p$ for $0 < p < 2$. Thus, we assume that

$$a = -1 - \varepsilon^p a_1, \quad 0 < p < 2. \quad (10)$$

We proceed to study the dynamics of (1). We set $\gamma = 1 - \frac{p}{2}$. As in [5, 6], we substitute the series

$$x(t, \varepsilon) = \varepsilon^{p/2} u(\tau, t_1) + \varepsilon^p x_2(t_1, \tau) + \varepsilon^{3p/2} x_3(t_1, \tau) + \dots, \quad (11)$$

into (1), where $\tau = \varepsilon^p t$, $t_1 = (\omega\varepsilon^{-\gamma} + \theta(\omega, \varepsilon) - \varepsilon^{1-\gamma}\omega + o(1))t$. The functions $x_2(t_1, \tau)$ and $x_3(t_1, \tau)$ are assumed to be π -periodic in the first argument. The dots denote terms of higher order of smallness in ε .

Let us collect together the coefficients of equal powers of ε . The equality of the coefficients of $\varepsilon^{3p/2}$ implies that the u must satisfy parabolic equation

$$\frac{\partial u}{\partial \tau} = \frac{1}{2} \frac{\partial^2 u}{\partial r^2} + a_1 u + (f_2^2 - f_3)u^3 \quad (12)$$

with boundary conditions

$$u(\tau, r) = -u(\tau, r + \frac{\pi}{\omega}). \quad (13)$$

For various ω we obtain various boundary value problems, each of which describes local dynamics in some part of a neighborhood of the zero solution to Eq. (1). Thus, as a normal form, we obtain the family of boundary value problems (12), (13), which depends on the continuous parameters ω . Generally, the dynamics of the problem depends on the parameter value.

Theorem 3. *Suppose that, given a positive value of ω , the boundary value problem (12), (13) has a bounded solution $u_*(\tau, r)$ defined for all $\tau \geq 0$.*

Then, the initial equation (1) has a solution asymptotic in discrepancy on the ray $t \geq 0$ of the form

$$x_*(t, \varepsilon) = \varepsilon^{p/2} u_*(\varepsilon^p t + o(\varepsilon^p), t_1) + o(\varepsilon^{p/2}).$$

An analogue of Theorem 2 is valid too.

Theorem 4. *Suppose that, for some $\omega > 0$, the boundary value problem (12), (8) has a solution $u_*(\tau, r)$ periodic in τ and only one multiplier of the problem linearized at u_* has absolute value 1.*

Then, the initial equation (1) has a periodic solution of the form

$$x_*(t, \varepsilon) = \varepsilon^{p/2} u_* \left(\varepsilon^p (1 + o(1)) t, \left(\frac{\omega}{\varepsilon^{1-p/2}} + \theta + o(1) \right) t \right) + o(\varepsilon^{p/2})$$

with the same stability properties.

Note that the solution x_* mentioned in Theorem 4 is a high-frequency oscillatory mode.

III. NUMERICAL ANALYSIS

It should be mentioned that, in a numerical analysis of the equations, the parameters p and a_1 may be determined not uniquely, which gives evidence for the abundance of dynamical modes of Eq. (1).

Let us use the results obtained above to analytically and numerically analyze concrete systems with fixed numerical parameters. Consider the equation

$$\frac{dx}{dt} + x = -(1 + \mu)x(t - T) + f_3 x^3(t - T).$$

The change of variables $t \rightarrow tT$ yields

$$\varepsilon \frac{dx}{dt} + x = -(1 + \mu)x(t - 1) + f_3 x^3(t - 1), \quad (14)$$

where $\varepsilon = T^{-1}$. Take $\varepsilon = 10^{-3}$, $\mu = 10^{-3}$ (we assume that these values are “sufficiently small”) and $f_3 = -1$.

Represent μ as $\mu = \varepsilon^p a_1$. Hence, the parameter p can be written as $p = 1 - \log_\varepsilon a_1$. We are interested in the values of a_1 that are neither too large nor too small relative to ε . For example, we may assume that a_1 belongs to the interval $(0.1, 10)$. So, p is in interval $0 < p < 2$.

For each $a_1 \in (0.1, 10)$, consider the normal form treating $\omega > 0$ as an arbitrary parameter:

$$\frac{\partial u}{\partial \tau} = \frac{1}{2} \frac{\partial^2 u}{\partial r^2} + a_1 u + u^3, \quad u(\tau, r) = -u(\tau, r + \frac{\pi}{\omega}). \quad (15)$$

Consider the solutions that are constant with respect to τ . They are determined by the equation

$$\frac{d^2 u}{dr^2} + a_1 u + u^3 = 0 \quad (16)$$

subject to the boundary conditions

$$u(r + \frac{\pi}{\omega}) = -u(r).$$

It is easy to show that Eq. (16) has a periodic solutions with a nonzero minimum period S . Let $u_0(r; a_1)$ is one of such solutions. Take $\omega = 2\pi S^{-1}$. Then, $u_0(r; a_1)$ is a solution of the boundary value problem and, therefore, of the normalized form. Note that du_0/dr vanishes exactly

once on an interval of length $S/2$. We linearize (15) on u_0 as follows:

$$\frac{\partial u}{\partial \tau} = \left(\frac{1}{2} \frac{\partial^2}{\partial r^2} + a_1 + 3u_0^2 \right) u, \\ u(\tau, r) = -u(\tau, r + \frac{S}{2}).$$

The linear operator on the right-hand side has one zero eigenvalue, and all its other eigenvalues are negative. Therefore, $u_0(r; a_1)$ is a stable solution of the normalized form. Hence, due to Theorem 4, the original equation has stable solutions close to

$$x(t; a_1, S) = \varepsilon^{p/2} u_0 \left(\left(\frac{2\pi}{S \varepsilon^{1-p/2}} + \theta(2\pi S^{-1}, \varepsilon) \right) t; a_1 \right).$$

Here we have two arbitrary parameters: a_1 and S . If we change them, then, generally, we get another solution of Eq. (14). Graphs of some solutions are shown at Fig. 1.

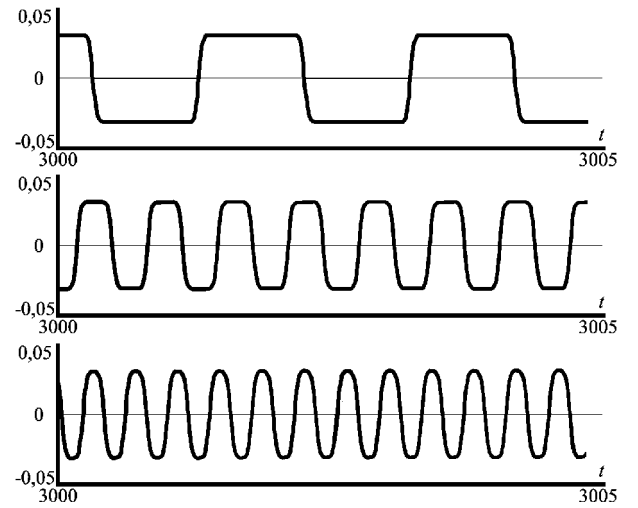


Fig. 1. Solutions of Eq. (14) in case $\mu = 10^{-3}$, $\varepsilon = 10^{-3}$, $f_3 = -1$, $3000 < t < 3005$. Additional parameters are for top plot: $a_1 = 5$, $p = 1, 23$, $\omega = 4$; for middle plot: $a_1 = 1$, $p = 1$, $\omega = 4$; for bottom plot: $a_1 = 1$, $p = 1$, $\omega = 3$.

Therefore, the number of periodic solutions to the original equation in the neighborhood of the equilibrium state increases unboundedly as $\varepsilon \rightarrow 0$. These analytical results are confirmed by the numerical results.

REFERENCES

- [1] S. P. Kuznetsov, Izv. Vyssh. Uchebn. Zaved., Radiofiz. 25, 1410-1428 (1982).
- [2] T. Kiliyas, K. Kutzer, A. Moegel, and W. Schwarz, Intern. J. Electronics 79, 737-753 (1995).
- [3] S. A. Kashchenko, Differ. Uravn. 25, 1448-1451 (1989).
- [4] S. A. Kashchenko, Differ. Uravn. 35, 1343-1355 (1999).
- [5] I. S. Kashchenko, Doklady Mathematics, Vol. 78, No. 1 (2008).
- [6] I. S. Kashchenko, Computational Mathematics and Mathematical Physics, Vol. 48, No. 12 (2008).

A New Quality Factor for the Comparison of Multiplier Architectures

Ahmed H. Darrat and Wolfgang Mathis
 Institute of Theoretical Electrical Engineering
 Leibniz University of Hannover
 Hannover, Germany
 Email: {darrat, mathis}@tet.uni-hannover.de

Abstract— In this paper we introduce a quality factor which enables the comparison of multiplier architectures with respect to the purity of the multiplication. We also propose an analytical method to derive closed-form expressions of the introduced quality factor in dependency of design parameters. This allows the designer to select the most suitable architecture for an application and choose the optimum values for the design parameters of the selected architecture. For illustration we use the introduced quality factor to compare between two basic multiplier architectures.

I. INTRODUCTION

Multiplication is an essential operation in different application fields of modern analog circuits. Multipliers are necessary components in neural networks and are widely used in communication systems for frequency conversion, phase detection, synthesizers, etc. A multiplier should ideally perform a linear product of two signals x and y yielding an output $z=Kxy$, where K is a multiplication constant [1,2]. Owing to the characteristics of the devices used for implementation, multipliers exhibit several non-idealities.

Although many works have been presented in the field of multipliers [1-3], this research field lacks a work which compares different architectures based on a systematic methodology, to help designers make the right choice for the relevant application. In order to make a comparison between different multiplier architectures, it is necessary to define a method that can be applied to all architectures and results in parameters that indicate the quality of the multiplier. Multipliers have several specification parameters, but since all are strongly dependant on the application field, there is no standard comparison metric [1]. Moreover, no metric exists that provides a conclusion on the quality of the mere functionality which is multiplication. The absence of a comparison method and a proper specification parameter hinders circuit

designers in selecting the most suitable multiplier architecture for their applications.

In this work a quality factor to indicate the purity of the multiplication performed by a multiplier is proposed. The introduced quality factor enables the comparison of multiplier architectures with respect to the purity of the multiplication. We also propose a method to derive closed-form expressions of the introduced quality factor in dependency of architecture and technology design parameters. This enables designers select the most suitable architecture for an application and choose the optimum values for the design parameters of the selected architecture. For illustration we use the proposed quality factor to compare between two basic multiplier architectures.

II. ANALYSIS OF NON-IDEALITIES IN MULTIPLIERS

The non-idealities in multipliers depend on the architecture as well as on the used devices [3]. For a designer to choose the most suitable architecture for an application, he/she must be able to compare the different multipliers with respect to their non-idealities for his/her specific application.

A. Taylor-series representation of the output

The output z of a multiplier can be approximated as a function of the inputs x and y through a Taylor series with two variables [4]

$$\begin{aligned}
 z \approx & f(x_0, y_0) + \left. \frac{\partial f(x, y)}{\partial x} \right|_{(x_0, y_0)} \Delta x + \left. \frac{\partial f(x, y)}{\partial y} \right|_{(x_0, y_0)} \Delta y \\
 & + \frac{1}{2!} \left[\left. \frac{\partial^2 f(x, y)}{\partial x^2} \right|_{(x_0, y_0)} \Delta x^2 + 2 \left. \frac{\partial^2 f(x, y)}{\partial x \partial y} \right|_{(x_0, y_0)} \Delta x \Delta y \right. \\
 & \left. + \left. \frac{\partial^2 f(x, y)}{\partial y^2} \right|_{(x_0, y_0)} \Delta y^2 \right] \\
 & + \frac{1}{3!} [\dots] + \dots,
 \end{aligned} \tag{1}$$

with $\Delta x = x - x_0$ and $\Delta y = y - y_0$, where (x_0, y_0) is the operating point. In order to determine the Taylor coefficients in this equation, the input-output description $z = f(x, y)$ of the system is needed. It must be N-times differentiable, where N is the order of the Taylor-series. Equation (1) corresponds to the following series representation [3]

$$z = \sum_{m,n=0}^N a_{mn} \cdot x^m \cdot y^n. \quad (2)$$

The coefficient a_{mn} represents the magnitude of the component $x^m y^n$ at the output of the system. a_{mn} can be determined directly from the Taylor coefficients calculated in (1). The coefficient a_{mn} can therefore be calculated as a function of the system's characteristics

$$a_{mn} = g(f(x, y)). \quad (3)$$

Since an ideal multiplier should only produce the component xy at its output, all other coefficients other than a_{11} are undesired and have to be equal to zero.

B. The Multiplication Purity Index (MPI)

According to this representation of the output we define the following parameter to indicate the quality of the multiplication performed by the system

$$MPI = \frac{|a_{11}|}{\sum_{m=0, n=0}^N |a_{mn}| - |a_{11}|}. \quad (4)$$

The Multiplication Purity Index (*MPI*) is the ratio of the desired component to the sum of all undesired components at the output of the multiplier. It therefore indicates the purity of the multiplication xy performed by a system with two inputs x and y . According to our definition, a multiplier with a higher *MPI* value produces a purer multiplication. An ideal multiplier should have an *MPI* of infinity.

Now consider the case of sinusoidal inputs $x(t) = A_1 \cos(\omega_1 t)$ and $y(t) = A_2 \cos(\omega_2 t)$. By substituting the functions of $x(t)$ and $y(t)$ into (2) and applying the trigonometric addition theorems, we obtain the following equation for the output $z(t)$:

$$z(t) = \sum_{i=-N, j=-N}^N b_{ij} \cdot \cos[(i\omega_1 + j\omega_2) \cdot t] \quad (5)$$

The coefficient b_{ij} represents the amplitude of the spectral component at the frequency $i\omega_1 + j\omega_2$. The coefficient b_{ij} can be determined in terms of the coefficients a_{mn} by comparing (2) to (5) and equating

the coefficients of both equations. The following equation shows the dependency of b_{11} on a_{mn} for $N=3$:

$$b_{11} = \frac{3}{8} a_{13} A_1 A_2^3 + \frac{1}{2} a_{11} A_1 A_2 + \frac{9}{32} a_{33} A_1^3 A_2^3 + \frac{3}{8} a_{31} A_1^3 A_2 \quad (6)$$

Note that b_{11} is provoked not only by a_{11} , but also by higher order coefficients of the Taylor series in (2).

C. The Spectral Multiplication Purity Index (SMPI)

According to the trigonometric product theorem, a multiplication of two sinusoidal signals with the frequencies ω_1 and ω_2 results in two spectral components, one at the sum frequency $(\omega_1 + \omega_2)$ and the other at the difference frequency $(\omega_1 - \omega_2)$ [4]. This implies that an ideal multiplier should contain only the spectral components with the coefficients b_{11} and b_{1-1} in its output. All other components at the output of the multiplier are undesired and can be categorized as non-idealities. Assuming $\omega_1 > \omega_2$, we define the Spectral Multiplication Purity Index (*SMPI*) based on the spectral components at the output as

$$SMPI = 20 \log_{10} \left(\frac{|b_{11}| + |b_{1-1}|}{\sum_{i=1, j=-N}^N |b_{ij}| - |b_{11}| - |b_{1-1}|} \right). \quad (7)$$

SMPI is given thereby in decibels, because the range of possible values is very large. According to (4), (6) and (7), $SMPI \neq MPI$. The advantage of *SMPI* over *MPI* is that, the calculation of *MPI* requires an analytical description of the input-output function $f(x, y)$, whereas for the calculation of *SMPI* only the spectral components of the output signal are needed. For complex multiplier circuits where an analytical description of the input-output function $f(x, y)$ is not derivable, a numerical calculation of *SMPI* after a spectral analysis of the system's output is possible. For the case that an analytical description of the input-output function $f(x, y)$ is derivable, both the *MPI* and the *SMPI* can be derived analytically as shown in the flow diagram of Fig. 1.

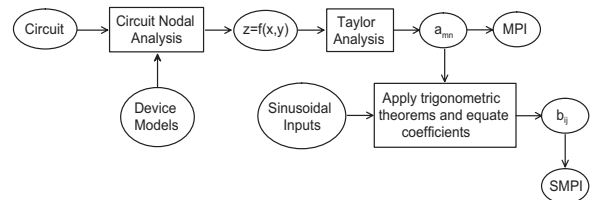


Figure 1. Flow diagram of the analytical derivation of *MPI* and *SMPI*

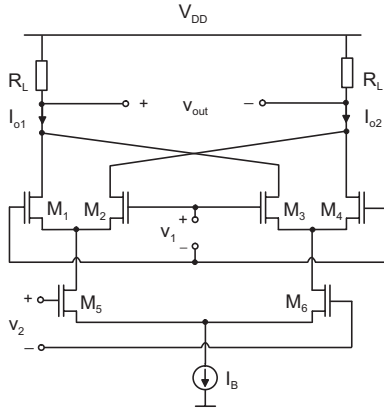


Figure 2. Gilbert MOS Multiplier

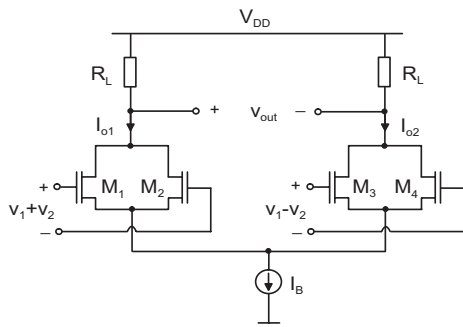


Figure 3. Square-law MOS Multiplier

III. COMPARISON OF TWO MULTIPLIER ARCHITECTURES

In this section we illustrate the use of *MPI* and *SMPI* by comparing two basic multiplier architectures. It is important to note that we here illustrate the analytical derivation of *MPI* and *SMPI*, which prerequisites the input-output description of the system. Nevertheless, a numerical calculation of *MPI* and *SMPI* is possible. For the numerical calculation of *MPI*, the Taylor coefficients of the input-output description of the system are needed, whereas for the numerical calculation of *SMPI* a spectral analysis of the output is required.

The two basic multipliers used for illustration are the Gilbert MOS multiplier and the square-law MOS multiplier. Both circuits are designed in the strong inversion operation mode. In the first part of this section we present both circuits. Their output functions are derived using the ideal quadratic model for the drain current of MOSFET in the strong inversion/saturation operation mode given by [5]

$$I_D = K_n (V_{GS} - V_{T0})^2, \text{ with } K_n = \mu_n C_{ox} W/L, \quad (8)$$

where K_n is the transconductance coefficient, W and L are the transistor's width and length, C_{ox} is the oxide capacitance, μ_n is the mobility coefficient of electrons and V_{T0} is the zero-bias threshold voltage.

A. The Gilbert MOS Multiplier

The Gilbert MOS multiplier shown in Fig. 2 consists of three differential pairs. The lower one has a constant bias-current and the upper two have bias currents controlled by v_2 . Using the simple MOSFET model given in (8), the output current can be derived to [1]

$$I_{out,s} = I_{o1} - I_{o2} \approx 2\sqrt{2K_{n1}K_{n2}}v_1v_2, \quad (9)$$

where K_{n1} and K_{n2} are the transconductance coefficients of the transistors M_1 - M_4 and M_5 - M_6 .

B. The square-law MOS Multiplier

The square-law MOS multiplier is shown in Fig. 2. Each of the transistor pairs M_1 - M_2 and M_3 - M_4 builds a squarer. The squaring is realized through the approximately quadratic characteristic of the MOSFET in the strong inversion/saturation operation mode. Using the MOSFET model of (8), the output current can be derived to [3]

$$I_{out,s} = I_{o1} - I_{o2} = 2K_nv_1v_2, \quad (10)$$

where K_n is the transconductance coefficient of the equally scaled and biased transistors.

C. Comparison of both architectures

The analytical derivation of the quality factors *MPI* and *SMPI* have been done as shown in the flow diagram of Fig. 1. In order to make a realistic comparison between the two presented multipliers, we have used a MOSFET model, which includes high field and short channel effects [5]. This model is given by

$$I_D \approx K_n [1 - \theta(V_{GS} - V_{T0})](V_{GS} - V_{T0})^2, \quad (11)$$

where θ is the mobility degradation factor.

The first step in the analytical calculation of *MPI* and *SMPI* is to derive the input-output function $z=f(x,y)$. Since we use the MOS-model of (11), we get relatively complex expressions for the input-output functions of both circuits compared to the simple expressions of (9) and (10). In order to retain the parameters in analytical form we have implemented the method symbolically in MAPLE. The order N of the Taylor-series was set to 3, which we found adequate for demonstrating the differences between

both circuits. The coefficients a_{mn} and b_{ij} as well as MPI and $SMPI$ for each circuit were determined analytically as closed-form expressions in dependency of the design parameters.

In order to reduce the number of parameters in these expressions, the technology (process) and some architecture design parameters have been set. As an example, figs. 4 and 5 show 3D-plots for MPI and $SMPI$ in dependency of the bias-current I_B and the width W of the transistors (assuming equal sizing). All other design parameters were set constant. The chosen range of values for both the bias-current I_B and the width W is typical for mixer applications in submicron technologies [6]. The differences between the results for MPI and $SMPI$ are due to the different definitions of each quality factor, which has been illustrated in (4), (6) and (7).

Figs. 4 and 5 show that the square-law multiplier has higher values of MPI and $SMPI$ for the chosen range of values of the design parameters I_B and W . This implies that the square-law architecture is a better multiplier for the chosen range of values of the design parameters. Having chosen the architecture, one can select the optimum design point for this circuit with respect to multiplication purity (MPI , $SMPI$), power consumption (I_B) and silicon area (W).

IV. CONCLUSION

A quality factor to indicate the purity of the multiplication performed by a multiplier has been introduced. Two definitions for the quality factor have been given; MPI (Multiplication Purity Index) and $SMPI$ (Spectral Multiplication Purity Index). Using this quality factor it is now possible to compare multiplier architectures with respect to the purity of the performed multiplication. Furthermore, a simple analytical method for deriving closed-form expressions of the introduced quality factor in dependency of architecture and technology design parameters was proposed. This enables designers to select the most suitable architecture for an application and choose the optimum values for the design parameters of the selected architecture. We have demonstrated the feasibility of the quality factor by using it in comparing two basic multiplier circuits. Since the introduced quality factor indicates the purity of the output signal with respect to the multiplication, all effects that lead to undesired components at the multipliers output, such as mismatch or noise, can be investigated. We believe that both the introduced quality factor and the

proposed method can be very useful in assisting designers in choosing the most suitable multiplier architecture for an application, and optimizing the design of the selected architecture for best performance.

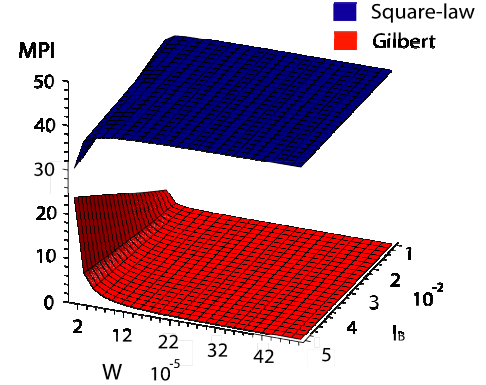


Figure 4. MPI against I_B and W for the square-law and the Gilbert multipliers in strong inversion

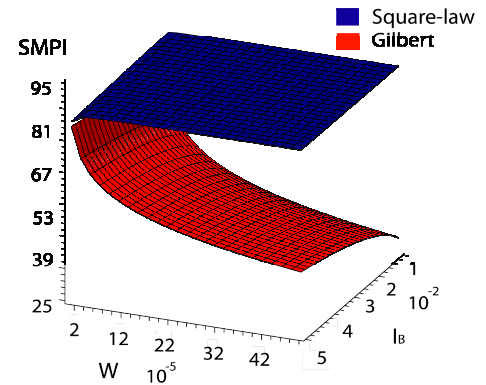


Figure 5. $SMPI$ against I_B and W for the square-law and the Gilbert multipliers in strong inversion

REFERENCES

- [1] G. Han and E. Sánchez-Sinencio, "CMOS Transconductance Multipliers: A Tutorial", IEEE Trans. Circuits and Systems-II: Analog and Digital Sig. Proc., vol. 45, no. 12, December 1998, pp. 1550–1563.
- [2] W-K. Chen, Feedback, Nonlinear, and Distributed Circuits, CRC Press 2009, Chapter 8: Synthesis and design of nonlinear circuits.
- [3] G. Giustolisi, G. Palmisano and G. Palumbo, "Analysis and Optimization of a novel CMOS multiplier", Int. J. Circ. Theor. Appl. 2001; 29:321-330.
- [4] I. Bronstein, K. Semendjajew, G. Musiol and H. Mühlig, "Handbook of Mathematics", Springer-Verlag GmbH, 2002.
- [5] Y. Tsidividis, Operation and modelling of the MOS Transistor, McGraw-Hill 1999, pp. 422-423.
- [6] M. Terrovitis and R. G. Meyer, Intermodulation distortion in current-commutating CMOS Mixers, IEEE J. solid-state circuits, vol. 35, no. 10, pp. 1461-1473, October 2000

Design of coupling for arbitrary lag synchronization in chaotic oscillators

Prodyot Kumar Roy

Department of Physics, Presidency College,

Kolkata 700 073, India

Email: pkpresi@yahoo.co.in

Ioan Grosu

Faculty of Engineering,

University of Medicine and Pharmacy, “Gr.T.Popa”,

Iasi, Romania

Email: igrosu@umfiasi.ro

Syamal Kumar Dana & Sourav Kumar Bhowmick

Central Instrumentation,

Indian Institute of Chemical Biology,

Kolkata 700 032, India

Email: skdana@iicb.res.in

Email: souravb1980@gmail.com

Abstract—We propose a design of unidirectional delay coupling for implementing arbitrary lag synchronization between two chaotic oscillators. The main advantage of the proposed method is that any desired value of lag can be set between the two oscillators, and further, the synchronization can be precisely controlled. The method is elaborated using numerical examples of the Hindmarsh-Rose neuron model, Rossler oscillator and a Sprott system.

I. INTRODUCTION

Coupled chaotic oscillators show different degrees of coherence either in amplitude and/or phase [1] depending upon the strength of the coupling. A complete synchronization (CS) [2] of amplitude and phase between chaotic oscillators is possible if the oscillators are identical and strongly coupled. In reality, as no two systems are identical, mismatch between the two play an important role on synchronization process: an almost CS can only be observed with strong coupling when its strength lies above a particular threshold value. Below this threshold, lag synchronization (LS) may be observed [3,4] in mismatched oscillators while phase synchronization (PS) [5] in general appear for further weaker coupling but above a second coupling threshold. Below this second threshold desynchronization takes place. The amplitudes of the coupled oscillators, in PS, remain almost uncorrelated in time, but always maintain phase differences less than a constant value either near zero (in-phase) or π (antiphase) [8]. On the contrary in case of LS, when the coupling strength lies between CS and PS, the coupled system oscillates in such a manner that the state variables of the two oscillators attain identical amplitudes but maintain a constant phase lag between them. This lag time, however, depends on the magnitude of mismatch between the

parameters and the coupling strength. And, as such, one cannot set an arbitrary time lag. And also, using the existing methods [9], one does not have any control over synchronization. For this, few researcher are even skeptic [4] regarding the experimental observation of LS since the amount of lag time often becomes of the same order as that of experimental uncertainty casting doubts on successful observation, particularly, in presence of noise. Nevertheless, intermittent lag synchronization (ILS) [4] is always possible to observe when the coupled oscillators develop LS with occasional interruption by intermittent loss of synchrony. The LS is also reported in time-delayed systems [10] under unidirectional delay coupling. The limitation of all such methods is their restriction on the amount of time lag and having no control over its magnitude, which is very important from the viewpoint of practical applications. It is true that alternative/modified methods of coupling for LS [11] or anticipating synchronization [12] are coming up to increase the lag time. No doubt these methods improve the result to certain extent, but the delay time still remains restricted to over a small range. On the contrary, our proposed design of coupling allows one achieving LS between two chaotic oscillators with an arbitrary lag time which may be of the order of the systems characteristic time or even multiples of it. We call this synchronization as arbitrary lag synchronization (ALS).

II. OPCL DELAY COUPLING

The unidirectional OPCL coupling was used earlier to realize CS in two identical chaotic oscillators [15] and two identical complex networks [16]. Later on, we extended [17] the theory to achieve CS and antisynchronization (AS) between two mismatched oscillators. Further we have shown how the scheme can be utilized to attain amplification/attenuation of chaos by introducing a

multiplicative factor in the goal dynamics. Now we attempt to use the same idea to realize ALS between two mismatched chaotic oscillators under unidirectional OPCL delay coupling.

We briefly outline the OPCL delay coupling method below.

A. Brief introduction of OPCL delay coupling

In [17] we discussed how a chaotic driver whose dynamics is described by $\dot{y} = f(y) + \Delta f(y)$, $y \in R^n$, ($\Delta f(y)$ contains the additional terms due to mismatch between the two oscillators) can be coupled to another chaotic oscillator so that the dynamics of the response oscillator is governed by $\dot{x} = f(x) + u(x, g)$, $x \in R^n$ ($u(x(t), g(t))$ is the coupling term) to achieve a goal dynamics $g(t) = \alpha y(t)$. Further, the multiplicative factor α appearing in the goal dynamics can be suitably chosen to obtain amplification or attenuation.

Now we propose to utilize the same idea to introduce time delay in the response signal. In other words, we modify our goal dynamics as $g(t) = \alpha y(t - \tau)$, so that the response signal synchronizes with the driver but with a time delay τ . The design of coupling u should be changed accordingly to satisfy the desired goal. We have found that the following choice of coupling satisfies our requirement:

$$u(x, g) = \dot{g} - f(g) + \left(H - \frac{\partial f(g)}{\partial g} \right) (x - \alpha y(t - \tau)). \quad (1)$$

Note that the form is similar to that in [17] but now contains the delay variables $y(t - \tau)$. In examples below we shall show that such a design of coupling works fine and one can set any desired value of τ independent of the system under consideration. Even, one can amplify or attenuate the signal according to one's own choice.

B. Numerical Simulation

Identical Oscillators

First we show the efficacy of OPCL delay coupling using two identical oscillators: the spiking-bursting Hindmarsh-Rose (HR) neuron model [18]. The driver equation is,

$$\begin{aligned} \dot{y}_1 &= y_2 - ay_1^3 + by_1^2 - y_3 + I, \\ \dot{y}_2 &= c - dy_1^2 - y_2, \\ \dot{y}_3 &= r\{S(y_1 + 1.6) - y_3\}. \end{aligned} \quad (2)$$

where y_1 is membrane potential, y_2 and y_3 are associated with fast and slow membrane currents, I is the input bias current to the neuron. The *Jacobian* of the model is

$$\frac{\partial f}{\partial y} = [-3ay_1^2 + 2by_1 \quad 1 \quad -1; -2dy_1 \quad -1 \quad 0; rS \quad 0 \quad -r]^T. \quad (3)$$

where $y = [y_1 \quad y_2 \quad y_3]^T$ (T denotes transpose of a matrix). The matrix H appearing in the coupling term can be obtained from the *Jacobian* of the model system as described in [17],

$$H = [p_1 \quad 1 \quad -1; p_2 \quad -1 \quad 0; rS \quad 0 \quad -r]^T. \quad (4)$$

We consider another identical HR system as response. The coupling for HR model is derived accordingly. The dynamical equations of the response HR oscillator including coupling terms are found to be,

$$\begin{aligned} \dot{x}_1 &= x_2 - ax_1^3 + bx_1^2 - x_3 + I \\ &\quad + a\alpha(\alpha^2 - 1)y_{1\tau}^3 + b\alpha(1 - \alpha)y_{1\tau}^2 + (\alpha - 1)I \\ &\quad + \{p_1 - 2b\alpha y_{1\tau} + 3a(\alpha y_{1\tau})^2\}(x_1 - \alpha y_{1\tau}), \\ x_2 &= c - dx_1^2 - x_2 + c(\alpha - 1) + d\alpha(\alpha - 1)y_{1\tau}^2 \\ &\quad + (p_2 + 2d\alpha y_{1\tau})(x_1 - \alpha y_{1\tau}), \\ \dot{x}_3 &= r\{s(x_1 + 1.6) - x_3\} + 1.6rs(\alpha - 1). \end{aligned} \quad (5)$$

where $y_{1\tau} = y_1(t - \tau)$.

The parameters (p_1, p_2) in are chosen as usual so as to satisfy the RH criterion (see [17] for details) so that the real part of all the eigenvalues of H are negative: $p_1 < r+1$ if we assume $p_2=0$. Accordingly, we select $p_1 = -3$ in our design of the coupling for implementing ALS

Numerical examples for two selected time delays are shown in Fig.1. Clearly the response signal (x_1 in blue) is following the driver signal (y_1 in red).

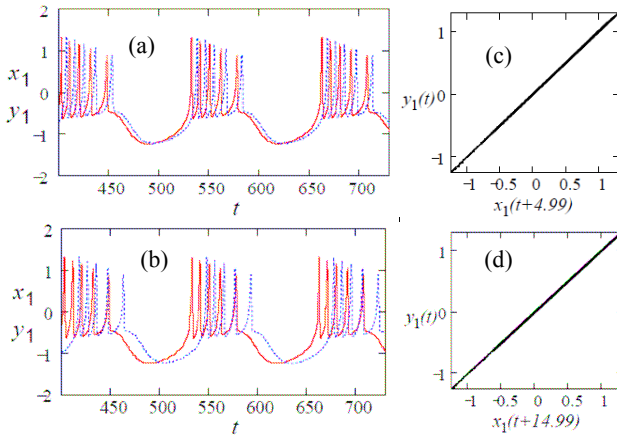


Fig.1. ALS in two identical Hindmarsh-Rose neuron models. Time series of two similar state variables x_1 and y_1 for time delays $\tau=4.99$ in (a), $\tau=14.99$ in (b). The corresponding synchronization manifolds are shown in (c) and (d) respectively.

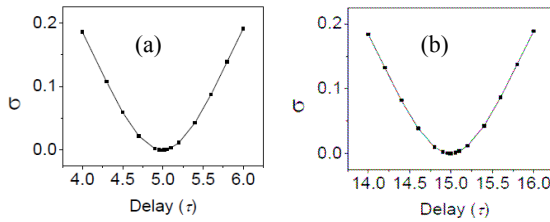


Fig.2. ALS in two identical Hindmarsh-Rose neuron models. The similarity function plots with the same data (as in Fig. 1.) in (a) and (b) for $\tau=4.99$, $\tau=14.99$ respectively confirm ALS.

C. Numerical Simulation

Mismatched Oscillators

To show that there is really no bar on the amount lag time to be set in, let us now consider the example of mismatched Rössler system (whose characteristic time is around six units) described by

$$\dot{x}_1 = -ax_2 - x_3; \dot{x}_2 = x_1 + bx_2; \dot{x}_3 = c + x_3(x_1 - d) \quad (6)$$

The driver Rössler oscillator with a mismatch is taken as

$$\begin{aligned} \dot{y}_1 &= -ay_2 - y_3 - \Delta ay_2; \dot{y}_2 = y_1 + by_2 + \Delta by_2 \\ \dot{y}_3 &= c + y_3(y_1 - d) + \Delta c - \Delta dy_3 \end{aligned} \quad (7)$$

(Δa , Δb , Δc , and Δd are mismatches in parameters).

The response oscillator with OPCL delay coupling turns out to be

$$\dot{x}_1 = -ax_2 - x_3 - \alpha \Delta ay_{2\tau}; \dot{x}_2 = x_1 + bx_2 + \alpha \Delta by_{2\tau}$$

$$\begin{aligned} \dot{x}_3 &= c + x_3(x_1 - d) + \alpha \Delta c + \alpha \Delta d y_{3\tau} + \alpha(1 - \alpha) y_{1\tau} y_{3\tau} \\ &\quad + (p_1 - \alpha y_{3\tau})(x_1 - \alpha y_{1\tau}) + (p_2 - \alpha y_{1\tau})(x_3 - \alpha y_{3\tau}) \end{aligned}$$

We used the notation $y_{i\tau} = y_i(t - \tau)$

(8)

The result of our simulation is shown in Fig.3.

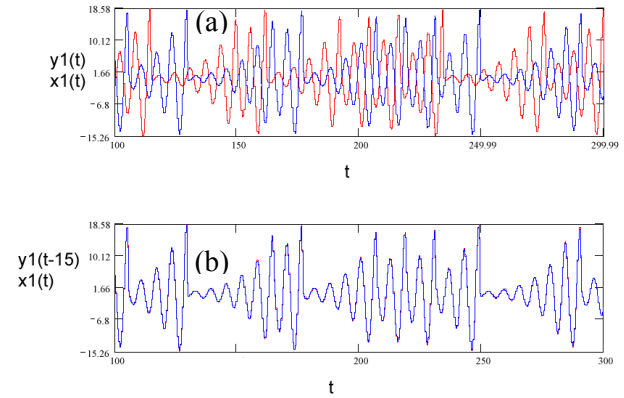


Fig.3. ALS in two mismatched Rössler system. Time series (after the transient) of driver signal y_1 (in red) and the response signal x_1 (in blue) for time delays $\tau=15$ in (a). The two series are overlap with each other in (b) when the time scale is shifted for the driver signal by 15 units corresponding to the lag time set for simulation.

We present another example of mismatched case, a Sprott system [19] that has single quadratic nonlinearity and hence the coupling is less complex and easier for practical implementation of OPCL coupling design as discussed in [17]. The Sprott system is,

$$\begin{aligned} \dot{x}_1 &= -ax_2, \quad \dot{x}_2 = x_1 + x_3, \\ \dot{x}_3 &= x_1 + x_2^2 - x_3. \end{aligned} \quad (9)$$

Another mismatched Sprott system taken as a driver is

$$\begin{aligned} \dot{y}_1 &= -ay_2 - \Delta ay_2, \quad \dot{y}_2 = y_1 + y_3, \\ \dot{y}_3 &= y_1 + y_2^2 - y_3 \end{aligned} \quad (10)$$

After coupling, the response (9) becomes

$$\begin{aligned}\dot{x}_1 &= -ax_2 - \alpha\Delta ay_2(t-\tau); \quad \dot{x}_2 = x_1 + x_3, \\ \dot{x}_3 &= x_1 + x_2^2 - x_3 + \alpha(1-\alpha)y_2(t-\tau)^2 \\ &\quad + (p - 2\alpha y_2(t-\tau))(x_2 - \alpha y_2(t-\tau)).\end{aligned}\quad (11)$$

The results are shown in Fig.4.

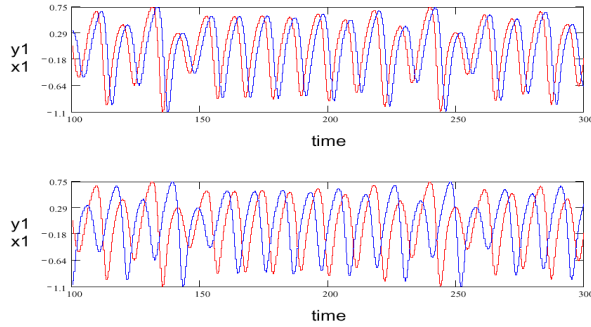


Fig.4. ALS in two mismatched Sprott circuit signals. The lag time being $\tau=2$ and $\tau=8$ units respectively confirming that one can set any arbitrary value of the lag time

The driver and the response are chaotic before coupling for ($a=0.225$, $\Delta a=0.025$). We choose in our design $p=-1$ and put control parameter $\alpha=1$. The time series of driver and response clearly indicates lag synchronization with delay time 2 and 8 units respectively.

III. CONCLUSION

We have shown that the OPCL coupling scheme can be suitably modified to include delay variables to obtain ALS. The main advantage of the method is that it allows one to set any arbitrary value of the delay time. Numerical results were presented for the Hindmarsh-Rose neuron model, Rossler oscillator and a Sprott system. Further, one can implement control over the synchronization but not discussed here for lack of space.

ACKNOWLEDGMENT

The work is partially supported by the Ministry of Education and Research, Romania and Ministry of Science & Technology, India. P.K.R. and S.K.D. also acknowledges partial support by BRNS, (DAE) Govt. of India.

REFERENCES

- [1] A.Pikovsky, M.Roseblum, J.Kurths, Synchronization: A Concept in Nonlinear Sciences, CUP, New York, 2001; S. Boccaletti, J. Kurths, G. Osipov, D.L. Valladares and C. Zhou, Phys. Rep. **366**, 1 (2002).
- [2] L.Pecora, T.Carroll, Phy.Rev.Lett. **64**, 821 (1990).
- [3] M.G. Rosenblum, A.S. Pikovsky and J. Kurths, Phy. Rev. Lett., **76**, 1804 (1996).
- [4] M.G. Rosenblum, A.S. Pikovsky and J. Kurths, Phy. Rev. Lett. **78**, 4193 (1997);
- [5] S.Taheriouni and Y.-C. Lai, Phy.Rev. E **59** (6), R6247 (1999); M.Zhan, C.W.Wei and C.-H.Lai, Phys.Rev. E **65**, 036202 (2002).
- [6] N. F.Rulkov, M.M.Suschik, L.S.Tsimring, Phy. Rev.E **51** (2), 980 (1995); H.D.I.Abarbanel, N.F.Rulkov, M.M.Sushchik, Phys. Rev. E, **53**, 4528 (1996).
- [7] A.E.Hramov, A.A.Koronovskii, Chaos **14** (3), 603 (2004); *ibid*, Physica D **206** (3-4) 252 (2005); A. E. Hramov, A.A.Koronovskii, M.K. Kurovskaya, and O.I. Moskalenko, Phy.Rev.E **71**, 056204 (2005).
- [8] L-Y.Cao, Y-C.Lai, Phys.Rev.E **58**, 382 (1998); V. Astakov et al, Int. J.Bifur.Chaos, **10** (4), 849 (2000); W.Liu et al, Phy.Rev.E **73**, 057203 (2006); C-M.Kim et al, Phy.Letts. A **320**, 39 (2003).
- [9] V.N.Belykh, G.V.Osipov, N.Kucklander, B.Blasius and J.Kurths, Physica D **200**, 81 (2004).
- [10] D.V.Senthilkumar and M.Lakshmanan, Phys. Rev. E **71**, 016211 (2005); S. Sivaprakasam, P. S. Spencer, P Rees, K. A. Shore, Optics letters **27** (14):1250-2 (2002).
- [11] K.Pyragas, T.Pyragiene, Phy.Rev.E **78**, 046217 (2008).
- [12] J.N. Blakely, M.W.Pruitt, N.J. Corron, Chaos **18**, 013117 (2008). G.Ambika and R.E.Amrithkar, PRE
- [13] V.B.Kazansteve, V.I.Nekorkin, V.I.Makarenko, R.Llinás, PNAS **100** (22), 13064-13068 (2003).
- [14] P.R.Bandyopadhyaya, S.N.Singh, D.P.Thivierge, A.M.Annaswamy, H.A.Leinhos, A.R.Fredette, D.N.Beal, IEEE Trans. Ocean Engg. **33** (4), 563-588 (2008).
- [15] E.A.Jackson, I.Grosu, Physica D **85**, 1(1995); I.Grosu, Phy.Rev.E **56**, 3709 (1997); I.Grosu, Int. J. Bifur. Chaos **17** (10), 3519 (2007).
- [16] C.Li, W.Sun, J.Kurths, Phy.Rev.E **76**, 046204 (2007).
- [17] I.Grosu, E.Padmanaban, P.K.Roy and S.K.Dana, Phy.Rev.Lett. **100**, 0234102 (2008); I.Grosu, R.Banerjee, P.K.Roy and S.K.Dana, Phy.Rev.E **80**, 016212 (2009).
- [18] J.L. Hindmarsh, R.M.Rose. Proc. R. Soc. London, Ser. B **221**, 87 (1984).
- [19] J. C. Sprott, Phys. Rev. E **50**, R647 (1994).

Desynchronization of Mean–Field Coupled Oscillators by Remote Virtual Grounding

Arūnas Tamaševičius and Skaidra Bumelienė
Plasma Phenomena and Chaos Lab.,
Semiconductor Physics Institute,
A. Goštauto 11, LT-01108 Vilnius, Lithuania
Email: tamasev@pfi.lt and skaidra@pfi.lt

Gytis Mykolaitis
Faculty of Fundamental Sciences,
Vilnius Gediminas Technical University,
Saulėtekio 11, LT-10223 Vilnius, Lithuania
Email: gytis@pfi.lt

Elena Tamaševičiūtė
Dept. of Mechanical and Process Engineering,
Swiss Federal Institute of Technology in Zürich,
CH-8092 Zürich, Switzerland
Email: elenata@student.ethz.ch

Raimundas Kirvaitis
Faculty of Electronics,
Vilnius Gediminas Technical University,
Naugarduko 41, LT-03227 Vilnius, Lithuania
Email: raimundas.kirvaitis@adm.vgtu.lt

Abstract—An extremely simple feedback technique has been proposed to desynchronize an array of the mean–field coupled FitzHugh–Nagumo type oscillators. A negative impedance converter based unit has been used for the remote virtual grounding of the coupling node of the array. The performance of the technique has been demonstrated both by means of numerical simulation and hardware experiments.

Keywords—oscillations; coupled oscillators; synchronization; desynchronization;

I. INTRODUCTION

Synchronization of coupled oscillators is a common phenomenon observed in a variety of fields in nature, science and engineering. It is widely investigated in physical, electronic, chemical, biological, and communication systems. However in some cases synchronization has rather contradictory impact. For example, synchrony in neuronal networks is very important for information processing in brain. While strong synchronization of neurons may cause essential tremor and Parkinson's disease. The standard therapy for patients is the electrical deep brain stimulation (DBS) with strong high frequency (~100 Hz) pulse trains. However, the DBS may cause side effects. A large number of advanced feedback and non-feedback techniques have been described in literature to avoid synchronization of interacting oscillators in general, and more specifically with the possible application to neuronal arrays, e.g. [1–5].

In this paper, we describe a very simple feedback technique for desynchronizing an array of FitzHugh–Nagumo type coupled oscillators (Fig. 1).

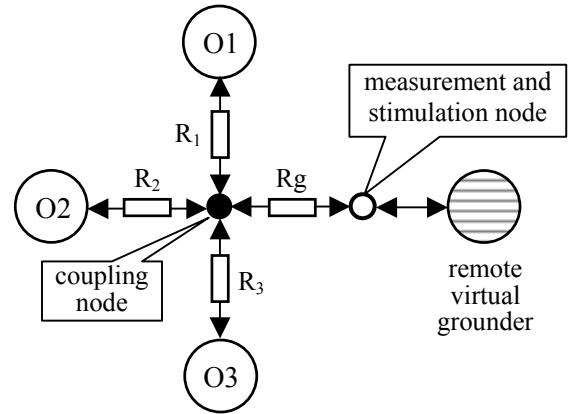


Fig. 1. Block diagram of three mean-field resistively coupled oscillators O1, O2, and O3 with remote virtual ground.

II. MATHEMATICAL BACKGROUND

An individual FitzHugh–Nagumo type oscillator is described by [6,7]:

$$\begin{aligned}\dot{x} &= -F(x) - y - c, \\ \dot{y} &= x - by,\end{aligned}\tag{1}$$

Here $F(x)$ is a nonlinear non-monotonous function. An array of N coupled oscillators is given by

$$\begin{aligned}\dot{x}_i &= -F_i(x_i) - y_i - c_i + k_i(z - x_i), \\ \dot{y}_i &= x_i - b_i y_i, \\ \varepsilon \dot{z} &= \sum_{i=1}^N k_i(x_i - z) = \sum_{i=1}^N k_i x_i - z \sum_{i=1}^N k_i\end{aligned}\tag{2}$$

Here z is a dynamical variable corresponding to the coupling node, $\varepsilon = R_0 C_0$ time constant of the coupling

node. Assuming negligibly small capacitance C_0 of the node ($\varepsilon \rightarrow 0$) we arrive to:

$$z = \sum_{i=1}^N k_i x_i / \sum_{i=1}^N k_i \equiv \bar{x}, \quad (3)$$

i.e. the coupling node potential is just the weighted mean of the main variables x_i . Then Eqs. (2) read:

$$\begin{aligned} \dot{x}_i &= -F_i(x_i) - y_i - c_i + k_i(\bar{x} - x_i), \\ \dot{y}_i &= x_i - b_i y_i. \end{aligned} \quad (4)$$

Let us apply very strong damping ‘ $-K_0 z$ ’ to the coupling node:

$$\varepsilon \dot{z} = \sum_{i=1}^N k_i x_i - z \sum_{i=1}^N k_i - K_0 z. \quad (5)$$

Again for $\varepsilon \rightarrow 0$

$$z = \sum_{i=1}^N k_i x_i / (\sum_{i=1}^N k_i + K_0). \quad (6)$$

If $K_0 \gg \sum_{i=1}^N k_i \approx N$, then $z \rightarrow 0$. In an electronic implementation (e.g. Fig. 4) the K_0 is an open-loop gain of an operational amplifier and reaches several hundreds of thousands. Thus Eqs. (2) read

$$\begin{aligned} \dot{x}_i &= -F_i(x_i) - y_i - c_i - k_i x_i, \\ \dot{y}_i &= x_i - b_i y_i. \end{aligned} \quad (7)$$

It is evident from (7), that the system effectively becomes uncoupled (the coupling term z vanishes). The only difference between the isolated oscillators (1) and the virtually decoupled oscillators (7) is the term ‘ $-k_i x_i$ ’. However, it involves only simple local damping, which does not cause any synchronization.

III. PSPICE SIMULATION

The coupled circuit in Fig. 1, where the oscillators O1, O2, O3 are presented in Fig. 2 and the remote virtual grounder (RVG) is shown in Fig. 4, has been simulated numerically using the Electronics Workbench Professional (the PSPICE based software). The LM741 type operational amplifiers (OA) and the 1N5820 type Schottky diodes (D1, D2) have been employed in the simulations. The typical output of an individual oscillator is presented in

Fig. 3, while the application circuit of the RVG unit is sketched in Fig. 5. The remote virtual ground is demonstrated to appear at the node #5 (Table 1).

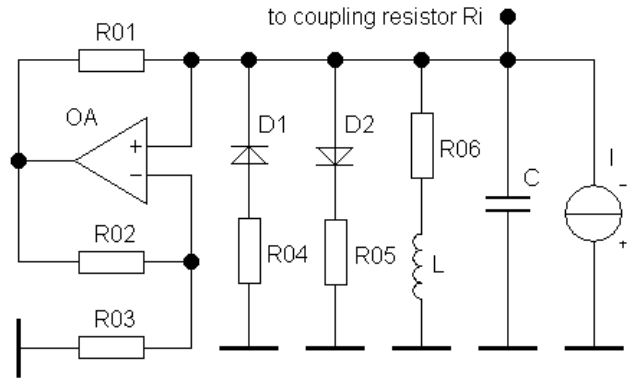


Fig. 2. Circuit diagram of the FitzHugh–Nagumo type oscillator. It is a slightly modified version of the circuit described in [6,7].

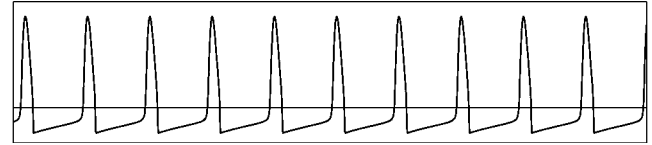


Fig. 3. Voltage across the capacitor C of the oscillator in Fig. 2. $L=1$ H, $C=330$ nF, $\rho=(L/C)^{1/2}=1.74$ k Ω , $R_{01}=R_{02}=1$ k Ω , $R_{03}=300$ Ω , $R_{04}=30$ Ω , $R_{05}=240$ Ω , $R_{06}=200$ Ω , $I=333$ μ A. Amplitude ≈ 1.5 V, inter-spike period ≈ 10 ms.

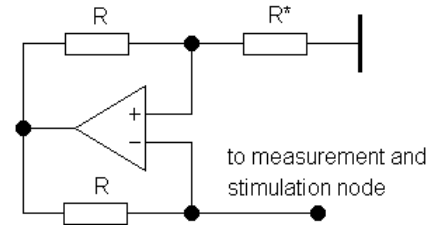


Fig. 4. Circuit diagram of the remote virtual grounder (RVG). It is a negative impedance converter based unit.

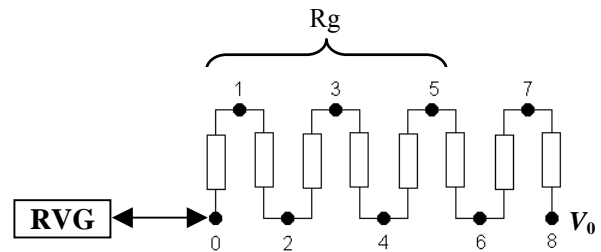


Fig. 5. Remote virtual grounding in a “distributed” resistive line. #0 is the measurement and stimulation node, #5 is the remote virtual grounding node ($V_5 \approx 0$, see Table 1); geometrically to be close to the coupling node. All resistors in the line are 4 k Ω each.

TABLE I. VOLTAGE DISTRIBUTION ALONG THE RESISTIVE LINE

Node	0	1	2	3	4	5 ^a	6	7
V_i/V_0	-1.7	-1.3	-1.0	-0.7	-0.3	0	0.3	0.7

^a exact voltage value at the node # 5 is $V_5/V_0 = -0.0007$.

The simulation results are presented in the form of the phase portraits, taken from different pairs of the oscillators (Figs. 6–8).

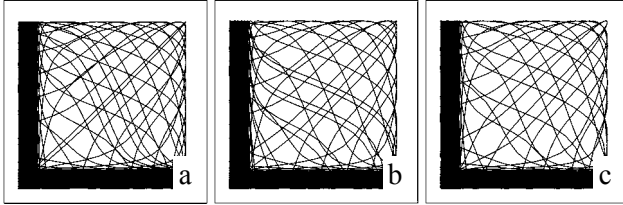


Fig. 6. Phase portraits from isolated oscillators. a) O2–O1, b) O3–O1, c) O3–O2. $I_1/I_2/I_3=333/349/313 \mu\text{A}$. $k_i=0$.

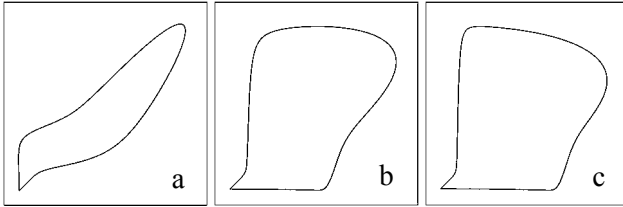


Fig. 7. Phase portraits from mean-field coupled oscillators. a) O2–O1, b) O3–O1, c) O3–O2. $I_1/I_2/I_3=333/349/313 \mu\text{A}$. $R_1=R_2=R_3=20 \text{ k}\Omega$, $k_i = \rho/R_i \approx 0.09$ (threshold value $k_{ith} \approx 0.05$).

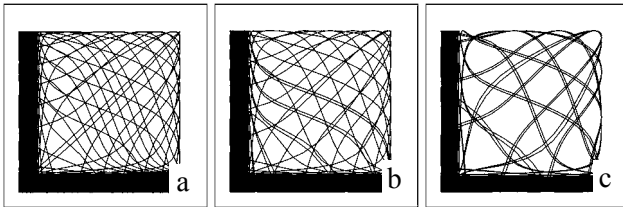


Fig. 8. Phase portraits from mean-field coupled oscillators with the remote virtual ground. a) O2–O1, b) O3–O1, c) O3–O2. $I_1/I_2/I_3=333/349/313 \mu\text{A}$, $R_1=R_2=R_3=20 \text{ k}\Omega$, $k_i = \rho/R_i \approx 0.09$, $R=10 \text{ k}\Omega$, $R^*=R_g=20 \text{ k}\Omega$. Note: it is important to set $R^* \cong R_g$.

Fig. 6, Fig. 7 and Fig. 8 indicate the uncoupled, synchronized and desynchronized states, respectively. The value of the mean field is illustrated with the time series of the voltage simulated at the coupling node (Fig. 9). The voltage of the coupling node becomes almost zero (Fig. 9b), when the remote virtual grounder is applied. Only a small ripple is observed on an enlarged scale (Fig. 9c).

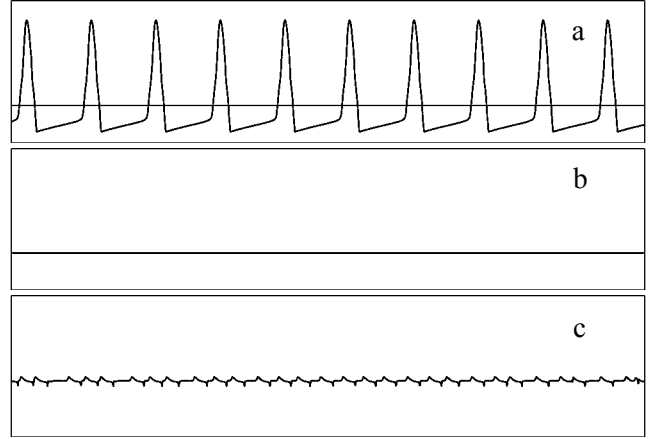


Fig. 9. Voltage simulated at the coupling node. a) Three coupled oscillators; amplitude $\approx 1.5 \text{ V}$. b) Three coupled oscillators with a remote virtual grounder. c) Plot (b) vertically zoomed in by a factor of 200; amplitude $\approx 2 \text{ mV}$. Circuit parameters are the same as in Fig. 7 and Fig. 8.

IV. HARDWARE EXPERIMENTS

Hardware experiments were carried out using the circuits described in the previous section III, namely three FitzHugh–Nagumo type oscillators (Fig. 2), resistively coupled in a star configuration, and the remote virtual grounder (Fig. 4). All the circuit elements and parameters were the same as in the numerical simulations, except the bias current I , that was set to the value of $220 \mu\text{A}$, because slightly different Schottky diodes (1N5817), had been used. In addition, the bias currents were the same ($I_1=I_2=I_3$) for all oscillators. The difference of the oscillators was due to the manufacturing spread of the element parameters (tolerance of the linear elements was 5%, and the mismatch of the diodes up to 10%). The output from an individual oscillator (Fig. 10) is in an excellent agreement with the simulated waveform (Fig. 3). The corresponding phase portraits in Fig. 11, Fig. 12, Fig. 13 and the time series in Fig. 14 for the coupled oscillators are also in a reasonable agreement with the numerical simulations.

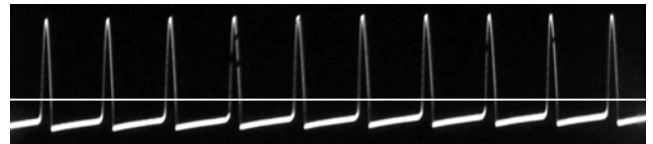


Fig. 10. Voltage across the capacitor C in the experimental FitzHugh–Nagumo oscillator. Amplitude $\approx 1.5 \text{ V}$, inter-spike period $\approx 10 \text{ ms}$. Nominal circuit parameters are the same as in Fig. 3. The bias current $I = 220 \mu\text{A}$.

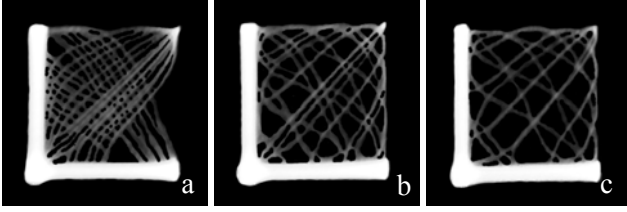


Fig. 11. Phase portraits from isolated oscillators. a) O2–O1, b) O3–O1, c) O3–O2. Nominal circuit parameters are the same as in Fig. 6. $I_1=I_2=I_3=220 \mu\text{A}$.

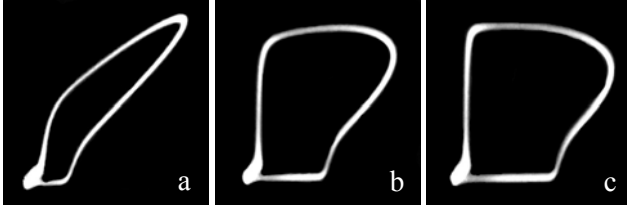


Fig. 12. Phase portraits from mean-field coupled oscillators. a) O2–O1, b) O3–O1, c) O3–O2. Nominal circuit parameters are the same as in Fig. 7. $I_1=I_2=I_3=220 \mu\text{A}$.

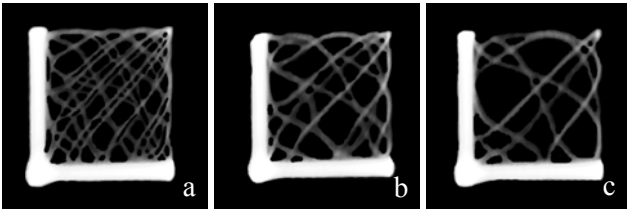


Fig. 13. Phase portraits from coupled oscillators with the remote virtual grounder. a) O2–O1, b) O3–O1, c) O3–O2. Nominal circuit parameters are the same as in Fig. 8. $I_1=I_2=I_3=220 \mu\text{A}$.

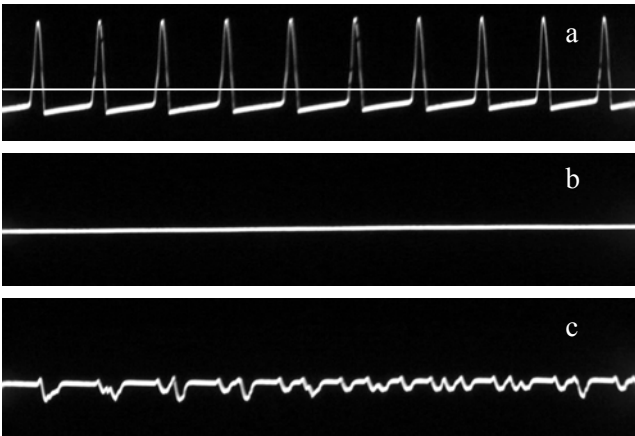


Fig. 14. Voltage measured at the coupling node. a) Three coupled oscillators; amplitude $\approx 1.5 \text{ V}$. b) Three coupled oscillators with remote virtual grounder. c) Photo (b) vertically zoomed in by a factor of 200; amplitude $\approx 2 \text{ mV}$. Nominal circuit parameters are the same as in Fig. 7 and Fig. 8. $I_1=I_2=I_3=220 \mu\text{A}$.

V. CONCLUSION

We have suggested desynchronizing mean-field coupled oscillators by using a remote virtual grounder, i.e. by resetting the voltage at the coupling node. Simulations have been performed and hardware experiments have been carried out with the FitzHugh–Nagumo oscillators. However we hope the similar technique can be applied to networks composed of other types of oscillators as well.

ACKNOWLEDGMENTS

The authors would like to thank Ruedi Stoop for stimulating this investigation. The work was partially supported by the EU Structural Funds via the Research Council of Lithuania within the Operational Programme for Human Resources Development for 2007–2013 under the measure VP1-3.1-ŠMM-07-V ‘Support to Research of Scientists and Other Researchers (Global Grant)’.

REFERENCES

- [1] O. V. Popovych, C. Hauptmann, and P. A. Tass, “Effective desynchronization by nonlinear delayed feedback,” *Phys. Rev. Lett.*, vol. 94, 164102, 2005.
- [2] O. V. Popovych, C. Hauptmann, and P. A. Tass, “Control of neuronal synchrony by nonlinear delayed feedback,” *Biol. Cybern.*, vol. 95, pp. 69–85, 2006.
- [3] P. A. Tass, *Phase Resetting in Medicine and Biology: Stochastic Modelling and Data Analysis*. Berlin: Springer, 2007.
- [4] K. Pyragas, O. V. Popovych, and P. A. Tass, “Controlling synchrony in oscillatory networks with a separate stimulation-registration setup,” *Eur. Phys. Lett.*, vol. 80, 40002, 2007.
- [5] T. Kano and S. Kinoshita, “Phase control of coupled oscillators using multilinear feedback,” in *Proc. NOLTA’09*, pp. 34–37, Sapporo, Japan, 2009.
- [6] E. Tamaševičiūtė, A. Tamaševičius, G. Mykolaitis, S. Bumelienė, R. Kirvaitis, and R. Stoop, “Electronic analog of the FitzHugh–Nagumo neuron model and noninvasive control of its steady state,” in *Proc. NDES’09*, pp. 138–141, Rapperswil, Switzerland, 2009.
- [7] A. Tamaševičius, E. Tamaševičiūtė, G. Mykolaitis, S. Bumelienė, R. Kirvaitis, and R. Stoop, “Neural spike suppression by adaptive control of an unknown steady state,” *Lecture Notes in Computer Science*, vol. 5768, pp. 618–627, 2009.

Nonlinear Observer Based Control of a Chaotic Phase Locked Loop

Mchiri Mohamed and Trabelsi Karim

SYSCOM Laboratory
Ecole Nationale d'Ingénieurs de Tunis, BP 37 Tunis
Belvédère 1002, Tunisia
Email: medmch@yahoo.fr

Belghith Safya

SYSCOM Laboratory
Ecole Nationale d'Ingénieurs de Tunis, BP 37 Tunis
Belvédère 1002, Tunisia
Email: Karim.Trabelsi@enig.rnu.tn

Abstract— This paper proposes a novel nonlinear observer to control a chaotic third order Phase Locked Loop (PLL). The design of the proposed observer is based on the high order sliding mode technique. By assuming that only the phase error of the PLL is known, the control strategy constructs a nonlinear observer based feedback law and then causes the phase error to behave in a desired way. The convergence of the observer is analyzed using the Lyapunov theory. Simulations results on PLL show the effectiveness and robustness of the proposed scheme.

I. INTRODUCTION

In recent years, control of chaotic systems has been an intensive research interest and several methods have been proposed [1-4]. From practical point of view, a direct access to actual states is not always available. Consequently, it is necessary to use a state-observer in order to estimate the state vector of the system under consideration and then construct the control law. In literature, the observer design for chaotic systems has been extensively studied and many types of observers have been used [5-9]. However, these methods do not consider the system uncertainties. To overcome this drawback, sliding mode observers have been developed [10-12]. They differ from traditional observers by the injection of a non-linear discontinuous term into the observer. This term, depending on the output estimation error, enables the observer to reject disturbances. The objective of this paper is to construct a non-linear observer based control design to force the solutions of the chaotic system to track a desired trajectory. We develop in the first step a novel observer based on sliding mode technique which guarantee an asymptotically convergence of the error estimation to zero. Then, we construct the control law based on the estimated states.

This paper is organized as follows. Section 2 displays the class of nonlinear chaotic systems under consideration. Section 3 presents the observer design and the convergence analysis. In Section 4 we consider the observer based control approach. Section 5 illustrates the main results by applying the proposed method for controlling a chaotic PLL and obtaining a desirable behavior. Finally, some conclusions are included in Section 6.

II. PROBLEM STATEMENT

The dynamics of the system under consideration are described by the following equation:

$$\dot{x}^{(n)} = f(x, \dot{x}, \dots, x^{(n-1)}, t) + u(t), \quad (1)$$

where $x \in R^n$ is the vector of generalized coordinates, $f(x, \dot{x}, \dots, x^{(n-1)}, t)$ is a nonlinear function depending on the time and $u(t)$ represent the control input. The form (1) includes a wide variety of chaotic systems such as third order Phase Locked Loop (PLL) and Duffing oscillator. The model (1) can be rewritten in the state-space form

$$\begin{cases} \dot{x}_1 = x_2 \\ \dot{x}_2 = x_3 \\ \vdots \\ \dot{x}_n = f(x_1, x_2, \dots, x_n, t) + u(t), \end{cases} \quad (2)$$

where $x_1 = x, x_2 = \dot{x}, \dots, x_n = x^{(n-1)}$. We assume here that only the state vector x is available for measurements. Hence, the goal is to find a nonlinear state observer for system (1) such that the error estimation tends to zero in finite time and by the availability of the state vector x only.

III. OBSERVER DESIGN

The proposed sliding mode observer has the following form

$$\begin{cases} \dot{\hat{x}}_1 = \hat{x}_2 + \lambda_1 * \text{sign}(e_1) \\ \dot{\hat{x}}_2 = \hat{x}_3 + \lambda_2 * g_1(e_1) * \text{sign}(\dot{e}_1) * \text{sign}(e_2) \\ \vdots \\ \dot{\hat{x}}_i = \hat{x}_{i+1} + \lambda_i * g_{i-1}(e_{i-1}) * \text{sign}(\dot{e}_{i-1}) * \text{sign}(e_i) \\ \vdots \\ \dot{\hat{x}}_n = f(x_1, \hat{x}_2, \dots, \hat{x}_n, t) + \lambda_n * \text{sign}(e_n) + u(t), \end{cases} \quad (3)$$

where \hat{x}_i , $i=1, \dots, n$, are the state estimations of the state vectors x_i , $i=1, \dots, n$, respectively and $g_i(e_i)$ is given by $g_i(e_i) = |e_i|^{1/2} * \text{sign}(e_i)$, $i=1..n-1$, $e_1 = x_1 - \hat{x}_1$ is the output error and $\text{sign}(\cdot)$ is the standard signum function. $\lambda_i, i=1, \dots, n$, are the observer gains to be defined later. By introducing the state errors $e_i, i=1, \dots, n$ as $e_i = x_i - \hat{x}_i$, the error system is given by:

$$\begin{cases} \dot{e}_1 = e_2 - \lambda_1 * \text{sign}(e_1) \\ \dot{e}_2 = e_3 - \lambda_2 * g_1(e_1) * \text{sign}(\dot{e}_1) * \text{sign}(e_2) \\ \vdots \\ \dot{e}_i = e_{i+1} - \lambda_i * g_{i-1}(e_{i-1}) * \text{sign}(\dot{e}_{i-1}) * \text{sign}(e_i) \\ \vdots \\ \dot{e}_n = F(x_1, x_2, \hat{x}_2, \dots, x_n, \hat{x}_n, t) - \lambda_n * \text{sign}(e_n), \end{cases} \quad (4)$$

We assume that all states of (1) are bounded by a positive constant M (which is possible for chaotic systems since they are bounded in a compact and convex region) and one can write $|F(x_1, x_2, \hat{x}_2, \dots, x_n, \hat{x}_n, t)| < M$ (5)

To demonstrate the asymptotically convergence of the error system to zero, we determine in the first step, the gain λ_1 (respectively λ_n) by defining a definite positive Lyapunov function V_1 (respectively V_n) as follows

$$V_1 = \frac{1}{2} e_1^2. \quad (6)$$

$$V_n = \frac{1}{2} e_n^2, \quad (7)$$

The time derivative of (6) gives

$$\begin{aligned} \dot{V}_1 &= e_1 \cdot \dot{e}_1 = e_1 \cdot (e_2 - \lambda_1 * \text{sign}(e_1)) \\ &\leq |e_1| \cdot |e_2| - \lambda_1 |e_1| \\ &< |e_1| \cdot (|e_2|_{\max} - \lambda_1) \end{aligned} \quad (8)$$

which is negative since $\lambda_1 > |e_2|_{\max}$. So, by choosing $\lambda_1 > |e_2|_{\max}$ the Lyapunov function V_1 is continually decreasing and the error e_1 tends asymptotically to zero. As before, V_n is continually decreasing and the error e_n tends asymptotically to zero since we have $\lambda_n > M$. Now, the second step consist on assuring an asymptotically convergence of all errors $e_i, i=2, \dots, n-1$, to zero. To this end, we will study the function \ddot{e}_i in the error trajectory $\dot{e}_i = f(e_i)$ for $i=2, \dots, n-1$, (see fig. 1). The second derivative of the system errors $e_i, i=2, \dots, n-1$ gives

$$\begin{cases} \ddot{e}_2 = \dot{e}_3 - \frac{\lambda_2}{2} |e_1|^{-1/2} |\dot{e}_1| \text{sign}(e_2) \\ \vdots \\ \ddot{e}_i = \dot{e}_{i+1} - \frac{\lambda_i}{2} |e_{i-1}|^{-1/2} |\dot{e}_{i-1}| \text{sign}(e_i) \\ \vdots \\ \ddot{e}_{n-1} = \dot{e}_n - \frac{\lambda_{n-1}}{2} |e_{n-2}|^{-1/2} |\dot{e}_{n-2}| \text{sign}(e_{n-1}), \end{cases} \quad (9)$$

Beginning with \ddot{e}_{n-1} . Since we have guaranteed the convergence of (e_n, \dot{e}_n) to $(0,0) \forall t \geq t_n$, the expression of \ddot{e}_{n-1} becomes

$$\begin{aligned} \ddot{e}_{n-1} &= \dot{e}_n - \frac{\lambda_{n-1}}{2} |e_{n-2}|^{-1/2} |\dot{e}_{n-2}| \text{sign}(e_{n-1}) \\ &= -\frac{\lambda_{n-1}}{2} |e_{n-2}|^{-1/2} |\dot{e}_{n-2}| \text{sign}(e_{n-1}), \quad \forall t \geq t_n, \end{aligned} \quad (10)$$

When studying \ddot{e}_{n-1} in the error trajectory $\dot{e}_{n-1} = f(e_{n-1})$, we have a negative decreasing function \ddot{e}_{n-1} in the first half (see fig.1 quadrant (1) and (2)). In the second half of $\dot{e}_{n-1} = f(e_{n-1})$ (quadrant (3) and (4)), we have $\ddot{e}_{n-1} \geq 0$ and increase and tend towards $e_{n-1} = \dot{e}_{n-1} = 0$ in finite time. Consequently and in the same way, we prove the finite time convergence of $(e_i, \dot{e}_i), i=2, \dots, n-2$, towards $e_i = \dot{e}_i = 0$ and for any observer gains $\lambda_i, i=2, \dots, n-1$.

IV. OBSERVER BASED CONTROL LAW

The control problem here is the design of a control law $u(t)$ such that the output signal $y(t)$ tracks a desired trajectory $y_d(t)$. The approach used in this section is based on the phase space reconstruction

technique [13]. Consider system (1), let $h(x)$ be the signal output and L_f the Lie derivative operator. We construct then the signal state

$$\begin{aligned}\sigma(t) &= (y(t), \dot{y}(t), \dots, y^{(n-1)}(t))^T \\ &= (h(x), L_f h(x), \dots, L_f^{(n-1)} h(x))^T \\ &= (\sigma_1, \sigma_2, \dots, \sigma_n)^T\end{aligned}\quad (11)$$

The i th Lie derivative operator is given by $L_f^i h(x) = \sum_{j=1}^n \frac{\partial L_f^{i-1} h(x)}{\partial x_j} f_j(x)$ and $f_j(x), j=1, \dots, n$ is given by model (2). The first derivate of $\sigma(t)$ gives:

$$\begin{aligned}\dot{\sigma}(t) &= (\dot{y}(t), \ddot{y}(t), \dots, y^{(n)}(t))^T \\ &= (L_f h(x), L_f^2 h(x), \dots, L_f^n h(x))^T\end{aligned}\quad (12)$$

For model (1), the state vector $\sigma(t)$ represents the signal $X = (x_1, x_2, \dots, x_n)$, so one can write

$$\dot{X} = A.X + B.v + u \quad (13)$$

where

$$A = \begin{pmatrix} 0 & 1 & 0 & \dots & 0 \\ 0 & 0 & 1 & \dots & 0 \\ \vdots & \vdots & \vdots & \dots & \vdots \\ 0 & 0 & 0 & \dots & 1 \\ 0 & 0 & 0 & \dots & 0 \end{pmatrix}_{n \times n}, B = \begin{pmatrix} 0 \\ 0 \\ \vdots \\ 1 \end{pmatrix} \in R^n,$$

and

$$v = L_f^n h(x) \quad (14)$$

(13) is a Brunowsky canonical form [14]. By introducing a complementary control input

$$r(t) = B.v + u(t) \quad (15)$$

(13) can be rewritten as

$$\dot{X}(t) = A.X(t) + r(t) \quad (16)$$

To guarantee the convergence of the error trajectory between $y(t)$ and $y_d(t)$ exponentially to zero, $r(t)$ can be chosen as

$$r(t) = -K.(y(t) - y_d(t)) \quad (17)$$

where $K = [k_1, k_2, \dots, k_n]^T$, $k_i, i=1, \dots, n$ are constants to be chosen such that the real parts of all eigenvalues of the closed loop system (13) are negative. From equations (15) and (17), the control input $u(t)$ is modified to be

$$u(t) = -K.(y(t) - y_d(t)) - B.\hat{v} \quad (18)$$

where \hat{v} is based on the estimated variables and equal to $\hat{v} = L_f^n h(\hat{x})$.

V. SIMULATIONS

Consider a third order PLL given by the following dynamic model

$$\begin{aligned}\ddot{\psi} &= -A\ddot{\psi} - B\dot{\psi} + C\left(\dot{\psi}^2 \sin(\psi) - \ddot{\psi} \cos(\psi)\right) \\ &\quad - D\dot{\psi} \cos(\psi) - E \sin(\psi) + u\end{aligned}\quad (19)$$

ψ is the phase error and u the control input of the system. The PLL exhibits a chaotic behavior for the following parameters $A=3.94; B=3.783; C=3; D=195; E=2250$. Figure 2 illustrates this behaviour. Let ψ be the output signal given by $y(t) = \psi(t) = x_1$ which is assumed to be only measured. As we want to design a controller for zero loops' phase error, the desired trajectory is chosen as $y_d = \text{const} = 0$. For simulations purposes, M is equal to 120 and the observer gains are taken as $\lambda_1=40, \lambda_2=10; \lambda_3=125$. For the design of the controller, we choose $k_1=22; k_2=160; k_3=389$. Figure 3 displays the errors estimation between the system states ($\psi, \dot{\psi}$ and $\ddot{\psi}$) and their estimated variables ($\hat{\psi}, \hat{\dot{\psi}}, \hat{\ddot{\psi}}$). Based on this figure, it is clear that estimated states converge in finite time and quickly to the real states of the PLL. Figure 4 displays the system response in the controlled case. It is easy to see that the phase error of the PLL quickly converges to the desired trajectory.

A comparison of our approach to control methods given in [4] and applied to a chaotic PLL shows the effectiveness of our strategy control from convergence rapidity point of view. Figure 5 display the transition time of the system response to the desired trajectory. Based on this figure, we show that our method allows better control results.

VI. CONCLUSION

A nonlinear observer based control approach of chaotic systems has been developed in this paper. The observer is based on sliding mode technique in order to estimate all states of the system. The constructed control law employs the estimated variables in order to derive the system from chaos to a fixed point. Theoretical results have been supported by numerical simulations applied to a third order chaotic PLL. These results are compared with those given in [4] showing then, the effectiveness of the proposed method.

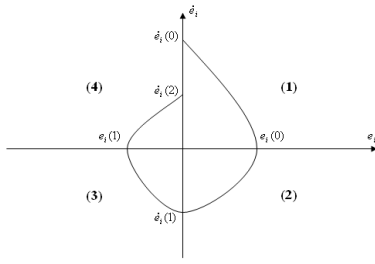


Fig.1. Finite time convergence observer.

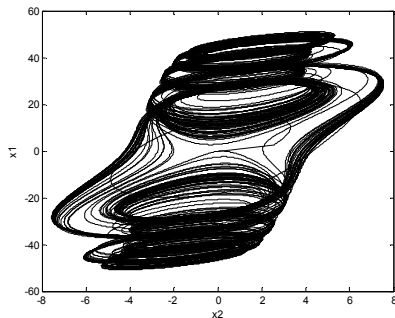


Fig.2. Strange attractor

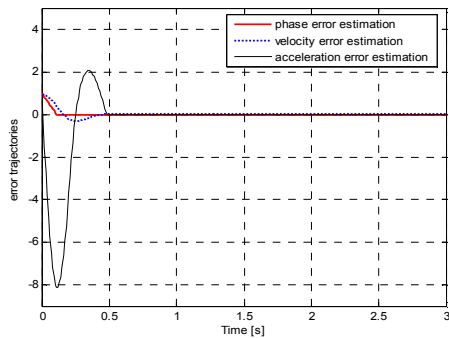


Fig.3. Different Errors estimation

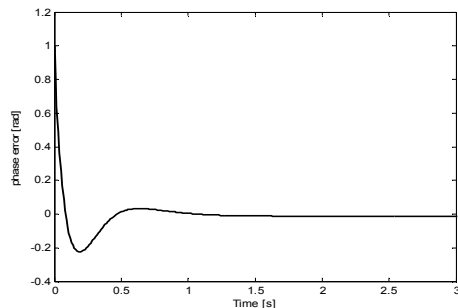


Fig.4. Phase error of the PLL in the controlled case

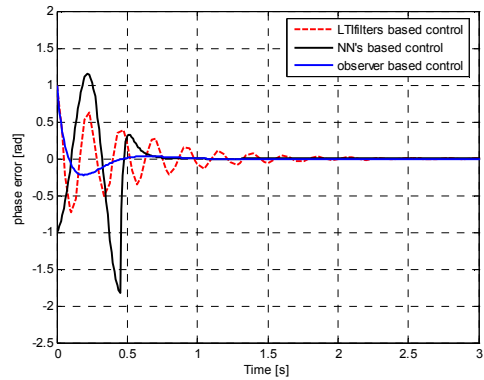


Fig.5. Transition to the regular solution

REFERENCES

- [1] E. Ott, C. Grebogi, and J.A. Yorke, "Controlling chaos", Phys. Rev. Lett. 64 (11), 1990, pp. 1196-1199.
- [2] A.M. Harb, and B.A.Harb, "Chaos control of 3rd Order PhaseLocked Loops using Backstepping Nonlinear Controller", Complexity International, 2002.
- [3] Ge SS, Wang C, and Lee TH, "Adaptive backstepping control of a class of chaotic systems". International Journal of Bifurcation & Chaos, (10), 2000, pp. 1149-1156.
- [4] Mchiri Mohamed, Belghith Safya, and Benjemaa Zouheir, "Neural Networks based control of chaotic phase locked loop", Proc. IEEE International Multi-Conference on Systems, Signals and Devices, Jordan, 2008.
- [5] Liao TL, "Observer-based approach for controlling chaotic systems", Phys Rev E, 57 (2), 1998, pp. 1604-1610.
- [6] Hua C, Guan X, Li X, and Peng S, "Adaptive observer-based control for a class of chaotic systems". Chaos, Solitons & Fractals, (22), 2004, pp. 103-110.
- [7] Wang J, Qiao GD, and Deng B, Observer-based robust adaptive variable universe fuzzy control for chaotic system. Chaos, Solitons & Fractals, (23), 2005, pp. 1013-1032.
- [8] S.H. Mahboobi, M. Shahrokhi, and H.N. Pishkenari, "Observer-based control design for three well-known chaotic systems", Chaos, Solitons & Fractals, (29), 2006, pp. 381-392.
- [9] Ercan Solak, Ömer Morgül, and Umut Ersoy, "Observer-based control of a class of chaotic systems", Physics Letters A, (279), 2001, pp. 47-55
- [10] C.X. Guo, Q.Y. Jiang, and Y.J. Cao, "Controlling chaotic oscillations via nonlinear observer approach", Chaos, Solitons and Fractals, 2006.
- [11] Aguilar-Lopez R, and Maya-Yescas R. "State estimation for nonlinear systems under model uncertainties: a class of sliding-mode observers", J Process Control, (15), 2005, pp. 363-370.
- [12] Han JQ. "Extended state observer of a class of uncertain systems", Control Decision, 10 (1), 1988, pp. 85-86.
- [13] Cao YJ, Zhang PX, and Cheng SJ, "Controlling chaotic systems via phase space reconstruction technique", International Journal of Bifurcation & Chaos, (13), 2003, pp. 557-568.
- [14] Isidori, A, "Nonlinear Control Systems: An Introduction", 2nd ed., Springer, NY, 1989.

Observer approach for synchronization of chaotic time delay Chua circuit :application to secure communication

Trabelsi Karim and Mchiri Mohamed

SYSKOM Laboratory
Ecole Nationale d'Ingénieurs de Tunis, BP 37 Tunis
Belvédère 1002, Tunisia
Email: karim_enit@yahoo.fr, medmch@yahoo.fr

Belghith Safya

SYSKOM Laboratory
Ecole Nationale d'Ingénieurs de Tunis, BP 37 Tunis
Belvédère 1002, Tunisia
Email: Karim.Trabelsi@enig.rnu.tn

Abstract—In this paper secure data transmission system based on synchronization of chaotic system is presented. The transmitter module consists of a chaotic generator which is the time delay feedback Chua circuit and an encryption mechanism (chaotic masking), in which the secret message (digital image) is added to the output of the chaotic generator. The receiver module consists of a non linear state observer design, driven by only one of the states of the time delay feedback Chua circuit; and a decryption mechanism. Simulations results prove the efficiency of the considered observer based cryptosystem: synchronization of the chaotic systems (transmitter-receiver) is obtained and the message signal is recovered.

I. INTRODUCTION

In recent years, Chua's circuit has become a standard model for studying chaos in systems described by finite-dimensional ordinary differential equations [1].

Synchronization of chaotic Chua's circuit with application to secure communication has also been investigated. However, a classic Chua's circuit is a third-order continuous-time autonomous system which can only produce low-dimensional chaos with one positive Lyapunov exponent.

On the other hand, it has been known that even a very simple first-order system with a time-delay feedback can produce very complex chaotic behaviors [2–5]. Mathematically, continuous-time systems with time-delay feedback can be described by delay differential equations that possess of infinite-dimensional state spaces and have the possibilities of producing high-dimensional hyperchaotic attractors with a large number of positive Lyapunov exponents.

This property has already stimulated the work on both analysis and design, and we have also witnessed a number of physically implemented chaotic time-delay systems for secure communication which claimed to have low detectability [6–7].

Several methods are proposed for chaotic cryptography. Among these methods we can cite *chaotic masking*, *chaotic shif keying*, *chaotic modulation*[8–10].

The communication system used in this work is based on the chaotic time delay feedback Chua circuit to transmit a digital image in a secure way. It consists of two steps: the first one assures the transmitter/receiver synchronization while the second step focuses on the encryption/decryption procedure. The synchronization is performed through a non linear state observer design, driven by the transmitted signal, and the encryption/decryption procedure is ensured by using the chaotic masking method [9–10].

The paper is organized as follows: In section II, we introduce the electronic structure and mathematical model of the time delay Chua's circuit and its chaotic behavior. In section III a non linear state observer is designed for this circuit and performances of the considered observer and the LMI observer approach[11] are compared. Section IV presented some simulations illustrate the efficiency of the considered observer-based cryptosystem: the “Lenna picture” is encrypted, transmitted, and decrypted. Finally, Section V concludes the paper.

II. TIME DELAY CHUA'S CIRCUIT

The chaotic generator consists of the time delay feedback Chua circuit [12] which is shown in figure(1)

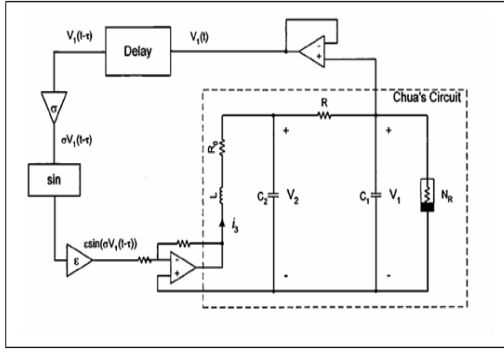


Fig. 1. Time delay feedback Chua circuit

A. Mathematical model

A time delay voltage feedback is added to the nominal Chua circuit. This system is described by the following system:

$$\begin{aligned} \dot{v}_1 &= \frac{1}{c_1} (G(v_2 - v_1) - f(v_1)) \\ \dot{v}_2 &= \frac{1}{c_2} (i_3 + G(v_1 - v_2)) \\ \dot{i}_3 &= -\frac{1}{L} (v_2 + r_0 i_3 + w(v_1(t - \tau))) \end{aligned} \quad (1)$$

Where v_1, v_2 and i_3 are the voltage across c_1 , the voltage across c_2 and the current through L , respectively. $G = \frac{1}{R}$ and

$$f(v_1) = G_b v_1 + \frac{1}{2} (G_a - G_b) (|v_1 + E| - |v_1 - E|) \quad (2)$$

is the v - i characteristic of the non linear resistor.

The time-delay function input is :

$$w(v_1(t - \tau)) = \varepsilon \sin(\sigma v_1(t - \tau)) \quad (3)$$

Where ε and σ are tow positive constants and τ represents the time delay.

B. Chaotic behavior :transmitter key definition

Now, using the mathematical model of the time delay Chua circuit, we study its chaotic behavior, for that some parameters are fixed in order to obtain such dynamics. To do so, we plotted the bifurcation diagram which is used to study the changes in the evolution of the solution's system with respect to changes in a chosen parameter. In this case, we plotted v_1 with the control parameter r_0 , so by varying its value from 1 to 50, keeping the other parameter fixed as following:

$R = 1950; c_1 = 10^{-8}; c_2 = 10^{-7}; L = 18,68.10^{-3}; \sigma = 0,5; \varepsilon = 0,2$ and $\tau = 0,001$

The bifurcation diagram is illustrated in the figure(2)

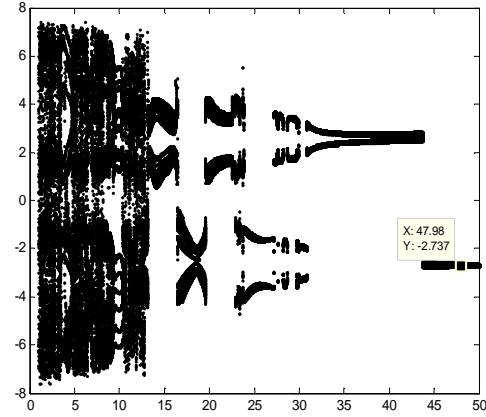


Fig. 2. Bifurcation diagram

As can be seen from the figure (2), the state variable v_1 is stable if r_0 is superior to 47.98, and then, if r_0 is inferior to this value the system dynamics follows usual period doubling rout to chaos.

In this work, we considered the parameter $r_0 = 1.2$ as a cryptosystem secret key (The value of this key is chosen in a way that makes the output behavior of the circuit be chaotic).

III. OBSERVER DESIGN

In this section, we are interested in the design of a nonlinear observer which ensures synchronization with the chaotic generator. In this work we consider the observer described in [13].

The dynamic model of the chaotic generator can be rewritten as:

$$\dot{x} = A \cdot x + B \cdot f(x, x_\tau) \quad (4)$$

With

$$\dot{x} = (\dot{v}_1, \dot{v}_2, \dot{i}_3)^T, A = \begin{pmatrix} -\frac{G}{c_1} & \frac{G}{c_1} & 0 \\ \frac{G}{c_2} & -\frac{G}{c_2} & \frac{1}{c_1} \\ 0 & -\frac{1}{L} & -\frac{r_0}{L} \end{pmatrix}, B = \begin{pmatrix} 1 & 0 \\ 0 & 0 \\ 0 & 1 \end{pmatrix}$$

$$\text{and } f(x, x_\tau) = \begin{pmatrix} -\frac{1}{c_1} f(v_1) \\ -\frac{1}{L} \omega(v_1(t - \tau)) \end{pmatrix}$$

The dynamic model of nonlinear observer is the following:

$$\dot{y} = A \cdot y + B \cdot f(y, y_\tau) + g(s(x, x_\tau) - s(y, y_\tau)) \quad (5)$$

Where $g: \mathbb{R}^2 \rightarrow \mathbb{R}^3$ is a suitably chosen nonlinear function; and $s: \mathbb{R}^3 \rightarrow \mathbb{R}^2$ is the synchronizing signal.

System (4) and (5) are said to be synchronizing, if $e(t) = x(t) - y(t) \xrightarrow{\infty} 0$. (6)

Let

$$s(x, x_\tau) = f(x, x_\tau) + Kx \quad (7)$$

with $K \in \mathbb{R}^{2 \times 3}$, and let :

$$g(s(x, x_\tau) - s(y, y_\tau)) = B(s(x, x_\tau) - s(y, y_\tau)) \quad (8)$$

Then system (6) becomes linear and time-invariant, and can be expressed as:

$$\dot{e} = Ae - BKe = Ae + Bu \quad (9)$$

Where $u = -Ke$ plays the role of a state feedback..

The error dynamic system is controllable if the controllability matrix $m = [B, AB, A^2B]$ is full rank.

In this case, a necessary and sufficient condition for the existence of a feedback gain matrix K such that the error converges to 0 is that all eigenvalues of the matrix $C = [A - BK]$ have negative real parts.

In this work, the chosen matrix m is full rank and we have to sent only one of the states of the time delay feedback Chua circuit to ensure the synchronization of the receiver, if we choose the state v_1 , the structure of the matrix K will be as the following :

$$K = \begin{pmatrix} k_{11} & 0 & 0 \\ k_{21} & 0 & 0 \end{pmatrix}$$

For $k_{11} = -10$ and $k_{21} = -50$, the eigenvalues of the matrix C are $(-45491; -5487 + 3100i; -5487 - 3100i)$; Substitute this matrix K into the observer dynamic and simulated it with Matlab we got the sum of squared errors (SSE) in state estimation as showed in figure(3) witch is shown the rapidity of the SSE convergence to 0 of the consider observer and the MLI method.

In this figure, we can observe that the SSE in the state estimation of three states, using the tow observer approach, is very low and satisfactory and it's clear that the considered nonlinear observer converges more rapidly (in less than 1.3 ms) than the LMI method [11]

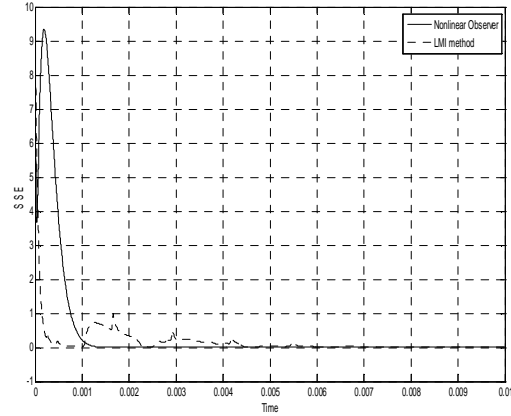


Fig.3. Comparative study: SSE using the tow observer approaches

IV. SECURE COMMUNICATION : IMAGE ENCRYPTION

The faculty of synchronizing the time delay Chua circuit makes the approach described in this paper, suitable for secure digital image transmission using the masking approach.

A. Communication scheme

In this work, we considered the scheme illustrated in figure(4)

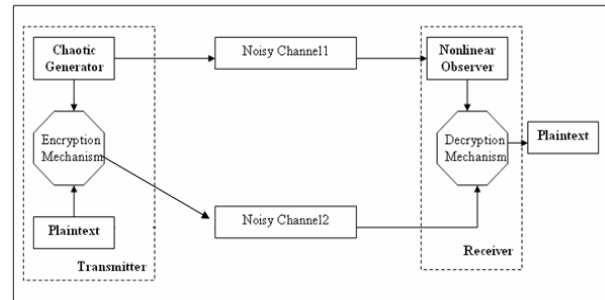


Fig. 4. Proposed communication scheme

In this scheme, the synchronization and the encoding are independent, indeed, two chaotic signals are sent by the transmitter. On the one hand, a first signal is aimed to the synchronization of the receiver. On the other hand, a second signal is used to encrypt the message: the information signal is injected in the second chaotic signal by the encryption mechanism to

create masked message. In order to recover the original signal and enhancing the security of the cryptosystem, the amplitude of the original signal must be small enough (compared with the amplitude of the chaotic signal), so; we choose the chaotic signal as following:

$$s(t) = m(t) + 3(v_1 + v_2) \quad (10)$$

where $m(t)$ is the original message,

After the synchronization step, the receiver recovers the message using the decryption mechanism ensured by the function:

$$\tilde{m}(t) = s(t) - 3(\tilde{v}_1 + \tilde{v}_2) \quad (11)$$

where \tilde{v}_1 and \tilde{v}_2 are given by the dynamic model of the observer.

B. Image encryption/decryption

In this work, we transform the images file on NRZ signal. The result of the encryption using the proposed chaos cryptosystem is illustrated in Figure(5). Figure(5.a) shows the original gray-level image of Lena, Figure(5.b) is the encrypted image and in Figure(5.c) the recovered image is successfully obtained.



Fig. 5. Image secure Transmission : (a) the original image, (b) the encrypted image, (c) the recovered image

V. CONCLUSION

In this paper, the problem of observer based synchronization and secure communication was addressed. We use the chaotic time delay Chua circuit as a transmitter. A first chaotic signal is sent to assure an observer-based synchronization. Then, a second chaotic signal is sent, in which the secret message (the gray-level image of Lena) is masked. For this purpose,

we prove that the considered observer design for synchronization is very low (in less than 1.3 ms) and satisfactory, converges more rapidly than the LMI method and it was successfully used as the receiver (the recovered image is successfully obtained). It is interesting to analyse, in further work, the influence of the noise present in the transmission channel on the deciphering quality in the receiver.

REFERENCES

- [1] L. O. Chua, C.W.Wu, A. Huang, and G.-Q. Zhong, "A universal circuit for studying and generating chaos-part I: Routes to chaos," *IEEE Trans. Circuits Syst. I*, vol. 40, pp. 732–742, Oct. 1993.
- [2] H. Lu and Z. He, "Chaotic behaviors in first-order autonomous continuous-time systems with delay," *IEEE Trans. Circuits Syst. I*, vol. 43, pp. 700–702, 1 1996.
- [3] O. Diekmann, S. A. van Gils, S. M. verduyn Lunel, and H.-O Walther, *Delay Equations: Functional-, Complex-, and Nonlinear Analysis*. Berlin, Germany: Springer-Verlag, 1995.
- [4] K. Ikeda and K. Matsumoto, "High-dimensional chaotic behavior in systems with time-delay feedback," *Physica D*, vol. 29, pp. 223–235, 1987.
- [5] P. Celka, "Delay-differential equations versus 1D-map: Application to chaos control," *Physica D*, vol. 104, no. 1, pp. 127–147, 1997.
- [6] B. Mensour and A. Longtin, "Synchronization of delay-differential equations with application to private communication," *Phys. Lett. A*, vol. 244, no. 1, pp. 59–70, 1998.
- [7] K. Paragas, "Transmission of signals via synchronization of chaotic time-delay systems," *Int. J. Bifurcation Chaos*, vol. 8, no. 5, pp. 1839–1842, 1998.
- [8] T. Yang, A survey of chaotic secure communication systems, *International journal of computational cognition*, Vol.2, N2, pp. 81-130, 2004.
- [9] Kiani-B, K. Fallahi, N. Pariz, H. Leung, A chaotic secure scheme using fractional chaotic systems based on an extended fractional Kalman filter, *Int. J. Communication in Nonlinear Science and Numerical Simulation*, pages 863-879, 2007.
- [10] E. Cherrier, M. Boutayeb, and J. Ragot, *Observers-Based Synchronization and Input Recovery for a Class of Nonlinear Chaotic Models*, *IEEE Trans. Circuits Syst. I*: Vol. 53, No. 9, pp. 1977–1988, Sept 2006
- [11] Zemouche, M. Boutayeb, and G. I. Bara. On observers design for nonlinear time-delay systems. In *2006 American Control Conference ACC'06*, Minneapolis, Minnesota, USA, June 2006.
- [12] Xiao Fan Wang, Guo-Qun Zhong, Kit-Sang Tang, Kim F. Man, and Zhi-Feng Liu, *Generating Chaos in Chua's Circuit via Time-Delay Feedback*, *IEEE Trans. Circuits Syst. I. Fundam Theory Appl.*, Vol. 48, No. 9, September 2001.
- [13] Shu yonglu, Tan Bangding, Lag Synchronization based on Nonlinear observer design for delay system, *IEEE*, pp 1396-1400, 2004.

Communication system with chaotic radiopulses in the real channels

L. V. Kuzmin

Institute of RadioEngineering and Electronics of RAS,
Mokhovaya st., 11/7
125009 Moscow, Russia
Email: lvk@cplire.ru

Abstract—Performance of wireless communication scheme with ultrawideband chaotic radiopulses in realistic channels is evaluated. The channels based on multipath channel models elaborated by IEEE 802.15.4a working group for ultrawideband wireless communication systems are considered. Error probability is numerically estimated and pathloss of chaotic radio pulses propagating over multipath channel are experimentally measured.

I. INTRODUCTION

Chaotic signals as information carriers for communication systems are widely studied theoretically and experimentally since 1990 when a special type of chaotic synchronization was introduced [1]. Further investigations showed low immunity of the chaotic synchronization to channel distortions, that yielded to the development of different modulation schemes improving characteristics of chaos-based systems in real channels, namely differential-chaos-shift-keying [2], chaotic-pulse-position-modulation [3] and direct chaotic communication scheme (DCCS) [4], [5] that was experimentally approved. DCCS means that chaotic signal is generated and modulated in microwave band without intermediate heterodyning. This scheme belongs to wideband or ultrawideband (UWB) communication systems, in which chaotic radiopulses are used as information symbols. It was shown that the performance of DCCS in white noise channel is comparable with the performance of communication systems based on an orthogonal signals. DCCS scheme allows us to design high-bitrate systems [4] as well as low-bitrate ones [5] due to possibility to design effective sources of chaotic signals of microwave band [5].

Recently theoretical DCCS performance was investigated in multipath channels [6] in the presence of significantly dominating multipath interference. The subject of this work is to evaluate the DCCS performance in the presence of additive white noise and multipath

interference, and to experimentally analyze the influence of multipath propagation on the chaotic radio pulses.

II. DCCS STRUCTURE AND CHANNEL MODEL

The schematic of DCCS structure [4] is depicted in the Fig. 1. Basically the DCCS modulator implements “On-Off keying” (OOK) modulation scheme: chaotic radio pulse of length τ_p is emitted to transmit symbol “1” and is not emitted to transmit symbol “0”. Between chaotic radio pulses a guard interval of length τ_g is inserted to prevent intersymbol interference.

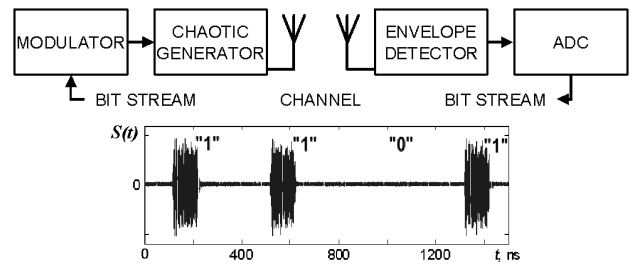


Fig. 1. DCCS structure (top) and chaotic radiopulses emitted to the air to encode symbols “1 1 0 1” (bottom)

The channel model considered here for numerical evaluation of the DCCS performance is based on the UWB multipath channel models adopted by IEEE working group developing an wireless channel models for UWB communications [7]:

$$y(t) = H(t) \otimes s(t) + n(t) \quad (1)$$

where $s(t)$ is a signal emitted by the transmitter to the air; $H(t)$ is a channel impulse-response; symbol \otimes means convolution; $n(t)$ is a additive white noise; $y(t)$ is a signal at the receiver input.

The channel impulse-response $H(t)$ corresponding to some relative position of the transmitter and the receiver, to some geometrical size of an accommodations and to

some indoor layouts is described by the i -th channel realization of response function $h^{(i)}(t)$ to δ -pulse [7]:

$$h^{(i)}(t) = X^{(i)} \sum_{l=0}^L \sum_{k=0}^K \alpha_{k,l}^{(i)} \delta(t - T_l^{(i)} - \tau_{k,l}^{(i)}) \quad (2)$$

$h^{(i)}(t)$ is formed as a sum of paths with statistically distributed amplitudes $\alpha_{k,l}^{(i)}$, cluster $T_l^{(i)}$ and path $\tau_{k,l}^{(i)}$ delays. The value $X^{(i)}$ represents log-normal shadowing.

Channel model (2) was designed on the basis of numerous experimental data and it can be considered as realistic channel model to describe nine different multipath environments: residential (CM1, 2), office (CM3, 4), outdoor (metropolitan suburban CM5,6), industrial (CM7, 8), farm (CM9). Models with odd numbers describe line-of-sight (LOS) case, even numbers correspond to the no-line-of-sight (NLOS) case. These multipath environments are typical for wireless personal area networks, where UWB communication systems are considered as promising applications.

The UWB receiver implemented in the DCCS is based on quadratic envelope detector with non-zero threshold. The receiver output is fed to the analogue-to-digital converter and then it is digitally processed to determine the positions with and without pulses.

Theoretical model of the noncoherent receiver assumes that the envelope detector forms the signal envelope $i(t) = \int_{t-\tau_p}^t y^2(p) dp$ of the chaotic radiopulses that can be expressed as

$$i(t) = e_p(t) + e_{pn}(t) + e_n(t) \quad (3)$$

where $e_p(t) = \int_{t-\tau_p}^t (h^{(i)}(p) \otimes s(p))^2 dp$ is the pulse energy corrupted by multipath; $e_{pn}(t) = 2 \int_{t-\tau_p}^t (h^{(i)}(p) \otimes s(p)) n(p) dp$ is the cross term

that equals to zero in average; and $e_n(t) = \int_{t-\tau_p}^t n^2(p) dp$ is the energy of white noise within pulse position.

It is assumed that symbol synchronization is established between the transmitter and the receiver. The receiver gathers energy within the pulse length τ_p and decides what symbol it receives: "0" or "1" according to the value of $i(t)$ that is compared with the threshold. The minimum error probability is achieved by means of preliminary estimated threshold on the basis of distribution of $i(t)$ for symbols "0" and "1" [4], [5].

III. DCCS PERFORMANCE

Performance characteristics, which are normally considered in wireless communications and we are interested in, are: energy loss of chaotic pulses due to multipath dispersion; bit-error-ratio (BER) as function of the signal-to-noise ratio (the ratio of the energy per bit to the noise spectral density E_b/N_0 for digital communication systems) for the given bitrate, i.e. for given τ_p , τ_g and for signal bandwidth Δf ; and pathloss exponent of UWB chaotic signal. Here the DCCS performance will be governed by the statistical properties of $i(t)$.

We consider the case when the guard interval length is longer than the channel response (Fig. 2a), white noise plays the dominant role at the receiver and the interpulse interference does not take place (Fig. 2b).

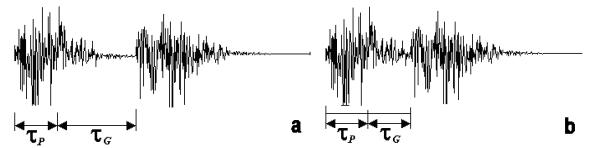


Fig. 2. Results of multipath propagation of two chaotic pulses when the guard interval τ_g is longer (a) and when it is shorter (b) than the channel response

A. Energy loss

The average pulse energy $\langle e_p \rangle$ at the receiver can be estimated as the product of averaged pulse power $\langle P_p \rangle$ by the pulse length $\langle e_p \rangle = \langle P_p \rangle \tau_p$. Due to noncoherent summation of paths the average pulse power is the sum of the path's power with amplitudes $\alpha_{k,l}$, i.e.

$P_p = \sum_{l=0}^{L_p} \sum_{k=0}^{K_p} (\alpha_{k,l}^{(i)})^2$, where L_p and K_p is the number of clusters and paths, respectively, coming in the receiver within the time interval τ_p . L_p and K_p are determined by the multipath channel environment: the smaller channel dispersion, the larger pulse energy coming in the receiver within the time interval τ_p . So, in order to achieve the maximum pulse power P_R , the pulse length τ_p must be matched with the channel impulse-response time. Under the assumption that the channel impulse-response energy is normalized to unity, i.e. $\sum_{l=0}^L \sum_{k=0}^K (\alpha_{k,l}^{(i)})^2 = 1$, the P_R is the estimate of the energy loss due to dispersion. Numerical estimates of this ratio are given in Fig. 3.

As can be seen in Fig. 3, the pulse energy loss rapidly decreases with increasing pulse length. Namely, for the pulse length $\tau_p = 10 ns$, for all channel types the average energy loss is no more than 4 dB. The pulse length $\tau_p =$

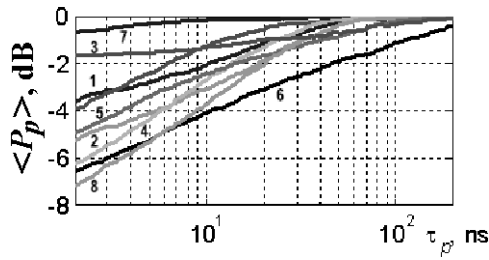


Fig. 3. Loss of the chaotic pulse energy due to multipath dispersion in the channels CM1...CM9

100 ns permits us to decrease the energy loss to 0 dB for all channel types.

B. Error probability

BER is governed by the variance and by the distribution of the pulse energy $i(t)$ corrupted by noise and multipath propagation effects. The pulse energy variance increases due to multipath dispersion and BER will also increase with respect to the BER corresponding to the pure noise channel. To evaluate the BER, direct numerical simulations were carried out.

Simulation results are shown in Fig. 4, where BER (P_b) is depicted versus E_b/N_0 for the following LOS channels: residential (CM1), outdoor (CM5) and farm (CM9). Estimates were obtained for the chaotic pulses of length τ_P equals to 5, 10 20 and 100 ns and the signal bandwidth $\Delta f = 2000$ MHz.

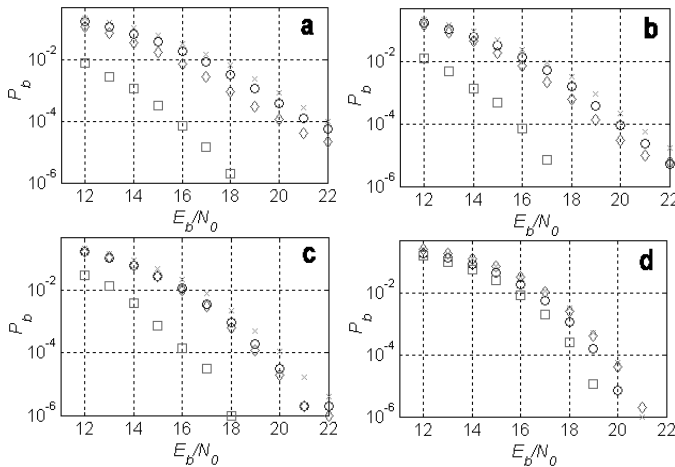


Fig. 4. BER (P_b) vs E_b/N_0 for residential (circle), outdoor (cross), farm (diamond) and AWGN channels (square) for the pulse length τ_P : 5 (a), 10 (b), 20 (c) and 100 ns (d).

As can be seen, if the pulse length τ_P is matched to the length of channel response, i.e. $\tau_p = 100$ ns here, the BER does not differ significantly from the BER for the

noise channel, and DCCS performance is practically the same as in noise channel taking into account that the pulse energy E_p should be corrected according to the loss due to the multipath dispersion (see Fig. 3).

IV. EXPERIMENTAL ESTIMATION OF CHAOTIC RADIO PULSE PROPAGATION

In order to experimentally demonstrate the multipath tails of chaotic radio pulses, to analyze variability of chaotic pulse envelope at the receiver output for different propagation conditions at different distances between the transmitter and the receiver, to evaluate the pathloss exponent of the UWB chaotic signals, we carried out the following experiment.

The scheme of experimental setup is depicted in Fig. 5. It consists of a generator of chaotic radio pulses, a logarithmic UWB receiver and an oscilloscope to record the signal waveforms (Fig. 5, top) for further computer analysis. A transistor oscillator operating in chaotic mode was used as the source of chaotic pulses [5]. The chaotic pulse length is set at $\tau_p = 100$ ns. The guard interval between pulses is $\tau_g = 300$ ns. The chosen guard interval length is enough to prevent interpulse interference. The pulse length value is enough to exclude the influence of the multipath dispersion and to correctly evaluate the pathloss exponent.

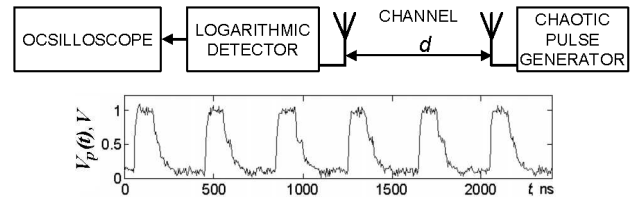


Fig. 5. The scheme of the experimental setup (top) and the envelope of the chaotic pulses at the logarithmic detector output (bottom)

Experiments were carried out in office area: in a corridor (height 4 m, length 40 m, width 3 m) and in a conference hall (length 20 m, height 4 m, width 16 m). The distance d between the transmitter and the receiver was varied from 1 to 20 m in the corridor and from 1 to 14 m in the conference hall. The transmitter and the receiver were located 1 m above the floor in the corridor and 2 m in the conference hall.

The output of the logarithmic detector is proportional to the logarithm of input power of chaotic radiopulses, i.e. $V_P(t) = K \lg(P_P(t)/P_0)$, where $V_P(t)$ is the envelope of the chaotic radiopulses at the detector output, K is the proportion coefficient, $P_P(t)$ is the power of chaotic radiopulses at the detector input and the P_0 is

a reference power value. Logarithmic detector allows to map exponential dynamical range of input power consisting of several orders of magnitude into a linear scale.

Experimental results are depicted in the Fig. 6, where the average envelopes of the chaotic radio pulses for different distances d between the transmitter and the receiver are shown for the corridor (to the left) and for the conference hall (to the right). The average envelopes were obtained by means of averaging envelopes of all pulses shown in Fig. 5b.

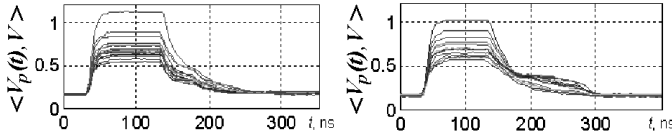


Fig. 6. Average envelopes in the corridor (left) and in the conference hall (right): upper curve corresponds to the minimum distance $d = 1$ m, lower one corresponds to the maximum d

The average envelope waveforms remain similar to each other at all distances between the transmitter and the receiver, which reflects the peculiar properties of the chaotic pulse propagation for the given indoor conditions and indicates good averaging of the power of paths coming to the receiver. It also should be noted that pathloss function shows no signs of small-scale fading-caused notches.

The pathloss P_L was calculated with the use of the average envelopes. The average amplitudes of the pulse envelopes are proportional to the pulse power, so the ratio of the given average envelope amplitudes to the amplitude of the envelope corresponding to $d = 1$ m (upper curves in the both figures) is the pathloss for the given channel.

Calculated pathloss P_L is depicted in Fig. 7, where the pathloss in the corridor and in the conference hall are shown at the left and at the right plots, respectively. Experimental pathloss estimates are rather well approximated by theoretical pathloss law $P_L(d) = -10n \lg(d/d_0)$, where $d_0 = 1$ m and $n = 1.75$ for the corridor and $n = 1.3$ for the conference hall. The obtained pathloss exponent values are close to the corresponding values estimated for LOS channels of IEEE 802.15.4a model [7].

V. CONCLUSIONS

Performance estimation shows that the communication scheme based on chaotic radiopulses is immune to strong

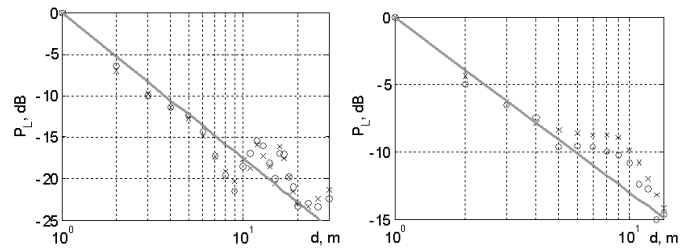


Fig. 7. Pathloss P_L in the corridor (left) and in the conference hall (right). Circles and crosses indicate two different series of measurements.

multipath conditions of signal propagation. Simulations with realistic channel models show that DCCS is suitable for wireless UWB networks operating in complex environments.

ACKNOWLEDGMENT

Authors acknowledge support from the Russian Foundation for Basic Research, grant No. 09-07-92651-IND-a.

REFERENCES

- [1] Pecora L. M., Carroll T. L., "Synchronization in Chaotic systems," *Phys. Rev. Lett.*, Vol. 64, No. 8, 821–824, 1990.
- [2] Kolumban G., Vizvari B., Schwarz W. et al. "Differential chaos shift keying: A robust coding for chaotic communication," *Proc. NDES'96*, Seville, Spain, 87–92, June 27–28 1996.
- [3] Rulkov N. F., Sushchik M. M., Tsimring L. S. et al. "Digital Communication Using Chaotic-Pulse-Position Modulation," *IEEE Trans. on Circuits and Syst.-I*, Vol. 48, No. 12, 1436–1444, 2001.
- [4] Dmitriev A.S., Kyarginsky B.Ye., Panas A.I. et al. Experiments on ultra wideband direct chaotic information transmission in microwave band," *Int. J. Bifurcation and Chaos*, Vol. 13, No 6, 1495, 2003.
- [5] Andreyev Yu. V., Dmitriev A. S., Efremova E. V. et al. "Qualitative theory of dynamical systems, chaos and contemporary communications," *Int. J. Bifurcation and Chaos*, Vol. 15, No 11, 3639–3651, 2005.
- [6] Kuz'min L. V., Morozov V. A. "Statistical Characteristics of an Ensemble of Ultrawideband Communications Channels under the Conditions of Multipath Signal Propagation in Rooms," *J. Communications Technology and Electronics*, Vol. 54, No 3, 313–322, 2009.
- [7] Channel Modeling Sub-committee Report Final. / IEEE P802.15.4a Working Group for Wireless Personal Area Networks (WPANs), Dec. 2004. <http://grouper.ieee.org/groups/802/15/pub/04/15-04-0662-02-004a-channel-model-final-report-r1.pdf>

Generation of the microwave dynamic chaos in ring self-oscillatory system on CMOS structure

Alexander Dmitriev and Elena Efremova

Kotel'nikov Institute of Radio Engineering and Electronics
of RAS,
Mohovaya st., 7-11, Moscow, 125009, Russia
Email: chaos@cplire.ru

Artem Nikishov

Moscow Institute of Physics and Technology,
141700, Institutskii st., 9, Dolgoprudnyi, Moscow
Region, 141700, Russia
Email: nikishov@cplire.ru

Abstract—Ring self-oscillatory system on CMOS structure, capable to generate microwave chaotic signal with uniform power spectral density, is proposed, implemented and investigated. System is realized as an integrated microcircuit on 180 nm CMOS technology process. Generation of chaotic oscillations with a maximum of spectral density in a range of frequencies 2.8 GHz – 3.8 GHz is obtained in experiments with microcircuit.

I. INTRODUCTION

Generation of dynamic chaos in the microwave frequencies range represents an interest for ultrawideband wireless communication systems [1-4]. Last years schemes and methods of calculation of microwave chaotic self-oscillatory systems with the lumped parameters, using transistors as active elements [5-6] have been proposed and developed. On the basis of these results ultrawideband radio- and microwave chaotic oscillators, realized on discrete elements [7-8], are created and experimentally investigated.

However, as it was noted in [9], for mass application of such devices it is necessary to realize them on basis of elements of modern functional electronics — monolithic integrated microcircuits. In the same paper possibility of such devices creation on an example of the Si-Ge-based microwave chaotic oscillator has been shown.

In the given work the microwave chaotic ring self-oscillatory system realized on CMOS-structure is proposed, implemented and investigated.

II. SYSTEM STRUCTURE

Unlike Si-Ge technology where typical active elements is bipolar transistor used in [9], CMOS transistors are used in CMOS technology. Beside this, boundary frequencies of active elements (so also gain

in an applied microwave range) for these two technologies essentially differ. If for Si-Ge technology 0,25 μm boundary frequency is 75 GHz, then it is only 35 GHz for CMOS technologies 0,18 μm . These two circumstances complicate realisation of the basic scheme of the chaotic oscillator with one active element on CMOS structure. Therefore in this work as initial chaotic self-oscillatory system the scheme with three amplifiers closed in a feedback loop [10] has been used.

The block-scheme of the chaotic self-oscillatory system on CMOS structure (fig. 1) consist of three identical two-cascade amplifiers and frequency selective circuit (FSC), closed in a feedback ring.

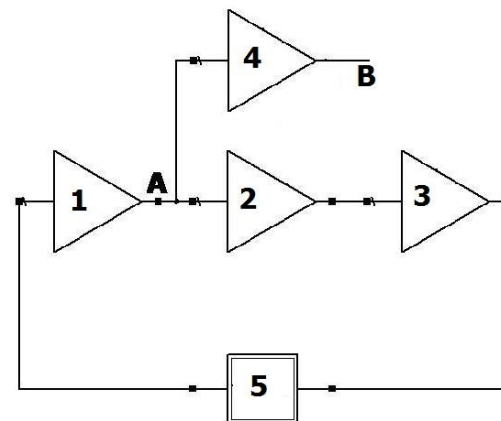


Fig. 1. Block scheme of the system. 1, 2, 3 – amplifiers; 4 – output buffer amplifier; 5 – frequency selective circuit; A –point of signal taken from a feedback ring; B – out

The first cascade of the each amplifier is an inverter (common-source circuit) with negative feedback. The second cascade is a buffer (common-drain circuit). The first cascade amplifies input signal. The second has gain of an order of unit, smaller level

of saturation in comparison with the first cascade and behave as a limiter. FSC (Fig.2), consisting of one RC and two LC sections, together with amplifiers frequency characteristic limits a power spectrum of oscillations to a demanded frequencies range.

Output signal is taken from a chaotic oscillations generation loop through the buffer amplifier.

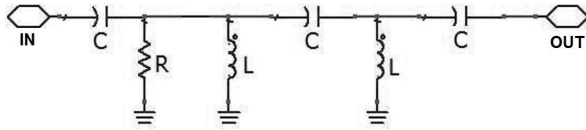


Fig.2. System frequency selective circuit

III. SIMULATION

Proposed system dynamics is investigated by means of considering the following questions: establishment of the fact of chaotic oscillations generation at certain parameters of the system; analysis of oscillations spectral characteristics; studying the bifurcation phenomena; determining the scenario of the chaotic oscillations evolution.

For simulation of the system, its model based on active and passive elements of the 180 nm CMOS technology process was designed according to block-scheme represented on the Figure 1.

Modelling was made in engineering package Advanced Design System (ADS).

As an observable variable signal voltage $U(t)$ on the system out (point B on the Fig. 1) was used.

An analysis of spectral characteristics of the model has shown that for the chosen values of system parameters at different supply voltage various oscillation modes, including chaotic, are observed. Single-frequency mode of oscillations is observed at a frequency close to 4 GHz when system amplifiers supply voltage is $U_a = 1.4$ V. The supply voltage increase up to $U_a = 1.5$ V leads to excitation of oscillations on the second frequency about 1 GHz. Then amplitudes of the double-frequency oscillation subharmonics become more intensive and, at last, oscillations become chaotic at $U_a = 1.8$ V (Fig. 3).

Evolution of oscillations is summarised on the single-parameter bifurcation diagram of oscillations modes (Fig. 4). Along axis U maximums of signal $U(t)$ are placed on given diagram at the adiabatic slow change of parameter U_a .

As follows from the diagram analysis, single-mode oscillations are excited at first time, when

supply voltage is sufficiently small. Then supply voltage increase leads to excitation of double-frequency oscillations mode and invariant torus is formed in oscillations phase space. The further voltage increase leads to structural reorganization of the resonances on the torus which finally comes to its subsequent destruction and transition to chaos. Such structural reorganization of the resonances is reflected in an increase of the number of oscillations spectral components.

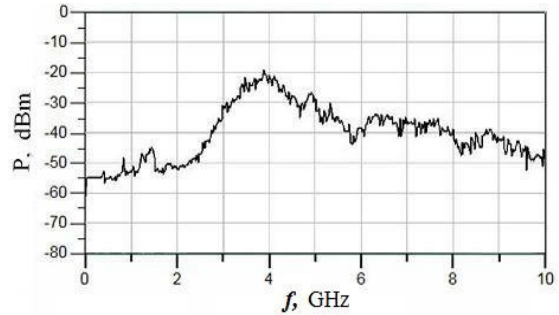


Fig.3. Chaotic oscillations power spectral density (modeling)

From the diagram, in particular, it is visible that zone of chaotic oscillations covers at least a range of supply voltage change from 1.8 V to 2.0 V that testifies to enough high stability of chaotic oscillations mode to change of this parameter.

Thus, chaotic oscillations are excited on the basis of double-frequency oscillations mode destruction. The described process illustrates a general principle of chaotic oscillations generation in proposed self-oscillatory system. Frequency range and bandwidth of the generated oscillations utterly corresponds to those of amplifiers used and the cutoff frequency of the FSC.

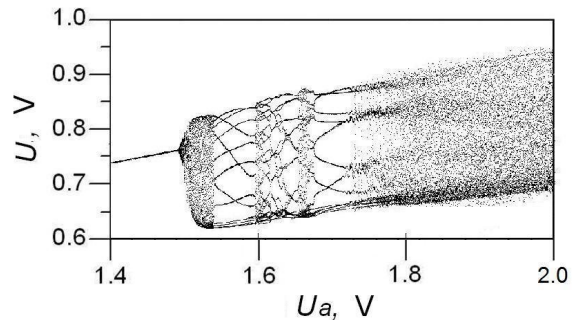


Fig.4. Single-parameter bifurcation diagram of oscillation modes. U_a – supply voltage, U – maxima of $U(t)$ signal

Possibility of double-frequency oscillations mode in the system is explained by the following circumstance. As follows from the phase-frequency response, represented on the figure 5, in the range from 0 to 10 GHz two frequencies have phase incursion $2\pi n$, where n is an integer. According to Nyquist-Mihaylov criterion, self-sustaining oscillations can excite on each of these frequencies in case the amplitude balance is fulfilled (feedback loop gain is above unit).

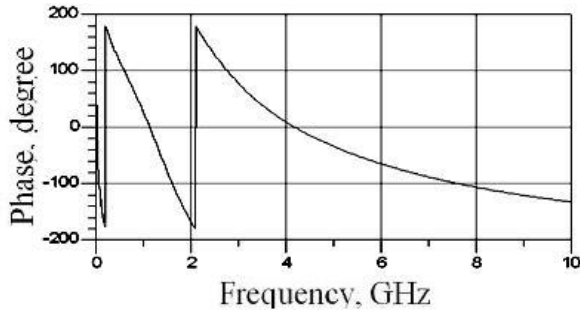


Fig.5. Phase frequency response of the system feedback loop

Analysis of the amplitude-frequency response shows that at supply voltage 1.4 V the feedback loop gain becomes more than unity at a frequency close to 4 GHz. So, at this frequency a first self-sustaining oscillation mode appears. Then, at supply voltage 1.5 V, the feedback loop gain becomes more than unity at both frequencies: close to 4 GHz and 1 GHz. So, self-sustaining oscillations are possible on these two frequencies.

According to the simulations results the basic power of the oscillations contains in the frequency band from 3.6 to 4.6 GHz and it is about -4 dBm. Consumed current is 25 mA at 1.8 voltage supply.

IV. EXPERIMENT

Using positive simulation results, an experimental realization of the proposed ring self-oscillatory system as an integrated CMOS microcircuit was made. Microcircuit topology size is about $0.8 \times 0.9 \text{ mm}^2$ (microcircuit in QFN package represented in the Figure 6). Frequency modes were adjusted by varying supply voltage in the range from 0 V to 3.5 V.

Self-oscillatory system on CMOS technology $0.18 \text{ }\mu\text{m}$ was implemented in software package Cadence IC. Possibility of its use for the analysis of systems with chaotic dynamics has been established in [9].

For experiments the microcircuit of the system was located in center of the QFN plastic package, and dice output pads are connected with package pads through slices of thin wires.

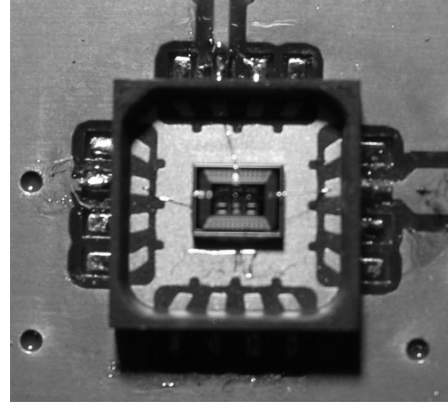


Fig.6. Microcircuit in QFN package.

Experimental investigation showed that single-mode oscillations excite at the frequency close to 3.2 GHz at supply voltage 1.5 V. With an increase of supply voltage to 1.7 V double-frequency oscillations mode appear (second frequency is about 600 MHz). Then amplitudes of the double-frequency oscillation subharmonics become more intensive and at supply voltage about 2.2V chaotic (Fig. 7) oscillations with uniform power-density spectrum and integrated power of about -6 dBm occur in the frequency band 2.8 - 3.8 GHz.

And you can see that experimental results are very close with results of modeling.

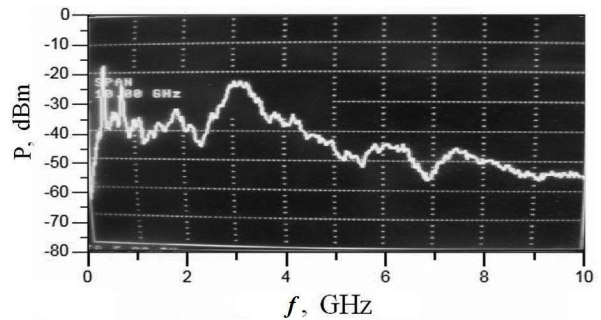


Fig.7. Chaotic oscillations power spectral density (experiment).

V. CONCLUSION

In the report microwave chaotic ring self-oscillatory system on CMOS structure capable to generate ultrawideband microwave chaotic signal

with uniform power spectral density, is proposed, implemented and investigated. The basic result of research is realization of system as an integrated microcircuit on technology 180 nm with the topology area less than 1 mm² and its activity demonstration in experiment.

Experimental realization of the device has confirmed simulation results. Chaotic oscillations have uniform power spectral density in frequency band from 2.8 GHz to 3.8 GHz and integrated output power reaches about -6 dBm.

It is possible to draw following conclusions by the results of simulations and experimental researches.

At first, oscillation modes which were observed in experiment qualitatively identical to oscillation modes which were observed at simulation. It means that theoretical conclusions about bifurcation phenomena based on the simulation are experimentally proved.

At second, chaotic oscillations are really excited on the basis of mechanism of double-frequency oscillations mode destruction.

Quantitative discrepancies between model and experiment are certainly observed. However it is explained by technological errors arising at microcircuits fabrication. But at simulations this errors were not considered because qualitative acknowledgements of theoretical assumptions (the scientific component) was important.

Thus, proposed microwave chaotic ring self-oscillatory system on CMOS structure can be used in different wireless communication applications as a compact device for UWB microwave chaotic signal generation.

ACKNOWLEDGMENT

This report is supported in part by the RFBR grant No. 09-02-00983-a and Russian Federation president grant for the state support of young Russian scientists No. MD-4131.2009.9.

REFERENCES

- [1] A.S. Dmitriev, B.E. Kyarginskii, N.A. Maksimov, et al., Radiotekhnika, No. 3, 9 (2000).
- [2] *Spec. Is.* on applications of nonlinear dynamics to electronic and information engineering // Proc. IEEE. 2002. V. 90. N 5.
- [3] A.S. Dmitriev and A.I. Panas, Dynamical Chaos: New Information Media for Communication Systems (Fizmatlit, Moscow, 2002) [in Russian].
- [4] *Mishagin K.G., Matrosov V.V., Shalfeev V.D. and etc.// Pis'ma v Zhurnal Tekhnicheskoi Fiziki, 2005, Vol. 31, No. 24, pp. 31–38.*
- [5] Dmitriev A.S., Panas A.I., Starkov S.O. // Int. J. of Bifurcation and Chaos. 1996. V. 6. N 5. P. 851–865.
- [6] A.S. Dmitriev and E.V. Efremova, Radiotekhnika, No. 8, 67 (2005).
- [7] E.V. Efremova, N.V. Atanov, and Yu.A. Dmitriev, Izv. Vyssh. Ucheb. Zaved., Priklad. Nelin. Dinam. 15, 23 (2007).
- [8] A.S. Dmitriev, E.V. Efremova, N.A. Maksimov, and E.V. Grigor'ev, Radiotekh. i elektron. (Moscow) 52, 1232 (2007) [J. Comm. Technol. Electron. 52, 1137 (2007)].
- [9] A.S. Dmitriev, E.V. Efremova and A. Yu. Nikishov// Technical Physics Letters. Volume 35, Number 12. pp. 1090-1092.
- [10] Nickishov A.Yu., Panas A.I., *Uspehi sovremennoy radioelektroniki*, 2008, 1. pp. 54–62. (In Russian).

INFLUENCE OF ELECTRON VELOCITY DISPERSION ON DYNAMICS OF ELECTRON BEAM WITH VIRTUAL CATHODE

S.A. Kurkin, A.E. Hramov, A.A. Koronovskii

Faculty of Nonlinear Processes, Saratov State University,
83, Astrakhanskaya, Saratov, 410012, Russia

e-mail: kurkinsa@gmail.com, hramovae@gmail.com, alexey.koronovskii@gmail.com

WWW: <http://nonlin.sgu.ru/>

Abstract—*The results of numerical study of initial electron velocity dispersion (external noise) influence on nonlinear dynamics of the electron beam with a virtual cathode and on the output characteristics of microwave devices based on electron beam with the virtual cathode (low-voltage vircators) are presented. It was discovered that the growth of initial electron velocity dispersion (the increase of the noise power) causes the suppression of virtual cathode oscillations in the system and hence the breaking of generation in the devices with the virtual cathode. It were obtained the character dependencies of spectra and output power of vircator radiation on the value of initial electron velocity dispersion.*

I. INTRODUCTION

A study of the microwave generators with a virtual cathode (vircators) is an important and actual application of nonlinear dynamics to modern problems of microwave electronics and telecommunications [1, 2]. The significance of such researches is determined by the distinctive features of vircators. Generators with the virtual cathode (VC) are characterized by a high output power, a simple construction (particularly vircators can operate without external focusing magnetic field), a possibility of a simple frequency tuning and regime switching. Therefore, vircators can be used as perspective controlled sources of microwave chaotic radiation. Such sources have wide application in modern devices for electronic system of information transmission based on the ideas of dynamical chaos [3, 4], noise radiolocation [5], non-linear antennas [6], etc.

The analysis of nonlinear oscillation processes in spatially extended systems with intensive beams of charged particles in the regimes of VC formation attracts great attention of scientific community [2, 7, 8]. It is well known [2, 7–9] that the systems with VC are characterized by the complex dynamics and can demonstrate a wide range of nonlinear phenomena, including dynamical chaos. Among the different elec-

tronic systems with VC the special interest is caused by the low-voltage vircator, in which the additional braking of the electron beam is used for to form VC [8]. In such systems VC may be formed in the non-relativistic electron beams with low current and low space charge density. As consequence, such compact non-relativistic electron systems may demonstrate periodic, narrow-band and wideband chaotic microwave oscillations.

It is well known that an initial velocity and angular distribution of injected electrons have a significant influence on the processes in the intensive electron beams with VC. Let us note, that the initial velocity dispersion can be considered as external noise effected on the chaotic oscillations of spatially extended system with VC. For example, the characteristics of chaotic oscillations in the traveling-wave tube (TWT) with collector-oscillator with VC are found to be determined by a value of the velocity dispersion of injected electrons [10]. This fact was used to improve the characteristics of the output radiation in the collector-generator system [11]. The experimental and theoretical studies of the influence of the electron velocity distribution on the chaotic oscillations in the electron beam in the regime of the VC formation were carried out in [12], with results showing a strong dependency of output characteristics of systems with VC on the noise characteristics. The theoretical results in this work were obtained by means of 1D numerical model. However, it is necessary often to take into account 2D effects in such systems [13–15]. At the present time there is a lot of results concerning the influence of the electron velocity dispersion on the characteristics of VC oscillations, but the systematic studies of such problem have not been carried out yet. An understanding of the noise influence on the electron beam with VC can make progress in the researches of the nonlinear dynamics of electronic systems and, as a consequence, in the development of the chaotic generators based on VC oscillations.

The present report deals with the theoretical numerical research of the influence of initial electron dispersion on output characteristics of radiation in the low-voltage vircator.

II. THEORETICAL STUDY OF LOW-VOLTAGE VIRCATOR WITH INITIAL ELECTRON DISPERSION

A. System under study and mathematical model

The typical scheme of the low-voltage vircator is presented in Fig. 1a. The generator consists of the electron-optical system 1-3 forming solid axially-cylindrical beam 4, drift space between grids 5 and 6, absorber 7, wideband microwave slow-wave system 8 (spiral system), microwave power output 9 and collector 10 for exhausted electrons of the beam. Oscillations in the system are generated by VC formed in the space between grids 5 and 6 due to the decelerating potential V_t putted on the output grid 6. The external axial magnetic field in the space between grids 5 and 6 is formed usually by the magnetic periodical focusing system (MPFS). The dimensionless parameter B is proportional to the external magnetic field amplitude on the symmetry axis of the drift space.

We have considered a time-dependent 2.5D model in which the dynamics of the electron beam in the drift space is described by a self-consistent set of Vlasov and Poisson equations [17]. The Vlasov kinetic equation for the electron beam motion analysis is solved numerically by the particle method [16]. In the cylindrical geometry the particles have the form of charged rings. In terms of dimensionless values (see, for example, [13]), the equations of motion in cylindrical coordinates for each particle are written as

$$\frac{dP_{ri}}{dt} - \gamma(z_i, \theta_i, r_i) r_i \left(\frac{d\theta_i}{dt} \right)^2 = -E_r - r_i B_z \frac{d\theta_i}{dt}, \quad (1)$$

$$\frac{dP_{\theta i}}{dt} + \gamma(z_i, \theta_i, r_i) \frac{dr_i}{dt} \frac{d\theta_i}{dt} = B_z \frac{dr_i}{dt} - B_r \frac{dz_i}{dt}, \quad (2)$$

$$\frac{dP_{zi}}{dt} = -E_z + r_i B_r \frac{d\theta_i}{dt}, \quad i = 1, \dots, N_0, \quad (3)$$

where $\gamma(z_i, \theta_i, r_i)$ is the relativistic factor. Here, z_i , r_i , and θ_i are the longitudinal, radial, and azimuthal dimensionless coordinates of the charged particles, $P_{zi} = \gamma \dot{z}_i$, $P_{ri} = \gamma \dot{r}_i$, $P_{\theta i} = \gamma r_i \dot{\theta}_i$ are longitudinal, radial, and azimuthal components of particles impulses, E_z and E_r are the longitudinal and radial electric field components, $B_z(z, r)$ and $B_r(z, r)$ are the longitudinal and radial components of the external magnetic field in the interaction space, $\beta_0 = v_0/c$,

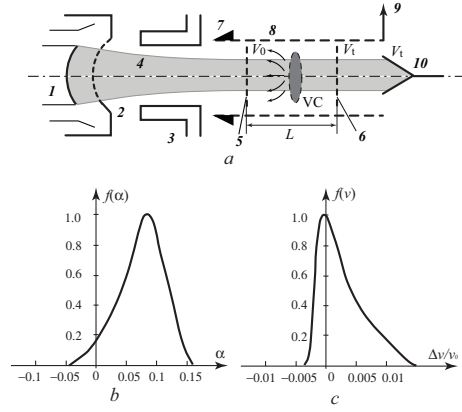


Fig. 1. (a) The scheme of the low-voltage vircator: (1) the cathode, (2) the grid, (3) the second anode of the electron gun, (4) the electron beam, (5) the input grid of the diode with accelerating potential V_0 , (6) the output grid of the diode gap with potential V_t , (7) the absorber, (8) the power output, (9) the energy output, and (10) the collector with potential V_t ; (b) and (c) the typical electron angular $f(\alpha)$ (b) and velocity $f(v)$ (b) distributions for the electron gun working in the regime of the temperature limiting of the current

where v_0 is the electron beam longitudinal velocity at the entrance of the system and c is the light speed. The fields do not have the azimuthal components due to the axial symmetry of the system. The subscript i denotes the number of the particle and N_0 is the full number of the particles used to model the charged particles beam. The initial conditions for the motion equations in the case of the initial electron dispersion absent are:

$$\dot{z}_i = v_0, \quad \dot{r}_i = 0, \quad \dot{\theta}_i = B_z(z_i, 0)/(2\gamma). \quad (4)$$

The second initial condition in (6) is determined by Busch's theorem.

The potential distribution in the interaction space was calculated self-consistently from Poisson's equation

$$\frac{1}{r} \frac{d\varphi}{dr} + \frac{d^2\varphi}{dr^2} + \frac{d^2\varphi}{dz^2} = \alpha^2 \rho, \quad (5)$$

where $\alpha = L\sqrt{|\rho_0|/V_0\epsilon_0}$ is the dimensionless control parameter which depends on the beam current as $\alpha \sim \sqrt{I}$ and is proportional to the length of the drift tube space as $\alpha \sim L$. Here V_0 is an accelerating potential. Poisson's equation (5) was solved with the standard boundary conditions $\varphi(z=0, r) = 0$, $\varphi(z=1, r) = 0$, $\varphi(z, r=R) = 0$, $\frac{d\varphi}{dr}\bigg|_{r=0} = 0$.

To model the wideband microwave power output the equivalent circuit method [18] is used.

To study physical processes in the low-voltage vircator taking into account the initial electron dispersion

we have considered the following model. The electrons of the axially symmetrical beam having the initial velocity and angular distributions are injected to the drift space. The velocity $f(\tilde{v})$ and angular $f(\tilde{\alpha})$ distributions of the injected electrons correspond to the experimentally ones reported in the work [12]. These distributions are characterized by the probability densities shown in Fig. 1b,c with dispersion values σ_α and σ_v , respectively. Note, that $\sigma_v = 0.01$ corresponds to the dispersion of the velocity distribution equals to 1%, and $\sigma_\alpha = 0.01$ – to dispersion of angular distribution equals to 0.01 radian.

The initial conditions for the motion equations of the large particles are the following:

$$\dot{z}_i = (v_0 + \tilde{v})\cos(\tilde{\alpha}), \quad \dot{r}_i = \tilde{v}\sin(\tilde{\alpha}). \quad (6)$$

These conditions specify the axial and radial initial velocities of the injected particles, respectively, while the noise processes, $\tilde{\alpha}$ and \tilde{v} , being determined by the distributions $f(\tilde{\alpha})$ and $f(\tilde{v})$.

B. Results of numerical study of nonlinear dynamics

The numerical simulation of the processes in the electron beam with VC in the low-voltage vircator has shown that the dynamics and characteristics of the output radiation of the low-voltage vircator are rather complex and depend on the values of the velocity and angular distributions of the injected electrons. The power spectra of the output radiation in the system obtained by means of the numerical simulation for the different values of the dispersion of electron velocity distribution σ_v and for the fixed value of dispersion of electron angular distribution $\sigma_\alpha = 0.016$ are presented in Fig. 2. As the dispersion σ_v increases, the output power spectrum is transformed considerably. The discrete power spectrum with a few fundamental harmonics and a noise pedestal around them corresponds to the small value of the velocity dispersion (Fig. 2a). With the growth of the dispersion σ_v the amplitude of the fundamental harmonics in the output power spectrum decreases (Fig. 2b). Finally, when the velocity dispersion reaches the critical value, the fundamental harmonics vanish completely, and the output power spectrum demonstrates only the noise pedestal (Fig. 2c). So, the presence of the considerable initial velocity dispersion in the low-voltage vircator (about 2.6%) leads to the suppression of the VC oscillations in the system and to the break of regular generation. It has been also obtained that the growth of the initial angular dispersion σ_α in the low-voltage vircator with the fixed value of velocity dispersion σ_v leads to the similar result.

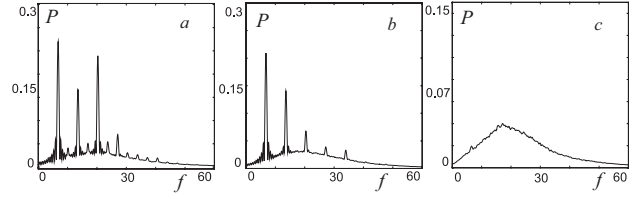


Fig. 2. Dimensionless output power spectra in the low-voltage vircator for $\alpha = 20$, $B = 7$, $\sigma_\alpha = 0.016$, $\sigma_v = 0.7\%$ (a), $\sigma_v = 1.3\%$ (b) and $\sigma_v = 2.6\%$ (c)

C. Microwave power of the generator

Let us consider now the dependence of the VC oscillation power in the low-voltage vircator on the value of the dispersion of electron velocity distribution σ_v . In Fig. 3 these dependencies are shown for the different parameters of the external magnetic field K (Fig. 3a) and beam currents α (Fig. 3b). All curves demonstrate the similar behavior. The output power of the generator decreases monotonously with the growth of the dispersion σ_v approaching asymptotically the constant value for any external magnetic field and beam current values (Fig. 3). The constant value of the output power of the low-voltage vircator corresponds to the power of noise generation of the device with suppressed VC oscillations (see Fig. 2c). There are the critical values of the velocity dispersion σ_v for the dependencies of the output power in Fig. 3, when the regular VC oscillations in the device are completely suppressed, with the power having reached the saturation point. The output power spectrum in Fig. 2c with no fundamental harmonics corresponds to this case. In this regime the low-voltage vircator can be used as the source of microwave noise-type signals. So, the decrease of the output power of the generator with the growth of the initial velocity dispersion σ_v is determined by the suppression of the VC oscillations in the system.

D. Physical processes

Finally, we consider the physical processes leading to the described behavior of the system and the suppression of the VC oscillations in the low-voltage vircator with the growth of the velocity or angular dispersion of the injected electrons. The analysis of the space-time diagrams of the electron beam in the system under study has shown that the suppression of the VC oscillations with the growth of initial electron dispersion is determined by the break of the main electron structure (VC) in the beam. When the initial dispersion is small, a non-stationary VC is formed in the system. It reflects periodically a part of electron

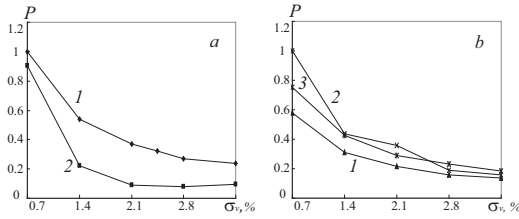


Fig. 3. Normalized dependencies of the output power of the low-voltage vircator on the value of the dispersion of the electron velocity distribution σ_v for $\sigma_\alpha = 0.016$, $a = 20$, $B = 7$ and $B = 40$ (a, curves 1 and 2 respectively) and $B = 7$, $a = 20$, $a = 25$ and $a = 30$ (b, curves 1, 2 and 3, respectively)

beam back to the injection plane, so the dynamics of VC leads to the regular density modulation of the reflected and passed parts of the electron beam. The character period of the VC oscillations in the system determines the fundamental harmonics in the output power spectrum (Fig. 2a) of the generator. The presence of the noise pedestal in the spectrum of output radiation is a consequence of a complex non-regular dynamics of electrons in the VC area and the initial dispersion of the injected electrons. When the initial dispersion exceeds the critical value the structure of VC in the electron beam is broken, because electrons in the system have large initial random velocity components. Consequently, the spectrum of output radiation demonstrates only the noise pedestal without fundamental spectral harmonics of VC the oscillations.

III. CONCLUSIONS

In conclusion, we have analyzed numerically the nonlinear dynamics and physical processes in the low-voltage system with VC with initial dispersion of injected electrons. We have discovered the considerable influence of the dispersion value on the nonlinear dynamics of VC and the output characteristics of the low-voltage vircator. The character dependencies of the output power of the generator on the initial dispersion of the injected electrons have been obtained. It was discovered that the increase of the initial velocity or angular dispersion of electrons leads to the suppression of the VC oscillations in the system and, hence, to the decrease of the output power of the generator.

This work has been supported by Russian Foundation for Basic Research (project 09-02-00255-a, 10-02-90432) and Federal special-purpose program "Scientific and educational personnel of innovation Russia" (2009-2013).

REFERENCES

- [1] V. L. Granatstein and I. Alexeff, *High Power Microwave Sources*, Artech House Microwave Library, 1987.
- [2] V. D. Alyokhin, A. E. Dubinov, V. D. Selemir et al., "Theoretical and experimental studies of virtual cathode microwave devices," *IEEE Trans. Plasma Sci.*, vol. 22, no. 5, pp. 954, 1994.
- [3] A. S. Dmitriev and A. I. Panas, *Dynamic chaos: novel type of information carrier for communication systems*, Fizmatlit, Moscow, 2002.
- [4] A. A. Koronovskii, O. I. Moskalenko, and A. E. Hramov, "On the use of chaotic synchronization for secure communication," *Physics-Uspekhi*, vol. 52, no. 12, 2009.
- [5] R. M. Narayanan and M. Dawood, "Doppler estimation using a coherent ultrawide-band random noise radar," *IEEE Trans. Antennas and Propagation*, vol. 48, pp. 868, 2000.
- [6] B.K. Meadows, T. H. Heath, J.D. Neff, et al., "Nonlinear antenna technology," *Proc. IEEE*, vol. 90, pp. 882–897, 2002.
- [7] A.E. Dubinov and V.D. Selemir, "Electronic devices with virtual cathodes (review)," *J. Commun. Techn. and Electronics*, vol. 47, pp. 575, 2002.
- [8] Yu. Kalinin, A. Koronovskii, A. Hramov, et al., "Experimental and theoretical investigations of stochastic oscillatory phenomena in a nonrelativistic electron beam with a virtual cathode," *Plasma Phys. Rep.*, vol. 31, pp. 938–952, 2005.
- [9] V. G. Anfinogentov and A. E. Hramov, "On the mechanism of occurrence of chaotic dynamics in a vacuum microwave generator with virtual cathode," *Radiophysics and Quantum Electronics*, vol. 41, no. 9, pp. 1137, 1998.
- [10] Yu.A. Kalinin, A.V. Mushtakov, and A.E. Hramov, "Studying chaotic microwave oscillations in a two with depressed collector," *Tech. Phys. Lett.*, vol. 33, pp. 655–657, 2007.
- [11] Yu.A. Kalinin, A. A. Koronovskii, and A. E. Hramov, "Chaotic wideband microwave oscillations in a hybrid system consisting of a traveling wave tube and a collector oscillator," *Tech. Physics*, vol. 53, no. 5, pp. 614–619, 2008.
- [12] Yu.A. Kalinin and A. E. Hramov, "Experimental and theoretical investigation into the effect of the electron velocity distribution on chaotic oscillations in an electron beam under virtual cathode formation conditions," *Tech. Physics*, vol. 51, no. 5, pp. 558–566, 2006.
- [13] A. E. Hramov, A. A. Koronovskii, M.Yu. Morozov, et al., "Effect of external magnetic field on critical current for the onset of virtual cathode oscillations in relativistic electron beams," *Phys. Lett. A*, vol. 372, pp. 876–883, 2008.
- [14] S. Gursharn and C. Shashank, "Secondary virtual-cathode formation in a low-voltage vircator," *IEEE Trans. on Plasma Sci.*, vol. 36, no. 3, pp. 694–700, June 2008.
- [15] S. A. Kurkin, A. E. Hramov, and A. A. Koronovskii, "Nonlinear dynamics and chaotization of virtual cathode oscillations in annular electron beam in uniform magnetic field," *Plasma Phys. Report*, vol. 35, no. 8, pp. 628–642, 2009.
- [16] C. K. Birdsall and A. B. Langdon, *Plasma physics, via computer simulation*, NY: McGraw-Hill, 1985.
- [17] T. M. Anderson, A. A. Mondelli, B. Levush, et al. "Advances in modelling and simulation of vacuum electron devices," *Proc. IEEE*, vol. 87, no. 5, pp. 804–839, 1999.
- [18] E. N. Egorov, Yu.A. Kalinin, A. A. Koronovskii, and A. E. Hramov, "Analysis of the dependence of the microwave generation power of a low-voltage vircator on controlling parameters," *Tech. Phys.*, vol. 52, no. 10, pp. 1387, 2007.

Observer Based Measurement of the Adenosine Diphosphate Concentration in Multimodal Oscillatory Pancreatic β -Cells

Klaus Röbenack

Institut für Regelungs- und Steuerungstheorie, Fakultät Elektrotechnik und Informationstechnik,
Technische Universität Dresden, D-01062 Dresden, Germany
Email: klaus.roebenack@tu-dresden.de

Abstract—Up to now, the concentration of adenosine diphosphate in a living pancreatic cell cannot be measured in real-time. However, these cells generate bursts of electrical activity. We use an electro-physiological model of the cell to derive an observer based estimation scheme using voltage measurement.

Index Terms—Nonlinear systems, multimodal oscillations, observer design, estimation.

I. INTRODUCTION

Insulin is secreted from pancreatic islets. For a better understanding of the mechanism behind the insulin secretion we study pancreatic β -cells. This is important to understand the development of type 2 diabetes.

Pancreatic cells show electric activity in term of multimodal oscillations. These oscillations are influenced by the concentrations of certain ions. In this context, one important substance is adenosine diphosphate. The real-time measurement of its concentration is practically not feasible. We use an well-accepted highly nonlinear electro-physiological model of pancreatic cells to derive an observer based estimation scheme. This paper extends the filter based approaches given in [1], [2].

The paper is structured as follows. In Section II we describe the electro-physiological model of pancreatic β -cells. This model is used in Section III to derive an estimation scheme. We draw some conclusions in Section IV.

II. CELL MODEL

Many cells can be modeled using the formalism derived by Hodgkin and Huxley [3]. A simple model describing the oscillations of pancreatic β -cells is given in [4]. We use the more complicated model developed in [5]. This model takes certain slow oscillation patterns (in the time range of seconds up to minutes) into account. In addition to ion channel and calcium dynamics, the

model in [5] also considers the ratio of adenosine diphosphate (ADP) to adenosine triphosphate (ATP) and the concentrations of the glycolytic intermediates, glucose 6-phosphate (G6P) and fructose 1,6-bisphosphate (FBP).

The membrane voltage V results from the differential equation

$$C_m \dot{V} = -I_K - I_{Ca} - I_{K(Ca)} - I_{K(ATP)} \quad (1)$$

with the membrane capacitance $C_m = 5300$ fF. The currents I_K and I_{Ca} are caused by K^+ potassium and Ca^{2+} calcium ions, respectively. The currents $I_{K(Ca)}$ and $I_{K(ATP)}$ are related to Ca and ADP sensitive K^+ ions. The ionic currents are given by

$$\begin{aligned} I_K &= g_K n (V - V_K) \\ I_{Ca} &= g_{Ca} m_\infty(V) (V - V_{Ca}) \\ I_{K(Ca)} &= g_{K(Ca)} \frac{Ca^2}{K_D^2 + Ca^2} (V - V_K) \\ I_{K(ATP)} &= g_{K(ATP)} o_\infty(ADP) (V - V_K) \end{aligned} \quad (2)$$

with the conductances $g_K = 2700$ pS, $g_{Ca} = 1000$ pS, the reversal potentials $V_K = -75$ mV, $V_{Ca} = 25$ mV, the calcium concentration Ca and the constant $K_D = 0.5 \mu M$. The activation variable n for the K^+ current I_K is governed by

$$\dot{n} = \frac{1}{\tau_n} (n_\infty(V) - n), \quad (3)$$

with the time constant $\tau_n = 20$ ms and the function

$$n_\infty(V) = \frac{1}{1 + e^{-(16+V)/5}},$$

where the voltage V is in mV. The function m_∞ defined by

$$m_\infty(V) = \frac{1}{1 + e^{-(20+V)/12}}.$$

can be interpreted as an activation variable of the Ca^{2+} current I_{Ca} . Similarly, o_∞ occurring in (2) is the activation variable of the current $I_{K(ATP)}$. The equivalent

circuit representation of model (1),(2) is shown in Fig. 1.

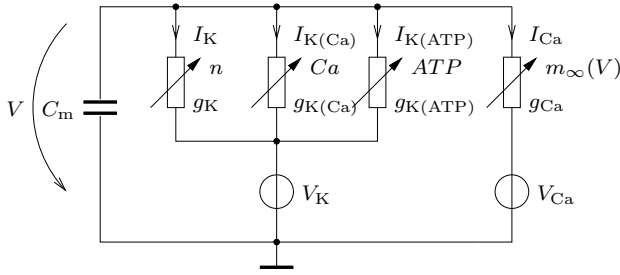


Fig. 1. Equivalent circuit representation of model (1),(2)

The calcium concentration Ca is modeled by the differential equation

$$\dot{Ca} = f_{\text{cyt}} (-\alpha I_{Ca} - k_{\text{PMCA}} Ca + J_{\text{er}}) \quad (4)$$

with the dimensionless constant $f_{\text{cyt}} = 0.01$. The constant $\alpha = 4.5 \times 10^{-6} \text{ fA}^{-1} \mu\text{Mms}^{-1}$ converts the current I_{Ca} to the Ca^{2+} flux and $k_{\text{PMCA}} = 0.2 \text{ ms}^{-1}$ is the calcium pump rate. The Ca^{2+} flux out of the endoplasmic reticulum is given by

$$J_{\text{er}} = p_{\text{leak}} (Ca_{\text{er}} - Ca) - k_{\text{SERCA}} Ca$$

with the leakage permeability $p_{\text{leak}} = 0.0002 \text{ ms}^{-1}$ and another pump rate $k_{\text{SERCA}} = 0.4 \text{ ms}^{-1}$. The calcium concentration Ca_{er} in the endoplasmic reticulum is modeled by the differential equation

$$\dot{Ca}_{\text{er}} = -f_{\text{er}} (V_{\text{cyt}}/V_{\text{er}}) J_{\text{er}} \quad (5)$$

with the constant $f_{\text{er}} = 0.01$ and the ratio $V_{\text{cyt}}/V_{\text{er}} = 31$.

In addition to the 4 differential equations (1), (3), (4), (5), the model in [5] consists of 3 further states, namely the concentrations of ADP , $G6P$ and FBP . This complicated 3-dimensional slow submodel is omitted here. Details can be found in [5].

The simulation of the pancreatic β -cell model was carried out for different parameter values of the conductances $g_{K(Ca)}$, $g_{K(ATP)}$ and the glucokinase reaction rate R_{GK} used in the second subsystem [5]. These parameter values are given in Tab. I.

For the numerical simulation of the first 4 differential equations (1)-(5) we used the initial values $V(0) = -60 \text{ mV}$, $n(0) = 0$, $Ca(0) = 0,1 \mu\text{M}$ and $Ca_{\text{er}}(0) = 185 \mu\text{M}$. The initial values of the additional 3-dimensional subsystem are $ADP(0) = 780 \mu\text{M}$, $G6P(0) = 200 \mu\text{M}$ and $FBP(0) = 40 \mu\text{M}$. The simulation results are shown in Fig. 2. Depending on the parameter values, the system exhibits different oscillation pattern.

TABLE I
DIFFERENT PARAMETER VALUES FOR THE SIMULATION

Mode	$g_{K(Ca)}$ in pS	$g_{K(ATP)}$ in nS	R_{GK} in s^{-1}
Compound	600	25	0.2
Slow	100	27	0.2
Fast	600	25	0.4
Subthreshold	100	30	0.2
Accordion	600	23	0.2

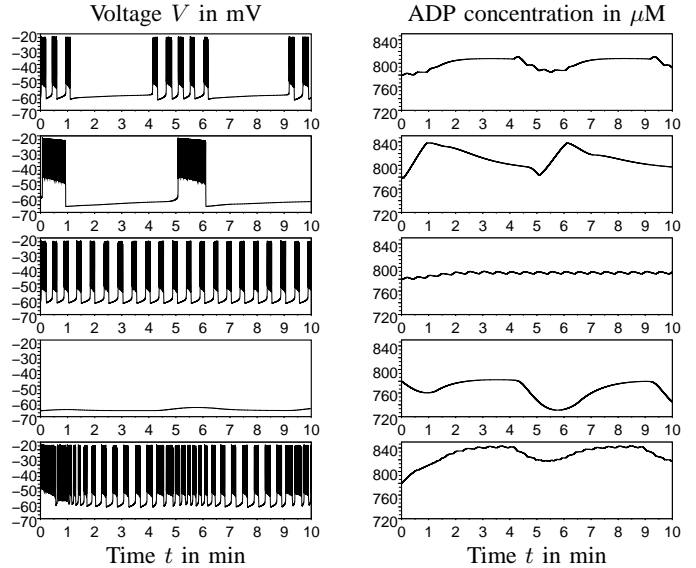


Fig. 2. Different oscillation patterns of the pancreatic β -cell model. In descending order of the rows: compound, slow, fast, subthreshold and accordon bursting.

III. OBSERVER BASE MEASUREMENT

A. State observer structure

Equations (1)-(5) can be rewritten as a 4-dimensional nonlinear state-space system

$$\dot{\mathbf{x}} = \mathbf{f}(\mathbf{x}) - \frac{1}{C_m} I_{K(ATP)} \quad (6)$$

with the state $\mathbf{x} = (V, n, Ca, Ca_{\text{er}})^T$, the current $I_{K(ATP)}$ as input and the measured voltage V as an output. To estimate the state we use an observer

$$\dot{\hat{\mathbf{x}}} = \mathbf{f}(\hat{\mathbf{x}}) + \mathbf{k}(V - \hat{V}) \quad (7)$$

with the estimated state $\hat{\mathbf{x}} = (\hat{V}, \hat{n}, \hat{Ca}, \hat{Ca}_{\text{er}})^T$ and the constant observer gain $\mathbf{k} = (k_1, k_2, k_3, k_4)^T \in \mathbb{R}^4$. The current $I_{K(ATP)}$ is omitted since it is not measured. To ensure convergence, the linear output injection with the gain \mathbf{k} must dominate the occurring nonlinearities. This usually implies large entries in the observer gain. Therefore, this observer is a high-gain observer [6]–[8]. Although there are several other possible approaches to

design an observer [9]–[13], the constant observer gain will simplify the reconstruction of the unknown input.

The observation error $\tilde{x} = x - \hat{x}$ is governed by the error dynamics

$$\dot{\tilde{x}} = f(x) - f(\hat{x}) - \frac{1}{C_m} I_{K(ATP)} - k(V - \hat{V}) . \quad (8)$$

B. Input reconstruction

Consider the error dynamics (8) near an equilibrium point with $\tilde{x} \approx 0$, i.e., $x \approx \hat{x}$. This implies $f(x) \approx f(\hat{x})$. For sufficiently large $k_1 > 0$ in k , the first differential equation of (8) can be simplified with $\dot{\tilde{x}} = 0$ to

$$0 \approx -\frac{1}{C_m} I_{K(ATP)} - k_1(V - \hat{V}) ,$$

or equivalently

$$I_{K(ATP)} \approx -k_1 C_m (V - \hat{V}) \quad (9)$$

This approximation can be used together with (2) to obtain an estimate \widehat{ADP} of the ADP concentration

$$\widehat{ADP} := o_\infty^{-1} \left(-\frac{k_1 C_m (V - \hat{V})}{g_{K(ATP)}(V - V_K)} \right) , \quad (10)$$

where o_∞^{-1} denote the inverse map of o_∞ .

In [5], the value of the activation variable o_∞ results from a difficult and lengthy calculation taking the balances between *ADP*, *ATP*, *G6P* and *FBP* into account. Here, we use the simulation data of the pancreatic cell model of all oscillation patterns shown in Fig. 2. It can be seen in Fig. 3 that o_∞ depends weakly nonlinear on the *ADP* concentration. We used a second order polynomial

$$ADP = p_0 + p_1 o_\infty + p_2 o_\infty^2 \quad (11)$$

to approximate the inverse map $o_\infty^{-1} : o_\infty \mapsto ADP$ required in (10). Using least squares we obtained the coefficients $p_0 = -949.57631 \mu\text{M}$, $p_1 = 378525.42 \mu\text{M}$ and $p_2 = -19041025 \mu\text{M}$. (Note that o_∞ is dimensionless.)

The measured voltage V quite often contains bursts, i.e., high frequency oscillations (see Fig. 2). These bursts also cause deviations of the *ADP* estimate \widehat{ADP} given in (10). We will suppress these disturbances using a low-pass filter with the continuous time transfer function

$$F(s) = \frac{a_0}{s^n + a_{n-1}s^{n-1} + \dots + a_1s + a_0} . \quad (12)$$

The filter coefficients a_0, \dots, a_{n-1} can be calculated using standard methods, e.g. one could use a Bessel, Butterworth or Cauer filter [14], [15]. In the time domain we

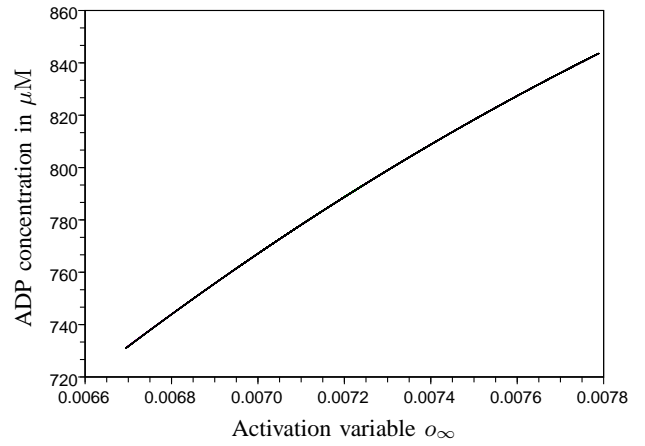


Fig. 3. Relation between o_∞ and *ADP* concentration

apply the filter (12) to \widehat{ADP} from (10) in order to define the final estimate \overline{ADP} of the concentration *ADP*:

$$\overline{ADP} := F\left(\frac{d}{dt}\right) \circ \widehat{ADP} . \quad (13)$$

The whole simulation and estimation scheme is shown in Fig. 4.

C. Numerical Results

The numerical simulation was carried out with SCILAB [16]. For the cell model we selected the compound bursting scheme (see Fig. 2 and Tab. I). For the observer (7) we used the initial values $\hat{V}(0) = -50 \text{ mV}$, $\hat{n}(0) = 0$, $\hat{Ca}(0) = 0.2 \mu\text{M}$ and $\hat{Ca}_{er}(0) = 150 \mu\text{M}$. Furthermore, we used the observer gain $k = (k_1, 0, 0, 0)^T$ with normalized value $k_1 = 100$ for V in mV and t in ms. For the filter (12), a 6th order Butterworth low-pass was designed having the radian cut-off frequency $\omega = 0.1 \text{ s}^{-1}$. The simulation results are shown in Fig. 5. A visual inspection suggests that the observer converges. The filtered signal \overline{ADP} yields a reasonable estimate of the *ADP* concentration.

Note that by the given form of the observer gain, only the first differential equation of the error dynamics (8) is directly influenced by the measurement. The convergence of the observer scheme suggests that system (6) is detectable [17], i.e., we rely on a weaker assumption that observability.

IV. CONCLUSION

In the paper we suggested an observer based approach to estimate the *ADP* concentration of a pancreatic β -cell measuring only the voltage on the cell's membrane. The method developed here requires a model of the cell's electro-physiological behavior. Our approach can

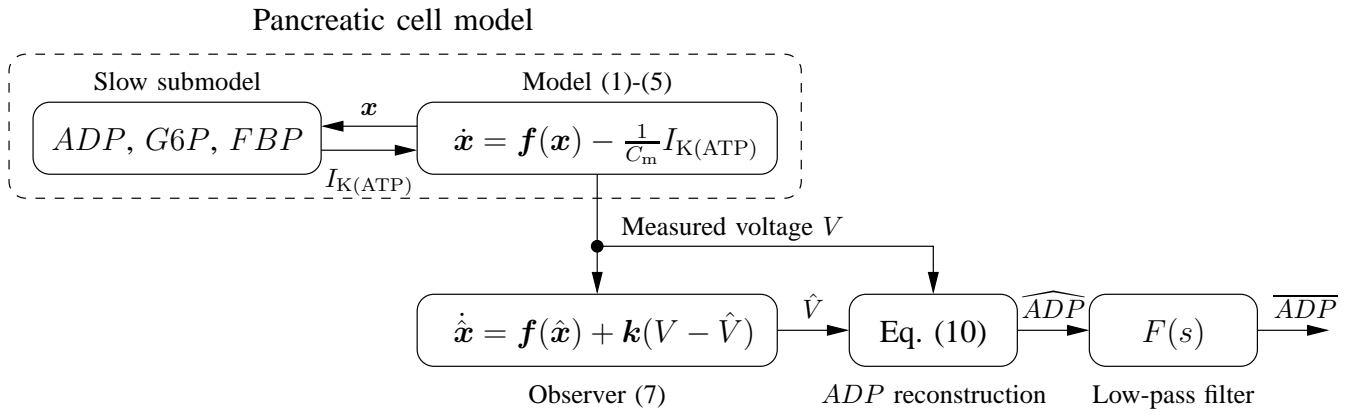


Fig. 4. Simulation and estimation scheme

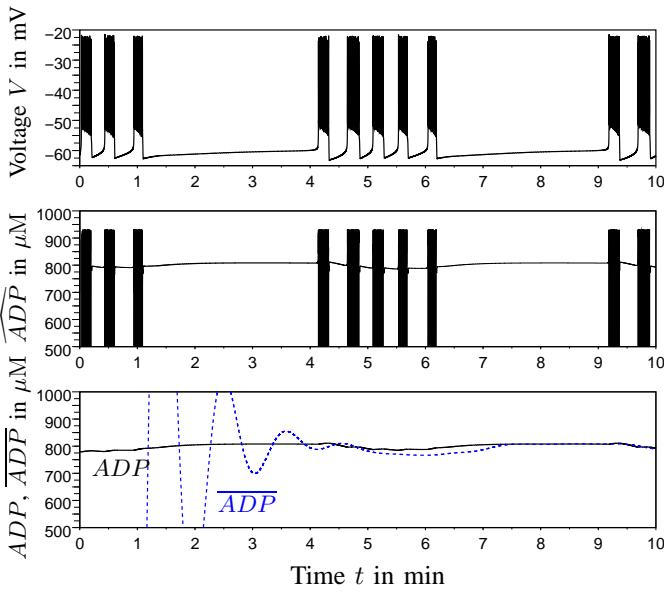


Fig. 5. ADP estimation from (simulated) voltage measurement

be implemented for a real-time measurement, which will be our next step. However, the disadvantage of our approach is the requirement of a reasonable precise cell model. Therefore, this method cannot be applied to unknown cell types.

ACKNOWLEDGMENT

The author would like to thank Assistant Professor Pranay Goel (Indian Institute of Science Education and Research, Pune) for many helpful discussions.

REFERENCES

- [1] K. Röbenack and P. Goel, "Observer based measurement of the input current into a neuron," *Mediterranean Journal of Measurement and Control*, vol. 3, no. 1, pp. 22–29, 2007.
- [2] —, "A combined observer and filter based approach for the determination of unknown parameters," *Int. J. Systems Science*, vol. 40, no. 3, pp. 213–221, Mar. 2009.
- [3] A. L. Hodgkin and A. F. Huxley, "A quantitative description of membrane current and its application to conduction and excitation in nerve," *Journal of Physiology*, vol. 117, pp. 500–544, 1952.
- [4] T. R. Chay and J. Keizer, "Minimal model for membrane oscillations in the pancreatic β -cell," *Biophysiological Journal*, vol. 42, pp. 181–190, 1983.
- [5] R. Bertram, L. Sation, M. Zhang, P. Smolen, and A. Sherman, "Calcium and glycolysis mediate multiple bursting modes in pancreatic islets," *Biophysical Journal*, vol. 87, pp. 3074–3087, 2004.
- [6] F. E. Thau, "Observing the state of nonlinear dynamical systems," *Int. J. Control*, vol. 17, no. 3, pp. 471–479, 1973.
- [7] S. Raghavan and J. K. Hedrick, "Observer design for a class of nonlinear systems," *Int. J. Control*, vol. 59, no. 2, pp. 515–528, 1994.
- [8] R. Rajamani, "Observers for Lipschitz nonlinear systems," *IEEE Trans. on Automatic Control*, vol. 43, no. 3, pp. 397–401, 1998.
- [9] E. A. Misawa and J. K. Hedrick, "Nonlinear observers — a state-of-the art survey," *Journal Dynamic Systems, Measurement, and Control*, vol. 111, pp. 344–352, Sep. 1989.
- [10] B. L. Walcott, M. J. Corless, and S. H. Žak, "Comparative study of non-linear state-observation techniques," *Int. J. Control*, vol. 45, no. 6, pp. 2109–2132, 1987.
- [11] H. Nijmeijer and T. I. Fossen, Eds., *New Directions in Nonlinear Observer Design*, ser. Lecture Notes in Control and Information Science. London: Springer-Verlag, 1999, vol. 244.
- [12] K. Röbenack, "Direct approximation of observer error linearization for nonlinear forced systems," *IMA Journal of Mathematical Control and Information*, vol. 24, no. 4, pp. 551–566, 2007.
- [13] K. Röbenack and A. F. Lynch, "High-gain nonlinear observer design using the observer canonical form," *IET Control Theory & Applications*, vol. 1, no. 6, pp. 1574–1579, 2007.
- [14] P. Denbig, *System Analysis and Signal Processing*. Boston: Addison-Wesley, 1998.
- [15] R. E. Thomas and A. J. Rosa, *The Analysis and Design of Linear Circuits*, 4th ed. Wiley, 2004.
- [16] S. L. Campbell, J.-P. Chancelier, and R. Nikoukhah, *Modeling and Simulation in Scilab/Scicos*. New York: Springer, 2006.
- [17] G. L. Amicucci and S. Monaco, "On nonlinear detectability," *J. Franklin Inst.*, vol. 335B, no. 6, pp. 1105–1123, 1998.

Spiking in Delay-Coupled FitzHugh-Nagumo Systems with Feedback

Anastasiia Panchuk

Institute of Mathematics,
National Academy of Sciences of Ukraine,
3, Tereshchenkivska str., 01601 Kiev, Ukraine
Email: nastyap@imath.kiev.ua

Abstract—We study two delay-coupled FitzHugh-Nagumo systems as the simplest representation of interacting neurons. It can be observed that adding delay coupling can cause periodic oscillations which coexist with a stable fixed point. We also demonstrate that self-feedback terms can provoke stable bursting patterns in the model.

Index Terms—Coupled excitable neurons, FitzHugh-Nagumo systems, spiking and bursting, delay differential equations.

I. INTRODUCTOIN

In the age of computers and technological progress, when science is developping so quickly that one major achievement is almost immediately followed by the next significant breakthrough, mankind finally dared lift the veil of mystery from this strange phenomenon named brain.

Since the end of the last century, study of neural networks picks up speed. Many works are devoted to modelling the brain as an ensemble of coupled nonlinear dynamical elements, capable of exchanging information between each other and producing different time regimes [1]–[6].

Quite often for representing a single neuron, a phase oscillator system is used. Thus, oscillatory behaviour of the individual system element is embedded in the model itself, and observable regular spiking is produced due to collective synchronization [7]–[9]. For instance, to characterize mutual dynamics of cells in certain brain areas, responsible for giving the onset to Parkinson's disease or epilepsy, a well-known Kuramoto model is considered [10]–[13].

The other approach was developed in 1961 by R. FitzHugh [14], and independently by J. Nagumo and co-authors [15] in 1962. They have deduced the simplest 2-dimensional system for studying the main characteristics of a neuron behaviour. Nowadays, this model is considered to be a canonical one and has been

studied in many papers (see, for instance, [16]–[19] and references therein).

II. MODEL

The purpose of this work is to study a model of two coupled neural elements, each being in the excitable regime (namely, not producing any self-sustained oscillation) and represented by a FitzHugh-Nagumo system. The elements are coupled so that each gets the delayed response from the other one: τ_1^C and τ_2^C are the delays and C is the coupling strength. In addition, it is assumed that each element receives a delayed feedback signal with the delay time τ_i^K , $i = 1, 2$ and feedback strength K . As it was shown in [23], the difference between τ_1^C and τ_2^C is not essential, therefore they are put to be equal $\tau_1^C = \tau_2^C = \tau^C$.

Adding all this up one can arrive to the following DDE system:

$$\begin{aligned} \epsilon \dot{x}_1 &= x_1 - \frac{x_1^3}{3} - y_1 + C(x_2(t - \tau^C) - x_1(t)) \\ &\quad + K(x_1(t - \tau_1^K) - x_1) \end{aligned} \quad (1a)$$

$$\dot{y}_1 = x_1 + a \quad (1b)$$

$$\begin{aligned} \epsilon \dot{x}_2 &= x_2 - \frac{x_2^3}{3} - y_2 + C(x_1(t - \tau^C) - x_2(t)) \\ &\quad + K(x_2(t - \tau_2^K) - x_2) \end{aligned} \quad (1c)$$

$$\dot{y}_2 = x_2 + a \quad (1d)$$

Everywhere below, if not specified differently, we put $\epsilon_1 = \epsilon_2 = 0.01$, $a = 1.3$, and $C = 0.5$.

III. VARIETY OF DYNAMICAL PATTERNS

Besides the only fixed point which is always stable (see [23]), the system (1) shows various regular spiking and bursting type patterns. Furthermore, several stable solutions can coexist for the same parameter values entailing high level multistability.

The Fig. 1 presents sample dynamics for the fixed delays τ_1^K and τ_2^K while the feedback strength K varies. Here, in each column of 3 plots the top subfigure represents time series for x_1, y_1 , the middle one shows the phase portrait, and in the the bottom one x_1 vs. x_2 are depicted.

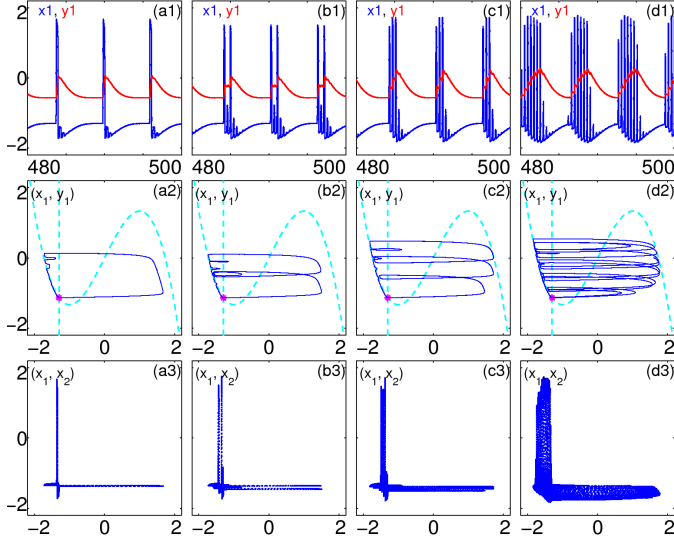


Fig. 1. Sample dynamics of the system (1) for $\tau_1^K = 0.4, \tau_2^K = 0.8$ with (a) $K = 0.2$, (b) $K = 0.3$, (c) $K = 0.32$, (d) $K = 0.4$. (The time series and phase space are shown only for x_1, y_1 . For x_2, y_2 they look similar).

One can see an expected transition from periodic spiking to bursting, in particular, with increasing K the activity (bursting) time interval enlarges.

In the Fig. 2 and 3 similar trajectory transformations are drawn, but for $\tau_1^K = 0.47, \tau_2^K = 1.2$ and $\tau_1^K = 0.8, \tau_2^K = 1.5$, respectively. However, there are noticeable differences between the three figures presented. Figs. 1(a), (b) and Figs. 2(a), (b) are almost the same, but for $\tau_1^K = 0.47, \tau_2^K = 1.2$, before the bursting dynamics, a periodic solution of smaller period can be obtained (Fig. 2(c)), which does not seem to be the case for $\tau_1^K = 0.4, \tau_2^K = 0.8$ (cf. Fig. 1(c)). To the other hand, for $\tau_1^K = 0.8, \tau_2^K = 1.5$ one observes diminuation of the solution period till chaotic-like dynamics arises, and we were not able to get any bursting.

IV. CLASSIFYING OSCILLATION REGIMES

As the dynamics of the system (1) is so diverse, some mean of its classification is needed. For this, one can calculate the autocorrelation function (ACF) of the solution series, or being precise, the lag where the ACF maximum is reached. Then this maximum's lag value equals roughly the solution period.

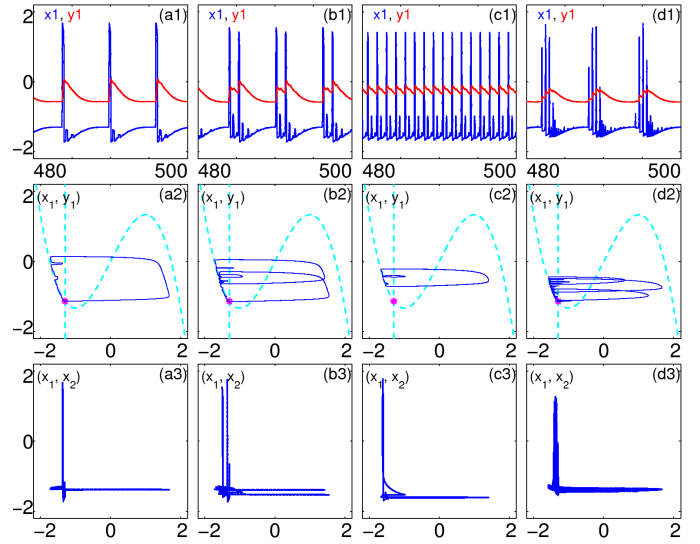


Fig. 2. Sample dynamics of the system (1) for $\tau_1^K = 0.47, \tau_2^K = 1.2$ with (a) $K = 0.2$, (b) $K = 0.28$, (c) $K = 0.3$, (d) $K = 0.42$

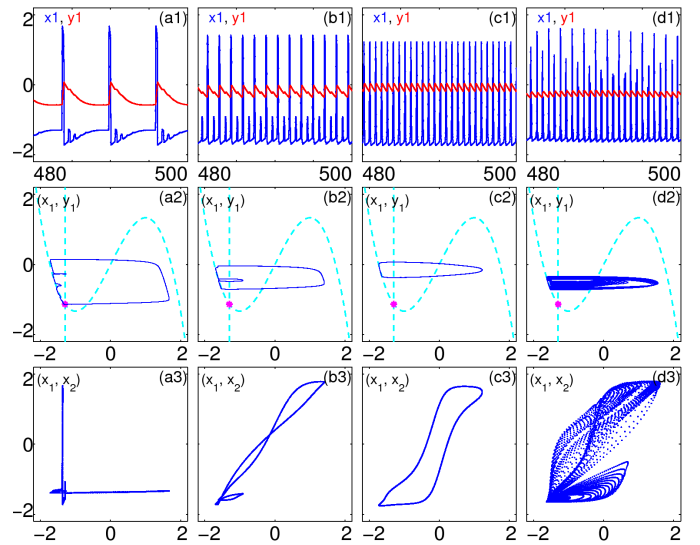


Fig. 3. Sample dynamics of the system (1) for $\tau_1^K = 0.8, \tau_2^K = 1.5$ with (a) $K = 0.2$, $K = 0.3$, $K = 0.4$, $K = 0.5$

In the Fig. 4, 2D bifurcation diagrams in the (K, τ_1^K) parameter space are plotted for $\tau^C = 3$ and $\tau_2^K = 2$. The initial conditions are taken differently for these plots: for (a) the history function was chosen in the shape of the cycle of period ≈ 6 (cf. “long cycle” in [23]), and for (b) the period of the initial function is about 2. As one can notice, the considered system is highly sensitive to the initial conditions.

In both figures, we plot all the solutions for which ACF maximum ≥ 0.8 , but those, with the calculated “period” (time lag of ACF maximum) greater than 7, are pointed with the same color as those, which have

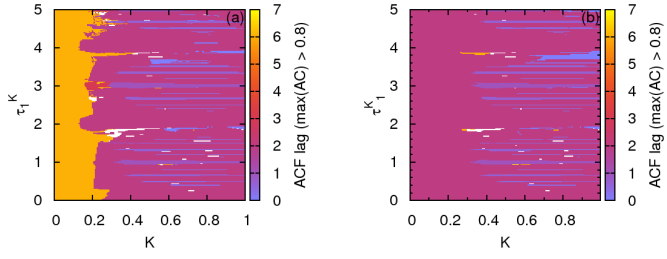


Fig. 4. Bifurcation diagrams in the (K, τ_1^K) -plane with $\tau^C = 3, \tau_2^K = 2$. The history function mimics the cycle of period (a) ≈ 6 ; (b) ≈ 2 .

period ≈ 7 . White color corresponds to the trajectories with ACF maximum < 0.8 .

The Fig. 5 depicts 2D diagrams in (τ_1^K, τ_2^K) space with different K values.

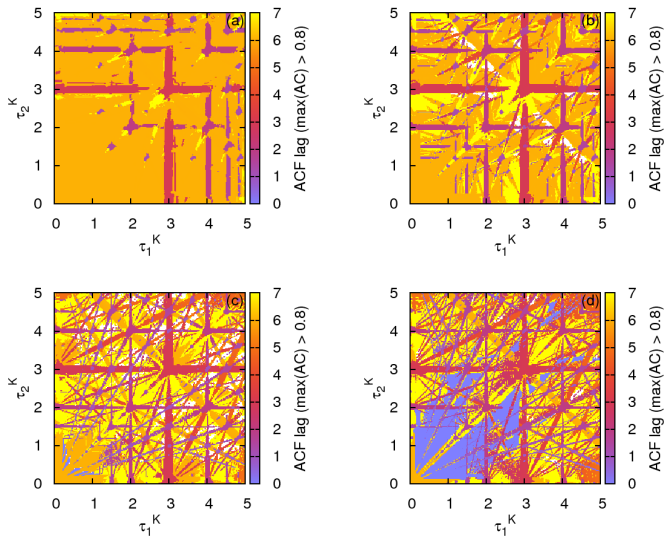


Fig. 5. Bifurcation diagrams in the (τ_1^K, τ_2^K) -plane with $\tau^C = 3$ and (a) $K = 0.2$; (b) $K = 0.3$; (c) $K = 0.4$; (d) $K = 0.5$.

It is observable that starting from some sufficiently large K -value, the regions where periodic solutions exist, accumulate around some lines, restraining the delay times to satisfy a certain law.

The Fig. 6(a), (b) show the color-coded bifurcation diagram in the (τ_1^K, τ_2^K) -plane for $K = 0.5$, and the same diagram with dashed black lines corresponding to the various laws $\tau_2^K = m/n\tau_1^K + r/s\tau^C$ (or $\tau_1^K = m/n\tau_2^K + r/s\tau^C$), where $m, n, r, s \in \mathbb{N}$, which is the same as $M\tau_1^K + N\tau_2^K + R\tau^C = 0$ with $M, N, R \in \mathbb{Z}$. (The similar relation was obtained in [24] for the 2D discrete system with several different delay terms). The Fig. 7 represents the lines corresponding to certain ratios of delay times (most of them are clearly visible in the Fig. 6(a)).

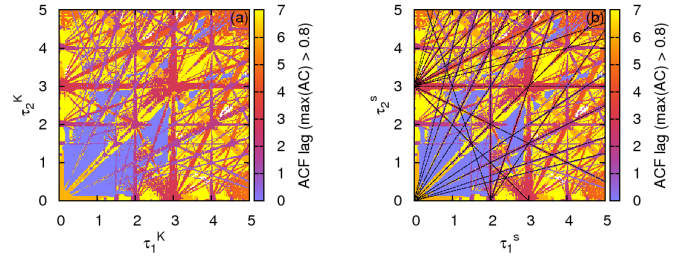


Fig. 6. Bifurcation diagram in the (τ_1^K, τ_2^K) -plane with $\tau^C = 3, K = 0.5$; (b) dashed black lines indicate certain ratios between τ_1^K, τ_2^K .

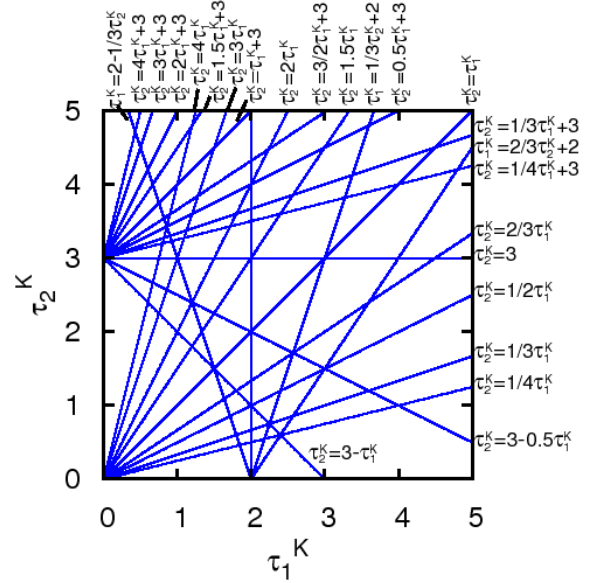


Fig. 7. Lines corresponding to different laws $M\tau_1^K + N\tau_2^K + R\tau^C = 0$ with $M, N, R \in \mathbb{Z}$.

Finally, in Fig. 8 bifurcation diagrams in the (τ_1^K, τ_2^K) parameter space for a constant $K = 0.5$ and different values of τ^C are depicted. Again one can see that for sufficiently large delay times periodic dynamics assembles around the lines corresponding to the law stated above.

V. CONCLUSION

In the present work for modelling interacting neural elements, two delay-coupled FitzHugh-Nagumo equation sets, including delayed feedback terms, were considered. Although each individual neuron is taken to be in the excitable regime (not generating any self-sustained oscillations), when coupled, they produce a great variety of spiking and bursting patterns. Thus, introducing delays entails significant complication of the system dynamics.

As it was also shown, the system is highly sensitive to the initial conditions, as well as it is rather responsive

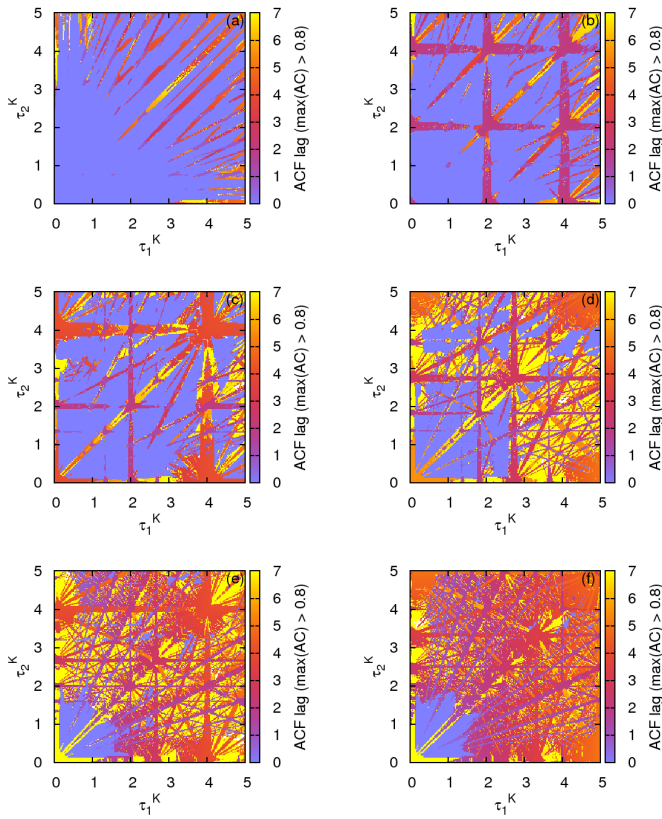


Fig. 8. Bifurcation diagrams in the (τ_1^K, τ_2^K) -plane with $K = 0.5$ and (a) $\tau^C = 0.37$; (b) $\tau^C = 1$; (c) $\tau^C = 2$; (d) $\tau^C = 2.73$; (e) $\tau^C = 4$; (f) $\tau^C = 5$.

to the parameter changes, especially, adjusting the delay times. It was observed, that the regions where low-frequency oscillations exist, accumulate mostly around some lines, restraining the delay times to satisfy a certain ratio.

ACKNOWLEDGMENT

This work was supported by DFG in the framework of Sfb 555.

The author would like to thank the Neural Dynamics group of Prof. Eckehard Schöll from Institute for Theoretical Physics of Technical University of Berlin for their kind hospitality and fruitful collaboration.

REFERENCES

- [1] H. Haken. *Brain Dynamics: Synchronization and Activity Patterns in Pulse-Coupled Neural Nets with Delays and Noise* (Springer Verlag GmbH, Berlin, 2006).
- [2] H. R. Wilson. *Spikes, Decisions, and Actions: The Dynamical Foundations of Neuroscience* (Oxford University Press, Oxford, 1999).

- [3] W. Gerstner and W. Kistler. *Spiking Neuron Models* (Cambridge University Press, Cambridge, 2002).
- [4] H. R. Wilson and J. D. Cowan. Excitatory and inhibitory interactions in localized populations of model neurons. *Biophysical Journal* 12, pp. 1–24 (1972).
- [5] A. Destexhe, D. Contreras, T. J. Sejnowski, and M. Steriade. A model of spindle rhythmicity in the isolated thalamic reticular nucleus, *J. Neurophysiol.* 72, pp. 803–818 (1994).
- [6] C. Zhou, L. Zemanova, G. Zamora, C. C. Hilgetag, and J. Kurths. Hierarchical organization unveiled by functional connectivity in complex brain networks, *Phys. Rev. Lett.* 97, p. 238103 (2006).
- [7] M. G. Rosenblum and A. Pikovsky. Controlling synchronization in an ensemble of globally coupled oscillators, *Phys. Rev. Lett.* 92, p. 114102 (2004).
- [8] O. V. Popovych, C. Hauptmann, and P. A. Tass. Effective desynchronization by nonlinear delayed feedback, *Phys. Rev. Lett.* 94, p. 164102 (2005).
- [9] M. Gassel, E. Glatt, and F. Kaiser. Time-delayed feedback in a net of neural elements: Transitions from oscillatory to excitable dynamics, *Fluct. Noise Lett.* 7, pp. L225–L229 (2007).
- [10] O. V. Popovych, Y. L. Maistrenko, and P. A. Tass. Phase chaos in coupled oscillators, *Phys. Rev. E* 71, p. 065201(R) (2005).
- [11] P. Ashwin, O. Burylko, Y. Maistrenko, and O. Popovych. Extreme sensitivity to detuning for globally coupled phase oscillators, *Phys. Rev. Lett.* 96, p. 054102 (2006).
- [12] Y. L. Maistrenko, B. Lysyansky, C. Hauptmann, O. Burylko, and P. A. Tass. Multistability in the Kuramoto model with synaptic plasticity, *Phys. Rev. E* 75, p. 066207 (2007).
- [13] P. Ashwin, O. Burylko, Y. Maistrenko. Bifurcation to heteroclinic cycles and sensitivity in three and four coupled phase oscillators, *Physica D* 237, pp. 454–466 (2008).
- [14] R. FitzHugh. Impulses and physiological states in theoretical models of nerve membrane, *Biophys. J.* 1, pp. 445–466 (1961).
- [15] J. Nagumo, S. Arimoto, and S. Yoshizawa. An active pulse transmission line simulating nerve axon., *Proc. IRE* 50, pp. 2061–2070 (1962).
- [16] N. Buric and D. Todorovic. Dynamics of fitzhughnagumo excitable systems with delayed coupling, *Phys. Rev. E* 67, p. 066222 (2003).
- [17] R. Toral, C. Masoller, C. R. Mirasso, M. Ciszak, O. Calvo. Characterization of the anticipated synchronization regime in the coupled FitzHughNagumo model for neurons, *Physica A* 325, pp. 192–198 (2003).
- [18] B. Lindner, J. García-Ojalvo, A. Neiman, and L. Schimansky-Geier. Effects of noise in excitable systems, *Phys. Rep.* 392, pp. 321–424 (2004).
- [19] H. Kitajima and J. Kurths. Synchronized firing of FitzHugh-Nagumo neurons by noise, *Chaos* 15, p. 023704 (2005).
- [20] M. A. Dahlem, G. Hiller, A. Panchuk, and E. Schöll. Dynamics of delay-coupled excitable neural systems, *Int. J. Bif. Chaos* 19, pp. 1–9 (2009).
- [21] E. Schöll, G. Hiller, P. Hövel, and M. A. Dahlem. Time-delayed feedback in neurosystems, *Phil. Trans. R. Soc. A* 367, pp. 1079–1096 (2009).
- [22] K. Pyragas. Continuous control of chaos by self-controlling feedback, *Phys. Lett. A* 170, pp. 421–428 (1992).
- [23] A. Panchuk, M. Dahlem, and E. Schöll. Regular spiking in asymmetrically delay-coupled FitzHugh-Nagumo systems, *arXiv:0911.2071v1 [nlin.AO]*
- [24] M. Zigzag, M. Butkovski, A. Englert, W. Kinzel and I. Kanter. Zero-lag synchronization of chaotic units with time-delayed couplings, *EPL* 85, 60005, 6pp. (2009).

Synchronization in Two Polygonal Oscillatory Networks Sharing a Branch

Yoko Uwate

UZH/ETH Zurich,
Winterthurerstrasse 190,
CH-8057 Zurich, Switzerland,
Email: yu001@ini.phys.ethz.ch

Yoshifumi Nishio

Dept. of Electrical and Electronic Engineering,
Tokushima University
2-1 Minami-Josanjima, Tokushima, Japan
Email: nishio@ee.tokushima-u.ac.jp

Ruedi Stoop

UZH/ETH Zurich,
Winterthurerstrasse 190,
CH-8057 Zurich, Switzerland,
Email: ruedi@ini.phys.ethz.ch

Abstract—In this study, synchronization phenomena observed in two coupled polygonal oscillatory networks sharing a branch is investigated. We focus on the phase difference between two oscillators which are coupled to the shared branch of the two polygonal networks. By computer simulations, we observe that synchronization state of the shared oscillators depends on the number of coupled oscillators of the each polygonal network.

I. INTRODUCTION

Synchronization, in particular, is one of the most important features that can be described and explored with the help of oscillators, because, upon their coupling, strongly correlated rhythms among the oscillators emerge, called synchronized states. Synchronization phenomena have been extensively reported in physical [1]–[4], biological [5],[6] and electrical [7],[8] systems.

Moreover, there are several types of polygonal network structures (e.g. Honeycomb structure and crystal structure) exists in the natural science. For the studies of large-scale network using coupled oscillators, a ring, a ladder and a two dimensional array structure are often investigated. However, there are not many discussions about coupled polygonal oscillatory networks by using electrical oscillators.

In this study, synchronization phenomena in two coupled polygonal oscillatory networks is investigated. Two polygonal oscillatory networks is shared a branch of two networks as shown in Fig. 1. First, we consider the two triangle oscillatory networks are shared by a branch. By using computer simulations and theoretical analysis, the phase difference and the amplitude of each oscillator are discussed. Furthermore, we investigate the phase difference between the shared oscillators when two polygonal (quadrilateral, pentagon, hexagon and heptagon) oscillatory networks are coupled.

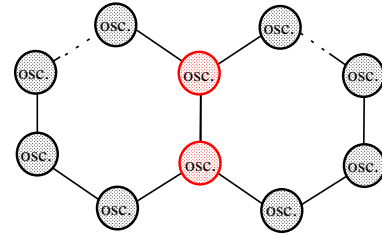


Fig. 1. General two coupled polygonal network oscillators.

II. TWO COUPLED TRIANGLE OSCILLATORY NETWORKS

We consider the two coupled triangle oscillatory networks sharing a branch as a first circuit model.

A. Circuit Model

The circuit model of two coupled triangle oscillatory networks sharing the branch is shown in Fig. 2.

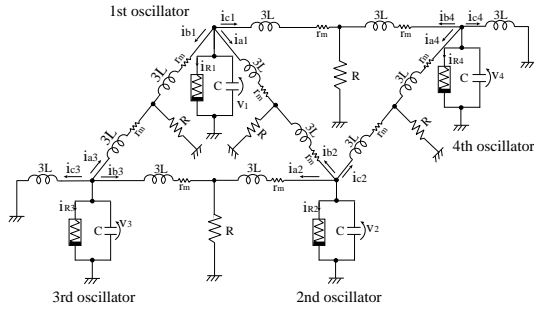
We assume that the $v_k - i_{Rk}$ characteristics of the nonlinear resistor in each oscillator is given by the following third order polynomial equation,

$$i_{Rk} = -g_1 v_k + g_3 v_k^3 \quad (g_1, g_3 > 0), \quad (1)$$

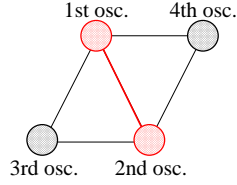
$$(k = 1, 2, 3, 4).$$

The normalized circuit equations governing the circuit in Fig. 2 are expressed as
[First oscillator]

$$\begin{cases} \frac{dx_1}{d\tau} = \varepsilon \left(1 - \frac{1}{3} x_1^2 \right) x_1 - (y_{a1} + y_{b1} + y_{c1}) \\ \frac{dy_{a1}}{d\tau} = \frac{1}{3} \left\{ x_1 - \eta y_{a1} - \gamma (y_{a1} + y_{b2}) \right\} \\ \frac{dy_{b1}}{d\tau} = \frac{1}{3} \left\{ x_1 - \eta y_{b1} - \gamma (y_{a3} + y_{b1}) \right\} \\ \frac{dy_{c1}}{d\tau} = \frac{1}{3} \left\{ x_1 - \eta y_{c1} - \gamma (y_{b4} + y_{c1}) \right\} \end{cases} \quad (2)$$



(a) Two coupled triangle oscillatory networks.



(b) Conceptual circuit model.

Fig. 2. Circuit model.

[Second oscillator]

$$\begin{cases} \frac{dx_2}{d\tau} = \varepsilon \left(1 - \frac{1}{3}x_2^2 \right) x_2 - (y_{a2} + y_{b2} + y_{c2}) \\ \frac{dy_{a2}}{d\tau} = \frac{1}{3} \left\{ x_2 - \eta y_{a2} - \gamma(y_{a2} + y_{b3}) \right\} \\ \frac{dy_{b2}}{d\tau} = \frac{1}{3} \left\{ x_2 - \eta y_{b2} - \beta\gamma(y_{a1} + y_{b2}) \right\} \\ \frac{dy_{c2}}{d\tau} = \frac{1}{3} \left\{ x_2 - \eta y_{c2} - \beta\gamma(y_{a4} + y_{c2}) \right\} \end{cases} \quad (3)$$

[Third oscillator]

$$\begin{cases} \frac{dx_3}{d\tau} = \varepsilon \left(1 - \frac{1}{3}x_3^2 \right) x_3 - (y_{a3} + y_{b3} + y_{c3}) \\ \frac{dy_{a3}}{d\tau} = \frac{1}{3} \left\{ x_3 - \eta y_{a3} - \gamma(y_{a3} + y_{b1}) \right\} \\ \frac{dy_{b3}}{d\tau} = \frac{1}{3} \left\{ x_3 - \eta y_{b3} - \gamma(y_{a2} + y_{b3}) \right\} \\ \frac{dy_{c3}}{d\tau} = \frac{1}{3} \left\{ x_3 - \eta y_{c3} \right\} \end{cases} \quad (4)$$

[Fourth oscillator]

$$\begin{cases} \frac{dx_4}{d\tau} = \varepsilon \left(1 - \frac{1}{3}x_4^2 \right) x_4 - (y_{a4} + y_{b4} + y_{c4}) \\ \frac{dy_{a4}}{d\tau} = \frac{1}{3} \left\{ x_4 - \eta y_{a4} - \gamma(y_{a4} + y_{c2}) \right\} \\ \frac{dy_{b4}}{d\tau} = \frac{1}{3} \left\{ x_4 - \eta y_{b4} - \gamma(y_{b4} + y_{c1}) \right\} \\ \frac{dy_{c4}}{d\tau} = \frac{1}{3} \left\{ x_4 - \eta y_{c4} \right\} \end{cases} \quad (5)$$

where

$$t = \sqrt{LC}\tau, \quad v_k = \sqrt{\frac{g_1}{3g_3}}x_k,$$

$$i_{ak} = \sqrt{\frac{g_1}{3g_3}}\sqrt{\frac{C}{L}}y_{ak}, \quad i_{bk} = \sqrt{\frac{g_1}{3g_3}}\sqrt{\frac{C}{L}}y_{bk},$$

$$\varepsilon = g_1\sqrt{\frac{L}{C}}, \quad \gamma = R\sqrt{\frac{C}{L}}, \quad \eta = r_m\sqrt{\frac{C}{L}},$$

$$(k = 1, 2, 3, 4).$$

In this equations, γ is the coupling strength and ε denotes the nonlinearity of the oscillators.

B. Synchronization Phenomena

For the computer simulations, we calculates Eqs. (2)-(5) using a fourth-order Runge-Kutta method with the step size $h = 0.005$. The parameters of this circuit model are fixed as $\varepsilon = 0.1$, $\gamma = 0.1$, $\eta = 0.0001$.

Figure 3 shows the time wave form of the voltage charged at the capacitance of each oscillator. From this figure, we can see that the first and the second oscillators are synchronized at in-phase (phase difference: 0 degree). While, the other combination oscillators synchronize with anti-phase (phase difference: 180 degree). Furthermore, the amplitude of between the first/second and the third/fourth oscillators has small difference. The phase plane of each combination oscillator is shown in Fig. 4.

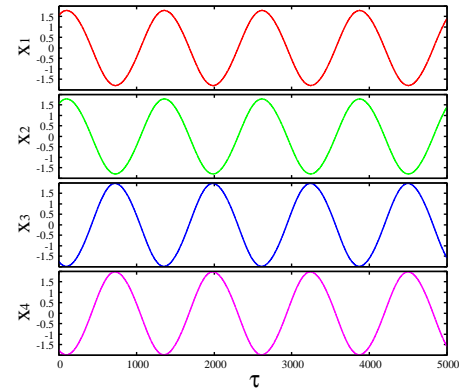


Fig. 3. Time wave form of the voltage charged at the capacitance of each oscillator.

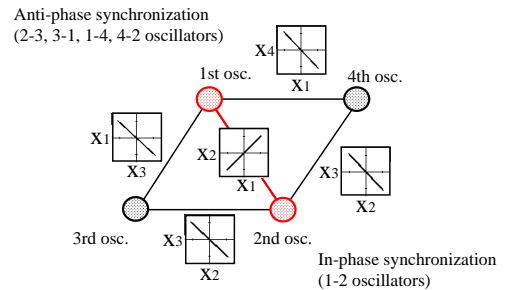


Fig. 4. Phase plane of each oscillator.

C. Theoretical Analysis

In this section, we explain the theoretical analysis by using the averaging method for the circuit equations (2)-(5) obtained from Fig. 2. Here, we consider the case of that the tiny resistance r_m does not exist ($\eta = 0$).

First, Eq (2) can be described by second order non-linear differential equation as follows.

$$\frac{d^2 x_1}{d\tau^2} + x_1 = \varepsilon(1 - x_1^2) \frac{dx_1}{d\tau} + \frac{1}{3}\gamma Y_1 \equiv F_1 \quad (6)$$

$$\frac{dY_1}{d\tau} + \frac{2}{3}\gamma Y_1 = x_1 + \frac{1}{3}x_2 + \frac{1}{3}x_3 + \frac{1}{3}x_4 \quad (7)$$

where,

$$Y_1 \equiv y_{a1} + y_{a3} + y_{b1} + y_{b2} + y_{b4} + y_{c1}.$$

Equation (7) is the first order linear differential equation. The solution is given as following equation.

$$Y_1 = e^{-\frac{2}{3}\gamma\tau} \int e^{\frac{2}{3}\gamma\tau} \left(x_1 + \frac{1}{3}x_2 + \frac{1}{3}x_3 + \frac{1}{3}x_4 \right) + C e^{-\frac{2}{3}\gamma\tau} \quad (8)$$

($C : \text{const.}$)

In the steady state, the second term of Eq. (8) becomes to zero.

Next, let assume the solution of Eq. (6) is

$$x_k(\tau) = \rho_k \sin(\tau + \theta_k). \quad (9)$$

We pay attention to treat the non-resonance system and apply for the averaging method to Eq. (6). We obtain ρ_1 and θ_1 as follows.

$$\begin{aligned} \dot{\rho}_1 &= \lim_{T \rightarrow \infty} \int_0^T \varepsilon F_1 \cos(\tau + \theta_1) d\tau \\ \dot{\theta}_1 &= \lim_{T \rightarrow \infty} \int_0^T \frac{\varepsilon}{\rho_1} F_1 \sin(\tau + \theta_k) d\tau \end{aligned} \quad (10)$$

By solving the above equations, Eqs. (11) and (12) are obtained.

$$\begin{aligned} \dot{\rho}_1 &= -\frac{\varepsilon^2 \rho_k}{8} (\rho_k^2 - 4) \\ &- \frac{\varepsilon \gamma}{3(4\gamma^2 + 9)} \left\{ 9\rho_1 + 2\gamma\rho_2 \sin(\theta_1 - \theta_2) \right. \\ &- 3\rho_2 \cos(\theta_1 - \theta_2) + 2\gamma\rho_3 \sin(\theta_1 - \theta_3) \\ &- 3\rho_3 \cos(\theta_1 - \theta_3) + 2\gamma\rho_4 \sin(\theta_1 - \theta_4) \\ &- \left. 3\rho_4 \cos(\theta_1 - \theta_4) \right\} \end{aligned} \quad (11)$$

$$\begin{aligned} \dot{\theta}_1 &= -\frac{\varepsilon \gamma}{3\rho_k(4\gamma^2 + 9)} \left\{ 6\gamma\rho_1 + 2\gamma\rho_2 \cos(\theta_1 - \theta_2) \right. \\ &- 3\rho_2 \sin(\theta_1 - \theta_2) + 2\gamma\rho_3 \cos(\theta_1 - \theta_3) \\ &- 3\rho_3 \sin(\theta_1 - \theta_3) + 2\gamma\rho_4 \cos(\theta_1 - \theta_4) \\ &- \left. 3\rho_4 \sin(\theta_1 - \theta_4) \right\} \end{aligned} \quad (12)$$

We also apply the averaging method to Eqs. (3)-(5) as similarity.

In the steady state,

$$\begin{aligned} \dot{\rho}_k &= 0 \quad \text{and} \quad \dot{\theta}_k = 0 \\ (k &= 1, 2, 3, 4). \end{aligned} \quad (13)$$

must be satisfied. We obtain the solutions as follows. For the amplitude:

$$\rho_k = \sqrt{4 - \frac{8\gamma}{3\varepsilon(4\gamma^2 + 9)}} \quad (14)$$

($k = 1, 2$).

$$\rho_k = 2 \quad (15)$$

$$(k = 3, 4).$$

For the phase difference:

$$\theta_1 - \theta_2 = 0. \quad (16)$$

$$\theta_3 - \theta_2 = \theta_3 - \theta_4 = \theta_4 - \theta_1 = \theta_4 - \theta_2 = \pi. \quad (17)$$

We confirm that the first and the second oscillators are synchronized at in-phase. Other combination oscillators synchronize with anti-phase. These theoretical results correspond with the computer simulation results. Table I summarizes the comparison between theoretical and simulation results when the parameters are set as $\varepsilon = 0.1$, $\gamma = 0.1$. From this table, we can see that they match very well.

TABLE I
COMPARISON BETWEEN THEORETICAL AND SIMULATION
RESULTS FOR THE AMPLITUDE.

	Theory	Simulation
ρ_1, ρ_2	1.765	1.790
ρ_3, ρ_4	2.000	1.979

D. Case for polygonal network ($N \geq 6$)

Finally, we investigate synchronization phenomena in several types of two coupled polygonal oscillatory networks as shown in Fig. 5. The computer simulation result of the phase difference between the shared oscillators of each network structure are summarized in Tab. II. From this table, we can see that the shared (the first and the second) oscillators are synchronized at anti-phase state when the number of the coupled oscillators of each polygonal network is even number. While in the case of that the number of the coupled oscillators of each polygonal network is odd number, the shared oscillators can not synchronized at anti-phase state.

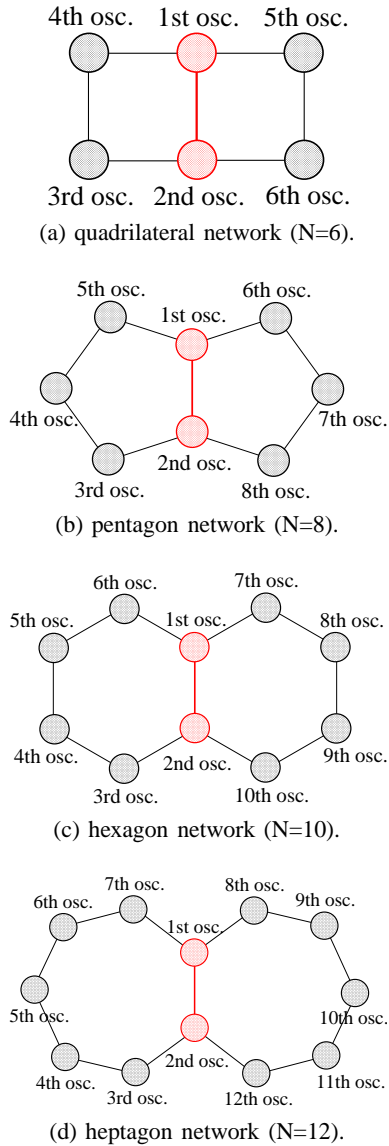


Fig. 5. Several types of two coupled polygonal oscillatory networks.

TABLE II
SYNCHRONIZATION STATES FOR DIFFERENT TYPES OF
POLYGONAL OSCILLATORY NETWORKS

Number of oscillators	Oscillator type	Phase
N=6 (quadrilateral)	Shared osc. (1-2)	180° (anti-phase)
	Independent osc.	180° (anti-phase)
N=8 (pentagon)	Shared osc. (1-2)	107.2°
	Independent osc.	152.8°
N=10 (hexagon)	Shared osc. (1-2)	180° (anti-phase)
	Independent osc.	180° (anti-phase)
N=12 (heptagon)	Shared osc. (1-2)	128.5°
	Independent osc.	158.7°

III. CONCLUSION

In this study, we investigated synchronization phenomena in two coupled polygonal oscillatory networks sharing the branch. By computer simulations, we confirmed that synchronization state of the shared oscillators depends on the number of coupled oscillators of the each polygonal network. We assume that the shared oscillators synchronize to make balance for whole system. In order to make clear the mechanism of such synchronization, to discuss a power consumption of coupled resistor and to analyze the stability of solutions obtained from the averaging method in detail are our future works.

REFERENCES

- [1] L.L. Bonilla, C.J. Perez Vicente and R. Spigler, "Time-periodic phases in populations of nonlinearly coupled oscillators with bimodal frequency distributions," *Physica D: Nonlinear Phenomena*, vol.113, no.1, pp.79-97, Feb. 1998.
- [2] J.A. Sherratt, "Invading wave fronts and their oscillatory wakes are linked by a modulated traveling phase resetting wave," *Physica D: Nonlinear Phenomena*, vol.117, no.1-4, pp.145-166, June 1998.
- [3] G. Abramson, V.M. Kenkre and A.R. Bishop, "Analytic solutions for nonlinear waves in coupled reacting systems," *Physica A: Statistical Mechanics and its Applications*, vol.305, no.3-4, pp.427-436, Mar. 2002.
- [4] I. Belykh, M. Hasler, M. Lauret and H. Nijmeijer, "Synchronization and graph topology," *Int. J. Bifurcation and Chaos*, vol.15, no.11, pp.3423-3433, Nov. 2005.
- [5] C.M. Gray, "Synchronous oscillations in neural systems: mechanisms and functions," *J. Computational Neuroscience*, vol.1, pp.11-38, 1994.
- [6] R. Stoop and C. Wagner, "Neocortex's architecture optimizes computation, information transfer and synchronizability, at given total connection length," *International Journal of Bifurcation and Chaos*, vol.17, no.7, pp.2257-2279, 2007.
- [7] T. Suezaki and S. Mori, "Mutual synchronization of two oscillators," *Trans. IECE*, vol.48, no.9, pp.1551-1557, Sep. 1965.
- [8] H.B. Fotsina and J. Daafouza, "Adaptive synchronization of uncertain chaotic colpitts oscillators based on parameter identification" *Physics Letters A*, vol.339, pp.304-315, May. 2005.

Chaos Control of the Chaotic Colpitts Oscillator

Arturo Buscarino, Luigi Fortuna and Mattia Frasca

Dipartimento di Ingegneria Elettrica
Elettronica e dei Sistemi, Facoltà di Ingegneria
Laboratorio sui Sistemi Complessi
Scuola Superiore di Catania
Università degli Studi di Catania
viale A. Doria 6, 95125 Catania, Italy.

Gregorio Sciuto

Dipartimento di Ingegneria Elettrica
Elettronica e dei Sistemi
Facoltà di Ingegneria
Università degli Studi di Catania
viale A. Doria 6, 95125 Catania, Italy.

Abstract—In this work, chaos control of the chaotic Colpitts oscillator is obtained through a new technique acting at the circuit level. It consists of the addition of a simple passive control network, constituted by a coupled inductor and a variable resistor. Numerical and experimental results demonstrate how by varying this external parameter different dynamics can be obtained.

I. INTRODUCTION

Since the discovery of chaos, the problem of controlling it, i.e., the problem of stabilization of equilibrium points or of some periodic orbit of the system (in general, the process that suppresses chaos) [1], [2], [3], [4], [5] attracted a lot of interest. Many different solutions have been proposed to solve this problem. In general, the techniques for chaos control can be classified in feedback and open-loop methods. Feedback methods usually allow the system to be stabilized in any of the unstable periodic orbits lying in the chaotic attractor, but require fast and accurate response to work properly. On the contrary, open-loop techniques exploit the effect of some (small) perturbations added to the system to modify the final state of the controlled dynamics.

Furthermore, when the problem of controlling electronic chaotic circuits is dealt with, issues such as easy of implementation and direct access to state variables may arise. In this case, some of the techniques for chaos control, although general, may require significant additional circuitry and/or may be of difficult implementation. For this reason, the research on control methods of direct applicability in specific chaotic circuits is an actual topic.

In this work, we discuss a new technique operating at the circuit level for chaos control in the Colpitts oscillator. The Colpitts oscillator [6], one of the simplest examples of an electronic oscillator, has been recently demonstrated to be able to exhibit chaotic behavior

[7]. It is therefore possible to design Colpitts oscillators able to generate high-frequency chaotic signals for communications applications [7]. Other configurations of this base circuit have been studied in [8] for inductorless implementations and in [9] for ultra-high frequency oscillations.

The paper is organized as follows: in Sec. II the control technique is discussed; in Sec. III the behavior of the circuit mathematical model is numerically investigated characterized with respect to the bifurcation parameter; in Sec. IV experimental results are discussed. Finally, Sec. V draws some concluding remarks.

II. THE CONTROLLED CHAOTIC COLPITTS OSCILLATOR

The starting point for the circuit introduced in this paper is the common base Colpitts oscillator reported in Fig. 1(a). This circuit belongs to the class of feedback oscillators. The feedback is provided by the inductor and the voltage divider made by the two capacitors, while R_2 and the voltage supply implement the polarization network for the transistor. According to the Barkhausen stability criterion, the parameters of this circuit can be chosen in order to obtain steady-state oscillations at a frequency determined by the two capacitors and the inductor and given by

$$f_0 = \frac{1}{2\pi\sqrt{L \cdot \left(\frac{C_1 C_2}{C_1 + C_2}\right)}} \quad (1)$$

Beyond the periodic regime, it has been found that this circuit is also able to generate chaotic signals, thus constituting one of the simplest chaotic oscillators [7]. Interestingly, the observed chaotic behavior is robust with respect to the type of the transistor used (a 2N2222 BJT in our experiments).

Following the analysis given in [7], the mathematical model of the chaotic Colpitts oscillator can be derived taking into account that, as it is experimentally verified, transistor $Q1$ only operates in forward active and cutoff regions. Therefore, the behavior of base current I_B can be modelled as a piece-wise linear function. The equations of the whole chaotic circuit can be thus written as follows:

$$\begin{aligned} C_1 \frac{dV_{C1}}{dt} &= I_L - \beta I_B \\ C_2 \frac{dV_{C2}}{dt} &= \frac{V_{ee} - V_{C2}}{R_2} + I_L + I_B \\ L \frac{dI_L}{dt} &= V_{cc} - V_{C1} - V_{C2} - I_L R_1 \end{aligned} \quad (2)$$

where

$$I_B = \begin{cases} 0 & \text{if } V_{BE} \leq V_{th} \\ \frac{V_{BE} - V_{th}}{R_{ON}} & \text{otherwise} \end{cases} \quad (3)$$

and β and R_{ON} are the forward current gain and the small-signal on-resistance of the base-emitter junction of the transistor, respectively.

The idea underlying the chaos control is to couple the inductor of the Colpitts oscillator with another inductor inserted in a passive circuit including a control parameter as shown in Fig. 1(b). The passive circuit in Fig. 1(b) is composed by the coupled inductor L_c and a resistor R_L . The inductor L_c is implemented by shaping a further conducting wire around the same coil core of the inductor L . The control exploits the mutual influence effect of the two coupled inductors: varying an element of the passive control network (the resistor R_L) the behavior of the chaotic Colpitts oscillator is controlled.

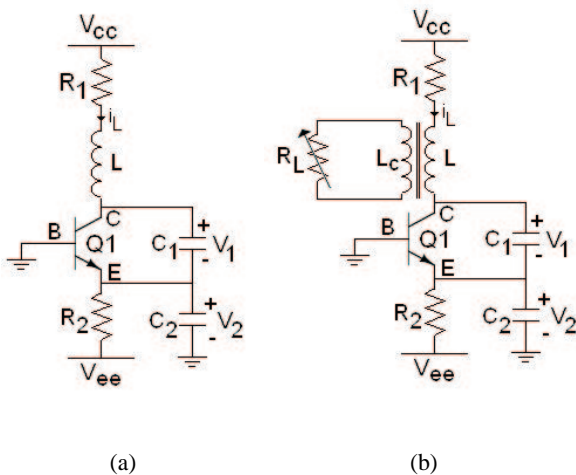


Fig. 1. (a) Chaotic Colpitts oscillator. (b) Controlled chaotic Colpitts oscillator. Components: $R_1 = 35\Omega$, $R_2 = 500\Omega$, $C_1 = 54nF$, $C_2 = 54nF$, $L = 98.5\mu H$, $L_c = 23\mu H$, $Q1 = BJT2N2222$, $R_L = 1k\Omega$ -potentiometer, $V_{cc} = 5V$, $V_{ee} = -5V$.

Introducing the control in Eqs. (2), they become:

$$\begin{aligned} C_1 \frac{dV_{C1}}{dt} &= I_L - \beta I_B \\ C_2 \frac{dV_{C2}}{dt} &= \frac{V_{ee} - V_{C2}}{R_2} + I_L + I_B \\ L \frac{dI_L}{dt} - M \frac{dI_2}{dt} &= V_{cc} - V_{C1} - V_{C2} - I_L R_1 \\ L_c \frac{dI_2}{dt} - M \frac{dI_L}{dt} &= -R_L I_2 \end{aligned} \quad (4)$$

or, equivalently:

$$\begin{aligned} C_1 \frac{dV_{C1}}{dt} &= I_L - \beta I_B \\ C_2 \frac{dV_{C2}}{dt} &= \frac{V_{ee} - V_{C2}}{R_2} + I_L + I_B \\ \frac{dI_L}{dt} &= \frac{L_c}{LL_c - M^2} \left(V_{cc} - V_{C1} - V_{C2} - I_L R_1 - \frac{M}{L_c} R_L I_2 \right) \\ \frac{dI_2}{dt} &= \frac{M}{LL_c - M^2} \left(V_{cc} - V_{C1} - V_{C2} - I_L R_1 - \frac{L}{M} R_L I_2 \right) \end{aligned} \quad (5)$$

where $M = k\sqrt{LL_c}$ represents the mutual inductance between L and L_c , given the coupling factor k .

The behavior obtained by inserting the proposed control in the chaotic Colpitts oscillator can be qualitatively studied taking into account some simple circuital considerations. When R_L is large (in the limit case $R_L \rightarrow \infty$, it is an open circuit), the current I_2 is very small (in the limit case, zero), and the passive control network has no influence on the chaotic Colpitts oscillator. Decreasing R_L the effect of the mutual inductance becomes more important. When R_L is small, the term $R_L I_2$ in the last equation of (4) becomes negligible and $\frac{dI_2}{dt} \simeq \frac{M}{L_c} \frac{dI_L}{dt}$. Substituting this in the third equation of (4), one can argue that Eqs. (4) become similar to (2) except for L which has to be substituted by $L - \frac{M^2}{L_c}$, with a net effect of decreasing the value of the equivalent inductor L . Finally, when R_L is very small, we expect that oscillations are suppressed, since the coupled inductor is short-circuited.

III. NUMERICAL RESULTS

The behavior of the mathematical model of the circuit as in Eqs. (5) has been investigated through numerical simulations for the values of components given in Fig. 1. The further parameters (β , R_{ON} and k) of the model have been fixed on the basis of their estimated values: $\beta = 200$, $R_{ON} = 100\Omega$ and $k = 0.8$.

Chaotic behavior has been observed when the circuit is not controlled ($R_L \rightarrow \infty$). Fig. 2 shows the waveforms of the simulated output v_c and the corresponding attractor.

The suitability of the chaos control approach is proven when R_L assumes finite values. Different periodic orbits can be stabilized. Fig. 3 shows three examples of the behavior of the controlled circuit for different values

of R_L . For $R_L = 100\Omega$ another chaotic attractor is obtained. Several other windows of periodic behavior and chaotic regions have been observed when R_L is varied.

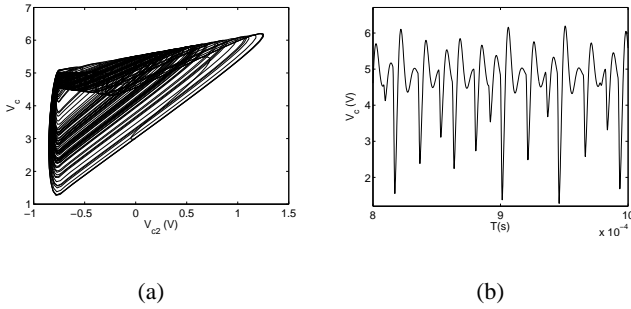


Fig. 2. Simulations of the not controlled Colpitts oscillator. (a) Projection on the plane $v_{C2} - v_C$ of the attractor. (b) Trend of v_c .

IV. EXPERIMENTAL CHARACTERIZATION

The behavior of system (5) has been experimentally investigated with respect to different values of the control parameter R_L . It has been found that for different values of R_L limit cycles of different periods can be stabilized. Furthermore, several windows of chaotic behavior have been also observed. Some examples are reported in Fig. 4. In particular, Fig. 4(a) shows the chaotic attractor obtained for $R_L = 925\Omega$ which corresponds to the nominal case of not controlled behavior. Decreasing R_L , stable limit cycles are obtained (Fig. 4(b) and Fig. 4(c)). Fig. 4(d) shows a chaotic attractor obtained for $R_L = 180\Omega$. Two other limit cycles obtained for $R_L = 90\Omega$ and $R_L = 35\Omega$ are shown in Fig. 4(e) and Fig. 4(f), respectively.

The complete experimental bifurcation diagram of the controlled chaotic Colpitts oscillator is shown in Fig. 5, showing the local maxima $V_{c,max}$ of the output signal V_c at different values of R_L . Waveforms have been acquired by using a NI USB6255 data acquisition board, with sampling frequency $f_s = 1000kHz$. As theoretically predicted, for $R_L \simeq 0$ a fixed point is obtained. For small values of R_L , a period-1 limit cycle is obtained. A cascade of period doubling bifurcations is then observed for increasing values of R_L , leading through the typical period-doubling route-to-chaos scenario to a first window of chaotic behavior. This window is followed by another window of periodic behavior that for further increasing values of R_L leads to the chaotic region observed in the not-controlled chaotic Colpitts oscillator. The attractors

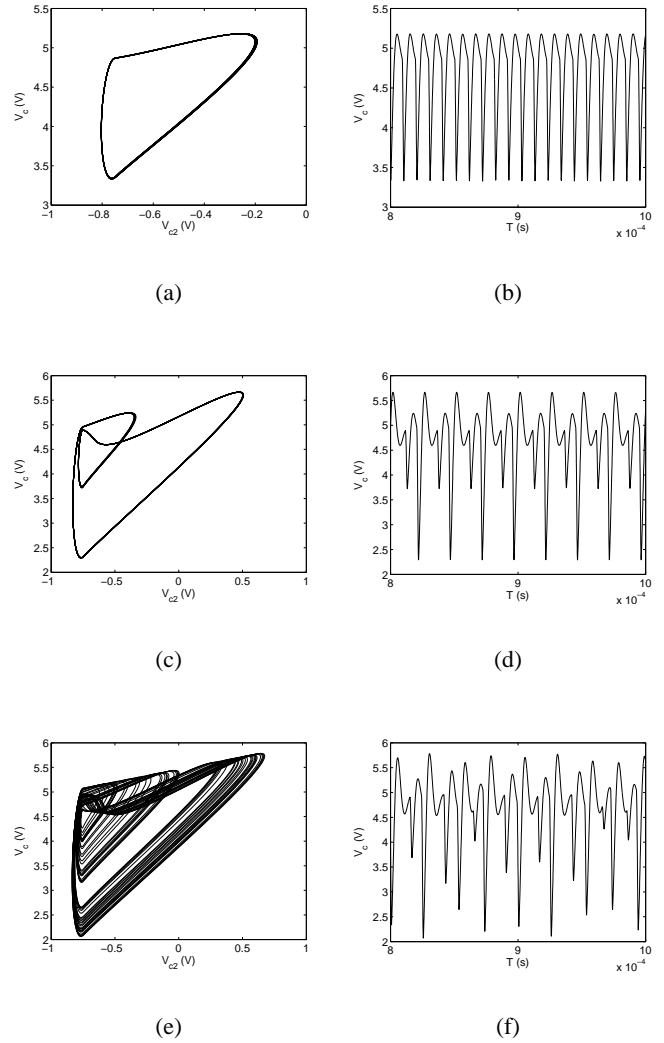


Fig. 3. Simulations of the not controlled Colpitts oscillator. (a) Projection on the plane $v_{C2} - v_C$ of the attractor for $R_L = 20\Omega$. (b) Trend of v_c for $R_L = 20\Omega$. (c) Projection on the plane $v_{C2} - v_C$ of the attractor for $R_L = 70\Omega$. (d) Trend of v_c for $R_L = 70\Omega$. (e) Projection on the plane $v_{C2} - v_C$ of the attractor for $R_L = 100\Omega$. (f) Trend of v_c for $R_L = 100\Omega$.

shown in Fig. 4 can be retrieved in the bifurcation diagram of Fig. 5 along with the other dynamical behaviors of the circuit.

V. CONCLUSIONS

In this paper, a new technique for chaos control in the chaotic Colpitts oscillator has been introduced. The technique exploits the coupling between a passive network coupled to the circuit through mutual inductors and the oscillator itself. The theoretical and experimental analysis allowed us to conclude that varying a resistor in the control network it is possible to control the behavior

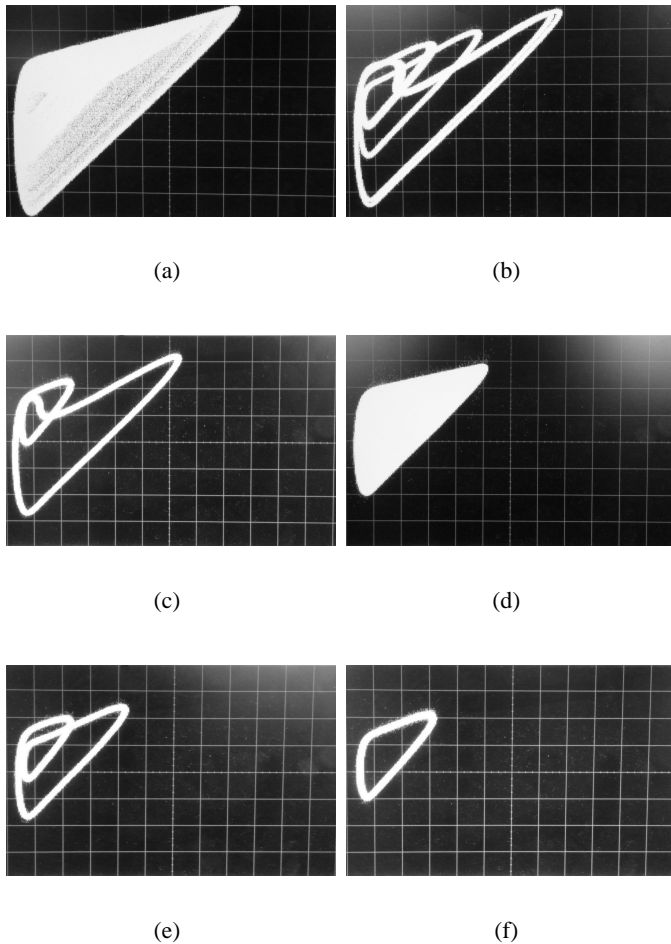


Fig. 4. Projection on the plane $v_{C2} - v_C$ of the attractor for different values of the control parameter R_L . Horizontal axis: 200mV/div ; vertical axis 500mV/div . (a) $R_L = 925\Omega$, (b) $R_L = 475\Omega$, (c) $R_L = 315\Omega$, (d) $R_L = 180\Omega$, (e) $R_L = 90\Omega$, (f) $R_L = 35\Omega$.

of the chaotic Colpitts oscillator in a simple and effective way. Several limit cycles can be stabilized. The complete bifurcation diagram with respect to this parameter also allowed to discover new windows of chaotic behavior not observed in the chaotic Colpitts oscillator, thus demonstrating the rich dynamics of this single-transistor chaotic circuit. Being passive and composed of only two elements, the control network has the advantage of a direct and easy implementation.

REFERENCES

- [1] G. Chen, "Controlling chua's global unfolding circuit family," *IEEE Trans. Circuits Syst. I Fundam. Theory Appl.* **40**, 11, pp. 829–832, 1993.
- [2] M. J. Ogorzalek, "Taming chaos: Part II control," *IEEE Trans. Circuits Syst. I Fundam. Theory Appl.* **40**, 10, pp. 700–706, 1993.
- [3] M. J. Ogorzalek, "Controlling chaos in electronic circuits," *Philosophical Transactions: Physical Sciences and Engineering* **353**, 1701, pp. 127–136, 1995.

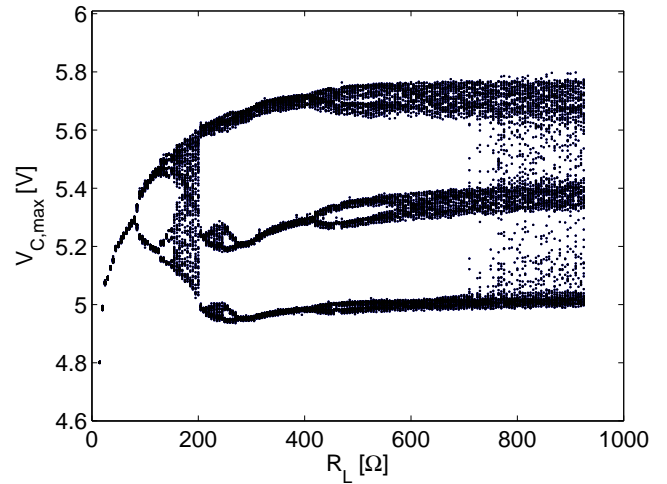


Fig. 5. Experimental bifurcation diagram of the controlled chaotic Colpitts oscillator.

- [4] T. Kapitaniak, L. Kocarev, and L. Chua, "Controlling chaos without feedback and control signals," *International Journal of Bifurcation and Chaos* **3**, 2, pp. 459–468, 1993.
- [5] G. Chen, X. Yu, *Chaos Control: Theory and Applications*, Lecture Notes in Control and Information Sciences, Springer, 2003.
- [6] E. H. Colpitts, "Oscillation generator", U.S.patent US001624537, 1927.
- [7] M. P. Kennedy, "Chaos in the Colpitts Oscillator", *IEEE Trans. Circuits Syst. I Fundam. Theory Appl.*, vol. 41, no. 11, pp. 771–774, 1994.
- [8] P. Arena, S. Baglio, L. Fortuna, G. Manganaro, "How State Controlled CNN Cells Generate the Dynamics of the Colpitts-Like Oscillator", *IEEE Trans. Circuits Syst. I Fundam. Theory Appl.*, vol. 43, no. 7, pp. 602–605, 1996.
- [9] J.Y. Effa, B.Z. Essimbi, J. Mucho Ngundam, "Synchronization of improved chaotic Colpitts oscillators using nonlinear feedback control", *Nonlinear Dynamics*, vol. 58, pp. 39–47, 2009.

Generalized synchronization in mutually coupled dynamical systems

Olga I. Moskalenko, Alexey A. Koronovskii, Alexander E. Hramov and Svetlana A. Shurygina

Faculty of Nonlinear Processes, Saratov State University,

83, Astrakhanskaya, Saratov, 410012, Russia

Email: moskalenko@nonlin.sgu.ru

Abstract—In present report the generalized synchronization regime onset in systems with a mutual type of coupling is analyzed. To define the mechanism of the synchronous regime arising the dependence of Lyapunov exponents on the coupling parameter is considered. The nearest neighbor method to mutually coupled dynamical systems is applied. The main results are illustrated using the examples of mutually coupled Rössler oscillators.

I. INTRODUCTION

Synchronization of chaotic oscillations is one of the most relevant directions of nonlinear dynamics attracting great attention of modern scientists [1]. The interest to it is connected both with a large fundamental significance of its investigation [2] and a wide practical applications, e.g., for the transmission of information, diagnostics of dynamics of some biological systems, control of chaos in the microwave systems, etc [3]–[7]. Several types of the synchronous chaotic system behavior are traditionally distinguished. They are phase [8], generalized [9], lag [10], complete [11], time scale synchronization [12] and others.

One of the most interesting types of the synchronous chaotic system behavior is the generalized synchronization (GS) regime [9], [13], [14]. Such type of chaotic synchronization has been firstly proposed for two unidirectionally coupled chaotic oscillators [9]. Later the concept of GS has been extended to the mutually coupled systems and networks of coupled nonlinear elements [13], [14]. At that, it should be noted that the GS regime has been investigated in detail only in unidirectionally coupled chaotic oscillators, whereas such type of chaotic synchronization in mutually coupled dynamical systems and complex networks has been analyzed poorly enough. Known works (see, e.g. [13], [14]) are directed to the development of new methods for the GS regime detection in such systems on the basis of the auxiliary system approach [15] proposed for unidirectionally coupled oscillators. At the same

time, the concept of the GS regime, the mechanisms of its arising and the correctness of application of the auxiliary system approach even in two mutually coupled dynamical systems remain still unclear.

In the present report we analyze the possibility of the GS regime existence in systems with a mutual type of coupling. Thereto we compute the spectrum of Lyapunov exponents (LE) and analyze its behavior with the coupling parameter value increasing. As would be shown bellow, the transition of the one of the positive LEs to the negative values could be treated as the GS regime onset in mutually coupled dynamical systems. We prove our assumptions by the nearest neighbor method proposed in [16].

II. GENERALIZED SYNCHRONIZATION REGIME

Generalized synchronization (GS) regime in unidirectionally coupled dynamical systems, the drive $\mathbf{x}_d(t)$ and response $\mathbf{x}_r(t)$ ones, means the presence of the unique functional relation $\mathbf{F}[\cdot]$ between their system states after the transient process is finished [9], i.e. $\mathbf{x}_r(t) = \mathbf{F}[\mathbf{x}_d(t)]$. It is clear that for two mutually coupled chaotic oscillators $\mathbf{x}_{1,2}(t)$ the definition of GS given above should be extended as the following $\mathbf{F}[\mathbf{x}_1(t), \mathbf{x}_2(t)] = 0$.

To reveal the presence of the GS regime in unidirectionally coupled dynamical systems the auxiliary system method [15] is frequently used. It is one of the accurate ones and simple enough for realization. Therefore, several attempts to apply such methods both for mutually coupled dynamical systems and complex networks are known in literature. In particular, in Ref. [13] the modification of the auxiliary system method for the analysis of GS in mutually coupled dynamical systems has been proposed. Due to such approach two auxiliary units $\mathbf{u}_{1,2}(t)$ being identical to the systems $\mathbf{x}_{1,2}(t)$ by the control parameter values but starting with other initial conditions should be introduced. At that, the system $\mathbf{x}_1(t)$ should

drive the oscillator $\mathbf{u}_2(t)$, whereas oscillator $\mathbf{x}_2(t)$ should drive the system $\mathbf{u}_1(t)$ (obviously, the type of coupling between the initial $\mathbf{x}_{1,2}(t)$ and auxiliary $\mathbf{u}_{1,2}(t)$ systems should be unidirectional). When the coupling parameter value increases the original and auxiliary system states can become coinciding after the initial transients, with two pairs of “identical” systems achieving synchronization at different coupling thresholds. When the first pair of “identical” oscillators (e.g., $\mathbf{x}_1(t)$ and $\mathbf{u}_1(t)$) becomes synchronized the so-called partial GS regime is observed. The case when both pairs of “identical” oscillators demonstrate coinciding oscillations corresponds to the complete GS regime (see for detail [13]).

Nevertheless, such modification of the auxiliary system approach gives the contradictory results. In particular, our calculations show that the synchronous regime (lag (LS) or even complete (CS) synchronization) between the systems $\mathbf{x}_{1,2}(t)$ arises before the complete GS onset in the terminology of Ref. [13] that conflicts with the definition of the GS regime itself, since the CS and LS regimes are partial cases of the GS and correspond to their strong forms [17].

Taking into account the arguments mentioned above one can draw a conclusion that the concept of the GS regime in the mutually coupled dynamical systems and complex networks demands reconsideration, with the auxiliary system approach in the form described in Ref. [13] being unapplicable for such systems.

Except the auxiliary system approach in the unidirectionally coupled dynamical systems the nearest neighbor method [9], [16] can be used for the GS regime detection. It is also possible to compute Lyapunov exponents to detect the presence of GS [18]. For unidirectionally coupled chaotic oscillators the negativity of the largest conditional Lyapunov exponent (computed for the response system) can be considered as a criterion of the GS presence [18].

Both methods mentioned above can be also applied for the systems with a mutual type of coupling. On the one hand, the nearest neighbor method may be used to detect the presence of the functional relation between the interacted system states, but it gives only approximate result [9], [16]. On the other hand, the Lyapunov exponent computation method is more accurate one, but the application of such method to the mutually coupled dynamical systems demands additional studies to be carried out. At the same time, the application of both methods together gives a clear view on the GS in the mutually coupled oscillators and networks. The next sections of our work are devoted to the detailed

description of the results obtained with the help of these methods.

III. LYAPUNOV EXPONENTS

Lyapunov exponents (LEs) are known to be a powerful tool for the analysis of the complex system dynamics. The spectrum of Lyapunov exponents allows to detect the qualitative changes of the system behavior when its control parameter is varied [18], [19]. It is clear that appearance of any type of chaotic synchronization can be detected by the changes in the behavior of Lyapunov exponent spectrum. In particular, as we have mentioned in Section II, the GS regime in unidirectionally coupled dynamical systems takes place when the largest conditional Lyapunov exponent becomes negative [18], [20]. The analogous situation takes place in mutually coupled dynamical systems, i.e., with the coupling parameter value increasing, one of the positive Lyapunov exponents passes through zero [10].

Transition of the positive Lyapunov exponent in the field of the negative values has been explained in literature (see, e.g. [10]) by the appearance of the LS regime (when the interacting systems demonstrate identical oscillations shifted in time). At the same time, the difference between the coupling parameter values corresponding to the points where the considered positive LE becomes negative and where the onset of LS is observed can be too large to be explained by the presence of intermittency near the boundary of LS regime.

In the present report we analyze in detail the relationship between the boundary of the LS regime and the critical line when one of the positive LEs passes through zero. For such purpose we consider two mutually coupled Rössler systems described by the following differential equations:

$$\begin{aligned}\dot{x}_{1,2} &= -\omega_{1,2}y_{1,2} - z_{1,2} + \varepsilon(x_{2,1} - x_{1,2}), \\ \dot{y}_{1,2} &= \omega_{1,2}x_{1,2} + ay_{1,2}, \\ \dot{z}_{1,2} &= p + z_{1,2}(x_{1,2} - c),\end{aligned}\tag{1}$$

where $\mathbf{x}_{1,2}(t) = (x_{1,2}, y_{1,2}, z_{1,2})^T$ are the vector-states of interacting systems, ε is a coupling parameter. The control parameter values have been selected by analogy with our previous works as $a = 0.15$, $p = 0.2$, $c = 10$. The parameters $\omega_{1,2}$ define the natural frequencies of the mutually coupled oscillations. In our investigations we have fixed $\omega_2 = 0.95$ and varied the ω_1 parameter in the range $[0.89; 1.01]$ providing the frequency mismatch of the oscillators.

To detect the presence of LS regime we have analyzed the behavior of the discrete maps obtained from the

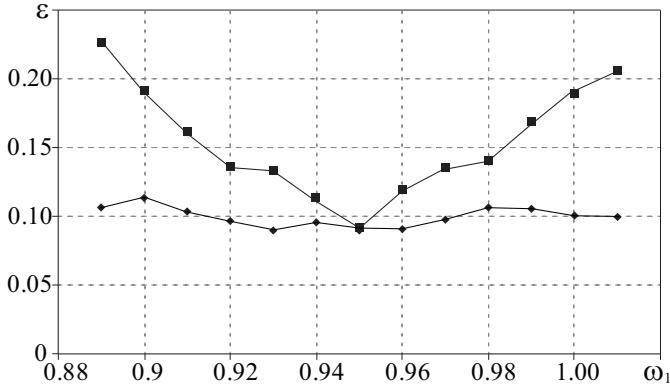


Fig. 1. The boundary of the LS regime onset (■) and the critical curve corresponding to zero crossing of one of the positive LE (◆) in mutually coupled Rössler oscillators (1)

original system (1) by means of Poincaré secant (as a secant planes we have used the planes $y_{1,2} = 0$, $\dot{y}_{1,2} < 0$). Taking into account the fact that the LS regime in the flow systems corresponds to the CS one in discrete maps [21] we have analyzed the CS regime onset in the maps reduced from (1). The boundary of the LS regime onset in system (1) is shown in Fig. 1 (numerically obtained data are marked by squares). In Fig. 1 the critical curve corresponding to the case when one of the positive LEs passes through zero is also shown (numerically obtained data are marked by diamonds). It is easy to see that the threshold of the LS regime grows with the value of the control parameter mismatch increasing, whereas the moment of the transition of the positive LE towards the negative values depends on the value of parameter detuning slightly. At the same time, the intermittent LS can be observed both before and after zero crossing of the positive LE or be non-observed at all. On the basis of calculations being made one can assume that the transition of the positive LE to the negative values could be connected with the GS regime onset in the mutually coupled dynamical systems. Nevertheless, such assumptions demand additional approval.

IV. NEAREST NEIGHBOR METHOD

To prove our assumptions that the zero pass of one of the positive LE could be connected with the GS regime onset in mutually coupled dynamical systems we apply the nearest neighbor method [9], [16] to the system under study. The main idea of such method consist in the fact that the presence of the functional relation between the interacting system states means that two close states (“origins”) in the phase space of the first system correspond to two close states (“images”) in

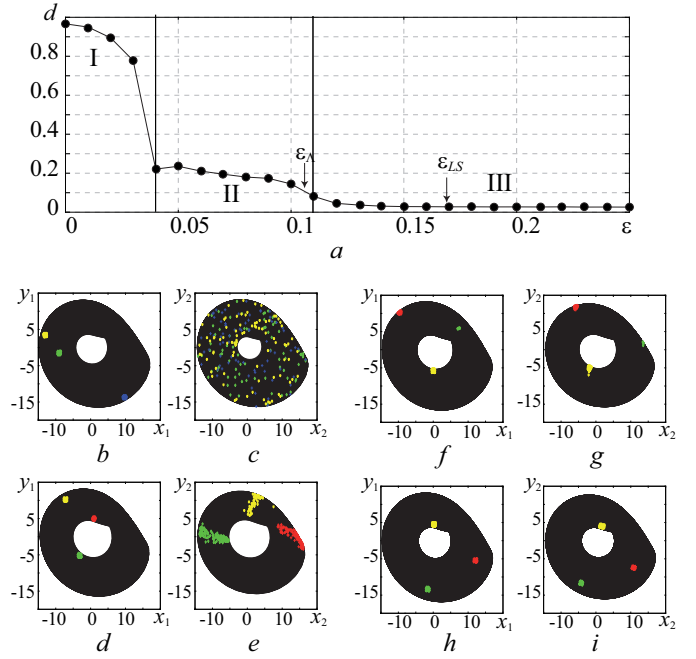


Fig. 2. (a) The quantitative measure of the GS regime onset d versus coupling parameter strength ε obtained for systems (1) with $\omega_1 = 0.99$. The critical values of the coupling parameter $\varepsilon_\Lambda = 0.106$ (the moment of zero crossing of one of the positive Lyapunov exponents) and $\varepsilon_{LS} = 0.169$ (the threshold of LS regime) are marked by arrows. (b–i) The phase portraits of Rössler oscillators for different values of the coupling parameter: (b–c) $\varepsilon = 0.01$ (the asynchronous state); (d–e) $\varepsilon = 0.05$ (the PS regime); (f–g) $\varepsilon = 0.12$ (the GS regime); (h–i) $\varepsilon = 0.18$ (the LS regime)

the phase space of the second system [9]. The principal advantage of such method is that it allows to detect the presence of a functional relation between two systems using only corresponding time series (independently on the way of their obtainment). Therefore, it could be easily applied to the data obtained both experimentally and numerically [16], [22], with the type of coupling (is it unidirectional or bidirectional) being not crucial. Although, as we have mentioned in Section II, such method is a rough enough, it can be used for the approval of the proposed theory.

In our calculations we have used the modification of the nearest neighbor method allowing to characterize the degree of the neighbor closeness quantitatively [16]. As a numerical indicator for the existence of a continuous function between the interacting systems the mean distance between images $\mathbf{x}_2^{n,nn}$ of nearest neighbors $\mathbf{x}_1^{n,nn}$ in the second system normalized by the average distance δ of randomly chosen states of the first system, i.e.

$$d = \frac{1}{N\delta} \sum_{n=0}^{N-1} \|\mathbf{x}_2^n - \mathbf{x}_2^{nn}\|, \quad (2)$$

where N is the number of randomly chosen points, has been calculated. If the GS regime takes place $d \rightarrow 0$, whereas $d \approx 1$ when the functional relation between the interacted system states is absent.

The dependence of the quantitative measure d mentioned above on the coupling parameter strength ε is shown in Fig. 2,a. One can easily see that such characteristics decreases monotonically with the coupling parameter value increasing. At that, the $(\varepsilon; d)$ -plane can be conventionally divided into 3 parts: I – $\varepsilon \in [0; 0.04)$ (the d -characteristics decreases very sharply indicating the transition from the asynchronous state to the phase synchronization (PS) regime at $\varepsilon_{PS} = 0.04$), II – $\varepsilon \in [0.04; 0.11)$ (the d -characteristics decreases slowly indicating occurrence of GS regime), III – $\varepsilon > 0.11$ ($d \approx 0$). The values of the coupling parameter corresponding to zero crossing of the positive LE ($\varepsilon_{\Lambda} = 0.106$) and onset of the LS regime ($\varepsilon_{LS} = 0.169$) are marked by arrows. It is easy to see that the value of d does not practically changes and remains close to zero in the range of coupling parameter $\varepsilon \in [\varepsilon_{\Lambda}, \varepsilon_{LS}]$ that leads to the conclusion that the GS regime arises before the LS one in mutually coupled dynamical systems as well as in the case of the unidirectionally coupled systems.

In Fig. 2,b-i the phase portraits of interacted Rössler systems (1) for different values of the coupling parameter strength are shown. At the phase portraits of the first system (b,d,f,h) three randomly chosen points and its nearest neighbors are marked by red, yellow and green, respectively. Fig. 2,c,e,g,i illustrates the images of the nearest neighbors of the first system mentioned above into the phase space of the second system. One can easily see that for a small values of the coupling parameter ($\varepsilon = 0.01$) all image points are distributed randomly on the whole attractor (c). With the coupling parameter value increasing the points become concentrated in a limited range of attractor, with the radius of such distribution decreasing when the coupling parameter grows (compare Fig. 2,e,g). Note, that the character of the images of the nearest neighbor location is practically the same in the case of GS (g) and LS (i) regimes. The only one difference between them consists in the fact that in the LS regime the representation points corresponding to the nearest neighbors are reflected practically in the same part of chaotic attractor (i) whereas in the GS regime they can be concentrated in a different regions (g).

V. CONCLUSION

In the present report the GS regime onset in systems with a mutual type of coupling is analyzed. The GS

regime onset is shown to be connected with the zero crossing of one of the positive Lyapunov exponents. The obtained results are proved by means of the nearest neighbor method.

ACKNOWLEDGMENT

This work has been supported by Federal special purpose programme “Scientific and educational personnel of innovation Russia (2009 - 2013)”, President Program for the support of young sciences with PHD degree (project MK-1225.2010.2) and Russian Foundation for Basic Research (project 09-02-92421).

REFERENCES

- [1] S. Boccaletti, J. Kurths, G. V. Osipov, D. L. Valladares, and C. S. Zhou, *Physics Reports*, vol. 366, pp. 1, 2002.
- [2] A. S. Pikovsky, M. G. Rosenblum, and J. Kurths, *Synchronization: a universal concept in nonlinear sciences*, Cambridge University Press, 2001.
- [3] R. Roy, *Nature*, vol. 438, pp. 298–299, 2005.
- [4] H. Jaeger and H. Haas, *Science*, vol. 304, pp. 78–80, April 2008.
- [5] L. Glass, *Nature (London)*, vol. 410, pp. 277–284, 2001.
- [6] A. N. Pavlov, O. V. Sosnovtseva, A. R. Ziganshin, N. H. Holstein-Rathlou, and E. Mosekilde, *Physica A*, vol. 316, pp. 233–249, 2002.
- [7] M. G. Rosenblum, A. S. Pikovsky, and J. Kurths, *Fluctuation and Noise Letters*, vol. 4, no. 1, pp. L53–L62, 2004.
- [8] M. G. Rosenblum, A. S. Pikovsky, and J. Kurths, *Phys. Rev. Lett.*, vol. 76, no. 11, pp. 1804–1807, 1996.
- [9] N. F. Rulkov, M. M. Sushchik, L. S. Tsimring, and H. D. I. Abarbanel, *Phys. Rev. E*, vol. 51, no. 2, pp. 980–994, 1995.
- [10] M. G. Rosenblum, A. S. Pikovsky, and J. Kurths, *Phys. Rev. Lett.*, vol. 78, no. 22, pp. 4193–4196, 1997.
- [11] L. M. Pecora and T. L. Carroll, *Phys. Rev. Lett.*, vol. 64, no. 8, pp. 821–824, 1990.
- [12] A. E. Hramov and A. A. Koronovskii, *Chaos*, vol. 14, no. 3, pp. 603–610, 2004.
- [13] Z. Zheng, X. Wang, and M. C. Cross, *Phys. Rev. E*, vol. 65, pp. 056211, 2002.
- [14] S. Guan, X. Wang, X. Gong, K. Li, and C. H. Lai, *CHAOS*, vol. 19, pp. 013130, 2009.
- [15] H. D. I. Abarbanel, N. F. Rulkov, and M. M. Sushchik, *Phys. Rev. E*, vol. 53, no. 5, pp. 4528–4535, 1996.
- [16] U. Parlitz, L. Junge, and W. Lauterborn, *Phys. Rev. E*, vol. 54, no. 2, pp. 2115–2117, 1996.
- [17] K. Pyragas, *Phys. Rev. E*, vol. 54, no. 5, pp. R4508–R4511, 1996.
- [18] K. Pyragas, *Phys. Rev. E*, vol. 56, no. 5, pp. 5183–5188, 1997.
- [19] A. E. Hramov, A. A. Koronovskii, and M. K. Kurovskaya, *Phys. Rev. E*, vol. 78, pp. 036212, 2008.
- [20] A. E. Hramov and A. A. Koronovskii, *Phys. Rev. E*, vol. 71, no. 6, pp. 067201, 2005.
- [21] A. A. Koronovskii, A. E. Hramov, and A. E. Khranova, *JETP Letters*, vol. 82, no. 3, pp. 160–163, 2005.
- [22] B. S. Dmitriev, A. E. Hramov, A. A. Koronovskii, A. V. Starodubov, D. I. Trubetskov, and Y. D. Zharkov, *Physical Review Letters*, vol. 102, no. 7, pp. 074101, 2009.

Chaotic Behavior of Hysteresis Cellular Nonlinear Networks and its Control

Angela Slavova
Institute of Mathematics and Informatics
Bulgarian Academy of Sciences
Sofia 1113, Bulgaria
slavova@math.bas.bg

Abstract- The main goal of this paper is to model and investigate Hysteresis Cellular Nonlinear Networks (CNN). Special type of memory-based relation between an input signal and an output signal in this circuit is introduced. Hysteresis reaction-diffusion model is studied from the point of view of local activity theory. Numerical simulations and discussions about the pattern formation in such model are presented. Feedback control is applied in order to stabilize the model.

Index terms- Hysteresis Cellular Nonlinear Networks, feedback, local activity theory, chaos, feedback control

I. INTRODUCTION

Hysteresis is defined as a rate independent memory effect. Such a setting occurs, for example, in the Weiss mean field theory of ferromagnetism [6], because of a positive feedback effect. In this model the bistability, and consequently the occurrence of hysteresis effects, corresponds to the presence of a sufficiently large positive feedback [7]. In the Weiss model of ferromagnetism it is shown that a nonlinear monotone constitutive law combined with a proper positive feedback effect can be transformed into a non-monotone law, and can then generate hysteresis. In this paper we shall show that monotone or non-monotone relationships generate hysteresis only in presence of suitable feedback effects. This work is devoted to mathematical modeling of pattern formation. Partial differential equations of diffusion type have long served as models for regulatory feedbacks and pattern formation in aggregates of living cells. We propose new receptor-based models for pattern formation and regulation in multicellular biological systems. The idea is that patterns are controlled by specific cell-surface receptors, which transmit to the cells signals responsible for their differentiation. The main aim of this work is to check which

aspects of self-organization and regeneration can be explained within the framework of CNNs.

II. FEEDBACK AND HYSTERESIS

Let us consider a circuit composed of an electric generator and two capacitors, characterized by the laws:

$$E_1 = f(D_1) \text{ , } E_2 = \frac{D_2}{\varepsilon} \text{ ,}$$

where f is a non-monotone function $R \rightarrow R$, ε is a positive constant, which represents electric permeability. If there elements are combined in series, then at equilibrium the charges of the two capacitors are equal $D_1 = D_2$. Then, denoting by V the generated electromotive force and by C_1 and C_2 two positive constants, we get [6]:

$$W = C_1 E_1 + C_2 E_2 = C_1 E_1 + \frac{C_2}{\varepsilon} D_1. \quad (1)$$

This condition will be named a load line (the potential W is the electric load). By eliminating E_1 , we get

$$W = C_1 f(D_1) + \frac{C_2}{\varepsilon} D_1 = g(D_1), \quad (2)$$

here g may be either monotone or non-monotone, depending on C_1 and C_2 . In this case hysteresis occurs in the D_1 versus W dependence.

Finally, let us show that the presence of a load line is mathematically equivalent to occurrence of a feedback effect. Usually this can be checked by means of a simple change of variable; however, these viewpoints can have different interpretations in applications. Assume that two variables w and z are related by a law:

$$w = f(z)$$

and that they are subject to a constraint (load line) depending on a third variable u :

$$z = g(u, w).$$

Then these two relations are equivalent to a feedback law relating u and w :

$$w = (f \circ g)(u, w). \quad (3)$$

Now we shall make a comparison between our general model of CNN and the feedback systems with hysteresis given above.

Let us consider our CNN model as the following system of equations:

$$\dot{x}_k(t) = -D_k x_k(t) + \sum_{all\ l} A_{k,l} y_l(t) + I_k, \quad (4)$$

$$z_k(t) = C_k(t) x_k(t) + \sum_{all\ l} A_{k,l} y_l(t) + I_k, \quad (5)$$

$$y_k(t) = sgm_k(x_k(t)). \quad (6)$$

It is obvious that we have the feedback system. In other words we have the following relations, defined by the (4)-(6):

$$y = f(x),$$

and from the other hand after solving (4) we get:

$$\begin{cases} x = g_1(y, x) \\ z = g_2(y, x). \end{cases}$$

If we denote vector $(g_1, g_2) = g$, then we get $y = (f \circ g)(y, x)$ which is a feedback law considered above.

Theorem 1 *Let $f(x)$ be a sigmoid, monotone increasing function. Assume that C_k is very large positive scalar, D_k - very large negative scalar and that $A_{k,l} > 1$. Then the CNN defined by (4)-(6) generates hysteresis.*

Proof:

Let us consider equation (4) and rewrite it in the form:

$$\dot{x}_k(t) = -D_k x_k(t) + F_1(y_k). \quad (7)$$

It is first order differential equation and therefore it is equivalent to the following integral equation:

$$x_k(t) = e^{D_k t} x_k(0) + \int_0^t e^{-D_k(t-s)} F_1(y_k(s)) ds. \quad (8)$$

Substituting (8) in (5) we get:

$$z_k(t) = C_k e^{D_k t} x_k(0) + \int_0^t C_k e^{-D_k(t-s)} F_1(y_k(s)) ds + F_1(y_k(t)). \quad (9)$$

Equations (8) and (9) define a feedback system of the type $y = (f \circ g)(y, x)$ given above. Under the conditions of the theorem, i.e. $A_{k,l} > 1$ and sufficiently large negative scalar D_k it follows that we have in this case very large positive feedback. According to [6] such kind of feedback leads to arising of hysteresis in the circuit. Thus, the theorem is proved.

As indicated earlier, hysteresis arises in systems having several equilibrium points.

We shall consider the following output function:

$$y = f(x) = \frac{x^3}{3} - x + c. \quad (10)$$

This can be done practically by introducing in the output circuit a special type of resistor known as a tunnel diode which exhibits a cubic characteristic function.

Let us denote by $a_q = A(l, l)$, $1 \leq q \leq n$. The following theorem hold.

Theorem 2 *If $a_q > 1$, $1 \leq q \leq n$, any equilibrium point \bar{x} of our CNN model (4) - (6) is unstable. After the transient has decayed to zero any trajectory of the system (4) - (6) will not converge to one stable equilibrium point. In other words we have hysteresis or bistability of the equilibrium points.*

The condition $a_q > 1$ possesses a very large positive feedback in our CNN, which can exhibit hysteresis according to the theory of ferromagnetism [6]. Since the trajectory of the system (4)-(6) is actually the solution of the differential equation (4) which is a first order differential equation [4], it means that after the transient has decayed to zero the trajectory will not converge to the stable equilibrium point if $a_q > 1$.

III. HYSTERESIS REACTION-DIFFUSION MODEL

A reaction-diffusion model involving a hysteretic functional was proposed by Hopfenstead and Jäger [5]. They assumed that the cell's growth had a hysteretic dependence on the amount of nutrients and acid present. Pattern formation in this model is caused by the initial instability of the ordinary differential equations (ODEs).

We consider one-dimensional epithelial sheet of length L . We denote the density of ligands by $v(x, t)$, where x and t are space and time coordinates, with x increasing from 0 to L along

the body column. The density of free receptors is denoted by $u(x, t)$. Consider a system of one reaction-diffusion equation and one ordinary differential equation (ODE):

$$\begin{cases} u_t = \Delta u + f(u, v) \\ v_t = g(u, v), \end{cases} \quad (11)$$

where the functions $f(u, v)$ and $g(u, v)$ present the rate of production of new free receptors and ligands, respectively and they are given by:

$$\begin{cases} f(u, v) = -c_1 \frac{u}{1+u^2} + \frac{b_1 u}{(1+u^2-u)(1+v)} \\ g(u, v) = -c_2 \frac{v}{1+v^2} + \frac{b_2 v}{(1+v^2-v)(1+u)}, \end{cases} \quad (12)$$

c_1 is the rate of decay of free receptors, c_2 is the rate of decay of ligands, $b_i > 0$, $i = 1, 2$ are constants.

We map hysteresis model (11), (12) into the following associated discrete-space version which we shall call hysteresis CNN model:

$$\begin{aligned} \frac{du_j}{dt} &= (u_{j-1} - 2u_j + u_{j+1}) + f(u_j, v_j) = U + f \\ \frac{dv_j}{dt} &= g(u_j, v_j) = g, 1 \leq j \leq N. \end{aligned} \quad (13)$$

The above system is actually a system of ODE which is identified as the state equation of an autonomous CNN made of N cells. For the output of our CNN model (13) we will take the standard sigmoid function [2].

The theory of local activity [3] provides a definitive answer to the fundamental question: what are the values of the cell parameter for which the interconnected system may exhibit complexity? Let us set $U = 0$ in the equilibrium equations:

$$\begin{aligned} U + f(u^e, v^e) &= 0, \\ g(u^e, v^e) &= 0. \end{aligned} \quad (14)$$

After solving the above system we get that it can have one, two or three real solutions and therefore we have three equilibrium points $E_i(u_i^e, v_i^e)$, $i = 1, 2, 3$.

Definition 1 A hysteresis CNN is said to be operating on the edge of chaos EC iff there is at least one equilibrium point E_i , $i = 1, 2, 3$ which is both locally active and stable when $U = 0$.

Theorem 3 Hysteresis CNN model for the system (11), (12) is operating in the edge of chaos regime iff $c_1 > b_1 > 0$, $c_2 > b_2 > 0$. For this parameter values, there is at least one equilibrium point which is both locally active and stable.

We shall perform simulations for the receptor-based CNN model (13):

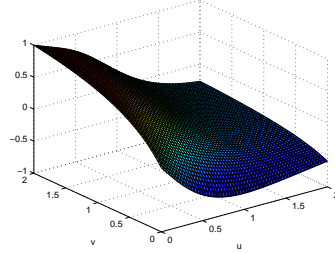


Fig.1. Stationary wave solution of the receptor-based CNN model for the following parameter set: $c_i, b_i \in [1, 2]$, $i = 1, 2$.

We can see from Fig. 1 that for small enough diffusion coefficients what is equal to the large enough domain size, we have formation of inhomogeneous solutions (fronts) which are stationary in time.

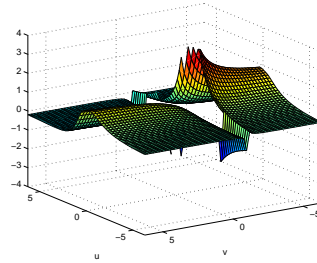


Fig.2. Spatio-temporal solution of the receptor-based CNN model for the following parameter set: $c_i, b_i \in [1, 2]$, $i = 1, 2$.

Simulations show that for the model (13) we can have a gradient-like solution for the density of free receptors (standing wave) which is stationary in time (see Fig.1) or a spatio-temporal solution oscillating in time (see Fig. 2). The hysteresis CNN cell [3] has two operating modes, namely, a bistable multivibrator mode and a relaxation oscillator mode. In the case of the bistable mode, the CNN gene design methodology [3] can be applied to hysteresis CNN. In the case of relaxation oscillator mode, the hysteresis CNN can generate various patterns and nonlinear waves. Furthermore, the hysteresis CNN has the function of both associative (static) and dynamic memories. The formation and persistence of the several peaks on Fig.2 are result of the bistability of

the reaction term. For such model we can have various stable solutions which are transitions between the stable steady states.

IV. CONTROL OF HYSTERESIS REACTION-DIFFUSION MODEL

In this section we propose a feedback control of our hysteresis reaction-diffusion model (13). We shall design a discrete-continuous regulator of CNN model in order to stabilize the chaotic motion to an admissible solution which is connected in some way to the original behaviour of the system (11),(12). Let us rewrite the CNN model (13) by the following simultaneous $2*N$ ordinary differential equations:

$$\begin{aligned} \frac{du_j}{dt} &= (u_{j-1} - 2u_j + u_{j+1}) + f(u_j, v_j) + z_{uj}, j = 1 \dots N, \\ \frac{dv_j}{dt} &= g(u_j) + z_{vj}, j = 1 \dots N, \end{aligned} \quad (15)$$

where z_{uj} , z_{vj} are controls and

$$\begin{cases} f(u, v) = -c_1 \frac{u}{1+u^2} + \frac{b_1 u}{(1+u^2-u)(1+v)} \\ g(u, v) = -c_2 \frac{v}{1+v^2} + \frac{b_2 v}{(1+v^2-v)(1+u)}, \end{cases} \quad (16)$$

Numbers of cells N lies in bounds $1 \leq N \leq 25$. Constant coefficients

$$c_j \in [0, 1], b_j \in [1, 2]. \quad (17)$$

Boundary conditions for (15) are

$$u(t, -1) = u(t, N + 1) = 0$$

and initial conditions are in the intervals

$$u(0, j) \in [0, 2], v(0, j) \in [0, 2].$$

We shall seek stabilized controls for (15), (16) as follows

$$z_{uj} = k_u v_j, \quad z_{vj} = k_v u_j + k_w v_j, \quad (18)$$

where the values of the scalar control coefficients k_u , k_v , k_w are to be found. After some calculations we obtain the following close-loop system's dynamical matrix [1] for them:

$$A_{cl} = \begin{bmatrix} A + (b_1 - c_1)E & k_u E \\ k_v E & (k_w - b_2 - c_2)E \end{bmatrix} \quad (19)$$

The simulation results are given on figures 3 and 4. They show that the proposed feedback control method allows so to stabilize the system's dynamics so to assign its rate of convergence.

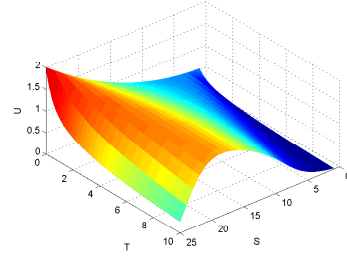


Fig.3. Spatio-temporal solution of the unstabilized receptor-based CNN model.

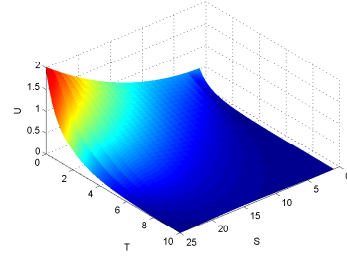


Fig.4. Spatio-temporal solution of the stabilized receptor-based CNN model, $\sigma = 0.5$.

References

- [1] G.Agranovich, E.Litsyn, A.Slavova, "Stabilizing Control of a Hysteresis Cellular Neural Network Model", *C.R.Bulg.Acad.Sci.*, vol.63, No.1, 2010.
- [2] L.O.Chua, L.Yang, "Cellular Neural Network: Theory and Applications", *IEEE Trans. CAS*, vol. 35, pp. 1257-1290, Oct. 1988.
- [3] L.O.Chua, Local activity in the origin of complexity, *Int.J.Bifurcations and Chaos*, 2005.
- [4] Hale, J., *Ordinary Differential Equations*, Wiley- Interscience, 1963.
- [5] F.Hoppensteadt, W.Jäger, "Pattern formation by bacteria". In S.Levin, editor, *Lecture Notes in Biomathematics: Biological Growth and Spread*, pp. 69-81, Heidelberg, Springer-Verlag, 1980.
- [6] Hodgdon M.L., Applications of a theory of ferromagnetic hysteresis, *IEEE Trans. Magn.*, 1988; MAG-24:218-221.
- [7] Hodgdon M.L., Mathematical theory and calculations of magnetic hysteresis curves, *IEEE Trans. Magn.*, 1988; MAG-24:3120-3122.

Focusing Time–Dependent Billiards as Maxwell’s Demon

Alexander Loskutov

Physics Faculty, Moscow State University,
119992 Moscow, Russia
Email: loskutov@chaos.phys.msu.ru

Alexei B. Ryabov

ICBM, University of Oldenburg,
26111 Oldenburg, Germany
Email: a.ryabov@icbm.de

Abstract—The Fermi acceleration is always inherent in completely chaotic time-dependent billiards. At the same time, the particle dynamics in nearly-integrable billiard systems can be more complex. Using a simplified approach, we investigate time-dependent stadium-like billiards and show that at a certain particle velocity a resonance between external periodical perturbations and the motion within stability islands of the unperturbed billiard can be observed. This resonance suppresses the Fermi acceleration of particles with velocities less than the resonance one. As a result, we observe separation of billiard particles by their velocities. This phenomenon may be treated as a peculiar billiard Maxwell’s Demon, when weak perturbations of a system leads the particle ensemble to separation. In other near-integrable billiard systems similar resonances can lead to differences in the acceleration of particles with velocities smaller or larger than a resonance value.

I. INTRODUCTION

A billiard dynamical system is generated by the free motion of a point mass particle (billiard ball) in a region Q with a piecewise-smooth boundary ∂Q and by the condition of the elastic collision from ∂Q . If the billiard boundary consists of dispersing and neutral components then such a billiard is said to be a dispersing one, or the Sinai billiard. One of the well know dispersing billiards is the Lorentz gas [1]. On the basis of the analysis of a 2D Lorentz gas a remarkable result has been obtained that the dynamics of purely deterministic systems may be ergodic with mixing and similar to the Brownian motion [2].

So-called focusing billiards include focusing components which can be connected by neutral ones. For some of such billiards one may prove that they possess the mixing property [3], [4]. The most know example of focusing billiards is “stadium”, or the Bunimovich billiards, which consist of two arcs and two rectilinear parallel segments joining them. Quite general conditions

of the chaoticity in 2D plane billiards are described in [5], [6] (see also references cited therein).

Billiards with boundaries, which oscillate according to one or another rule, represent a natural physical generalization of classical billiard systems. Indeed, the Lorentz gas has been proposed for the description of the motion of electrons between heavy ions in the lattice of metals. In the reality, however, ions should weakly oscillate near their equilibrium state. Moreover, some important problems of mathematical physics can be described by non-stationary billiard models (see [7]).

It is obvious that in time-dependent billiards the velocity of billiard particles changes from a collision to collision. After a collision event the billiard particle gains or loses its energy depending on whether the billiard boundary is approaching (i.e. there is a head-on collision) or receding (i.e. there is a head-tail collision).

A model of particle acceleration by elastic collisions with massive moving obstacles has been suggested by E.Fermi to explain the origin of high energy cosmic rays [8]. Fermi argued that in a typical environment the probability of a head-on collision is greater than the probability of a head-tail collision, so particles would, on average, be accelerated. In this problem, dynamical properties of billiards play a principal role: if it possesses the chaotic behavior then the boundary perturbation may lead to the particle acceleration [9], [10], [11], [12]. It was also found that new effects may be observed if the static billiard is a nearly integrable system [13]. Depending on the initial velocity value the particle ensemble in time-dependent billiards may be accelerated or decelerated.

This phenomenon can be treated as a specific (billiard) Maxwell’s Demon. In 1871 Maxwell proposed a peculiar arrangement (Demon) which could select the gas of molecules containing in two chambers connected through a small hole. These chambers, following to the second

thermodynamics law, are at the equilibrium state. Demon could hypothetically work against this law by separation of molecules by their velocities and the further chamber selection.

In the present paper we consider nearly integrable stadium-like billiards with periodically perturbed boundaries and describe the origin of the increase and decrease of the particle velocity.

II. TIME-DEPENDENT BILLIARDS

First let us describe the billiard models which used in the present paper for simulations. Suppose that the focusing components are arcs of a circle of the radius R and of the angle measure 2Φ , and they are symmetrically placed with respect to the vertical billiards axis (Fig.1a). Introduce also dynamical variables as shown in Fig.1b.

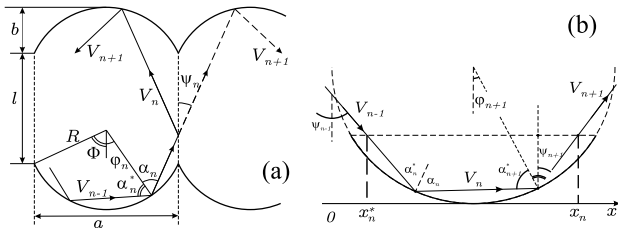


Fig. 1. Coordinates in a stadium.

Let us suppose now that the focusing components of the billiard boundary are perturbed periodically, $U(t) = U_0 f(\omega(t + t_0))$, where ω is the oscillation frequency. If the amplitude of billiard oscillations is sufficiently small, i.e. $U_0/\omega \ll l$, then we can neglect the boundary displacement with respect to the characteristic billiard size. In this approximation the billiard map reads as

$$V_n = \sqrt{V_{n-1}^2 + 4V_{n-1} \cos \alpha_n^* U_n + 4U_n^2}, \quad (1)$$

$$\alpha_n = \arcsin \left(\frac{V_{n-1}}{V_n} \sin \alpha_n^* \right),$$

$$\alpha_{n+1}^* = \alpha_n$$

$$t_{n+1} = t_n + \frac{2R \cos \alpha_n}{V_n}, \quad (2)$$

$$\varphi_{n+1} = \varphi_n + \pi - 2\alpha_n \pmod{2\pi},$$

if $|\varphi_{n+1}| \leq \Phi$, and

$$\psi_n = \alpha_n - \varphi_n,$$

$$\varphi_{n+1} = \psi_n - \alpha_{n+1}^*,$$

$$x_n = \frac{R}{\cos \psi_n} [\sin \alpha_n + \sin (\Phi - \psi_n)],$$

$$x_{n+1}^* = x_n + l \tan \psi_n \pmod{a},$$

$$\alpha_{n+1}^* = \arcsin \left[\sin (\psi_n + \Phi) - \frac{x_{n+1}^*}{R} \cos \psi_n \right],$$

$$t_{n+1} = t_n + \frac{R(\cos \varphi_n + \cos \varphi_{n+1} - 2 \cos \Phi) + l}{V_n \cos \psi_n}, \quad (3)$$

if $|\varphi_n + \pi - 2\alpha_n| > \Phi$. Expressions (2) correspond to a series of successive collisions with one component, and expressions (3) describe transition from one focusing component to another. The only approximation that we used is the smallness of the boundary displacement.

A. Particle separation

We carried out numerical simulations of maps (1)–(3) in two cases. In the first case we considered “classical” fully chaotic billiards in the form of a classical stadium. In the second case we assumed that $l \gg a \gg b$ and investigated a nearly integrable billiard system.

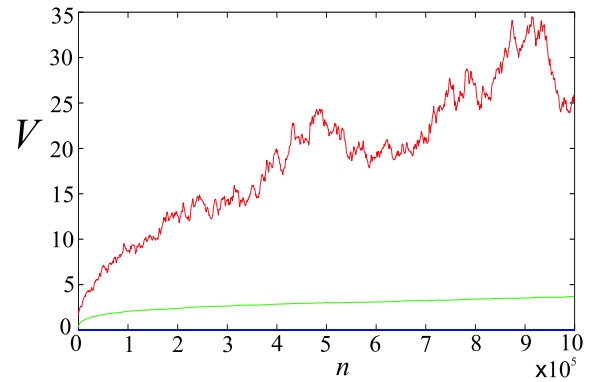


Fig. 2. The average (green), minimal (blue), and maximal (red) velocities of an ensemble of 5000 particle as a function of the number of collisions: $l = 2$, $a = 0.5$, $b = 0.25$, $U_0 = 0.01$, $\omega = 1$ and $V_0 = 0.1$.

Fig. 2 shows the dependence of the average, maximum and minimum velocities in the ensemble of particles on the number of collisions for a fully chaotic stadium. The average particle velocity (the central green curve) follows a power law $\bar{V}(n) \sim n^\gamma$, $\gamma = 0.44$. Thus, the Fermi acceleration phenomenon is inherent in this time-dependent billiard. To characterize the spread of particles we also plotted the minimal (the lower blue curve) and maximal (the red broken curve) velocity in the ensemble.

The most intriguing behavior of the particle velocity we observe in nearly integrable billiards. In this case $b \ll l$, and the phase space of the system contains regions with regular and stochastic dynamics. If the initial velocity of particles is sufficiently large then the average particle velocity grows, and the velocity distribution function becomes wider with the number of collisions (Fig. 3a,b). If however, the initial velocity is small

enough, then the average particle velocity slows down up to a small value V_{fin} , and the particle distribution approaches to a stationary one with a relatively small variance (Fig. 3c,d).

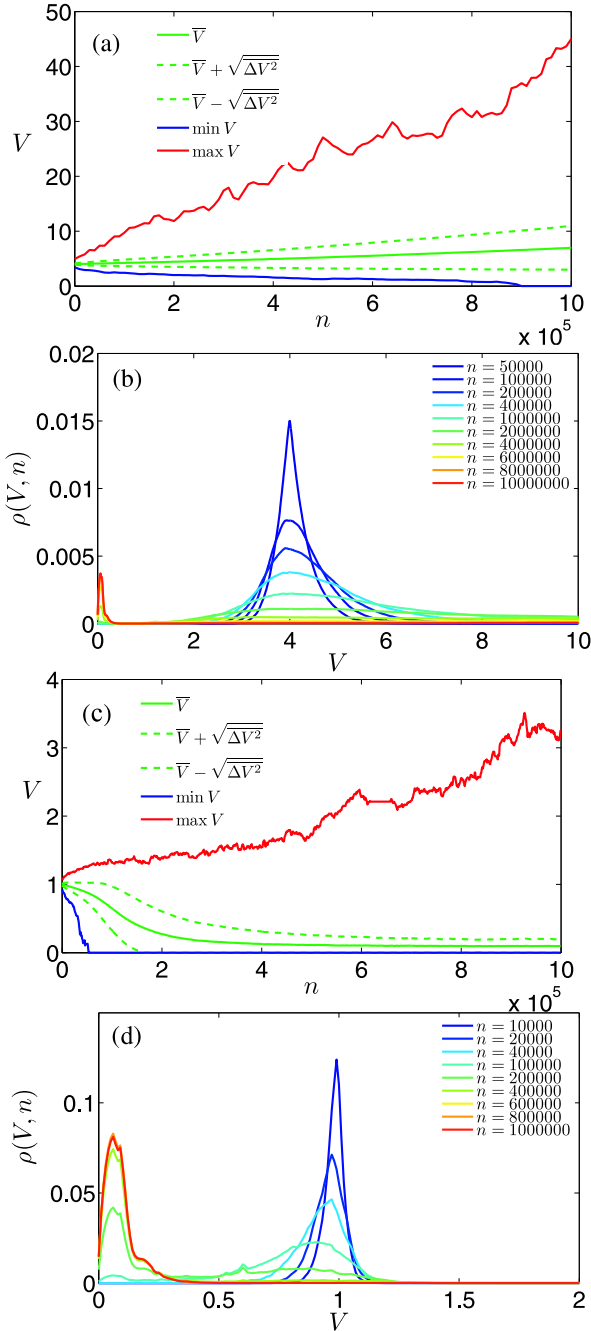


Fig. 3. (a) The dynamics of initially "fast" particles, $V_0 = 4$. (b) The evolution of the velocity distribution function, corresponding to panel (b). (c), (d) The same for initially "slow" particles, $V_0 = 1$. For each case an ensemble of 20 000 particles has been considered. $l = 1$, $a = 0.5$, $b = 0.01$, $\omega = 1$, $U_0 = 0.005$

Note, however, that in the last case there is a small

probability for particles to leave the region of small velocities. In particular, the maximal velocity of the ensemble grows (Fig. 3c). However, these events are rare and do not influence the particle distribution during the observation time. But their role can be crucial on an extremely long simulation period. This is due to the fact that for "fast" particles the probability to return into the region of small velocities decreases with time, because these particles will on average be accelerated, while the probability to leave the small velocity region will be almost constant.

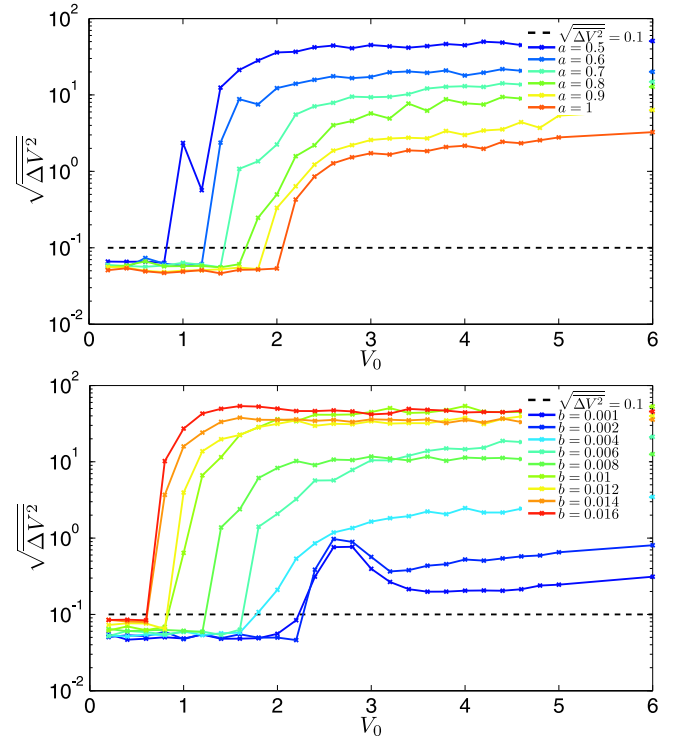


Fig. 4. The standard deviation $\sqrt{\Delta V^2}$ of the velocity distribution after 10^7 collisions as a function of the initial velocity plotted for different a and b . The black dashed line shows a threshold value between narrow (the deceleration of particles) and wide (the acceleration of particles) distributions. Each data point is calculated for an ensemble of 400 particles. $l = 1$, $a = 0.5$, $b = 0.01$, $\omega = 1$, $U_0 = 0.005$.

To find the velocity at which the particle separation occurs we investigated the width (standard deviation, $\sqrt{\Delta V^2}$) of the particle velocity distribution after 10^7 collisions as a function of the initial velocity for different billiard parameters a and b (see Fig. 4). For calculations of each point we used an ensemble of 400 trajectories. This analysis shows that $\sqrt{\Delta V^2}$ undergoes a first-order phase transition at a critical value V_c of the initial velocity. If $V_0 < V_c$ then the variance of the velocity

distribution approaches to a small value. At the same time, $V_0 > V_c$ leads to a non-stationary distribution with an unlimited variance which grows with the number of collisions. Furthermore, the velocity distribution function (Fig. 3b and 3d) has a bimodal form. This is an additional hint that we observe a first-order phase transition characterized by two attracting states.

We should make two comments here. Firstly, for some parameters values (e.g., for $b = 0.004$ and $b = 0.001$) particle separation is very slow and the number of steps 10^7 is not enough to clearly see it. As a result, these transitions look much smoother and resemble a second-order phase transition. However, analyzing the dynamics of velocity distribution functions, we still observe separation of particles into two groups with relatively high and low velocities. Secondly, curves for $b \leq 0.002$ in bottom Fig. 4 have a local maximum when V_0 is slightly larger than V_c . This maximum occurs due to the fact that for small b random fluctuations of the velocity diminish. As a result, the variance is relatively small if the initial velocity is large. If however, the initial velocity is a little larger than V_c , then a fraction of particles which are decelerated and turn out to be trapped in a small velocity region, gives an essential additional impact in the variance. This leads to a local maximum of the variance at this values of the velocity.

III. DISCUSSION

The phase portrait of a nearly integrable billiard configuration with the fixed boundary consists of stochastic layers and stable fixed points surrounded by stability islands. In a vicinity of a fixed point the particle motion can be represented as rotation around this point with a certain period. All trajectories are located either on elliptical invariant curves or in the stochastic layer.

In time-dependent billiards the whole phase space may become accessible. In this case the resonance behavior can be observed: The particle follows a spiral trajectory approaching the fixed point and leaves its neighborhood [13]. There is a essential difference in the dynamics of velocity of particles moving within the stochastic layer and within the stability islands. In the stochastic area, the angles of incidence can be large and the flights between collisions can be long, while in the regular area successive collisions occur almost at the same incidence angles and in regular intervals of time. As a result, in the stochastic area the velocity changes more chaotically and slower than in the vicinity of fixed points. In particular, detailed analysis shows that the average change of velocity vanishes in the

stochastic area, while there are areas of acceleration and deceleration within the stability islands [14]. Note that this is true only if the particle can occasionally enter and leave regular regions. If however, a particle moves along an invariant curve of the perturbed system then the change of total velocity tends to zero.

To get an insight into the mechanism of the particle separation by their velocities, consider a particle with $V < V_r$, where $V_r = V_c$ is a resonance velocity. The particle enters into the vicinity of a fixed point if the phases of rotation and boundary oscillations are close to each other. Since $V < V_r$, the rotation around the fixed point will be slower, and the phase delay will increase. Finally, the particle will return in the stochastic area. However, if the particle enters the regions of regular motion at the phase when it decelerates due to collisions with boundaries, then the phase delay will increase even faster, and the particle can leave this area after only a few head-tail collisions, which decrease its velocity. At the same time, if the particle initially accelerates in the regular region, then the phase delay will increase slower, and the particle can stay in this area longer. As a result, the velocity growth will be compensated by a further velocity decrease. Similar ideas show that a particle with $V > V_r$ will rather have accelerating collisions and then return to the stochastic area. We believe that this mechanism breaks the symmetry and leads to the separation of particles by their velocities (for detailed explanations see [14]).

REFERENCES

- [1] I. P. Cornfeld, S. V. Fomin, Ya. G. Sinai. *Ergodic Theory* (Springer, Berlin 1982)
- [2] L. A. Bunimovich, Ya. G. Sinai, *Commun. Math. Phys.* **78**, 479 (1981)
- [3] L. A. Bunimovich, *Commun. Math. Phys.* **65**, 295 (1979)
- [4] L. A. Bunimovich, *Chaos* **1**, 187 (1991)
- [5] S. Tabachnikov. *Geometry and billiards* (Amer. Math. Soc., 2005)
- [6] N. Chernov, R. Markarian. *Introduction to the Ergodic Theory of Chaotic billiards* (IMPA Press, Rio de Janeiro, Brazil, 2003)
- [7] A. Loskutov, *Physics – Uspekhi* **50**, 939 (2007)
- [8] E. Fermi, *Phys. Rev.* **75**, 1169 (1949)
- [9] A. Loskutov, A. B. Ryabov, L. G. Akinshin, *J. Phys. A* **33**, 7973 (2000)
- [10] R. E. de Carvalho, F. C. Souza, E. D. Leonel, *Phys. Rev. E* **73**, 066229 (2006)
- [11] A. L. Livorati, D. Ladeira, E. D. Leonel, *Phys. Rev. E* **78**, 056205 (2008)
- [12] E. D. Leonel, D. F. M. Oliveira, A. Loskutov, *Chaos* **19**, 033142 (2009)
- [13] A. Loskutov, A. Ryabov, *J. Stat. Phys.* **108**, 995 (2002)
- [14] A. B. Ryabov, A. Loskutov, *J. Phys. A: Math. Theor.* **43**, 125104 (2010)

Noise-induced Phenomena in a Bio-inspired Chemical Sensor Array

Kazuki Nakada, Katsumi Tateno, Hatsuo Hayashi, and Kiyonori Yoshii
 Graduate School of Life Science and Systems Engineering,
 Kyushu Institute of Technology,
 2-4 Hibikino, Wakamatsu-Ku, Kitakyushu 808-0196 Japan.
 Email: nakada@brain.kyutech.ac.jp

Abstract—For the development of a bio-inspired chemical sensor array, a computational model has been proposed in our previous work. The model consists of three functional parts: the chemical sensor, the random pulse generator, and the stochastic synchronizer, converting the concentration of chemical substances into the degree of stochastic synchronization of elements. In this work, we focus on resonate-and-fire neuron circuits that receive common random pulses for the stochastic synchronizer part. We evaluated cross correlation coefficients of outputs of the circuits as the degree of synchronization with circuit simulations. As a result, the circuits synchronized with others depending on the statistical properties of the random pulses. Furthermore, we considered how the dynamical properties of the circuits affect stochastic synchronization.

I. INTRODUCTION

For the development of a bio-inspired chemical sensor array, we focus on the functional roles of a network of mouse taste bud cells (TBCs). The information processing in sensory coding includes the TBCs can be represented as stochastic processes due to the probabilistic neurotransmitter release and action potential generation with fluctuation. On the basis of the physiological properties of the TBCs, a computational model for chemical sensor arrays has been proposed in our previous work [1]. The model consists of three functional parts: the chemical sensor as an array of electrochemical transducers, the random pulse generator that converts the outputs from the first part into a sequence of random pulses, and the stochastic synchronizer that receives the random pulses and detect the concentration of chemical substances as the degree of stochastic synchronization.

For a practical chemical sensor array, it is the demand to operate correctly under nonideal conditions as constraints: a limited number of sensing elements with nonuniformity and probabilistic behavior. Biological sensor arrays in nature could find solutions to fulfill the demand [4]-[5]. By learning from these solutions, we have considered to utilize noise-induced nonlinear phenomena, such as noise shaping [3], stochastic resonance [4] and coherence resonance [6]-[10], and noise-induced synchronization [12]-[14] and clustering [15], increasing the signal-to-noise ratio (SNR), dynamic range (DR), and information transfer ratio in information processing.

In this context, a computational model that utilizes noise-induced synchronization for detecting the concentration of chemical substances has been proposed [1]. It has also been

implemented on a software platform with commercial alcohol sensors [16] and on a hardware platform [20], [21].

In this work, focusing on hardware implementation of the stochastic synchronizer part, we investigated noise-induced nonlinear phenomena in an uncoupled array nonidentical resonate-and-fire neuron (RFN) circuits [18] that receive common strong random pulses. Through SPICE (Simulation Program with Integrated Circuit Emphasis) simulations, we evaluated cross correlation coefficients of the outputs of the circuits as the degree of stochastic synchronization. As a result, each circuit synchronized with others depends on the statistical properties of the random pulses. Furthermore, we considered how the dynamical properties of the circuits affect stochastic synchronization.

II. COMPUTATIONAL MODEL FOR A CHEMICAL SENSOR ARRAY.

We here explain a computational model for a chemical sensor array [1], [2]. The model consists of three functional parts.

The first part is the chemical sensor part constructed from an array of nonidentical electrochemical transducers. This part outputs analog signals with fluctuation and noise depending on the concentration of chemical substances. The second part is the random pulse generator part. It consists of an array of individual integrators that converts each output of the elements of the first part into a sequence of random pulses. When the number of the integrators increases, the interpulse interval (IPI) of the summation of the outputs becomes close to the Poisson process. The third part is the stochastic synchronizer part constructed from uncoupled nonidentical neuron models. It receives the random pulses and each element synchronizes with others depending on the statistical properties of the random pulses. As a result, the concentration of chemical substances can be detected as the degree of stochastic synchronization [1]. Finally, the model converts the concentration of chemical substances into the degree of stochastic synchronization of the elements [1], [2].

III. CIRCUIT IMPLEMENTATION

We here explain the resonate-and-fire neuron (RFN) circuit [19] for constituting the stochastic synchronizer part of the computational model for a chemical sensor array.

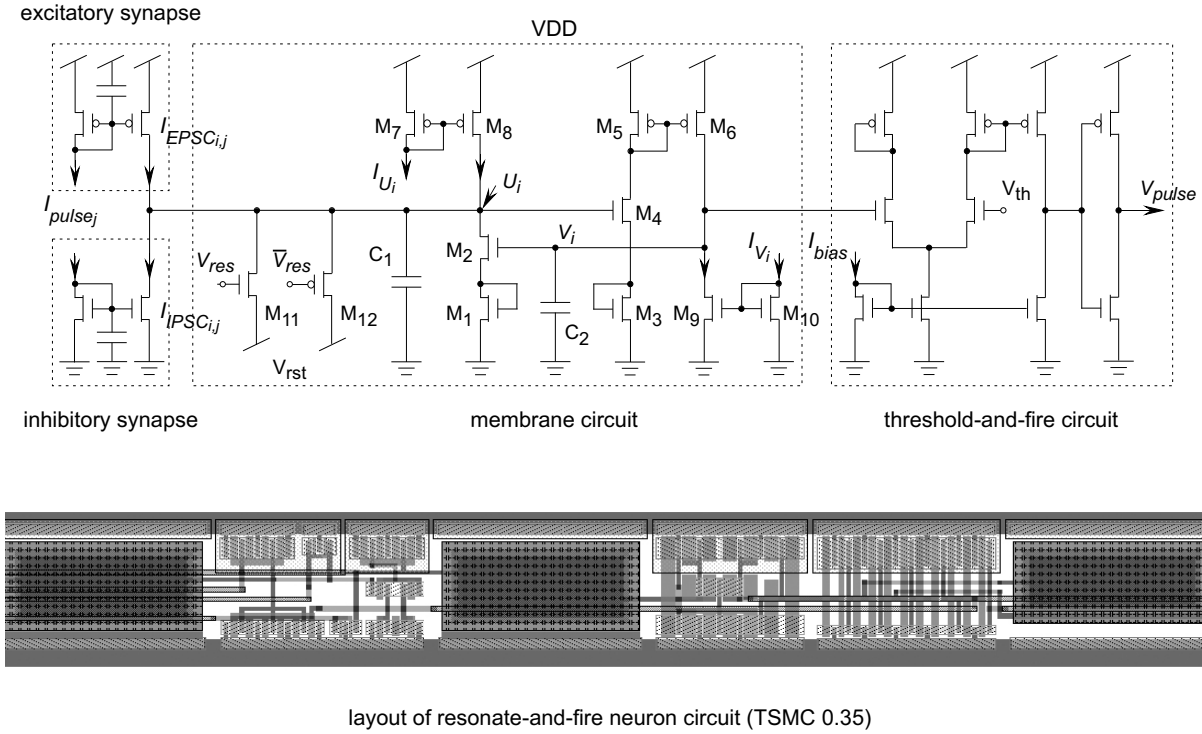


Fig. 1. Schematic diagram and chip layout of the resonate-and-fire neuron (RFN) circuit. The circuit consists of a membrane circuit, a threshold-and-fire circuit, and excitatory and inhibitory synaptic circuits. The membrane circuit has second-order dynamics containing two state variables U (a current-like variable) and V (a voltage-like variable).

The circuit consists of a membrane circuit, a threshold-and-fire circuit, and current-mirror integrators as excitatory and inhibitory synaptic circuits (Fig.1). The dynamics of the circuit are as follows:

$$C \frac{dU}{dt} = -g(U - V_{rst}) + I_{in} + \bar{I}_U - S I_{no} \exp\left(\frac{\kappa_n^2}{\kappa_n + 1} \frac{V}{V_T}\right) \quad (1)$$

$$C \frac{dV}{dt} = S I_{no} \exp\left(\frac{\kappa_n^2}{\kappa_n + 1} \frac{U}{V_T}\right) - \bar{I}_V \quad (2)$$

where U and V correspond to the current- and voltage-like state variables, respectively. C represents the capacitance, g the conductance for a transistor M_{11} , V_{rst} the reset voltage, and I_{in} the summation of the post-synaptic currents, I_{EPSC} and I_{IPSC} , through the excitatory and inhibitory synaptic circuits, respectively. Currents, \bar{I}_U and \bar{I}_V , are described as follows:

$$\bar{I}_U = \alpha I_{U_i} \left(1 + \frac{VDD - U}{V_{E,p}}\right) \quad (3)$$

$$\bar{I}_V = \beta I_{V_i} \left(1 + \frac{V}{V_{E,n}}\right) \quad (4)$$

where I_{U_i} and I_{V_i} represent the bias currents for the current mirrors, VDD the power-supply voltage, and α and β the

dimensionless constants:

$$\alpha = \left(1 + \frac{VDD - V_{g1}}{V_{E,p}}\right)^{-1} \quad (5)$$

$$\beta = \left(1 + \frac{V_{g2}}{V_{E,n}}\right)^{-1} \quad (6)$$

where V_{g1} and V_{g2} represent the gate voltages of M_7 - M_8 and M_9 - M_{10} , which are determined by the bias currents I_{U_i} and I_{V_i} .

The equilibrium point of the membrane circuit, (U_o, V_o) , can easily be calculated, and the stability of the point can be analyzed by the eigenvalues of the Jacobian matrix of the membrane circuit,

$$J = \begin{bmatrix} -\frac{I_{U_i}}{V_{E,p} + VDD - V_{g1}} & -\frac{\kappa_n^2}{\kappa_n + 1} \frac{I_{V_o}}{V_T} \\ \frac{\kappa_n^2}{\kappa_n + 1} \frac{I_{U_o}}{V_T} & -\frac{I_{V_i}}{V_{E,n} + V_{g2}} \end{bmatrix} \quad (7)$$

where I_{U_o} and I_{V_o} represent the equilibrium current at the equilibrium point. The leak conductance g is close to zero as M_{11} turns off. We used diode-connected transistors M_1 and M_3 to obtain small coefficients for I_{U_o} and I_{V_o} , and short transistors that have small Early voltages for M_7 - M_{10} to obtain small coefficients for I_{U_i} and I_{V_i} .

Consequently, the equilibrium point becomes a focus. In this case, the circuit dynamics is qualitatively equivalent to the membrane dynamics of the resonate-and-fire neuron model

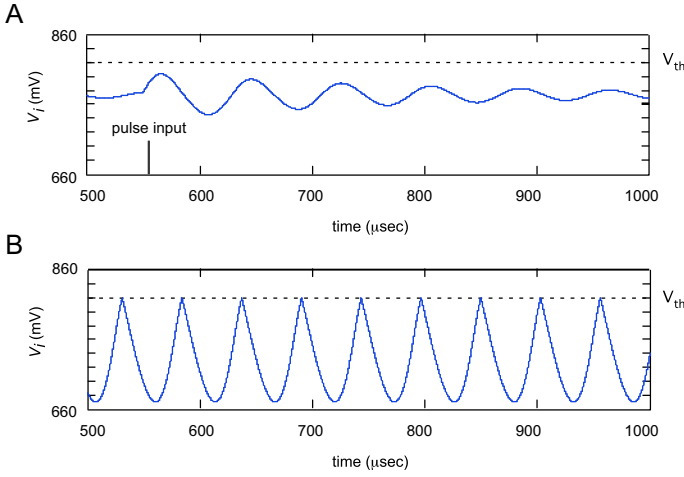


Fig. 2. Typical behavior of a RFN circuit in (A) an excitable state and (B) a periodic firing state.

near the equilibrium point [17]. Furthermore, the circuit has a voltage-dependent resonant frequency at the resting state as in the case of analogous to biological neurons.

According to the relative location of the equilibrium point and the threshold V_{th} , the RFN circuit has two states: an excitable state and a periodic firing state. In the excitable state, the circuit fires when the voltage V exceeds V_{th} driven by external pulse inputs. By increasing the bias current I_{V_i} to bring the the equilibrium point close to the threshold V_{th} , the circuit becomes a periodic firing state. In the periodic firing state, the circuit fires repetitively.

IV. SIMULATION RESULTS

We investigated stochastic synchronization properties of an array of uncoupled nonidentical RFN circuits using the circuit simulator SPICE. We used a set of the model parameters for the TSMC 0.35- μm CMOS process.

Through the following simulations, the supply voltages were set at $V_{DD} = 1.5$ V, $V_{th} = 820$ mV, and $V_{rst} = 750$ mV, the bias currents were set at $I_{U_i} = I_{V_i} = 10$ nA, and $I_{bias} = 250$ nA, and the capacitance were set at $C = 2$ pF. We introduced excitatory pulse inputs (amplitude: 1.5 V and width: 0.1 μsec) as synaptic currents into the circuit. The capacitances for the synaptic circuits were set at $C_p = 0.02$ pF.

We firstly describe the typical behavior of a single RFN circuit. When the circuit was in an excitable state, the circuit exhibited a damped subthreshold oscillation in response to an excitatory pulse input (Fig. 2A). When the bias current I_{V_i} increases from 10 nA to 17 nA, the circuit becomes a periodic firing state and exhibits a repetitive firing pattern (Fig. 2B).

We further describe the behavior of an array of uncoupled nonidentical RFN circuits in response to common strong random pulses. We set Gaussian-distributed values with a low coefficient of variation (CV) for the bias currents I_{U_i} and I_{V_i} of the circuits, and therefore each circuit had an individual resting potential and resonant frequency according

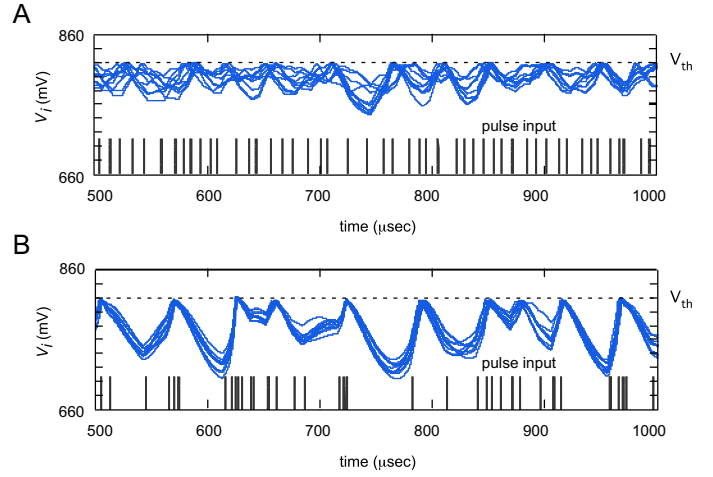


Fig. 3. Stochastic synchronization in an array of uncoupled nonidentical RFN circuits (the number of circuits equals to 10) driven by random pulses with Gamma-distributed IPIs (the mean of IPIs = 10 μsec). Multiple waveforms are the outputs of the circuit. The degree of stochastic synchronization increased with the increase of the CV of IPIs as in the case of (A) $CV = 1/\sqrt{10}$ and (B) $CV = 1$.

to (7). We introduced common random pulses with Gamma-distributed interpulse intervals (IPIs) into the array of the circuits. The degree of synchronization among the circuits was increased with the increase of the CV of the IPIs in the presence of nonuniformity of the individual circuits, as shown in Fig. 3. The mean of the IPIs also affected the degree of synchronization when the CV of the IPIs decreased.

Figure 4 shows the relationship between the degree of synchronization and the CV of of the random pulses, in which the degree of synchronization is represented as the cross correlation coefficient of the waveforms of the voltage V_i . This result also shows that the circuits synchronized when Poisson pulses were introduced ($CV=1$).

We considered effects of the dynamical properties of the circuit on stochastic synchronization. We increased the mean of the bias current I_{V_i} from 10 nA to 20 nA so that the circuits entered the periodic firing state from the excitable state. We introduced common Poisson random pulses into the circuits. Figure 5 shows the relationship between the degree of synchronization and the mean IPIs of the Poisson pulses. The degree of synchronization decreased when the circuits were in the periodic firing state as compared to the excitable state.

V. CONCLUDING REMARKS

In biological information processing, a population of cells may effectively use their correlations in order to transmit information even in a noisy environment [5]. Noise-induced nonlinear phenomena such as noise-induced synchronization increases correlations between uncoupled cells. In practice, the computational model described here effectively use such a

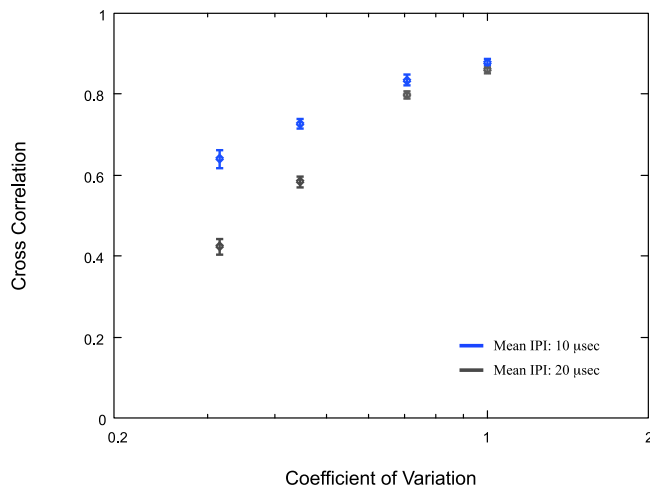


Fig. 4. Cross correlation coefficients of the output waveforms of the circuits as the degree of stochastic synchronization when Gamma pulses were introduced into the array of the circuits.

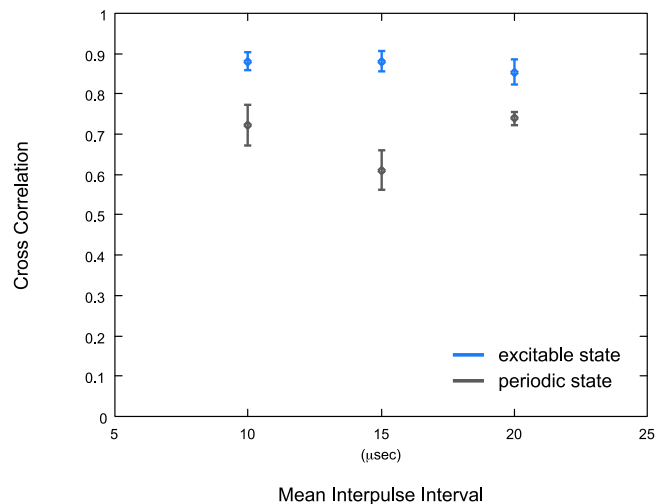


Fig. 5. Cross correlation coefficients of the output waveforms of the circuits as the degree of stochastic synchronization when Poisson pulses were introduced into the array of the circuits.

phenomenon to reduce the nonuniformity of sensing elements on sensory processing [1].

In this work, focusing on hardware implementation of the part of the computational model, we have investigated noise-induced nonlinear phenomena in an array of uncoupled nonidentical RFN circuits [18] that received common random pulses. We have evaluated the cross correlation coefficients as the degree of stochastic synchronization through SPICE simulations. As a result, the circuits synchronized with others depending on the statistical distribution of the random pulses. Furthermore, we have considered the effects of the dynamical properties of the circuits on stochastic synchronization. The degree of synchronization increased when the element circuits were in an excitable state. These results provide valuable insight into strategies for designing of a chemical sensor array on a silicon chip.

REFERENCES

- [1] K. Tateno, K. Yoshii, Y. Ohtubo, and T. Miki, "A network model toward a taste bud inspired sensor," *Brain-inspired IT III, Int. Congress Series*, Elsevier, pp. 52-55, 2007.
- [2] K. Tateno, J. Igarashi, K. Nakada, T. Miki, Y. Ohtubo, and K. Yoshii, "Signal detection inspired by mouse taste receptor cells," presented at *The 2009 International Symposium on Nonlinear Theory and its Applications*, Sapporo, Japan, Oct. 18-21, 2009.
- [3] M. J. Chacron, B. Lindner, and A. Longtin, "Noise shaping by interval correlations increases information transfer," *Phys. Rev. Lett.* 92, 080601, 2004.
- [4] J. J. Collins, C. C. Chow, and T. T. Imhoff, "Stochastic resonance without tuning," *Nature*, 376, pp. 236-238, 1995.
- [5] A. Neiman, X. Pei, D. Russell, W. Wojtenek, L. Wilkens, F. Moss, H. A. Braun, M. T. Huber, and K. Voigt, "Synchronization of noisy electrosensitive cells in the paddlefish," *Phys. Rev. Lett.* 82, pp. 660-663, 1999.
- [6] S. Pikovsky and J. Kurths, "Coherence resonance in a noise-driven excitable system," *Phys. Rev. Lett.* 78, pp. 775-778, 1997.
- [7] C. Zhou, J. Kurths, and B. Hu, "Array-enhanced coherence resonance: nontrivial effects of heterogeneity and spatial independence of noise," *Phys. Rev. Lett.* 87, 098101, 2001.
- [8] Y. Shinohara, T. Kanamaru, H. Suzuki, T. Horita, and K. Aihara, "Array-enhanced coherence resonance and forced dynamics in coupled FitzHugh-Nagumo neurons with noise," *Phys. Rev. E* 65, 051906, 2002.
- [9] R. C. Hilborn and R. J. Erwin, "Coherence resonance in models of an excitable neuron with noise in both the fast and slow dynamics," *Phys. Lett. A*, vol. 322, no. 1-2, pp. 19-24, 2004.
- [10] S. Reinker, Y.-X. Li, and R. Kuske, "Noise-induced coherence and network oscillations in a reduced bursting model," *Bulletin of Mathematical Biology*, vol. 68, no. 6, pp. 1401-1427, 2006.
- [11] A. Neiman and D. F. Russell, "Synchronization of noise-induced bursts in noncoupled sensory neurons," *Phys. Rev. Lett.* 88, 138103, 2002.
- [12] R. V. Jensen, "Synchronization of randomly driven nonlinear oscillators," *Phys. Rev. E* 58, 6907, 1998.
- [13] J. Teramae and D. Tanaka, "Robustness of the noise-induced phase synchronization in a general class of limit cycle oscillators," *Phys. Rev. Lett.* 93, 204103, 2004.
- [14] H. Nakao, K. Arai, K. Nagai, Y. Tsubo, and Y. Kuramoto, "Synchrony of limit-cycle oscillators induced by random external impulses," *Phys. Rev. E* 72, 026220, 2005.
- [15] H. Nakao, K. Arai, and Y. Kawamura, "Noise-induced synchronization and clustering in ensembles of uncoupled limit-cycle oscillators," *Phys. Rev. Lett.* 98, 184101, 2007.
- [16] J. Igarashi, K. Tateno, K. Nakada, T. Miki, Y. Ohtubo, and K. Yoshii, "A chemical sensor array inspired by mouse taste buds," *Brain-Inspired Information Technology, Studies in Computational Intelligence*, vol. 266, pp.159-164, Springer, 2010.
- [17] E. M. Izhikevich, *Dynamical Systems in Neuroscience: The Geometry of Excitability and Bursting*, The MIT press, 2007.
- [18] K. Nakada, J. Igarashi, T. Asai, and H. Hayashi, "Noise effects on performance of signal detection in an analog VLSI resonate-and-fire neuron," in *proc. IEEE Int. Symposium on Circuits and Systems*, pp. 5183-5186, Island of Kos, Greece, 2006.
- [19] K. Nakada, T. Asai, and H. Hayashi, "Analog VSI implementation of resonate-and-fire neuron," *Int. J. Neural Systems*, vol. 16, no. 6, pp. 445-456, 2006.
- [20] K. Nakada, K. Tateno, H. Hayashi, and K. Yoshii, "Functional properties of resonate-and-fire neuron circuits for bio-inspired chemical sensor array," *Brain-Inspired Information Technology, Studies in Computational Intelligence*, vol. 266, pp.129-133, Springer, 2010.
- [21] K. Nakada, J. Igarashi, T. Asai, K. Tateno, H. Hayashi, Y. Ohtubo, T. Miki, K. Yoshii, "Stochastic synchronization and array-enhanced coherence resonance in a bio-inspired chemical sensor array", in *proc 11th IEEE International Conference on Computational Science and Engineering*, San Paulo, Brazil, Nov. 16-18, 2008.

Explicit model predictive control for the start-up and orbital stabilization of a boost converter

Axel Schild and Jan Lunze

Faculty of Electrical Eng. & Information Sciences,
Ruhr-Universitaet Bochum,
44780 Bochum, Germany
Email: {schild,lunze}@atp.rub.de

Wolfgang Schwarz

Faculty of Electrical Eng. & Information Technology,
Dresden University of Technology,
01062 Dresden, Germany
Email: Wolfgang.Schwarz@mailbox.tu-dresden.de

Abstract—This paper addresses the design of optimal switching laws that jointly solve the problems of start-up and orbital stabilization for a boost converter. After summarizing the concept of model predictive control for smooth systems, it is outlined first, how MPC can be extended to power converters that fall into the class of switched autonomous systems and, second, that the optimal control can be represented in terms of relatively simple stationary switching surfaces in the state space. Simulation results demonstrate the feasibility and the good control-loop performance.

I. INTRODUCTION

A switching power converter transforms a constant dc input voltage into a dc dominated output voltage of desired level. The working principle relies on switching the *power stage* between different circuit topologies, here called *operation modes*, in the correct order at adequate time instants. Typically, power converters are operated by *periodic switching laws*, where expedient circuit topologies are pre-selected and arranged into a periodic mode schedule by the designer. This reduces the effective control input to the *transition times*.

The design of the control law, which processes state measurements into transition times, has a long and rich history. Many works synthesize fixed-frequency *time-driven* switching laws by exploiting the technique of averaging. The latter yields a nonlinear *average model* with *duty cycles* as continuous-valued constrained control inputs, for which the controller can then be designed using linear and nonlinear control theory [1]. The presence of input and state constraints together with advances in controller hardware have recently fuelled the interest for the application of model predictive control [2], [3]. It was shown that fix-frequency MPC laws achieve 1. a fast start-up while obeying constraints, 2. an excellent output tracking as well as 3. a good

disturbance attenuation. However, the high switching frequency may cause unnecessary mode transitions and, thus, high switching losses. Also, orbital stability, which is a central element of stationary converter specifications, is not ensured by equilibrium stability of the averaged closed-loop system [4].

The systematic synthesis of *event-driven* switching laws, which make no a-priori assumptions on the switching frequency, has been investigated only quite recently. In contrast to fixed-frequency control, an *event-driven* switching law is implemented directly in terms of switching surfaces in the state space that switch the circuit topology whenever being intersected by the state trajectory. [5] showed that the associated hybrid design problem can be translated into an equivalent periodic feedback design problem of discrete-time systems. Exploiting the idea of optimal control and continuation, [6] presented a scheme for designing polyhedral switching surfaces, that achieve an optimal transient loop behavior in the presence of state constraints as well as orbital stability of a desired limit cycle at stationary operation. A central benefit of the new approach is that the resulting switching law is simple to implement and evaluate. Also, it avoids unnecessary mode transitions.

The central contribution of this paper is an extension of model predictive control to the design of *event-driven* switching laws of switching power converters by using the results of [6]. Simulation results illustrate the feasibility as well as the good loop performance, both in the transient and stationary operating regime.

II. BOOST CONVERTER MODEL AND CONTROL OBJECTIVES

For ease of presentation, this work focusses on the design of an optimal periodic switching law for a simple boost converter circuit in continuous-conduction mode

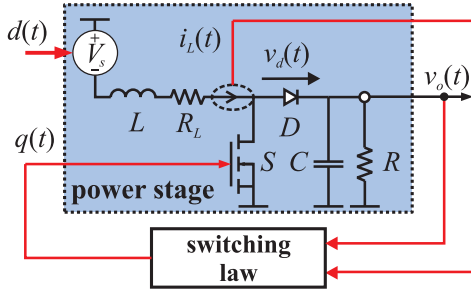


Fig. 1. Schematics of the boost converter power stage

(Fig. 1). The power stage constitutes a bimodal switched system. Mode $q = 1$ is associated with switch S being closed and mode $q = 0$ with S open. The circuit dynamics are described by a second-order switched affine system

$$\dot{\mathbf{x}}(t) = \mathbf{A}_q \mathbf{x}(t) + \mathbf{b}_q \quad (1)$$

with the state $\mathbf{x}(t) = (i_L(t) \ v_o(t))^T$ and

$$\mathbf{A}_0 = \begin{pmatrix} \frac{-R_L}{L} & \frac{-1}{L} \\ \frac{1}{C} & \frac{-1}{RC} \end{pmatrix}, \quad \mathbf{A}_1 = \begin{pmatrix} \frac{-R_L}{L} & 0 \\ 0 & \frac{-1}{RC} \end{pmatrix}$$

$$\mathbf{b}_0 = \left(\frac{V_s - V_d}{L} \ 0 \right)^T, \quad \mathbf{b}_1 = \left(\frac{V_s}{L} \ 0 \right)^T$$

Parameter values are $V_s = 12 \text{ V}$, $L = 1 \text{ mH}$, $R_L = 0.25 \Omega$, $C = 20.5 \text{ F}$, $V_d = 0.4 \text{ V}$ and $R = 50 \Omega$. The switching time, at which the k -th mode transition is executed, is denoted by τ_k . The corresponding state value $\mathbf{x}(\tau_k) = \mathbf{x}_k$ is called the switching point and the distance $\delta_k = \tau_{k+1} - \tau_k$ is called the activation duration of the k -th mode. Finite or infinite sequences of values τ_k , \mathbf{x}_k , and δ_k are indicated by τ , \mathbf{x} and δ .

Problem 1: Given the model (1) and a mode schedule $q^\circ = (1, 0)$ to be periodically executed, determine switching surfaces \mathcal{S}_q in the state space that 1. orbitally stabilize the boost converter at a feasible limit cycle Γ around a reference voltage $V_{\text{ref}} = 18 \text{ V}$ with a ripple of $|\Delta v_o| < 0.5 \text{ V}$ and 2. realize a fast start-up without excessive inductor currents $i_L(t)$ above 1 A .

An admissible limit cycle with a period of $T = 50 \text{ s}$ is depicted in Fig. 2. Its switching points (rectangles) are

$$\mathbf{x}_1 = (0.67 \text{ A} \ 17.91 \text{ V})^T, \quad \mathbf{x}_0 = (0.46 \text{ A} \ 18.23 \text{ V})^T$$

This cycle is to be stabilized in the following.

III. EXPLICIT MODEL PREDICTIVE CONTROL FOR SWITCHED DYNAMICAL SYSTEMS

A. The concept of model predictive control

Model predictive control provides an approach to solve an intractable optimal feedback control problem by

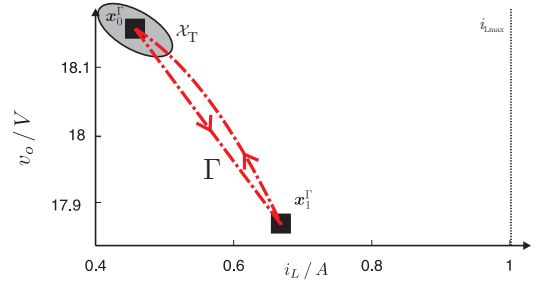


Fig. 2. Admissible limit cycle satisfying the design specifications

repeatedly solving *open-loop* finite-horizon optimization problems during the operation of a plant [7]. Originally, this control scheme was introduced for uniformly sampled smooth nonlinear discrete-time systems

$$\mathbf{x}_{k+1} = \mathbf{f}(\mathbf{x}_k, \mathbf{u}_k, \mathbf{d}_k) \quad (2)$$

with states \mathbf{x} , continuous-valued control inputs \mathbf{u} , disturbances \mathbf{d} and a smooth vector field \mathbf{f} . Having obtained a new state measurement \mathbf{x}_k at the k -th sample time t_k , a constrained optimization problem $\pi(\mathbf{x}_k, N)$ of the form

$$\min_{\boldsymbol{\nu}_k} J_{[0,N]}(\boldsymbol{\xi}_k, \boldsymbol{\nu}_k) = \sum_{j=0}^{N-1} g_j(\boldsymbol{\xi}_{j|k}, \boldsymbol{\nu}_{j|k}) + g_N(\boldsymbol{\xi}_{N|k}) \quad (3)$$

$$\text{s. t. } \boldsymbol{\xi}_{j+1|k} = \mathbf{h}(\boldsymbol{\xi}_{j|k}, \boldsymbol{\nu}_{j|k}), \quad \boldsymbol{\xi}_{0|k} = \mathbf{x}_k \quad (4)$$

$$\mathbf{c}_k(\boldsymbol{\xi}_{j|k}, \boldsymbol{\nu}_{j|k}) \leq \mathbf{0}, \text{ for } k = 0..p-1 \quad (5)$$

$$\mathbf{c}_N(\boldsymbol{\xi}_{N|k}) \leq \mathbf{0} \quad (6)$$

is solved. Here, an undisturbed model (4) of system (2) is used to predict the evolution $\boldsymbol{\xi}_k$ from the current state \mathbf{x}_k onwards over the next N samples into the future. From the resulting optimal input sequence $\boldsymbol{\nu}_k^*$, only the first element is applied as the k -th input

$$\mathbf{u}_k = \boldsymbol{\kappa}_N(\mathbf{x}_k, k) = \boldsymbol{\nu}_{0|k}^* \quad (7)$$

to the plant. $\boldsymbol{\kappa}_N(\mathbf{x}_k, k)$ defines the *model predictive feedback control law*, which is in general of time-varying nature. The remaining predicted input sequence is reused as an initial guess for the subsequent optimization problem $\pi(\mathbf{x}_{k+1}, N)$ to be solved at the $(k+1)$ -st sample time, at which a new state measurement becomes available. Clearly, the MPC principle still works, if the time between each new optimization varies.

Under the assumption of 1. having a perfect model (4), 2. the absence of disturbances, 3. that $g_k(\mathbf{0}, \mathbf{0}) = g_N(\mathbf{0}) = 0$ and 4. that the terminal cost term $g_N(\boldsymbol{\xi})$ over-bounds the infinite-horizon residual costs, i.e. $g_N(\boldsymbol{\xi}_{N|k}) \geq V(\boldsymbol{\xi}_{N|k}) = \min_{\boldsymbol{\nu}} J_{[N,\infty]}(\boldsymbol{\xi}_k, \boldsymbol{\nu}) < \infty$,

asymptotic stability of the origin (or any other equilibrium, if the g_j are adjusted properly) is guaranteed for the closed-loop system using (7). In the face of a moderate model mismatch and exogenous disturbances, the resulting control-loop is practically stable. Transient performance can be traded against computational complexity by increasing the horizon N .

The over-bounding property 4 can be enforced by following a *quasi-infinite horizon* (QIH) strategy. Here, the idea is constrain ξ_N at the end of the prediction horizon to a neighborhood of the origin, in which $\pi(x_k, \infty)$ can be approximated sufficiently well by its unconstrained linearization at $(x, u) = (0, 0)$

$$\begin{aligned} \min_{\nu_k} \sum_{j=0}^{\infty} \Delta \xi_{j|k}^T \frac{\partial^2 g_j}{\partial \xi^2} \Delta \xi_{j|k} + 2 \Delta \xi_{j|k}^T \frac{\partial g_j^2}{\partial \xi \partial \nu} \Delta \nu_{j|k} \\ + \Delta \nu_{j|k}^T \frac{\partial^2 g_j}{\partial \nu^2} \Delta \nu_{j|k} \text{ s. t.} \\ \Delta \xi_{j+1|k} = \frac{\partial h}{\partial \xi} \Delta \xi_{j|k} + \frac{\partial h}{\partial \nu} \Delta \nu_{j|k}, \Delta \xi_{0|k} = \Delta x_0 \end{aligned}$$

As known, this linearized problem yields a closed-form solution $\Delta \nu_{j|k}^* = \mathbf{k}^T \Delta \xi_{j|k}$ and the value function $V(\Delta \xi) = \Delta \xi^T \mathbf{X} \Delta \xi$ is a quadratic form, with \mathbf{X} being the solution to the Lyapunov equality

$$\begin{aligned} \mathbf{X} \begin{pmatrix} \frac{\partial h}{\partial \xi} & \frac{\partial h}{\partial \nu} \mathbf{k}^T \end{pmatrix}^T \mathbf{X} \begin{pmatrix} \frac{\partial h}{\partial \xi} & \frac{\partial h}{\partial \nu} \mathbf{k}^T \end{pmatrix} \\ + \left(\frac{\partial^2 g_j}{\partial \xi^2} + 2 \frac{\partial^2 g_j}{\partial \xi \partial \nu} \mathbf{k}^T + \mathbf{k} \frac{\partial^2 g_j}{\partial \nu^2} \mathbf{k}^T \right) = \mathbf{0} . \quad (8) \end{aligned}$$

Consequently, it is possible to select a $\gamma > 0$ and \mathbf{P} large enough, such that $g_N(\xi) = \xi^T \mathbf{P} \xi \geq V(\xi)$, $\forall \xi \in \mathcal{X}_T = \{\xi : \xi^T \mathbf{P} \xi \leq \gamma\}$. To minimize the performance loss, the over-bounding should be least conservative.

B. Model predictive control applied to a boost converter

The MPC scheme from the last subsection can be extended to the boost converter by replacing the model (4) by the return map [8]

$$\mathbf{x}_{c+1} = \begin{pmatrix} \mathbf{I} & \mathbf{0} \end{pmatrix} e^{(\mathbf{A}_0 \delta_0)} e^{(\mathbf{A}_1 \delta_1)} \begin{pmatrix} \mathbf{x}_c \\ 1 \end{pmatrix}, \tilde{\mathbf{A}}_q = \begin{pmatrix} \mathbf{A}_q & \mathbf{b}_q \\ \mathbf{0}^T & 0 \end{pmatrix}.$$

Clearly, this map constitutes a nonlinear discrete-time system with a state \mathbf{x}_c that coincides with the switching point at each re-activation of mode $q = 1$, and a continuous-valued control input δ° denoting the activation duration sequence for the cycle q° .

Furthermore, we need to formalize the verbal specifications of Problem 1 into a discrete-time performance metric and discrete-time state constraints. Suitable

choices for these are

$$g_k(\mathbf{x}_k, \delta) = \begin{cases} \mathbf{x}_k^T \mathbf{Q}_k \mathbf{x}_k, & k < N \\ \mathbf{x}_N^T \mathbf{P} \mathbf{x}_N, & k = N \end{cases} \quad (9)$$

$$\mathbf{c}_k(\mathbf{x}_k, \delta) = \begin{cases} \int_0^\delta I(t) dt, & k < N \\ \mathbf{x}_N^T \mathbf{P} \mathbf{x}_N - \gamma < 0, & k = N \end{cases} \quad (10)$$

$$I(t) = \begin{cases} i_L(t) & 1 & \text{if } i_L(t) \geq 1.01 \\ 400(i_L(t) - 0.99)^2 & \text{if } 0.99 \leq i_L(t) \leq 1.01 \\ 0 & \text{if } i_L(t) \leq 0.99 \end{cases}.$$

The quadratic term of (9) accounts for the orbital stability requirement as long as the weighting matrix \mathbf{Q}_k is positive definite. The *transcribed* constraints (10) can be evaluated numerically. Both (9) and (10) are sufficiently smooth functions, which makes derivative-based iterative solvers for nonlinear programs applicable.

All that remains is to choose \mathbf{P} , γ according to the QIH-strategy. For this, stabilizing switching planes have to be computed according to the algorithm in [5]. With these, a periodic Lyapunov equality similar to (8) can be solved numerically. The resulting \mathbf{X} and $\gamma = 0.01$ define terminal costs g_N and a terminal region \mathcal{X}_T that together ensure orbital stability.

C. Explicit representation of the MPC law

For a fast switching power converter, it is impossible to iteratively solve the complex algebraic optimization problem (3)-(6) on-line at the beginning of each period. Fortunately, it was shown in [6] that the solution to such a finite-horizon problem can be expressed in terms of stationary switching surfaces by imposing mild restrictions onto the dynamics, the costs and the constraints. The resulting *time-invariant* MPC law $\delta^\circ = \kappa_{\tilde{q}^\circ}(\mathbf{x}_c)$, which returns the complete optimal activation duration sequence for the schedule q° at the beginning of each switching cycle, defines the optimal surfaces as

$$\mathcal{S}_q^* = \{\mathbf{x} : \mathbf{e}_q^T \kappa_{\tilde{q}^\circ}(\mathbf{x}_c) = 0\} \quad (11)$$

with the q -th unit vector \mathbf{e}_q . [6] provides a numerically efficient algorithm to compute polyhedral approximations $\tilde{\mathcal{S}}_q^*$ of \mathcal{S}_q^* , which uses ideas from predictor-corrector continuation, nonlinear optimization and optimal perturbation control. Such polyhedral surfaces $\tilde{\mathcal{S}}_q^*$ are efficiently tested for intersection within s by exploiting ideas from the field of collision detection [9].

IV. SIMULATION RESULTS

For the converter model and the control specifications of Section II, the explicit model predictive control law was computed in terms of two polyhedral surfaces $\tilde{\mathcal{S}}_0^*$

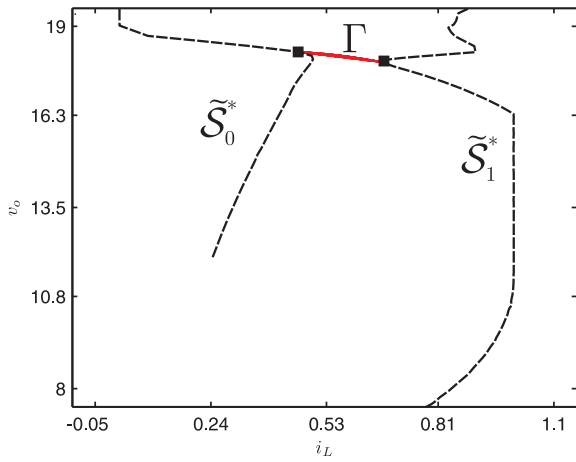


Fig. 3. Switching surfaces implementing the MPC law

and \tilde{S}_1^* . Fig. 3 depicts these surfaces in state space, together with the desired limit cycle Γ . Each surface \tilde{S}_q^* constitutes a polygon of approximately 200 sections. As can be seen, it is certainly possible to use far less polygon sections without degrading the closed-loop performance considerably. Figure 4 shows a simulation result of the start-up behavior under strong disturbances affecting the input source V_S . The first two subfigures illustrate that the state $x(t)$ is quickly taken from its initial value $x_0 = (0 \text{ A } 6 \text{ V})^T$ to a close neighborhood of Γ within four switchings. At the beginning, the inductor is maximally charged while energy is simultaneously transferred to the capacitor at the output. The first activation period of mode $q = 1$ is short to prevent violation of the current constraint. The subsequent energy transfer to the capacitor is interrupted ($q = 0$ is deactivated), when the outgoing energy flow first exceeds the incoming flow.

In summary, nearly time-optimal start-up is achieved

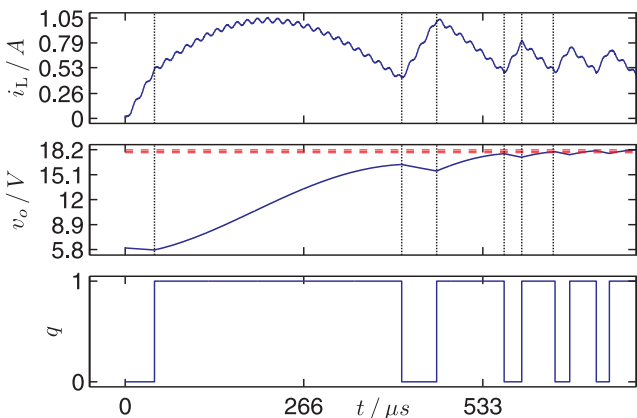


Fig. 4. Simulation of the closed-loop start-up behavior

without violating the constraint on the inductor current, without voltage overshoot and without the execution of unnecessary mode transitions (see third subplot). Once the state reaches a neighborhood of Γ the power converter settles to a stationary periodic operation.

Even though, disturbances cause heavy inductor current oscillations and the capacitor is chosen relatively small, the output voltage is almost left unaffected. This is due to the *infinite sampling rate* property of an explicit MPC law, which allows for compensating disturbance effects immediately.

V. CONCLUSION

At the academical example of a boost converter, it was shown how to use model predictive control in the design of optimal switching surfaces in the state space. Simulation results illustrate the good loop performance for a known constant load and a fixed reference voltage. How to relax these two restriction is subject to ongoing research. The potential for applying this control concept at high power converters should be investigated as well.

ACKNOWLEDGMENT

This work is supported by the Deutsche Forschungsgemeinschaft (LU462/21-3)

REFERENCES

- [1] R. W. Erickson and D. Maksimovic, *Fundamentals of Power Electronics*. Kluwer Academic Pub, 2001.
- [2] T. Geyer, G. Papafotiou, and M. Morari, "On the optimal control of switch-mode dc-dc converters," in *HSCC'04*. Philadelphia: Springer-Verlag, 2004, pp. 342–356.
- [3] A. Beccuti, G. Papafotiou, and M. Morari, "Explicit model predictive control of the boost dc-dc converter," in *Proceedings of the 2nd IFAC Conference on Analysis and Design of Hybrid Systems*, 2006.
- [4] D. Hamill, J. Deane, and D.J. Jeffries, "Modeling of chaotic dc-dc converters by iterated nonlinear mappings," *IEEE Trans. on Power Elec.*, vol. 7, pp. 25–36, 1992.
- [5] A. Schild, J. Lunze, J. Krupar, and W. Schwarz, "Design of generalized hysteresis controllers for dc-dc switching power converters," *IEEE Trans. Power Electron.*, vol. 24, pp. 138–147, 2009.
- [6] A. Schild, X. Ding, M. Egerstedt, and J. Lunze, "Design of optimal switching surfaces for switched autonomous systems," in *Proc. of 42nd IEEE CDC*. Shanghai, China: IEEE, 2009, pp. 5293–5298.
- [7] R. Findeisen, L. Imsland, F. Allgöwer, and B. A. Foss, "State and output feedback nonlinear model predictive control: An overview," *European Journal of Control*, vol. 9, pp. 190–206, 2003.
- [8] A. Schild and J. Lunze, *The HYCON Handbook of Hybrid Systems Control Theory-Tools-Applications*. Cambridge Press, 2009, ch. 6.5 Abstract models of hybrid systems, pp. 231–247.
- [9] C. Ericson, *Real-Time Collision Detection*. Elsevier LTD, Oxford, 2005.

Chaos based networking systems sharing a common nonlinearity

M. Santhiah and P. Philominathan

Department of Physics,
P.G and Research Department of Physics,
A.V.V.M. Sri Pushpam College,
Poondi, Thanjavur - 613 503,
India.

Email: philominathan@gmail.com

Abstract—This paper suggests a simple mechanism of sharing a common nonlinearity among the linear oscillators to exhibit some interesting phenomena. Here, we present fourth-order nonautonomous circuit capable of showing a large variety of dynamical behaviours in three different modes of operation. In particular, a new phenomenon of coexistence of attractors leading to torus behaviour when two identical oscillators sharing a common nonlinearity and many spatio-temporal patterns when more oscillators sharing a nonlinearity are presented. The results of numerical simulations, hardware experimental realization and analytical studies are presented.

Key words: Bifurcations; chaos; nonlinear electronic circuits.

I. INTRODUCTION

Ever since the invention of chaos, the application of dynamic chaos in many diversified fields has an exponential growth. It is an established fact that electronic circuits are representatives of many physical systems and can be represented by differential or partial differential equations. This leads to exhibit many kinds of natural phenomena from chaotic electronic circuits. The concept of nonlinear element by Chua and its' subsequent studies allowed many possibilities of exploring chaotic dynamical systems [?]. Motivated by many research activities in nonlinear electronic circuits, we wish to present some suggestions regarding the implementation of two identical linear oscillators sharing a common

nonlinearity. In particular, much attention has been given to explore the novel features of the present circuit with experimental, numerical and analytical results. Moreover, this study is expected to open up certain unexplored aspects exist in certain nonlinear electronic systems which could mimic many kinds of natural phenomena and it is expected that these phenomena be analyzed by using differential equations. From the technical point of view, our study provides a clue for the potential applications in controlling of chaos, secure communication systems, torus-synchronization etc.

II. DESCRIPTION OF MODEL CIRCUIT

A. Experimental Setup

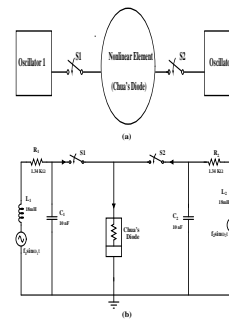


Fig. 1. (a) Block diagram of two LCR oscillators sharing Chua's diode through switches. (b) Schematic circuit diagram of Fig. 2(a).

The experimental circuit that we have employed here is a simple nonautonomous MLC

circuit and a forced LCR circuit connected in parallel. The combined circuit is shown in Fig. 2(b). The nonlinear resistive element, that is, Chua's diode employed in the circuit is to cater the needs of the two linear oscillators and to provide both periodic and chaotic domains experimentally. For analysis, we use the parameter set as: $C_1 = C_2 = 10nF$, $L_1 = L_2 = 18mH$, $R_1 = R_2 = 1.34k\Omega$. The circuit is driven by two external forcing sources whose amplitudes (f_1, f_2) and frequencies (ω_1, ω_2) are considered as the control parameters.

1) *State Equations*: The state equations for the schematic in Fig. 2(b) are the following:

$$C_1 \frac{dv_1}{dt} = i_{L1} - h(\langle v \rangle) \quad (1)$$

$$C_2 \frac{dv_2}{dt} = i_{L2} - h(\langle v \rangle) \quad (2)$$

$$L_1 \frac{di_{L1}}{dt} = -i_{L1} R_1 + f_1 \sin(\omega_1 t) - v_1 \quad (3)$$

and

$$L_2 \frac{di_{L2}}{dt} = -i_{L2} R_2 + f_2 \sin(\omega_2 t) - v_2 \quad (4)$$

where v_1 and v_2 , the voltages across C_1 and C_2 and i_{L1} and i_{L2} , the current through the inductance L_1 and L_2 are the four state variables that describe the dynamics of the system.

In this implementation, since the nonlinear element is connected parallel to C_1 and C_2 , the current flow across it is controlled by the voltages v_1 and v_2 of the capacitors and hence its performance is restricted to a linear combination, specifically the arithmetic mean of these potentials ($\langle v \rangle$). The argument of the nonlinear function is given as,

$$h(\langle v \rangle) = G_b \langle v \rangle + \frac{1}{2}(G_a - G_b) [|\langle v \rangle + B_p| - |\langle v \rangle - B_p|] \quad (5)$$

The slopes of the nonlinear characteristic $h(\langle v \rangle)$ in Eq. (5) are defined by $G_a = -0.756mA/V$ and $G_b = -0.409mA/V$.

B. Experimental realization

The circuit model described here is the most suited one to have both the processes and its' adaptability to set in any mode of operations is explained in the following:

1) *Mode(1)*: If the states of the switches are set as S1-ON and S2-OFF, we have the standard nonautonomous MLC circuit. By increasing the amplitude from zero upwards, the circuit exhibits the complex dynamics of bifurcation and chaos.

2) *Mode(2)*: If the states of the switches are set as S1-OFF and S2-ON, and by setting the frequency to $8.890KHz$ and varying the amplitude from $0.0365V_{rms}$ to $0.107V_{rms}$, the period doubling route to chaos can be observed as in mode(1). From the mode(1) and mode(2), one can understand that the dynamical behaviours just mimic the dynamics of the MLC circuit.

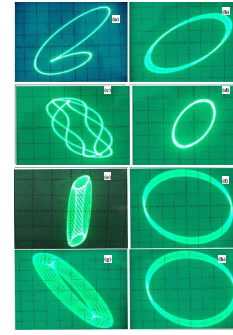


Fig. 2. Experimental phase portraits in the $(v_1 - i_{L1})$ and $(v_2 - i_{L2})$ planes. (a-b) $\nu_1 (= \frac{\omega_1}{2\pi}) = 16 KHz$, $\nu_2 = 8 KHz$, $f_1 = 0.00707 V_{rms}$ and $f_2 = 0.03535 V_{rms}$; (c-d) $\nu_1 = 24 KHz$, $\nu_2 = 9 KHz$, $f_1 = 0.006364 V_{rms}$ and $f_2 = 0.0707 V_{rms}$; (e-f) $\nu_1 = 1.433 KHz$, $\nu_2 = 2.786 KHz$, $f_1 = 0.00707 V_{rms}$ and $f_2 = 0.28284 V_{rms}$; (g-h) $\nu_1 = 8.2123 KHz$, $\nu_2 = 12.4586 KHz$, $f_1 = 0.06363 V_{rms}$ and $f_2 = 0.35355 V_{rms}$.

3) *Mode(3)*: To study the performance of the circuit [Eqs. (1)-(4)] which includes the paradigm of sharing of nonlinearity, the states of the switches S1 and S2 should have to be in ON condition. In order to understand the behaviour of the chosen circuit in mode(3), the following observations are carried out by keeping $f_1 = f_2 = 0.107V_{rms}$, $\omega_1 = 8.890KHz$ and $\omega_2 = 8.8KHz$.

- When S1 is ON and S2 is OFF the circuit exhibits a double-scroll chaotic attractor.
- When S1 is kept ON and S2 is also switched to ON, the existence of double-scroll attractor is controlled to exhibit period-1 limit cycle.

- The same behaviour of transition from chaotic attractor to period-1 limit cycle is observed when S2 is made ON at first and then S1- ON.

Further, we varied the amplitudes ω_1 , ω_2 and the frequencies f_1 , f_2 to understand the more interesting behaviour of circuit. Experimentally observed phase portraits in $(v_1 - i_{L_1})$ and $(v_2 - i_{L_2})$ planes for various values of frequencies and amplitudes are shown in Fig. 3.

III. NUMERICAL STUDIES

For numerical analysis, the circuit Eqs. (1)-(5) are converted into a normalized form. The normalized circuit equations are given by,

$$\dot{x}_1 = y_1 - f(x) \quad (6)$$

$$\dot{y}_1 = F_1 \sin(\omega_1 t) - \beta_1 y_1 - \beta_1 x_1 \quad (7)$$

$$\dot{x}_2 = y_2 - f(x) \quad (8)$$

$$\dot{y}_2 = F_2 \sin(\omega_2 t) - \beta_2 y_2 - \beta_2 x_2 \quad (9)$$

where,

$$f(x) = f(\langle x \rangle) = \begin{cases} b\langle x \rangle + a - b, & \langle x \rangle \geq 1 \\ a\langle x \rangle, & |\langle x \rangle| \leq 1 \\ b\langle x \rangle - a + b, & \langle x \rangle \leq -1 \end{cases} \quad (10)$$

Here (\cdot) dot denotes differentiation with respect to τ , $\langle \cdot \rangle$ refers arithmetic mean and $f(x)$ denotes the current through the nonlinear element. The dynamics of Eqs. (6)-(10) depends on the parameter a and b . In order to investigate the dynamics of this circuit, we numerically integrated Eqs. (6)-(10) using fourth-order Runge-Kutta algorithm with the fixed parameters $a = -1.022$, $b = -0.55$, $\beta_1 = \beta_2 = 1.0$, while varying the frequencies ω_1 or ω_2 or the drive amplitudes F_1 or F_2 .

Using the above model [Fig. 2(b)], the dynamical behaviour based on numerical simulation are summarized below.

As discussed in the experimental studies, the circuit performance in three different modes of operation are also numerically examined. For

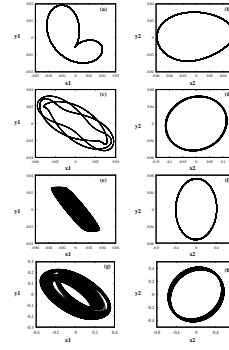


Fig. 3. Numerically observed phase portraits in the (x_1, y_1) and (x_2, y_2) planes. **(a-b)** $\omega_1=1.346432$, $\omega_2=0.673216$, $F_1=0.01$, $F_2=0.05$; **(c-d)** $\omega_1=2.019648$, $\omega_2=0.673216$, $F_1=0.009$, $F_2=0.1$; **(e-f)** $\omega_1=2.1038$, $\omega_2=0.673216$, $F_1=0.01$, $F_2=0.4$; **(g-h)** $\omega_1=0.618034$, $\omega_2=0.3345$, $F_1=0.09$, $F_2=0.5$.

mode(1) and mode(2) operations, one could expect the dynamical behaviour of the conventional MLC circuit. But, for the mode(3) operation, we observe few ordered patterns which includes the influence of forces present in the entire circuit.

IV. ANALYTICAL STUDIES

Earlier sections have vividly described both experimental and numerical realizations and it is quite obvious from the experimental observations that the potential developed across each energy components seem to be constant in mode(3). This unique feature paved way to investigate the analytical aspects of the proposed circuit given by Eqs. (6)-(10). Then, the unified second order differential equation will be of the form

$$\ddot{y}_1 = -\beta_1 \dot{y}_1 - \beta_1 y_1 - \frac{a}{2} \beta_1 y_1 - \frac{a}{2} \dot{y}_1 + \frac{a}{2} F_1 \sin \omega_1 t - \beta_1 \frac{a}{2} y_2 - \frac{\beta_1 a}{\beta_2 2} \dot{y}_2 + \frac{\beta_1 a}{\beta_2 2} F_2 \sin \omega_2 t + F_1 \omega_1 \cos \omega_1 t \quad (11)$$

and when considering $y_1 = y_2$ and $\dot{y}_2 = \dot{y}_1$, we obtain the subspace divided into three regions.

$$\begin{aligned} D_{-1} &= \{(t, y, \dot{y}) \mid \langle x \rangle < -1\} \\ D_0 &= \{(t, y, \dot{y}) \mid |\langle x \rangle| \leq 1\} \\ D_{+1} &= \{(t, y, \dot{y}) \mid \langle x \rangle > 1\} \end{aligned}$$

For mode(3), the stability determining eigenvalues of the indicial equation $\lambda^2 + K_1\lambda + K_2$ in the D_0 region are found to be real and distinct, on the other hand, in the region $D_{\pm 1}$, there exists a pair of complex conjugate eigenvalues. Now Eq. (15) in each of the regions as,

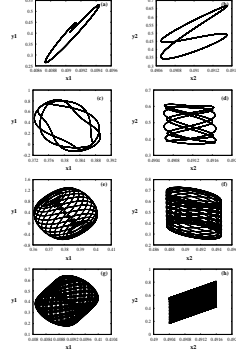


Fig. 4. Analytical phase portraits in the (x_1, y_1) and (x_2, y_2) planes. **(a-b)** $\omega_1=1.346432$, $\omega_2=0.673216$, $F_1=0.035$, $F_2=0.045$; **(c-d)** $\omega_1=2.019648$, $\omega_2=0.673216$, $F_1=0.05$, $F_2=0.15$; **(e-f)** $\omega_1=2.1038$, $\omega_2=0.673216$, $F_1=0.35$, $F_2=0.2$; **(g-h)** $\omega_1=0.618034$, $\omega_2=0.3345$, $F_1=0.09$, $F_2=0.5$.

$$\ddot{y}_1 + K_1\dot{y}_1 + K_2y_1 = E_1 \cos(\omega_1 t) + E_2 \sin(\omega_1 t) + E_3 \sin(\omega_2 t) \quad \text{for } |\langle x \rangle| \leq -1 \quad (12)$$

and

$$\ddot{y}_1 + K_3\dot{y}_1 + K_4y_1 = E_4 \cos(\omega_1 t) + E_5 \sin(\omega_1 t) + E_6 \sin(\omega_2 t) + \beta_1 \Delta. \quad (13)$$

where,

$$\Delta = a - b \quad \text{for } D_{+1} \text{ region}$$

$$\Delta = b - a \quad \text{for } D_{-1} \text{ region}$$

Eqs. (12) and (13) can be solved analytically to obtain y_1 and y_2 , which can be then differentiated to get \dot{y}_1 and \dot{y}_2 . From Eq. (6) and Eq. (8), x_1 and x_2 can be evaluated. The phase portraits of analytical solutions in the $(x_1 - y_1)$ and $(x_2 - y_2)$ phase space shown in Fig. 5 agrees with the experimental and numerical results obtained in earlier sections.

V. CONCLUSION

In this paper, the fascinating ordered and chaotic phenomena have been accomplished in a versatile model circuit using a well known paradigm of nonlinear circuit, namely, Chua's circuit and their results are presented. The possible ways and means by which a single nonlinearity can be exploited by a network of linear oscillators have been shown here with efficient experimental, numerical and analytical studies.

REFERENCES

- [1] Chua, L. O., Disoer, C. A. & Kuh, E.S. [1987] *Linear and Nonlinear Circuits* (Mc Graw-Hill Book co., Singapore).
- [2] Lakshmanan, M. & Rajasekar, S. *Nonlinear Dynamcis: Integrability, Chaos and Patterns* (Springer, Berlin).
- [3] Nishio, Y & Ushida, A. [2002] "Chaotic wandering and its analysis in simpled coupled chaotic circuits," *IEICE Trans. Fundamentals* E-85-A, 248-255.
- [4] Rafeal Martinez-Guerra. & Wen Yu. [2008] "Chaotic synchronization and secure communication via sliding-mode observer," *Int. J. Bifurcation and Chaos* 18, 235-243.

Music Score Recognition System for a Robot controlling a Theremin

Kristina Kelber and Nils Wabnik
Faculty of Electrical Engineering,
University of Applied Sciences Dresden,
Friedrich-List-Platz 1, D-01069 Dresden, Germany
Email: kelber@et.htw-dresden.de

Carlos Hernández Franco
Dept. of Communications,
Polytechnic University of Valencia,
Camino de Vera s/n, 46022, Valencia, Spain
Email: chernan@dcom.upv.es

Abstract—This paper is focussed on a MatLab-based music score recognition system, which is developed to read printed music scores and to generate a MIDI structure. This structure is used to control two robotic arms playing a Theremin without physical contact. The whole system is developed for teaching engineering students at the involved universities.

I. INTRODUCTION AND DESCRIPTION OF THE OVERALL PROJECT

The Theremin is an early electronic musical instrument, invented in 1920 by Lev Sergeyevich Termen, who discovered its function by chance during research on proximity sensors. The Theremin is played without being touched. Two metal antennas sense the position of the players hands, which act as the grounded plate (the performers body being the connection to ground) of a variable capacitor in an LC circuit. The horizontal antenna is used for volume control (changing the amplitude of the signal), while the vertical one is used for the pitch (changing the frequency). Its signal processing principle is depicted in fig. 1. To control the pitch, two

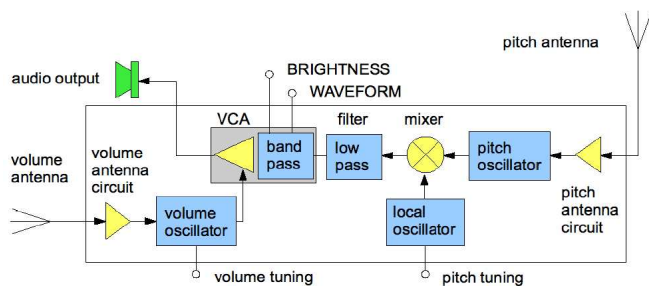


Fig. 1. Signal processing principle of the Theremin [1]

radio frequency oscillators are used. One operates at a fixed frequency, the other is controlled by the performers distance from the pitch antenna. The difference between

the frequencies of the two oscillators at each moment allows the creation of a difference tone in the audio frequency range.

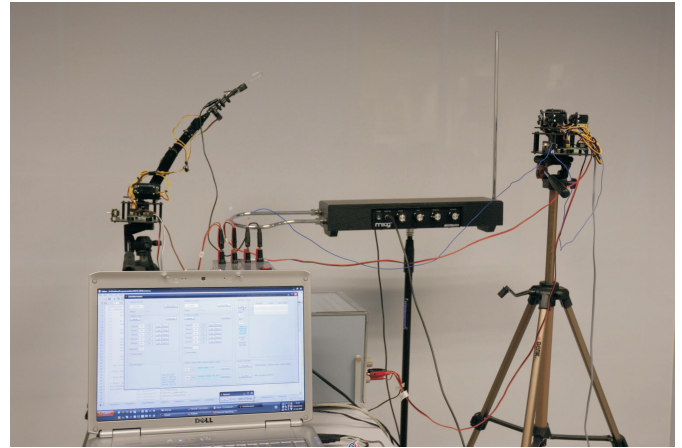


Fig. 2. Experimental setup: Moog Etherwave Theremin, two Lynx-5 robotic arms, and a laptop to control the robots.

In this project, players hands are replaced by two robotic arms as shown in fig. 2. The robots are controlled by a MatLab script, which reads musical information from a MIDI file. Now, an optical vision system for the robot is added. This paper is focussed on a simple and fast music score recognition system, which is developed as the basis of the vision system and is implemented in MatLab, too. The whole project, which is intended to be used for teaching (lab experiments, demonstrations), is described in [8].

II. REQUIREMENTS AND LIMITATIONS FOR THE OPTICAL VISION SYSTEM

A. Requirements

For development and test of the system, score sheets of A4 paper size, produced by the software LilyPond

[7], are used. Investigations show, that for detection of all necessary details (such as dotted notes) a minimum resolution of 100dpi is required. At present, an image size of approx. 1200 x 1700 pixel (corresponding to a resolution of 145dpi) is used for each A4 page.

B. Limitations

Simply moving his right hand by something near 50 cm enables the player of the Theremin to cover a usable pitch range of approximately c2 to c7 (MIDI 36 to MIDI 96) [6]. Unfortunately, the working range of the robotic arm is not that large. In the recent setup it is restricted to the range of c3 to f5 (MIDI 48 to MIDI 77). Therefore, music score recognition is limited to that range as well during this first stage of development.

As the Theremin is only able to produce one single tone per time, it is assumed that there are single notes only at the sheet.

Furthermore, due to the speed limit of the robotic arms, the minimum duration of a note is 0.2ms. Therefore, only notes and breaks down to 1/8 are analysed.

III. MUSIC SCORE RECOGNITION ALGORITHM

Optical Music Recognition (OMR) has been developed for over three decades to read printed music scores by a computer system. An overview of the state of the art is given e.g. [4]. Many of the algorithms, described there, consist of the following four modules:

- 1) staff line identification,
- 2) musical object location,
- 3) musical feature classification, and
- 4) musical semantics.

The upper part of one of the example images, which is used to depict the image processing algorithm and its results, is shown in fig. 3.

A. Staff line detection

The most widely used method for detecting staff lines is based on horizontal projections [5]. A horizontal projection maps a two-dimensional array into a one-dimensional vector by recording the number of black pixels in each row of the image in the corresponding entry in the vector. Under such a projection, staff lines appear as distinct maximums in that vector that can be detected easily [4] (see fig. 4 for example). Lets assume, the length of the staff lines exceeds a certain percentage (e.g. 0.8) of the paper width. Then, for maximums less than that percentage, the staff sheet has been rotated. The angle of rotation can be determined and corrected based on a Hough transform for (staff) lines and the horizontal

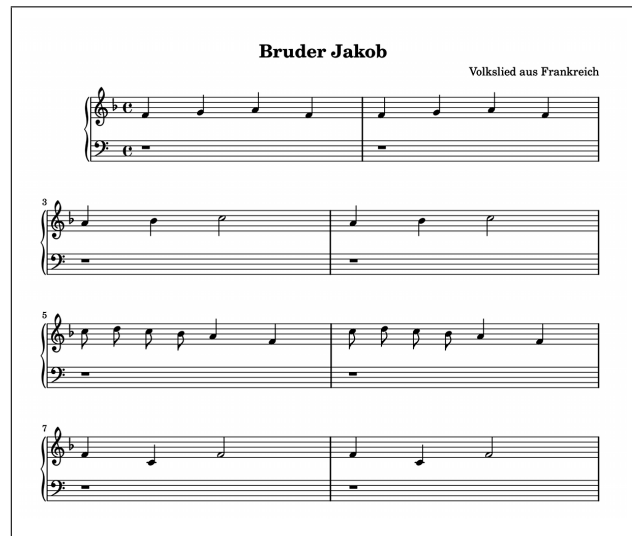


Fig. 3. Upper part of an example image of a musical score

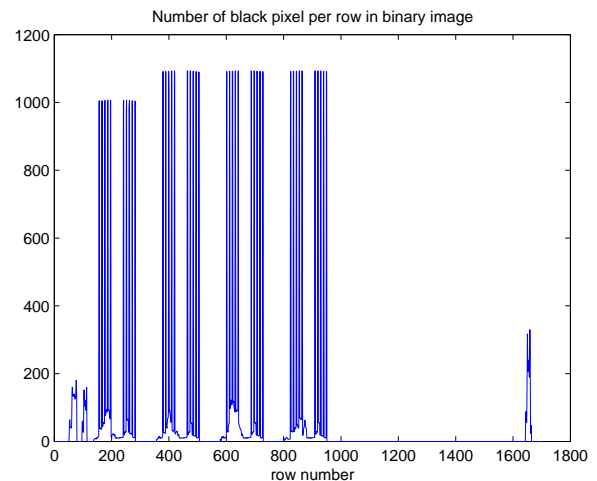


Fig. 4. Horizontal projection of the example image

projection is repeated. Afterwards, always five staff lines are grouped to one staff, which forms the region of interest (ROI) for further processing (e.g. fig. 5).

B. Musical object location

For object location, which is based on a flood-fill algorithm in general, staff lines are either ignored or removed. Due to the limitations mentioned in sec. II-B, a simplified approach can be used here, which is based on vertical projection of the ROI of each staff. As an example, fig. 6 shows the vertical projection of the ROI of the first staff. As the average number of pixels related to staff lines in each row is known from staff line detection (no. of values above threshold in the vector of horizontal projection, 10 pixel for fig. 6), it can be

ROI of staff no. 1



Fig. 5. Region of interest of first staff

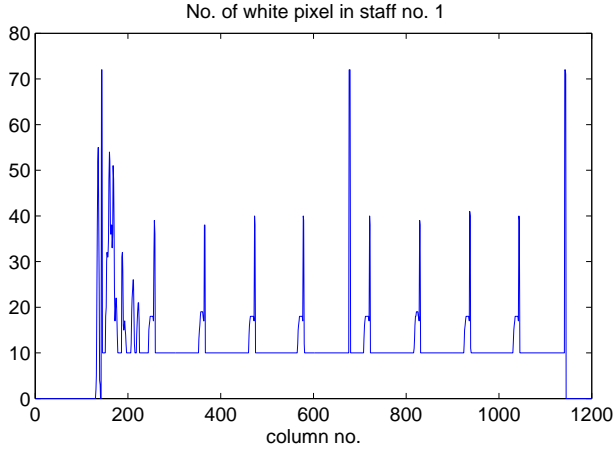


Fig. 6. Vertical projection of the Region of interest of first staff

subtracted from the vector of vertical projection. Now, musical symbols are separated by zeros in that vector and the horizontal range of its bounding box can be determined.

C. Musical feature classification and semantics

OMR often works on a sub-symbol level. Primitives, such as note heads, stems, beams, or flags, are classified based on template matching, Hough transform or projections. Afterwards, primitives are grouped to musical symbols using musical knowledge [4]. Other approaches are based on the analysis of the bounding box dimension [4], on morphological detection and connected components analysis to recognize the symbols, followed by a reasoning module [2] or on template matching of complete symbols [3].

In this project, template matching in time and frequency range as well as projections have been implemented and compared. It turned out, that the approach based on vertical projection of the ROI of each staff is the fastest as it reduces the problem from 2D to 1D signal processing. Furthermore, it is less sensitive to scaling and it easily provides all symbols in correct order, due to the fact, that the ROI of the staff is processed from left to right. The algorithm for detecting the musical symbols within the ROI of the staffs is described in fig. 7.

for all staffs
find <i>clef</i>
find <i>beat sign</i>
if $distance(beat\ sign, clef) > threshold$
look for <i>accidentals</i>
for all beats
while $symbol \neq beat\ bar$
recognize <i>notes/breaks</i>
if $\sum notes/breaks < beat\ sign$
search for <i>dotted notes</i>
if $beat\ bar = repeat\ mark$
store <i>repeat info</i> in structure
if $beat\ bar = double\ bar$
check for new <i>accidentals/beat sign</i>

Fig. 7. Algorithm for detecting musical symbols

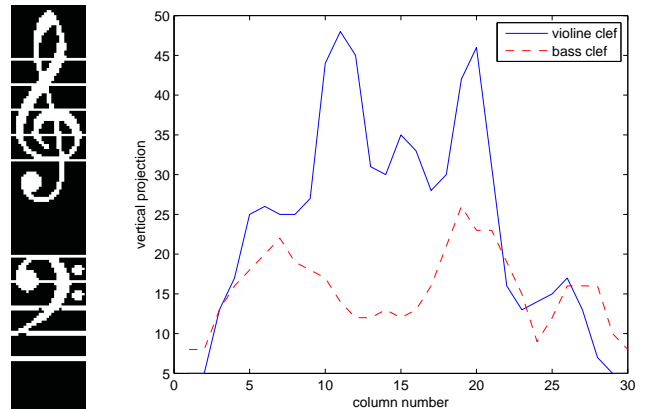


Fig. 8. Violine clef, bass clef, and their vertical projections

First, clef, beat sign (if any), and accidentals (if any) are detected at the beginning of each ROI. Clefs and accidentals can be easily distinguished based on their vertical projections (see fig. 8 for an example). For the beat sign, template matching by XOR of the scaled ROI of the symbol and the templates is used.

Afterwards, notes and breaks are recognized based on vertical and horizontal projections. As an example, fig. 9 shows some notes and their vertical projections. Due to the different shapes, this projection can be used to determine the *duration* of the note, which is 1/1, beat bar, 1/2,

1/8, 1/4, 1/8 in that example. A horizontal projection

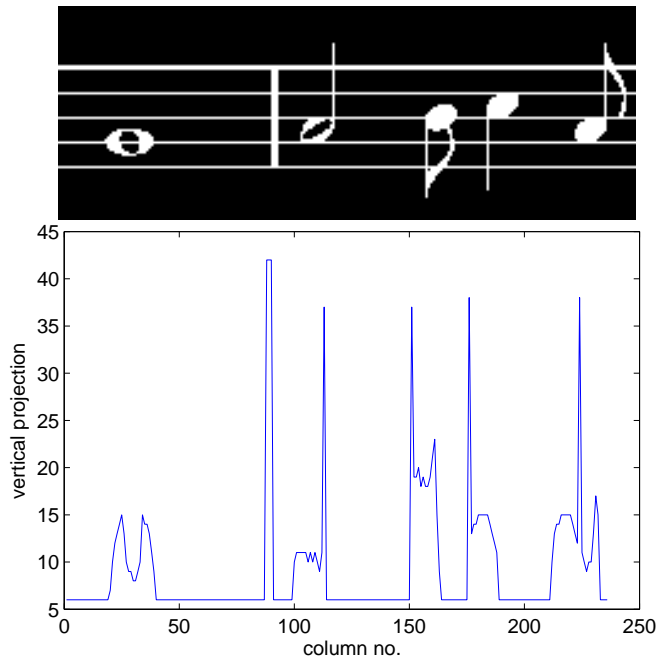


Fig. 9. Notes and their vertical projections

of the ROI of each single note is used to determine its *pitch*. As an example, fig. 10 shows these projections for the first four notes in fig. 9. Ignoring the values related to projections of the staff lines, one obtains maximums which results in g4, a4, h4, and c5.

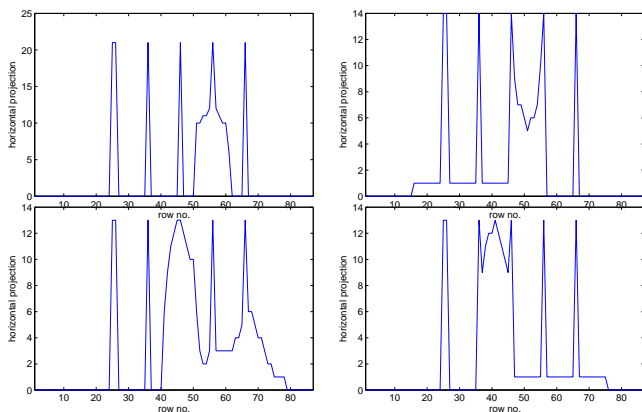


Fig. 10. Horizontal projections of the first four notes in fig. 9

When a beat bar is found, it is checked whether the durations of all detected notes and breaks corresponds to the beat sign. If not, it is searched for missed notes. In case of a double beat bar, it is looked for new accidentals and beat sign. Accidentals in front of notes are currently not analysed, but will be allowed later on.

All processed symbols are stored in a MatLab structure staff by staff and beat by beat. In cases, where no accidental or beat sign is detected, its value is taken from the previous staff.

Finally, a MIDI structure is generated from the MatLab structure and it is used to control the robotic arms.

IV. CONCLUSION & FUTURE WORK

A MatLab-based music score recognition system has been developed. It is now able to analyse musical score sheets and to build a MIDI structure, which can be used to control two robotic arms playing a Theremin. In the future, the processing speed of the MatLab script should be further optimized and the number of musical symbols to be recognized will be extended in order to analyse more complex score sheets for other instruments, like piano or violin, too.

The main purpose of developing the whole system, depicted in fig. 2, is to introduce engineering students to a wide range of problems in an exciting way. The Theremin can be used to explain basics of circuit theory and the operation of the robotic arms for control theory. Several digital signal processing algorithms can be investigated and compared using the optical vision system and a new module for sound analysis and synthesis which is just under development.

REFERENCES

- [1] Nils Wabnik: *Implementation of an artificial vision system for the robotic arms controlling the electronic musical instrument Theremin*, diploma thesis, University of Applied Sciences Dresden, 2009.
- [2] B.R. Modayur, V. Ramesh, R.M. Haralick, and L.G. Shapiro: MUSER: A prototype musical score recognition system using mathematical morphology, *Machine Vision and Applications*, vol. 6, pp. 140-150, 1993.
- [3] M. Engelhardt, R. Sonderegger: *Virtual Pianist*, diploma thesis, Hochschule für Technik, Rapperswil, 2001.
- [4] D. Bainbridge, T. Bell: The Challenge of Optical Music Recognition, *Computers and the Humanities*, vol. 35, pp. 95121, 2001.
- [5] D. Blostein, H.S. Baird: A Critical Survey of Music Image Analysis, In *Structured Document Image Analysis*. Ed. H.S. Baird, H. Bunke, K. Yamamoto, Springer-Verlag, Berlin, pp. 405-434, 1992.
- [6] *Understanding, costumizing, and hot-rodding your Etherwave Theremin*, Moog Music Inc., 2003.
- [7] Software available at <http://lilypond.org/>
- [8] C. Hernández Franco, K. Kelber: Digital Signal Processing Applied to Musical Hyper Instruments, accepted for International Technology, Education and Development Conference (INTED2010), Valencia / Spain, March, 2010.

A Cochlear Active Transmission-Line Model without Wave Reflection

Tohru Kohda and Takao Une
Dept. Informatics, Kyushu University
Email: kohda@csce.kyushu-u.ac.jp
une@kairo.csce.kyushu-u.ac.jp,

Kazuyuki Aihara
Institute of Industrial Science,
Tokyo University
Email: aihara@sat.t.u-tokyo.ac.jp

Abstract—Two simplifying assumptions were made in a frequency-domain formulation of an integrable 1D transmission-line cochlear model: (1) the parallel impedance representing the basilar membrane impedance is a series *LRC* circuit whose resonant frequency varies exponentially with the distance x from the stapes; and (2) the characteristic impedance $Z_0(s)$ with the complex angular frequency s is independent of x so that no wave reflection occurs which comes from the nonuniformity of the parallel and/or the longitudinal impedance, except at the stapes and helicotrema. When $Z_0(s)$ is real (respectively, complex), we can get an integrable passive (respectively, active) model. In this paper, we review a cascaded transmission-line model consisting of two active sections and one passive one. Such an active-passive-active model is shown to give a solution to Zweig et. al.'s cochlear compromise problem and Zwislocki's sharp maximum vs. wave reflection paradox and provide a computational model for simulating Kemp echo.

I. INTRODUCTION

The classical nonuniform transmission-line model of the cochlea is characterized by two quantities as functions of distance x from the stapes and the complex angular frequency $s = \sigma + j\omega$ with the angular frequency ω and a real-valued σ (see for review [1]–[5]): (1) the distributed parallel impedance representing the basilar membrane impedance $Y^{-1}(x, s)$; and (2) the series impedance representing the reticular lamina and outer hair cell, as well as the fluid that connects adjacent parallel sections together, $Z(x, s)$, as shown in Fig.1, where $E, P_0, U_0, P_L, U_L, Z_G$, and Z_L denote the eardrum pressure, stapes pressure at $x = 0$, stapes volume velocity, pressure difference at the helicotrema ($x = L$), fluid volume velocity at the helicotrema, middle ear transfer characteristic and helicotrema characteristic, respectively. Furthermore, $P(x, s), U(x, s), U_b(x, s)$ denote the pressure difference between two scalae at x ,

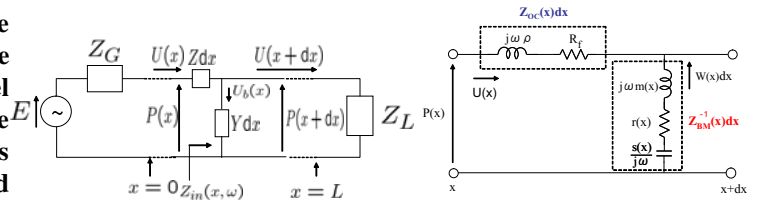


Fig. 1. Left: Simplified cochlea transmission-line model with the series impedance $Z(x, s)$ and parallel admittance $Y(x, s)$ per unit length; Right: $Z(x, s)$ and $Y(x, s)$ of classical models.

fluid volume velocity, basilar membrane velocity, respectively. In electrical communication engineering, instead of $Y(x, s)$ and $Z(x, s)$, the characteristic impedance $Z_0(x, s) (= \sqrt{Z(x, s)/Y(x, s)})$ and the propagation constant $\gamma(x, s) (= \sqrt{Z(x, s)Y(x, s)})$ are often discussed.

Unlike in most of well-known cochlear transmission-line models, we have previously given cochlear transmission-line models [6], [7], where $Z_0(x, s)$ is independent of x , i.e., $Z_0(x, s) = Z_0(s)$ but the propagation constant is a function of x and s so that no wave reflection occurs which comes from the nonuniformity of $Y(x, s)$ and/or $Z(x, s)$, except at the stapes and helicotrema. Furthermore, we have shown that when $Z_0(s)$ is real (respectively, complex), the resulting transmission-line becomes a passive integrable cochlear model [6] (respectively, an active [7] and hybrid one [8]).

In this paper, we briefly review that such a class of cochlear transmission-line models without wave reflection has good agreement with physiological experimental data [9]–[11]. Furthermore, we give frequency characteristics and travelling wave in such models.

II. NONUNIFORM TRANSMISSION-LINE MODEL WITH CONSTANT CHARACTERISTIC IMPEDANCE

A number of cochlear mechanics have been proposed (see for review [1]–[5]). In the well-known cochlear

transmission-line models, the pressure difference $P(x, s)$ across the scala media and the volume velocity $U(x, s)$ of the fluids at x are assumed to satisfy the nonuniform transmission-line equations as shown in Fig.1:

$$\frac{\partial P(x, s)}{\partial x} = -Z(x, s)U(x, s), \quad (1)$$

$$\frac{\partial U(x, s)}{\partial x} = -Y(x, s)P(x, s). \quad (2)$$

Under the condition that as shown in the right figure of Fig. 1, the longitudinal coupling is fluid coupling, *e.g.*,

$$Z(x, s) = \nu(x) + s\mu(x) \quad (3)$$

and the scala media is modeled mechanically as a linear array of harmonic oscillators, *i.e.*,

$$Y^{-1}(x, s) = sm(x) + r(x) + k(x)/s, \quad (4)$$

the solution $P(x, s)$ and $U(x, s)$ to the above nonuniform transmission-line equations are given by the use of the WKB approximation technique (see for review [12],[13]).

On the other hand, two simplifying assumptions were made in two integrable transmission-line models of the cochlea [6], [7]: (1) $Y^{-1}(x, s)$ is a series LRC circuit whose resonant frequency is given by $\beta(x) = \beta_0 e^{-ax}$; and (2) $Z(x, s)$ is determined by the characteristic impedance $Z_0(s)$ which is independent of x , namely, $Z(x, s) = Z_0^2(s)Y(x, s)$ so that no wave reflection occurs which comes from the nonuniformity of $Y(x, s)$ and/or $Z(x, s)$, except at the stapes and/or helicotrema. Thus the second assumption gives an integrable transmission-line equations:

$$\frac{\partial P(x, s)}{\partial x} = -Z_0(s)\gamma(x, s)U(x, s), \quad (5)$$

$$\frac{\partial U(x, s)}{\partial x} = -\frac{\gamma(x, s)}{Z_0(s)}P(x, s). \quad (6)$$

Not using the WKB approximation technique, we can get the solutions of $P(x, s)$ and $U(x, s)$ in a rigorous form:

$$P(x, s) = A_d e^{-\Gamma(d, x; s)} + B_d e^{\Gamma(d, x; s)} \quad (7)$$

$$U(x, s) = \frac{A_d}{Z_0(s)} e^{-\Gamma(d, x; s)} - \frac{B_d}{Z_0(s)} e^{\Gamma(d, x; s)} \quad (8)$$

where

$$\Gamma(d_0, d_1; s) = \int_{d_0}^{d_1} \gamma(x, s) dx \quad (9)$$

and A_d and B_d are constants to be determined by the boundary conditions at $x = d$. The first terms of $P(x, s)$ and $U(x, s)$, $A_d e^{-\Gamma(d, x; s)}$ and $\frac{A_d}{Z_0(s)} e^{-\Gamma(d, x; s)}$,

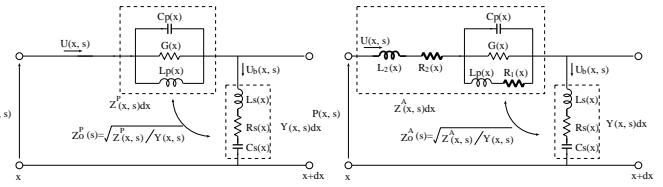


Fig. 2. Left:Short section of a passive electrical transmission-line; Right:Short section of an active electrical transmission-line.

respectively are referred to as the incident waves and the second terms $B_d e^{\Gamma(d, x; s)}$ and $\frac{B_d}{Z_0(s)} e^{\Gamma(d, x; s)}$ are referred to as the reflection waves.

Note that both of $P(x, s)$ and $U(x, s)$ are to be wave-reflectionless, defined by

$$P(x, s) = A_0 e^{-\Gamma(0, x; s)}, U(x, s) = \frac{A_0}{Z_0(s)} e^{-\Gamma(0, x; s)} \quad (10)$$

if and only if both of the generator impedance $Z_G(s)$ and the load impedance $Z_L(s)$ in the transmission-line, as shown in Fig.1, are matched to the characteristic impedance $Z_0(s)$. (*i.e.*, $Z_G(s) = Z_L(s) = Z_0(s)$.) Namely, such a transmission-line satisfies the maximum power-transfer theorem in the circuit theory. Thus this assumption is quite distinct from the assumptions in most of well-known transmission-line models that the characteristic impedance is a function of x and s and the propagation constant is independent of x .

Assuming that the parallel impedance is a series LRC circuit, defined by

$$Y^{-1}(x, s) = sL(x) + R(x) + \frac{1}{sC(x)}, \quad (11)$$

(together with the condition that $L(x) = L_0 e^{ax}$, $C(x) = C_0 e^{ax}$, $R(x) = R_0$), or the resonant frequency and the loss function are defined by

$$\beta(x) = \frac{1}{\sqrt{L(x)C(x)}} = \beta_0 e^{-ax}, \quad \beta_0 = \frac{1}{\sqrt{L_0 C_0}}, \quad (12)$$

$$\delta(x) = R(x) \sqrt{\frac{C(x)}{L(x)}} = \delta_0, \quad \delta_0 = R_0 \sqrt{\frac{C_0}{L_0}}. \quad (13)$$

We have get a passive transmission-line model [6] with a resistive characteristic impedance $Z_0(s) = Z_0^P = r$ and hence with a parallel LGC circuit $Z(x, s) = Z^P(x, s)$, as shown in Fig.2. Furthermore, we have shown that several numerical results of the passive model give good agreement with the experimental data by Békésy and Rhode (see Figs. 4-7).

On the other hand, an inductive characteristic impedance $Z_0^A(s) = r + sM$ and hence $Z(x, s) =$

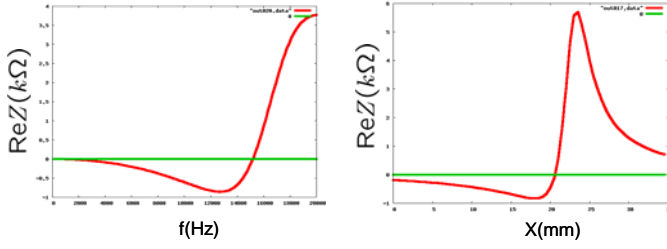


Fig. 3. Real parts of the series impedance Z in the active transmission-line model as a function of f and x .

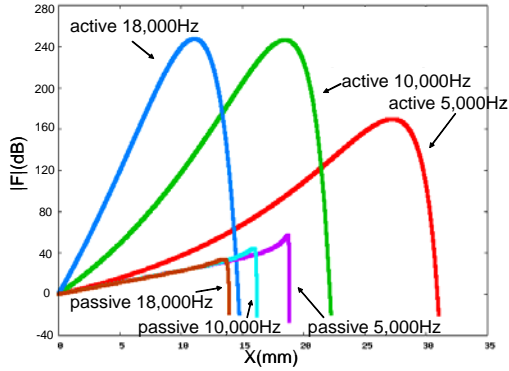


Fig. 4. Amplitude characteristics of the transfer function in the active transmission-line model as a function of place x .

$Z^A(x, s) = Z_0^A(s)^2 Y(x, s)$, (together with the condition that $L(x) = L_0 e^{ax}$, $C(x) = C_0 e^{ax}$, $R(x) = R_0 e^{-ax}$) led us to get a locally active model [7], [8] with sharp frequency characteristics as reported by Sellick *et al.* (see Figs. 4 and 6). The continued-fraction expansion of $Z^A(x, s)$ gives a network synthesis of $Z^A(x, s)$, represented by a parallel $LGC - L$ in series circuit with locally negative resistances $R_1(x)$ and $R_2(x)$ as shown in Fig.3.

Let us introduce the input impedance and the reflection coefficient of the transmission-line at x , respectively defined by

$$Z_{in}(x, \omega) = \frac{P(x, \omega)}{U(x, \omega)}, \quad (14)$$

$$\rho(x, \omega) = \frac{B_0 e^{\Gamma(0, x, \omega)}}{A_0 e^{-\Gamma(0, x, \omega)}} = \frac{Z_{in}(x, \omega) - Z_0(\omega)}{Z_{in}(x, \omega) + Z_0(\omega)}. \quad (15)$$

The assumption that $Z_G = Z_L = Z_0(\omega)$ gives

$$P(x, \omega) = P(0, \omega) e^{-\Gamma(0, x, \omega)}, \quad U_b(x, \omega) = Y(x, \omega) P(x, \omega). \quad (16)$$

Figures 4-7 show numerical results of the basilar membrane velocity in active/passive models as a function of

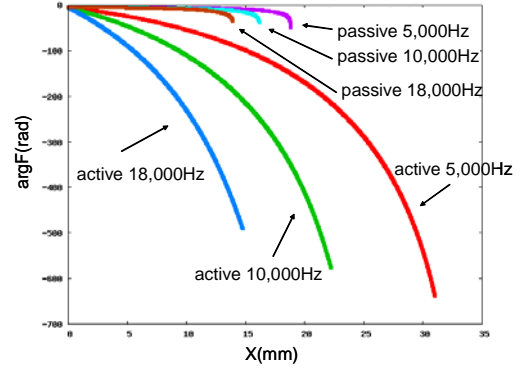


Fig. 5. Phase characteristics of the transfer function in the active transmission-line model as a function of place x .

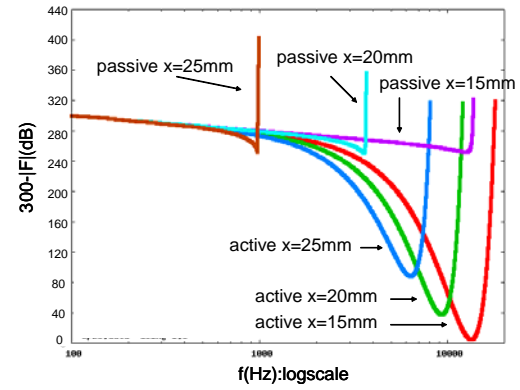


Fig. 6. Amplitude characteristics of the transfer function in the active transmission-line model as a function of frequency f .

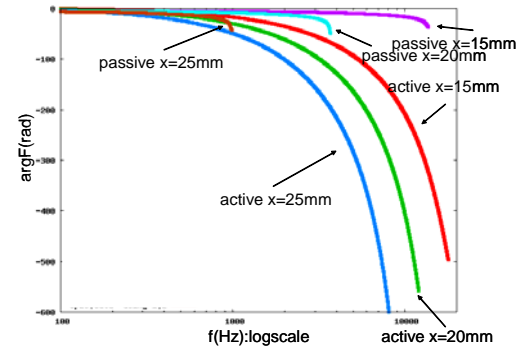


Fig. 7. Phase characteristics of the transfer function in the active transmission-line model as a function of frequency f .

x and f , respectively. The parameters of these models are given as

$$\begin{cases} \text{Active : } r = 36.0, M = 2.3 \times 10^{-4}, L_0 = 1.78 \times 10^{-6}, \\ \quad R_0 = 1.5, C_0 = 2.78 \times 10^{-6}, a = 0.08, \\ \text{Passive : } r = 3.4, L_0 = 2.385 \times 10^{-7}, R_0 = 1.45, \\ \quad C_0 = 2.132 \times 10^{-7}, a = 0.263. \end{cases}$$

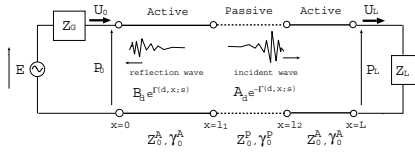


Fig. 8. Cascaded transmission-line model which consists of two active sections with $Z_0^A(s)$ and $\gamma^A(x, s)$ in the $(0, \ell_1)$ and (ℓ_2, L) regions and one passive section in the (ℓ_1, ℓ_2) region with $Z_0^P(s)$ and $\gamma^P(x, s)$ in order to make savings of active mechanisms, where $\Gamma(d_0, d_1; s) = \int_{d_0}^{d_1} \gamma(y, s) dy$ with $\gamma(y, s) = \gamma^A(y, s)$ or $\gamma^P(y, s)$.

III. ACTIVE-PASSIVE-ACTIVE MODELS WITH CONSTANT CHARACTERISTIC IMPEDANCE

In this paper, we present a cascaded transmission-line model [8] which consists of two active sections in the $(0, \ell_1)$ and (ℓ_2, L) regions and one passive section in the (ℓ_1, ℓ_2) region in order to make savings of active mechanisms, as shown in Fig.8. Such a cascaded active-passive-active (APA) transmission-line can be easily solved by using both of four reflection coefficients $\rho(x, s)$ and input impedances $Z_{in}(x, s)$ at $x = 0, \ell_1, \ell_2, L$ as follows:

$$\begin{aligned} \rho(0, s) &= \frac{(1 + \rho(\ell_1, s))Z_0^P - (1 - \rho(\ell_1, s))Z_0^A}{(1 + \rho(\ell_1, s))Z_0^P + (1 - \rho(\ell_1, s))Z_0^A} e^{-2\Gamma^A(0, \ell_1; s)}, \\ \rho(\ell_1, s) &= \frac{(1 + \rho(\ell_2, s))Z_0^A - (1 - \rho(\ell_2, s))Z_0^P}{(1 + \rho(\ell_2, s))Z_0^A + (1 - \rho(\ell_2, s))Z_0^P} e^{-2\Gamma^P(\ell_1, \ell_2; s)}, \\ \rho(\ell_2, s) &= \frac{Z_L - Z_0^A}{Z_L + Z_0^A} e^{-2\Gamma^A(\ell_2, L; s)}, \end{aligned}$$

and $Z_{in}(x, s)$ is calculated by fomula (15). (In the case, fomula (15) Z_0 is treated as Z_0^A or Z_0^P). Such an APA model with only 7 parameters *i.e.*, $a, \beta_0, \delta_0, \text{Re}Z_0, \text{Im}Z_0, \ell_1, \ell_2$, as well as $Z_G(s)$ and $Z_L(s)$, provides a computational model in the following sense: (1) both of the transfer characteristic $P(x, s)/E$ and the input impedance at the eardrum $Z_T(s)$, defined by

$$Z_T(s) = Z_G(s) + Z_{in}(0, s) \quad (17)$$

can be easily obtained; and (2) the application of the Inverse Laplace Transform to $Z_T(s)$ gives the model response for simulating Kemp echo. In particular, this model is shown to give a concrete model of the antiresonator as a possible secondary resonance of the cochlear partition [14] and furthermore to provide a simple solution to the cochlear compromise problem [12] and the sharp maximum versus wave reflection paradox [15].

IV. CONCLUSIONS

We have reviewed a class of transmission-line with the constant characteristic impedance and given a cascaded transmission-line model consisting of two active sections with the complex-valued constant characteristic impedance and one passive one with the constant real-valued characteristic impedance. Such an active-passive-active model has been shown to give a solution to the the cochlear compromise problem [12] and sharp maximum *vs.* wave reflection paradox [15] and provide a computational model for simulating Kemp echo using the inverse Laplace transform of the input imedance at the eardrum. This work was supported in part by ERATO Aihara Complexity Modelling Project, JST, and Grants-in-Aid for Scientific Research of Japan Society for the Promotion of Science, no.20360174.

REFERENCES

- [1] J.B.Allen, "Cochlear Micromechanics-A Physical Model of Transduction," *J. Acoust.Soc.Am.*, **68**-6, pp. 1660-1670,1980.
- [2] De Boer, E, "Auditory physics. Physical principles in hearing theory. I,II,III,"*Phy. Rep.*, respectively, **62**, pp.87-174, 1980, **105**, pp.141-226, 1984, **203**, pp.125-231, 1991.
- [3] E.deBoer, "On Equivalence of Locally Active Models of the Cochlea," *J.Acoust.Soc.Am.*, **98**-3, pp. 1400-1409,1995.
- [4] J.B.Allen,"Nonlinear Cochlear Signal Processing," March 13,2001
- [5] The workshop on Auditory Mechanisms: the 1st in a series in 1983, the 10th in 2008, the 11th will be held in 2011.
- [6] Y.Oono and T.Kohda, "A Distributed-Parameter Model for Representing the Basilar Membrane Displacement", *Trans. IEICE*, **57**-D-8, pp. 463-470, 1974, (*in Japanese*).
- [7] T.Kohda, "An Active One-Dimensional Cochlear Model as a Modification of a Passive Model", *J.Acoust.Soc.Jpn.*, **41**-8, pp. 519-526, 1985, (*in Japanese*).
- [8] T.Kohda, "A cochlear active transmission-line Model with Longitudinal Antiresonance Coupling," Proc. of Int. Symp. on Recent Developments in Auditory Mechanics, editors: H. Wada, T. Takasaka, K.Ikeda, K. Ohyama, T.Koike, World Scientific, pp.174-180, 2000
- [9] G.V.Békésy,*Experiments in Hearing*, McGraw-Hill Book Co., New York, 1960.
- [10] W.S.Rhode, "Observation of the basilar membrane in squirrel monkeys using Mössbauer technique," *J.Acoust. Soc. Am.*49, 1218-1231, 1971.
- [11] P.M.Sellick, R.Patuzzi and B.M.Johnstone, "Measurement of basilar membrane motion in the guinea pig using the Mössbauer technique," *J. Acoust. Soc. Am.* 72, 131-141, 1982.
- [12] G.Zweig, R.Lipes, and J.R.Pierce, "The Cochlear Compromise," *J.Acoust.Soc.Am.*, **59**-4, pp. 975-982, 1976.
- [13] G. Zweig, "Finding the impedance of the organ of Corti," *J. Acoust. Soc. Am.* 89, 1229-1254, 1991.
- [14] J.J.Zwislocki, "Tectorial Membrane: A Possible Effect on Frequency Analysis in the Cochlea," *Science*, **204**, pp. 639-641, 1979.
- [15] J.J.Zwislocki, "Sharp Vibration Maximum in the Cochlea Without Wave Reflection," *Hearing Research*. **9**, pp. 103-111, 1983.

Automatic Discovery of Subgoals in Reinforcement Learning using Betweenness Centrality Measures

Parham Moradi

Department of Computer Science
Amirkabir University of Technology
Tehran, Iran
pmoradi@aut.ac.ir

Ali Ajdari Rad, Alireza Khadivi and Martin Hasler

School of Computer and Communication Sciences
Ecole Polytechnique Fédéral de Lausanne,
Lausanne, Switzerland
{ali.ajdarirad,alireza.khadivi,martin.hasler}@epfl.ch

Abstract— The standard reinforcement learning methods do not scale up well for complex tasks and a solution to this drawback is to decomposing a learning task into a set of subgoals. In this paper we propose a new algorithm for identifying and evaluating subgoals automatically based on a new complex network centrality measure. Investigating two benchmark problems, the results show that the proposed method outperforms current well-known centrality based approaches.

I. INTRODUCTION

Reinforcement Learning (RL) is an approach for autonomous agents to improve their performance while interacting with an environment [1]. In the Reinforcement Learning framework, the interaction of the agent and an environment can be represented by a Markov Decision Process (MDP) framework. A finite MDP is a tuple $\langle S, A, T, R \rangle$, where S is a finite set of states, A is a finite set of actions, $T: S \times A \times S \rightarrow [0, 1]$ is a state transition probability function and $R: S \times A \rightarrow \mathbb{R}$ is a reward function. At each decision stage, the agent is in a state $s \in S$ and executes an action $a \in A$ with probability $T(s, a, s')$ which leads to state $s' \in S$ and obtains a reward $r \in \mathbb{R}$ which is an either static or stochastic function of the current state and the action performed by the agent. The agent's goal is to find a map from states to actions, called policy, which maximizes the expected discounted reward over time, $E\{\sum_{t=0}^{\infty} \gamma^t r_t\}$, where $\gamma < 1$ is a discount factor and r_t is the reward obtained at time t .

Standard RL methods do not scale up well for complex tasks. There are two principal approaches for improving RL performance in complex environments. The first approach is to apply approximates of a value function and the second approach is decomposing a learning task into a set of simpler subtasks [3-4], leading to skills. This decomposition leads to the reduction of the size of an agent's state space and expedites the learning procedure. To represent skills, we use the options framework [3]. An option is a

temporally-extended action, specified by a triple $\langle I, \pi, \beta \rangle$ where I denotes the option's initiation set, i.e., the set of states in which the option can be invoked; π is the option's policy, mapping states belonging to I to a sequence of actions; and β denotes the option's termination condition, where $\beta(s)$ denotes the probability that the option terminates in state s . In this paper, the Macro-Q-Learning algorithm [3] is exploited to optimize policies for agent's actions, i.e. primitive actions and options. Using a skill means that the agent follows the policy of that skill until it reaches a termination node. Due to the longer execution time of skills comparing to the primitive actions, the penalty, i.e. negative reward, assigned to a skill is higher than primitive actions. Consequently, developing useless skills leads to low learning performance. A common way is to define a set of subgoals consisting in reaching some strategic states. These states are believed to have crucial importance to reach and help accomplishing the task considerably. Appropriate selection of skills effectively simplifies learning of the task. The skills could be predefined by the designer but it is not usually easy to find them for complex tasks [3-4]. Therefore, it is preferable that the agent acquires these skills automatically which in fact is the goal of this paper.

There are three approaches to identify subgoals automatically. The first approach is frequency based and uses the information how often a state has been visited by the agent [5-6]. Next is policy based in which the agent, first learns a task and then analyzes the learned policy for certain structural properties [7-8]. Finally, the third method is graph theoretic approaches where the agent's transition history is mapped to a graph and then, the states within strongly connected regions are identified as subgoals [9-14]. Menache *et al.* [9] have used the Max Flow-Min Cut algorithm to find bottleneck states while in [10-12] the states space is partitioned using some graph clustering

algorithms. On the other hand, Simsek and Barto [13] and Ajdari et al. [14] showed that the node centrality-based measures can be utilized as an effective measure not only for finding but also evaluating the subgoals.

According to the definition and application of skills, Ajdari et al. [14] characterized the candidate subgoals as follows. The candidate subgoals should (a) frequently contribute in solutions to be reused in several tasks, (b) lie on rather long and hard-to-find solutions to be used for the abstraction of subgoals, and (c) have some centrality property to decrease the average time of exploration. In addition to above conditions, from the computational complexity point of view, the skill acquisition method must be applicable for problems with a large state space. There are several centrality measures that numerically quantify the importance of nodes in a graph [15] including betweenness centrality, closeness centrality, stress centrality, graph centrality and connection graph stability (CGS) centrality [14].

Here, we propose a new algorithm for identifying and evaluating subgoals automatically. Investigating two benchmark problems, the results show that the proposed method outperforms current well-known centrality based methods. The rest of the paper is organized as follows; in section 2 the proposed method is presented. The benchmark tasks, simulation and results are described in section 3 and section 4 contains concluding remarks.

II. PROPOSED METHOD

Our proposed algorithm is as follows: (1) the agent starts exploring the environment until stop conditions are met, (2) the agent's state space history is mapped to a graph, (3) the nodes of the obtained graph are scored based on CGS centrality (4), the top most scored nodes, i.e. nodes with score higher than a predefined threshold, are considered as candidate subgoals, (5) the set of candidate subgoals is reduced to the most important subgoals, (6) for each subgoal, a skill is developed and is added to the agent's action set. Afterwards, the agent can either select a primitive action or a skill, in each state and updates its corresponding policy based on gained reward.

A. Subgoal set discovery

For subgoal identification and selection, recently, we proposed a node centrality measure called *connection graph stability (CGS) centrality* which is defined as the weighted sum of the path length of shortest paths crossing a node [14]. This measure fulfills all three mentioned properties for detecting nodes related to useful skills. The CGS concept was first introduced by Belykh *et al.* [16] as a score assigned to the edges of the graph to find a sufficient condition for synchronization in a network of coupled dynamical systems. It is worth mentioning that the computational complexity of this measure and node betweenness

centrality is similar by exploiting Brandes algorithm [15] with minor modifications to involve the length of the paths. In order to find subgoals, the nodes with a CGS value less than a threshold are eliminated while the rest are considered as candidate subgoals and are preserved for further investigation. This is due to fact that it is highly expected that the subgoals are within the high-centrality nodes. We will show that the proposed method is not sensitive to this threshold.

B. Subgoal set pruning

Normally, the neighboring nodes of the most central nodes have also high centrality values and using a simple thresholding may result in redundant nearby subgoals. To avoid such results, we propose to create a properly weighted graph of candidate subgoals. This graph will be decomposed into a set of clusters with one main subgoal in each. By definition, a cluster is a subset of nodes which are strongly connected to each other, but are weakly connected to the nodes outside. We start with a complete graph whose nodes are the candidate subgoals and assign the edge weights as follows,

$$W_{ij} = \frac{C_{ij}}{S_j}, \quad (3)$$

where W_{ij} is the weight of the edge connecting nodes i and j , S_j is the node CGS score of j , and C_{ij} presents the co-betweenness centrality of nodes i and j , defined as the number of shortest paths that make use of nodes i and j simultaneously [17]. Using this weighting scheme, the candidate subgoals that are highly correlated, i.e. lie on many similar shortest paths, become highly coupled, while the rest are rather loosely coupled.

In order to find the main subgoals, the weighted graph is divided into some clusters using the Fast Newman clustering algorithm which has been proved to have both good performance and low computational complexity i.e. $O(md \log n)$, where n and m are number of nodes and edges, respectively and d is the depth of the dendrogram describing the network community structure [2]. After clustering, the nodes with maximum node CGS in their own clusters are taken as the final subgoals.

C. Creating skills

In this paper, we focus on subgoal identification. However, there is also some prior knowledge about proper selection of the initiation set and the policy of each skill that can be extracted from the state transition graph. But for the sake of simplicity, we consider all nodes of the graph as initiation set of each skill and the probabilities of the policy are set equal. Further investigation on this topic is under progress.

III. SIMULATION AND RESULTS

A. Environments and benchmarks

The proposed method is tested on two benchmark tasks namely “grid room” and “taxi driver” worlds which are briefly introduced in this section.

Two-room grid world shown in figure 1.a, consists of two rooms connecting each other through two doors. The agent is located at a randomly selected start point and asked to find a randomly selected goal point. The agent has four primitive actions, namely to move up, down, left and right. In the corresponding state transition graph, the cells are represented as nodes which are connected to their four neighbors. Then, we randomly select 60 tasks (namely 60 pairs <start, goal> locations). Each task is performed 100 times (episodes). The agent receives a reward of 1000 at the goal state and a reward -1 for all other states. To set the exploitation and exploration trade-off, our agents select out of policy, i.e. random, actions with probability of 0.1, i.e. the agent uses an ϵ -greedy policy [1] with $\epsilon = 0.1$. The learning rate α and the discount factor γ are set to 0.1 and 0.9 respectively.

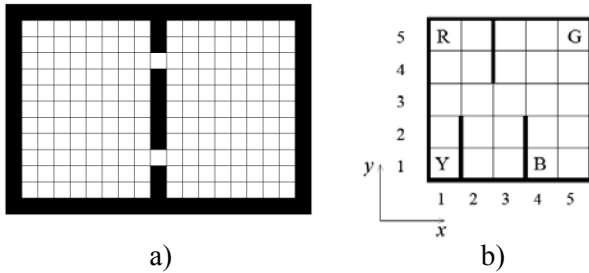


Figure 1 a) two-room grid world domain b) Taxi driver domain.

Taxi driver world, shown in figure 1.b, consists of a 5x5 grid with 4 special cells (RGBY). A passenger should be picked up from a cell and then dropped off in a destination cell, where the pickup and drop off nodes are two randomly chosen cells from the set of RGYB nodes. The corresponding graph of state transition graph consists of two identical grids (one for the case that the taxi is searching for the passenger and one for the case when the taxi has picked up a passenger and is looking for the drop off location) that are connected through a pair of nodes belonging to the set of RGBY nodes (the nodes where a change of state is possible). In each episode, the location of the taxi is chosen randomly. The taxi must pick up the passenger and deliver him, using the primitive actions up, down, left, right, Pickup, Putdown. For each iteration, a sequence of 300 episodes was considered. The taxi receives a reward of +20 for successfully delivering the passenger, -10 for attempting to pickup or drop off the passenger at incorrect locations and -1 for other actions. The other parameters were set same as in the two-room grid problem.

B. Results

Fig 2.a and 2.b show the result of the node CGS centrality scoring of the corresponding graphs of the

mentioned benchmark problems. The lighter color of cells corresponds to the higher centrality scores. As it was expected the nodes around main subgoals, e.g. neighbors of hallway doors in the two-room grid world, have also high centrality scores.

The next step is the elimination of the redundant subgoals which can be done by thresholding or, as it is proposed, by clustering. By varying the threshold, different numbers of nodes are extracted as subgoals. For example, in the grid world, when the threshold is set to 0.3, there are 22 candidate subgoals extracted as it is marked in figure 2.a by either ‘C’ or ‘F’ symbols. In the taxi world, the candidate subgoals, extracted when the threshold was set to 0.4, are presented in figure 2.b. It can be seen from figure 2.a and 2.b that most of founded candidate subgoals are neighboring states, since they lie on the same paths with the doorways and therefore centrality scores of these nodes are rather high. Thus, the thresholding step will detect these states as candidate subgoals. If we considered these redundant subgoals for creating skills we may create some complexity and additional penalties to an agent while obtaining no benefits. Actually, if we set the threshold to $t=0.95$ we would just extract the doorways which are the most effective subgoals in the grid world. No such threshold can be found that lead to extraction of only principal subgoals in the taxi world, since the cells (2, 3) and (4, 3) have higher centrality values comparing to the RGBY cells.

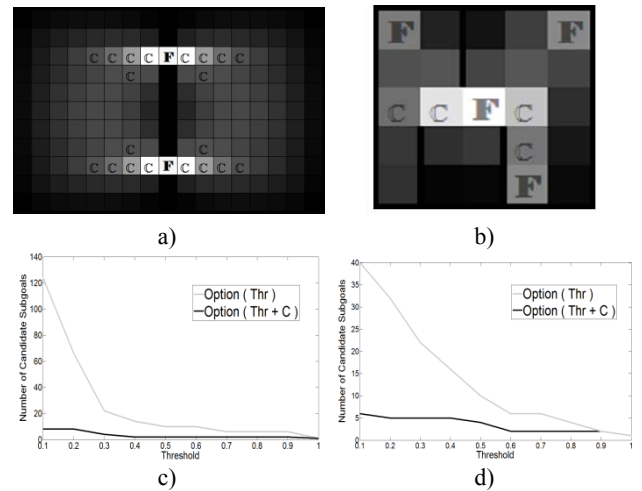


Figure 2 The assigned node CGS score to the (a) two-room grid and (b) taxi driver domain. The number of identified subgoals resulted from thresholding and applying the clustering approach as the function of the threshold values (c) two-room grid and (d) taxi driver domain. Further descriptions are given in the text.

The final subgoals can be identified using our proposed clustering approach. In the figures 2.a and 2.b final subgoals are specified with symbol ‘F’ in the corresponding cells. It can be seen that the proposed step is able to identify the final subgoals precisely. Figure 2.c and 3.d compares the number of identified subgoals using thresholding and the proposed approaches when the threshold value slides from zero,

i.e. extract all nodes, to one, i.e. extract no node. It can be seen that our method has effectively reduced the sensitivity of appropriate threshold selection.

After identifying useful subgoals, skills are developed according to each found set of nodes based on the option framework. Here, we compare the result of subgoal identification based on thresholding and on clustering approaches. For this purpose, we repeat the experiments for the case that the agent extracts the subgoals by thresholding or by applying the proposed clustering approach on the candidate subgoals. Figure 4 shows the average obtained reward in a two room grid world when the threshold was set to 0.3. In this figure, the gained reward as the function of episodes is shown for three different configurations, namely, (a) 'without option' where the agent uses standard RL, i.e. just trained based on primitive actions, (b) 'thresholded option' where the agent extracts the subgoals based on thresholding of the candidate subgoals and then selects two subgoals among them randomly, and (c) 'clustered thresholded options' where the agent extracts the final subgoals by the proposed approach. In this experiment the agent was able to gain higher than 95% of the maximum average reward after only 8 episodes when the subgoals were extracted using the proposed approach while this point is reached by 'thresholded option' and 'without skill' approaches after 18 and 84 episodes respectively. It is worth mentioning that if the agent does not develop skills it will gain more reward in average in the very first episodes because in these episodes the policies of the skills are not optimized yet and this will lead to a large amount of penalty. We report the same qualitative trend in taxi world task.

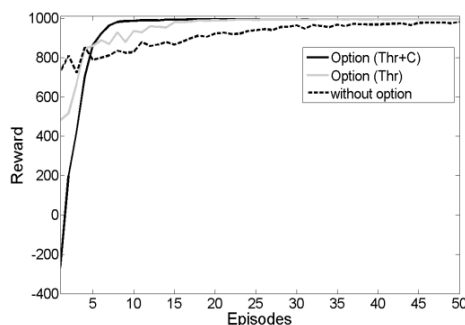


Figure 4 Average reward obtained in a two-room grid world when the agent use standard RL, i.e. without options, use options extracted from thresholding, i.e. Option (Thr), and options extracted from thresholding consequenced by clustering approaches, i.e. Option (Thr+C).

IV. CONCLUSION

In this paper, a novel graph theoretic based subgoal discovery method is presented. The main contribution of the method is to utilize complex network theory measures for improving the subgoal identification process in the option framework. In particular, the CGS centrality was defined and applied for candidate

subgoal ranking and extraction. Then, co-betweenness measure of the extracted candidates were used to create a weighted graph of candidates where a low cost clustering algorithm can be used to extract principal subgoals as the cluster centers. Our method results in identifying useful subgoals to improve the agents learning performance to reach the main goal.

ACKNOWLEDGMENT

This work has been supported by Swiss NSF through Grant No 200021-112081/1.

REFERENCES

- [1] Sutton, R., and Barto, A., "Reinforcement Learning: An Introduction". MIT Press, Cambridge, 1998.
- [2] Khadivi, A. and Hasler, M., "A Weighting Scheme for Enhancing Community Detection in Networks," Accepted in ICC 2010.
- [3] Sutton, R., and Precup, D., "Between MDPs and Semi-MDPs A Framework for Temporal Abstraction in Reinforcement Learning". Artificial Intelligence, Vol. 112, pp.181-211, 1999.
- [4] Barto, A., and Mahadevan, S., "Recent advances in hierarchical reinforcement learning", Discrete Event Systems Journal, 13, pp. 41-77, 2003.
- [5] Digney, B., "Learning hierarchical control structure for multiple tasks and changing environments", Proceedings of the Fifth Conference on the Simulation of Adaptive Behavior, 1998.
- [6] McGovern, A., & Barto, A. G. (2001). Automatic discovery of subgoals in reinforcement learning using diverse density. Proceedings of the 18th International Conference on Machine Learning (pp. 361-368). Morgan Kaufmann.
- [7] Goel, S., and Huber, M., "Subgoal discovery for hierarchical reinforcement learning using learned policies", In Proceedings of the 16th International FLAIRS Conference, pp. 346-350, 2003.
- [8] Asadi, M., and Huber, M. "Reinforcement learning acceleration through autonomous subgoal discovery", In Proceedings of the International Conf. on Machine Learning, Models, Technologies and Applications, pp. 69-74, 2005.
- [9] Menache, I., Mannor, S., and Shimkin, N., "Q-Cut -Dynamic discovery of sub-goals in reinforcement learning", Proceedings of the 13th European Conference on Machine Learning, pp. 295-306, 2002.
- [10] Mannor, S., Menache, I., Hoze, A., Klein, and U., "Dynamic abstraction in reinforcement learning via clustering", Proceedings of the Twenty-First International Conference on Machine Learning, pp. 560-567, 2004.
- [11] Şimşek, Ö. and Barto, A., "Identifying useful subgoals in reinforcement learning by local graph partitioning", Proceedings of the 22nd International Conference on Machine Learning (ICML), 2004.
- [12] Shen, J., Gu, G., and Liu, H., "Automatic option generation in hierarchical reinforcement learning via immune clustering", Systems and Control in Aerospace and Astronautics, pp.500-504, 2006.
- [13] Şimşek, Ö. and Barto, A., "Skill characterization based on betweenness", Advances in Neural Information Processing Systems (NIPS), pp.1497-1504, 2009.
- [14] Ajdari Rad, A., Moradi, P. and Hasler, M., "Automatic Skill Acquisition in Reinforcement Learning using Connection Graph Stability Centrality", accepted in ISCAS 2010.
- [15] Brandes, U., "A Faster Algorithm for Betweenness Centrality", Journal of Mathematical Sociology, vol. 25, issue 2, pp.163-177, 2001.
- [16] Belykh, V., Belykh, I., and Hasler, M., "Connection graph stability method for synchronized coupled chaotic systems", Physica D, vol.195/1-2, pp. 159-187, 2004.
- [17] Kolaczyk, E. D., D. B. Chua, et al. (2007). "Co-Betweenness: A Pairwise Notion of Centrality." CoRR abs/0709.3420.

Prediction of Time-Series Data using PSpice and Runge-Kutta Method

Kazuhisa YOSHIMATSU, Toru TANAKA
and Masayuki YAMAUCHI

Dept. of Electronics and Computer Eng.,
Hiroshima Institute of Technology,
2-1-1, Miyake, Saeki-ku, Hiroshima 731-5193, JAPAN.
Email: yoshimatsu.k@gmail.com

Yoshifumi NISHIO

Dept. of Electrical and Electronic Eng.,
Tokushima University,
2-1, Minami-Jyosanjiima, Tokushima, JAPAN.

Abstract—Prediction of time-series data in natural world are very important. For example, if nonlinear time-series data are predictable, we can take adequate action for problem of weather. In this study, we propose two prediction methods for time-series data using coupled oscillators system. We predict chaos time-series data like the natural phenomena by these methods. The chaos time-series data are made by the Chua's circuit. The prediction results of time-series data are compared with two our methods. We show possibility of predictable by actual circuit.

I. INTRODUCTION

Predictions of the time-series data of natural world are very important for human, and a lot of researches are carried out up to now[1][2]. A lot of things of the natural world such as the atom, neurons, and planets are oscillating. These are connected by each other, and operate as a system. Therefore, time-series data of a lot of natural things are oscillatory solutions. Coupled oscillators system can make complex phenomena[3][4].

The time-series data is generally predicted with statistics, a state space model, a Karman filter and so on. We think that the oscillatory solution should be used for the prediction.

In our previous study, we proposed a method using Runge-Kutta method and normalized equations of lattice oscillator[5]. However, the prediction was used numerical equations without features of the OP-Amps. Further, an input signal source was optimized for normalization of circuit equations. Therefore, to make an actual circuit of this prediction system is hard.

In this study, the lattice oscillators constructed by van der Pol oscillators are simulated using Runge-Kutta method and PSpice, and predict the time-series data of the Chua's circuit. Simulations by PSpice include features of OP-Amp, and include the input signal source that is constructed by only a voltage source. Additionally, values of all elements is used realistic values.

The prediction results of time-series data using PSpice are compared from the prediction results using Runge-Kutta method.

We show possibility of predictable by the actual circuit of our method by using PSpice.

II. PREDICTION USING RUNGE-KUTTA METHOD

A. Circuit model for Runge-Kutta method

In this study, 9 van der Pol oscillators are coupled as a lattice by inductors(see Figs. 1(a) and 1(b)), and we predict time-series data by this circuit. In this method, an arbitrary signal $f(t)$, that is synthesized and predicted, is presented as a current of an inductor L_{out2} , because circuit equations should be normalized and simplified(see Fig. 1). Therefore, an input part is substituted the inductor L_{out2} and an arbitrary voltage signal source. An output signal $h(t)$ of the voltage signal source is shown as follows:

$$h(t) = \frac{1}{L_{out2}} \int f(t) dt. \quad (1)$$

In this method, we can predict in ideal condition because the measurement instrument and input power source are considered. Each oscillator are called $OSC(k, l)$. In our method, future time-series data are predicted from past time-series data by a circuit which is like a filter. Therefore, to input past time-series data from outside is needed. The time-series data is input to each oscillator through each outside inductor L_{out} . Each oscillator includes a negative resistance, an inductor L , and a capacitor C . Prediction results are gotten as time-series data of a voltage of $OSC(k, l)$. We want to analyze this circuit by using Runge-Kutta method. Therefore, normalized equations of this circuit should be used. The parameters of this circuit are set as Figs. 1(a) and 1(b). The all oscillators are used same parameters, and the all coupling inductors are used same inductance. All inductors L_{out2} for inputting time-series data are used one value. The voltage of each oscillator is called $v_{(k, l)}$. Moreover, the electric current that flows to the inductor of each oscillator is named $i_{(k, l)}$. An arbitrary time-series data are input from an inductor L_{out2} and voltage signal source. We control the voltage signal source to be a current of L_{out2} is the arbitrary time-series data synthesis and prediction time-series data are output as the current $i_{(1, 1)}$ of $OSC(1, 1)$. The nonlinear resistance of each oscillator is approximated as follows.

$$f(v_{(k, l)}) = -g_1 v_{(k, l)} + g_3 v_{(k, l)}^3. \quad (2)$$

The circuit equation is normalized by the following equations.

$$t = \sqrt{LC}\tau, \quad i_{(k,l)} = \sqrt{\frac{Cg_1}{3Lg_3}}x_{(k,l)}, \quad v_{(k,l)} = \sqrt{\frac{g_1}{3g_3}}y_{(k,l)}, \quad (3)$$

$$\alpha_{(k,l)-(m,n)} = \frac{L}{L_{(k,l)-(m,n)}}, \quad \varepsilon_{(k,l)} = g_1 \sqrt{\frac{L}{C}}.$$

[corner]

$$\begin{aligned} \frac{dx_{(k_0,l_0)}}{d\tau} &= y_{(k_0,l_0)}, \\ \frac{dy_{(k_0,l_0)}}{d\tau} &= -x_{(k_0,l_0)} + \alpha_{(k_1,l_1)-(k_2,l_2)}(x_{(k_3,l_3)} - x_{(k_0,l_0)}) \\ &\quad + \alpha_{(k_4,l_4)-(k_5,l_5)}(x_{(k_6,l_6)} - x_{(k_0,l_0)}) + \alpha_{out(k_0,l_0)}(x_s - x_{(k_0,l_0)}) \\ &\quad + \varepsilon_{(k_0,l_0)}(y_{(k_0,l_0)} - \frac{1}{3}y_{(k_0,l_0)}^3). \end{aligned} \quad (4)$$

$$(k_0, l_0, k_1, l_1, k_2, l_2, k_3, l_3, k_4, l_4, k_5, l_5, k_6, l_6) =$$

$$\begin{cases} \text{top-left} : (0, 0, 0, 0, 0, 1, 0, 1, 0, 0, 1, 0, 1, 0), \\ \text{top-right} : (0, 2, 0, 1, 0, 2, 0, 1, 0, 2, 1, 2, 1, 2), \\ \text{bottom-left} : (2, 0, 2, 0, 2, 1, 2, 1, 1, 0, 2, 0, 1, 0), \\ \text{bottom-right} : (2, 2, 2, 1, 2, 2, 2, 1, 1, 2, 2, 2, 1, 2). \end{cases}$$

[center($k = 1$ and $l = 1$)]

$$\begin{aligned} \frac{dx_{(1,1)}}{d\tau} &= y_{(1,1)}, \\ \frac{dy_{(1,1)}}{d\tau} &= -x_{(1,1)} + \alpha_{(1,0)-(1,1)}(x_{(1,0)} - x_{(1,1)}) \\ &\quad + \alpha_{(1,1)-(1,2)}(x_{(1,2)} - x_{(1,1)}) + \alpha_{(0,1)-(1,1)}(x_{(0,1)} - x_{(1,1)}) \\ &\quad + \alpha_{(1,1)-(2,1)}(x_{(2,1)} - x_{(1,1)}) \\ &\quad + \varepsilon_{(1,1)}(y_{(1,1)} - \frac{1}{3}y_{(1,1)}^3). \end{aligned} \quad (5)$$

[side]

$$\begin{aligned} \frac{dx_{(k_0,l_0)}}{d\tau} &= y_{(k_0,l_0)}, \\ \frac{dy_{(k_0,l_0)}}{d\tau} &= -x_{(k_0,l_0)} + \alpha_{(k_1,l_1)-(k_2,l_2)}(x_{(k_3,l_3)} - x_{(k_0,l_0)}) \\ &\quad + \alpha_{(k_4,l_4)-(k_5,l_5)}(x_{(k_6,l_6)} - x_{(k_0,l_0)}) \\ &\quad + \alpha_{(k_7,l_7)-(k_8,l_8)}(x_{(k_9,l_9)} - x_{(k_0,l_0)}) + \alpha_{out(k_0,l_0)}(x_s - x_{(k_0,l_0)}) \\ &\quad + \varepsilon_{(k_0,l_0)}(y_{(k_0,l_0)} - \frac{1}{3}y_{(k_0,l_0)}^3). \end{aligned} \quad (6)$$

$$(k_0, l_0, k_1, l_1, k_2, l_2, k_3, l_3, k_4, l_4, k_5, l_5, k_6, l_6, k_7, l_7, k_8, l_8, k_9, l_9) =$$

$$\begin{cases} \text{top} : (0, 1, 0, 0, 0, 1, 0, 0, 0, 1, 0, 2, 0, 2, 0, 1, 1, 1, 1, 1), \\ \text{left} : (1, 0, 1, 0, 1, 1, 1, 1, 0, 0, 1, 0, 0, 0, 1, 0, 2, 0, 2, 0), \\ \text{right} : (1, 2, 1, 1, 1, 2, 1, 1, 0, 2, 1, 2, 0, 2, 1, 2, 2, 2, 2, 2), \\ \text{bottom} : (2, 1, 2, 0, 2, 1, 2, 0, 2, 1, 2, 2, 2, 2, 1, 2, 2, 2, 1, 2). \end{cases}$$

Each nonlinearity and coupling parameter must be adjusted individually, because we synthesize and predict time-series data by these circuit equations. Therefore, each ε and α are renamed as $\varepsilon_{(k,l)}$ and $\alpha_{(k,l)-(m,n)}$.

B. Prediction method using Runge-Kutta method

We use a time-series data of Chua's circuit as an original time-series data. Parameters of Chua's circuit on pp.24 of [6] are used. The original time-series data is assumed as $f(t)$. A prediction of the original time-series data is assumed as $g(t)$.

The original time-series data of continuous data are divided

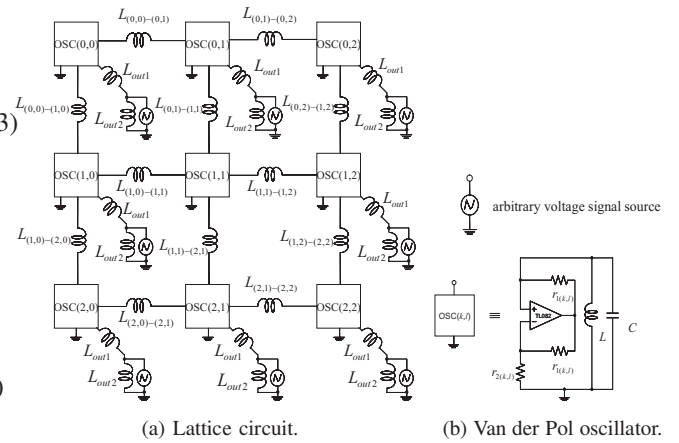


Fig. 1. Circuit model for Runge-Kutta method.

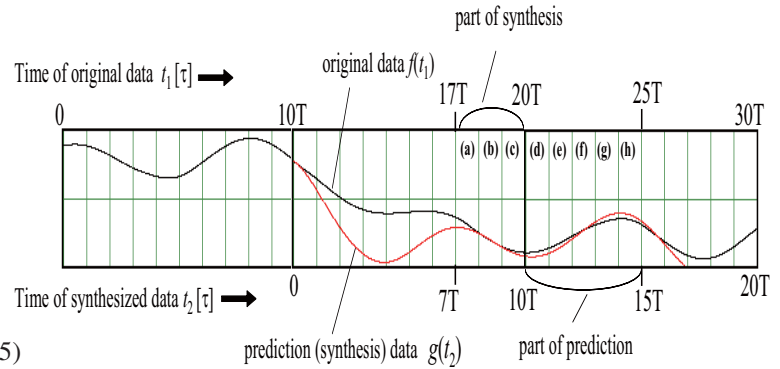


Fig. 2. Relation between synthesis time-series data and original time-series data (Runge-Kutta method).

by time period of arbitrary length T , and are predicted. Our system is predicted future time-series data from past time-series data. The details of procedure of our method are shown as follows, and an example of synthesis and prediction are shown in Fig. 2.

- 1) The original data from $f(0)$ to $f(10T)$ is added to our system, and data from $g(0)$ to $g(10T)$ is synthesized at the same time. The original data are shown in Fig. 2. The synthesis data are shown in Fig. 2. In the Fig. 2, time axis of synthesis data differs from time axis of original data.
- 2) The synthesized data $g(t): (7T \leq t \leq 10T)$ are adjusted to values close to $f(t): (17T \leq t \leq 20T)$ by changing each parameter and eighteen initial values of oscillators. Each initial value is set plus $f(10T)$ or minus $f(10T)$ independently.
- 3) The original time-series data from $f(10T)$ to $f(20T)$ is added to the adjusted system, and time-series data from $g(10T)$ to $g(20T)$ is synthesized at the same time. The synthesis data $g(t): (10T < t \leq 20T)$ are considered as prediction data.
- 4) A prediction period is fixed from $10T$ to $15T$ because to predict for long time is difficult.

If the time-series data $g(t): (10T < t \leq 15T)$ is close to $f(t): (20T < t \leq 25T)$, we can consider that $g(t): (10T < t \leq 15T)$ predicts the original time-series data (see Fig. 2). We

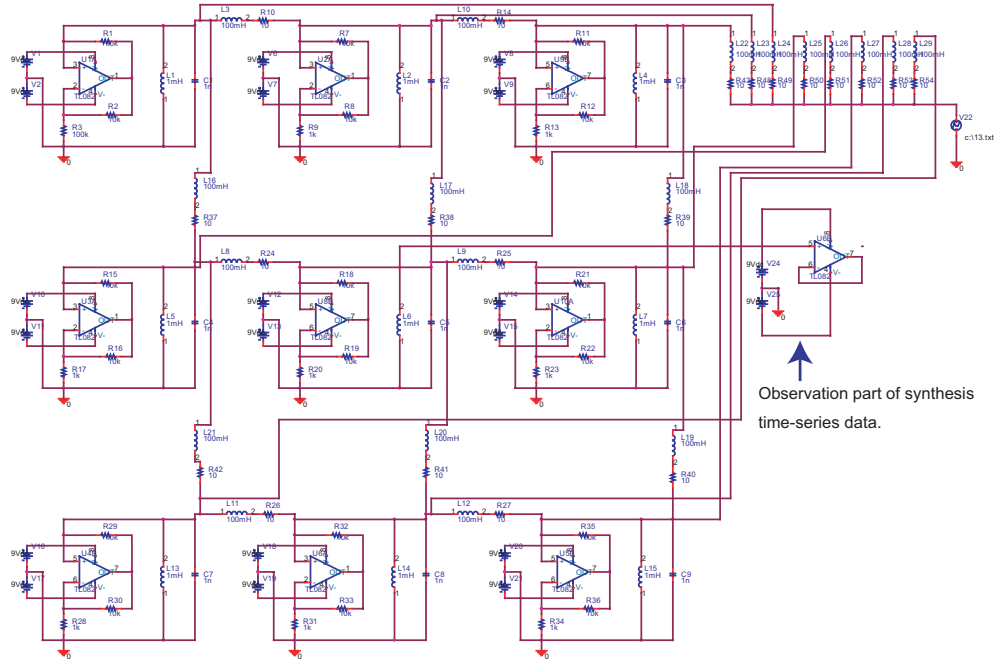


Fig. 3. Circuit model for PSpice(OP-Amp:TL082).

predict long time data repeating this method.

III. PREDICTION USING PSpICE

In this section, we predict the same time-series data by PSpice.

A. Circuit model for PSpice

The prediction circuit for PSpice is shown in Fig.3. This circuit and above circuit are same circuit basically. However, in this circuit, we conscious an actual circuit. This circuit includes registers of coupling inductors. Original time-series data are input from an arbitrary voltage signal source. Synthesis and prediction time-series data are output as the voltage $v_{(1,1)}$ of OSC(1,1). The capacitances are used from 1500nF to 1nF. The resistances are used from 10Meg Ω to 10 Ω . The inductances are used from 150mH to 0.1 μ H.

B. Prediction method using PSpice

We basically predict time-series data by same method, which is shown in above section. The details of procedure of our method are shown as follows, and an example of synthesis and prediction are shown in Fig.4.

- 1) The original data from $f(0)$ to $f(2T)$ (α) is added to our system, and data from $g(0)$ to $g(2T)$ (β) is synthesized at the same time(see Fig.4).
- 2) The synthesized data $g(t) : (T \leq t \leq 2T)$ are adjusted to values close to $f(t) : (7T \leq t \leq 8T)$ by changing many parameters and many initial values of oscillators. We adjust all parameters as like full solution search. However, when the synthesis data is very close to original data, we stop to adjust the parameters. Therefore, we can think a probability of global minimum, which our

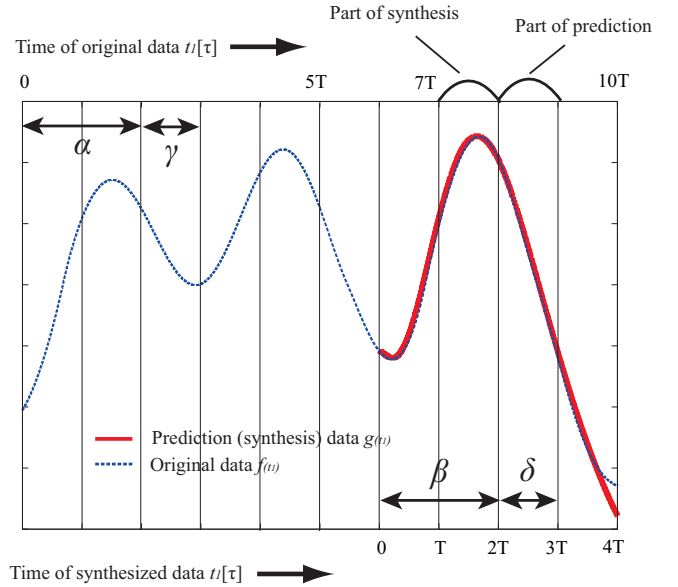


Fig. 4. Relation between synthesis time-series data and original time-series data (PSpice).

results is, is low. Each initial values is set plus $f(6T)$, minus $f(6T)$ or 0, independently.

- 3) The original time-series data from $f(t) : (2T < t \leq 3T)$ (γ) is added to the adjusted system, and time-series data from $g(t) : (2T < t \leq 3T)$ (δ) is synthesized at the same time. The synthesis data $g(t) : (2T < t \leq 3T)$ are considered as prediction data.
- 4) A prediction period is fixed from $2T$ to $3T$ because to predict for long time is difficult.

If the time-series data $g(t) : (2T < t \leq 3T)$ is close to $f(t) : (8T < t \leq 9T)$, we can consider that $g(t) : (2T < t \leq 3T)$ predicts the original time-series data (see Fig.4). We predict

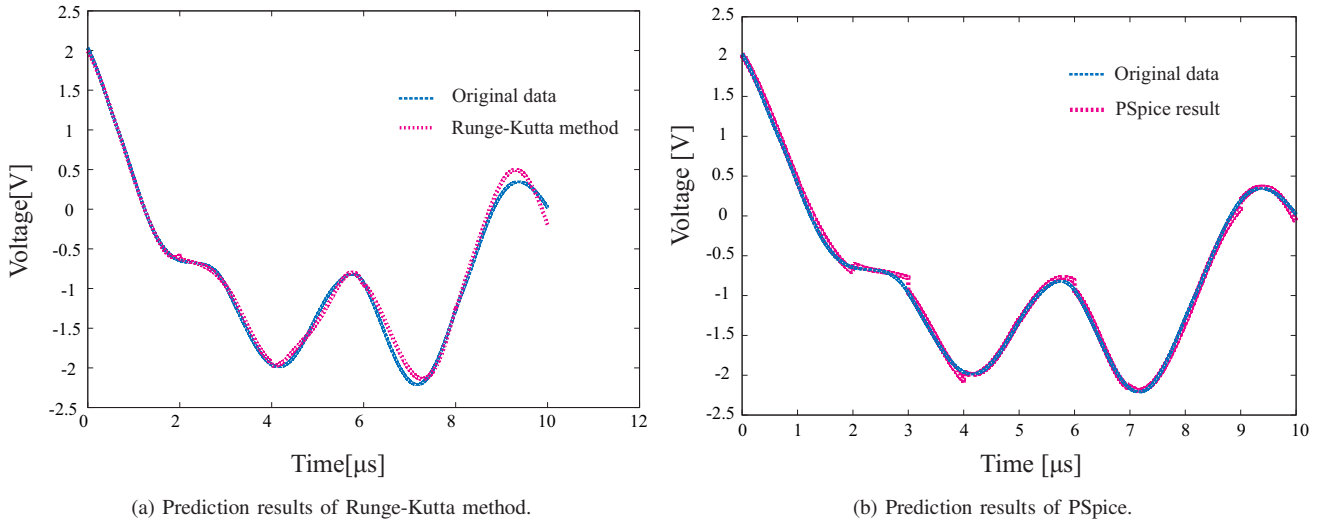


Fig. 5. Prediction results

TABLE I

COMPARISON OF MEAN ABSOLUTE ERRORS AND ERROR RATES.

		0-T	T-2T	2T-3T	3T-4T	4T-5T	5T-6T	6T-7T	7T-8T	8T-9T	9T-10T
Runge-Kutta	Mean absolute errors	0.010766	0.005188	0.009479	0.049336	0.024742	0.043291	0.131468	0.017386	0.084017	0.054813
	Error rate[%]	0.5409	0.8552	0.9861	2.5543	1.2519	3.0564	6.4987	0.8130	6.6471	11.022
PSpice	Mean absolute errors	0.032161	0.037112	0.035688	0.006525	0.001489	0.028941	0.012496	0.006792	0.040905	0.001294
	Error rate[%]	1.5909	5.2871	4.3139	0.2968	0.0749	2.1890	0.5778	0.3102	3.0528	0.3540

long time data repeating this method.

IV. COMPARISON BETWEEN PREDICTION RESULTS OF RUNGE-KUTTA METHOD AND PSpice.

The composite prediction result using Runge-Kutta method and the original data are shown in Fig.5(a). The composite prediction result using PSpice and the original data are shown in Fig.5(b). We can confirm that the result of PSpice is better than the result of Runge-Kutta method. However, the Runge-Kutta method synthesizes during $3T$, and predicts during $5T$. In other hand, PSpice synthesizes during T , and predicts during T . We can think that to obtain good results by using PSpice are easier than to obtain good results by using Runge-Kutta method. However, the adjustment of our method using PSpice is difficult.

The error rates are shown in Table I.

The mean error rate is calculated as follows:

$$\text{The error rate} = \frac{\text{Mean absolute errors}}{\text{Maximum amplitude}} \times 100 \text{ [\%]} \quad (7)$$

The result of PSpice is better than the result of Runge-Kutta method in 7 domains of 10 domains. The mean error rates of PSpice results are large in the domain where change is sharp. Because the adjustment of our method using PSpice is difficult. In the Runge-Kutta method, a mean error rate between the prediction time-series data and the original time-series data is 3.42%. In PSpice, a mean error rate is 1.80%.

V. CONCLUSION

In this study, the lattice oscillator constructed by van der Pol oscillators was simulated using Runge-Kutta method and PSpice, and we predicted the time-series data of the Chua's circuit using the lattice oscillator. Moreover, the prediction

results of time-series data using PSpice were compared with results using Runge-Kutta method. The mean error rates in our methods using Runge-Kutta method and using PSpice were 3.42% and 1.80%, respectively. Therefore, we can say that we were able to predict well. In other words, we can think that possibility of predictable by the actual circuit of our method is shown. However, synthesis using Runge-Kutta method was easier than synthesis using PSpice, because the changed parameter is few, and the time efficiency is good. The mean error rate in our system using Runge-Kutta method enough is small. Therefore, we can think that prediction efficiency is good when the Runge-Kutta method is used.

VI. ACKNOWLEDGEMENTS

This research is supported by the Grants-in-Aid for Young Scientific Research (B) (No. 19760270) from the Japan Society for the Promotion of Science.

REFERENCES

- [1] Sapankevych, N and Sankar, R, "Time Series Prediction Using Support Vector Machines: A Survey," *IEEE COMPUTATIONAL INTELLIGENCE MAGAZINE*, May 2009.
- [2] T. Matsumoto, Y. Nakajima, M. Saito, J. Sugi and H. Hamagishi, "Reconstructions and Predictions of Nonlinear Dynamical Systems: A Hierarchical Bayesian Approach," *IEEE TRANSACTIONS ON SIGNAL PROCESSING*, vol. 49, no. 9, Sept. 2001.
- [3] L. L. Bonilla, C. J. Pérez Vicente and R. Spigler, "Time-Periodic Phases in Populations of Nonlinearly Coupled Oscillators with Bimodal Frequency Distributions," *Physica D: Nonlinear Phenomena* vol. 113, issues 1, pp. 79–97, Feb. 1998.
- [4] M. Yamauchi, M. Okuda, Y. Nishio and A. Ushida, "Analysis of Phase-Inversion Waves in Coupled Oscillators Synchronizing at In-and-Anti-Phase," *IEICE Trans. Fundamentals*, vol.E86-A, no.7, pp.1799-1806, July 2003.
- [5] T.Imoto, S.Yamane and M.yamauchi "Prediction of Chaos Time-series Data using Coupled Oscillators System," *Proc. of SSJW'08*, pp.32-35, 2008.
- [6] K. Aihara, *Chaos*, Saiensu-sha Co., Ltd. Publishers, 1990(in Japanese).

Circuit Implementation of an A/D Converter Based on the Scale-Adjusted β -Map Using a Discrete-Time Integrator

Yoshihiko Horio^{*}, Kenya Jin'no[†], Tohru Kohda[‡], and Kazuyuki Aihara[§]

^{*} Dept. of Electrical & Electronic Eng., Tokyo Denki University,
Tokyo, 101-8457, Japan, Email: horio@eee.dendai.ac.jp

[†] Dept. of Electrical & Electronics Eng., Nippon Institute of Technology,
Saitama, 345-8501, Japan, Email: jinno@ieee.org

[‡] Dept. of Computer Science & Communication Eng., Kyushu University,
Fukuoka, 819-0395, Japan, Email: kohda@csce.kyushu-u.ac.jp

[§] Institute of Industrial Science, Tokyo University,
Tokyo, 153-8505, Japan, Email: aihara@sat.t.u-tokyo.ac.jp

Abstract—We propose a circuit technique to implement an A/D converter based on a scale-adjusted β -map utilizing a discrete-time integrator, which is a basic and preferred circuit element in integrated circuits. We, then, propose switched-capacitor (SC) scale-adjusted β A/D converter circuits in order to verify the proposed technique. In addition, we confirm the proposed circuits through SPICE simulations with ideal circuit elements. Moreover, we apply the proposed circuits to a chaos generator, which is robust against non-idealities of the circuit elements and noise.

I. INTRODUCTION

A data conversion method based on a β -map (β -converter) was proposed [1]. The β -converter is more stable than the pulse code modulation (PCM) type converters in a sense that the PCM-type converters suffer from deviations of the threshold value of the quantizer, mismatches of the gain of the internal amplifier, and circuit noise. In the worst case, the PCM converters will diverge. In contrast, $\sum \Delta$ -type converters are stable; however, usually its input signal should be oversampled in order to obtain reasonable accuracy. The β -converter is robust against device and parameter mismatches in the circuit like $\sum \Delta$ -type converters; at the same time, the β -converter has almost optimal rate distortion property like PCM-type converters.

Recently, in order to further improve the performance of the β -converter, interval analyses were used to propose a decoding algorithm and a guideline for the circuit design parameters, which minimize the decoding errors [2]–[4]. In addition, a data-conversion method based on a scale-adjusted β -map (scale-adjusted β -converter) was proposed where the gain of the internal amplifier and the tolerance of the quantizer threshold can be independently

determined, which alleviates restrictions on the circuit design [2]–[4]. The scale-adjusted β -converter includes the original β -converter as its special case.

Block diagrams for circuit implementation of the β - and scale-adjusted β -converters (analog-to-digital (A/D) converters) were given in Refs. [1] and [4], respectively. However, the proposed schematic diagrams are not suitable for actual circuits, in particular, for integrated circuit implementation of these A/D converters.

In this paper, we propose a circuit technique to realize the scale-adjusted β A/D converter utilizing a discrete-time integrator, which is a basic and preferred circuit element in integrated circuits, as a core element. We, furthermore, propose switched-capacitor (SC) scale-adjusted β A/D converter circuits in order to verify the proposed technique. In addition, we show the validity of the SC scale-adjusted β A/D converter circuits through SPICE simulations with ideal circuit elements.

Because the β -map and the scale-adjusted β -map are eventually locally onto, trajectories from all initial conditions (the inputs for the converters in this case) will be confined within a finite interval. Therefore, the proposed A/D converter circuits can be used as a chaos generator, which is robust against deviations and mismatches of circuit parameters, by only altering the clock waveforms of the A/D converter circuits. Moreover, different chaotic dynamics can be easily obtained by altering the circuit parameters. Another advantage of the circuit is that we can easily determine the initial condition by the input of the circuit. A SPICE simulation result for the proposed chaos generators is also shown.

II. DATA CONVERTER BASED ON THE SCALE-ADJUSTED β -MAP

The scale-adjusted β -map $S(\cdot)$ [2]-[4] is given by

$$S(x) = \begin{cases} \beta x, & x \in [0, \gamma\nu), \\ \beta x - s(\beta - 1), & x \in [\gamma\nu, s), \end{cases} \quad (1)$$

where $\nu \in [s(\beta - 1), s)$ is a threshold parameter, $1 < \beta < 2$ is a radix of the conversion, $\gamma = 1/\beta$, and $s > 0$ is a scaling parameter. When $s = (\beta - 1)^{-1}$, the scale-adjusted β -map is equivalent to the β -map $C(\cdot)$ [1] given by

$$C(x) = \begin{cases} \beta x, & x < \gamma\nu, \\ \beta x - 1, & x \geq \gamma\nu. \end{cases} \quad (2)$$

By introducing a discrete-time t_n (n is an integer), eq. (1) can be written as a one-dimensional discrete-time dynamical system as

$$\begin{aligned} x(t_{n+1}) &= S(x(t_n)) \\ &= \begin{cases} \beta x(t_n), & x(t_n) \in [0, \gamma\nu), \\ \beta x(t_n) - s(\beta - 1), & x(t_n) \in [\gamma\nu, s). \end{cases} \end{aligned} \quad (3)$$

Moreover, we define a binary variable $b(t_n) \in \{0, 1\}$ as

$$b(t_n) = Q_\theta(x(t_n)) = \begin{cases} 0, & x(t_n) \in [0, \theta), \\ 1, & x(t_n) \in [\theta, s), \end{cases} \quad (4)$$

where $Q_\theta(\cdot)$ is a quantizer with its threshold of $\theta = \gamma\nu$. As a result, eq. (3) can be rewritten as

$$x(t_{n+1}) = \beta x(t_n) - b(t_n)s(\beta - 1). \quad (5)$$

Now, we sample an analog input signal x_{input} at $t = t_1$. That is,

$$x(t_1) = x_{input}. \quad (6)$$

Then, by iterating eq. (5) from $t = t_1$ to $t = t_L$ (L is a bit-length), we obtain a binary output sequence $BS(x_{input})$ which corresponds to the analog input x_{input} as

$$BS(x_{input}) = (b_L b_{L-1} \cdots b_1)_{\beta, s}, \quad (7)$$

where $b_n = b(t_n)$ ($n = 1, 2, \dots, L$), $b_1 = b(t_1)$ is the LSB, and $b_L = b(t_L)$ is the MSB.

The tolerance σ_ν of the threshold parameter ν is given as [2]-[4]

$$\sigma_\nu = s(2 - \beta). \quad (8)$$

Therefore, the threshold θ of the quantizer $Q_\theta(\cdot)$ can be fluctuated within the tolerance σ_θ given by

$$\sigma_\theta = \gamma\sigma_\nu = \gamma s(2 - \beta) = s(2\gamma - 1). \quad (9)$$

Therefore, a large fluctuation of θ is acceptable in circuit implementation.

On the other hand, the value of β can be estimated from two output bit-sequences by solving the characteristic equation [1], [4]. Therefore, the scale-adjusted β A/D converter is also robust against the deviation of β from its optimal value.

III. IMPLEMENTATION OF THE SCALE-ADJUSTED β A/D CONVERTER WITH A DISCRETE-TIME INTEGRATOR

A block diagram of the A/D converter based on the scale-adjusted β -map was given in Ref. [4]. However, the diagram is not suitable for a practical circuit, in particular, for an integrated circuit.

By the way, a discrete-time integrator is a most common circuit element for the sampled-data analog circuits. The reasons for this would be; 1) Many useful and practical circuit configurations for the discrete-time integrators, which are insensitive to the non-idealities and mismatches of the circuit devices, parasitic devices, and noise, are already available; 2) Circuit techniques for the discrete-time integrators such as switched-capacitor (SC) and switched-current (SI) circuits are readily available and mature with accumulated knowledge through a large number of working examples.

Therefore, we implement the A/D converter based on the scale-adjusted β -map given by eq. (5) with the discrete-time integrator as follows. We first rewrite eq. (5) and eq. (4) using the z -transformation as

$$X(z) = \beta X(z)z^{-1} - B(z)z^{-1}s(\beta - 1), \quad (10)$$

$$B(z) = Q_\theta(X(z)), \quad (11)$$

where $X(z)$ and $B(z)$ are z -domain variables for $x(t_n)$ and $b(t_n)$, respectively. Form the above equations, we finally obtain

$$X(z) = s(1 - \beta) \cdot \frac{z^{-1}}{1 - \beta z^{-1}} \cdot Q_\theta(X(z)). \quad (12)$$

This result shows that we can realize the A/D converter based on the scale-adjusted β -map using a discrete-time backward-Euler damped-integrator with damping factor of β , and the quantizer $Q_\theta(\cdot)$.

IV. SC CIRCUIT IMPLEMENTATION OF THE SCALE-ADJUSTED β A/D CONVERTER

We use a SC circuit technique, as an illustration, to implement the scale-adjusted β A/D converter with a SC integrator. Let us consider a SC integrator circuit shown in Fig. 1. The z -domain transfer function of this circuit

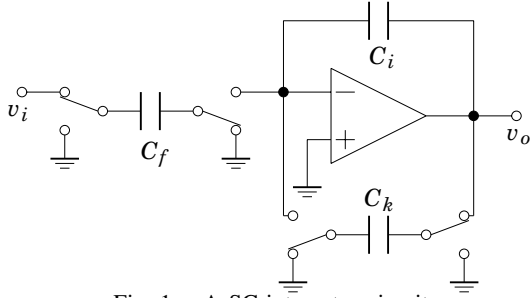


Fig. 1. A SC integrator circuit.

is given by

$$V_o(z) = \frac{C_f}{C_i} \cdot \frac{z^{-1}}{1 - \left(1 + \frac{C_k}{C_i}\right) z^{-1}} \cdot V_i(z), \quad (13)$$

where $V_o(z)$ and $V_i(z)$ are z -domain variables for v_o and v_i in Fig. 1, respectively. By comparing eq. (12) and eq. (13), we see that we can implement eq. (12) with the SC integrator in Fig. 1 by setting

$$\begin{aligned} V_o(z) &= X(z), & V_i(z) &= Q_\theta(X(z)), \\ \frac{C_f}{C_i} &= s(1 - \beta), & \frac{C_k}{C_i} &= \beta - 1. \end{aligned} \quad (14)$$

However, $1 < \beta < 2$ implies $-1 < 1 - \beta < 0$. Therefore, C_f/C_i should be negative, which is impossible with real capacitors. Therefore, we introduce a negative quantizer $\widetilde{Q}_\theta(\cdot)$ as

$$\widetilde{Q}_\theta(\cdot) \equiv -Q_\theta(\cdot) \quad (15)$$

Then, we can modify the assignments in eq. (14) as

$$\begin{aligned} V_o(z) &= X(z), & V_i(z) &= \widetilde{Q}_\theta(X(z)), \\ \frac{C_f}{C_i} &= s(\beta - 1), & \frac{C_k}{C_i} &= \beta - 1. \end{aligned} \quad (16)$$

As a result, $C_f/C_i > 0$.

A possible SC circuit for the scale-adjusted β A/D converter is shown in Fig. 2. The clock waveforms that drive the circuit are shown in Fig. 3.

In the above implementation, the capacitor value of C_f depends on both s and β ; therefore, the freedom in the circuit design is restricted. In order to solve this problem, we introduce a quantizer $\widetilde{Q}_\theta^S(\cdot)$ whose binary output level takes 0 and $-s$ instead of 0 and 1 as

$$\widetilde{Q}_\theta^S(\cdot) = -s \times Q_\theta(\cdot) = s \times \widetilde{Q}_\theta(\cdot). \quad (17)$$

By replacing $\widetilde{Q}_\theta(\cdot)$ in Fig. 2 by $\widetilde{Q}_\theta^S(\cdot)$, we can realize the scale-adjusted β A/D converter with the same circuit configuration in Fig. 2 by setting

$$\begin{aligned} V_o(z) &= X(z), & V_i(z) &= \widetilde{Q}_\theta^S(X(z)), \\ \frac{C_f}{C_i} &= \beta - 1, & \frac{C_k}{C_i} &= \beta - 1. \end{aligned} \quad (18)$$

In this implementation, the binary sequence b_n^S obtained from the circuit is

$$-b_n^S = -s \cdot b_n = \widetilde{Q}_\theta^S(x(t_n)). \quad (19)$$

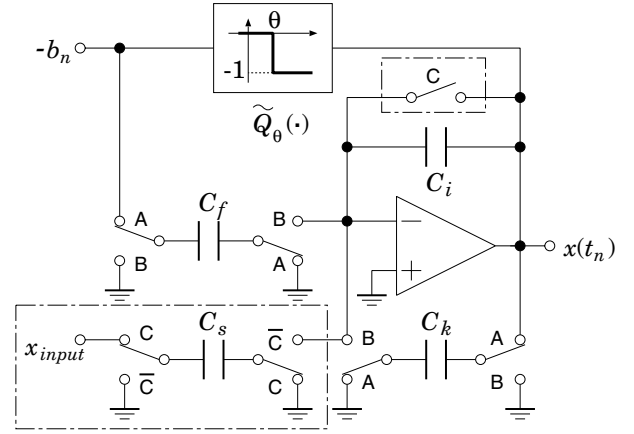


Fig. 2. A possible SC circuit for the scale-adjusted β A/D converter. The circuits inside the chain lines and the clock ϕC can be omitted for a chaos generator when a setting for the initial condition is not needed.

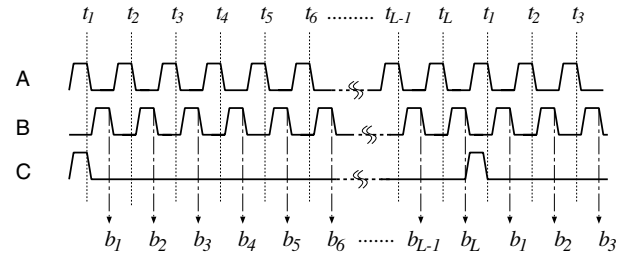


Fig. 3. The clock waveforms driving the circuit in Fig. 2 for the bit-length of L . The sample-timings for the binary sequence b_i are also shown.

V. APPLICATION TO A CHAOS GENERATOR

If we set $L = \infty$, the circuit in Fig. 2 works as a chaos generator with the output chaotic sequence $x(t_n)$. The initial condition of the circuit can be easily set by x_{input} . If the initial condition does not need to be determined, the circuits inside the chain lines in Fig. 2 and the clock ϕC can be omitted.

The trajectory of $x(t_n)$ of the circuit is eventually confined within an invariant interval ranging from $\nu - s(\beta - 1)$ to ν . Therefore, the proposed circuit can stably and robustly generate chaotic attractors even with inevitable circuit non-idealities and noise.

VI. SPICE SIMULATIONS

The SC scale-adjusted β A/D converter circuit in Fig. 2 was simulated by SPICE with ideal devices in order to confirm the circuit implementation. The value of β is usually estimated from the output binary sequences [1]-[4]. However, we assume in the simulations that the value of β is known because the aim of the simulations is to confirm the functionalities of the circuit under ideal conditions. We chose $\beta = 5/3$, $s = 3$ for simulations.

We, first, simply checked the output bit-sequence b_i obtained from the circuit. Table I shows examples of the obtained bit-sequences and those obtained from numerical calculations for $L = 8$. As shown in the table, the proposed circuit correctly converts the input x_{input} to the binary bits.

Second, conversion errors were calculated from the SPICE simulation results. We use $L = 13$ to obtain an equivalent resolution of 2^{-8} . The results are shown in Fig. 4 for different values of the quantizer threshold $\theta = \gamma\nu$ when the input x_{input} was altered. We also derived the conversion errors for different values of input x_{input} when we changed θ as shown in Fig. 5. From these figures, the proposed circuit properly converts the input signal x_{input} regardless of the value of θ . This demonstrates the robustness of the proposed circuit against the deviations of θ .

Finally, we set $L = \infty$ in the proposed circuit to realize a chaotic generator. Figure 6 shows an example of the chaotic attractor obtained from the SPICE simulation with $\theta = 1.44$. As shown in the figure, the chaotic attractor is confined within the interval $(\nu - s(\beta - 1) = 0.4 \leq y(t_n) \leq \nu = 2.4)$.

VII. CONCLUSION

We have proposed the technique to realize the A/D converter based on the scale-adjusted β -map using the discrete-time integrator. The discrete-time integrator is most useful, common, and preferred circuit element in integrated circuits. Therefore, the proposed technique is suitable to integrate the scale-adjusted β A/D converter as an IC form. In addition, we have shown possible SC circuits for the scale-adjusted β A/D converter. The SPICE simulation results with the proposed circuit have confirmed the validity of the proposed technique and the SC circuit implementation. Moreover, we have derived the robust chaotic generator from the SC scale-adjusted β A/D converter circuit. This work was supported in part by ERATO Aihara Complexity Modelling Project, JST, and Kakenhi (20300085).

REFERENCES

- [1] I. Daubechies, R.A. DeVore, C.S. Güntürk, and V.A. Vaishampayan, 'A/D conversion with imperfect quantizers,' IEEE Tans. on Info. Theory, 52, 3, 874–885, 2006.
- [2] S. Hironaka, T. Kohda, and K. Aihara, 'Markov chain of binary sequences generated by A/D conversion using β -encoder,' in Proc. NDES, 261–264, Tokushima, Japan, 2007.
- [3] S. Hironaka, T. Kohda, and K. Aihara, 'Negative β -encoder,' in Proc. NOLTA, 564–567, Budapest, Hungary, 2008.
- [4] T. Kohda, S. Hironaka, and K. Aihara, 'Negative β -encoder,' Preprint, archiv:0808.2548v2[cs.IT], 28 July, 2009. <http://arxiv.org/abs/0808.2548>

TABLE I
OUTPUT BIT-SEQUENCES FROM THE SPICE SIMULATIONS AND NUMERICAL CALCULATIONS WITH $L = 8$.

Input x_{input}	Threshold θ	Output Bits		
		SPICE	Numerical	Error
0.1	1.21	00001000	00001000	0
	1.5	00000110	00000110	0
	1.79	00000101	00000101	0
0.5	1.21	01000100	01000100	0
	1.5	00110101	00110101	0
	1.79	00110100	00110100	0
0.95	1.21	10010100	10010100	0
	1.5	10010100	10010100	0
	1.79	01110101	01110101	0

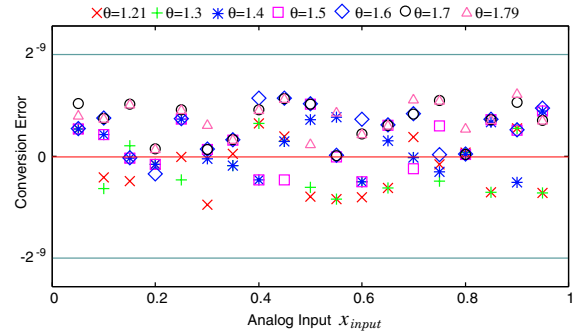


Fig. 4. Conversion errors for different values of θ when x_{input} was swept.

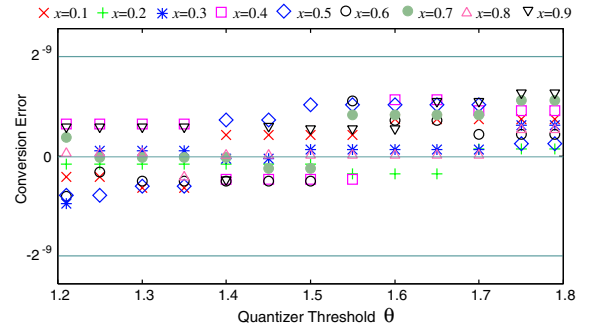


Fig. 5. Conversion errors for different values of x_{input} when θ was swept.

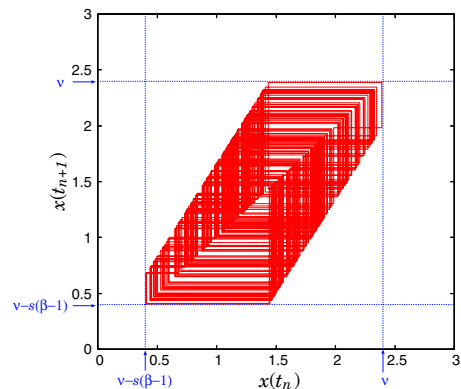


Fig. 6. A chaotic attractor from the circuit in Fig. 2 with $L = \infty$ and $\theta = 1.44$.

Peak Search Algorithm of Frequency Characteristics with Unstable Region

Hiroshige Kataoka

Dept. Electrical and Electronic Eng., Dept. Electrical and Electronic Eng., Dept. Electrical and Electronic Eng.,
Tokushima University, Tokushima University, Tokushima University,
Tokushima 770-8506, JAPAN Tokushima 770-8506, JAPAN Tokushima 770-8506, JAPAN
hiroshige@ee.tokushima-u.ac.jp yamagami@ee.tokushima-u.ac.jp nishio@ee.tokushima-u.ac.jp

Yoshihiro Yamagami

Yoshifumi Nishio

Abstract—For designing PCBs (printed circuit boards), it is very important to find out the locations and the frequencies giving large peak values of the voltages. Electrostatic capacity exists between the wire lines of PCBs. The characteristics of the capacitors depend on the distance between the wire lines. From this reason, we have to analyze circuits including nonlinear capacitors. In that case, the frequency characteristics become distorted, compared with linear circuits. If the distortion becomes large, the characteristics has unstable region. In this article, we propose a SPICE-oriented algorithm to analyze frequency characteristics with unstable region and to find the peaks of the frequency characteristics.

I. INTRODUCTION

In this study, we propose a SPICE-oriented algorithm to analyze frequency characteristics of nonlinear circuits and to find more exact peak voltages of the frequency characteristics. Although they may be found by the standard transient analysis of SPICE, it is difficult to find the exact peaks when the quality factor (Q) is very large. In the SPICE, analysis is every fixed spacing. Because of this, we may pass over them if we choose a large step size. Furthermore, the frequency characteristics of nonlinear circuits often have unstable regions. Such regions cannot be obtained the standard methods using SPICE. In our algorithm, we derive the sine-cosine circuit [1][2] from the nonlinear circuit. Next, the Fourier transformation circuit [3] is used to obtain the response of nonlinear elements. When we analyze this circuit with the transient analysis of SPICE, we may pass over the exact peaks. In order to avoid this problem, we apply the differentiator and the nonlinear limiter [4]. Finally, we apply the STC (solution trace circuit) [5] to obtain the frequency characteristics even when the curve has unstable regions.

Section 2 shows how to use the sine-cosine circuits

and the Fourier transformation circuit. Section 3 explains the peak search algorithm with the differentiator and the nonlinear limiter. Section 4 explains the tracing of the frequency characteristics curve by using STC. Illustrated example of the proposed algorithm is shown in Sec. 5 and Sec. 6 concludes the article.

II. SPICE-ORIENTED HARMONIC BALANCE ALGORITHM

A. Sine-cosine transformation

Sine-cosine transformation based on the HB (harmonic balance) method such that the determining equation is solved by transient analysis of SPICE. We discuss the sine-cosine circuit corresponding to the determining equation of the HB method. If we set the voltage through a capacitor C

$$v_C = V_{CS} \sin \omega t + V_{CC} \cos \omega t, \quad (1)$$

the current i_C is given by

$$i_C = C \frac{dv_C}{dt} = -\omega C V_{CC} \sin \omega t + \omega C V_{CS} \cos \omega t. \quad (2)$$

Thus, the coefficients of $\sin \omega t$ and $\cos \omega t$ are described by

$$I_{CS} = -\omega C V_{CC}, \quad I_{CC} = \omega C V_{CS}. \quad (3)$$

Namely, the capacitor is replaced by coupled voltage-controlled current sources in the sine-cosine transformation of the HB method. In the same way, let the current through an inductor L be

$$i_L = I_{LS} \sin \omega t + I_{LC} \cos \omega t. \quad (4)$$

Then, the voltage v_L is given by

$$v_L = L \frac{di_L}{dt} = -\omega L I_{LC} \sin \omega t + \omega L I_{LS} \cos \omega t. \quad (5)$$

Thus, the coefficients of $\sin \omega t$, $\cos \omega t$ are described by

$$V_{LS} = -\omega L I_{LC}, \quad V_{LC} = \omega L I_{LS}. \quad (6)$$

Namely, the inductor is replaced by coupled current-controlled voltage sources in the sine-cosine transformation.

As an example, Fig. 1 shows a LRC ladder circuit and Fig. 2 shows the corresponding sine-cosine circuits.

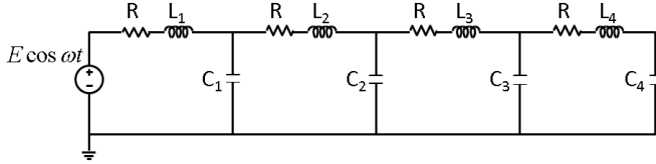


Fig. 1. LRC ladder circuit.

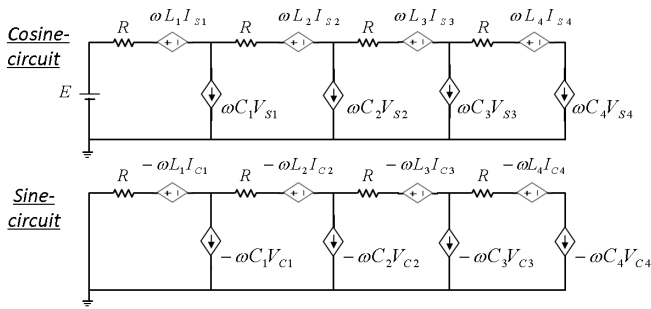


Fig. 2. Sine-cosine circuit for Fig.1.

B. Fourier transformation circuit

In this study, we use the Fourier transformation circuit in order to realize the characteristics of nonlinear capacitors. Figure 3 shows the Fourier transformation circuit. Suppose the input and output waveforms as follows:

$$\begin{cases} i(t) = I_1 \cos \omega t + I_2 \sin \omega t \\ v(t) = V_1 \cos \omega t + V_2 \sin \omega t \end{cases} \quad (7)$$

The characteristics of the electric current which flows through a capacitor can be indicated as

$$i = dq/dt = (\partial q / \partial v)(dv/dt). \quad (8)$$

From Eq. (8), the coefficients for electric charge $q(t)$ of $\sin \omega t$, $\cos \omega t$ are described by

$$q(t) = -\frac{1}{\omega} I_2 \cos \omega t + \frac{1}{\omega} I_1 \sin \omega t. \quad (9)$$

From this, input of Fourier transformation circuit model $i(t)$ is changed as

$$q(t) = Q_1 \cos \omega t + Q_2 \sin \omega t, \quad (10)$$

and from Eq. (8), the characteristics of a nonlinear capacitor is expressed with an equation using $q(t)$ and v as $v = G(q)$. We expand $G(q)$ to Fourier series,

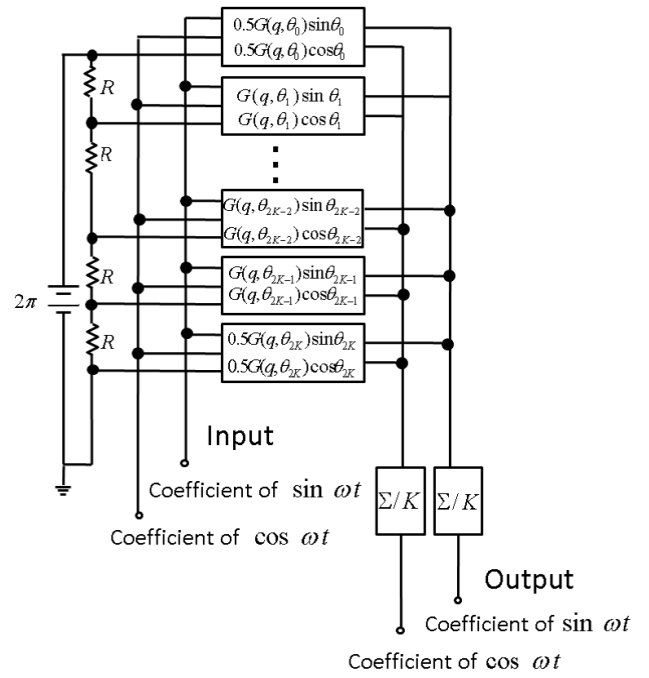


Fig. 3. Fourier transformation circuit.

and obtain the coefficients of the voltages by using the trapezoidal formula as follows.

$$\begin{aligned} V_1 &= \frac{1}{\pi} \int_0^{2\pi} (G(q) \cos \omega t) d(\omega t) \\ &= \frac{1}{2K} (G_0 + G_{2K}) + \frac{1}{K} (G_1 \cos \frac{\pi}{K} \\ &\quad + G_2 \cos \frac{2\pi}{K} + \dots + G_{2K-1} \cos \frac{(2K-1)\pi}{K}), \end{aligned} \quad (11)$$

$$\begin{aligned} V_2 &= \frac{1}{\pi} \int_0^{2\pi} (G(q) \sin \omega t) d(\omega t) \\ &= \frac{1}{K} (G_1 \sin \frac{\pi}{K} + G_2 \sin \frac{2\pi}{K} \\ &\quad + \dots + G_{2K-1} \sin \frac{(2K-1)\pi}{K}). \end{aligned} \quad (12)$$

where

$$\begin{aligned} \int_a^b G(q) d(\omega t) &= \frac{h}{2} (G_0 + G_{2K}) \\ &\quad + h(G_1 + G_2 + \dots + G_{2K-1}), \\ h &= \frac{\pi}{K}, G_i = G(q(t_i)), \\ \omega t_i &= 0, \pi/K, \dots, (2K-1)\pi/K, 2\pi. \end{aligned} \quad (13)$$

K is a number which divides the region of a to b .

III. PEAK SEARCH ALGORITHM

We search the peaks by using differentiator and non-linear limiter. The frequencies ω at the peak voltages satisfy

$$\frac{d|v(\omega)|}{d\omega} = 0, \quad (14)$$

on the characteristics curve. Hence, $|v(\omega)|$ need to be firstly differentiated by a differentiator. In order to find the exact peak points, the output is limited and expanded with a nonlinear limiter, which consists of a limiter and nonlinear diode as shown in Fig. 4.

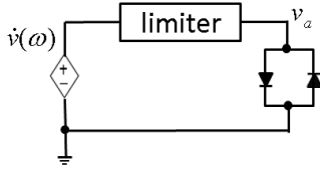


Fig. 4. Nonlinear limiter.

We suppose the characteristics of the limiter as follows:

$$v_a = \begin{cases} -V_{max} & : \text{ for } v_{in} < -V_L \\ k v_{in} & : \text{ for } -V_L \leq v_{in} \leq V_L \\ V_{max} & : \text{ for } V_L < v_{in} \end{cases}, \quad (15)$$

The output of the nonlinear limiter is given by

$$i_{out} = \begin{cases} I_s \exp(\lambda v_a) & : \text{ for } v_a > 0 \\ -I_s \exp(-\lambda v_a) & : \text{ for } v_a < 0 \end{cases}, \quad (16)$$

as shows in Fig. 5.

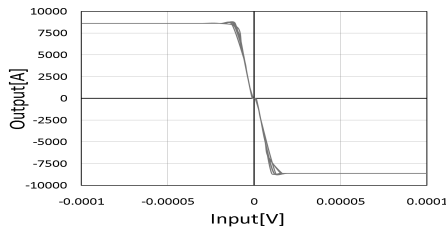


Fig. 5. Characteristics of nonlinear limiter.

The expansion factor of k is large enough. In order to complicate the analysis, we include nonlinear diodes in nonlinear limiter. Thus, the analysis near the zero points (an input of Fig. 5) is executed with a very small step size. In our algorithm, the nonlinear limiter is connected to differentiator. Input of the nonlinear limiter is equal to the slope of the voltage wave. From this reason, we can analyze the curve finely around peak voltages.

IV. TRACE FOR UNSTABLE REGION

Since we set time as frequency, we can not analyze unstable region. In this section, we explain STC (solution trace circuit) for change a horizontal axis into a voltage v_ω from time (namely, frequency).

STC is based on the arc-length method [6][7]. Those voltages are differentiated with respect to the time t

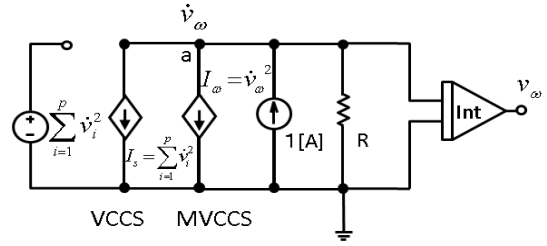


Fig. 6. STC (Solution trace circuit).

instead of the arc-length s by using differentiators. They are transformed to the corresponding voltage sources with current controlled voltage source (CCVS). Next, each voltage is squared and transformed to the current source. We have

$$I_s = \sum_{i=1}^p \left(\frac{dv_i}{dt} \right)^2 \quad (17)$$

as shown in Fig. 6. If we set the voltage of node a as v_ω , $I_\omega = v_\omega^2$ can be obtained by multiplier and voltage controlled current source VCCS (MVCCS). Thus, the additional constant current source in Fig. 6 realize to satisfying the arc-length method by Eq. (17). Then, the node voltage v_ω is integrated to obtain v_ω . Note that R in Fig. 6 is a very large resistance used only to avoid the L-J cut-set.

In this study, v_ω in Fig. 6 is equal to ω in the main circuit. The value of new v_ω depends on voltages of main circuit, and the voltages depend on the last v_ω . Repeating the calculations, the STC traces the value of ω .

V. ILLUSTRATIVE EXAMPLE

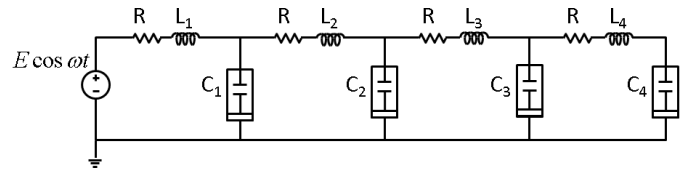


Fig. 7. LRC ladder circuit including nonlinear capacitor.

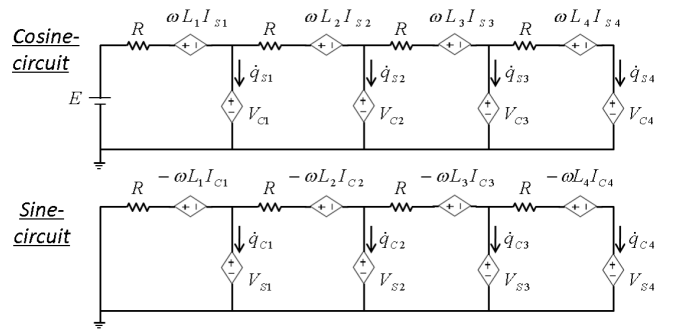


Fig. 8. Sine-cosine circuit for Fig. 7.

As an example we consider the LRC ladder circuit including nonlinear capacitors as Fig. 7. Figure 8 is the sine-cosine circuit for Fig. 7. In Fig. 7, $L_1 = L_2 = L_3 = L_4 = 0.1H$, and the nonlinear characteristics of C_1, C_2, C_3, C_4 are the same. We set $K = 10$ and the characteristics of the nonlinear capacitors are $G(q) = q + 0.8q^3$. The voltages of the CCVS in Fig. 7 are inputted to the STC. We set v_ω in Fig. 6 as ω for the frequency characteristics.

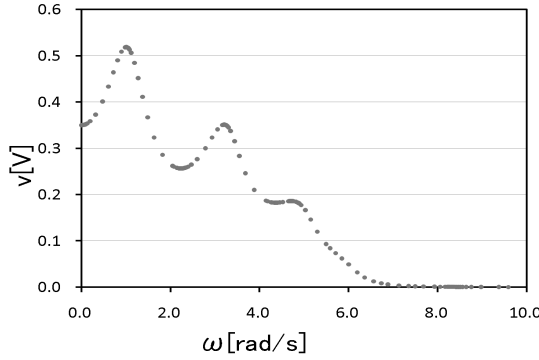


Fig. 9. Plot of frequency characteristics for $R=0.1\Omega$.

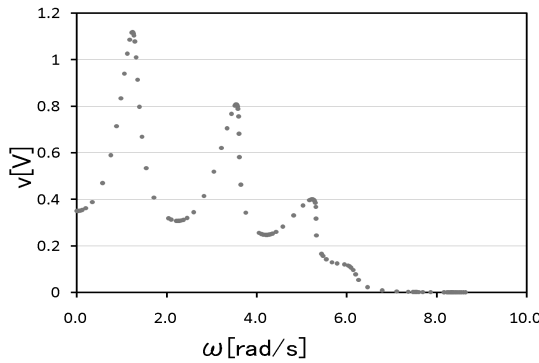


Fig. 10. Plot of frequency characteristics for $R=0.05\Omega$.

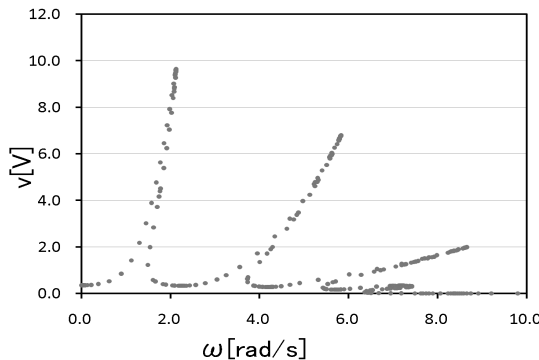


Fig. 11. Plot of frequency characteristics for $R=0.01\Omega$.

The simulated results are shown in Figs. 9, 10 and 11 for the cases of $R = 0.1\Omega$, 0.05Ω and 0.01Ω ,

respectively. The horizontal axis is ω and the vertical axis is the voltage through the nonlinear capacitor C_4 . We name the peaks of the curves as peak1, peak2, peak3 and peak4 from the left. We can see that the peaks of the curves become inclined as reducing the resistance (this corresponds to increase the effect of the nonlinearity). Although the unstable region appears in the case of $R = 0.01\Omega$, we could trace the curve successfully as shown in Fig. 11. We can also notice that the step size around the peak becomes smaller by the effect of the nonlinear limiter. We should mention that each frequency characteristics curve could be obtained by a single run of the transient analysis of SPICE.

VI. CONCLUSIONS

We have proposed a SPICE-oriented algorithm to analyze frequency characteristics with unstable region and to find the peaks of the frequency characteristics. By combining the sine-cosine circuits, the Fourier transformation circuit, the nonlinear limiter and the solution tracing circuit, the frequency characteristics curve can be obtained even if the curve has unstable region. The simulation results of the LRC ladder circuit with nonlinear capacitors showed the efficiency of the proposed method. The analysis of printed circuit boards using our proposed method is our future research.

REFERENCES

- [1] T. Kinouchi, Y. Yamagami, Y. Nishio and A. Ushida, "Spice-Oriented Harmonic Balance Volterra Series Methods," Proc. of NOLTA'07, pp.513-516, 2007.
- [2] T. Tang and M.S. Nakhla, "Analysis of High-Speed VLSI Interconnect Using the Asymptotic Waveform Evaluation Technique," IEEE Trans. Computer-Aided Design, vol.11, pp.341-352, 1992.
- [3] J. Kawata, Y. Taniguchi, M. Oda, Y. Yamagami, Y. Nishio and A. Ushida, "Spice-Oriented Frequency-Domain Analysis of Nonlinear Electronic Circuits," IEICE Trans. Fundamentals, vol.E90-A, no.2, pp.406-410, 2007.
- [4] A. Kusaka, T. Kinouchi, Y. Yamagami, Y. Nishio and A. Ushida, "A Spice-Oriented Frequency Domain Analysis of Electromagnetic Fields of PCBs," Proc. of NCSP'09, pp.526-529, 2009.
- [5] Y. Inoue, "DC Analysis of Nonlinear Circuits Using Solution-Tracing Circuits," Trans. IEICE(A), vol.J74-A, pp.1647-1655, 1991.
- [6] E. Ikeno and A. Ushida, "The Arc-length Method for the Computation of Characteristic Curves," IEEE Trans. Circuits Syst., vol.23, pp.181-183, 1976.
- [7] A. Ushida and L.O. Chua, "Tracing Solution Curves of Nonlinear Equations with Sharp Turning Points," Int. J. Circuit Theory Appl., vol.12, pp.1-21, 1984.

An Experimental Investigation of PWM-1 Controlled Circuit with Time Delay

Kenichi Tasaki, Hiroyuki Asahara, Takuji Kousaka

Faculty of Engineering Oita University, 700 Dannoharu, Oita, Japan

e-mail: {tasaki, asahara}@bifurcation.jp, takuji@cc.oita-u.ac.jp

URL: <http://nonlinear.jp/>

Abstract—In this paper, we examine the effect of switching delay in a PWM-1 controlled circuit based on the laboratory experiment. First, we propose a circuit model containing switching delay and explain its behavior. Then, we derive the Poincaré maps to analyze the properties. Finally, we discuss the effect of switching delay by using the Poincaré map and one dimensional bifurcation diagrams. Moreover, we show the bifurcation phenomena in a circuit with switching delay.

I. INTRODUCTION

In the electrical engineering, pulse-width modulation (PWM) is used as a control method of power conversion circuit [1]-[4]. In particular, the pulse-width modulation of the first kind (PWM-1) has a property that the switch shifts only once in each time of period. Maity *et al.* reported the nonlinear property of discrete map and the existence of bifurcation phenomena in a PWM-1 controlled buck converter [5]. However, the narrow analysis of it is difficult due to the reason that its circuit dynamics is described by high dimensional system. Thus, we have proposed a simplest circuit model that is constructed by the switching part of PWM-1 controlled buck converter circuit as one of the effective way to examine the fundamental property of PWM-1 controlled circuit [6].

On the other hand, most of the previous researches assumed that the switching action behaves ideally. However, the various unexpected effect occur with the switching action in the practical systems. Banergee *et al.* reported switching nonidealities and its greatly influences into the circuit dynamics based on the laboratory experiment [7]. Therefore, we have studied the dynamical effect of missed switching action in a simplest interrupted system [8]. However, there is no study about the influence of missed switching action in an interrupted electric circuit with PWM-1 control.

In this paper, we discuss the effect of switching delay in a PWM-1 controlled circuit based on the laboratory experiment. First, we propose a simplest circuit model containing switching delay and explain its behavior.

Then, we derive the Poincaré map to analyze the properties in a circuit with switching delay. Finally, we discuss the effect of switching delay and the bifurcation phenomena in a circuit with switching delay by using the experimental results.

II. DYNAMICS OF THE CIRCUIT

We propose an interrupted electric circuit with switching delay in Fig. 1, where the circuit is constructed by the switching part of PWM-1. In this figure, the capacitance voltage v is sampled at the beginning of the clock interval by the sample hold amplifier (S/H). Then, it is compared with the reference voltage by the comparator (C), and control signal is generated. Here, we artificially make a time delay t_d into the control signal by using some logical elements. Now, we set the circuit parameters as : $R = 20[\text{k}\Omega]$, $C = 0.1[\mu\text{F}]$, $E_1 = 0.0[\text{V}]$, $E_2 = 3.0[\text{V}]$, $T = 2.0[\text{ms}]$. Moreover, the circuit equation is defined as

$$RC \frac{dv}{dt} = \begin{cases} -v + E_1 & : \text{switch A} \\ -v + E_2 & : \text{switch B} \end{cases} \quad (1)$$

Next, we explain the dynamics of the circuit. Figure 2 (a) shows the behavior of PWM-1 controlled circuit with ideal switching. In this figure, $S(t)$ corresponds to the reference voltage, where v_U and v_L means the maximum and minimum voltage. Let us suppose that v_k is the initial value at $t = kT$. Basic switching rule of the circuit with ideal switching is classified into three types. If the parameters satisfy $v_U \leq v_k$, the switch keeps state A until the next clock arrives. Also, the switch remain state B until the next clock pulse appears if the condition $v_k \leq v_L$ is satisfied. On the other hand, the switch obeys state A during the time t_a under the condition of $v_L < v_k < v_U$, and then it changes to state B. Note that t_a is the time that v_k becomes equal to the reference voltage $S(t)$.

On the other hand, time delay t_d arises with the every switching action in a PWM-1 controlled circuit with switching delay (see Fig. 2 (b)). We know that the

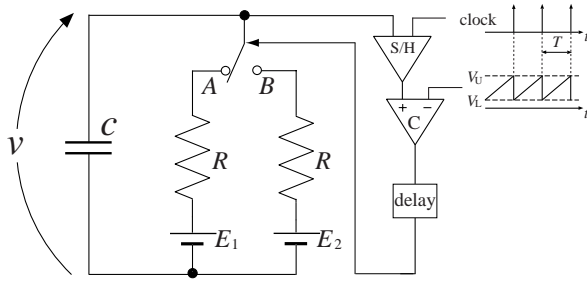


Fig. 1. PWM-1 controlled circuit with switching delay.

appearance of switching delay makes almost all of the behavior of waveform during the clock interval different, however the fundamental switching logic is same as the ideal switching case. Figure 2 (c) shows the experimental result of the capacitance voltage in the circuit with switching delay.

III. POINCARÉ MAP

We firstly define the three types of borders D_1 , D_2 and D_3 to classify the waveform in the circuit with switching delay.

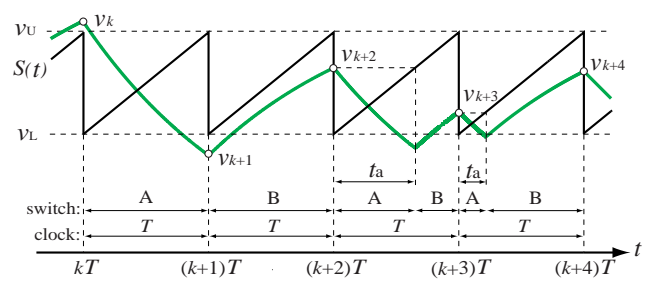
$$D_1 = v_U, D_2 = v_L, D_3 = \frac{(T - t_d)(v_U - v_L)}{T} + v_L \quad (2)$$

Note that the border D_3 is only used in a circuit with switching delay. If the waveform starts at D_3 , the switch changes from state A to B when the next clock pulse arrives. Using these borders, the waveform during the duration of clock interval can be classified into nine types in the circuit with switching delay. Note that we need the information of v_k and v_{k-1} that is the solution at $t = kT$ and $t = (k-1)T$ to classify the consecutive waveform. This means that the circuit with switching delay must be described by two dimensional discrete system. Thus, we define the variable function u_k that satisfies $u_{k+1} = v_k$. Poincaré map in the circuit with switching delay is described by the following equations.

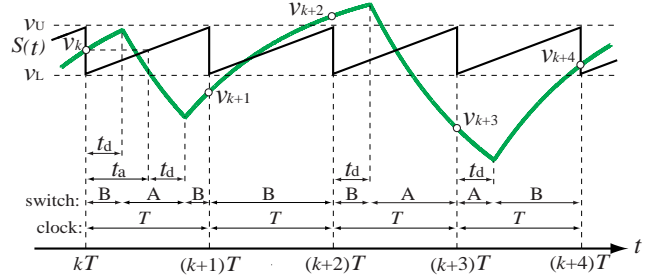
$$\mathbf{x}_{k+1} = \mathbf{A}_{dj}\mathbf{x} + \mathbf{B}_{dj}, \mathbf{x} \in I_{dj} \quad (j = 1, 2 \dots 9) \quad (3)$$

Here, \mathbf{x} is defined as $\mathbf{x} = [u_k \quad v_k]^T$, and the \mathbf{A}_{dj} and \mathbf{B}_{dj} ($j = 1, 2 \dots 9$) are given by

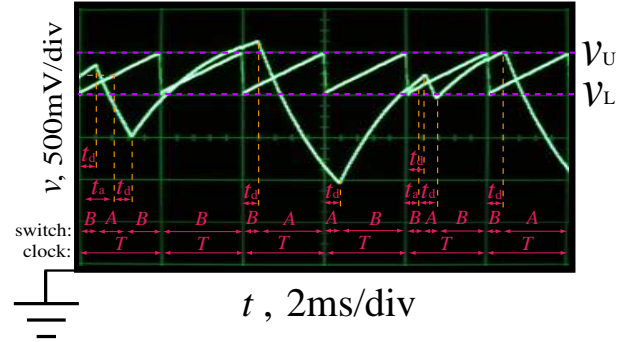
$$\begin{aligned} \mathbf{A}_{dj} &= \begin{bmatrix} 0 & 1 \\ 0 & e^{-\frac{T}{RC}} \end{bmatrix}, \\ \mathbf{B}_{d1} &= \begin{bmatrix} 0 \\ E_1 + (E_2 - E_1)e^{-\frac{-T+t_d}{RC}} - E_2e^{-\frac{T}{RC}} \end{bmatrix}, \\ \mathbf{B}_{d2} &= \begin{bmatrix} 0 \\ E_2 + (E_1 - E_2)e^{-\frac{-T+t_d+t_a(v_k)}{RC}} \\ + (E_2 - E_1)e^{-\frac{-T+t_d}{RC}} - E_2e^{-\frac{T}{RC}} \end{bmatrix}, \\ \mathbf{B}_{d3} &= \begin{bmatrix} 0 \\ E_2(1 - e^{-\frac{T}{RC}}) \end{bmatrix}, \quad \mathbf{B}_{d4} = \begin{bmatrix} 0 \\ E_1(1 - e^{-\frac{T}{RC}}) \end{bmatrix}, \end{aligned}$$



(a) Example of the waveform (Ideal switching).



(b) Example of the waveform (Switching delay).



(c) Experimental result (Switching delay).

Fig. 2. Behavior of the waveform.

$$\begin{aligned} \mathbf{B}_{d5} &= \begin{bmatrix} 0 \\ E_2 + (E_1 - E_2)e^{-\frac{-T+t_d+t_a(v_k)}{RC}} - E_1e^{-\frac{T}{RC}} \end{bmatrix}, \\ \mathbf{B}_{d6} &= \begin{bmatrix} 0 \\ E_2 + (E_1 - E_2)e^{-\frac{-T+t_d}{RC}} - E_1e^{-\frac{T}{RC}} \end{bmatrix}, \\ \mathbf{B}_{d7} &= \begin{bmatrix} 0 \\ E_1 + (E_2 - E_1)e^{-\frac{-T+t_d}{RC}} + (E_1 - E_2)e^{-\frac{t_a(v_k)+t_d-2T}{RC}} \\ - E_1e^{-\frac{T}{RC}} \end{bmatrix}, \\ \mathbf{B}_{d8} &= \begin{bmatrix} 0 \\ E_2 + (E_1 - E_2)e^{-\frac{-T+t_a(v_k)+t_d}{RC}} + (E_2 - E_1)e^{-\frac{-T+t_d}{RC}} \\ + (E_1 - E_2)e^{-\frac{t_a(v_k)+t_d-2T}{RC}} - E_1e^{-\frac{T}{RC}} \end{bmatrix}, \\ \mathbf{B}_{d9} &= \begin{bmatrix} 0 \\ E_2 + (E_1 - E_2)e^{-\frac{-2T+t_d+t_a(u_k)}{RC}} - E_1e^{-\frac{T}{RC}} \end{bmatrix}. \end{aligned} \quad (4)$$

Here, $t_a(x)$ is expressed in the following equations.

$$t_a(x) = \frac{x - v_L}{v_U - v_L} T \quad (5)$$

Poincaré map in the circuit with ideal switching can be defined in the same way. Note that we let the Poincaré map in the circuit with ideal switching as the two dimensional discrete system to compare the circuit with switching delay in this paper. Furthermore $I_{ij} (j = 1, 2, 3)$ and $I_{dj} (j = 1, 2 \cdots 9)$ correspond to the existence region of the classified waveform in a circuit with ideal switching and a circuit with switching delay (see Fig. 3).

IV. EXPERIMENTAL RESULT

Figure 3 shows the Poincaré map in a circuit with ideal switching and a circuit with switching delay based on the laboratory experiment. It is clear that the time delay t_d greatly influences into the circuit dynamics, because the new types of region are constructed in a circuit with switching delay. We notice that a part of the Poincaré map B_{d7} , B_{d8} and B_{d9} depend on the values of u_k and v_k (see Eq. (4)). In other words, the Poincaré map in the circuit with switching delay is described by the two dimensional discrete system. However the Poincaré map in the circuit with ideal switching is also described by one dimensional discrete system because its all regions depend on only the value of v_k [6]. Therefore we attribute that the structure of Poincaré map is varied due to the appearance of switching delay. Then we discuss the bifurcation phenomena in a circuit with switching delay. Figure 4 exhibits the one dimensional bifurcation diagram in a circuit with ideal switching and a circuit with switching delay, respectively. Additionally, Fig. 5 shows the corresponding

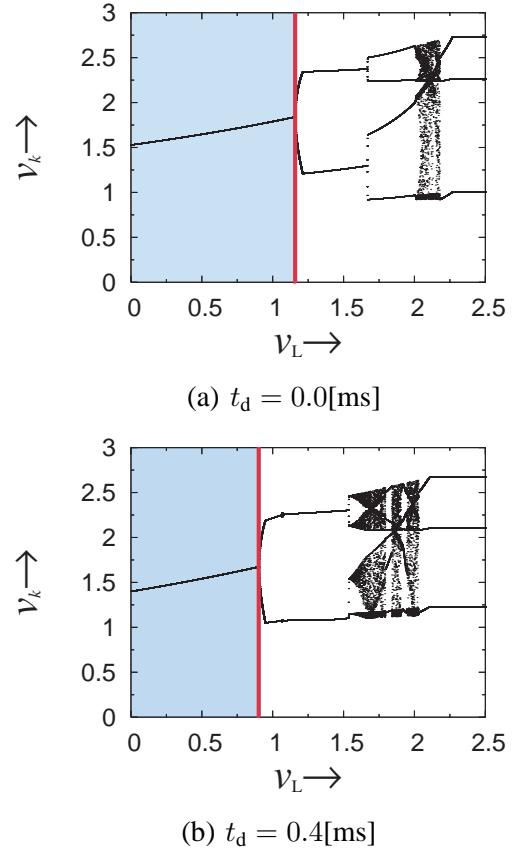
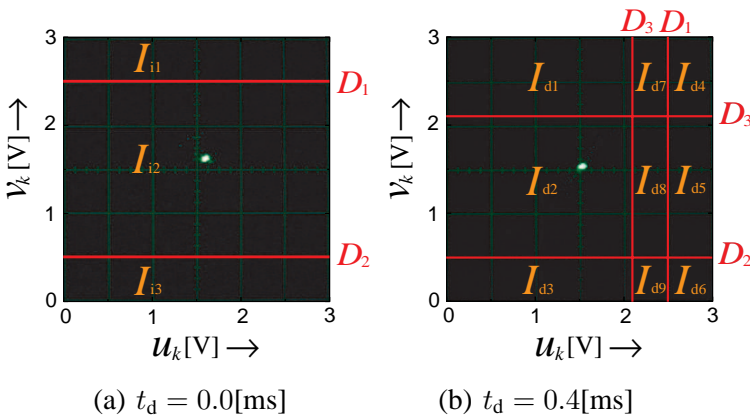


Fig. 4. One parameter bifurcation diagram. ($T = 2.0$ [ms] and $v_U = 2.5$ [V])

experimental results with Fig. 4 (b). We can observe various kinds of periodic waveforms and chaotic attractor. For example, there is the period-1 waveform at $v_L = 0.5$ [V] (see Figs. 5 (a)). Also, the period-1 waveform becomes the period-2 waveform through the period doubling bifurcation at $v_L = 0.91$ [V]. Moreover, the period-6 waveform exists at $v_L = 1.8$ [V] (see Figs. 5 (c)). After that border-collision bifurcation occurs and the chaotic attractor is generated at $v_L = 1.9$ [V]. This results show that the period doubling bifurcation or border-collision bifurcation concern the behavior of the waveform in the circuit with switching delay.

Finally, we examine the effect of switching delay with the one dimensional bifurcation diagram. We can observe that the appearance of switching delay makes the existence region of the periodic waveform and chaotic attractor different. For example the existence region of the period-1 waveform becomes small. It is occurred depending on the period doubling bifurcation, and the red line in these figures show the appearance of a period doubling bifurcation. The specific condition of the period doubling bifurcation at red line is given by

$$e^{-\frac{T}{RC}} + \frac{E_1 - E_2}{v_U - v_L} T e^{\frac{-T + t_d + t_a(v_k)}{RC}} + 1 = 0. \quad (6)$$

Fig. 3. Experimental results of the Poincaré map. ($v_U = 2.5$ [V], $v_L = 0.5$ [V] and $T = 2.0$ [ms])
26-28 May 2010, Dresden, Germany

Thus, the existence region of the period-1 waveform is reduced by switching delay because the time delay t_d is a positive value in Eq. (6).

Consequently, the period doubling bifurcation or the border-collision bifurcation relate to the behavior of the waveform in the circuit with switching delay. Moreover, the appearance of switching delay exerts an influence on the circuit dynamics because it makes the structure of Poincaré map and the existence region of the various kinds of waveform different from the circuit with ideal switching.

V. CONCLUSION

In this paper, we examined the effect of switching delay and show the bifurcation phenomena in the simplest circuit model based on laboratory experiment. As a result, the period doubling bifurcation or border-collision bifurcation relate to the behavior of the waveform in the circuit with switching delay. Moreover, the appearance of switching delay has an effect on the circuit dynamics because it makes the structure of Poincaré map and the existence region of the various kinds of waveform different from the circuit with ideal switching. Concretely, the Poincaré map in the circuit with switching delay is described by two dimensional discrete system and the existence region of the period-1 waveform is reduced by switching delay. In addition, we consider that a similar effect and bifurcation phenomena are observed in the PWM-1 controlled high dimensional circuit, because our circuit model is constructed by the switching part of PWM-1 controlled buck converter circuit.

REFERENCES

- [1] S. Banerjee and G. C. Verghese, Eds., *Nonlinear Phenomena in Power Electronics: Attractors, Bifurcations, Chaos, and Nonlinear Control*, New York: IEEE Press, 2001.
- [2] M. di Bernardo and C. K. Tse, "Chaos in Power Electronics: An Overview," *Chaos in Circuits and Systems*, chapter 16. World Scientific, pp. 317–340, 2002.
- [3] B. Robert and C. Robert, "Border-Collision Bifurcations in a One-Dimensional Piecewise Smooth Map for a PWM Current-Programmed H-Bridge Inverter," *International Journal of Control*, Vol. 75, No. 16 & 17, pp. 1356–1367, 2002.
- [4] A. El Aroudi and R. Leyva, "Quasi-periodic route to chaos in a PWM voltage-controlled DC-DC boost converter," *IEEE Trans. Circuits Syst. I, Fundam. Theory Appl.*, Vol. 48, No. 8, pp. 967–978, 2001.
- [5] S. Maity et al., "Bifurcation Analysis of PWM-1 Voltage-Mode-Controlled Buck Converter Using the Exact Discrete Model," *IEEE Trans. Circuits Syst. I, Fundam. Theory Appl.*, Vol. 54, No. 5, pp. 1120–1130, 2007.
- [6] S. Tomonaga et al., "Bifurcation Phenomena Observed in a Switched Dynamical System with PWM-1 Control," 17th International Workshop on Nonlinear Dynamics of Electronic Systems pp. 46–49, 2009.
- [7] S. Banerjee et al., "Dynamical Effects of Missed Switching in Current-Mode Controlled dc-dc Converters," *IEEE Trans. Circuit and Syst. part I*, Vol. 51, No. 12, pp. 649–654, 2004.
- [8] Takuji Kousaka and Hiroyuki Asahara, "Dynamical mechanism for interrupted circuit with switching delay" *IEICE Electronics Express*, Vol. 6 No. 12 pp.806-810, 2009.

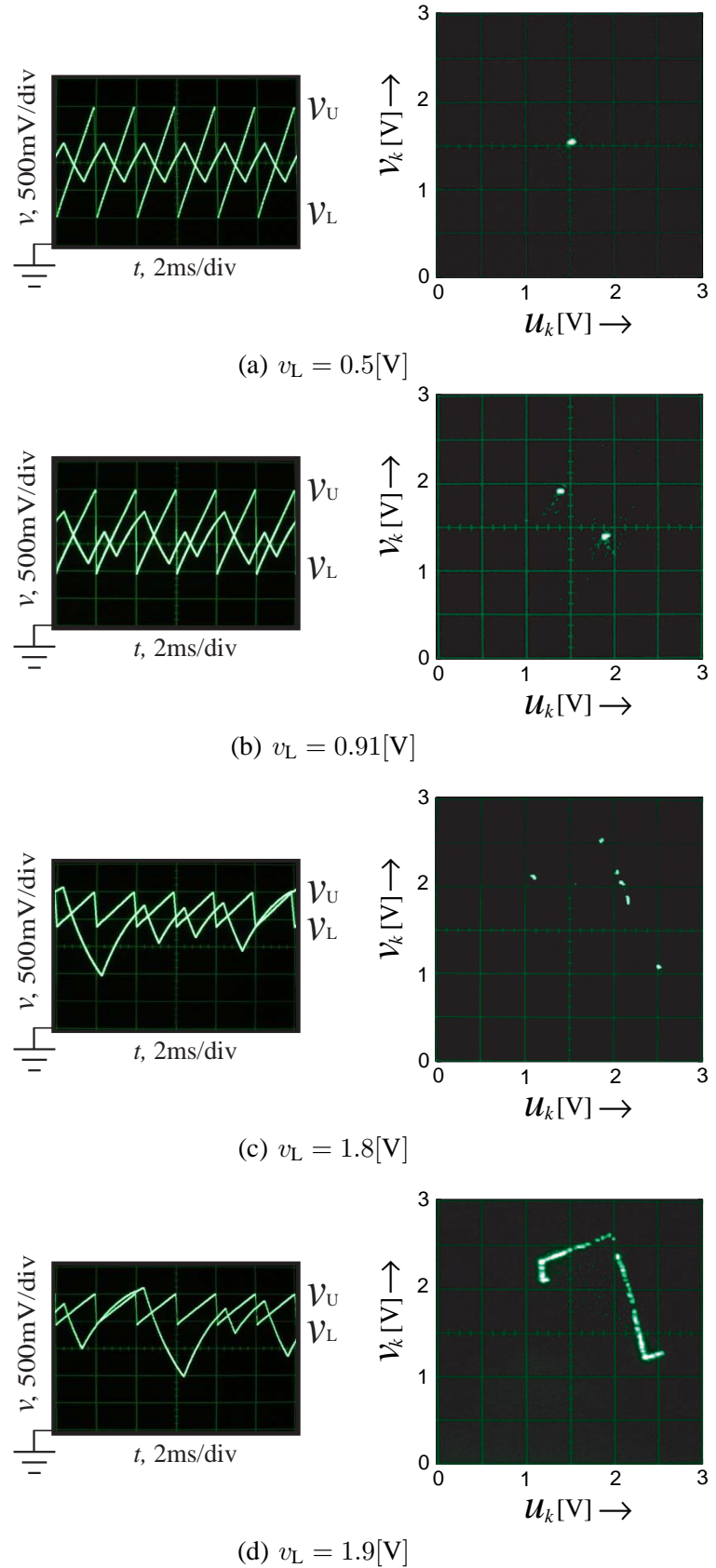


Fig. 5. Experimental result. ($v_U = 2.5[V]$, $T = 2.0[ms]$ and $t_d = 0.4[ms]$)

Qualitative Mechanism of DC/DC Converter containing Spike Noise

Hiroyuki Asahara and Takuji Kousaka

Faculty of Engineering Oita University, 700 Dannoharu, Oita, Japan

Email: asahara@bifurcation.jp and takuji@cc.oita-u.ac.jp

http : //nonlinear.jp/

Abstract—The main purpose of this paper is to clarify the qualitative mechanism in the current mode controlled buck-boost converter containing spike noise. First, we explain the basic switching rule in the circuit with ideal switching and the circuit with spike noise, respectively. Then, the Poincaré map is derived for the rigorous analysis. Finally, we show some analytical results based on the Poincaré map. In particular, we pay attention to the dynamical effect of spike noise in the circuit including discontinuous conduction mode (DCM).

I. INTRODUCTION

Power conversion DC/DC converters are widely used in the field of electrical engineering, and have been thoroughly studied in the past decade under the assumption of the theoretical switching action [1]–[4]. However, there are various kinds of unavoidable switching non-idealities such as time delay via the circuit's elements (switching delay), high frequency ripple (spike noise) and so on. In particular, Ref. [5] reported that the above missed switching actions make the bifurcation structure of DC/DC converters different, and greatly influences into the circuit dynamics. Although, there is no paper that have analyzed the effect of missed switching actions except for Refs. [5]–[7]. Therefore, we have proposed a simplest class of interrupted electric circuit and its mathematical model based on the switching action of the converter circuit operated in continuous conduction mode (CCM), and analyzed it in detail [8], [9]. However, dynamical effect of missed switching action in the circuit dynamics including discontinuous conduction mode (DCM) does not studied at all. To develop the fundamental circuit theory of DC/DC converters, we need to examine the effect of missed switching action in the circuit dynamics with DCM.

This paper addresses the first step to analyze the dynamical effect of missed switching action in the circuit dynamics with DCM. The current mode controlled buck-boost converter is used as the circuit model. First, we

explain the behavior of the waveform in the circuit with ideal switching and the circuit with spike noise, respectively. Then, we classify the consecutive waveform during the clock interval utilizing the critical value, and derive the Poincaré map for the rigorous analysis. Finally, we discuss the qualitative mechanism of the circuit with spike noise based on the Poincaré map. In particular, we pay attention to the effect of spike noise in the circuit dynamics containing DCM.

II. CIRCUIT AND SWITCHING RULE

Figure 1 shows the current mode controlled buck-boost converter. In this paper, we let the capacitance voltage v is a constant value E_0 , under the assumption of the capacitance C and resistance R are large enough for the clock interval T . Thus, the circuit equation is given by

$$\frac{di}{dt} = \begin{cases} \frac{E_d}{L}, & : \text{state 1} \\ -\frac{E_0}{L}, & : \text{state 2} \\ 0, & : \text{state 3} \end{cases} \quad (1)$$

where state 1, state 2 and state 3 are defined as

- state 1: S conducting, D blocking and $0 < i < i_{\text{ref}}$
- state 2: S blocking, D conducting and $0 < i < i_{\text{ref}}$

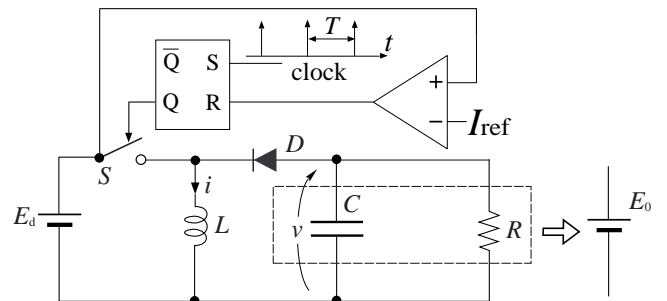


Fig. 1. Current mode controlled buck-boost converter

- state 3: S and D both blocking and $i = 0$.

Let us suppose that $\tau = t/(RC)$ and $y = i/I_{\text{ref}}$ are used as the dimensionless variables. Moreover, we set a variable $M = E_0/E_d$ in the following analysis.

Figure 2 shows the behavior of the waveform in the circuit with ideal switching and the circuit with spike noise. Note that the detailed analysis in the circuit with ideal switching has been already conducted in Ref. [4], however, we show the conceptual diagram of the waveform in the circuit with ideal switching in terms of the comparison between the circuit with spike noise. Here, the operation time of spike noise does not influence into the circuit dynamics so much, because it is short enough for the clock interval [5]. Thus, we ignore the operation time of spike noise in the following analysis to study the fundamental property of the circuit (see Fig. 2 (b)). The basic switching rule falls into three types as follows:

- 1) the switch changes from state ON to OFF if the waveform hits the reference value,
- 2) the switch changes from state OFF to ON if the clock pulse is impressed when the switch is set at state OFF,
- 3) the switch keeps state OFF until the next clock pulse is impressed if the waveform reaches to zero,

where the switching rule 2) does not be applied if the maximum size of spike noise h reaches to the reference value. In addition, the circuit dynamics includes DCM

if the waveform reaches to zero.

III. POINCARÉ MAP

Basic behavior of the waveform during a duration of clock interval T in the circuit with spike noise is classified into five types (see Fig. 3) by the critical values D_1 , D_2 , D_3 and D_4 .

$$D_1 = 1 - T, \quad D_2 = 1 - T + \frac{1}{M}, \quad D_3 = 1 - h, \quad D_4 = MT \quad (2)$$

Note that we need the information of y_k and y_{k-1} that is the waveform at $\tau = kT$ and $\tau = (k-1)T$ to classify the waveform during the clock interval. In addition, we define the variable function x_k that satisfies $x_{k+1} = y_k$, and let I_{sj} ($j = 1 \sim 10$) that are the regions of the classified waveforms.

$$\begin{aligned} I_{s1} &= \{x_k, y_k \mid y_k < D_1\}, \\ I_{s2} &= \{x_k, y_k \mid D_1 \leq y_k < D_3 \text{ or } (D_3 \leq y_k, x_k \leq D_1)\}, \\ I_{s3} &= \{x_k, y_k \mid D_2 \leq y_k, x_k \leq D_1\}, \\ I_{s4} &= \{x_k, y_k \mid D_3 \leq y_k, D_1 < x_k\}, \\ I_{s5} &= \{x_k, y_k \mid D_3 \leq y_k < D_4, D_1 < x_k\}, \\ I_{s6} &= \{x_k, y_k \mid D_1 \leq y_k < D_3 \text{ or } (D_3 \leq y_k < D_2, x_k \leq D_1)\}, \\ I_{s7} &= \{x_k, y_k \mid D_1 \leq y_k < D_2\}, \\ I_{s8} &= \{x_k, y_k \mid D_2 \leq y_k < D_3 \text{ or } (D_3 \leq y_k, x_k \leq D_1)\}, \\ I_{s9} &= \{x_k, y_k \mid D_4 \leq y_k, D_3 \leq y_k, D_1 < x_k\}, \\ I_{s10} &= \{x_k, y_k \mid D_3 \leq y_k, D_1 < x_k\}, \end{aligned} \quad (3)$$

Therefore, we can define the Poincaré map in the circuit with spike noise as follows:

$$x_{k+1} = \begin{cases} \begin{bmatrix} y_k \\ y_k + 1 \end{bmatrix}, & (x_k, y_k) \in I_{s1} \\ \begin{bmatrix} y_k \\ -M(y_k + T - 1) + 1 \end{bmatrix}, & (x_k, y_k) \in I_{s2}, I_{s6}, I_{s7} \\ \begin{bmatrix} y_k \\ 0 \end{bmatrix}, & (x_k, y_k) \in I_{s3}, I_{s8} \\ \begin{bmatrix} y_k \\ y_k - MT \end{bmatrix}, & (x_k, y_k) \in I_{s4}, I_{s9} \\ \begin{bmatrix} y_k \\ 0 \end{bmatrix}, & (x_k, y_k) \in I_{s5}, I_{s10} \end{cases} \quad (4)$$

The consecutive waveform during the clock interval is classified into three types in the circuit with ideal switching by using the border D_1 and D_2 . Likewise, we call the region in the circuit with ideal switching as I_{i1} , I_{i2} and I_{i3} in the following analysis. Note that the circuit with ideal switching is described by the one dimensional discrete system. However, we treat it as the two dimensional discrete system in order to compare the circuit with spike noise.

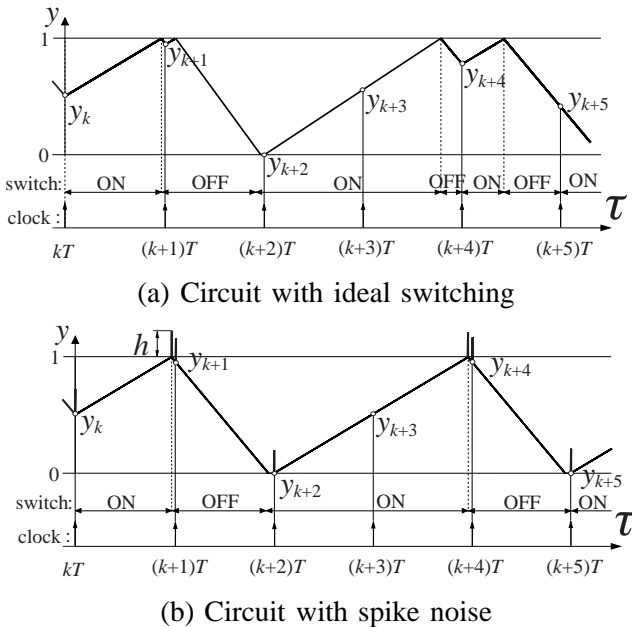


Fig. 2. Conceptual diagrams of the waveform in the circuit

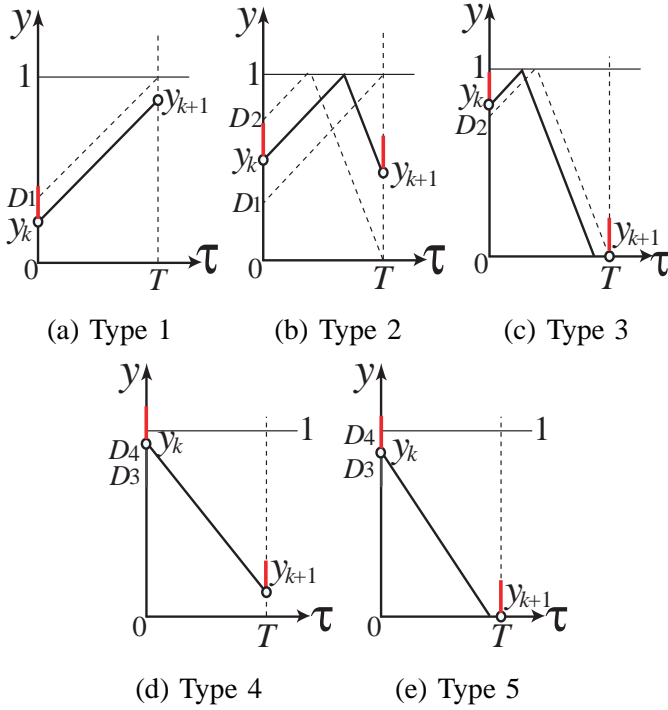


Fig. 3. Classified waveforms during the clock interval

IV. QUALITATIVE MECHANISM

Figures 4 and 5 show the structure of Poincaré map in the circuit with ideal switching and the circuit with spike noise. Note that behavior of the waveform during the clock interval in color-coded red, blue, purple, green and orange regions correspond to Fig. 3 (a), (b), (c), (d) and (e), respectively. Now, we can define the four types of Poincaré map in the circuit with spike noise as follows:

- 1) case 1 : $h \neq 0$ and $D_4 < D_3$ and $0 \leq 1 - MT$,
- 2) case 2 : $h \neq 0$ and $D_3 \leq D_4$ and $0 \leq 1 - MT$,
- 3) case 3 : $h \neq 0$ and $D_3 < D_2$ and $1 - MT < 0$,

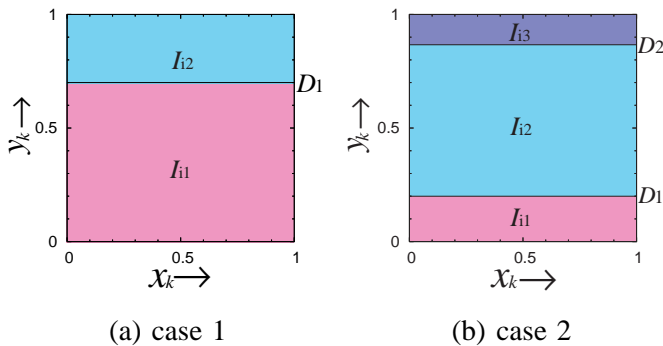


Fig. 4. Structure of the Poincaré map (ideal switching)

4) case 4 : $h \neq 0$ and $D_2 \leq D_3$ and $1 - MT < 0$, where case 1–4 are shown in Fig. 5. Structure of the Poincaré map in the circuit with spike noise different in form compared with the circuit with ideal switching. We find out that the new type of switching rule that is the switch keeps state OFF during the clock interval greatly influences into the circuit dynamics (see green or orange regions in Fig. 5). Figures 6 and 7 show the examples of waveform and its corresponding Poincaré map in the circuit with ideal switching and the circuit with spike noise. It is clear that appearance of spike noise causes the new region I_{s4} , I_{s5} and I_{s9} . In particular, region I_{s4} makes the new mapping point in the Poincaré map (see Fig. 6 (b)). As the results, some effects of spike noise such as expansion of the invariant set, appearance of the coexisting attractor can be observed in the circuit. On the other hand, spike noise can make the operation time of DCM long. For example, we can observe that the region I_{s5} constructs the new mapping point in the Poincaré map, and makes the operation time of DCM long in Fig. 7 (b). In general, it can be said that the circuit dynamics with spike noise tend to be in DCM in the lower parameter value of T compared with the circuit dynamics with ideal switching under the condition of $D_2 \leq D_3$. Note that spike noise does not influence into the circuit behavior under the condition of $D_3 \leq D_2$

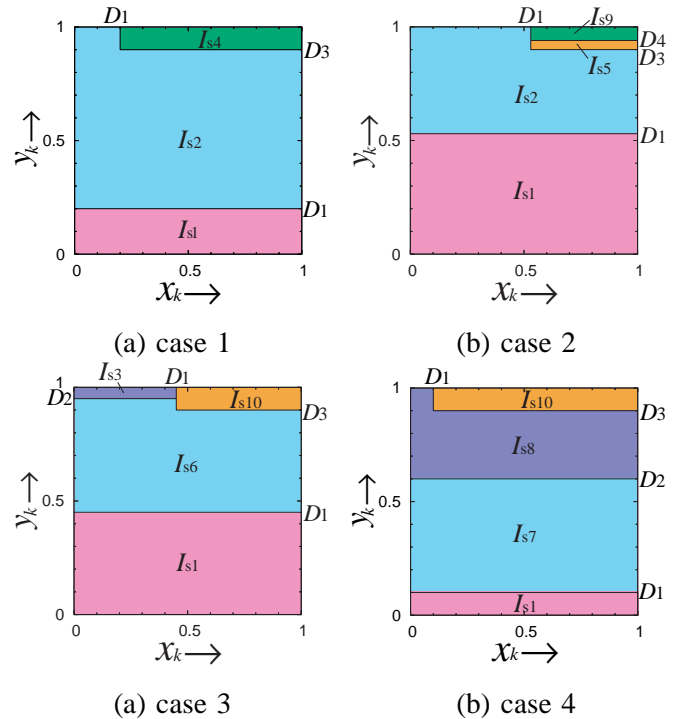
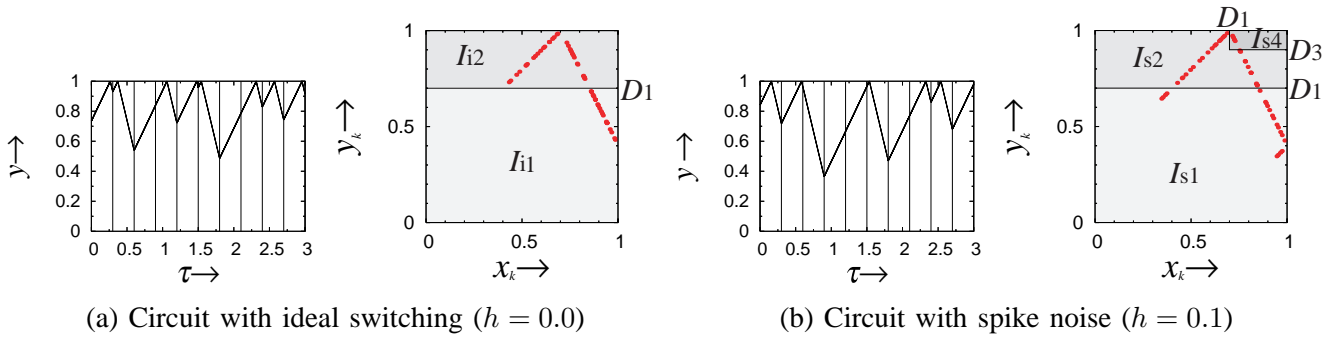
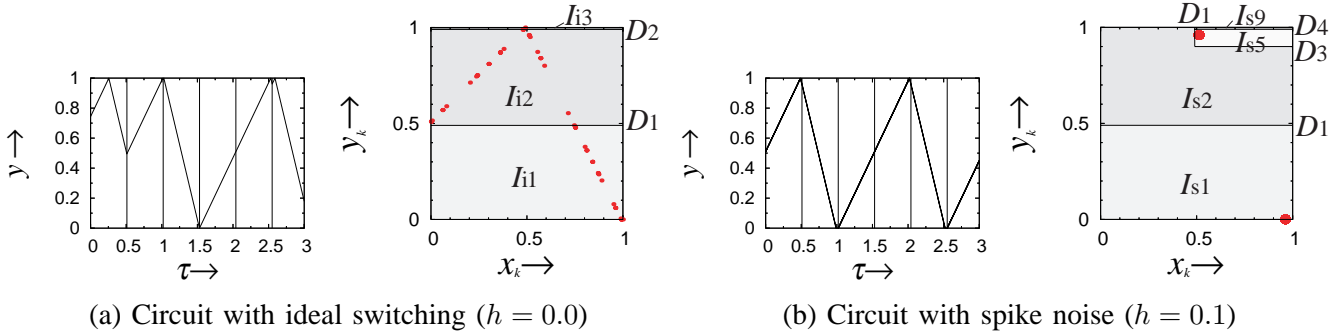


Fig. 5. Structure of the Poincaré map (spike noise)

Fig. 6. Examples of the waveform and its Poincaré map in the circuit dynamics does not including DCM ($T = 0.3$, $M = 2.0$).Fig. 7. Examples of the waveform and its Poincaré map in the circuit dynamics including DCM ($T = 0.51$, $M = 2.0$).

in the circuit, because both of the circuit dynamics with ideal switching and spike noise including DCM at the same time under the condition of $D_3 \leq D_2$. Consequently, we can conclude that appearance of spike noise makes the new type of waveform that the switch keeps state OFF during the clock interval (see Fig. 3 (d), (e)), and effects in the circuit dynamics.

V. CONCLUSION

We have analyzed the buck-boost converter containing spike noise based on the Poincaré map. First, we explained the basic switching rule in the circuit. Then, the Poincaré map in the circuit with spike noise was derived for the rigorous analysis. Finally we discuss the qualitative mechanism and dynamical effect of spike noise in the circuit based on the Poincaré map. As the results, we could be conducted that (1) appearance of spike noise makes the new type of waveform that the switch keeps state OFF during the clock interval, and effects in the circuit dynamics (2) the circuit dynamics with spike noise tend to be in DCM in the lower parameter value of T compared with the circuit dynamics with ideal switching under the condition of $D_2 \leq D_3$ (3) spike noise did not influence into the circuit dynamics under the condition of $D_3 \leq D_2$. Detailed bifurcation analysis

in the circuit dynamics with DCM and investigation into the effect of missed switching action in more high dimensional system is our future work to be studied.

REFERENCES

- [1] D.C. Hamill and J.H.B. Deane., "Modeling of chaotic dc-dc converters by iterated nonlinear mappings," *IEEE Transaction on Power Electronics* vol. 7-(1), pp. 25–36, 1992
- [2] M. di Bernald and C. K. Tse., *Chaos in Power Electronics: An overview*, Chaos in Circuits and Systems, chapter 16. World Scientific, pp.317–340, 2002.
- [3] C. K. Tse., *Complex Behavior of Switching Power Converters*, Boca Raton: CRC Press, 2003.
- [4] T. Kabe *et al.*, "Analysis of Piecewise Constant Models of Current Mode Controlled DC-DC Converters," *IEICE TRANS. FUNDAMENTALS*, vol.E90-A, no.2, 2007.
- [5] S. Banerjee, S. Parui, A. Gupta, "Dynamical Effects of Missed Switching in Current-Mode Controlled dc-dc Converters," *IEEE Trans. Circuits and Syst. part II*, Vol.51, No.12, pp.649–654, 2004.
- [6] T. Maruyama *et al.*, "Chaos in an Auto Gain Controlled Oscillator Containing Time Delay," *IEICE Transaction on Electronics, Information and Communication Engineers A*, Vol. 72, pp. 1814–1820, 1989. (In Japanese)
- [7] M. Kuboshima and T. Saito., "Bifurcation from a chaos generator including switched inductor with time delay," *IEICE Transaction on Fundamentals of Electronics*, Vol. 80, pp. 1567–1571 1997.
- [8] H. Asahara and T. Kousaka., "Experimental Validation of a Hybrid Dynamical System with Switching Delay," *Journal of Signal Processing*, Vol. 13, No. 4, pp. 307–310, 2009.
- [9] H. Asahara, T. Suzui, T. Kousaka., "Dynamical Effect of the Spike Noise in a System Interrupted by Own State and a Periodic Interval," *IEICE Transaction on Fundamentals A*, Vol. 92, pp. 596–603, 2009. (In Japanese)

Two-Compartment Phenomenological Model of Dopaminergic Neuron

Denis Zakharov and Vladimir Nekorkin

Nonlinear Dynamics Department,
Institute of Applied Physics of the RAS,
46, Ulyanov St., 603950 Nizhny Novgorod, Russia
Email: zakharov@neuron.appl.sci-nnov.ru

Alexey Kuznetsov

Department of Mathematical Sciences,
Indiana University-Purdue University Indianapolis,
402 N. Blackford St., Indianapolis, IN 46202, USA
Email: askuznet@iupui.edu

Abstract— We have constructed a two-compartment model of the dopaminergic neuron based on the FitzHue-Nagumo oscillators with nonlinear recovering for each compartment. The compartments correspond to the soma and dendrites differing by the value of small parameter. The influence of stimuli (applied current for the somatic compartment and synaptic activation for the dendritic compartment) on the model has been studied. We have shown that activation of AMPA and NMDA synaptic currents leads to neuron firing high-frequency bursts. The mechanisms underlying the high-frequency oscillations are investigated.

Dopaminergic neurons situated in the midbrain and basal ganglia play a key role in motor activity and behavioral response formation. They are active and generate periodical or irregular spike trains as well as high frequency bursts [1,2] (fig. 1). The frequency of periodic or irregular spike train is 1-5 Hz, whereas the frequency of spikes in the bursts may exceed 20 Hz [2,3]. Long-term depolarization of the soma of the neuron is not able to produce the high frequency burst because it results in suppression of neuron activity [4,5]. But it is possible to speak about correlation between high-frequency bursts and activation of NMDA- and AMPA-receptors. It was shown [6-8] that *in vitro* slices stimulation of NMDA-receptors may evoke such bursts. The role of AMPA-receptors has not been fully understood. On the one hand, there are some papers (for example, [9]), in which it was demonstrated that only activation of NMDA-receptors may produce high-frequency burst generation. On the other hand, in [10] it was shown that it is necessary to combine activation of receptors of both types for obtaining high-frequency generation.

Recently the phenomenological [11], and Hodgkin-Huxley-like [12-14] models of the dopaminergic neuron were proposed. These models

consist of electrically coupled compartments. The first compartment describes soma dynamics, whereas the other compartments (at least one) mimic dendrites behavior. In the framework of the phenomenological model based on FitzHue-Nagumo oscillators [11] and Hodgkin-Huxley-like [12, 13] models it was demonstrated that high-frequency bursts generation cannot be a result of the soma stimulation by the applied current. In the model based on the Hodgkin-Huxley equations [14] the influence of applied current on the soma compartment and action of NMDA- and AMPA-receptors stimulation on dendritic one are studied. It was shown that activation of NMDA-receptors may initiate high-frequency bursts, whereas activation of AMPA-receptors leads to suppression of neuron activity. Disadvantages of this model are complexity and a great amount of model parameters. The goal of our work was construction of a simple model describing different mechanisms of high-frequency burst generation. As distinct from the model in [11] we used FitzHue-Nagumo oscillators with nonlinear recovering for describing compartments and also investigated the influence of NMDA- and AMPA-receptors activation.

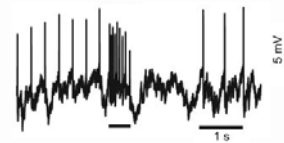


Fig. 1. An oscillogram of high-frequency activation *in vitro* of a dopaminergic neuron in black matter of midbrain induced by synaptic stimulation of NMDA- and AMPA-receptors [10] (stimulation duration is shown by black line).

I. MODEL

The model consists of two compartments imitating behavior of the soma and the dendrite (fig.

2). Each compartment is described by FitzHue-Nagumo equations in the form [15]:

$$\begin{aligned}\dot{u}_s &= f(u_s) - v_s + j_s + j_{stis} + d(u_s - u_d), \\ \dot{v}_s &= \varepsilon_s(g(u_s) - v_s), \\ \dot{u}_d &= f(u_d) - v_d + j_d + j_{stid} + d(u_d - u_s), \\ \dot{v}_d &= \varepsilon_d(g(u_d) - v_d), \\ j_{stis} &= j_{ext}, \\ j_{stid} &= g_{NMDA}(u_d)(E_{NMDA} - u_d) + g_{AMPA}(E_{AMPA} - u_d), \\ g_{NMDA} &= \frac{\bar{g}_{NMDA}}{1 + 0.28[Mg]e^{-0.08u_d}}.\end{aligned}$$

Indexes s and d correspond to the compartments describing the soma and the dendrite, respectively. Variables u_s and u_d qualitatively represent membrane potentials of the compartments, variables v_s and v_d model dynamics of calcium ion concentration. ε_s and ε_d are small parameters determining slowness of variables v_s and v_d in comparison with u_s and u_d . Because of different sizes of the soma and the dendrite, the value of the somatic small parameter ε_s is much smaller than the value of the dendritic small parameter ε_d (further, for definiteness $\varepsilon_s=0.06$, $\varepsilon_d=0.6$). Parameter d is electric coupling strength.

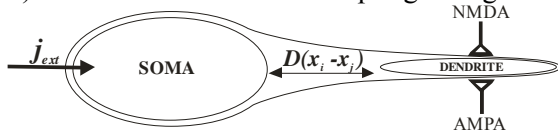


Fig. 2. Schematic representation of the model.

Functions $f(u)$ and $g(u)$ have the following form:

$$\begin{aligned}f(u) &= u - u^3/3, \\ g(u) &= \begin{cases} \alpha u, & u \leq 0, \\ \beta u, & u \geq 0. \end{cases}\end{aligned}\quad (2)$$

Control parameters j_s and j_d determine spontaneous activity of the compartments (without external stimuli). j_{stis} represents the action of applied current (for the somatic compartment), j_{stid} describes the action of synaptic stimuli (for the dendritic compartment). g_{AMPA} is AMPA-channel maximum conductivity, g_{NMDA} is maximum conductivity of NMDA-channel, E_{NMDA} and E_{AMPA} are reversal potentials of the channels. In our work conductivity of AMPA-receptors did not depend on variable u . The form of NMDA-receptors conductivity $g_{NMDA}(u)$ was taken from [8]. Concentration of Mg^{2+} was considered to be constant.

II. DYNAMICS OF THE ISOLATED COMPARTMENTS OF THE MODEL

A. Bifurcation Analysis

As compartments of the model are described by the same FitzHue-Nagumo equations with different values of small parameters, we considered bifurcations of a compartment:

$$\begin{aligned}\dot{u} &= f(u) - v + j + j_{sti}, \\ \dot{v} &= \varepsilon(g(u) - v),\end{aligned}\quad (3)$$

for different values of parameters ε , j and α without external stimulus ($j_{sti}=0$).

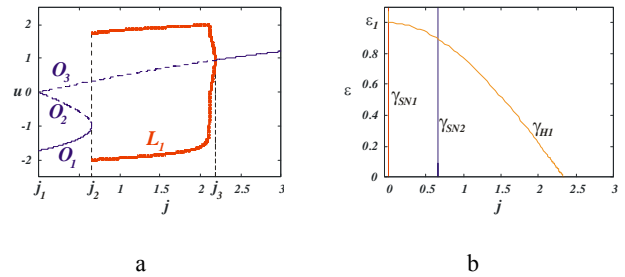


Fig. 3. One-parametric (a) and two-parametric (b) bifurcation diagrams for $\alpha=0.01$. In (a) the heavy line shows the limit cycle, thin lines demonstrate equilibria (O_1 , O_2 and O_3); solid and dashed lines correspond to stable and unstable solution, respectively. In (b) curves γ_{SN1} and γ_{SN2} correspond to saddle-node bifurcations, curve γ_{HI} corresponds to Andronov-Hopf bifurcation.

Consider the case $\varepsilon=0.1$ and $\alpha=0.01$. For $j < j_1$ only one stable equilibrium – stable node O_1 exists on phase plane (fig. 3a). At $j=j_1$ saddle-node bifurcation takes place, and saddle O_2 and unstable node O_3 appear. Three equilibria co-exist on the phase plane of system (3) up to the value of the control parameter $j=j_2$ ($j \in (j_1, j_2)$). A saddle-node separatrix loop bifurcation occurs here: O_1 and O_2 disappear, and a limit cycle L_1 is born from heteroclinic connection. At $j=j_3$ Andronov-Hopf bifurcation takes place: limit cycle disappears and equilibrium O_3 becomes stable. Thus, for the values of control parameter $j \in (j_2, j_3)$ on the phase plane of system (3) there exists only one stable attractor – limit cycle L_1 . Note that as the limit cycle was born from heteroclinic connection, its period tends to infinity for $j \rightarrow j_2$.

Such bifurcation scenario holds true within some interval of values of parameter α . Also there are two more ways of limit cycle birth (homoclinic bifurcation or subcritical Andronov-Hopf

bifurcation), but these cases will not be considered here.

A two-parametric bifurcation diagram for system (3) is presented in fig. 3b. Position of the curves corresponding to saddle-node bifurcations does not depend on parameter ε . As Andronov-Hopf bifurcation takes place at smaller values of parameter j , at $\varepsilon = \varepsilon_l$ there is a merge point of curves γ_{SN1} and γ_{H1} . This means that for $\varepsilon > \varepsilon_l$ there is no periodic solution. In other words, with increasing parameter ε the interval of parameter j , in which oscillations are observed, increases and then disappears.

B. Action of External Stimuli on Isolated Compartments

Here we consider the action of applied current j_{ext} and synaptic currents initiated by activation of AMPA- and NMDA-receptors on isolated somatic and dendritic compartments. For definiteness, let us set parameter values in the following way: $j_s = j_d = 0.48$, $\beta = 3$, $E_{NMDA} = 0$, $E_{AMPA} = 0$, $[Mg] = 10$. As was mentioned above, experimental data indicates that applied current cannot initiate substantial increase of compartment frequency, whereas synaptic stimuli are able to do so [6-10]. For instance, this concerns NMDA-current. In our model soma oscillations have an almost constant amplitude and their frequency weakly increased with the growth of parameter j_{ext} up to $j_{ext} \approx 2.25$ (fig. 4a,b). In the neighborhood of this value, the oscillation amplitude abruptly reduces to zero, while the frequency rapidly grows. Such behavior is attributed to disappearance of the limit cycle (which is the image of oscillations on the phase plane) through the supercritical Andronov-Hopf bifurcation. For the dendritic compartment, increasing of applied current results in oscillations with slower amplitude (in comparison with the soma) and rapid growth of frequency, but leads to fast activity suppression.

Activation of AMPA-receptors decreases the amplitude of soma oscillation and increases the frequency severalfold (fig. 4c,d). For the same stimulus, oscillation of the dendritic compartment has rapidly increasing amplitude and quickly decreasing amplitude. Activation of NMDA-receptors results in smaller reducing of both compartment oscillations and does not suppress their activity in a wider interval of parameter g_{NMDA} (fig. 4e,f). The frequency of soma oscillations grows only slightly, whereas dendritic

frequency increases severalfold. So, in our model activation of AMPA- and NMDA-receptors leads to different consequences: activation of both types of receptors results in drastic frequency growth, but activation of AMPA-receptors rapidly decreases oscillation amplitude, and then suppresses activity.

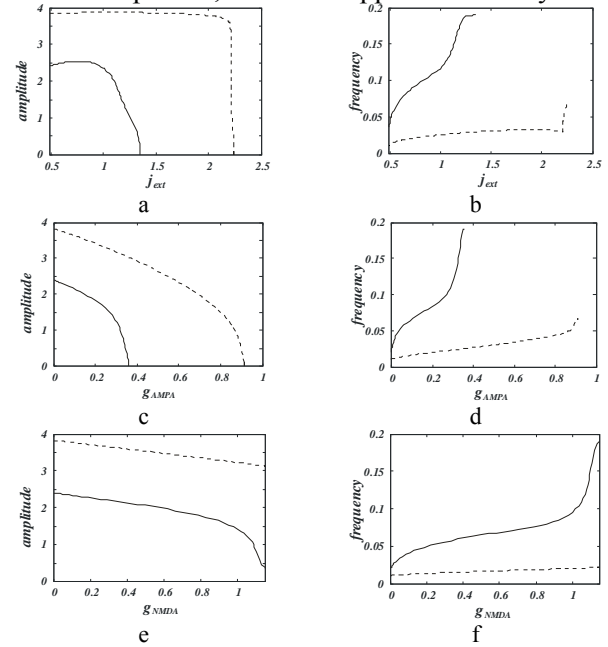


Fig. 4. Dependence of amplitude and frequency of the isolated compartments on applied current and conductivity of synapses with AMPA- and NMDA-receptors. Dashed curves correspond to the soma, solid curves correspond to the dendrite.

III. ACTION OF EXTERNAL STIMULI ON THE INTEGRAL MODEL

Electric coupling synchronizes the compartments of the model but, as the compartments are non-identical, full synchronization in system (1) is impossible. Nevertheless, even for small values of the coupling strength, frequency synchronization is observed. So we fixed the coupling strength value so as to obtain frequency synchronization ($d=5$).

Stimulation of AMPA-receptors substantially increases the frequency of oscillations and at the same time reduces their amplitude (fig. 5a,b). At $g_{AMPA} \approx 0.8$ there is suppression of neuron activity through the supercritical Andronov-Hopf bifurcation. Activation of NMDA-receptors in the same interval of parameter values results in weak reducing of oscillation amplitude only (fig. 5b). The frequency of oscillations grows slower than for activation of AMPA-receptors, hence higher values of g_{NMDA} are needed for obtaining comparable frequency (fig. 5c).

Consider parameter g_{NMDA} varying in time. Assume that (as in fig. 6a) at $t=350$ the value of g_{NMDA} increases jumpwise from 0 up to 0.4, and at $t=750$ the action of stimulation ceases. During stimulation the oscillation frequency rapidly increases, whereas the amplitude remains almost unchanged. After the end of stimulation, the neuron returns to the regime of low-frequency oscillations.

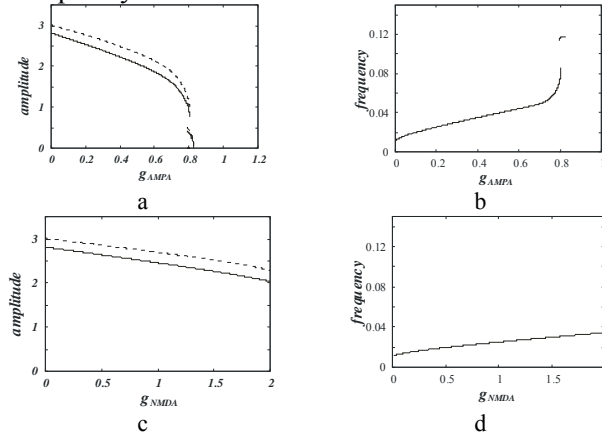


Fig. 5. Dependence of amplitude and frequency of system (1) on conductivity of synapses with AMPA- and NMDA-receptors. Dashed curves correspond to the soma ($\epsilon_s=0.06$), solid curves correspond to the dendrite ($\epsilon_d=0.6$).

IV. CONCLUSION

In the presented work we constructed the two-compartment model of dopaminergic neuron on the basis of FitzHue-Nagumo oscillators with nonlinear recovering. The compartments corresponded to the soma and the dendrite differing by the values of small parameters ϵ_s and ϵ_d ($\epsilon_s \ll \epsilon_d$). As a result the dendritic compartment had a wider region of external stimuli (j_{ext} , g_{AMPA} , g_{NMDA}) in which oscillations exist in comparison with the somatic compartment. In other words, somatic periodic activity had a rougher character than the dendritic one. Note that as was the case for the model proposed in [14], only such a functional feature underlies frequency limitation.

We considered the case of limit cycle birth through heteroclinic connection. A characteristic feature of this scenario is zero frequency (infinite period) at the bifurcation point. Any minimal external stimulus at the point results in rapid growth of oscillation frequency. It is the class 1 of spiking system by classification in [16].

Stimulation of AMPA-receptors and applied current have the same impact on the frequency of the isolated compartments. Similarly to [14], such

stimulation rapidly increases the frequency of dendrite oscillations and at the same time suppresses activity. The frequency of soma oscillations changes slower. In contrast to the model [14], there is a small difference between the amplitude of the soma and of the dendrite. As a result, activation of AMPA receptors leads to rapid reducing of oscillation amplitude but not to activity suppression as it was in [14]. Stimulation of NMDA receptors has a weaker impact. On the other hand, neuron activity suppression does not occur in a wide range of parameter g_{NMDA} . Such structural stability may underlie reliable observation of experimental oscillation frequency growth in the case of NMDA-receptors activation, whereas AMPA intensity should be set more accurately to avoid oscillation suppression.

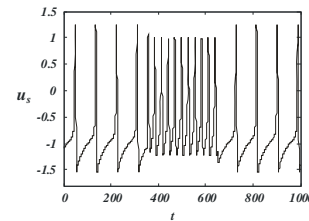


Fig. 6. High frequency burst oscillogram initiated by short time activation of NMDA-receptors (g_{NMDA} changes jumpwise from 0 at $t=350$ up to 1,2 and back to 0 at $t=750$, $j_s=j_d=0.48$).

ACKNOWLEDGMENT

The authors appreciate the support of the Russian Foundation for Basic Research (grants 08-02-97035, 09-02-91061), the Federal Agency of Education (contract № P942) and the National Science Foundation (grant DMS-0817717).

REFERENCES

- [1] P. Celada, et al., *Neuroscience* **89**, 813 (1999).
- [2] B. I. Hyland, et al., *Neuroscience* **114**, 475 (2002).
- [3] P. G. Overton and D. Clark, *Brain Res. Rev.* **25**, 312 (1997).
- [4] T. Kita, H. Kita, and S. T. Kitai, *Brain Res.* **372**, 21 (1986).
- [5] C. D. Richards, et al., *Neuroscience* **80**, 545 (1997).
- [6] P. Overton and D. Clark, *Synapse* **10**, 131 (1993).
- [7] H. Morikawa, et al., *J. Neurosci.* **23**, 149 (2003).
- [8] Y.-X. Li, R. Bertram, and J. Rinzel, *Neuroscience* **71**, 397 (1996).
- [9] C. L. Christoffersen, L. T. Meltzer, *Neuroscience* **67**, 373 (1995).
- [10] S. N. Blythe, et al., *J. Neurophysiol.* **97**, 2837 (2007).
- [11] G. S. Medvedev, N. Kopell, *SIAM J. Appl. Math.* **61**, 1763 (2001).
- [12] C. J. Wilson and J. C. Callaway, *J. Neurophysiol.* **83**, 3084 (2000).
- [13] G. S. Medvedev et al., *J. Comput. Neurosci.* **15**, 53 (2003).
- [14] A. S. Kuznetsov, et al., *J. Neurophysiol.* **95**, 932 (2006).
- [15] S. Binczak et al., *Electronics Letters* **39**, 961 (2003).
- [16] E. M. Izhikevich, *Int. J. Bif. and Chaos* **10**, 1171 (2000).

An adaptive coupling scheme for the Kuramoto model of complex networks

Bo Ning*, Jian-Li Hou*, Quansheng Ren[†], and Jianye Zhao*[‡]

*Department of Electronics, Peking University, Beijing, China 100871

[†]Mathematics in the Sciences, Max-Planck Institute, Leipzig, Germany 04103

[‡]Email: phdzjy@263.net

Abstract—There are significant interests in the research of complex network theories in recent years. One of the most attractive aspects is the synchronization of complex networks. Enlightened from the ideas of spike-timing dependent plasticity (STDP), we improve and extend an adaptive principle to complex networks with different degrees and frequency distributions within the context of the Kuramoto model. This paper mainly investigates the adaptive scheme in two kinds of complex networks. Comparing with other weighted or unweighted coupling schemes, it is shown that the adaptive coupling scheme has a better performance in phase synchronization and communication efficiency.

Index Terms—Complex networks, Phase synchronization, Adaptive coupling scheme, Heterogeneities.

I. INTRODUCTION

Since the seminal work on the small-world phenomenon by Watts and Strogatz [1], the structure and dynamics of complex networks have recently attracted lots of interests from a variety of fields [2]. In particular, the synchronization of complex networks has various applications and important research value [3, 4]. Among various different synchronization states, such as complete (CS), phase (PS), lag (LS) and generalized (GS) synchronization [5], PS [6] occupies a crucial position. In real world complex systems, such as brain and rhythmical activities, information is exchanged over the network mostly in the form of timing, such as frequency and phase, but not amplitude [7]. To study this case, the Kuramoto model [8] has been a paradigm [9].

In the collective dynamics of emergence phenomenon, efficiency is an important issue in the context of information transmission and processing, and in problems of synchronization, it is related to the connection cost [10, 11]. In order to improve the efficiency of synchronization and reduce the connection cost, heterogeneity is a key factor that one must affront [12].

In recent years, the characterization of spike-timing dependent plasticity (STDP) has attracted increasing interests [13, 14]. Enlightened from these ideas, some of us have proposed an adaptive principle [15] to generalize the Kuramoto model for the study of highly regular lattices. In this paper, we improve and extend the principle to complex networks with heterogeneous frequency and degree distributions. By simulating two kinds of complex networks and comparing the adaptive coupling scheme, it is shown that the adaptive scheme could suppress the negative effects of the heterogeneity and the phase synchronization is enhanced obviously. The remainder of the paper is organized as follows. In Sec. II, we present the new adaptive coupling scheme. Numerical experiments are carried out in Sec. III. Section IV summarizes our conclusions.

II. ADAPTIVE AND WEIGHTED COUPLING SCHEME

We consider the dynamics of an ensemble of N coupled oscillators on top of complex networks within the context of the Kuramoto model (KM). The original KM corresponding to a uniform, all-to-all, and sinusoidal coupling is described by the equations:

$$\dot{\theta}_i = \omega_i + \frac{\lambda}{N} \sum_{j=1}^N \sin(\theta_j - \theta_i) \quad (i = 1, \dots, N). \quad (1)$$

Here ω_i are natural frequencies distributed with a given probability density $g(\omega)$, θ_i are phases of individual oscillators, and λ is the coupling constant. The factor $1/N$ is introduced in order to ensure a good behavior of the model in the thermodynamic limit $N \rightarrow \infty$. In order to study the KM on top of complex networks, we reformulate Eq. 1 to the form:

$$\dot{\theta}_i = \omega_i + \sum_{j=1}^N \lambda_{ij} A_{ij} \sin(\theta_j - \theta_i) \quad (i = 1, \dots, N), \quad (2)$$

where λ_{ij} is the coupling strength between pairs of connected oscillators. A_{ij} is the connectivity matrix, i.e. $A_{ij} = 1$ if i is connected to j and $A_{ij} = 0$ otherwise.

In a previous work [15], some of us proposed a new adaptive coupling scheme ($\dot{K}_{ij} = \varepsilon [|\sin(\gamma(\theta_i - \theta_j))| K_{ij}]$) for the KM on top of regular lattices based on the essential ideas of STDP. In this paper, we develop the adaptive coupling scheme. The recent development of the weighted coupling structure aiming at the heterogeneity in topology is introduced to the new adaptive scheme [20]. The elements of the coupling matrix describing interaction between two oscillators, for instance i and j , are controlled by the following equation:

$$\frac{d\lambda_{ij}}{d(t)} = \varepsilon \left[\frac{1}{k_i^\beta} |\sin(\gamma(\theta_i - \theta_j))| \lambda_{ij} \right]. \quad (3)$$

In actual cases of weakly coupled oscillators, the phase parameter could not be obtained directly, but is represented in sine or cosine form. This is why we adopt the sinelike form in the paper. The simulation results showed that the average coupling costs of the linear and the sinelike adaptive schemes are the same [15]. For different settings of γ , the adaptive scheme corresponding to $\gamma = 0.5$ has the best performances in the average coupling cost and synchronization speed.

Rewriting the dynamic equation (3) as

$$\frac{d\lambda_{ij}}{d(\varepsilon t)} = \frac{1}{k_i^\beta} |\sin(\gamma(\theta_i - \theta_j))| \lambda_{ij},$$

we see that the parameter ε , as the time scale, only determines the evolution rate of the dynamic equation. Larger ε will accelerate the global synchronization. The combination of the parameters ε and k_i^β could adjust the adaptation range of the dynamical coupling. For fixed ε and $\beta > 0$, the larger degree a node has, the smaller coupling strength could be achieved. We adopt $\beta = 1$ to improve the performance in the aspect of the heterogeneity in topology [16]. The adaptation function $|\sin(\gamma(\theta_i - \theta_j))|$ implies that the coupling coefficients grow stronger for the pairs of oscillators which have larger phase incoherence. Fig. 1 shows the learning curves of the adaptation function for different values of γ . The curves are similar with the curve of the additive STDP learning law. The learning curve of STDP could be symmetric about origin [18] or a shifted point in X-axis [17], while the learning curve we used is symmetric about Y-axis. This difference could be ascribed to the directionality of coupling.

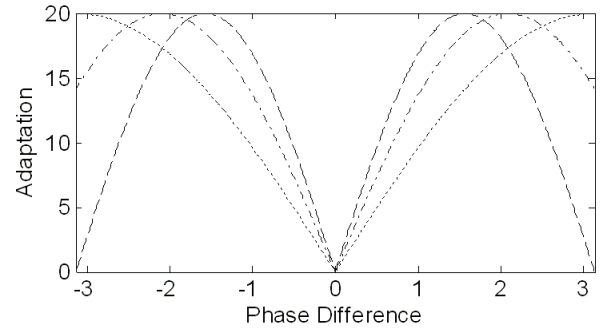


Fig. 1. The learning curves of the adaptation functions with different γ : $\gamma = 0.5$ (...), $\gamma = 0.75$ (-.-), and $\gamma = 1.0$ (-).

III. NUMERICAL EXPERIMENTS

A. Scale-free Networks

Heterogeneities both in the degrees and intrinsic frequency distributions could restrain synchronization in scale-free networks accordingly [19]. Therefore, we use the new adaptive coupling scheme (Eq.3) to enhance the synchronization of scale-free networks.

The scale-free network is produced following the BA procedure [19, 20]. Starting from a set of m_0 nodes, a new node is introduced to m ($m \leq m_0$, $m = 3$ has been set) older ones at each time step. The natural frequencies ω_i and the initial values of θ_i were randomly drawn from a uniform distribution in the interval $(-0.5, 0.5)$ and $(-\pi, \pi)$, respectively. In order to determine which pairs of nodes are synchronized and find out the clusters, we utilize the procedure proposed in [21]. The dynamical coherence of every pair of connected oscillators can be written like this:

$$D_{ij} = A_{ij} \left| \lim_{t \rightarrow \infty} \frac{1}{\Delta t} \int_{t_r}^{t_r + \Delta t} e^{i[\theta_i(t) - \theta_j(t)]} dt \right|, \quad (4)$$

where t_r is the starting time of integral. Based on the coherence matrix the authors defined a new order parameter [21]:

$$r_{link} = \frac{1}{2N_l} \sum_{i=1}^N \sum_{j=1}^N D_{ij} \quad (5)$$

which measures the fraction of links that are synchronized in the network. $N_l = \sum_{i=1}^N k_i$ is the total number of the degrees. We define the measure of average wiring cost as the average of the coupling strength over all connections in the network:

$$Cost = \left(\sum_{i=1}^N \sum_{j=1}^N K_{ij} \right) / N_l \quad (6)$$

where is the coupling strength of the connection between node i and j .

Here we compare performances of five different coupling schemes under the same configurations and average wiring cost (Eq. 6):

$$\text{1st Scheme : } \lambda_{ij}^{adp} = \varepsilon \left[\frac{1}{k_i^\beta} |\sin(\gamma(\theta_i - \theta_j))| \lambda_{ij} \right], \quad (3)$$

$$\text{2nd Scheme : } \lambda_{ij}^{d\&f} = C_{d\&f} |\omega_i - \omega_j|^\mu / k_i^\beta, \quad (7)$$

$$\text{3rd Scheme : } \lambda_{ij}^{dgr} = C_{dgr} / k_i^\beta, \quad (8)$$

$$\text{4th Scheme : } \lambda_{ij}^{frq} = C_{frq} |\omega_i - \omega_j|^\mu, \quad (9)$$

$$\text{5th Scheme : } \lambda_{ij}^{equ} = C_{equ}. \quad (10)$$

and are set to be 1 in the schemes. The weights of the second coupling schemes (Eq. 7) correlate with both the heterogeneities in intrinsic frequency and reverse degrees while the third (Eq. 8) the fourth (Eq. 9) coupling schemes correlate with the heterogeneity in intrinsic frequency or reverse degrees respectively. The fifth scheme (Eq. 10) has coupling distribution with equal strength. In the last four schemes, the constants C are set with different values to achieve different coupling strength.

Fig. 2 displays the obtained order parameters versus the average wiring cost of the five coupling schemes. From the figures we see that the adaptive coupling scheme (1st Scheme) has the best performance of global synchronization. In order to achieve large fractions ($r_{link} \geq 80\%$ in Fig. 2) of all possible links that are synchronized in network, the adaptive coupling scheme has faster speed than the other four schemes.

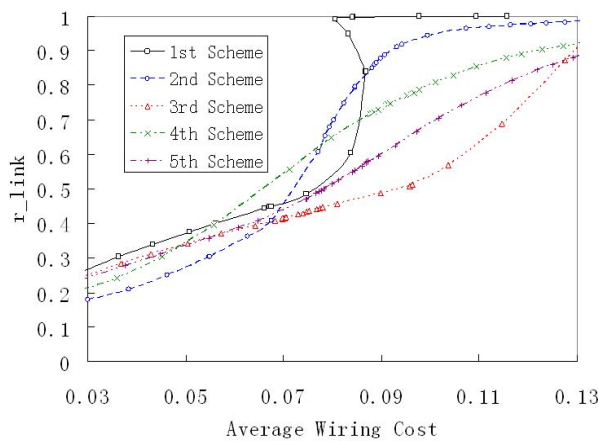


Fig. 2. r_{link} of the five schemes under same average wiring cost on top of the scale-free network. The network size is 1000.

B. Modular Networks

Many complex networks in nature have several levels and are composed of certain sub-networks with differentiated internal and external connectivity that form communities. This kind of networks is named as Modular Networks [22]. An example of these modular networks is the mammalian brain [23]. In light of the results of above sub-sections we apply the adaptive scheme to modular networks in this sub-section. A common benchmark of random network with community structure on several hierarchical levels [22] is utilized. We prescribe 16 areas that represent the first organizational level, each one embedding 16 nodes. At the second organization level of the network, we prescribe 4 compartments, each one embedding four different areas of the first level. The initial values of θ_i are randomly selected from a uniform distribution in the interval $(-\pi, \pi)$.

We compare the adaptive scheme with constant coupling scheme in modular networks under same configurations and same average wiring cost. The synchronization matrix B is utilized to describe the collective behavior of the oscillator system. The elements of the synchronization matrix B of clusters could have only two values, i.e. 0 and 1. If the value is 1, it implies that the corresponding pair of oscillators have synchronized. We multiply the elements of matrix B with the frequencies, and visualize them with color code in the two columns of Fig. 3.

From the figures we see that when the average wiring cost is extremely small (0.0064, for instance), the two schemes could not achieve synchronization either in all areas (Fig. 3 a1 and a2). However, when the first organizational level of the adaptive coupling scheme has achieved synchronization (Fig. 3 b2) and the average wiring cost achieves 0.021, only a few areas of the constant scheme achieve synchronization on the first organization level, whereas in the rest areas only a few nodes get synchronized (Fig. 3 b1). Moreover, when the average wiring cost achieves 0.0434, the second organizational level of the adaptive scheme achieves synchronized (Fig. 3 c2), but the constant coupling scheme only gets synchronized on the first level and none compartments in the second level is synchronized (Fig. 3 c1). These imply that the adaptive coupling scheme has better synchronization performance than constant coupling scheme in efficiency.

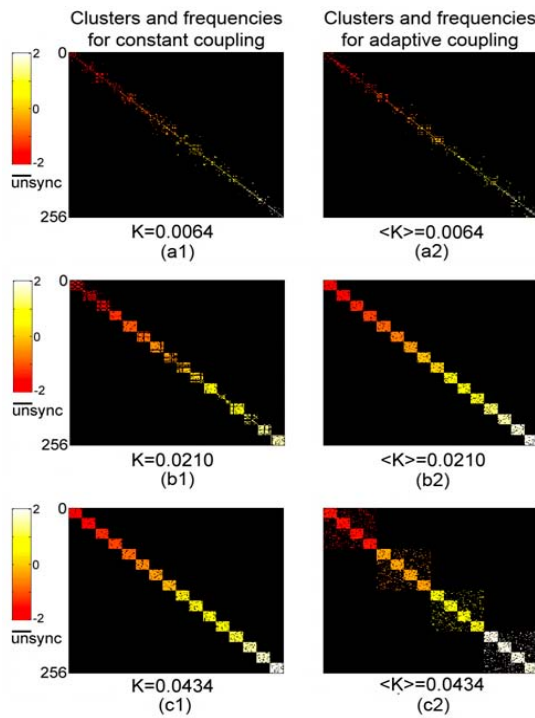


Fig. 3. We represent the clusters and frequencies of the oscillators. The plots of the two-dimension figures denote the items of the synchronization matrix B . The color code denotes the frequency. The average wiring cost is labeled under each figure.

IV. CONCLUSION

In this paper we investigate the synchronization issues of a developed adaptive coupling scheme in complex networks of Kuramoto phase oscillators. Our main concern is the migration of the negative effects introduced by the heterogeneities in intrinsic frequency and degree distributions. The idea of the adaptive coupling law is enlightened from the developments of the brain and neural science, especially from the character of the STDP. We study the adaptive coupling scheme on top of two kinds of complex networks. Simulation results reveal that the adaptive scheme has good performance in efficiency and could achieve a more reasonable coupling dynamics.

ACKNOWLEDGMENT

This work is supported by NSF China, Grand No.60704040.

REFERENCES

- [1] D.J. Watts, S.H. Strogatz, "Collective dynamics of 'small-world' networks," *Nature*, vol. 393, pp.440-442, Apr. 1998.
- [2] S. Boccaletti, V. Latora, Y. Moreno, M. Chavez, and D.-U. Hwang, "Complex networks: Structure and dynamism," *Phys. Rep.*, vol.424, pp.175-308, Feb. 2006.
- [3] S.H. Strogatz, *Sync: The Emerging Science of Spontaneous Order*, New York: Hyperion, 2003.
- [4] S.C. Manrubia, A.S. Mikhailov, D.H. Zanette, *Emergence of Dynamical Order: Synchronization Phenomena in Complex Systems*, Singapore: World Scientific, 2004.
- [5] S. Boccaletti, J. Kurths, G. Osipov, D.L. Valladares, and C.S. Zhou, "The synchronization of chaotic system," *Phys. Rep.*, vol.366, pp.1-101, Jan. 2002.
- [6] M.G. Rosenblum, A.S. Pikovsky, J. Kurths, "Phase synchronization of chaotic oscillators," *Phys. Rev. Lett.*, vol.76, pp.1804-1807, Mar. 1996.
- [7] M.I. Rabinovich, P. Varona, A.I. Selverston, and H.D.I. Abarbanel, "Dynamical principles in neuroscience," *Rev. Mod. Phys.*, vol.78, pp.1213-1265, Nov. 2006.
- [8] Y. Kuramoto, *Chemical Oscillations, Waves, and Turbulence*, New York: Springer, 1991.
- [9] J. A. Acebrón, L.L. Bonilla, C.J.P. Vicente, F. Ritort, and R. Spigler, "The Kuramoto model: A simple paradigm for synchronization phenomena," *Rev. Mod. Phys.*, vol.77, pp.137-185, Apr. 2005.
- [10] V. Latora, M. Marchiori, "Efficient behavior of small-world networks," *Phys. Rev. Lett.*, vol.87, pp.198701, Oct. 2001.
- [11] V. Latora, M. Marchiori, "Economic small-world behavior in weighted networks," *Eur. Phys. J. B* vol.32, pp.249-263, Apr. 2003.
- [12] T. Nishikawa, A.E. Motter, Y.C. Lai, F.C. Hoppensteadt, "Heterogeneity in oscillator networks: Are smaller worlds easier to synchronize?," *Phys. Rev. Lett.*, vol.91, pp.014101, Jul. 2003.
- [13] L. F. Abbott, S. B. Nelson, "Synaptic plasticity: taming the beast," *Nat. Neurosci.*, vol.3, pp.1178-1183, Nov. 2000.
- [14] G.Q. Bi, M. Poo, "Synaptic modification by correlated activity: Hebb's postulate revisited," *Annu. Rev. Neurosci.*, vol.24, pp.139-166, Mar. 2001.
- [15] Q.S. Ren, J.Y. Zhao, "Adaptive coupling and enhanced synchronization in coupled phase oscillators," *Phys. Rev. E*, vol.76, pp. 016207, Jul. 2007.
- [16] A.E. Motter, C.S. Zhou, J. Kurths, "Enhancing complex-network synchronization," *Europhys. Lett.*, vol.69, pp.334-340, Feb. 2005.
- [17] T. Nowotny, V.P. Zhigulin, A.I. Selverston, H.D.I. Abarbanel, M.I. Rabinovich, "Enhancement of synchronization in a hybrid neural circuit by spike-timing dependent plasticity," *J. Neurosci.*, vol.23(30), pp.9776-9785, Oct. 2003.
- [18] V.P. Zhigulin, M.I. Rabinovich, R. Huerta, and H.D.I. Abarbanel, "Robustness and enhancement of neural synchronization by activity-dependent coupling," *Phys. Rev. E*, vol.67, pp.021901, Feb. 2003.
- [19] A.-L. Barabási, R. Albert, "Emergence of scaling in random networks," *Science*, vol.286, pp.509-512, Oct. 1999.
- [20] A.-L. Barabási, R. Albert, H. Jeong, "Mean-field theory for scale-free random networks," *Physica A*, vol.272, pp.173-187, Oct. 1999.
- [21] J. Gómez-Gardeñes, Y. Moreno, "Synchronizability determined by coupling strengths and topology on complex networks," *A. Arenas, Phys. Rev. E*, vol.75, pp.066106, Jun. 2007.
- [22] A. Arenas, A. Díaz-Guilera, C.J. Pérez-Vicente, "Synchronization reveals topological scales in complex networks," *Phys. Rev. Lett.* vol.96, pp.114102, Mar. 2006.
- [23] O. Sporns, G. Tononi, R. Kötter, "The human connectome: A structure description of the human brain," *PLoS Comput. Biol.* vol.1, pp.0245, Sep. 2005.

Improved Divided Chaotic Associative Memory for Successive Learning

Yohei TAKAMORI

School of Computer Science
Tokyo University of Technology
1404-1 Katakura, Hachioji, Tokyo, Japan
Email: takamori@osn.cs.teu.ac.jp

Yuko OSANA

School of Computer Science
Tokyo University of Technology
1404-1 Katakura, Hachioji, Tokyo, Japan
Email: osana@cs.teu.ac.jp

Abstract—In this paper, we propose an Improved Divided Chaotic Associative Memory for Successive Learning (IDCAMS). The proposed model is based on the Divided Chaotic Associative Memory for Successive Learning (DCAMS) which was proposed in order to improve the storage capacity. In most of the conventional neural network models, the learning process and the recall process are divided, and therefore they need all information to learn in advance. In the IDCAMS, the learning process and the recall process are not divided and its one-to-many associations ability is superior to that of the DCAMS.

Index Terms—Successive Learning, Associative Memory, Chaotic Neural Network, Multi-Winner Competition

I. INTRODUCTION

Recently, neural networks are drawing much attention as a method to realize flexible information processing. Neural networks consider neuron groups of the brain in the creature, and imitate these neurons technologically. Neural networks have some features, especially one of the important features is that the networks can learn to acquire the ability of information processing. In the field of neural network, many models have been proposed. Many of those models, the learning process and the recall process are divided, and therefore they need all information to learn in advance.

However, in the real world, it is very difficult to get all information to learn in advance. So we need the model whose learning and recall processes are not divided. As such model, the Improved Chaotic Associative Memory for Successive Learning (ICAMS)[1] and the Divided Chaotic Associative Memory for Successive Learning (DCAMS)[2] have been proposed. However, their one-to-many associations ability is low.

In this paper, we propose an Improved Divided Chaotic Associative Memory for Successive Learning (IDCAMS). The proposed model is based on the

DCAMS. In the proposed IDCAMS, the learning process and the recall process are not divided. When an unstored pattern set is given to the network, the IDCAMS can learn the patterns successively. Moreover, the one-to-many associations ability of the proposed IDCAMS is superior to that of the conventional DCAMS.

II. IMPROVED DIVIDED CHAOTIC ASSOCIATIVE MEMORY FOR SUCCESSIVE LEARNING

A. Outline of IDCAMS

Here, we explain the outline of the proposed Improved Divided Chaotic Associative Memory for Successive Learning (IDCAMS). The proposed IDCAMS has three stages; (1) Pattern Search Stage, (2) Distributed Pattern Generation Stage and (3) Learning Stage.

When an unstored pattern set is given to the network, the proposed IDCAMS distinguishes an unstored pattern set from stored patterns and can learn the pattern set successively. When a stored pattern set is given, the IDCAMS recalls the patterns. When an unstored pattern set is given to the network, the IDCAMS changes the internal pattern for input pattern set by chaos[3] and presents other pattern candidates (we call this the Pattern Search Stage). When the IDCAMS can not recall the desired patterns, the distributed pattern is generated by the multi-winners competition[4] (Distributed Pattern Generation Stage), and it learns the input pattern set as an unstored pattern set (Learning Stage).

B. Structure of IDCAMS

The proposed IDCAMS is a kind of the hetero-associative memories. Figure 1 shows the structure of the IDCAMS. This model has an Input/Output Layer (I/O Layer) composed of conventional neurons and some Distributed Representation Layers (DR Layers) composed of chaotic neurons[3]. In this model, there are the

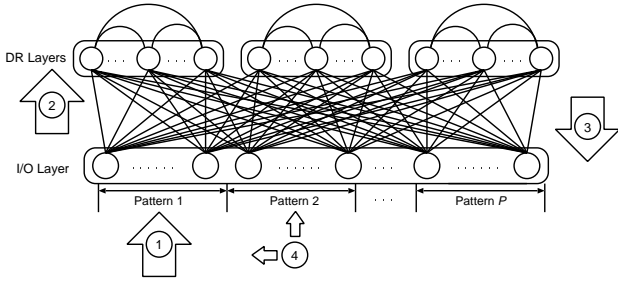


Fig. 1. Structure of Proposed IDCAMSL.

connection weights between neurons in each DR Layer and the connection weights between the Input/Output Layer and each DR Layer. As shown in Fig.1, the Input/Output Layer has plural parts. The number of parts is decided by depending on the number of patterns included in the pattern set. In the case of Fig.1, the Input/Output Layer consists of P parts corresponding to the patterns 1~ P . In this model, when a pattern set is given to the Input/Output Layer, the internal pattern corresponding to the input patterns is formed in the DR Layer. Then, in the Input/Output Layer, an output pattern set is recalled from the internal pattern. The IDCAMSL distinguishes an unstored pattern set from stored patterns by comparing the input patterns with the output patterns.

In this model, the output of the r th DR Layer at the time $t+1$, $x_i^{D_r}(t+1)$ is given by the following equations.

$$x_i^{D_r}(t+1) = \phi^D(\xi_i^r(t+1) + \eta_i^r(t+1) + \zeta_i^r(t+1)) \quad (1)$$

$$\xi_i^r(t+1) = k_s \xi_i^r(t) + \sum_{j=1}^M v_{ij}^r A_j(t) \quad (2)$$

$$\eta_i^r(t+1) = k_m \eta_i^r(t) + \sum_{j=1}^{N_r} w_{ij}^r x_j^{D_r}(t) \quad (3)$$

$$\zeta_i^r(t+1) = k_r \zeta_i^r(t) - \alpha_r(t) x_i^{D_r}(t) - \theta_i^r(1 - k_r) \quad (4)$$

In Eqs.(1)~(4), M is the number of neurons in the Input/Output Layer, v_{ij}^r is the connection weight between the neuron j in the Input/Output Layer and the neuron i in the r th DR Layer, N_r is the number of neurons in the r th DR Layer, w_{ij}^r is the connection weight between the neuron i and the neuron j in the r th DR Layer, $\alpha_r(t)$ is the scaling factor of the refractoriness in the r th DR Layer at the time t , k_s , k_m and k_r are the damping factors, and θ_i^r is the threshold of the neuron i in the r th DR Layer. $\phi^D(\cdot)$ is the following output function:

$$\phi^D(u_i) = \tanh(u_i/\varepsilon) \quad (5)$$

where ε is the steepness parameter.

The output of the neuron j in the Input/Output Layer corresponding to the internal pattern in the r th DR Layer

at the time t , $x_j^{IO_r}(t)$ is given as follows.

$$x_j^{IO_r}(t) = \phi^{IO} \left(\sum_{i=1}^{N_r} v_{ij}^r x_i^{D_r}(t) \right) \quad (6)$$

$$\phi^{IO}(u) = \begin{cases} 1 & , u \geq 0 \\ -1 & , u < 0 \end{cases} \quad (7)$$

C. Pattern Search Stage

In the Pattern Search Stage, until the IDCAMSL recalls the desired patterns, the following two procedures are repeated. If the IDCAMSL can not recall the desired patterns, when the stage is repeated T_s times (In this paper, T_s is set 10), the IDCAMSL finishes the stage.

1) *Pattern Assumption*: In the proposed IDCAMSL, only when the input patterns are given to all parts of the Input/Output Layer, the patterns are judged. When the input pattern $A_j(t)$ is similar to the recalled pattern $x_j^{IO_r}(t)$, the IDCAMSL can assume that input patterns is one of the stored patterns. The IDCAMSL outputs the pattern formed by the internal pattern in the DR Layer. The similarity rate $s(t)$ is defined by

$$s(t) = \max_r (s_1(t), \dots, s_r(t), \dots, s_R(t)) \quad (8)$$

$$s_r(t) = \frac{1}{M} \sum_{j=1}^M A_j(t) x_j^{IO_r}(t) \quad (r = 1, \dots, R) \quad (9)$$

where R is the number of the DR Layers and $s_r(t)$ is the similarity between the input pattern and the output pattern at the time t in the r th DR Layer. The IDCAMSL regards the input patterns as a stored pattern set, when the similarity rate $s(t)$ is larger than the threshold s^{th} ($s(t) \geq s^{th}$).

2) *Pattern Search*: When the IDCAMSL assumes that the input patterns are an unstored pattern set, the IDCAMSL changes the internal pattern $x_i^{D_r}(t)$ for the input pattern by chaos and presents the other pattern candidates.

In the chaotic neural network, it is known that dynamic association can be realized if the scaling factor of the refractoriness $\alpha_r(t)$ is suitable. Therefore in the proposed model, $\alpha_r(t)$ is changed as follows:

$$\alpha_r(t) = ((\alpha_{max}^r(t) - \alpha_{min}) \times (1 - s_r(t)) + \alpha_{min}) / \alpha_{DIV} \quad (10)$$

$$\alpha_{max}^r(t) = M v_{max}^r + N_r w_{max}^r \quad (11)$$

$$v_{max}^r = \max(|v_{11}^r|, \dots, |v_{ij}^r|, \dots, |v_{NM}^r|) \quad (12)$$

$$w_{max}^r = \max(|w_{11}^r|, \dots, |w_{ii'}^r|, \dots, |w_{NN}^r|) \quad (13)$$

where α_{min} is the minimum of α , $\alpha_{max}^r(t)$ is the maximum of α in the r th DR Layer at the time t , and α_{DIV} is the constant.

D. Distributed Pattern Generation Stage

In the Distributed Pattern Generation Stage, the distributed pattern corresponding to the input patterns is generated by the multi-winners competition[4].

In the proposed IDCAMSL, only one distributed pattern is generated in the r^* -th DR Layer. r^* is decided by

$$r^* = \underset{r}{\operatorname{argmin}} \left(s_{max}^1, \dots, s_{max}^r, \dots, s_{max}^R \right) \quad (14)$$

$$s_{max}^r = \max \left(s_r^1, \dots, s_r^p, \dots, s_r^P \right) \quad (15)$$

$$s_r^p = \frac{1}{M_p} \sum_{j=1}^{M_p} A_j^p(t) x_j^{IO_{rp}}(t) \quad (16)$$

where R is the number of DR Layers, P is the number of parts decided by depending on the number of patterns included in the pattern set, $A_j^p(t)$ is the strength of the external input j of the part p at the time t , $x_j^{IO_{rp}}(t)$ is the output of the neuron j of the part p in the Input/Output Layer corresponding to the internal pattern in the r -th DR Layer at the time t , s_r^p is the similarity rate between $A_j^p(t)$ and $x_j^{IO_{rp}}(t)$ and M_p is the number of neurons of the part p in the Input/Output Layer.

In the proposed model, r^* is decided by Eqs.(14)~(16). Therefore, patterns that have common parts are properly stored in different module.

1) Calculation of Outputs of Neurons in I/O Layer:

When the input pattern $A(t)$ is given to the Input/Output Layer, the output of the neuron j in the Input/Output Layer x_j^{IO} is given by

$$x_j^{IO} = \phi^{IO}(A_j(t)). \quad (17)$$

The output function $\phi^{IO}(\cdot)$ is given by Eq.(7).

2) Calculation of Initial Output of Neurons in DR Layer:

The output of the neuron i in the r^* -th DR Layer $x_i^{D_{r^*}(0)}$ is calculated by

$$x_i^{D_{r^*}(0)} = \phi^D \left(\sum_{j=1}^M v_{ij}^{r^*} x_j^{IO} \right) \quad (18)$$

where $v_{ij}^{r^*}$ is the connection weight from the neuron j in the Input/Output Layer to the neuron i in the r^* -th DR Layer and M is the number of neurons in the Input/Output Layer. The output function $\phi^D(\cdot)$ is given by Eq.(5).

3) Competition between Neuron in DR Layer:

The competition dynamics is given by the following equation:

$$x_i^{D_{r^*}} = \phi^D \left(\sum_{i'=1}^{N_{r^*}} w_{ii'}^{r^*} x_{i'}^{D_{r^*}} \right) \quad (19)$$

where $x_{i'}^{D_{r^*}}$ is the output of the neuron i' in the r^* -th DR Layer, $w_{ii'}^{r^*}$ is the connection weight between the neuron i and the neuron i' in the r^* -th DR Layer and N_{r^*} is the number of neurons in the r^* -th DR Layer.

E. Learning Stage

In the Pattern Search Stage, if the IDCAMSL can not recall the desired pattern set, it learns the input pattern set as an unstored pattern set. The Learning Stage has two phases; (1) Hebbian Learning Phase and (2) anti-Hebbian Learning Phase. By this learning, the connection weights are changed to learn the input patterns.

1) *Hebbian Learning Phase:* In the Hebbian Learning Phase, until the similarity rate $s(t)$ becomes 1.0, the update of the connection weights is repeated.

If the signs of the outputs of two neurons are same, the connection weight between these two neurons is strengthened.

The connection weight between the Input/Output Layer and the DR Layer $v_{ij}^{r^*}$ and the connection weight in the DR Layer $w_{ii'}^{r^*}$ are updated as follows:

$$v_{ij}^{r^*(new)} = v_{ij}^{r^*(old)} + \gamma_v^+ x_i^{D_{r^*}(comp)} A_j(t) \quad (20)$$

$$w_{ii'}^{r^*(new)} = w_{ii'}^{r^*(old)} + \gamma_w^+ x_i^{D_{r^*}(comp)} x_{i'}^{D_{r^*}(comp)} \quad (21)$$

where γ_v^+ is the learning rate of the connection weight $v_{ij}^{r^*}$ in the Hebbian Learning Phase, and γ_w^+ is the learning rate of the connection weight $w_{ii'}^{r^*}$ in this phase.

2) *Give Up Function:* When the similarity rate $s(t)$ does not become 1.0 even if the connection weights are updated T_n times, the IDCAMSL gives up to memorize the pattern set. If the IDCAMSL gives up to learn the pattern set, the anti-Hebbian Learning Phase is not performed.

3) *Anti-Hebbian Learning Phase:* The anti-Hebbian Learning Phase is performed after the Hebbian Learning Phase. In this phase, the connection weights $v_{ij}^{r^*}$ and $w_{ii'}^{r^*}$ are changed in the opposite direction in the case of the Hebbian Learning Phase. The anti-Hebbian learning makes the relation between the patterns is learned without destroying the stored patterns.

In this phase, $v_{ij}^{r^*}$ and $w_{ii'}^{r^*}$ are updated by

$$v_{ij}^{r^*(new)} = v_{ij}^{r^*(old)} - \gamma_v^- x_i^{D_{r^*}(comp)} A_j(t) \quad (22)$$

$$w_{ii'}^{r^*(new)} = w_{ii'}^{r^*(old)} - \gamma_w^- x_i^{D_{r^*}(comp)} x_{i'}^{D_{r^*}(comp)} \quad (23)$$

where γ_v^- ($\gamma_v^- > \gamma_v^+ > 0$) is the learning rate of the connection weight $v_{ij}^{r^*}$ in this phase, and γ_w^- ($\gamma_w^- > \gamma_w^+ > 0$) is the learning rate of the connection weight $w_{ii'}^{r^*}$ in this phase.

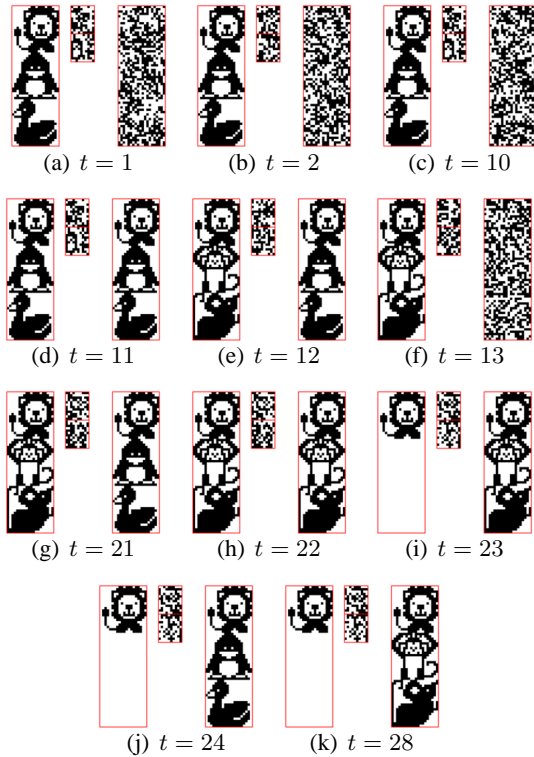


Fig. 2. Successive Learning in Proposed Model.

III. COMPUTER EXPERIMENT RESULTS

In this section, we show the computer experiment results to demonstrate the effectiveness of the proposed IDCAMSL.

A. Successive Learning and One-to-Many Associations

Figure 2 shows the successive learning and one-to-many associations in the proposed IDCAMSL. As seen in Fig.2, the patterns “lion”, “penguin” and “duck” were given to the network at $t=1$ and “lion”, “monkey” and “mouse” were given to the network at $t=12$. Then these pattern sets were trained as new patterns. At $t=23$, the pattern “lion” was given to the network, then the IDCAMSL recalled pattern sets corresponding to the input pattern. From these results, we confirmed that the proposed IDCAMSL can learn patterns successively and realize one-to-many associations.

B. One-to-Many Associations Ability

Here, we examined the one-to-many associations ability of the proposed IDCAMSL. In this experiment, we used the IDCAMSL which has 200 neurons in the Input/Output Layer and 300 neurons in the DR Layer. We used random patterns which have one-to-many relations, and the only common parts were given to the network

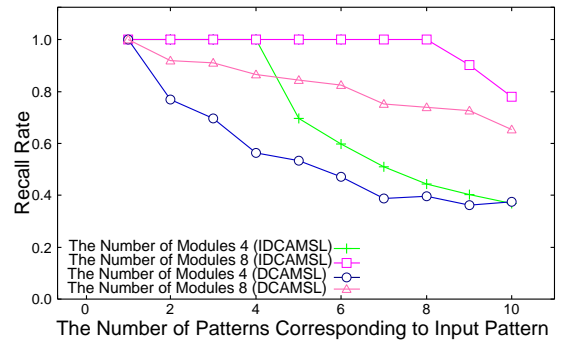


Fig. 3. One-to-Many Associations Ability.

in this experiment. Figure 3 shows the average of 100 trials. In this figure, the horizontal axis is the number of patterns in one-to-many relation, and the vertical axis is the ratio of the number of recalled patterns divided by the number of patterns corresponding to the input pattern. In this figure, the one-to-many associations ability of the Divided Chaotic Associative Memory for Successive Learning (DCAMSL)[2] is also shown for reference. From these results, we confirmed that the one-to-many associations ability of the proposed IDCAMSL is superior to that of the conventional DCAMSL.

IV. CONCLUSIONS

In this paper, we have proposed the Improved Divided Chaotic Associative Memory for Successive Learning (IDCAMSL) based on the DCAMSL[2]. In the proposed IDCAMSL, the learning and recall processes are not divided. When an unstored pattern set is given to the network, the IDCAMSL can learn the pattern successively. We carried out a series of computer experiments and confirmed that the proposed IDCAMSL can learn patterns successively and realize one-to-many associations, and the one-to-many associations ability of the IDCAMSL is superior to that of the conventional DCAMSL.

REFERENCES

- [1] T. Ikeya, T. Sazuka, A. Hagiwara and Y. Osana : “Improved chaotic associative memory for successive learning,” Proceedings of IASTED Artificial Intelligence and Applications, Innsbruck, 2007.
- [2] T. Hada and Y. Osana : “Divided chaotic associative memory for successive learning,” Proceedings of International Conference on Neural Information Processing, Auckland, 2008.
- [3] K. Aihara, T. Takabe and M. Toyoda : “Chaotic neural networks,” Physics Letter A, Vol.144, No.6,7, pp.333–340, 1990.
- [4] J. T. Huang and M. Hagiwara : “A multi-winners self-organizing neural network,” IEEE International Conference on System, Man and Cybernetics, pp.2499–2504, 1997.

Network motifs in STDP-driven neuronal networks

Quansheng Ren*, Kiran M. Kolwankar*[†], Areejit Samal* and Jürgen Jost*

*Max Planck Institute for Mathematics in the Sciences, Inselstr. 22, 04103 Leipzig, Germany.

Email: quren@mis.mpg.de Telephone: (49) 341-9959535

[†]Department of Physics, Ramniranjan Jhunjhunwala College, Ghatkopar (W), Mumbai 400 086, India

Abstract—We study motif abundance profile in neural network models wherein the strengths of the synapses are governed by spike-timing-dependent plasticity (STDP) and compare that with the profile of real *C. elegans* neural network to identify robust qualitative features.

I. INTRODUCTION

Developments in network theory has led to statistical concepts and tools to study the structure and dynamics of complex networks [1]. Using these concepts, it was shown that large-scale structure of neuronal networks have scale-free and small-world properties [2], [3]. For a better understanding, it is necessary to identify factors determining the structure of neuronal networks. Apart from genetical aspects and geometric constraints, some self-organization process may be envisaged to play an important role in determining the connectivity structure of neuronal networks. Since a neural network processes different sensory inputs, it should thereby adapt itself to its experiences. In biological scenario, we have the learning scheme of *spike-timing-dependent synaptic plasticity* (STDP) [4] which says that a synapse is strengthened when the presynaptic neuron fires shortly before the postsynaptic one, and the synapse is weakened instead when this temporal order is reversed. In particular, during the development of neuronal network, some synapses may become extremely weak to be entirely eliminated. For example, it is known that the brain has a very dense population of synaptic connections just after the birth and most of these connections are pruned in the course of development [5]. Such a pruning takes place even in the smaller size *C. elegans* network [6]. This pruning is reflected by the irreversible deletion of synapses with strength below a certain threshold.

Recent initial explorations to test this line of thinking have been encouraging leading to important insights on large-scale structure of neuronal networks [7], [8]. In Ref.[7], some of us have considered a simple model of coupled chaotic maps wherein the coupling strengths changed according to a STDP learning rule. It was shown

that starting from a globally coupled network a stationary network with a broad degree distribution was obtained [7]. Similar results were obtained in Ref.[8] using a continuous Fitzugh-Nagumo model. These developments suggest that the STDP learning dynamics may play an important role in determining the structure of neural networks. In order to confirm this conjecture, a closer investigation of the local network structure within realistic neuron model networks driven by STDP learning rule needs be performed.

In this paper, we have studied realistic neuronal models with STDP learning rule and show that STDP-driven evolved networks are similar to the real network in *C. elegans* in their local wiring structure. We have compared the local structure of STDP-driven evolved networks with real *C. elegans* network by studying the occurrence of different network motifs. Network motifs are patterns (sub-graphs) that recur within the network much more often than expected at random [9]. The characterization of complex networks using their network motif profile has become very popular owing to the fact that different subnetworks are thought to carry out different functions in the network and the abundance of certain subnetworks can decide the overall character of the network.

II. METHODS

A. Neuron models

In this paper, we study two neuronal models: the Leaky Integrate-and-Fire (LIF) model and the Hodgkin-Huxley (HH) model using the NEST Simulation Tool [10]. The parameter values for our simulations of the LIF model were taken from Ref. [11] and HH model from Ref. [12]. We do not consider inhibitory synapses that are extremely rare between interneurons in the *C. elegans* network [13]. In both models, the synaptic conductance $g_i(t)$ is given by $g_i(t) = g_m \sum_{j=1}^N w_{ij}(t) \sum_k f(t - t_j^k)$, where N is the number of neurons, g_m is the maximum value of the synaptic conductance, w_{ij} is the weight of the synaptic connection from the i th neuron to the j th neuron, $f(t)$ describes the shape of the postsynaptic

current, t_j^k is the timing of the k th spike of the j th neuron.

B. STDP learning rule

In our simulations, the weights of different synaptic connections, w_{ij} , get modified (Δw_{ij}) via a STDP learning rule which depends on the temporal difference $\Delta t = t_j - (t_i + \tau_d)$, where t_j and t_i are the spike time of the postsynaptic neuron j and presynaptic neuron i , respectively, and τ_d is the delay time of the spike transmission from neuron i to neuron j . The weight modification factor Δw_{ij} is given by the equation:

$$\Delta w_{ij}(\Delta t) = \begin{cases} \lambda \exp(-|\Delta t|/\tau_+) & \text{if } \Delta t \geq \tau_d \\ -\lambda \alpha \exp(-|\Delta t|/\tau_-) & \text{if } \Delta t < \tau_d, \end{cases} \quad (1)$$

where learning rate $\lambda = 0.0001$ and w_{ij} are constrained in the range $[0, 1]$. α introduces a possible asymmetry between the scale of potentiation and depression and the time constants τ_+ and τ_- control the width of the time window.

C. Network Motifs

We have used the Mfinder software [9] by U. Alon's group to determine the three-node network motifs in our STDP-driven networks. The abundance of each subgraph i is quantified by the Z-score, $z_i = \frac{N_i^{real} - \langle N_i^{rand} \rangle}{std(N_i^{rand})}$, where N_i^{real} is the abundance of subgraph i in the real network, $\langle N_i^{rand} \rangle$ and $std(N_i^{rand})$ are the mean and standard deviation of abundance of subgraph i in an ensemble of 1000 random networks generated by preserving the same number of incoming, outgoing and mutual edges at each node compared to the real network. If $z_i > 0$ ($z_i < 0$) then the subgraph i is over-represented (under-represented) and is designated as a motif (anti-motif) [9]. The significance profile (SP) of different subgraphs in a network is the vector of Z-scores normalized to length 1: $SP_i = z_i / \sqrt{\sum_{i=1}^{13} z_i^2}$. SP shows the relative significance of subgraphs and is important for comparison of networks of different sizes and degree sequences [14].

III. EVOLUTION OF NEURAL NETWORKS WITH STDP

A. Basic phenomena

We start our simulations of the STDP-driven pruning process with an all-to-all connected network where neurons are stimulated by different periodic patterns repeatedly with period $T_{pattern}$. We truncate all the patterns from Poisson spike trains with the same average firing rate $f_{Poisson} = 50\text{Hz}$. This average firing rate corresponds to a 20ms spike interval and is consistent

with the width of STDP time window. In all cases, the peak synaptic conductances and the neuron potentials are initialized with a random uniform distribution. Most of the peak synaptic conductances are pushed toward zero or g_m after development. The threshold for synaptic pruning is set to $g = 0.005\text{nS}$. We analyze the occurrence of triad motifs in the resulting steady-state network of the investigated neuronal models.

We follow the above-outlined approach to study four cases with different configurations. We refer to the first case as “basic configuration”, and the later cases are variations of the first case. In the “basic configuration”, we simulate a network of $N = 100$ LIF neurons which is similar in size to the *C. elegans* subnetwork of somatic interneurons. An asymmetric time window $\tau_+ = 16.8\text{ms}$ and $\tau_- = 33.7\text{ms}$ was used in the STDP rule which provides a reasonable approximation of the observed synaptic modification in actual experiments [15]. We take $\alpha = 0.525$ along with the asymmetric time window resulting in the ratio $A_- \tau_- / A_+ \tau_+ = 1.05$ similar to that in Ref. [11]. We set the other parameters as follows: the synaptic delay $\tau_d = 10\text{ms}$, the maximum peak synaptic conductance $g_m = 0.3\text{nS}$, and the period of input patterns $T_{pattern} = 2\text{s}$. We also study three variations of the “basic configuration”: “Symmetric configuration”, where the asymmetric time window is replaced with a symmetric one ($\tau_+ = \tau_- = 20.0\text{ms}$), and $\alpha = 1.05$ to preserve the ratio $A_- \tau_- / A_+ \tau_+ = 1.05$; “HH model configuration”, where LIF model is replaced by the HH model; “Large network configuration”, where the network size is enlarged to 200 neurons, and $g_m = 0.2\text{nS}$. For all four cases, we repeat our simulations 10 times with different input patterns and initial values.

The SPs of triads for the four configurations mentioned above along with that for the *C. elegans* neuronal network is shown in Fig. 1. It is seen that all four STDP-driven evolved networks have very similar SPs with triads 7, 9 and 10 as motifs, and triads 1, 2, 4, and 5 as anti-motifs, as in the SP of the *C. elegans* network which belongs to the second superfamily reported in [14]. The SP curves for the four STDP-driven evolved networks are even more similar to the *C. elegans* subnetwork of interneurons. We find that this phenomenon does not depend on the neuron model, the symmetry of the time window or the network size, and thus must reflect some intrinsic characteristic of STDP. Recently, it was shown that the three motifs, feedforward loop (FFL; triad 7) and the mixed-feedforward-feedback loops (MFFL1, MFFL2; triad 9, 10) perform important neural computation and cognition tasks in the cell providing

an explanation for the abundance of these motifs in the real network [16]. Our results show that STDP may be a potential mechanism which could develop these important motifs abundant in neuronal networks in second superfamily [14].

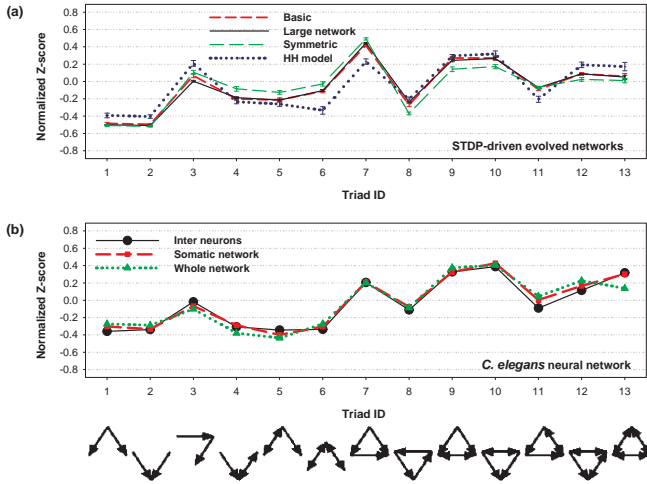


Fig. 1. Comparison of SPs for (a) four different STDP-driven evolved networks and (b) *C. elegans* neuronal networks (the sub-network of somatic interneurons, the somatic network, the whole neuronal network using the old wiring diagram [17]). We also show the triad subgraph dictionary in this figure.

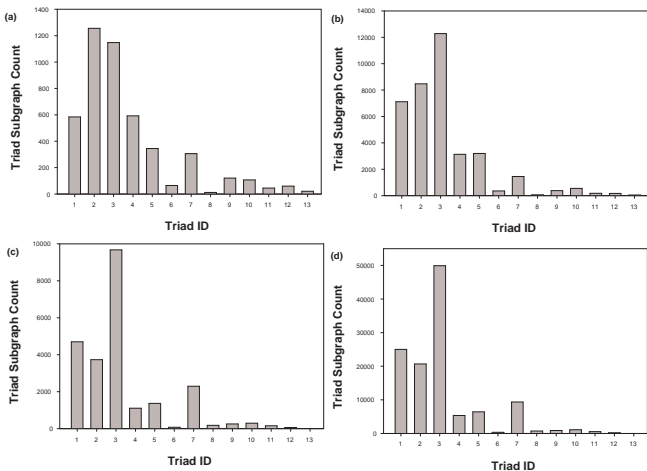


Fig. 2. Comparison of triad frequency spectra for STDP-driven evolved networks and *C. elegans* neuronal network. (a) subnetwork of somatic interneurons and (b) somatic network in *C. elegans*. STDP-driven evolved networks in (c) basic and (d) large network configurations.

There are small differences between our evolved networks and the subnetwork of interneurons in *C. elegans* like triads 1, 2 and 8 have relatively lower negative SP, while triads 3 and 7 have relatively higher positive

SP compared to the *C. elegans* neuronal network (cf. Fig. 1). STDP tends to form feedforward structures [18] and reflect the causal relations between neurons, which could lead to over-representation of cascades (triad 3) and FFL (triad 7), and under-representation of cycles (triad 8). On the other hand, we have neglected other mechanisms such as short-term plasticity and hundreds of gap connections that are present in *C. elegans*. The neuron models and parameter setting may also be different from *C. elegans*. Since, all these factors could influence the results and have not been accounted in the simulated models, the reported similarities between the evolved and real networks are even more striking. In Fig. 2 we see that the STDP-driven evolved network for the “basic configuration” even develops a similar triad frequency spectra as that of *C. elegans*.

B. The role of neuronal inputs.

We have simulated neurons with other spike trains such as stochastic Poisson spike trains and periodic regular patterns apart from periodic patterns obtained from Poisson spike trains. For these different spike trains, we either do not obtain a steady distribution of peak synaptic conductances or else find a similar SP. The complexity of correlations between neuronal inputs is crucial for the similarities in SPs.

Based on our simulations, there seems to be two ways to achieve a constant distribution of peak synaptic conductances through STDP: one to use constant temporal correlations between inputs and the other through repeated input of the same temporal sequences [19]. To investigate the first case, we utilize a simple method to generate sufficiently complex temporally correlated inputs: A non-periodic Poisson spike train with average firing rate 50Hz is randomly delayed 100 times to generate the inputs for 100 neurons. The random delay time T_d follows a uniform distribution between [1ms, T], and we have studied two cases: T=20ms and T=200ms. Considering that the width of time window in STDP and average spike interval are both ≈ 20 ms, the case T=20ms corresponds to a simple relation structure of temporal correlations between neuronal inputs, while the case T=200ms corresponds to a more complex relation structure. In Fig. 3(a), we see for the case T=200ms, the SP is quite similar to that of network of interneurons in *C. elegans*, and the only difference lies in the abundance of triad 12. However, for the case T=20ms, we do not obtain similar result. Thus, STDP may play a fundamental role in development of the local structure of neuronal networks, but we should also pay attention to the complexity

of correlations between neuronal inputs. However, this simple scheme of temporally correlated inputs did not generate a triad frequency spectrum similar to that of *C. elegans* (cf. Fig. 3(b-c)). For the case $T=200\text{ms}$, we get more triads corresponding to feedforward structures, i.e. cascades (triad 3), FFL (triad 7) and MFFL (triad 9 and 10), but did not obtain any subgraph corresponding to triads 6, 8 and 11. This may be because the correlation scheme we utilize here is not complex enough compared to real scenario. In *C. elegans*, because of the stochastic characteristic in the environment, inputs of interneurons could have very complex temporal correlations.

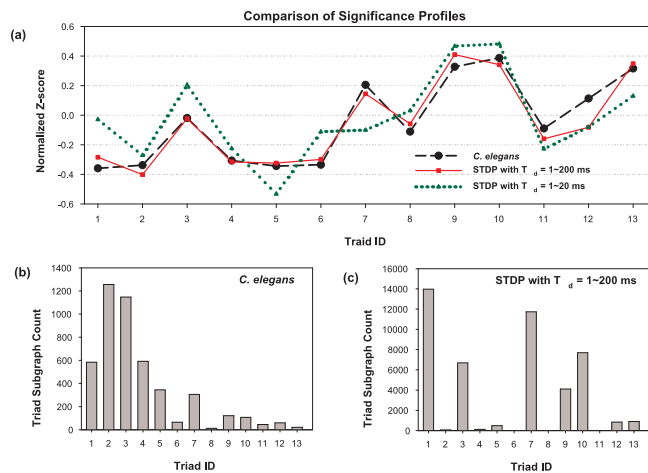


Fig. 3. Comparison of SPs and triad frequency spectra for the *C. elegans* interneuron subnetwork and STDP-driven evolved networks with correlated stochastic inputs.

IV. CONCLUSIONS

Our simulations mimic the STDP pruning process during course of development within realistic neuronal models where neurons are stimulated with periodic or complex temporally correlated spike trains. In the resultant STDP-driven evolved networks, three triads FFL, MFFL1 and MFFL2, which perform important neural computation and cognition tasks, were over-represented compared to randomized networks. The SPs of STDP-driven evolved networks are similar to that in the *C. elegans* neuronal network, especially the subnetwork of interneurons. Also, the triad frequency spectrum of STDP-driven evolved network in certain configurations is similar to that of *C. elegans*. The exact role of neuronal input in determining the network structure is yet not clear but it seems some amount of complexity is needed. The sparsity of the *C. elegans* neuronal network could be also achieved by the STDP-driven evolved network. These observations suggest that STDP-driven self-organization

could be a candidate mechanism to generate the local structure of *C. elegans* neuronal network.

ACKNOWLEDGMENT

KMK acknowledges support from Department of Science and Technology (DST), India and JJ from Volkswagen Foundation.

REFERENCES

- [1] R. Albert, A.-L. Barabasi, Statistical mechanics of networks, Rev. Mod. Phys. 74 (2002) 47–97.
- [2] V. M. Eguíluz, D. R. Chialvo, G. A. Cecchi, M. Baliki, A. V. Apkarian, Scale-free brain functional networks, Phys. Rev. Lett. 94 (1) (2005) 018102.
- [3] C. J. Stam, J. C. Reijneveld, Graph theoretical analysis of complex networks in the brain, Nonlinear Biomedical Physics 1 (2007) 3.
- [4] H. Markram, J. Lübke, M. Frotscher, B. Sakmann, Regulation of synaptic efficacy by coincidence of synaptic APs and EPSPs, Science 275 (1997) 213–215.
- [5] D. L. Bishop, T. Misgeld, M. K. Walsh, W.-B. Gan, J. W. Lichtman, Axon branch removal at developing synapses by axosome shedding, Neuron 44 (4) (2004) 651 – 661. doi:DOI: 10.1016/j.neuron.2004.10.026.
- [6] W. Wadsworth, Axon pruning: *C. elegans* makes the cut, Current Biology 15 (2005) R796–R798.
- [7] J. Jost, K. M. Kolwankar, Evolution of network structure by temporal learning, Physica A 388 (2009) 1959.
- [8] C.-W. Shin, S. Kim, Self-organized criticality and scale-free properties in emergent functional neural networks, Phys. Rev. E 74 (2006) 045101(R).
- [9] R. Milo, S. Shen-Orr, S. Itzkovitz, N. Kashtan, D. Chklovskii, U. Alon, Network motifs: Simple building blocks of complex networks, Science 298 (2002) 824–827.
- [10] M.-O. Gewaltig, M. Diesmann, Nest (neural simulation tool), Scholarpedia 2 (4) (2007) 1430.
- [11] S. Song, K. D. Miller, L. F. Abbott, Competitive hebbian learning through spike-timing-dependent synaptic plasticity, Nature Neuroscience 3 (9) (2000) 919–926.
- [12] R. D. Traub, R. Miles, Neuronal Networks of the Hippocampus, Cambridge University Press, Cambridge UK., 1991.
- [13] L. R. Varshney, B. L. Chen, E. Paniagua, D. H. Hall, D. B. Chklovskii, Structural properties of the *Caenorhabditis elegans* neuronal network Submitted.
- [14] R. Milo, S. Itzkovitz, N. Kashtan, R. Levitt, S. Shen-Orr, I. Ayzenshtat, M. Sheffer, U. Alon, Superfamilies of evolved and designed networks, Science 303 (2004) 1538–1542.
- [15] G. Q. Bi, M. M. Poo, Synaptic modification by correlated activity: Hebb's postulate revisited, Annu. Rev. Neurosci. 24 (2001) 139–166.
- [16] C. Li, Functions of neuronal network motifs, Phys. Rev. E 78 (2008) 037101.
- [17] J. G. White, E. Southgate, J. N. Thomson, S. Brenner, The structure of the nervous system of the nematode *Caenorhabditis elegans*, Phil. Trans. R. Soc. Lond. B 314 (1986) 1–340.
- [18] N. Masuda, H. Kori, Formation of feedforward networks and frequency synchrony by spike-timing-dependent plasticity, J. Comput. Neurosci. 22 (2007) 327–345.
- [19] T. Nowotny, M. I. Rabinovich, Spatial representation of temporal information through spike-timing-dependent-plasticity, Phys. Rev. E 68 (2003) 011908.

An Exactly Solvable Chaotic Circuit

Ned J. Corron, Mark T. Stahl, and Jonathan N. Blakely
 U. S. Army Research, Development and Engineering Command
 RDMR-WSS, Redstone Arsenal, Alabama 35898 USA
 ned.corron@us.army.mil

Abstract— We report the construction and operation of a novel chaotic electronic oscillator for which a detailed model admits an exact analytic solution. The circuit is modeled by a hybrid dynamical system including both a continuous differential equation and a discrete switching condition. The analytic solution is written as the linear convolution of a symbol sequence and a fixed basis pulse, similar to conventional communications waveforms. Waveform returns sampled at switching times are conjugate to a shift map, effectively proving the circuit is chaotic. We show the analytic solution accurately reconstructs a measured waveform, thereby confirming the efficacy of the circuit model.

I. INTRODUCTION

It is commonly assumed that the complexity of chaos precludes straightforward analytic solution. However, this is not necessarily true [1-2]. For difference equations, it has been explicitly shown that trajectories of the shift map and baker's map can be written as the convolution of a random process and an acausal basis pulse [3]. A similar construction is available for analogous continuous-time waveforms [4-6]. Yet in some sense, these toy systems are of limited interest, since they are not derived as an accurate model for a real physical system.

In this paper, we report the construction and operation of a novel chaotic electronic oscillator for which a detailed model admits an exact analytic solution. The oscillator is a hybrid circuit, containing both analog and digital components. A mathematical model contains a second order differential equation coupled to a switching condition controlling a binary state. Importantly, the model admits an exact analytic solution, which is written as a linear convolution of a binary sequence and a fixed basis pulse. Successive returns at discrete transition times exactly satisfy a shift map, thereby proving the oscillator is chaotic.

In operation, the electronic circuit generates waveforms that closely agree with the analytic solution. Sampled at switching times, the circuit generates a shift map consistent with the analytic model. Using symbols extracted from a measured

waveform, we construct the corresponding analytic solution and find it closely matches the observed waveform. Together, these observations confirm that the exactly solvable analytic model provides a good representation of the electronic circuit.

II. ELECTRONIC CIRCUIT

A hybrid electronic oscillator, with both analog and digital components, is shown in Fig. 1. This circuit was constructed using commercially available, discrete components on a solderless breadboard. The analog operational amplifiers are all type TL082, which are powered using ± 15 V. The diodes are all type 1N4148. The digital integrated circuit is a dual positive-edge-triggered D flip flop (SN54LS74AJ), which is powered with +5 V. The digital and analog components share a common ground.

In the figure, certain analog components are grouped by dashed boxes. The grouping labeled $-R$ comprises an active circuit realizing a negative resistor. The grouping labeled L is an impedance converter providing a nearly ideal inductor. Also significant is the capacitor labeled C , which connects $-R$ and L to a virtual ground provided by an operational amplifier. For the nominal circuit values shown in the figure, we have $C = 1.3 \mu\text{F}$, $L = 2.7 \text{ H}$, and $-R$ is tunable by a variable resistor.

The left side of this circuit is a standard RLC harmonic oscillator, except the resistance is negative. Thus, this part of the circuit is modeled as

$$C \frac{dv}{dt} - \frac{v}{R} + i = 0, \quad L \frac{di}{dt} = v - v_s \quad (1)$$

where v is the tank voltage, i is the current through the inductor, and v_s is a feedback voltage applied to the inductor. We introduce the dimensionless time

$$\tau = \frac{t}{T} \quad (2)$$

where

$$T = 2RC\omega \sqrt{\frac{L}{4R^2C - L}} \quad (3)$$

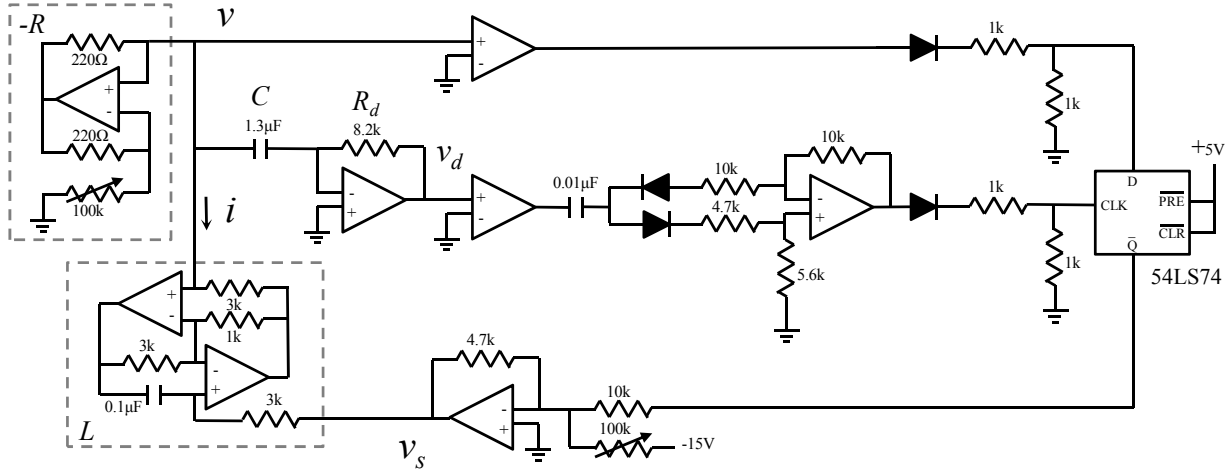


Fig. 1. Chaotic hybrid oscillator circuit.

and $\omega = 2\pi$. As we show below, the period T is the return time for the oscillator. Equations (1) are then written as

$$\frac{d^2v}{d\tau^2} - 2\beta \frac{dv}{d\tau} + (\omega^2 + \beta^2)(v - v_s) = 0 \quad (4)$$

where the parameter

$$\beta = \frac{T}{2RC} \quad (5)$$

is the dimensionless negative damping. For the circuit, we only consider $0 < \beta \leq \ln 2$.

The right side of the schematic contains digital logic circuitry. In the top trace, an operational amplifier is configured as a comparator to detect the sign of the voltage v . The subsequent diode and voltage divider convert the saturated amplifier output to digital logic levels. The middle trace uses a current-to-voltage converter to give

$$v_d = -R_d C \frac{dv}{dt} \quad (6)$$

where R_d is the feedback resistor. A second comparator then detects the sign of this voltage. The following capacitor, diodes, and difference amplifier generate a short trigger pulse for any transition in the comparator output. Thus, the middle trace generates a trigger pulse whenever the derivative of the tank voltage v changes sign. This trigger signal is also scaled to digital logic levels.

The logic signals from the top two traces control a flip flop in a 54LS74 integrated circuit. The flip flop is configured here to store the sign of the tank voltage at the last transition in the sign of dv/dt . This output is

fed back to the oscillator via the bottom trace. A summing circuit with fixed gain shifts the digital signal to the symmetric levels $\pm V$, and the feedback signal v_s is applied to the tank inductor.

As such, the feedback circuit is modeled by the switching condition

$$\frac{dv}{dt} = 0 \Rightarrow v_s = V \operatorname{sgn}(v) + V_0 \quad (7)$$

meaning that, whenever the derivative of the tank voltage v passes through zero, the feedback voltage v_s is set to the sign of the tank voltage times the fixed magnitude V . Furthermore, the feedback voltage is held constant until the next trigger event when the derivative dv/dt vanishes. An offset voltage V_0 is included to account for any small, yet unavoidable, asymmetry in the electronic circuit.

III. ANALYTIC SOLUTION

The circuit dynamics are modeled by the ordinary differential equation (4) with the switching equation (7). Defining the dimensionless states

$$u = \frac{v - V_0}{V}, \quad s = \frac{v_s - V_0}{V} \quad (8)$$

we obtain the dimensionless hybrid system

$$\ddot{u} - 2\beta\dot{u} + (\omega^2 + \beta^2)(u - s) = 0 \quad (9)$$

and

$$\dot{u}(\tau) = 0 \Rightarrow s(\tau) = \operatorname{sgn}(u(\tau)) \quad (10)$$

where a dot represents a derivative with respect to the dimensionless time τ .

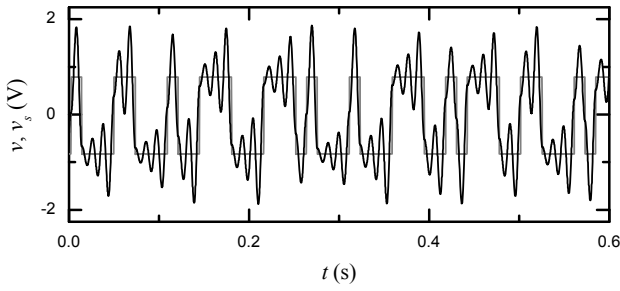


Fig. 2. Typical time series measured from the circuit. The oscillating waveform is the tank voltage v , while the square wave is the discrete switching state v_s .

Significantly, an exact analytic solution to the hybrid system (9) and (10) can be found [6]. Here we write the solution as

$$u(\tau) = \sum_{m=-\infty}^{\infty} s_m \cdot P(\tau - m), \quad s(\tau) = s_{[\tau]} \quad (11)$$

where the square brackets indicate the largest integer less than or equal to the argument, and s_m is a sequence of binary symbols, ± 1 . The basis pulse is

$$P(\tau) = \begin{cases} (1 - e^{-\beta})\rho(\tau), & \tau < 0 \\ 1 - e^{-\beta}\rho(\tau), & 0 \leq \tau < 1 \\ 0, & 1 \leq \tau \end{cases} \quad (12)$$

where

$$\rho(\tau) = e^{\beta\tau} \left(\cos \omega\tau - \frac{\beta}{\omega} \sin \omega\tau \right) \quad (13)$$

is the oscillatory component. The veracity of this solution can be confirmed by direct substitution.

We note the solution (11) satisfies $\dot{u}(n) = 0$, $\dot{u}(n + 1/2) = 0$, and $\text{sgn}(u(n + 1/2)) = \text{sgn}(u(n))$ for all integer n . Thus, the switching transitions defined by equation (10) only occur at integer dimensionless times. Significantly, successive returns at integer times satisfy the recursion relation

$$u(n+1) = e^{\beta}u(n) - (e^{\beta} - 1) \cdot s_n \quad (14)$$

which is a shift map with slope e^{β} . For $\beta > 0$, the slope of the return map is everywhere greater than one. Since the map is also closed on the unit interval for $\beta \leq \ln 2$, the shift map (14) is necessarily chaotic, implying the hybrid system is also chaotic.

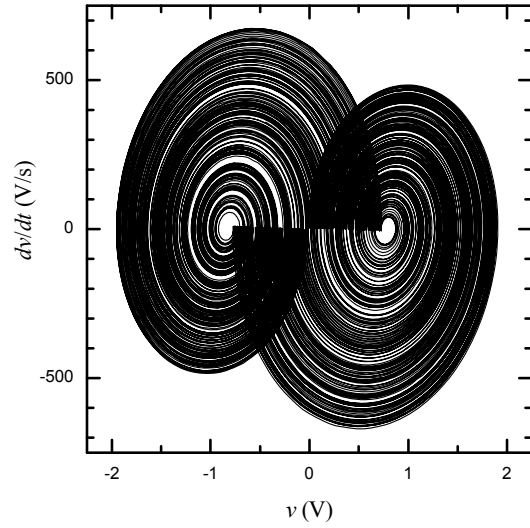


Fig. 3. Phase space projection of measured circuit waveforms.

IV. MEASURED WAVEFORM DATA

The negative resistor was adjusted to obtain chaotic dynamics. For $R \sim 6.5 \text{ k}\Omega$, the circuit oscillates chaotically with a fundamental frequency near 84 Hz. Waveforms v , v_d , and v_s were sampled at 100 kHz using a data acquisition device and a PC. To reduce sampling noise, the oversampled data were smoothed using a running average over a window of ten samples.

Fig. 2 shows a typical measured time series for the tank voltage v . Also shown is the corresponding digital signal v_s , which switches between two fixed points, $\pm V$. After each switching event, the tank voltage exhibits growing oscillations about the fixed point. When the oscillation gets large, a switching event is triggered. Fig. 3 shows a phase space projection of v and v_d for a four-second trajectory. From analysis of the measured signal v_s , we estimate the amplitude scale $V = 0.81 \text{ V}$ and offset $V_0 = -0.02 \text{ V}$.

Using the nominal circuit values and equations (3) and (5), we estimate $T = 0.012 \text{ s}$ and $\beta \doteq 0.7 \sim \ln 2$. However, more precise estimates for T and β are derived from analysis of the measured waveform. Using transitions detected in v_s , we determine the return times t_n where $dv/dt = 0$ and $|v - V_0| < V$. The average return time is $T = \langle t_{n+1} - t_n \rangle$, which gives $T = 0.0119 \text{ s}$. A return map for the successive returns $v(t_n)$ is shown in Fig. 4. This map is in agreement with the analytic solution (14), which predicts the slope

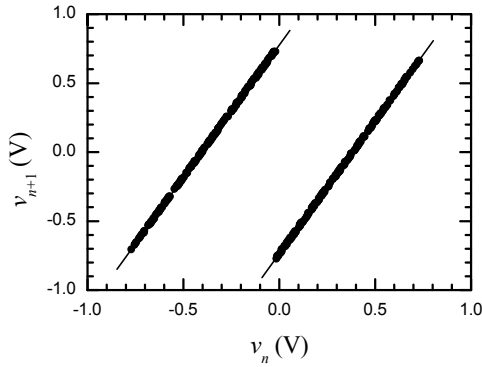


Fig. 4. Successive return map with lines fit to measured data.

$e^\beta > 1$. Using a linear least squares fit to each segment of the measured return map, we obtain $e^\beta = 1.92$, so that $\beta = 0.65$.

We also directly confirm the agreement between the oscillator circuit and the analytic model. From the measured switching signal v_s , we extract the symbol sequence s_n . For the 4-second waveform, a total of 336 symbols are obtained. Using these symbols and the precise estimates of T and β , the corresponding analytic waveform is constructed using equations (8) and (11). We note the sum in the analytic model is evaluated for just the known symbols, so the analytic solution is not exact; however, the exponential nature of the neglected terms implies the error in the truncated solution is negligible. A typical portion of the measured waveform and analytic solution are shown in Fig. 5(a). In this plot, the two waveforms overlap and are indistinguishable, which indicates remarkable agreement. In Fig. 5(b), the difference Δv between the measured waveform and analytic solution is shown on a finer scale. The close agreement between the two waveforms confirms the reliability of the circuit model.

V. CONCLUSIONS

In this paper we showed a chaotic oscillator circuit that is accurately modeled by an exactly solvable hybrid system. Although the circuit oscillates at low frequencies (~ 84 Hz), a higher frequency version of this oscillator may prove useful for technological applications of chaos. For example, the circuit provides an antipodal chaotic waveform, which may be preferable for proposed chaotic communication approaches based on encoding message signals in symbolic dynamics [7-8]. The existence of a fixed basis pulse suggests that a simple matched filter may be realized for detecting and decoding the received

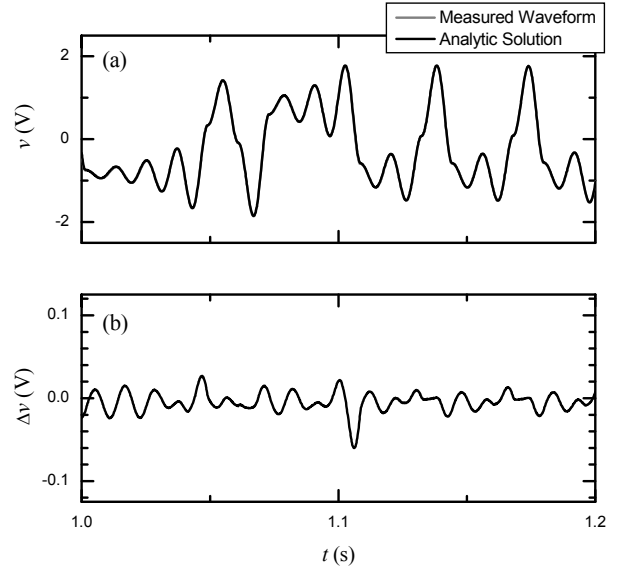


Fig. 5. A typical time series showing (a) measured circuit waveform and corresponding analytic solution and (b) magnified (20x) difference Δv between measured and analytic waveforms.

symbols. Along these lines, we have recently identified a significant relationship to the synthesis of reverse-time chaos with linear filters [9]. The development and application of a practical matched filter for chaotic oscillators is the subject of our current research efforts.

REFERENCES

- [1] S. Katsura and W. Fukuda, "Exactly solvable models showing chaotic behavior," *Physica A*, vol. 130, 597-605, April 1985.
- [2] K. Umeno, "Method of constructing exactly solvable chaos," *Phys. Rev. E*, vol. 55, pp. 5280-5284, May 1997.
- [3] D. F. Drake and D. B. Williams, "Linear, random representations of chaos," *IEEE Trans. Signal Process.*, vol. 55, pp. 1379-1389, April 2007.
- [4] S. T. Hayes, "Chaos from linear systems: implications for communicating with chaos, and the nature of determinism and randomness," *J. Phys. Conf. Series*, vol. 23, pp. 215-237, October 2005.
- [5] Y. Hirata and K. Judd, "Constructing dynamical systems with specified symbolic dynamics," *Chaos*, vol. 15, art. 033102, September 2005.
- [6] N. J. Corron, "An exactly solvable chaotic differential equation," *Dyn. Contin. Discrete Impuls. Syst. A*, vol. 16, pp. 777-788, November 2009.
- [7] S. Hayes, C. Grebogi, and E. Ott, "Communicating with chaos," *Phys. Rev. Lett.*, vol. 70, pp. 3031-3034, 17 May 1993.
- [8] E. M. Bollt, "Review of chaos communication by feedback control of symbolic dynamics," *Int. J. Bifurcations Chaos*, vol. 13, pp. 269-285, February 2003.
- [9] N. J. Corron, S. T. Hayes, S. D. Pethel, and J. N. Blakely, "Chaos without nonlinear dynamics," *Phys. Rev. Lett.*, vol. 97, art. 024101, 14 July 2006.

Complex dynamics in a new PWL chaotic circuit

Arturo Buscarino, Luigi Fortuna and Mattia Frasca

Dipartimento di Ingegneria Elettrica Elettronica e dei Sistemi, Facoltà di Ingegneria

Laboratorio sui Sistemi Complessi, Scuola Superiore di Catania

Università degli Studi di Catania, viale A. Doria 6, 95125 Catania, Italy.

Abstract—In this paper, starting from the dissipative form of the nonlinear oscillator proposed in [1], a new non-autonomous PWL chaotic circuit is designed and implemented. The circuit has been then experimentally investigated and the bifurcation diagram with respect to the frequency of the forcing signal has been experimentally derived.

I. INTRODUCTION

Since its discovery, chaos has attracted the interest of circuit engineers. On one hand, it allowed to correctly characterize phenomena appearing in some circuits and that, before, were classified as parasitic, unwanted, or multiple coexisting oscillations. On the other hand, circuit engineers directed their efforts towards the design and implementation of chaotic waveform generators. In many cases, the design of such circuits started from the equations of a mathematical model and allowed the study and characterization of the system dynamics. Electronic circuits have been in fact used to study a wide range of complex dynamics, also including strange non-chaotic attractors [2], multi-scroll attractors [3], and synchronization [4].

In this work, we take into account the following equations:

$$\begin{aligned}\dot{x} &= y - a_1x \\ \dot{y} &= -bx - a_2y + \sin(\omega t) + s(x)\end{aligned}\quad (1)$$

with $s(x) = \frac{1}{2}(|5x+1| - |5x-1|)$. Eqs. (1) represent the dissipative form of the system studied in [1]. In fact, in the limit of zero dissipation ($a_1 = a_2 = 0$) they can be rewritten as:

$$\ddot{x} + bx = \sin(\omega t) + s(x) \quad (2)$$

In the theoretical study of the conservative system (2), performed in [1], chaotic behavior in the Smale sense for $\omega = \sqrt{2}$ is proven.

In this work, we experimentally characterize this system, by implementing an analog electronic circuit governed by Eqs. (1) and showing some examples of

the different dynamics that can be obtained by varying the frequency of the forcing signal.

As it can be noticed, the nonlinearity of system (1) is a piecewise-linear (PWL) function. Since the beginning of the studies on chaos in electrical circuits, this way to define a nonlinearity has provided a simple and efficient tool for the design and analysis of chaotic circuits. The most paradigmatic autonomous circuit able to show chaotic behavior, i.e. the Chua's circuit [5], is indeed based on a PWL nonlinearity.

PWL nonlinearity is also commonly found in nonautonomous chaotic circuits. For instance, the dissipative oscillator consisting in a resistor-inductor-diode series introduced in [6] has been analyzed by using a PWL approximation of its nonlinearity. The authors disclosed, by means of circuital simulations, a period-doubling route to chaos. Other examples of PWL dissipative nonautonomous oscillators can be found in [7], [8].

Given the nature of the nonlinearity of system (1), among possible approaches for the design and implementation of electronic circuits modelling dynamical systems the approach based on the concept of State Controlled Cellular Nonlinear Network (SC-CNN) has been chosen since it provides an easy alternative design method, particularly advantageous in the case of PWL nonlinearities.

A Cellular Nonlinear Network (CNN) [9] is an analog signal processing system based on the local interaction of simple first-order nonlinear circuits: the CNN cells. The SC-CNN [10] consists in a generalization of the CNN paradigm in which CNN cells locally share information not only about their outputs, but also about their state variables. SC-CNNs have been used to implement different examples of dynamical systems [10], [11], [12].

II. THE ELECTRONIC CIRCUIT

A CNN can be defined as an array of locally interconnected first-order systems, the so-called CNN cells [9], [13]. The generic CNN cell is characterized by a state variable x_j , by an output variable y_j , and by a set of

tunable parameters that defines the interactions between cells. Among the numerous applications of CNNs (e.g. image processing and spatio-temporal phenomena emulation [14], locomotion control [15], and so on), we are interested to the property that any arbitrary dynamical system can be implemented suitably choosing the set of parameters and, thus, suitably connecting the CNN cells [10], [16], [17].

Since a CNN cell is a first-order dynamical system, the implementation of the model in Eqs. (1) requires two interconnected CNN cells. For the sake of simplicity, in the following the state equations of a SC-CNN made of two cells are given:

$$\begin{aligned} \dot{x}_1 &= -x_1 + a_{11}y_1 + a_{12}y_2 + s_{11}x_1 + s_{12}x_2 + i_1 \\ \dot{x}_2 &= -x_2 + a_{21}y_1 + a_{22}y_2 + s_{21}x_1 + s_{22}x_2 + i_2 \\ y_1 &= 0.5(|x_1 + 1| - |x_1 - 1|) \\ y_2 &= 0.5(|x_2 + 1| - |x_2 - 1|) \end{aligned} \quad (3)$$

where it should be mentioned that using the standard operational amplifiers (OP-AMPs) [10] a more general output nonlinearity is actually implemented: $y_j = 0.5(|\alpha x_j + 1| - |\alpha x_j - 1|)$.

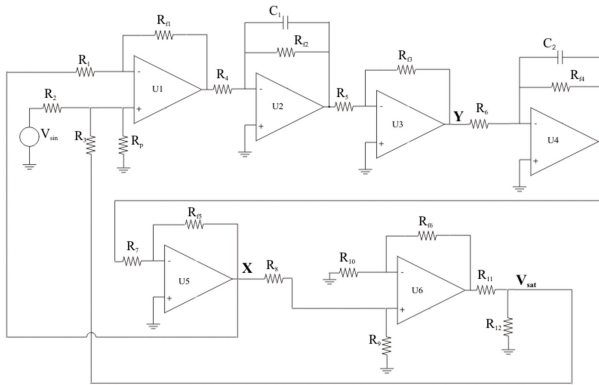


Fig. 1. The new dissipative circuit. The values of the components are the following: $R_1 = R_5 = R_7 = R_{f1} = R_{f3} = R_{f5} = R_p = 1k\Omega$, $R_2 = R_3 = R_{12} = 2k\Omega$, $R_4 = R_6 = 3.3k\Omega$, $R_8 = R_{10} = 5k\Omega$, $R_9 = R_{f6} = 470k\Omega$, $R_{11} = 16.5k\Omega$, $R_{f2} = R_{f4} = 330k\Omega$, $C_1 = C_2 = 100nF$.

In order to implement an electrical analogue of the second-order differential equation (2), let us first rewrite Eq. (2) in terms of a system of two first-order differential equations as follows:

$$\begin{aligned} \dot{x} &= y \\ \dot{y} &= -bx + \sin(\omega t) + s(x) \end{aligned} \quad (4)$$

where $s(x) = \frac{1}{2}(|5x + 1| - |5x - 1|)$.

To let the state variables x and y oscillate within the voltage supply limits, Eq. (4) need to be scaled. The state variables are scaled by a factor $\frac{1}{2}$, and the time variable by a factor $k = 3000$ which also permits a faster observation of the system behavior. The scaled system reads as follows:

$$\begin{aligned} \frac{dX}{d\tau} &= kY \\ \frac{dY}{d\tau} &= k(-bX + \frac{1}{2}\sin(k\omega\tau) + \frac{1}{2}S(X)) \end{aligned} \quad (5)$$

where $S(X) = \frac{1}{2}(|10X + 1| - |10X - 1|)$ and $k\tau = t$.

Comparing Eqs. (5) to Eqs. (3) the values of the CNN parameters can be derived. In particular: $a_{11} = a_{12} = a_{22} = 0$, $a_{21} = \frac{k}{2}$, $s_{11} = s_{22} = 1$, $s_{12} = k$, $s_{21} = -bk$, $i_1 = 0$, $i_2 = \frac{k}{2}\sin(k\omega\tau)$, and $\alpha = 10$. A SC-CNN with two cells and the parameters listed above has been then designed. The complete scheme is reported in Fig. 1.

The architecture of the circuit follows the approach described in [10], [11] where the state variables of the system to be implemented are associated to voltages across the capacitors of the circuitual analogue and OP-AMPs are used to implement the CNN cells. In fact, suitable configurations of the OP-AMPs allow to implement inverting and non-inverting adders, integrators, and nonlinear elements following standard design guidelines [18]. In particular, referring to the circuit shown in Fig. 1, the two state variables X and Y of Eqs. (5) are associated with the voltage across the two capacitors C_1 and C_2 , respectively, and the nonlinearity is simply implemented by taking into account the saturation of the OP-AMP U_6 . The other OP-AMPs are: U_2 and U_4 (arranged in a Miller configuration) perform the integration of \dot{X} and \dot{Y} , U_3 and U_5 (arranged in an inverting configuration with gain $G = -1$) invert the sign of the state variable; U_1 is an algebraic adder.

The analysis carried out above is based on ideal assumptions on the circuit elements. However, it should be noticed that dissipative terms are introduced, and for this reason the real dynamics of the circuit is represented by Eqs. (1). In our case the dissipative terms are associated with the non-ideal behavior of the Miller integrators. In fact, the transfer functions of such blocks (OP-AMPs U_2 and U_4) do not have a zero pole (as in the integrator ideal case). More precisely, the low frequency pole of such transfer functions is placed in $s = -\frac{1}{R_{fi}C_i}$ which implies a dissipative term $\frac{1}{kR_{fi}C_i}$. Hence, the equations of the circuit read as follows:

$$\begin{aligned} \frac{dX}{d\tau} &= k \left(\frac{R_{f4}R_{f5}}{R_6R_7} Y - \frac{1}{kR_{f4}C_2} X \right) \\ \frac{dY}{d\tau} &= k \frac{R_{f2}R_{f3}}{R_4R_5} \left(-\frac{R_{f1}R_{f5}}{R_1R_7} X + \frac{R_{f1}}{R_2} \sin(\Omega\tau) + \right. \\ &\quad \left. + \frac{R_{f1}}{R_3} V_{sat} - \frac{1}{kR_{f2}C_1} Y \right) \end{aligned} \quad (6)$$

where $\Omega = k\omega$ and V_{sat} is the PWL nonlinearity. The values of the components are reported in the caption of Fig. 1 and match Eqs. (6) with $k = 3000$. In particular, we have set $\frac{R_{f3}}{R_5} = 1$, $\frac{R_{f5}}{R_7} = 1$, $\frac{R_{f1}R_{f5}}{R_1R_7} = 1$, $\frac{R_{f1}}{R_2} = \frac{1}{2}$ and $\frac{R_{f1}}{R_3} = \frac{1}{2}$. The dissipative terms are $\frac{1}{kR_{f4}C_2} = \frac{1}{kR_{f2}C_1} = 0.01$.

III. EXPERIMENTAL CHARACTERIZATION

The circuit has been realized in a discrete-components board and has been extensively investigated. It has been experimentally observed that a fundamental parameter is the frequency of the sinusoidal forcing signal, which motivated a deep analysis performed with respect to this parameter. In fact, varying the frequency of the forcing signal, a wide range of dynamical behaviors, from limit cycles to chaotic attractors, has been observed. All the data collected in the experiments have been acquired by using a data acquisition board (National Instruments AT-MIO 1620E) with sampling frequency $f_s = 200\text{kHz}$ for $T = 4\text{s}$ (i.e. 800000 samples for each time series).

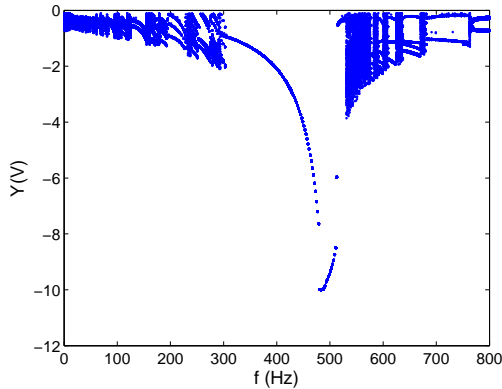


Fig. 2. Experimental bifurcation diagram of variable Y with respect to the forcing frequency. $f = \frac{\Omega}{2\pi}$ ranges from 1Hz to 800Hz.

In [1] it is shown how system (2) exhibits a chaotic behavior for the nominal value of the parameter $\omega = \sqrt{2}$. For our electrical analogue this corresponds to a frequency of the forcing signal $f = 675\text{Hz}$. At this frequency, the dissipative system also exhibits a chaotic attractor as shown in Fig. 3(a).

We have then investigated a much larger range of frequency with respect to [1] and found many other

regions of chaotic behavior. The experimental bifurcation diagram with respect to the forcing frequency $f = \frac{\Omega}{2\pi}$ is shown in Fig. 2. For frequencies below 25Hz, the system periodically oscillates. Increasing the forcing frequency, sudden windows of chaotic behavior have been observed. For further increases of the forcing frequency other periodic behaviors have been observed. Examples of the dynamical behavior exhibited by the circuit are shown in Figs. 3 and 4.

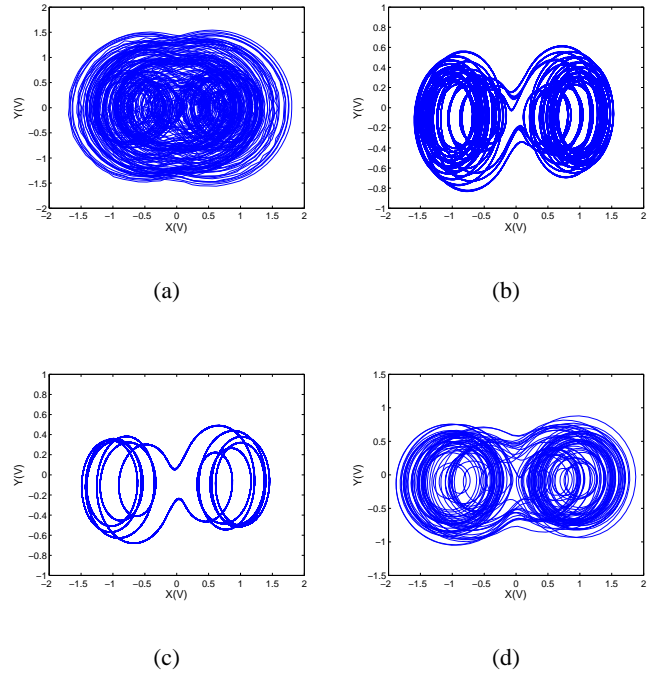


Fig. 3. Phase planes $X-Y$ for different forcing frequencies $f = \frac{\Omega}{2\pi}$: (a) $f = 675\text{Hz}$, (b) $f = 25\text{Hz}$, (c) $f = 40\text{Hz}$, (d) $f = 65\text{Hz}$.

A large window of periodic behavior has been observed in the range of the forcing frequency 307–515Hz in which the system evolves on a periodic orbit whose amplitude increases for $f < 480\text{Hz}$. Then the amplitude of the periodic orbit collapses and a new window of chaotic behavior is observed. Furthermore, in two distinct ranges of the forcing frequency, i.e. 517–529Hz, and 575–579Hz, transient chaos [19] has been also found. In Fig. 5(a), showing the trend of the two state variables, the transition from a chaotic to a periodic behavior is illustrated. In Fig. 5(b) the corresponding trajectories in the phase plane are shown.

IV. CONCLUSIONS

The analysis of nonlinear nonautonomous circuits like Duffing or Van der Pol oscillators disclosed their

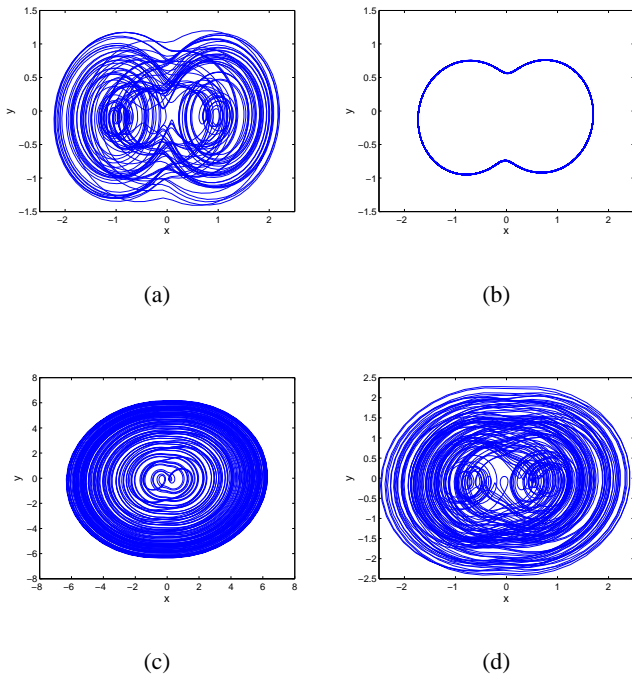


Fig. 4. Phase planes $X-Y$ for different forcing frequencies $f = \frac{\Omega}{2\pi}$: (a) $f = 170\text{Hz}$, (b) $f = 270\text{Hz}$, (c) $f = 488\text{Hz}$, (d) $f = 550\text{Hz}$.

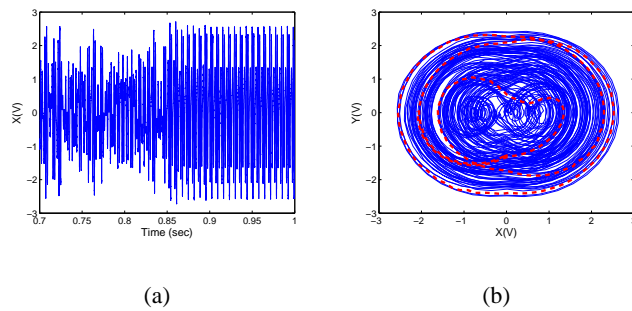


Fig. 5. Transient chaos for $f = 579\text{Hz}$. (a) Trend of the state variable X and (b) phase plane $X-Y$, in blue the transient chaotic trajectories, in dashed line (red) the steady-state limit cycle.

capability to show complex (and in particular chaotic) behavior. In this paper, starting from a nonlinear mathematical model of a nonautonomous oscillator introduced in [1], we discussed its physical implementation through a SC-CNN based circuit. The non-ideal characteristic of circuital elements and, in particular, of integrators based on OP-AMPs is responsible for the introduction of dissipative terms. Thus, the implemented circuit is the dissipative form of the original nonautonomous circuit. It has been deeply experimentally investigated, in particular with respect to the frequency of the forcing sinusoidal

signal, in order to characterize its dynamical behavior. As in the conservative case, we found that the frequency of the forcing signal is a fundamental parameter for the dissipative circuit, giving rise to a wide range of dynamical behaviors.

REFERENCES

- [1] A. Pokrovskii, O. Rasskazov, D. Visetti, "Homoclinic trajectories and chaotic behaviour in a piecewise linear oscillator", *Discrete Cont Dyn-B* **8**, 943–970, 2007.
- [2] E.J. Ngamga, A. Buscarino, M. Frasca, L. Fortuna, A. Prasad, J. Kurths, "Recurrence analysis of strange nonchaotic dynamics in driven excitable systems", *Chaos* **18**, 013128, 2008.
- [3] J. Lü, G. Chen, "Generating multiscroll chaotic attractors: theorems, methods and application", *Int. J. Bif. and Chaos* **16**, 775–858, 2006.
- [4] L.M. Pecora, T.L. Carroll, "Synchronization in chaotic systems", *Phys. Rev. Lett.* **61**, 821–824, 1990.
- [5] L.O. Chua, T. Matsumoto, M. Komuro, "The double scroll", *IEEE Trans. Circuits Syst.* **32**, 798–818, 1985.
- [6] A. Azzouz, R. Duhr, M. Hasler, "Transition to chaos in a simple nonlinear circuit driven by a sinusoidal voltage source", *IEEE Trans. Circuits Syst.* **30**, 913–914, 1983.
- [7] M.P. Kennedy, L.O. Chua, "Van der Pol and Chaos", *IEEE Trans. Circuits Syst.* **33**, 974–980, 1986.
- [8] S. Özoguz, A.S. Elwakil, "On the Realization of Circuit-Independent Nonautonomous Pulse-Excited Chaotic Oscillator Circuits", *IEEE Trans. Circuits Syst.-II* **51**, 552–556, 2004.
- [9] L.O. Chua, T. Roska, "The CNN paradigm", *IEEE Trans. Circuits Syst.-I* **40**, 147–156, 1993.
- [10] P. Arena, S. Baglio, L. Fortuna, G. Manganaro, "Chua's circuit can be generated by CNN cells", *IEEE Trans. Circuits Syst.-I* **42**, 123–125, 1995.
- [11] P. Arena, S. Baglio, L. Fortuna, G. Manganaro, "How state controlled CNN cells generate the dynamics of the Colpitts-like oscillator", *IEEE Trans. Circuits Syst.-I* **43**, 602–605, 1996.
- [12] F. Zou, J.A. Nossek, "A chaotic attractor with Cellular Neural Networks", *IEEE Trans. Circuits Syst.* **38**, 811–812, 1991.
- [13] L.O. Chua, T. Roska, *Cellular Neural Networks and Visual Computing: Foundations and Applications (Paperback)*, (Cambridge University Press), 2005.
- [14] L.O. Chua, *CNN: A Paradigm for Complexity*, (World Scientific, Singapore/River Edge: NJ), 1998.
- [15] M. Frasca, P. Arena, L. Fortuna, *Bio-Inspired Emergent Control Of Locomotion Systems*, World Scientific Series on Nonlinear Science, Series A Vol. 48, 2004.
- [16] M. Bucolo, L. Fortuna, M. Frasca, M.G. Xibilia, "A generalized Chua cell for realizing any continuous n-segment piecewise-linear function", *Int. J. Bif. Chaos* **11**, 2517–2527, 2001.
- [17] L. Fortuna, A. Rizzo, M.G. Xibilia, "Modeling complex dynamics via extended PWL-based CNNs", *Int. J. Bif. Chaos* **13**, 3273–3286, 2003.
- [18] A.S. Sedra, K.C. Smith, *Microelectronic Circuits*, (Oxford University Press, USA), 2003.
- [19] C. Grebogi, E. Ott, J.A. Yorke, "Crises, sudden changes in chaotic attractors, and transient chaos", *Physica D* **7**, 181–200, 1983.

Shil'nikov Chaos and Mixed-mode Oscillation in asymmetry-induced Chua Circuit

Satyabrata Chakraborty and Syamal Kumar Dana
Central Instrumentation, Indian Institute of Chemical Biology
(Council of Scientific and Industrial Research), Kolkata 700032, India
e-mail: skdana@iicb.res.in

Abstract—Experimental evidences of *Shil'nikov type homoclinic chaos and mixed-mode oscillations* (MMOs) are presented in asymmetry-induced Chua's oscillator. The asymmetry plays a crucial role in the related homoclinic bifurcations. The asymmetry is introduced in the circuit by forcing a DC voltage or by coupling a second Chua circuit in resting state.

I. INTRODUCTION

The *Shil'nikov type homoclinic chaos* [1, 2] deals with a saddle focus with real and complex conjugate eigenvalues, $(\gamma, \sigma \pm j\omega)$ in 3D systems. The trajectory of the homoclinic chaos escapes spirally from the saddle focus in 2D eigenspace and re-injects into it along the stable eigendirection for systems with $\gamma < 0$, $\sigma > 0$ and $|\gamma/\sigma| > 1$. A reverse direction of the trajectory of the homoclinic chaos is seen when $\gamma > 0$, $\sigma < 0$ and $|\gamma/\sigma| > 1$. In period-parameter space, the period of limit cycle (period- n : $n^0, n=1, 2, 3, \dots$) increases asymptotically with a control parameter as it approaches a homoclinic orbit and in close vicinity of this bifurcation point, instabilities appear yet bounded to the saddle focus.

Several numerical studies [3-11] showed evidences of MMOs as a transition route to the *Shil'nikov type homoclinic chaos* with control parameter in slow-fast systems. The MMO is defined as a periodic oscillation with alternate appearance of large amplitude oscillations and low amplitude oscillations of different time scales. The sequence of MMOs is observed in the intermediate periodic regimes of the parameter space of the dynamical system. The MMOs is denoted by L^s , where L and s are the number of large and small amplitude oscillations respectively. The L remains fixed for a set of selected system parameters. The number of small oscillation (s) is stable in a periodic window but it is highly irregular in chaotic windows. For different

sets of selected parameters, MMOs with $L = 1, 2, 3, \dots$ may be observed. As a control parameter is tuned to the homoclinic point, the number of small oscillations increases while the trajectory moves closer and closer to a saddle. However, for a fixed L , the number of small oscillations s increases in the alternate periodic windows intermediate to chaotic windows in parameter space. Finally, the state of homoclinic chaos denoted by L^∞ is reached when the number of small oscillations s becomes finitely very large but highly irregular, which is reflected as large fluctuations in return time of homoclinic spiking.

In this paper, we report experimental observations of the *Shil'nikov type homoclinic chaos* in Chua's circuit from a viewpoint of induced asymmetry. In Chua circuit, like many other systems, the dynamics usually changes with a parameter from stable equilibrium to limit cycle by supercritical Hopf bifurcation and to chaos via period-doubling (PD). With further changes in parameter, the system shows period-adding bifurcation when a sequence of periodic windows appear intermediate to chaotic windows in parameter space. The periodic windows are created via SN bifurcation of the chaotic states while the periodic states again move to chaotic states via PD. Subsequently, the dynamics follows a reverse PD before moving to period-1 and then to unstable limit cycle via subcritical Hopf bifurcation. The original Chua circuit model has inversion symmetry. It has two inherent time scales: one for both the revolving cycles around either of the symmetric equilibrium points and another the large cycle covering the two symmetric scrolls. However, these two time scales cannot help inducing homoclinic bifurcation. A third time scale is introduced in the Chua circuit by inducing asymmetry in the system using either an external DC forcing or by coupling (unidirectional or bi-directional) another Chua circuit in resting state. One of the double scroll attractors

thereby shrinks in size and creates an additional time scale in the overall dynamics. In fact, the asymmetry plays a crucial role in the observation of MMOs and homoclinic chaos.

II. EXPERIMENTAL SET UP: ASYMMETRIC CHUA'S CIRCUIT

The forced Chua circuit is shown in Fig.1. A DC voltage is forced at the C_1 capacitor node to induce asymmetry in the attractor. The model of the asymmetry-induced Chua's circuit is given by

$$\begin{aligned} \frac{dV_{C_1}}{dt} &= \frac{G}{C_1}(V_{C_2} - V_{C_1}(1 + \frac{1}{R_p}) - \frac{1}{C_1}f(V_{C_1}) + \frac{1}{R_c C_1}(V_0 - V_{C_1})) \\ \frac{dV_{C_2}}{dt} &= \frac{1}{C_2}[I_L - G(V_{C_2} - V_{C_1})] \\ \frac{dI_L}{dt} &= -\frac{1}{L}(V_{C_2} + r_0 I_3) \end{aligned} \quad (1)$$

and

$$f(V_{C_1}) = \begin{cases} G_b V_{C_1} + (G_b - G_a)E & \text{if } V_{C_1} < -E \\ G_a V_{C_1} & \text{if } -E \leq V_{C_1} \leq E \\ G_b V_{C_1} + (G_a - G_b)E & \text{if } V_{C_1} > E \end{cases} \quad (2)$$

where $G=1/R_1$ and G_a, G_b are the slopes in the inner and outer regions [12] respectively of the piecewise linear characteristic $f(V_{C_1})$. The slopes G_a and G_b are determined by

$$G_a = (-\frac{1}{R_2} - \frac{1}{R_4}), \quad G_b = (\frac{1}{R_3} - \frac{1}{R_4}) \quad (3)$$

The state variables V_{C_1} , V_{C_2} are the voltages measured at nodes of capacitors C_1 and C_2 respectively and, and I_L is the current through the inductance L respectively. The DC source V_{dc} is connected to the Chua's circuit using a voltage divider network using resistances R_x and R_y , where $V_0 = V_{dc}(1 + R_x/R_y)$. The DC forcing induces asymmetry in the double scroll attractor when one of the scrolls is shrunk in size and thereby one additional time scale is introduced, which characterizes the small amplitude oscillation. To facilitate fine control of the strength of asymmetry, a series resistance R_c is connected between the voltage divider and the V_{C_1} node of the Chua's circuit. The original model has three stable foci, one near the origin with eigenvalues $(\gamma, -\sigma \pm j\omega)$ and other two at inversion symmetric positions with

eigenvalues $(-\gamma, \sigma \pm j\omega)$. The basic characteristic of the eigenvalues of all the saddle foci remains unchanged in the asymmetric system.

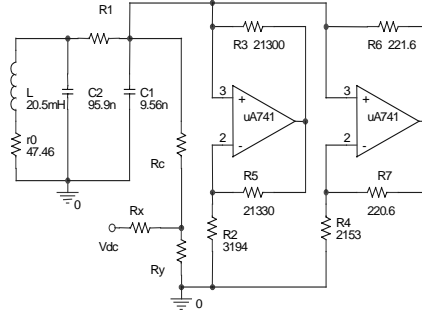


Fig.1: Asymmetric Chua's oscillator: $\pm 9V$ supply

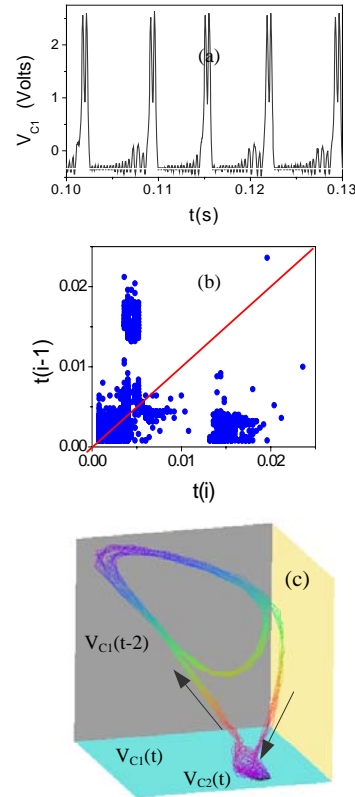


Fig.2: Homoclinic chaos in asymmetry-induced Chua's Circuit: (a) time series of experiment for $R_1=1370.1\Omega$, $R_c=47.25k\Omega$, $R_x=9.33k\Omega$, $R_y=1.73k\Omega$ in lower plot, (b) return time of small amplitude oscillations, (c) 3D trajectory in the right plot is reconstructed using experimental time series of $V_{C_1}(t)$, $V_{C_2}(t)$ and delayed $V_{C_1}(t-2)$ along the X-axis, Y-axis and Z-axis respectively. $R_1=1370.1\Omega$, $R_c=47.25k\Omega$, $R_x=9.33k\Omega$, $R_y=1.73k\Omega$.

III. HOMOCLINIC CHAOS

For selected R_1 and R_C , a time series from experiment is shown in Fig.2(a), which gives clear evidence of *Shil'nikov type homoclinic chaos* as a train of high amplitude spikes with irregular switching to small amplitude oscillations. The time series of the homoclinic chaos is seen as a MMO ($2^s:L=2$) with fluctuating number of small amplitude oscillation (s). The number of small amplitude oscillations decides the time interval of the large amplitude spiking, whose successive time intervals are highly uncorrelated as reflected in the time series as well as in the return time of large amplitude oscillations in Fig.2(b). For stable small amplitude oscillations, the return time must show a fixed point along the 45° line. We have calculated the time interval of the maxima of small amplitude oscillations from the measured time series instead of calculating the time interval of large amplitude oscillations, and then the successive time intervals $t(i)$ are plotted against the previous interval $t(i-1)$ as shown in Fig.2(b). As a result we find interesting multivalued structure in the return map, which is an important signature [13-15] of homoclinic chaos. This confirms the complexity of the small amplitude oscillations, which causes large fluctuations in the time interval of the large amplitude oscillations.

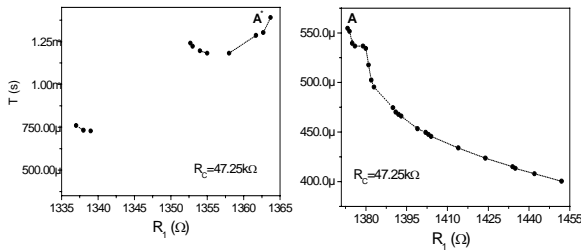


Fig.3: Period parameter bifurcation $R_C=47.25k\Omega$, $R_x=9.33k\Omega$, $R_y=1.73k\Omega$.

The 3D trajectory of *Shil'nikov chaos* as obtained from experiment is shown in Fig.2(c). The trajectory moves towards the saddle focus at one end along its stable eigendirection indicated by the arrows. When the trajectory comes in close proximity to this saddle focus, it escapes out spirally. Next it spirals in towards the saddle focus origin before totally escaping away along the unstable eigendirection of

this saddle focus. Finally the trajectory takes two global turns around the third saddle focus at the other end before reinjecting into the first saddle focus. In reality, the trajectory of the 3D unstable orbit approaches homoclinicity to two different saddle foci, one at the origin and the other at one end of the attractor.

In our experiment, we set the asymmetry by $R_x=9.33k\Omega$, $R_y=1.73k\Omega$ and $R_C=47.25k\Omega$, and then decrease R_1 from 1524Ω . As R_1 is decreased, the circuit dynamics moves from stable focus to limit cycle via supercritical Hopf bifurcation at $R_1=1524\Omega$ and a transition to 2-band chaos occurs via a sequence of PD. The period-parameter bifurcation in Fig.3 shows asymptotic increase in period with decrease in R_1 indicating an approach to homoclinicity. A large amplitude limit cycle 2^0 for $R_1=1373.3\Omega$ is seen at the highest point (A) of the right bifurcation diagram in Fig.3. The instability started just beyond this point with further decrease in R_1 and the instabilities continue until $R_1=1363.7\Omega$ when it stops with the re-appearance of another large amplitude limit cycle (2^0) which corresponds to the top (A*) of the left bifurcation diagram in Fig.3. A stable limit cycle (period-2) reappears [16] at $R_1=1339\Omega$, which moves to 1^0 (period-1) limit cycle at $R_1=1337\Omega$ via reverse PD and finally loses stability via subcritical Hopf bifurcation for $R_1<1337\Omega$. Each of the local maxima in the period-parameter bifurcation, indicates an approach to homoclinicity, however, it is difficult to observe them in a single experiment due to their extreme sensitivity to control parameter. We focus, in our first experiment, on evidences of homoclinicity related to MMO (2^s) in the R_1 interval of $(1363.7\Omega, 1373.3\Omega)$. In the parameter interval, $R_1=[1363.7\Omega, 1373.3\Omega]$, several complex behaviors such as MMO, homoclinic chaos are observed [16]. We observed a sequence of MMOs interspersed by chaotic states in the parameter interval of $R_1=(1363.7\Omega, 1373.3\Omega)$ as a route to homoclinic chaos (2^s) at $R_1=1370.1\Omega$. However, it becomes very difficult to identify the periodic MMOs, in this experiment, due to their extremely narrow interval in the selected parameter space.

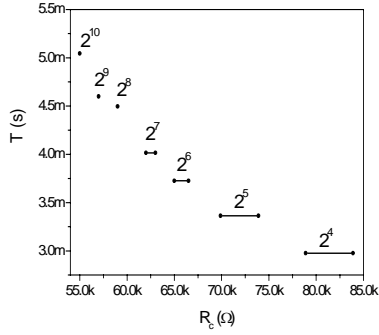


Fig.4: Mixed Mode Oscillation: $R_1=1357\Omega$ and $R_x=1858\Omega$, $R_y=333\Omega$. Period of MMO is plotted in parameter space. Intermediate to the periodic windows of MMOs ($L=2$) with increasing number ($s=4, 5, 6, 7, 8, 9, 10$) of small amplitude oscillations, there exist chaotic windows.

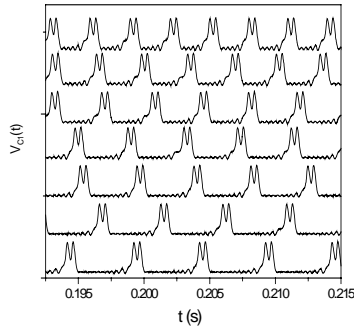


Fig.5: Experimental Mixed Mode Oscillations. $R_1=1357\Omega$ and $R_x=1858\Omega$, $R_y=333\Omega$. Mixed mode oscillations from top to bottom for $L=2$ and $s=4, 5, 6, 7, 8, 9, 10$. R_C values are 78.9kΩ, 69.9kΩ, 65kΩ, 62kΩ, 59kΩ, 57kΩ and 55kΩ respectively.

IV. MIXED MODE OSCILLATION

We set up a second experiment with parameters, $R_x=1858\Omega$, $R_y=333\Omega$ and find similar sequence of events as described above but with clear evidences of periodic MMO. For selected $R_C=47.14k\Omega$, the parameter $R_1=1357\Omega$ is tuned to observe homoclinic chaos. However, we observed the sequences of periodic MMOs with intermediate chaotic states when we use R_C as a control parameter keeping other parameters unchanged. The period-parameter bifurcation in Fig.4 shows devil's staircases with asymptotic increase in period while approaching homoclinicity with decrease in R_C . We are able to

observe a sequence of periodic MMOs (2^s) with a maximum number of small oscillations $s=10$ for $R_C=55k\Omega$. The interval in R_C parameter for the MMO becomes narrower with increasing small oscillation (s). It is evident that as R_C is slowly tuned from 85kΩ corresponding the MMO ($s=4$) to 55kΩ ($s=10$), the interspike intervals increase by two fold. Thus, by fine-tuning the asymmetry parameter, we are able to reach a close vicinity of the homoclinic orbit with much larger ($s \gg 10$) number of small oscillations. The time series of periodic MMOs are shown in Fig.5. The Y-scale is arbitrarily chosen since different time series are either scaled up or down for visual clarity.

V. CONCLUSION

Experimental evidence of Shil'nikov type homoclinic chaos is presented in asymmetry-induced Chua circuit. The asymmetry is induced by DC voltage forcing which plays a crucial role in the process of transition to homoclinic chaos. Interesting to note that we observed similar kind of homoclinic chaos and MMOs in two Chua circuits coupled either in unidirectional or bi-directional mode when one of them is in resting state.

REFERENCES

- [1] S.Wiggins, Introduction to Applied Nonlinear Dynamical Systems and Chaos (Springer-verlag, NY, 1990)
- [2] Y.A.Kuznetsov, Elements of Applied Bifurcation Theory,(Springer-Verlag, NY, 1995)
- [3] V.Petrov, S.K.Scott and K.Showalter, *J.Chem.Phys.* **97** (9), 6191 (1992).
- [4] T.Peacock, T.Mullin, *J.Fluid.Mech.*, **432**, 369 (2001).
- [5] R.Herrero, R.Pons, J.Farjas, F.Pi, G.Orriols, *Phys.Rev.E* **53** (6), 5627 (1996).
- [6] J.J.Healy, D.S.Broomhead, K.A.Cliffe, R.Jones, T.Mullin, *Physica D* **48**, 322 (1991).
- [7] P.Gaspard,X.-J.Wang, *J.Stat.Phys.* **48**, 151 (1987).
- [8] Marc T.M..Koper, *Physica D*, **80**, 72-94 (1995).
- [9] A.Goryachev, P.Strizhak, R.Kapral, *J.Chem Phys.*, (1997).
- [10] S.Rajesh,G.Ananthakrishna, *Physica D***140**, 193, (2000).
- [11] P.Glendinning, J.Abshagen, T.Mullin, *Phys.Rev.E***64**, 036208 (2001).
- [12] M.P.Kennedy, *IEEE Trans.Cir.Systs.*,CAS-**40**, (1993).
- [13] A.N.Pisarchik,R.Meucci,F.T.Arecchi, *Eur.Phys.J. D***13**, 385 (2001).
- [14] E.Allaria, F.T.Arecchi, A.Di Garbo, M.Meucci, *Phys.Rev.Lett.*, **86** (5),791 (2001).
- [15] I.P.Marino, E.Allaria, R.Meucci, S.Boccaletti, F.T.Arecchi, *CHAOS*, **13** (1), 286 (2003)
- [16] S.K.Dana, S.Chakraborty and G.Aanathakrishna, *PRAMANA-J.Physics* **64** (3), 443 (2005).

Penetration and Reflection Mechanisms of Phase-Inversion Waves in Lattice Oscillators

Hitoshi ABURATANI, Suguru YAMANE
and Masayuki YAMAUCHI

Department of Electronics and Computer Engineering,
Hiroshima Institute of Technology
2-1-1, Miyake, Saeki-ku, Hiroshima, Japan
Email: ab.hitoshi247@gmail.com

Yoshifumi NISHIO

Department of Electrical and Electronic Engineering,
Tokushima University
2-1 Minami-Josanjima, Tokushima, Japan

Abstract—We observe and analyze particular synchronization phenomena on a lattice of coupled oscillators. Wave-motion phenomena which propagate phase differences can be observed on the system in steady states, when the system has nonlinearity. We call this wave-motion phenomena “phase-inversion waves.” The phase-inversion waves have some behaviors, which are propagation, reflection, extinction, and penetration. In this paper, a penetration mechanism between a vertical phase-inversion wave and a horizontal phase-inversion wave is made clear. Furthermore, a reflection mechanism between two phase-inversion waves is made clear.

I. INTRODUCTION

In this world, there are synchronization phenomena in every where[1]. The synchronization phenomena are existing among atoms, sea waves, planets and so on. There are synchronization phenomena also among humans as rumors, trends, and so on. Therefore, the synchronization phenomenon is researched in various fields. For example, there is research of synchronization phenomena of a lot of fireflies[2]. We investigate and analyze the synchronization phenomena on the coupled oscillator systems[3]. In our previous study, we discovered the wave-motion which propagates phase difference, which is around 180 degrees, between adjacent oscillators on coupled oscillators system as a ladder and as a lattice. We call the wave-motion “phase-inversion wave.” The phase-inversion waves can be observed in steady states[4]. There are the phase-inversion wave propagating to vertical direction and the phase-inversion wave propagating to horizontal direction on the lattice coupled oscillators system.

In this study, attracting forces to in-phase or anti-phase synchronization are investigated on one parameter-set where the phase-inversion waves can be observed. A penetration mechanism between the vertical phase-inversion wave and the horizontal phase-inversion wave and reflection mechanism between two phase-inversion waves are made clear by instantaneous frequencies of each oscillator, phase differences between adjacent oscillators, and the attracting forces.

II. CIRCUIT MODEL

A lot of van der Pol oscillators are coupled by inductors L_0 as a lattice(see Fig. 1). The number of column and the number of row of this system are assumed as “ $M+1$ ” and “ $N+1$.” We

name each oscillator $OSC(k,l)$. A voltage of each oscillator is named $v_{(k,l)}$, and a current of inductor of each oscillator is named $i_{(k,l)}$ (see Fig. 1). The circuit equations of this circuit model are normalized by Eq. (1), and the normalized circuit equations are shown as Eqs. (2)–(6).

$$\begin{aligned} i_{(k,l)} &= \sqrt{\frac{Cg_1}{3Lg_3}}x_{(k,l)}, \quad v_{(k,l)} = \sqrt{\frac{g_1}{3g_3}}y_{(k,l)}, \\ t &= \sqrt{LC}\tau, \quad \frac{d}{d\tau} = “ \cdot ”, \quad \alpha = \frac{L}{L_0}, \quad \varepsilon = g_1\sqrt{\frac{L}{C}}. \end{aligned} \quad (1)$$

[Corner-top] (left: $(a,b)=(0,1)$. right: $(a,b)=(N,N-1)$.)

$$\begin{aligned} \frac{dx_{(0,a)}}{d\tau} &= y_{(0,a)}, \\ \frac{dy_{(0,a)}}{d\tau} &= -x_{(0,a)} + \alpha(x_{(0,b)} + x_{(1,a)} - 2x_{(0,a)}) \\ &\quad + \varepsilon(y_{(0,a)} - \frac{1}{3}y_{(0,a)}^3). \end{aligned} \quad (2)$$

[Corner-bottom] (left: $(a,b)=(0,1)$. right: $(a,b)=(N,N-1)$.)

$$\begin{aligned} \frac{dx_{(M,a)}}{d\tau} &= y_{(M,a)}, \\ \frac{dy_{(M,a)}}{d\tau} &= -x_{(M,a)} + \alpha(x_{(M-1,a)} + x_{(M,b)} \\ &\quad - 2x_{(M,a)}) + \varepsilon(y_{(M,a)} - \frac{1}{3}y_{(M,a)}^3). \end{aligned} \quad (3)$$

[Center] ($0 < k < M$. $0 < l < N$.)

$$\begin{aligned} \frac{dx_{(k,l)}}{d\tau} &= y_{(k,l)}, \\ \frac{dy_{(k,l)}}{d\tau} &= -x_{(k,l)} + \alpha(x_{(k+1,l)} + x_{(k-1,l)} + x_{(k,l+1)} + x_{(k,l-1)} \\ &\quad - 4x_{(k,l)}) + \varepsilon(y_{(k,l)} - \frac{1}{3}y_{(k,l)}^3). \end{aligned} \quad (4)$$

[Edge]

(top: $(a,b)=(0,1)$. bottom: $(a,b)=(M,M-1)$. both: $0 < l < N$.)

$$\begin{aligned} \frac{dx_{(a,l)}}{d\tau} &= y_{(a,l)}, \\ \frac{dy_{(a,l)}}{d\tau} &= -x_{(a,l)} + \alpha(x_{(a,l-1)} + x_{(a,l+1)} + x_{(b,l)} - 3x_{(a,l)}) \\ &\quad + \varepsilon(y_{(a,l)} - \frac{1}{3}y_{(a,l)}^3). \end{aligned} \quad (5)$$

(left: $(a,b)=(0,1)$. right: $(a,b)=(N,N-1)$. both: $0 < k < M$.)

$$\begin{aligned} \frac{dx_{(k,a)}}{d\tau} &= y_{(k,a)}, \\ \frac{dy_{(k,a)}}{d\tau} &= -x_{(k,a)} + \alpha(x_{(k-1,a)} + x_{(k+1,a)} + x_{(k,b)} - 3x_{(k,a)}) \\ &\quad + \varepsilon(y_{(k,a)} - \frac{1}{3}y_{(k,a)}^3). \end{aligned} \quad (6)$$

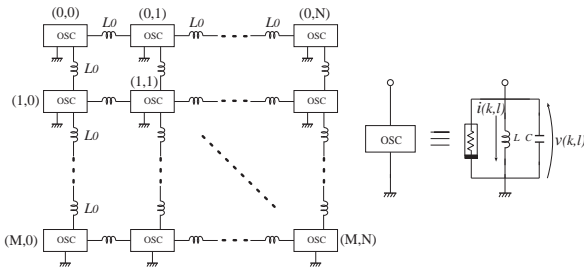


Fig. 1. Circuit Model.

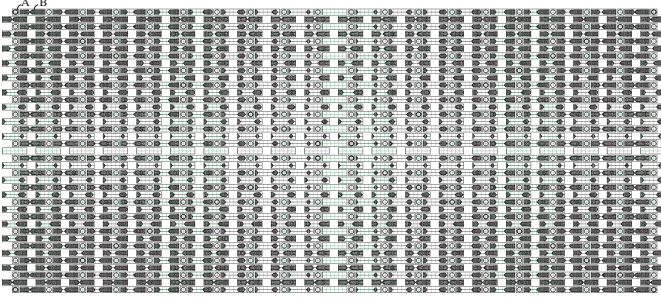


Fig. 2. The phase-inversion waves on 20x20 oscillators(α :an attractor of each oscillator(current vs. voltage), β :a sum of voltages of adjacent oscillators(sum of voltage vs. time)).

The α corresponds to the coupling parameter of each oscillator. The ε corresponds to the nonlinearity of each oscillator. This system is simulated by the fourth order Runge-Kutta methods using Eqs. (2)-(6). The phase-inversion waves are shown in Fig. 2. Figure 2-A expresses attractor of each oscillators. Figure 2-B expresses itinerancy of phase difference sum of voltages of adjacent oscillators is shown along the time.

III. ATTRACTING FORCE

Attracting forces to in-phase or anti-phase synchronization are investigated on one parameter-set where the phase-inversion waves can be observed(see Fig.3). Attracting forces are observed as follows:

- 1) The phase differences between all adjacent oscillators are fixed as arbitrary value in the lattice system.
- 2) The phase difference between OSC(1,4) and OSC(1,5) after one period from initial value is analyzed along the initial phase difference is changed.

A vertical axis of Fig.3 expresses a variation of phase difference per one cycle. An upper direction shows attracting force to in-phase. A downward direction shows attracting force to anti-phase. A horizontal axis shows initial phase differences. Therefore, the length of line shows a attracting forces at each phase difference. Attracting force to in-phase is the strongest in 40 degrees. Attracting force to anti-phase is the strongest in 130 degrees.

IV. BEHAVIOR OF PHASE-INVERSION WAVES

We can observed some behaviors of phase-inversion waves on above systems. These behaviors are a propagation, a reflection at an edge, a reflection between phase-inversion waves, distinction and a penetration. Moreover, these behaviors can be classified by frequencies, because three frequencies are observed in steady states. The synchronizations for vertical

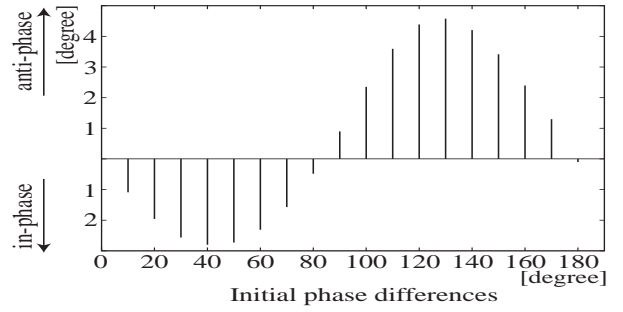


Fig. 3. Attracting forces.

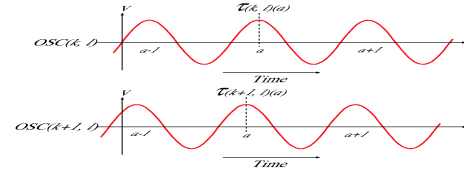


Fig. 4. The detection method of frequencies and the phase differences.

direction and for horizontal direction needs to be considered, because this system is 2 dimensional array. Therefore, three type synchronizations are observed as follows:

- 1) OSC(k, l)–OSC($k, l+1$), OSC(k, l)–OSC($k, l-1$), OSC(k, l)–OSC($k+1, l$), and OSC(k, l)–OSC($k-1, l$): in-phase synchronization.
- 2) {(OSC(k, l)–OSC($k, l+1$) and OSC(k, l)–OSC($k, l-1$): in-phase synchronization. OSC(k, l)–OSC($k+1, l$), and OSC(k, l)–OSC($k-1, l$): anti-phase synchronization.} or {OSC(k, l)–OSC($k, l+1$), and OSC(k, l)–OSC($k, l-1$): anti-phase synchronization. OSC(k, l)–OSC($k+1, l$), and OSC(k, l)–OSC($k+1, l$): int-phase synchronization.}
- 3) OSC(k, l)–OSC($k, l+1$), OSC(k, l)–OSC($k, l-1$), OSC(k, l)–OSC($k+1, l$), and OSC(k, l)–OSC($k+1, l$): anti-phase synchronization.

In this paper, we call the 1st type synchronization “in-and-in-phase synchronization.” The 2nd type synchronization is called “in-and-anti-phase synchronization.” The 3rd type synchronization is called “anti-and-anti-phase synchronization.” An each instantaneous frequency $f_{(k,l)}$ of OSC(k, l) is obtained in each synchronization type. In the 1st situational synchronization, $f_{(k,l)}$ is f_{in-in} . In the 2nd situational synchronization, $f_{(k,l)}$ is $f_{in-anti}$. In the 3rd situational synchronization, $f_{(k,l)}$ is $f_{anti-anti}$.

These behaviors are shown in Table I. There is a disappearance by collision of two phase-inversion waves other than these phenomena.

V. MECHANISM

We analyze about the penetration and reflection of the two phase-inversion waves.

The phase-inversion wave shows in Fig.2. The mechanisms are made clear using instantaneous frequency of each oscillator and phase difference between adjacent oscillators. The coupling parameter is fixed as $\alpha = 0.01$, and nonlinearity is fixed as $\varepsilon = 0.05$. An equation of the instantaneous frequency

TABLE I
CHARACTERISTICS OF THE PHASE-INVERSION WAVES.

Names of behaviors	Itinerancies of instantaneous frequencies	Phenomena
Propagations	$f_{in-in} \Leftrightarrow f_{in-anti}$, & $f_{in-anti} \Leftrightarrow f_{anti-anti}$	The phase-inversion waves propagate to vertical direction or horizontal direction. The vertical phase-inversion waves move from the horizontal phase-inversion waves independently.
Penetrations	$f_{in-in} \Leftrightarrow f_{anti-anti}$	Two phase-inversion waves arrives at an oscillator from vertical direction and horizontal direction, and each phase-inversion wave penetrates each other.
Reflections at an edge	$f_{in-in} \Leftrightarrow f_{in-anti}$, & $f_{in-anti} \Leftrightarrow f_{anti-anti}$	When an phase-inversion wave arrives at an edge, the phase-inversion wave reflects and propagates to where they came from. Sometime this phenomenon is happened with penetration.
Reflections between two phase-inversion waves	$f_{in-in} \Leftrightarrow f_{in-anti}$, & $f_{in-anti} \Leftrightarrow f_{anti-anti}$	When two phase-inversion waves coming from the opposite directions arrive to two adjacent oscillator at same time, the phase-inversion waves reflect and propagate to where they came from.

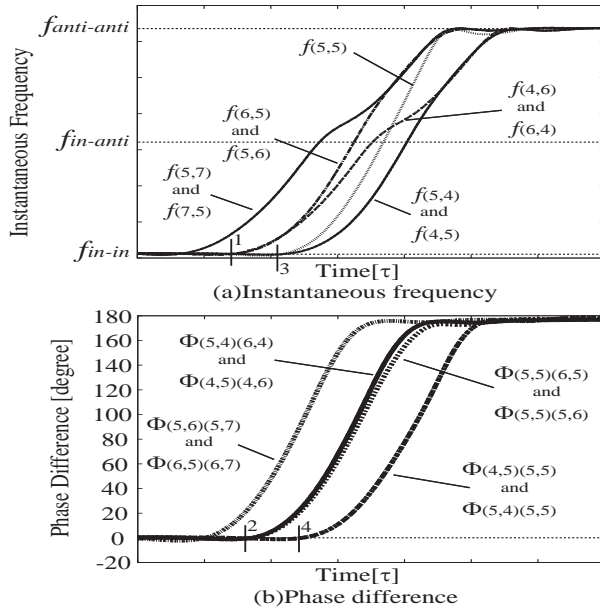


Fig. 5. Transitions of phase difference and frequencies by penetration a phase-inversion wave.

of $OSC(k, l)$ is calculated as follows. The instantaneous frequency is named $f_{(k,l)}(a)$ where “a” expresses the number of times of the peak value of the voltage. Time of a peak value of the voltage of $OSC(k, l)$ is assumed as $\tau_{(k,l)}(a)$ (see Fig.4). Similarly, $\tau_{(k+1,l)}(a)$ and $\tau_{(k,l+1)}(a)$ are decided. The $f_{(k,l)}(a)$ is obtained by Eq.(7).

$$f_{(k,l)}(a) = \frac{1}{\tau_{(k,l)}(a) - \tau_{(k,l)}(a-1)}. \quad (7)$$

The phase difference is calculated as follows. A phase difference between $OSC(k, l)$ and $OSC(k+1, l)$ and a phase difference between $OSC(k, l)$ and $OSC(k, l+1)$ are calculated. The phase differences are assumed as $\Phi_{(k,l)(k+1,l)}(a)$ and $\Phi_{(k,l)(k,l+1)}(a)$ respectively (see Fig.4). The $\Phi_{(k,l)(k+1,l)}(a)$ and $\Phi_{(k,l)(k,l+1)}(a)$ are obtained by Eq.(8).

$$\begin{aligned} \Phi_{(k,l)(k+1,l)}(a) &= \frac{\tau_{(k,l)}(a) - \tau_{(k+1,l)}(a)}{\tau_{(k,l)}(a) - \tau_{(k,l)}(a-1)} \times 360 \text{ [degree]} \\ \Phi_{(k,l)(k,l+1)}(a) &= \frac{\tau_{(k,l)}(a) - \tau_{(k,l+1)}(a)}{\tau_{(k,l)}(a) - \tau_{(k,l)}(a-1)} \times 360 \text{ [degree].} \end{aligned} \quad (8)$$

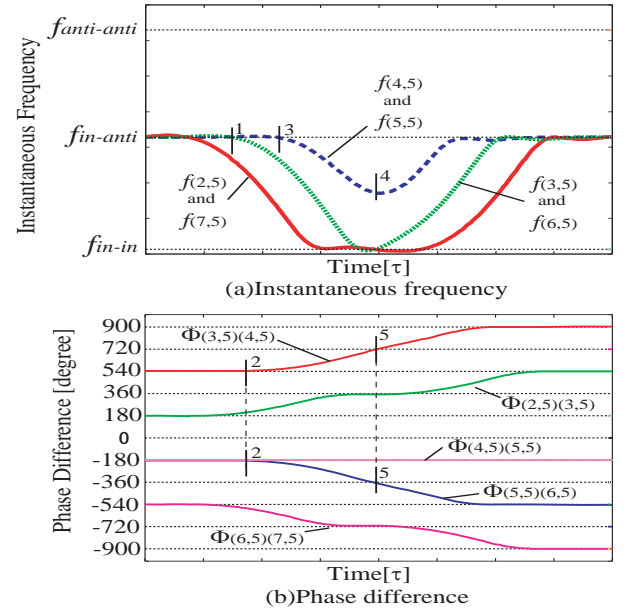


Fig. 6. Transitions of phase difference and frequencies by reflection between two phase-inversion wave.

A. Penetration Mechanism

We can observe the phenomenon of penetration. A mechanism of penetration is shown in Tab. II and Fig. 5. The vertical axis of Fig. 5(a) is the instantaneous frequency, and horizontal direction is time. The vertical axis of Fig. 5(b) expresses the phase differences, and horizontal direction expresses time.

B. Reflection mechanisms between two phase-inversion waves

We can observe the reflection phenomenon between two phase-inversion waves which are arrives at two adjacent oscillators at same time from opposite directions respectively. We shows mechanism in Table III. In Fig.6(a), the vertical axis is the instantaneous frequencies, and the horizontal axis is time. In Fig.6(b), the vertical axis is the phase differences, and the horizontal axis is the time.

VI. CONCLUSION

An attracting forces to in-phase and to anti-phase were made clear by all adjacent oscillators being fixed as arbitrary phase

TABLE II
PENETRATION MECHANISM(SEE FIG.5).

no.	Vertical direction	Horizontal direction
0	Now, phase-inversion waves, which changes phase states from in-phase synchronization to anti-phase synchronization, are arrived at oscillators of 7th row line from oscillators of 8th row line.	Now, phase-inversion waves, which changes phase states from in-phase synchronization to anti-phase synchronization, are arrived at oscillators of 7th column line from oscillators of 8th column line.
1	$\Phi_{(6,5)(7,5)}$ is increasing toward 180 degrees. $f_{(6,5)}$ slowly starts to increase from f_{in-in} to $f_{in-anti}$, after $\Phi_{(6,5)(7,5)}$ start to increase, because an attracting force to in-phase is weak around 0 degree(see Fig.3). $f_{(6,4)}$ also starts to increase from f_{in-in} , because a phase-inversion wave of adjacent vertical direction arrives at 6th row line at the same time. $f_{(6,4)}$ changes toward $f_{in-anti}$, because horizontal wave does not arrives at OSC(6,4) yet.	$\Phi_{(5,6)(5,7)}$ is increasing toward 180 degrees. $f_{(5,6)}$ slowly starts to increase from f_{in-in} to $f_{in-anti}$, after $\Phi_{(5,6)(5,7)}$ start to increase, because an attracting force to in-phase is weak around 0 degree(see Fig.3). $f_{(4,6)}$ also starts to increase from f_{in-in} , because a phase-inversion wave of adjacent vertical direction arrives at 6th column line at the same time. $f_{(4,6)}$ changes toward $f_{in-anti}$, because horizontal wave does not arrives at OSC(4,6) yet.
2	$\Phi_{(5,5)(6,5)}$ and $\Phi_{(5,4)(6,4)}$ start to increase toward 180 degrees, because $f_{(6,5)}$ and $f_{(6,4)}$ increase toward $f_{in-anti}$.	$\Phi_{(5,5)(5,6)}$ and $\Phi_{(4,5)(4,6)}$ start to increase toward 180 degrees, because $f_{(5,6)}$ and $f_{(4,6)}$ increase toward $f_{in-anti}$.
3	A horizontal phase-inversion wave and a vertical phase-inversion wave arrives at OSC(5,5). $f_{(5,5)}$ starts to increase to $f_{anti-anti}$ by horizontal phase-inversion wave and vertical phase-inversion wave rapidly. $f_{(4,5)}$ and $f_{(5,4)}$ start to increase from f_{in-in} to $f_{anti-anti}$, because $\Phi_{(5,4)(6,4)}$ and $\Phi_{(4,5)(4,6)}$ start to increase toward 180 degrees.	
4	Therefore, $\Phi_{(4,5)(5,5)}$ starts to increase toward 180 degrees because $f_{(5,5)}$ increases toward $f_{anti-anti}$. Because an attracting force to anti-phase is weak around 180 degrees, $\Phi_{(4,5)(5,5)}$ arrives at 180 degrees slowly(see Fig.3).	Therefore, $\Phi_{(5,4)(5,5)}$ starts to increase toward 180 degrees because $f_{(5,5)}$ increases toward $f_{anti-anti}$. Because an attracting force to anti-phase is weak around 180 degrees, $\Phi_{(5,4)(5,5)}$ arrives at 180 degrees slowly(see Fig.3).
The phase-inversion waves penetrate each other by above mechanism.		

TABLE III
REFLECTION MECHANISM BETWEEN TWO PHASE-INVERSION WAVES(SEE FIG.6).

no.	upside	down side
0	Now the phase states of horizontal direction are fixed in in-phase synchronization. The phase states of vertical directions around OSC(5,5) are anti-phase synchronization. The phase-inversion wave changing from anti-phase to in-phase synchronization arrives on 3rd row and 6th row line from 0th row line and 9th row line respectively.	
1	$f_{(3,5)}$ starts to decrease from $f_{in-anti}$ to f_{in-in} , because $\Phi_{(2,5)(3,5)}$ started to change from anti-phase to in-phase. $f_{(3,5)}$ slowly changes, because an attracting force is weak force around anti-phase synchronization(see Fig.3).	$f_{(6,5)}$ starts to decrease from $f_{in-anti}$ to f_{in-in} , because $\Phi_{(6,5)(7,5)}$ started to change from anti-phase to in-phase. $f_{(6,5)}$ slowly changes, because an attracting force is weak force around anti-phase synchronization(see Fig.3).
2	$\Phi_{(3,5)(4,5)}$ starts to changing from anti-phase to in-phase, because $f_{(3,5)}$ started to decrease from $f_{in-anti}$ to f_{in-in} .	$\Phi_{(5,5)(6,5)}$ starts to change from anti-phase to in-phase, because $f_{(5,5)}$ started to decrease from $f_{in-anti}$ to f_{in-in} .
3	$f_{(4,5)}$ starts to decrease from $f_{in-anti}$ to f_{in-in} slowly, because $\Phi_{(3,5)(4,5)}$ started to change from anti-phase to in-phase.	$f_{(5,5)}$ starts to decrease from $f_{in-anti}$ to f_{in-in} slowly, because $\Phi_{(5,5)(6,5)}$ started to change from anti-phase to in-phase.
4	$\Phi_{(4,5)(5,5)}$ are fixed anti-phase, because the frequencies of OSC(4,5) and OSC(5,5) are same itinerancy. Therefore, $f_{(4,5)}$ and $f_{(5,5)}$ stop between $f_{in-anti}$ and f_{in-in} , and $f_{(4,5)}$ and $f_{(5,5)}$ start to increase to $f_{in-anti}$ again.	
5	$\Phi_{(3,5)(4,5)}$ can not stop at in-phase synchronization, because reflection phase-inversion wave arrives in a moment again.	$\Phi_{(4,5)(5,5)}$ can not stop at in-phase synchronization, because reflection phase-inversion wave arrives in a moment again.
Two phase-inversion waves reflect by above mechanism.		

difference.

A penetration mechanism between the vertical phase-inversion wave and horizontal phase-inversion wave was made clear by instantaneous frequencies of each oscillator, phase differences between adjacent oscillators and the attracting forces. Furthermore, a reflection mechanism between two phase-inversion waves was made clear by instantaneous frequencies of each oscillator, phase differences between adjacent oscillators and the attracting forces.

ACKNOWLEDGEMENTS

This research is supported by the Grants-in-Aid for Young Scientific Research (B) (No. 19760270) from the Japan Society

for the Promotion of Science.

REFERENCES

- [1] B. Schechter, "How the brain gets rhythm," *Science*, vol. 274, no. 5286, pp. 339-340, Oct. 1996.
- [2] N. Ohba, "Flash Communication Systems of Japanese Fireflies," *Integrative and Comparative Biology*, vol. 44, pp. 225-233, June 2004.
- [3] T. Endo and S. Mori, "Mode Analysis of Two-Dimensional Low-Pass Multimode Oscillator," *IEEE Trans. Circuits and Syst.*, vol. 23, no. 9, pp. 517-530, Sept. 1976.
- [4] M. Yamauchi, M. Okuda, Y. Nishio and A. Ushida, "Analysis of Phase-Inversion Waves in Coupled Oscillators Synchronizing at In-and-Anti-Phase," *IEICE Trans. Fundamentals*, vol. E86-A, no. 7, pp. 1799-1806, July 2003.

Data Clustering based on Hebbian Learning in Inhomogeneous Coupled Map Lattices

Thomas Ott & Urs Mürset

Institute of Applied Simulation,

ZHAW Zurich University of Applied Sciences, Switzerland

E-mail: ottt@zhaw.ch, murs@zhaw.ch

Abstract—We outline a novel clustering algorithm based on Hebbian-like learning in inhomogeneous coupled map lattices. The algorithm is nonparametric and the number of clusters does not have to be specified. It is capable of detecting clusters of complex shape and it can distinguish between clusters and noisy background data. The clustering resolution can be controlled by two parameters. We report on the properties of the algorithm and we discuss its advantages and potential drawbacks.

I. INTRODUCTION

The problem of finding appropriate groupings in a data set is referred to as clustering problem. In the last few decades numerous different clustering methods have been developed. They can be roughly divided into parametric and nonparametric approaches. Parametric approaches rely on some specification of the data structure. Nonparametric approaches, in contrast, make no or few assumptions about the clusters. Some nonparametric approaches, such as superparamagnetic clustering ([1], [2]), rely on the idea that clusters can emerge on the basis of local interactions between data items by means of self-organisation. In [3] an algorithm was proposed that exploits the idea of cluster self-organisation based on Hebbian-like learning in integrate-and-fire networks, making the clusters arise out of the interplay between neural activity and changes in network connectivity. In this contribution we adapt and implement the idea of Hebbian learning for clustering using coupled map lattices, unifying the ideas presented in [3] and [4]. Compared to integrate-and-fire networks, the simulation of coupled map lattices is potentially faster since it puts the dynamics on a more abstract level. We outline our concept of Hebbian clustering with coupled map lattices by means of a 2D test data set and we report on a nontrivial 3D example.

II. HEBBIAN LEARNING IN COUPLED MAP LATTICES

We first translate a given d -dimensional data distribution with N points $\{r_i\}$ into an undirected graph by connecting each point to its k nearest neighbours. To each edge (i, j) of the resulting graph a positive connection strength is appointed according to

$$J_{(i,j)} = \exp(-(r_i - r_j)^2 / (2a)^2), \quad (1)$$

where the scaling factor a is equal to the average distance of connected points. $J_{(i,i)}$ is set to zero. Following the principles sketched in [4], a real variable $x_i \in [-1, 1]$ is assigned to each point. The time evolution of these variables is given by

$$x_i(t+1) = \frac{1}{C_i} \sum_j J_{ij} f(x_j(t)) \quad (2)$$

where $C_i = \sum_j J_{ij}$ and $f(x) = 1 - 2x^2$ is the logistic map. The variables x_i are randomly initialised. During the time evolution, they are updated in a fixed but arbitrary order. After each update of a variable x_i , the weights $J_{(i,j)}$ are adapted according to a Hebbian-like learning rule: If the value of a connected variable x_j is synchronised, i.e. within a certain learning window τ , then the connection $J_{(i,j)}$ is strengthened until it reaches a maximum at 1, otherwise it is weakened:

$$\begin{aligned} \text{If } |x_i - x_j| < \tau : \quad & J_{(i,j)} = \max(1, d_1 J_{(i,j)}) \\ \text{If } |x_i - x_j| \geq \tau : \quad & J_{(i,j)} = J_{(i,j)} / d_2 \end{aligned} \quad (3)$$

where $d_1 > 1$ is the strengthening factor and $d_2 > 1$ is the weakening divisor. In order to eliminate one parameter we set $d_2 = k$. The choice of the other parameters is discussed below. A complete update of all the variables is called an iteration. After a couple of iterations the network structure enters a stable phase (see below) and the update process is terminated. The final clusters correspond to the final connectivity components. In Fig. 1 this idea is illustrated by means of a 2D test set consisting of $N = 900$ points.

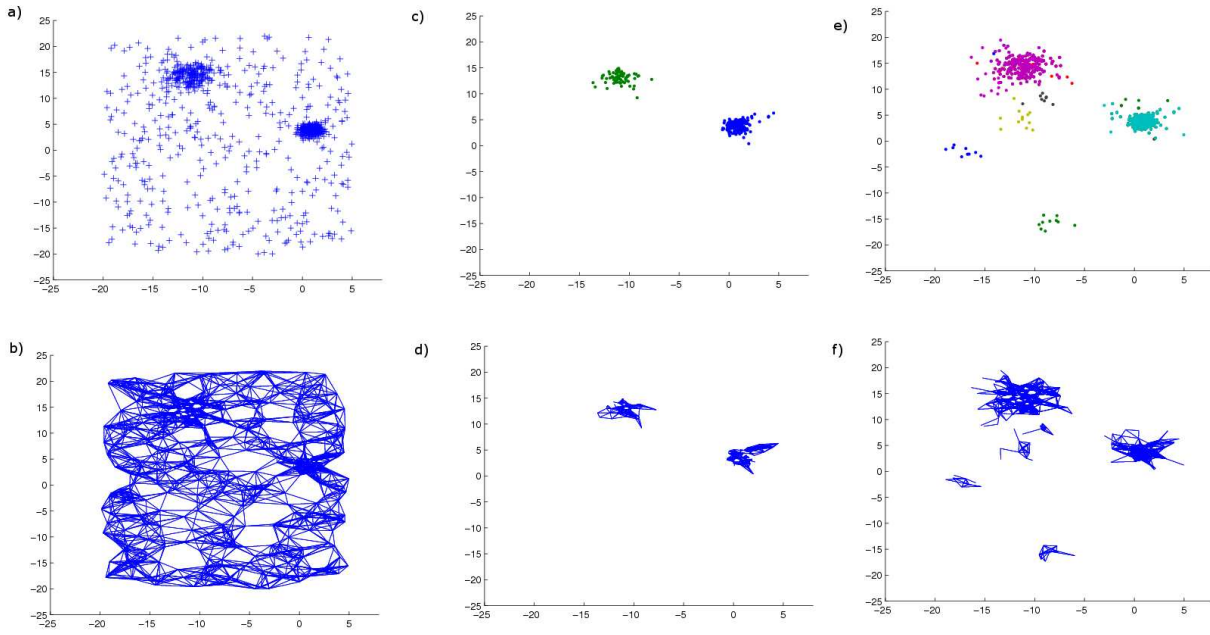


Fig. 1. a) 2D test distribution with two clusters ($N_1 = 200$ and $N_2 = 300$) embedded into a background distribution ($N_3 = 400$). b) Corresponding connectivity graph for $k = 10$. c) For the parameters $d_1 = 1.1, d_2 = k, \tau = 0.2$, two clusters were identified. d) The identification is based on the resulting connectivity graph. e, f) The parameters $d_1 = 1.1, d_2 = k, \tau = 0.3$ reveal more clusters.

A. Termination and Cluster Identification

The self-organisation at work ensures that almost all the weights quickly tend to either 0 or 1. In Fig. 2, based on the 2-dimensional toy example shown in Fig. 1, the fraction of weights with $0.05 < J_{(i,j)} < 1$ is depicted for various learning window sizes in dependence on the number of iterations. It shows a rapid decay of this fraction below about 5%, independent of the window size. Hence after a couple of iterations, the network structure ceases to change (up to some small changes).

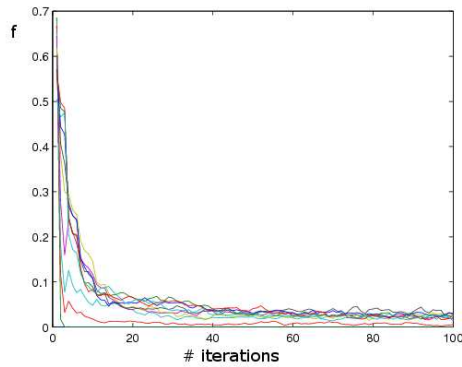


Fig. 2. Fraction f of connections with intermediate weight $0.05 < J_{(i,j)} < 1$ in dependence on the number of iterations for different learning window sizes ($0 < \tau < 2$).

On the basis of this observation, the algorithm is terminated if 1) either the fraction of weights with $0.05 < J_{(i,j)} < 1$ is smaller than 5% or if 2) a maximal predefined number of iterations is reached, for which 50 was chosen. The choice of the values 0.05, 5% and 50 is somewhat arbitrary. Similar values can be chosen without a relevant effect on the results.

After termination, the clusters are identified as the strong connection components of the final network, i.e. connections smaller than 1 are cut and the components of the resulting graph are determined.

B. Role of Learning Rule Parameters

The influence of τ :

The size of the learning window τ influences the clustering resolution. For small values, synchronisation is difficult and only a few small clusters are detected, corresponding to the regions of highest data density. For intermediate values, usually more and larger clusters can be found. They merge to bigger units for larger values of τ . Clear clusters are typically stable over a longer interval of τ . We demonstrate the role of τ by means of a 2D example with two clear cluster structures embedded into a background distribution ($N_1 = N_2 = 200, N_3 = 100, k = 10, d_1 = 1.1$, see Fig. 3 a)). Over a substantial interval between about 0.1 and 0.6, two

clusters, consisting of about 200 points each, dominate the scenery. Hence the average cluster size for this interval is around 200 (Fig. 3 b)). It is smaller for somewhat larger values of τ since a couple of small clusters emerge and the number of clusters increases (Fig. 3 c)). Finally, the average cluster size increases for very large values of τ since the clusters are merged. The number of clusters for large τ oscillates between 1 and 2, revealing a certain instability of the algorithm in this range, which is due to different initial conditions (see C).

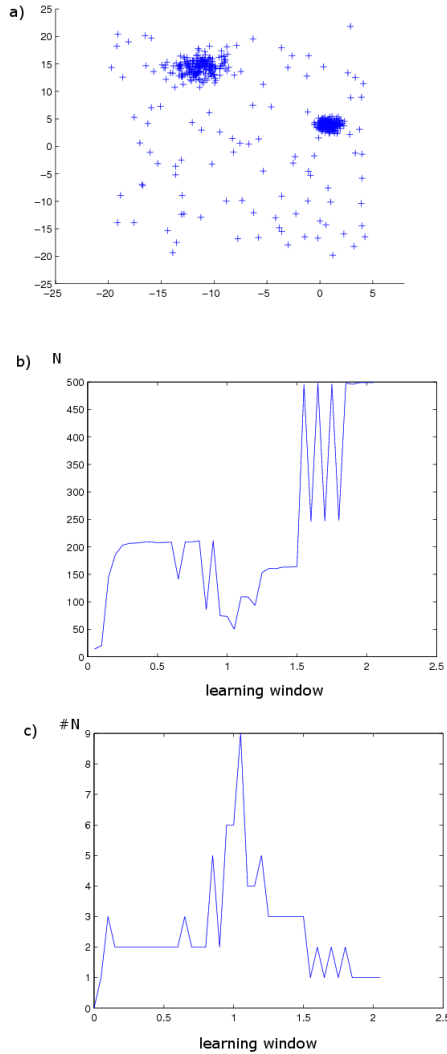


Fig. 3. (a) 2D test set with 500 points. b) Average cluster size N in dependence on the learning window size τ . c) Number of clusters $\#N$ in dependence on the learning window size τ .

The influence of d_1 :

d_1 plays a similar role as τ . For small values only very dense regions can cluster. We thus find many

small clusters. For large values all the connections are strengthened, which results in one big cluster only. For the window size used $\tau = 0.2$, the two clusters shown in Fig. 3 a) can be found for intermediate values of d_1 in the range between 1.1 and 1.3. In this region, two clusters of about the size 200 can be found (Fig. 4 a) and b)).

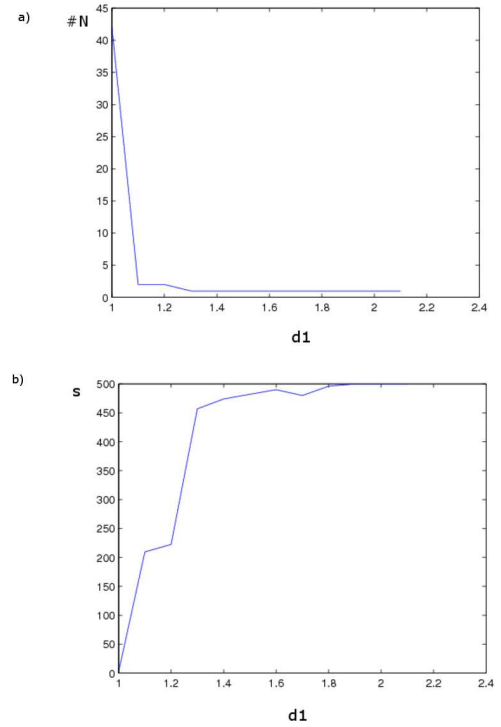


Fig. 4. a) Number of clusters $\#N$ in dependence on the learning factor d_1 b) Average cluster size s in dependence on d_1 .

The influence of k :

k does not influence the results significantly. This observation confirms the picture of a robust self-organisation of the network structure resulting from the learning rule used.

C. Initial Conditions

The random initialisation of the network variables $\{x_i\}$ can lead to an accidental strengthening of weak connections in the beginning, which can influence the final results in an undesired direction. We found that the problem can be removed by introducing a settling phase in the beginning during which learning is disabled.

III. 3D EXAMPLE

In [3] a 3-dimensional data set was introduced with two entangled rings embedded into a background dis-

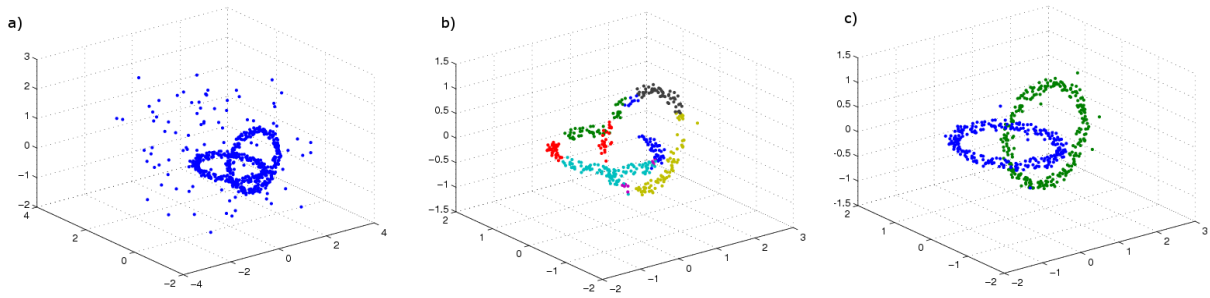


Fig. 5. a) Non-trivial clustering task with two rings embedded in a background distribution ($N = 620$ points in total). Clusters found for the parameters b) $k = d_2 = 5, d_1 = 1.05, \tau = 0.22$ and c) $k = d_2 = 5, d_1 = 1.05, \tau = 0.3$.

tribution. The corresponding clustering task is nontrivial and it cannot be solved by most standard algorithms such as K-means clustering. Hebbian clustering approaches, in contrast, can solve the task with ease. In Fig. 5 the results of our approach are shown for two different parameter choices. Compared to Hebbian clustering with integrate-and-fire networks, the results seem to be a bit more sensitive to the choice of the parameters (compare results in [3]). However, when choosing appropriate parameters, the individualities of the two rings can be worked out perfectly. The example clearly demonstrates two advantages of the approach: It is able to determine clusters of arbitrary shape and it provides an integrated noise cleaning since it is able to distinguish clusters from a background distribution.

We also compared the time performance of integrate-and-fire networks with our approach. The comparison yields almost identical running times with slight advantages for coupled map lattices. Both algorithms have an inherent time complexity of the order $O(N^2)$, where N is the size of the data set.

IV. CONCLUSION

We demonstrated that the idea of clustering based on Hebbian learning can be adapted for coupled map lattices. The mechanism of cluster formation is similar to Hebbian clustering in integrate-and-fire networks presented in [3]. Since coupled map lattices are defined by rather simple dynamics compared to integrate-and-fire networks, we expected that clustering with coupled map lattices would be a bit faster, but the current implementation in Matlab did not show a clear speed advantage. The number and the size of the resulting clusters depend on the choice of the learning parameters. They allow the resolution or granularity of the clustering to be controlled. This fact, however, raises the question how the optimal clustering resolution should be chosen.

Clear cluster structures can be detected by scanning a whole range of possible learning values since clear clusters typically occur in a longer interval. Compared to integrate-and-fire networks, Hebbian clustering with coupled map lattices seems to be rather more sensitive to the choice of the parameters. Moreover, the detailed results seem to be slightly dependent on the initial condition, whereas integrate-and-fire networks are almost completely unsuceptible to the initialisation. Fortunately, the influence of the initial condition can be successfully removed by introducing a settling phase without learning.

In future work, we intend to test a slightly adapted Hebbian learning rule, based on mutual information. This measure was used in [4] to determine the synchronicity of two elements and we believe that it is less susceptible to parameter changes. Furthermore, inspired by the paradigm of self-organising maps (e.g. [5]), we want to shift the focus to the question of how Hebbian learning clustering can be utilised to visualise high-dimensional data.

REFERENCES

- [1] M. Blatt, S. Wiseman, E. Domany. Superparamagnetic Clustering of Data. In *Phys. Rev. Lett.* 76, pp. 3251–3254, 1996.
- [2] T. Ott, A. Kern, W.-H. Steeb, R. Stoop. Sequential Clustering: Tracking Down the Most Natural Clusters. In *J. Stat. Mech.*, P11014, 2005.
- [3] F. Landis, T. Ott, R. Stoop. Hebbian Self-Organizing Integrate-and-Fire Networks for Data Clustering. In *Neural Computation* 22(1), pp. 273–288, 2010.
- [4] L. Angelini, F. De Carlo, C. Marangi, M. Pellicoro, S. Stramaglia. Clustering Data by Inhomogeneous Chaotic Map Lattices. In *Phys. Rev. Lett.* 85(3), pp. 554–557, 2000.
- [5] S. Haykin. *Neural Networks - A Comprehensive Foundation* Prentice-Hall Inc., 1999.

Transient Dynamics and Metastable States in an Ensemble of Synaptically Coupled Morris-Lecar Neurons

Vladimir I. Nekorkin, Dmitry V. Kasatkin and Aleksey S. Dmitrichev
Institute of Applied Physics of the Russian Academy of Sciences,
46 Ulyanov Street, 603950, Nizhny Novgorod, Russia
Email: kasatkin@neuron.appl.sci-nnov.ru

Abstract—A novel dynamical model of synaptic transmission based on the FitzHugh-Nagumo system with nonlinear recovery properties was proposed. The model accounts for typical features of synaptic transmission such as synaptic threshold and delay. The dynamics of an ensemble of Morris-Lecar neurons interconnected by means of such synaptic couplings was investigated. It was shown that an ensemble demonstrate various structurally stable modes of transient dynamics in the form of sequential transitions between different metastable oscillatory states.

I. INTRODUCTION

Many neurophysiologic experiments have indicated that some neural processes related, for example, with performing of different cognitive tasks (memory, attention, psychomotor coordination, and so on) are accompanied only by transient activity at the level of individual neurons or small enough groups of neurons [1-3]. As a result of such processes a certain sequence of transitional activity phases appears in neural network. It is clear that such activity of neural networks cannot be understood within the framework of classical models of nonlinear dynamics which are based on the concept of attractor because here the main effect is achieved long before the system reaches its neighborhood. Therefore, to adequately describe transient and sequential neural processes a novel class of models should be developed. One of the popular points of view is that such models should be based primarily on the concept of metastable states. Transient dynamics here is formed by sequential switching between these states. Recently several phenomenological models based on the metastable states concept have been proposed [4-7]. These models operate with variables characterizing averaged activity of neural networks. To describe the dynamics of such variables either a generalized Lotka-Volterra system or a Wilson-Cowan system is used. It has been shown that under ap-

propriate conditions a stable heteroclinic channel appears in the phase space of the models. This channel represents a mathematical image of transient activity. Indeed, the channel is formed by a set of trajectories in the vicinity of a heteroclinic skeleton which consists of saddles and unstable separatrices which connect their surroundings. Each trajectory of the channel sequentially passes the neighborhoods of saddle fixed points "staying" there for some (finite) time. However, the models have significant limitations. First of all, they do not account for dynamical properties of individual neurons. Another limitation consists in significant simplification of architecture and properties of interneuron synaptic couplings.

In this work we propose a model demonstrating various structurally stable transient dynamics and taking into account individual properties of neurons. The model represents an ensemble consisting of three Morris-Lecar neurons [8]. The transition of excitation between them is realized by means of chemical synapses.

II. MODEL

Consider an ensemble of three neurons with excitatory synapses. The dynamics of such ensemble can be described by the following system of ordinary differential equations:

$$C \frac{dv_i}{dt} = -g_L(v_i - v_L) - g_{Ca}M_\infty(v_i)(v_i - v_{Ca}) - (1)$$

$$-g_K n_i(v_i - v_K) + I_i^{ext} - g_{syn} s_i(v_i - v_{rev}),$$

$$\frac{dn_i}{dt} = \frac{n_\infty(v_i) - n_i}{\tau_n(v_i)}, \quad (2)$$

$$\frac{dr_i}{dt} = f_1(r_i) - s_i - k_1, \quad (3)$$

$$\frac{ds_i}{dt} = \varepsilon(f_2(r_i) - s_i - k_2 - \mu \sum_{\substack{j=1, \\ j \neq i}}^3 H(v_j - \theta_{ji})), \quad (4)$$

$$i, j = 1, 2, 3.$$

The neurons dynamics is given by the two-variable Morris-Lecar (ML) neuronal model (1)-(2), equations (3)-(4) describe synaptic couplings between neurons. Here, the variables v_i , n_i correspond to the membrane potential and the state of activation of K^+ channels of the i -th neuron, C is the capacitance of the membrane. The parameters g_L , g_{Ca} , g_K are the maximal conductances associated with the leak, Ca^{2+} and K^+ transmembrane currents, respectively; v_L , v_{Ca} , v_K are the corresponding reversal potentials; I_i^{ext} are the external currents. The voltage-dependent gating functions $M_\infty(v)$, $n_\infty(v)$ and $\tau_n(v)$ are given by:

$$\begin{aligned} M_\infty(v) &= 0.5 \left[1 + \tanh \left(\frac{v - v_1}{v_2} \right) \right], \\ n_\infty(v) &= 0.5 \left[1 + \tanh \left(\frac{v - v_3}{v_4} \right) \right], \\ \tau_n(v) &= \left[\phi \cosh \left(\frac{v - v_3}{2v_4} \right) \right]^{-1}, \end{aligned}$$

where $v_1 = -0.01$, $v_2 = 0.15$, $v_3 = 0$, $v_4 = 0.3$, $\phi = 1$. The coupling between neurons is defined by adding the synaptic current term $-g_{syn}s_i(v_i - v_{rev})$ to the right side of equation (1). The parameter g_{syn} is the maximal synaptic conductance and v_{rev} is the synaptic reversal potential. The variable s_i characterizes how the postsynaptic conductance depends on the presynaptic potentials v_j , ($j \neq i$). To describe the dynamics of synaptic interneuron interaction we introduce a phenomenological model in the form of equations (3),(4), where

$$\begin{aligned} f_1(r) &= r - \frac{r^3}{3}, \\ f_2(r) &= \begin{cases} \alpha r, & r < 0 \\ \beta r, & r \geq 0 \end{cases}, \\ H(x) &= (1 + \exp(-\frac{x}{K_p}))^{-1}, \end{aligned}$$

$K_p = 0.001$, $\alpha = 0.5$, $\beta = 2$, $\varepsilon = 0.005$, $\mu = 0.07$, $k_1 = -0.666$, $k_2 = -0.5$. The parameters θ_{ji} characterize the initial times of synaptic activation processes caused by input information signals. In the ML neuronal model (equations (1),(2)) values of parameters are fixed as follows: $C = 1$, $g_L = 0.1$, $g_{Ca} = 1.1$, $g_K = 2$, $v_L = -0.5$, $v_{Ca} = 1$, $v_K = -0.7$, $g_{syn} = 0.0409$, $v_{rev} = 0.5$, $I_i^{ext} = 0.13$, ($i = 1, 2, 3$). With these parameter values the uncoupled single neuron is in the rest state.

III. SYNAPTIC COUPLING DYNAMICS

The term $-s_i g_{syn}(v_i - v_{rev})$ in the right side of equation (1) models synaptic current that can changes

the membrane potential of the i -th neuron v_i . Activation variable s_i shows the dependence of postsynaptic conductance on presynaptic potential v_j . Here, we propose a new phenomenological dynamical model of synapse possessing the threshold features and realistic form of synaptic current as well as synaptic delay.

The FitzHugh-Nagumo system (equations (3),(4) with $\mu = 0$) in the parameters region, where it has three equilibrium states, was used here for describing dynamics of variable s_i . Let us consider in detail an activation process of synaptic coupling in our model. If the condition $v_j < \theta_{ji}$ is satisfied for all the neurons membrane potentials, then all the functions $H(v_j - \theta_{ji}) \approx 0$ and equations (3),(4) can be rewritten as follows:

$$\begin{aligned} \frac{dr_i}{dt} &= f_1(r_i) - s_i - k_1, \\ \frac{ds_i}{dt} &= \varepsilon(f_2(r_i) - s_i - k_2). \end{aligned} \quad (5)$$

Under the chosen parameter values, the system (5) has a phase portrait presented in fig. 1a. In this case, for any initial conditions the system comes to the rest state associated with stable equilibrium state O_1 . Parameters k_1 and k_2 are chosen such, that the ordinate of this equilibrium state is equal to zero. There is also saddle equilibrium state O_2 in phase plane. Stable separatrix of this state defines the activation threshold of the system. Assume that at some moment the potential of the j -th neuron exceeds θ_{ji} value. Then, function $H(v_j - \theta_{ji})$ rapidly takes on the value equal to unity (H is close to Heaviside function) and for throughout the period when $v_j > \theta_{ji}$, equations (3),(4) are written in the form:

$$\begin{aligned} \frac{dr_i}{dt} &= f_1(r_i) - s_i - k_1, \\ \frac{ds_i}{dt} &= \varepsilon(f_2(r_i) - s_i - k_2 - \mu). \end{aligned} \quad (6)$$

At the same time, the initial conditions for system (3),(4) are defined by dynamics of the previous system (5) and correspond to its equilibrium state O_1 . In fig. 1b the phase portrait of system (6) is presented. In this case there is only one attractor of the system – stable limit cycle L . Note, that transformation of the phase portrait, presented in fig. 1a, into the one, illustrated in fig. 1b is realized through Andronov-Hopf bifurcation, loop of separatrix W_1^s and W_1^u and saddle-node bifurcation of limit cycle. However, appearing modes have no significant influence on dynamics of system (3),(4), because the function $H(v_j - \theta_{ji})$ takes one of two possible values 0 or 1 rather quickly. The trajectory of system (6), originating from equilibrium state O_1 returns to the vicinity of stable

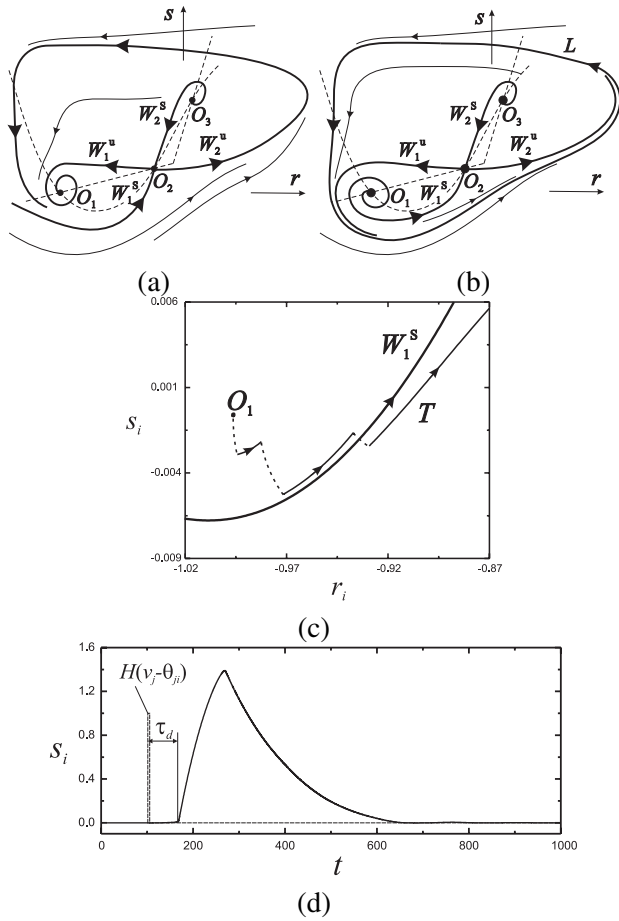


Fig. 1. Phase portraits of system (3),(4) for: (a) $v_j < \theta_{ji}$; (b) $v_j > \theta_{ji}$. (c) Fragment of trajectory forming in system (3),(4) as a result of processes of its activation and inactivation; (d) Evolution of variable $s_i(t)$ caused by changing of membrane potential v_j .

limit cycle L in accordance with dynamics of system (6). When the variable v_j becomes less than θ_{ji} , the system dynamics is described by equations (5), i.e. the trajectory returns to the vicinity of equilibrium state O_1 . Therefore, dynamics of synapse is caused by both systems (5) and (6) in turn. If the excess of potential v_j over θ_{ji} is multiple, then some trajectory T (fig. 1c) appears in the phase plane of variables (r_i, s_i) . This trajectory consists of fragments of trajectories of systems (6) (dot line) and system (5) (solid line) in turn. If the representation point finds itself to the right of separatrix W_1^s after the presynaptic potential ceases to increase, then the system returns to the vicinity of equilibrium state O_1 according to system (5) dynamics. This process is followed by “powerful” pulse change of variable r , i.e. activation of synaptic coupling. In this case evolution of variable s has a typical form for synaptic current (fig. 1d). Separatrix W_1^s defines activation threshold for synaptic coupling.

The time needed for the representation point to find itself to the right of separatrix W_1^s determines synaptic delay in our model. Thus, the parameters θ_{ji} in system (1)-(4) control the start of synaptic processes and synaptic delay is defined by dynamical properties of two “joining” nonlinear systems.

IV. TRANSIENT DYNAMICS

Consider dynamics of the model (1)-(4). All the neurons are in the rest state at the initial moment. Suppose one of the neurons (for example, the second one) to be affected by external current (information signal). It causes change of membrane potential $v_2(t)$. When the variable $v_2(t)$ exceeds the value of θ_{2i} synaptic coupling between the second and the i -th neurons may be activated. In the phase plane of system (3),(4) there appears trajectory T which in some time exceeds the threshold corresponding to separatrix W_1^s , and causes an increase of variable s_i (fig. 1d). Increasing of variable s_i means appearance of synaptic current coming to the i -th neuron.

In the presence of synaptic current, the dynamical system (1),(2), describing the i -th neuron, is non-autonomous and is defined in three-dimensional phase space. System (3),(4) contains small parameter ε , and, therefore variation of variable s_i in time is rather slow in comparison with the evolution of variables v_i, n_i . Therefore, to the first approximation one can suppose variable s_i in system (1),(2) to be a quasistatically varying parameter. The bifurcation diagram of system (1),(2) where s_i is playing a role of parameter is presented in fig. 2a. If $s_i < s_d \approx 0.724$, the system has the only stable equilibrium state P_1 . When $s_i = s_d$, saddle-node bifurcation of limit cycles takes place. Two limit cycles arise in phase plane – stable C^s and unstable C^u (fig. 2a). Further increasing of s_i leads to collapse of unstable limit cycle. For $s_i = s_h \approx 1.092$, the equilibrium state loses its stability as a result of subcritical Andronov-Hopf bifurcation. For $s_i > s_f \approx 1.327$, two more equilibrium states appear – saddle P_2 and unstable P_3 (fig. 2a). Therefore, if $s_i > s_h$, the only attractor of system (1),(2) is stable limit cycle C^s . In non-autonomous phase space, a one-parametric s_i -set of stable equilibrium states P_1 and limit cycles C^s form stable one-dimensional $M_{st}^s(0)$ and two-dimensional $M_c^s(0)$ integral manifolds, respectively. For $0 < \varepsilon \ll 1$, there are integral manifolds $M_{st}^s(\varepsilon)$ and $M_c^s(\varepsilon)$ close to $M_{st}^s(0)$ and $M_c^s(0)$ in system (1),(2). Fig. 2b illustrates a numerically obtained trajectory in non-autonomous phase space laying in manifolds $M_{st}^s(\varepsilon)$ and $M_c^s(\varepsilon)$. The trajectory includes an oscillating part

related to the phase of transient oscillating activity of a neuron, and the part corresponding to the phase of rest state of a neuron.

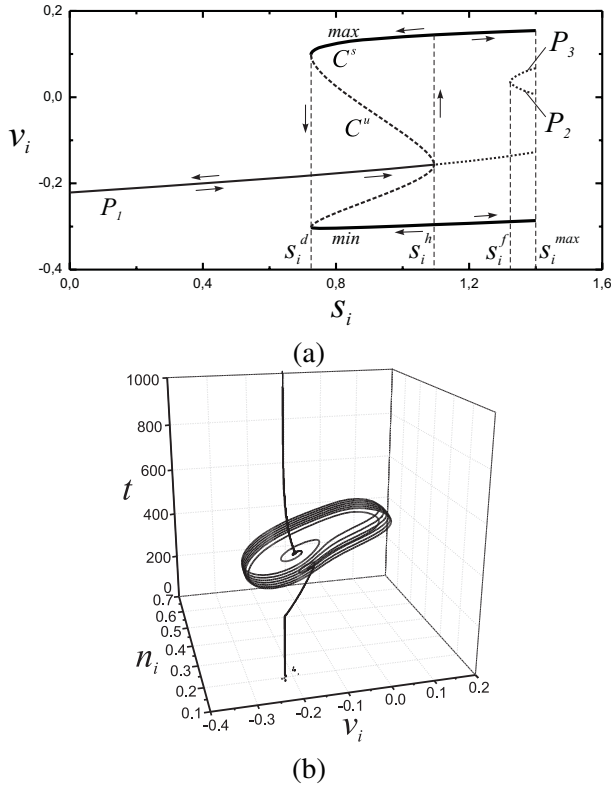


Fig. 2. Dynamics of system (1),(2) for changing s_i value. (a) One-parametric bifurcation diagram; (b) The trajectory forming in non-autonomous phase space for changing $s_i(t)$.

We considered the process of activation of a neuron and described dynamical mechanism of arising of the process. Activation of other neurons of the ensemble occurs analogously. As a result, some transient sequence of oscillating phases of activity occurs in the ensemble. Compile a matrix Θ of θ_{ji} , where $\theta_{jj} = 0$, ($j = 1, 2, 3$). Numerical investigation of system (1)-(4) has shown, that any Θ matrix corresponds to some sequence (“path”) of transient states of activity of neurons of the ensemble. In fig. 3 we present two transient sequences corresponding to two different Θ matrices, where θ_{ji} takes one of three values: $-0.2, -0.146, 0.2$. Transient dynamics of system (1)-(4) does not necessarily consist in changing of a sequence of single activation neurons. It has been found, that the phases of activity of neurons may be not single and may take place irregularly.

V. CONCLUSION

In this work we propose a new dynamical model of synaptic coupling based on the FitzHugh-Nagumo

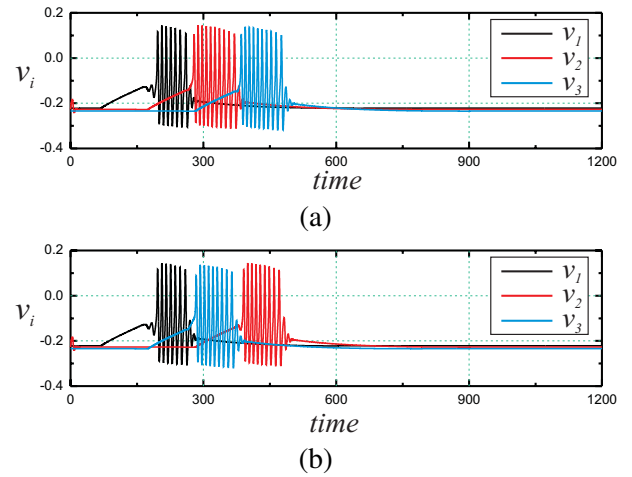


Fig. 3. Examples of transient dynamics of system (1)-(4) corresponding to two different Θ matrices: (a) $\theta_{21} = -0.2, \theta_{12} = \theta_{23} = -0.146, \theta_{13} = \theta_{32} = \theta_{31} = 0.2$; (b) $\theta_{21} = -0.2, \theta_{13} = \theta_{32} = -0.146, \theta_{12} = \theta_{23} = \theta_{31} = 0.2$.

system with nonlinear recovery properties. The model accounts for important properties of synapses such as synaptic threshold and delay. Synaptic delay in the model is not introduced artificially but is formed by its non-trivial dynamics. The duration of delay depends on the amplitude of external stimulus. By means of such synaptic couplings we form an ensemble of globally coupled Morris-Lecar neurons and study its dynamics. We show that such ensemble demonstrates various structurally stable regimes of transient dynamics in the form of sequential transitions between different metastable oscillatory states.

ACKNOWLEDGMENT

The authors would like to thank the support of the Russian Foundation for Basic Research (grants 08-02-97035, 09-02-91061, 09-02-00719) and the Federal Agency of Education (contract P942).

REFERENCES

- [1] O. Mazur, G. Laurent. *Neuron* **48**, 661 (2005)
- [2] M. Stopfer, V. Jayaraman, G. Laurent. *Neuron* **39**, 991 (2003)
- [3] L. M. Jones, A. Fontanini, B. F. Sadacca et al. *PNAS* **104**(47), 18772 (2007)
- [4] M. Rabinovich, A. Volkovskii, P. Lecanda et al. *Physical Review Letters* **87**, 068102 (2001)
- [5] V. S. Afraimovich, V. P. Zhigulin, M. I. Rabinovich. *Chaos* **14**(4), 1123 (2004)
- [6] M. I. Rabinovich, R. Huerta, V. S. Afraimovich. *Physical Review Letters* **97**, 88103 (2006)
- [7] M. I. Rabinovich, R. Huerta, P. Varona et al. *Biological Cybernetics* **95**, 519 (2006)
- [8] C. Morris, H. Lecar. *Biophysical Journal* **35**, 193 (1981)

Bifurcations in memristive oscillators

Fernando Corinto

Department of Electronics

Politecnico di Torino, Torino (Italy)

e-mail: fernando.corinto@polito.it

Alon Ascoli

Department of Electronics

Politecnico di Torino, Torino (Italy)

e-mail: alon.ascoli@polito.it

Marco Gilli

Department of Electronics

Politecnico di Torino, Torino (Italy)

e-mail: marco.gilli@polito.it

Abstract—The aim of this manuscript is to explain the interesting nonlinear dynamical behavior of a cell belonging to a class of memristor oscillators we aim to couple through memristors and/or resistors for the realization of networks for pattern recognition tasks. In particular, we shall first study existence, location and stability of the equilibria of the dynamical system. Then we shall summarize the theoretical methodology we used to prove that such a system may undergo a Heteroclinic bifurcation and a Hopf bifurcation.

I. INTRODUCTION

The memristor (i.e. memory-resistor) is a bipole characterized by a nonlinear relationship between the time integrals of current and voltage. It was discovered by Chua back in 1971 [1]. In 1976 [2] introduced a more general class of dynamical systems, the so-called memristive systems, which includes the memristor as a special case. Recently in [3] the notion of memristive systems was further extended to encompass capacitive and inductive devices. The first experimental proof of the existence of a memristor in nature was realized at Hewlett-Packard Labs in 2008 [4] by exploiting the coupling between solid-state electronic and ionic transports occurring in a nanoscale device under an external bias voltage.

The inclusion of memristive systems in integrated circuits may considerably extend the circuit functionality. Memristive systems could be employed for the realization of ultra-dense non-volatile memories. Furthermore, their use in electronic neural networks could allow the reproduction of complex neural processes. For example, coupling among adjacent electronic neurons of a network performing associative memory operations was recently realized through memristor emulators in [5].

In this work we shall first detect a suitable mathematical model for a class of oscillators employing memristive bipoles, including, as a sub-class, the nonlinear memristor oscillators derived from Chua's oscillators by replacing Chua's diodes with memristors in [6], where an incorrect mathematical model was presented

and analyzed for each oscillator. We shall then get a thorough understanding of the dynamics of a simple second-order oscillator from that sub-class. We shall give some details of the theoretical methodology we adopted to prove that such a dynamical system may display both an Heteroclinic Bifurcation and a Hopf Bifurcation.

II. MEMRISTIVE OSCILLATORS

In this section we shall determine an appropriate mathematical model for a whole class of oscillators with memristive bipoles. Oscillators from this class shall be later used to design associative and dynamic memories.

A linear bipole is characterized by the following constitutive equations:

$$L(D)u(t) = y(t) \quad (1)$$

where u and y denote the input and output to the linear bipole respectively, and $L(D)$ is a linear rational function of the time-differential operator $D = \frac{d}{dt}$. On the other hand, the constitutive equations of a memristive bipole may be written as:

$$y = g(x, u, t)u, \quad Dx = f(x, u, t) \quad (2)$$

where u and y are the input and output to the memristive bipole respectively, $f(\cdot)$ is a scalar continuous function defining the time evolution of the state variable x of the memristive bipole and $g(\cdot)$ is the scalar nonlinear Lipschitz input-output response of the memristive bipole. Connecting the one port of a linear bipole with that of a memristive bipole, depending on the choice of the input and output variables to the bipoles, one of the two Kirchhoff's Laws will impose a connection constraint on (1) and (2), thus yielding the general Lur'e model of an oscillator with a memristive bipole:

$$L(D)u(t) = -g(x, u, t)u, \quad Dx = f(x, u, t) \quad (3)$$

The constitutive equations of a memristor are:

$$y = g(x, u, t)u = h(x)u, \quad Dx = u \quad (4)$$

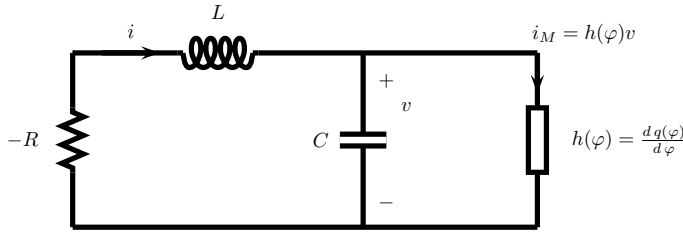


Fig. 1. A second-order oscillator with a voltage-controlled memristor.

Inserting (4) into (3) yields the general Lur'e model of an oscillator with a memristor:

$$L(D)u(t) = -h(x)u \quad (5)$$

$$Dx = u \quad (6)$$

It is crucial to realize that (5)-(6) are redundant and may thus be rewritten in a more compact form. In fact, integrating both sides of (5), that is multiplying each side of (5) by $D^{-1} = \int dt$, using (6) and defining $h(x) = \frac{dk(x)}{dx}$, we get:

$$L(D)x = -k(x). \quad (7)$$

The class of oscillators modeled by (7) includes as a subclass all the memristor oscillators presented in [6], whose authors, however, presented and studied an incorrect redundant mathematical model for each oscillator, thus drawing wrong conclusions regarding the corresponding dynamical behavior.

III. SECOND-ORDER MEMRISTOR OSCILLATOR

Our final aim is to propose networks of oscillators modeled by (7) and coupled through resistors or memristors for pattern recognition tasks. To this end, let us pick one of the circuits presented in [6], the second-order oscillator with a voltage-controlled memristor shown in Figure 1. Applying Kirchhoff's Laws to the circuit and modeling the memristor with (4), where $u = v$ and $y = i_M$ denote the voltage across and the current through the memristor respectively, we get the equations in terms of currents and voltages:

$$i_M = h(\varphi)v, \quad CDv = i - i_M, \quad Ri - v = LDi \quad (8)$$

where i is the current flowing through the inductor and x represents the flux φ through the memristor. Integrating both sides of each equation in (8) and observing that $v = D\varphi$, an equivalent set of equations in terms of charges and fluxes is obtained:

$$q_M = q(\varphi), \quad CD\varphi = q_L - q_M, \quad Rq_L - \varphi = LDq_L \quad (9)$$

where q , q_L and q_M denote the charges in the capacitor, the inductor and the memristor respectively. After a few algebraic manipulations (9) may be turned into the following non-redundant state equations:

$$Dx_1 = \alpha x_2 - \alpha q_M(x_1) \quad (10)$$

$$Dx_2 = -\xi x_1 + \beta x_2 \quad (11)$$

where $\alpha = \frac{1}{C}$, $\beta = \frac{R}{L}$ and $\xi = \frac{1}{L}$, while the state variables are defined as $x_1 = \varphi$ and $x_2 = q_L$. Note that the order of the dynamical system (10)-(11) is 2. The authors in [6] derived the state equations of the oscillator from (8), thus presenting and analyzing a redundant third-order dynamical system and drawing incorrect conclusions with regard to the dynamic behavior of the oscillator.

It is straightforward to derive the Lur'e model of (10)-(11). For reasons of limited available space, here we report only the final expression omitting the calculations, which will appear in a more extended version of this paper:

$$L(D)x_1 = -q_M(x_1) \quad (12)$$

where $q_M(x_1)$ denotes the flux-dependent charge in the memristor and $L(D) = \frac{D^2 - \beta D + \alpha \xi}{\alpha(D - \beta)}$. As expected from Section II, (12) could be derived from (7) after setting x to x_1 and $k(x)$ to $q_M(x_1)$. The charge-flux nonlinear relationship of the memristor is set to $q_M(x_1) = bx_1 + (a - b)(\frac{1}{2}(|x_1 + 1| + |x_1 - 1|))$. The equilibria of (10)-(11) are the intersections on the $x_1 - x_2$ plane between the line $x_2 = \frac{\xi x_1}{\beta}$ and $x_2 = q_M(x_1)$. Let us assume that $b > a > 0$. In this case we have:

- 1) a single equilibrium point, i.e. $\mathbf{x}_0 = (\bar{x}_1, \bar{x}_2) = (0, 0)$, if $\frac{\xi}{\beta} < a$ or if $\frac{\xi}{\beta} > b$;
- 2) ∞ equilibria, i.e. $(\tilde{x}_1, \tilde{x}_2) \in \{(x_1, x_2) \in \mathbf{R}^2 : x_2 = ax_1 \ \forall x_1 \in [-1, 1]\}$, if $\frac{\xi}{\beta} = a$;
- 3) 3 equilibria, i.e. $\mathbf{x}_0, \mathbf{x}_+, \mathbf{x}_- = (\hat{x}_1, \hat{x}_2) = \left(\frac{\beta(a-b)}{\xi-\beta b}, \frac{\xi(a-b)}{\xi-\beta b}\right)$ and $\mathbf{x}_- = -\mathbf{x}_+$, if $a < \frac{\xi}{\beta} < b$.

Here we shall consider the most interesting case, that is case 3 in the above list. The Jacobian matrix of (10)-(11) is:

$$J = \begin{pmatrix} -\alpha\{b + \frac{a-b}{2}[\text{sgn}(x_1 + 1) - \text{sgn}(x_1 - 1)]\} & \alpha \\ -\xi & \beta \end{pmatrix} \quad (13)$$

The trace and determinant of (13) at \mathbf{x}_0 are $\tau_0 = \beta - a\alpha$ and $\Delta_0 = \alpha(\xi - a\beta)$ respectively. Note that in this case $\Delta_0 > 0$, therefore the stability of the origin depends on the sign of τ_0 . It follows that the origin is unstable for $\alpha < \frac{\beta}{a}$. The sign of $\Delta_0 - \frac{\tau_0^2}{4}$ will establish how trajectories behave in the neighborhood of the origin. It turns out that spiral behavior occurs for $\alpha_1 < \alpha < \alpha_2$,

where $\alpha_{1,2} = \frac{2\xi - a\beta \pm \sqrt{4\xi(\xi - a\beta)}}{a^2}$, while nodal behavior is observed otherwise.

The trace and determinant of (13) at \mathbf{x}_+ are $\tau_+ = \beta - b\alpha$ and $\Delta_+ = \alpha(\xi - b\beta)$ respectively (the same holds for \mathbf{x}_-). Note that in this case $\Delta_+ < 0$, therefore \mathbf{x}_+ exhibits an unstable saddle behavior. The sign of τ_+ will establish which of the two real eigenvalues is larger in absolute value. It turns out that for $\alpha > \frac{\beta}{b}$ the evolution of the system along the stable manifold is faster than along the unstable manifold. Unlike the position of the equilibria, their stability depend on α .

Furthermore, we theoretically proved that dynamical system (10)-(11) may undergo a Heteroclinic Bifurcation from which a stable limit cycle is born. Due to the limited available space, we shall present the details in a future manuscript. Here we summarize our methodology. Focusing on the $x_1 - x_2$ state plane, after derivation of the analytical expressions for the stable and unstable manifolds of the saddles we then detected the intersections of the same manifolds with the $x_1 = \pm 1$ lines. We then analytically solved (10)-(11) within the linear region characterized by $|x_1| < 1$ and derived the necessary conditions for the existence of a Heteroclinic orbit, that is the necessary conditions for the system to evolve through the specified linear region from the intersection of the unstable manifold of \mathbf{x}_- with the $x_1 = -1$ line to the intersection of the stable manifold of \mathbf{x}_+ with the $x_1 = 1$ line. One of the two conditions yields the analytical expression of the time interval, call it Δt , needed for the state-space trajectory to follow the above mentioned path as a function of parameters a, b, ξ, β and α , while the other one imposes a constraint on the relationship among these parameters. If both these conditions are satisfied, the dynamical system (10)-(11) exhibits a Heteroclinic Bifurcation. Let us set $a = 0.02, b = 2, \xi = 0.1$ (in Figure 1 we choose $L = 10$) and $\beta = 0.1$ (in Figure 1 we assume $R = 1$). In Figure 2 we show the eigenvalues $\lambda_{1,2} = \frac{\tau_\zeta}{2} \pm \frac{\sqrt{\tau_\zeta^2 - 4\Delta_\zeta}}{2}$ where ζ denotes 0 for \mathbf{x}_0 (left) and + for \mathbf{x}_+ (right). Note that the eigenvalues for \mathbf{x}_- are identical to those for \mathbf{x}_+ . In agreement with the above theory, in this particular case \mathbf{x}_0 is an unstable node for $0 < \alpha < 0.0253$, an unstable focus for $0.0253 < \alpha < 5$, a stable focus for $5 < \alpha < 989.9747$ and a stable node for $\alpha > 989.97$. On the other hand both \mathbf{x}_+ and \mathbf{x}_- are saddles for any value of α (for $\alpha < 0.05$ the positive eigenvalue is larger than the negative one in absolute value). Also, as parameter α is gradually increased, this particular dynamical system first has no stable attractors for $0 < \alpha < 0.17$, then a stable cycle is born as

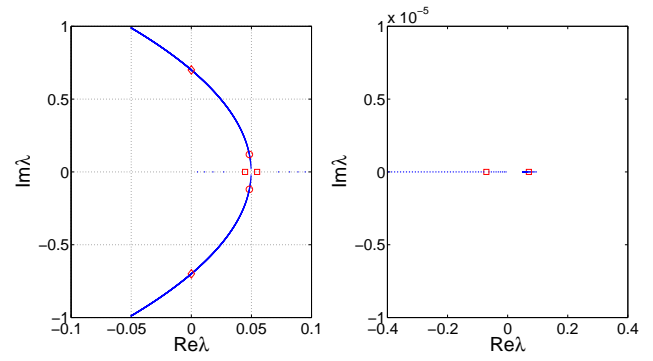


Fig. 2. Left: Eigenvalues of the origin, that is \mathbf{x}_0 , as parameter α is swept from 0.005 to 10 with a step interval of 0.005. Highlighted are the eigenvalues relative to the cases when the origin \mathbf{x}_0 is about to turn from an unstable node to an unstable focus (red squares, $\alpha = 0.025$), when a stable limit cycle is born as a result of a Heteroclinic Bifurcation (red circles, $\alpha = 0.17$), and when the cycle collides with the origin that turns from an unstable focus to a stable focus according to a Hopf Bifurcation (red diamonds, $\alpha = 5$). Right: Eigenvalues of \mathbf{x}_+ as parameter α is swept from 0.005 to 10 with a step interval of 0.005. Note the location of the eigenvalues $\lambda_{1,2} = \pm 0.0707$ (red squares) for $\alpha = 0.05$, below (above) which the absolute value of the positive real eigenvalue is greater (smaller) than that of the negative real eigenvalue.

a result of a Heteroclinic Bifurcation for $\alpha = 0.17$ (this value of α is derived from the second of the two conditions for the existence of a Heteroclinic orbit, while the other condition yields $\Delta t = 10.9731s$). As α is further increased, the period and amplitude of the cycle shrink until the cycle itself collides with the origin and a Hopf Bifurcation takes place for $\alpha = 5$. For larger values of α the only stable attractor of the system is the origin. The left plot of Figure 3 depicts the 3 equilibria (red asterisk markers) together with the steady-state attractors of the system for three different values of α , that is close to its birth (black curve, $\alpha = 0.171$), when it appears to be considerably reduced in size (blue curve, $\alpha = 1$), and close to its collision with the origin (red curve, $\alpha = 4.9675$). On the other hand, the right plot of Figure 3 reports the time waveform of the flux oscillation x_1 for $\alpha = 1$. In order to capture the nonlinear oscillations, the Describing Function (DF) Technique [7], [8] was applied to the Lur'e model of the oscillator (12). Here we shall only summarize our theoretical findings. Letting $x_1(t) \approx A + B \sin \omega t$, where A and B denote the bias and the amplitude of the flux oscillation respectively, we first derived the DF approximation for the nonlinearity $q_M(x_1)$ through long analytical calculation of integrals [8], then we expanded (12) (equating bias values, sine and cosine coefficients on each side) to finally get a set

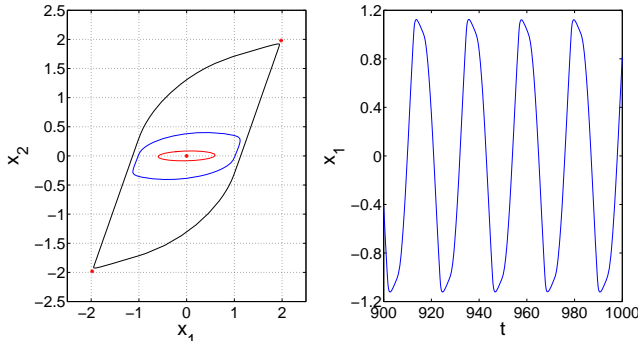


Fig. 3. Left: Steady-state attractor of the dynamical system after numerical integration of (10)-(11) for $a = 0.02$, $b = 2$, $\xi = 0.1$ and $\beta = 0.1$. Parameter α is set to a value of 4.9675, i.e. close to the occurrence of the Hopf bifurcation (red curve), of 1, where the size of the cycle is smaller than at the cycle birth (blue curve) and of 0.171, close to the appearance of the Heteroclinic bifurcation (black curve). Here the equilibria of the system for our particular parameter choice, i.e. the origin $\mathbf{x}_0 = (0, 0)$ and the two saddles $\mathbf{x}_+ = (1.98, 1.98)$ and $\mathbf{x}_- = -(1.98, 1.98)$, are shown with red asterisk markers (note that the position of the equilibria does not depend on α). Right: Time waveform of $x_1 = \varphi$ after numerical integration of (10)-(11) for $a = 0.02$, $b = 2$, $\xi = 0.1$, $\beta = 0.1$ and $\alpha = 1$.

of three DF algebraic equations. From the first of these we determined the analytical expression for ω :

$$\omega = \sqrt{\alpha\xi - \beta^2} \quad (14)$$

The corresponding graph of ω versus α for $a = 0.02$, $b = 2$, $\xi = 0.1$ and $\beta = 0.1$ is reported on the left plot of Figure 4 for $0.17 < \alpha < 4.99$. The expressions for the bias A and the amplitude B of the nonlinear oscillation may not be analytically determined from the other two DF algebraic equations; however, one of them is an identity for $A = 0$. Inserting this value for A into the other one, solving the resulting equation for B with $a = 0.02$, $b = 2$, $\xi = 0.1$ and $\beta = 0.1$, the behavior of the amplitude of the flux oscillation as a function of α is reported on the right of Figure 4. Note that for $\alpha > 5$ the origin turns from an unstable into a stable focus (see left plot of Figure 2) and limit cycle behavior disappears, as expected from our previous theoretical findings. For $a = 0.02$, $b = 2$, $\xi = 0.1$ and $\beta = 0.1$ and setting $\alpha = 1$ (choose $C = 1$ in Figure 1), numerical solution to the DF algebraic equations yield $A = 0$, $B \approx 1.12$ and $\omega \approx 0.3$. This is confirmed by numerical integration of (10)-(11) for our special parameter choice and it is clear from the left plot of Figure 3.

IV. CONCLUSIONS

In this work we investigated the interesting nonlinear dynamical behavior exhibited by a Memristor Oscillator

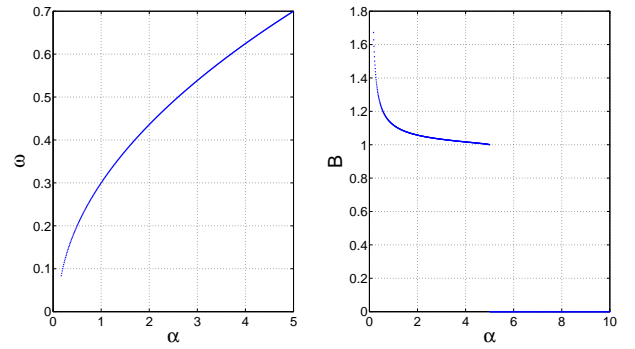


Fig. 4. Left: Plot of (14) as parameter α is swept from 0.17 to 4.99 with a step interval of 0.01. Right: Behavior of the amplitude B of the flux oscillation as parameter α is swept from 0.17 to 10 with a step interval of 0.01 according to the numerical technique explained in the text.

belonging to a class of cells used in Networks for Associative and Dynamic Memory applications. In particular, we presented a theoretical methodology to give evidence of the occurrence of Heteroclinic and Hopf Bifurcations in such a dynamical system.

ACKNOWLEDGEMENTS

This work was partially supported by the *CRT Foundation*, under the project no. 2009.0570, by the Istituto Superiore Mario Boella and the regional government of Piedmont.

REFERENCES

- [1] L. O. Chua, "Memristor: the missing circuit element," *IEEE Transactions on Circuit Theory*, vol. 18, no. 5, pp. 507-519, 1971.
- [2] L. O. Chua, and S. M. Kang, "Memristive devices and systems," *Proc. IEEE*, vol. 64, no. 2, pp. 209-223, 1976.
- [3] M. Di Ventra, Yu. V. Pershin, and L. Chua "Circuit elements with memory: memristors, memcapacitors and meminductors," *Proc. IEEE*, vol. 97, no. 10, pp. 1717-1724, 2009.
- [4] D. B. Strukov, G. S. Snider, D. R. Stewart, and R. S. Williams "The missing memristor found," *Nature*, vol. 14, pp. 80-83, 2008.
- [5] Yu. V. Pershin, and M. Di Ventra "Experimental demonstration of associative memory with memristive neural networks," arXiv:0905.2935, 2009.
- [6] M. Itoh, and L. Chua, "Memristor oscillators," *International Journal of Bifurcation and Chaos*, vol. 18, pp. 3183-3206, 2008.
- [7] F. Corinto, M. Bonnin, and M. Gilli, "Weakly connected oscillatory network models for associative and dynamic memories," *International Journal of Bifurcation and Chaos*, Vol. 17, pp. 4365-4379, 2007.
- [8] M. Bonnin, F. Corinto, and M. Gilli, "Periodic oscillation in weakly connected cellular nonlinear networks," *IEEE Transactions on Circuits and Systems I*, vol. 55, no. 6, pp. 1671-1684, July 2008.
- [9] M. Itoh, and L. O. Chua, "Star cellular neural networks for associative and dynamic memories," *Int. J. Bifurcation and Chaos*, vol. 14, pp. 1725-1772, 2004.

On the Chaos Associative Memory with Tchebycheff Activation Function

Masahiro Nakagawa

Faculty of Electrical Eng.,
Nagaoka University of Technology,
Kamitomioka 1603-1, Nagaoka, Niigata 940-2188
Japan
Email: masanaka@vos.nagaokaut.ac.jp

Abstract—In this paper we shall put forward a novel chaos neuron model and investigate the dynamic properties of memory retrievals. The present artificial neuron model is defined by such periodic input-output mapping as the Tchebycheff function of the second kind. It is apparently shown that the present neural network with a periodic activation function has an ability of the retrievals of the embedded patterns superior than the conventional neural network with such a monotonous mapping. This advantage is considered to be as a result of the nonmonotonous property of the periodic mapping which involves a chaotic behaviour of the neurons. It is also found that the present chaos neuron model has a remarkably larger memory capacity than the conventional association system with the monotonous dynamics. These findings are considered to result from the chaotic dynamics to avoid at an unfavourable spurious states.

I. INTRODUCTION

To date the associative models have been extensively investigated on the basis of the autocorrelation characteristics of the embedded patterns. Since the foundations of the retrieval model by Anderson[1], Kohonen[2], and Nakano[3], many works related to such an association model of the inter-connected neurons with a autocorrelation matrix have been reported by Amari[4], Amit et al.[5] and Gardner[6]. So far it has been known that the capacity of the autocorrelation associative model is estimated as $\sim 0.15N$ at most for N neuron systems. This is considered as the result of the unfavourable spurious memory states increasing drastically with the increasing network size or N . In addition, as is well known nowadays, the performance is usually

depressed especially for the strongly correlated (or non-orthogonal) embedded patterns (L). To avoid this problem, a few chaotic neural networks have been investigated by Inoue and Nagayoshi[7], Aihara et al.[8], Nakagawa and Okabe[9], Nakamura and Nakagawa[10], Kasahara and Nakagawa[11]. Therein chaotic behaviour has been shown to be available for the optimization problems or the memory retrievals. Very recently the neuro-dynamics with a nonmonotonous mapping have been very recently reported by Morita[12], Yanai & Amari[13]. They noticed that the nonmonotonous mapping in a neuron dynamics provides an advantage of the memory capacity compared with the conventional associatron with a monotonous mapping. This improvement of the autocorrelation association model was explained as a result of a certain orthogonalization of the apparent synaptic weight matrix[13]. That is, a nonmonotonous neuron dynamics involves itself a one-step orthogonalizing procedure in the dynamic retrieval process. Further, as a special case of the nonmonotonous mapping, we have put forward a periodic activation function to realise a novel chaos neuron[14-16]. Therein we have elucidated that such a chaos neural network has a noticeable advantage in memory searching and the auto-associative model superior than the previous chaos neuron model with a monotonous activation function[8-10].

In this work, let us propose a noble association model with a periodic mapping instead of the previously investigated nonmonotone ones[12,13]. In practice the Tchebycheff function of the second kind is introduced in the nonlinear neuron dynamics in similar to the previous work[14-16]. Such a periodic mapping is found to have an ability to escape from an unfavourable spurious metastable state as a result of such a nonmonotonous property of the mapping as well as the resultant chaotic behaviour of the neurons.

In addition the presently proposed chaotic dynamics will be found to promote the memory capacity of the neural network. In the next section a theoretical framework will be reviewed to construct the periodic dynamics related to chaos. Then some computational results will be given in **III** to show the ability with respect to the memory capacity. Finally a few concluding remarks will be addressed in **IV** to show the effect of the chaos in the present neuro-dynamics.

II. THEORY

We shall start with deriving the dynamic rule for the present neural network. For this purpose let us define the internal state and the corresponding output of the i th neuron as σ_i and s_i , respectively, which have to be related each other in terms of the following nonlinear mapping[13,14] in terms of the Tchebycheff function,

$$s_i = \sin\left(\frac{\nu}{\tau} \sin^{-1} \sigma_i\right) \quad (0 < \tau \leq 1) \quad (1)$$

where ν is a constant.

Then the Lyapunov function E may be defined as

$$E = -\frac{1}{2} \sum_{i=1}^N \sum_{j=1}^N w_{ij} s_i s_j + \frac{1}{2} \sum_{i=1}^N \lambda_i \left\{ \int ds_i \sigma_i^\dagger + \int ds_i^\dagger \sigma_i \right\} \quad (2)$$

where λ_i ($1 \leq i \leq N$) are constants to be determined as mentioned below, \dagger denoted the conjugate quantities and $H_d / N w_{ij}$ is the connection matrix defined as,

$$w_{ij} = \sum_{r=1}^L e_i^{(r)} e_j^{\dagger(r)} ; \quad (3)$$

here $e_i^{(r)}$ ($1 \leq i \leq N, 1 \leq r \leq L$) are the binary embedded vectors to be retrieved.

The updating dynamics may be introduced as

$$\sigma_i(t+1) = \sigma_i(t) - \eta \frac{\partial E}{\partial s_i^\dagger} , \quad (4)$$

where η is a constant. Substituting eq.(2) into eq.(4), one finds

$$\sigma_i(t+1) = (1 - \lambda_i) \sigma_i(t) + \eta \sum_{j=1}^N w_{ij} s_j(t) . \quad (5)$$

So as to assure the equilibrium point at a retrieval

point together with $\sigma_i(t+1) = \sigma_i(t)$, $s_i(t+1) = s_i(t)$, $\nu / \tau = 1$ as well as eq.(1), one has the following constraint,

$$\eta = \lambda_i . \quad (6)$$

For the present model, the Frobenius-Perron equation is defined as

$$p(\sigma) = \int_{-1}^{+1} d\xi p(\xi) \delta(\sigma - f(\xi)) . \quad (7)$$

From eqs.(1) and (7), the invariant measure $p(\sigma)$ eventually leads to

$$p(\sigma) = \frac{1}{\pi \sqrt{1 - \sigma^2}} . \quad (8)$$

Hence the Lyapunov exponent is readily derived as

$$\lambda = \int_{-1}^{+1} d\xi p(\xi) \log \left| \frac{df(\xi)}{d\xi} \right| = \log \alpha (\alpha = \nu / \tau) \quad (9)$$

Therefore it has to be noted that the chaos strength may be controlled in terms of the parameter α .

Finally we shall concentrate our interest on the control method of the parameter τ in eq.(4). As expected by eq.(9) with a fixed ν , τ is closely related to the chaotic behaviour of the neuron. Therefore τ has to be even smaller than 1 so as to involve the chaos dynamics. On the other hand, in order to accomplish a complete association, τ must be controlled towards 1 near a complete retrieval point, where only one overlap is to become +1 or -1 whereas all the others must completely vanish. According to this respect, we may control τ in the following manner,

$$\tau(t+1) = \tau(t) + \kappa(1 - \tau(t)) \quad (10)$$

where κ is a relaxation parameter to control τ . Finally τ is to be reset to a sufficiently small constant ε according to the following condition as

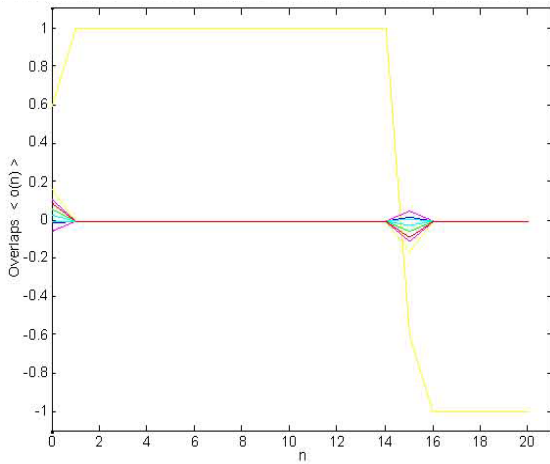
$$\text{if } t = 0 \text{ or } \|s(t+1) - s(t)\| < \varepsilon \rightarrow \tau(t) = \varepsilon . \quad (11)$$

III. RESULTS

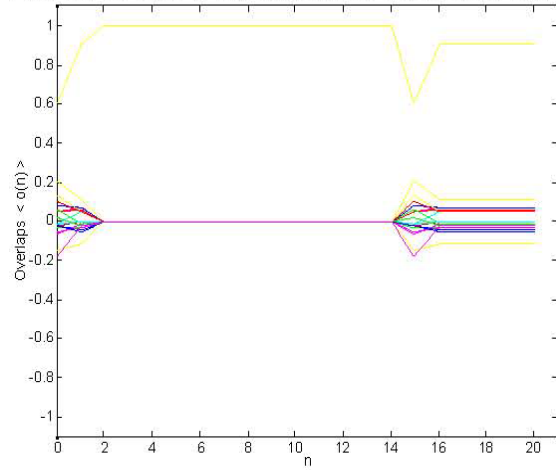
In this section let us show the association properties of the present model in comparison with the

monotonous dynamic system.

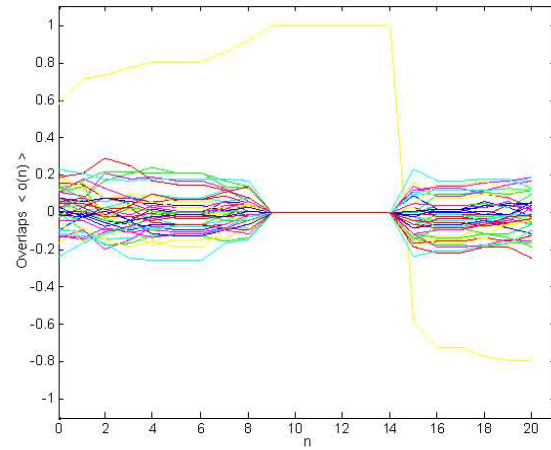
First of all we shall present a few examples of the dynamic behaviour of the present chaotic model. Here κ and ε are set to 0.8 and 10^{-6} , respectively, below if not mentioned. The initial state $s_i(0)$ ($1 \leq i \leq N$) was also set to a random pattern which is apart from an embedded pattern with the Hamming distance H_d . The embedded pattern vectors were randomly picked up from 2^N patterns to be different each other. Hereafter the number of neurons is set to 100 if not mentioned. In Fig. 1(a)-(c), the dynamics for the memory retrievals are depicted for the several loading rates L/N . Herein the Hamming distance H_d , i.e. the distance from a target pattern to be retrieved, was set to 20.



(a) $L/N=0.1$



(b) $L/N=0.2$



(c) $L/N=0.4$

Fig.1 The overlap dynamics during the memory retrievals for the several loading rates L/N .

From this result, one may confirm the advantage of the presently proposed chaos associative memory model with the Tchebycheff activation function in comparison with the conventional non-chaotic models[1]-[6].

Then let us present the memory retrieval properties for 200 trials for different set of the embedded vectors in Figs.2(a) and (b) for a few Hamming distances H_d/N .

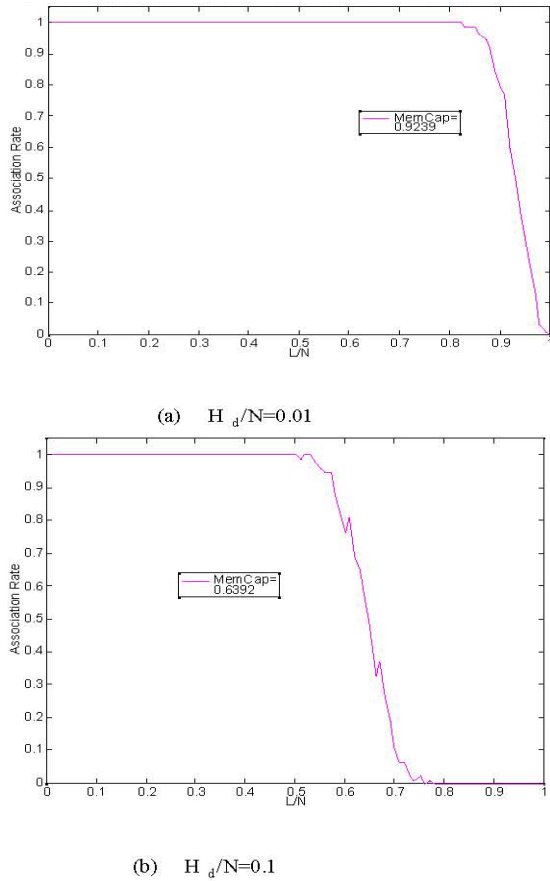


Fig.2 Memory retrieval properties.

To conclude this work, we shall present memory capacities, which are defined as the area of the memory retrieval curves in Fig.2, for the present model in Fig.3.

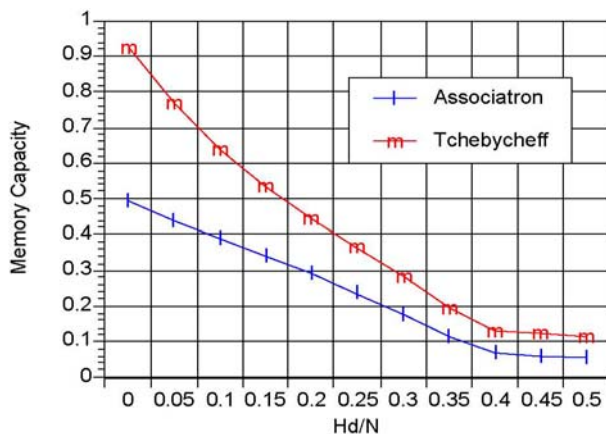


Fig. 3 Memory capacities vs the Hamming distance.

IV Conclusions

In this paper we have proposed a chaotic memory retrieval model with a periodic function as an activation function which relates the internal state σ to the output s . In practice the Tchebycheff function of the second kind was utilised so as to involve chaotic dynamics in the autoassociative memory. Although such a periodic mapping does no longer assure the monotonous decreasing of the energy, it may prevent the system from an unfavourable trapping at spurious states. At the same time the dynamic memory retrieval characteristics of such a chaos neural network is found to be improved in comparison with the conventional models including the chaos neural networks with the monotonous mapping[9-11].

REFERENCES

- [1] J.A.Anderson:Math. Biosci.**14**(1972)197.
- [2] T.Kohonen: **IEEE Trans.C-21**(1972)353.
- [3] K.Nakano: **IEEE Trans. SMC-2**(1972)380.
- [4] S.Amari: Biol. Cybern.**26**(1977)175.
- [5] D.J.Amit, H.Gutfreund, and H. Sompolinsky:Phys. Rev. Lett.**55** (1985)1530.
- [6] E. Gardner: J. Phys. **A19**(1986)L1047.
- [7] M.Inoue and A.Nagayoshi: Phys.Lett.**A158**(1991)373.
- [8] K.Aihara, T.Numajiri, G.Matsumoto, and M.Kotani: Phys. Lett. **A116** (1986)313.
- [9] M.Nakagawa and M. Okabe: J. Phys. Soc.of Jpn.**61**(1992)L1121.
- [10] K.Nakamura and M.Nakagawa:J. Phys. Soc. of Jpn.**62**(1993)2942.
- [11] T. Kasahara and M. Nakagawa: IEICE Trans. on Fundamentals A (1994, in press).
- [12] M.Morita :Neural Networks **6**(1993)115-126.
- [13] Hiro-F.Yanai and S.Amari: Proc. of ICNN'93, San Francisco (1993)1385-1390.
- [14] M. Nakagawa: Proc. of ICONIP'94, Seoul,Vol.1 (1994)609.
- [15] M. Nakagawa: Proc. of ICDC'94,Tokyo,Vol.2 (1994) pp.603-607.
- [16] M. Nakagawa: J. Phys.Soc.Jpn.**64**(1995)pp.1023-1031.
- [17] M. Nakagawa:IEICE Trans. on Fundamentals E78-A (1995)pp.412-423

Detecting unstable periodic spatio-temporal states of spatially extended chaotic systems

Alexander E. Hramov and Alexey A. Koronovskii
Faculty of Nonlinear Processes; Saratov State University;
Astrakhanskaya, 83, Saratov, 410012, Russia; Email: aeh@nonlin.sgu.ru

Abstract—In this paper we have proposed the method of detection of unstable periodic spatio-temporal states of spatially extended chaotic systems. The application of this method is illustrated by consideration of two different systems: (i) fluid model of Pierce diode which is one of the fundamental system of the physics of plasmas and (ii) complex one-dimensional Ginzburg-Landau equation demonstrating different regimes of spatio-temporal chaos.

I. INTRODUCTION

Unstable periodic orbits (UPOs) embedded into chaotic attractors are well-known to play an important role in the dynamics of systems with a small number of degree of freedom [1]. The chaotic regime may be characterized by means of the set of UPOs [2]. A universal and powerful tool for exploration of chaotic dynamics, UPOs proved to be especially efficient in context of chaotic synchronization [3], [4] and the problem of chaos controlling [5]. In the last case UPOs may be stabilized by means of the weak influence on system dynamics by small variation of control parameter [5] or with the delay feedback [6].

In spatially extended systems the unstable periodic spatio-temporal states (UPSTSs) exist [7] which are similar to UPOs in chaotic systems with a small number of degree of freedom. In particular, chaotic dynamics of spatially extended systems may be controlled by stabilizing such UPSTSs [8]. Therefore, one of the important problems connected with the study of distributed chaotic system is finding these UPSTSs. It is appropriate to suggest that the methods aimed at the search of UPOs of dynamical systems with small dimension of phase space may be adapted to spatially extended systems. The method proposed by D. Lathrop and E. Kostelich [9], as an example, had been used to pick out UPSTSs for the fluid model of Pierce diode [10]. This method is based on the obtaining of the histograms describing the frequency of system returning to the vicinity of UPOs (in low-dimensional systems) or UPSTSs (in spatially distributed

systems), respectively. Nevertheless, this method applied to spatially extended systems is rather imprecise and time-consuming.

In this report we describe the modification of the method of P. Schmelcher and F. Diakonov (SD-method) [11], [12] allowing precise detection of UPSTSs in spatially extended chaotic systems [13]. As the example of analysis of spatially extended chaotic system we consider the complex Ginzburg-Landau equation (CGLE) and the fluid model of Pierce diode.

II. DETECTION OF UPSTS OF CHAOTIC DYNAMICS IN THE PIERCE DIODE

As the primary system under study we have used the fluid model of Pierce diode [14], [15] being one of the simplest beam-plasma systems demonstrating chaotic dynamics. It consists of two plane infinite grids pierced by the electron beam (see. Fig. 1). The entrance charge density ρ_0 and velocity v_0 are maintained constant. The space between the grids is evenly filled by the neutralizing ions with density $|\rho_i/\rho_0| = 1$. The dynamics of this system is defined by the only parameter, the so-called Pierce parameter $\alpha = \omega_p L/v_0$, where ω_p is the plasma frequency, L is the distance between grids. With $\alpha > \pi$ Pierce instability develops, which leads to the appearance of the virtual cathode. At the same time, with $\alpha \sim 3\pi$, the instability is limited by non-linearity and the regime of complete passing of the electron beam through the diode space can be observed. In this case the system can be described by the partial differential equations:

$$\frac{\partial v}{\partial t} + v \frac{\partial v}{\partial x} = \frac{\partial \varphi}{\partial x}, \quad \frac{\partial \rho}{\partial t} = -\frac{\partial(v\rho)}{\partial x}, \quad \frac{\partial^2 \varphi}{\partial x^2} = \alpha^2(\rho - 1), \quad (1)$$

with the boundary conditions:

$$v(0, t) = 1, \quad \rho(0, t) = 1, \quad \varphi(0, t) = \varphi(1, t) = 0. \quad (2)$$

In equations (1)–(2) the non-dimensional variables (space charge potential φ , density ρ , velocity v , space coordinate x and time t) are used (see [15], [16]).



Fig. 1. Schematic diagram of Pierce diode

One of the core problems related to the spatially extended system consideration is the infinite dimension of the “phase space” W^∞ . As a consequence, the state $\mathbf{U}(x, t)$ of the system of study should be considered instead of vector $\mathbf{x}(t)$ in \mathbb{R}^n as in the case of the flow systems. For the system (1) this state $\mathbf{U}(x, t) = (v(x, t), \rho(x, t), \varphi(x, t))^T$ is the vector of the functions characterizing the system dynamics. After the transient finished the set of the states $\mathbf{U}(x, t)$ may be considered as attracting subspace W^s of the infinite-dimensional “phase space” W^∞ of the spatially extended system under study. If the dimension of this subspace is finite, the finite-dimensional space \mathbb{R}^m of variables may be used to describe the dynamics of the spatially extended system.

In is well-known that SD-method was developed to the UPOs detection in the systems with discrete time, although it may be also applied to the flow systems [12] by means of reducing them to maps with the help of Poincaré secant. In order to apply the SD method to an extended system, we assume that its infinite-dimensional phase space possesses the low-dimensional attracting invariant subspace W^s , and the desired solution lies in this subspace. Further, we construct the auxiliary system $\mathbf{y}(t)$ in which the vector field \mathbf{y} is in one-to-one correspondence with W^s .

The stationary states $\mathbf{U}^0(x, t) = \mathbf{U}^0(x)$ of the spatially extended system correspond to the fixed points in the phase space of the auxiliary system, while the periodic spatio-temporal states of (1) are in one-to-one correspondence with the periodic orbits of the finite-dimensional system $\mathbf{y}(t)$. Therefore, UPSTs of spatially extended system may be found by means of the detection of UPOs of the auxiliary finite-dimensional system.

There are many well-known methods for applying low-dimensional variable space to describe the behavior of the spatially extended system, among which a typical one is the mode expansion method. Therein we propose the use of the variables taken from several points x_i of the extended system space to construct the finite dimensional system

$$\mathbf{y}(t) = (\rho(x_1, t), \dots, \rho(x_m, t))^T, \quad (3)$$

where m is the dimension of the auxiliary system, $x_i = iL/(m+1)$, $i = \overline{1, m}$. In comparison with the other known methods (for example, Galerkin method), such approach allows us to undergo easily from the spatially extended system state $\mathbf{U}(x, t)$ to the low-dimensional vector $\mathbf{y}(t)$ without any additional calculations.

For the system under study (1) we have estimated the dimension of the auxiliary vector $\mathbf{y}(t)$ as $m = 3$. This assumption is based on the results of the consideration of the finite-dimensional model of the Pierce diode dynamics obtained with the help of Galerkin method [15].

To confirm meeting of the requirements of the one-to-one correspondence between state $\mathbf{U}(x, t)$ of the spatially extended system and vector $\mathbf{y}(t)$ of the constructed auxiliary system with the small number of degree of freedom we have used the neighbour method [17]. We have examined that the distance $d(\mathbf{y}_1, \mathbf{y}_2) = \|\mathbf{y}_1 - \mathbf{y}_2\|$ between two vectors $\mathbf{y}_1 = \mathbf{y}(t_1)$ and $\mathbf{y}_2 = \mathbf{y}(t_2)$ taken in the arbitrary moments of time t_1 and t_2 is close to zero if and only if the distance $S(\mathbf{U}_1, \mathbf{U}_2)$ between two different states $\mathbf{U}(x, t_1)$ and $\mathbf{U}(x, t_2)$ of the spatially extended system taken in the same moments of time t_1 and t_2 is also small. The distance $S(\mathbf{U}_1, \mathbf{U}_2)$ has been defined as

$$S(\mathbf{U}_1, \mathbf{U}_2) = \left(\int_0^1 \|\mathbf{U}_1 - \mathbf{U}_2\|^2 dx \right)^{1/2}, \quad (4)$$

where $\|\cdot\|$ is Euclidian norm. According to the neighbour method it means that there is the one-to-one correspondence between $\mathbf{U}(x, t)$ and $\mathbf{y}(t)$, therefore we can use the constructed auxiliary low dimensional system $\mathbf{y}(t)$ to find UPTSTs by means of SD-method.

Having constructed the auxiliary flow system (3) we can use SD-method to detect UPOs in it and UPSTs in the initial spatially extended chaotic system (1), respectively. In \mathbb{R}^3 space a plane $\rho(x = 0.25, t) = 1.0$ has been selected as Poincaré secant. Let us denote the vectors $\mathbf{y}(t_n) = (1, \rho(0.5, t_n), \rho(0.75, t_n))^T$ corresponding to the n -th crossing the selected secant surface by the trajectory $\mathbf{y}(t)$ as \mathbf{y}_n . Then the description of the system dynamics can be made with the help of the discrete map

$$\mathbf{y}_{n+1} = \mathbf{G}(\mathbf{y}_n), \quad (5)$$

where $\mathbf{G}(\cdot)$ is the evolution operator. Obviously, it is impossible to find the analytical form for the operator \mathbf{G} , but numerical integration of the initial system of partial differential equations (1) can give us a sequence of values $\{\mathbf{y}\}_n$, generated by the map (5).

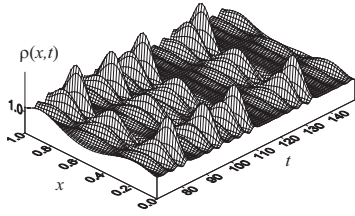


Fig. 2. The spatio-temporal dynamics of the charge density $\rho(x, t)$ of the electron beam of Pierce diode. The oscillations for the selected control parameter value $\alpha = 2.858\pi$ are chaotic both in space and time

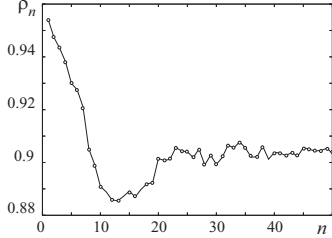


Fig. 3. The dependence of $\rho_n(x = 0.75)$ upon the number of iteration of SD-method for the UPSTS of the length 1

SD-method for picking out UPOs in the map (5) supposes consideration of the following map [12]:

$$\mathbf{y}_{n+1} = \mathbf{y}_n + \lambda \mathbf{C} [\mathbf{G}(\mathbf{y}_n) - \mathbf{y}_n], \quad (6)$$

where $\lambda = 0.1$ is the method constant and \mathbf{C} is a certain matrix of the set \mathbf{C}_k . Each of matrices \mathbf{C}_k should have only one non-vanishing entry $+1$ or -1 in row and column, i.e., they are orthogonal. In works [11], [12] it was shown that map (6) under the appropriate choice of the matrix \mathbf{C} allows to stabilize effectively the unstable saddle periodical orbits of systems (5) and (3). A trajectory of transformed system (6) starting in the domain of attraction of a stabilized fixed point converges to it. Therefore, the UPOs of a chaotic dynamical system (5) can be obtained by iterating the transformed systems (6) using a robust set of initial conditions.

The system (6) allows to find only the UPOs of length 1. To consider UPOs of length p the map

$$\mathbf{y}_{n+1} = \mathbf{y}_n + \lambda \mathbf{C} [\mathbf{G}^p(\mathbf{y}_n) - \mathbf{y}_n], \quad (7)$$

should be considered instead of (6) where $\mathbf{G}^{(p)}(\cdot)$ is p -times iterated map (5). As far as the spatially extended system and the auxiliary flow system are considered, only the p -th crossing of the Poincaré secant by the trajectory $\mathbf{y}(t)$ should be taken into account.

So, by numerical iteration of the map (7) with different values of p one can find the set of the unstable periodic spatio-temporal states of the extended system (1). However, there is a problem concerning with searching the

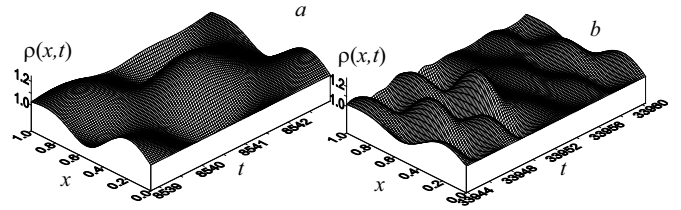


Fig. 4. The distribution of space charge density $\rho(x, t)$ corresponding to the unstable spatio-temporal states with the following lengths p periods T : (a) $p = 1$, $T = 4.2$; (b) $p = 4$, $T = 18.9$

state $\mathbf{U}(x, t_{n+1})$ at the moment t_{n+1} based on the known vector \mathbf{y}_{n+1} . Indeed, we know only the coordinates of the state $\mathbf{y}(t_{n+1})$ in the Poincaré secant but we don't know the corresponding distribution of $\rho(x, t_{n+1})$, $v(x, t_{n+1})$ and $\varphi(x, t_{n+1})$, and, correspondingly, we do not know the state $\mathbf{U}(x, t_{n+1})$ of the extended system (1). However, as we have determined above with the help of the nearest neighbours method the state $\mathbf{y}(t_{n+1})$ in the Poincaré secant uniquely defines the corresponding state $\mathbf{U}(x, t_{n+1})$ belonging to the attracting finite-dimensional subspace W^s of the infinite-dimensional phase space W^∞ . To obtain this spatially state $\mathbf{U}(x, t_{n+1})$ mentioned above we have used the following procedure. The system of partial differential equations (1) is integrated (and vector $\mathbf{y}(t)$ is calculated) until some vector $\mathbf{y}(t_s)$ is close to the required one \mathbf{y}_{n+1} with some demanded precision: $\|\mathbf{y}_{n+1} - \mathbf{y}(s)\| < 10^{-3}$. When this condition is satisfied, the state $\mathbf{U}(x, t_s)$ corresponding to the found vector $\mathbf{y}(s)$ are considered as the required one $\mathbf{U}(x, t_{n+1})$ and then the next iteration according to (7) should be done.

The spatio-temporal chaotic dynamics of the charge density $\rho(x, t)$ in the Pierce diode is shown in Fig. 2 for $\alpha = 2.858\pi$. Applying the modified SD-method allows to find the demanded periodical time-space states. The convergence of the iteration procedure (7) is illustrated by Fig. 3 which shows the dependence of the density $\rho_n(x = 0.75)$ in the moments of time when the trajectory $\mathbf{y}(t)$ in \mathbb{R}^3 space crosses the Poincaré secant upon the number of iteration n of the SD-method when the UPSTS of the length $p = 1$ is studied. One can see clearly that the iteration process of SD-method converges to the value corresponding to the unstable time-periodical spatio-temporal state of the system. Fig. 4 shows the distribution $\rho(x, t)$ corresponding to the USTSs with different periods T detected by means of SD-method.

III. DETECTION OF UPSTS IN CGLE

To show the universality of the proposed approach we also report the results of detecting the UPSTSs for

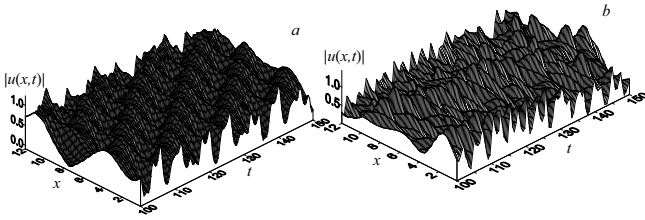


Fig. 5. The spatio-temporal dynamics $|u(x,t)|$ of the Ginzburg-Landau equation for the length (a) $L = 12.63$ and (b) $L = 13.25$

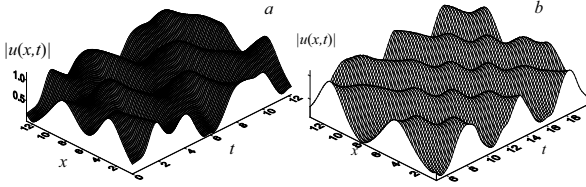


Fig. 6. The evolution of the module $|u(x,t)|$ corresponding to the UPSTSs with: (a) $p = 1$, $T = 12.1$ ($L = 12.63$; $m = 3$); (b) $p = 3$, $T = 20.2$ ($L = 13.25$, $m = 4$)

the one-dimensional complex Ginzburg-Landau equation (CGLE). The CGLE is a fundamental model for the pattern formation and turbulence description [18].

We have considered one-dimensional CGLE

$$\partial u / \partial t = u - (1 - i\alpha)|u|^2 u + (1 + i\beta)\partial^2 u / \partial x^2 \quad (8)$$

with periodical boundary conditions $u(L, t) = u(0, t)$. All calculations were performed for a fixed system parameters $\alpha = \beta = 4$ and random initial conditions.

The system length L has been chosen as the control parameter. In our study we examined two values of the control parameter: $L_1 = 12.63$ and $L_2 = 13.25$. For both these values L CGLE demonstrates the spatiotemporal chaotic regime (Fig. 5). One can see easily that the second case is characterized by more complex irregular spatio-temporal chaotic dynamics. Indeed, in the first case ($L = 12.63$) the chaotic dynamics is characterized by only one positive Lyapunov exponent $\Lambda_1 = 0.04$, while the second chaotic regime ($L = 13.25$) is characterized by two positive Lyapunov exponents $\Lambda_1 = 0.10$ and $\Lambda_2 = 0.07$. Applying the modified SD-method to the spatially extended CGLE we can find the demanded UPSTSs as well as for the fluid model of Pierce diode. We have constructed the vector (3) of the auxiliary low dimensional system as $\mathbf{y}(t) = (u(x_1, t), \dots, u(x_m, t))^T$, where m is the dimension of the auxiliary system vector, $x_i = iL/m$, $i = \overline{1, m}$.

In contrast to the fluid model of Pierce diode the dimension m of the auxiliary vector $\mathbf{y}(t)$ is unknown for CGLE. Therefore, we have to try to find UPSTSs by means of the SD-method (7) for the different values of

the dimension m starting from the minimal dimension value $m = 3$. If the required UPSTS is not found for the selected value of the auxiliary vector dimension m^* , the SD-method procedure should be repeated for the greater dimension value $m = m^* + 1$. For the system length $L = 12.63$ the dimension of the auxiliary system $m = 3$ is found to be adequate for the correct UPSTSs detection. As it was mentioned above the system behavior is characterized by one positive Lyapunov exponent. For the more complicated case $L = 13.25$ (when the behavior of CGLE is characterized by two positive Lyapunov exponents) the dimension of the auxiliary vector should be taken as $m = 4$ for UPSTSs to be detected successfully.

Fig. 6a shows the evolution of the profile $|u(x,t)|$ corresponding to the UPSTS with period $T = 12.1$ detected by means of SD-method for the system length $L = 12.63$, when the dimension of the auxiliary vector has been chosen as $m = 3$. The analogous evolution of the profile $|u(x,t)|$ with $T = 20.2$ is shown in Fig. 6b for $L = 13.25$ and $m = 4$.

IV. CONCLUSION

We have proposed the method of the detection of UPSTSs of spatially extended chaotic systems which is the extension of the well known SD-method. The effectiveness of this method is illustrated by the consideration of the fluid model of Pierce diode and CGLE.

ACKNOWLEDGEMENTS

This work has been supported by Russian Foundation of Basic Research (grant 09-02-00255; 09-02-92421) and Federal special-purpose programme ‘‘Scientific and educational personnel of innovation Russia’’ (2009–2013).

REFERENCES

- [1] Cvitanović P., Phys. Rev. Lett. 61 (1988) 2729.
- [2] Carroll T.L., Phys. Rev. E 59 (1999) 1615.
- [3] Pikovsky A.S., Zaks M., Rosenblum M.G., Osipov G.V., Kurths J., Chaos 7 (1997) 680.
- [4] Hramov A.E., Koronovskii A.A., Kurovskaya M.K., Moskalenko O.I., Phys. Rev. E 71 (2005) 056204.
- [5] Ott E., Grebogi C., Yorke J., Phys. Rev. Lett. 64 (1990) 1196.
- [6] Pyragas K., Phys. Lett. A 170 (1992) 421.
- [7] Franceschini G., Bose S., Schöll E., Phys. Rev. E 60 (1999) 5426.
- [8] Boccaletti S., Bragard J., Arecchi F. Phys. Rev. E 59 (1999) 6574.
- [9] Lathrop D.P., Kostelich E.J., Phys. Rev. A 40 (1989) 4028.
- [10] Rempen I.S., Hramov A.E., BRAS: Physics 68 (2004) 1998.
- [11] Schmelcher P., Diakonov F.K., Phys. Rev. Lett. 79 (1997) 4734.
- [12] Pingel D., Schmelcher P., Diakonov F. PRE 64 (2001) 026214.
- [13] Hramov A., Koronovskii A. Europhys. Lett. 80 (2007) 10001.
- [14] Godfrey B.B. Phys. Fluids 30, (1987), 1553.
- [15] Hramov A.E., Rempen I.S. Int. J. Electronics 91 (2004) 1.
- [16] Filatov R., Hramov A., Koronovskii A. PLA 358 (2006) 301.
- [17] Pecora L.M., Carroll T.L., Heagy J.F. PRE 52 (1995) 3420.
- [18] Aranson I.S., Kramer L. Rev. Modern Phys. 74 (2002) 99.

Phase-flip bifurcation in a system of time-delay coupled oscillators

Vladimir Klinshov and Vladimir Nekorkin

Nonlinear dynamics and optics division,

Institute of Applied Physics RAS,

Nizhny Novgorod, Russia

Email: vklin@neuron.appl.sci-nnov.ru

Abstract—The phase-flip bifurcation is studied in a simple model of two oscillators coupled with time delay. The dynamics the system is analytically studied, and the dynamical mechanism of the effect is discovered and explained.

I. INTRODUCTION

Synchronization of coupled oscillators is an universal fundamental effect and has been observed and studied in many fields of physics, engineering, chemistry and medicine (see, for example, [1-5]). One of important problems in this direction is to examine the effect of time delay on synchronization of coupled oscillators systems. Time-delayed coupling can present in most physical and biological systems like optical laser devices, electromechanical systems, physiological systems, etc. This time delay can arise from finite propagation speed of signals or from other reasons.

Studying of synchrony of oscillators with time-delayed coupling has been the topic of a number of recent investigations. One of interesting effects observed in time-delay coupled systems is the so-called phase-flip bifurcation [6,7]. This bifurcation corresponds to sharp change of synchronization mode from in-phase to anti-phase while smooth varying of time delay. Phase-flip bifurcation was demonstrated in a series of systems, such as coupled Rossler oscillators, semiconductor lasers with optical feedback, coupled van der Pol-Fitzhugh-Nagumo neurons, Chua oscillators and other.

In the present report we suggest a simple model of time delay-coupled oscillators in which we analytically study synchronization and phase-flip bifurcation. The results of our study discover the dynamical mechanisms underlying this effect.

II. MODEL

As the base model of our study we consider two oscillators with cycle periods $T_1 = 1/\omega_1$ and $T_2 = 1/\omega_2$

and describe them by their phases φ_j with $d\varphi_j/dt = \omega_j$. These phases vary in interval $[0;1]$, and at $\varphi_j = 1$ the j -th oscillator reaches threshold, emits a pulse and resets its phase to zero. The coupling between the oscillators is organized as follows. Each pulse, emitted by one of oscillators, reaches another and acts on it after some time delay τ . An input pulse yields a state change of the oscillator that consists in phase shift $\Delta\varphi_j = -\mu \sin \varphi_j$ that depends on its present phase value and coupling strength μ :

$$\varphi_j^{\text{new}} = \varphi_j + \Delta\varphi_j.$$

This pair of delay-coupled oscillators is formally described by the following dynamical system:

$$\frac{d\varphi_k}{dt} = \omega_k - \mu \sum_{j=1}^{+\infty} \delta(t - (t_j^m + \tau)) \sin \varphi_k,$$

where $k, m = \overline{1, 2}$ and $k \neq m$. Here t_j^k are the moments of k -th unit firing: $\varphi_j(t_j^k) = 1$. The summarizing is carried out by the moments $t_j^m + \tau$ when pulses from m -th oscillator act on k -th oscillator.

For the convenience of further studying let us introduce a vector $\vec{\xi}$, characterizing the state of system as follows:

$$\vec{\xi} = \{\varphi_1, \varphi_2, x_1^1, x_2^1, \dots, x_1^2, x_2^2, \dots\},$$

where $x_j^k = t - t_j^k$ is time, passed from the moment t_j^k of k -th oscillators firing.

All the components of vector $\vec{\xi}$ grow uniformly almost all the time expect a countable set of moments in which some specific events take place. These events are: 1) firing of one of units, either 2) action of a pulse on one of units. Let us determine the moments when the nearest of these events takes place if we have system state $\vec{\xi}$ in moment t .

The nearest firing of k -th unit takes place in the moment $t' = t + \theta_k$, where

$$\theta_k = \frac{1 - \varphi_k}{\omega_k}.$$

In this case vector $\vec{\xi}$ changes as follows:

$$\begin{aligned}\varphi_k(t') &= 0, \\ \varphi_m(t') &= \varphi_m(t) + \omega_m \theta_k, \\ x_1^k(t') &= 0, \\ x_j^k(t') &= x_{j-1}^k(t) + \theta_k, \\ x_j^m(t') &= x_j^m(t) + \theta_k,\end{aligned}$$

where $m \neq k$.

The nearest pulse arrival to the k -th unit from another takes place in the moment $t + \vartheta_k$, where

$$\vartheta_k = \tau - x_{n_m}^m,$$

where $n_m = \max_{j>0} \{j | x_j^m < \tau\}$.

In this case the components of $\vec{\xi}$ change as follows:

$$\begin{aligned}\varphi_k(t') &= \varphi_k(t) + \omega_k \vartheta_k + \mu f(\varphi_k(t) + \omega_k \vartheta_k), \\ \varphi_m(t') &= \varphi_m(t) + \omega_m \vartheta_k, \\ x_j^{k,m}(t') &= x_j^{k,m}(t) + \vartheta_k.\end{aligned}$$

To define the nearest of these events we compare the values $\theta_1, \theta_2, \vartheta_1, \vartheta_2$ and find the minimal value of them, which corresponds the nearest event. Using equations this we construct a map $G : \vec{\xi}(t) \mapsto \vec{\xi}(t')$ that defines the system state transformation between the nearest events.

III. SYNCHRONIZATION

Let's proceed to studying of mutual synchronization possibility in the system of two time-delay coupled oscillators. Let both units oscillate synchronously with some common period T . We introduce a Poincare secant $\varphi_2 = x_1^2 = 0$ and study how the system state changes during one period T between two moments of second unit firing t_j^2 and t_{j+1}^2 . During this time the events consisting in oscillators firing or pulses actions may occur in different sequences. For example, the sequence may be the following: the first unit fires, then it gets a pulse from the second unit, then the second units fires, and then it gets a pulse from the first unit, and so on. For each sequence of these events we can get a corresponding expression for Poincare map. Generalizing

these expressions for all possible cases, we'll get after some analysis the following map:

$$H = \begin{cases} \overline{\varphi_1} &= \omega_1(T - \Delta) + a, \\ \overline{x_1^1} &= T - \Delta, \\ \overline{x_j^{1,2}} &= x_{j-1}^{1,2} + T, \end{cases}$$

where

$$\begin{aligned}\Delta &= \frac{1 - \varphi_1 - b}{\omega_1}, \\ T &= \frac{1 - c}{\omega_2}, \\ a &= -\mu(1 - \alpha) \sin(\omega_1(\tau - \Delta - x_{n_2}^2)), \\ b &= -\mu\alpha \sin(\varphi_1 + \omega_1(\tau - x_{n_2}^2)), \\ c &= -\mu \sin(\omega_2(\tau - x_{n_1}^1)), \\ n_1 &= \left\lceil \frac{\tau + \Delta}{T} \right\rceil, \\ n_2 &= \left\lceil \frac{\tau}{T} \right\rceil + 1, \\ \alpha &= \begin{cases} 0, & \Delta < \tau \bmod T, \\ 1, & \Delta > \tau \bmod T, \end{cases}\end{aligned}$$

if $n_1 = 0$ we take $x_0^1 = -\Delta$.

Synchronous modes of the system corresponds to fixed points of the Poincare map H . Finding these fixed points we get after some analysis:

$$\begin{aligned}x_j^1 &= jT - \Delta, \\ x_j^2 &= (j - 1)T, \\ \varphi_1 &= \omega_1(T - \Delta) + a.\end{aligned}$$

This fixed point corresponds to a periodical solution of the system, which means mutual synchronization of oscillators. Looking at the form of this solution one can see that the values T and Δ have easy physical sense. T is just a common period of units firing, and Δ is a time delay between instants of first and second units firing, or interpulse delay. Using the previous system we get the following equations for T and Δ .

$$\begin{aligned}-\mu \sin(\omega_1((\tau - \Delta) \bmod T)) &= 1 - \omega_1 T, \\ -\mu \sin(\omega_2((\tau + \Delta) \bmod T)) &= 1 - \omega_2 T.\end{aligned}$$

Solving these equations we can get the expressions for the values of T and Δ that fully characterize synchronous mode of the system dynamics. Linearizing the map H near its fixed point we can study the stability of the corresponding periodical solution.

IV. RESULTS AND DISCUSSION

We now present our results for synchronization of two oscillators interacting with time delay obtained with the help of mathematical formalism described above. The series of diagrams in Fig. 1 represents the characteristics of periodical solutions of the system. We plot the value of relative interpulse delay Δ/T versus the coupling time lag τ . Solid lines correspond to stable solutions, dashed lines correspond to unstable ones. The coupling strength $\mu = 0.1$, the intrinsic frequencies of the units are $\omega_1 = 1$ and $\omega_2 = 1.01$ in Fig. 1a, $\omega_1 = 1$ and $\omega_2 = 1.1$ in Fig. 1b.

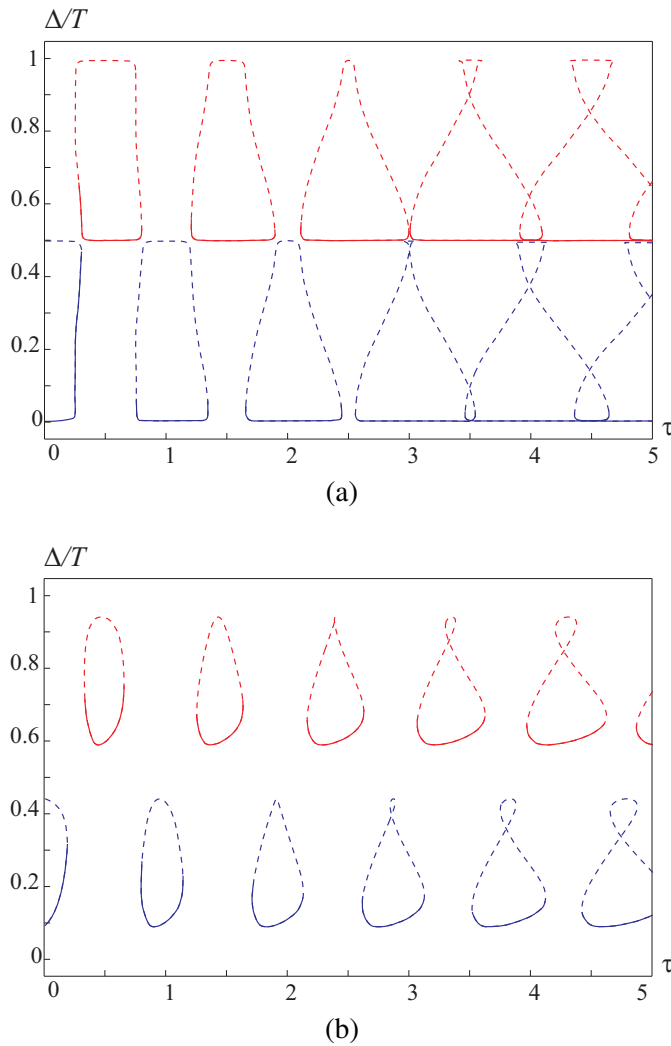


Fig. 1. Synchronization modes of the system for (a) $\omega_1 = 1$, $\omega_2 = 1.01$ and (b) $\omega_1 = 1$, $\omega_2 = 1.1$. Solid line correspond to stable solutions, dashed lines correspond to unstable ones. Blue color corresponds to in-phase synchronization, red color corresponds to anti-phase synchronization.

As we can see, the system has a number of periodical solutions which exist in definite intervals of time lag τ . In each such interval a pair of stable and unstable solutions exists. On the border of each such interval the corresponding fixed points disappear through saddle-node bifurcation. This means that synchronization of oscillators is possible inside these intervals (the so-called synchronization intervals). The size of these intervals decreases with grow of frequency mismatch between the oscillators (compare Figs. 1a and 1b).

The value of interspike delay Δ strongly differs from one synchronization interval to another. Depending on the relative interspike delay Δ/T we will speak about "in-phase" and "anti-phase" synchronization. Synchronization is called "in-phase", if $\Delta/T \in [0; 0.25)$ or $\Delta/T \in [0.75; 1)$; synchronization is "anti-phase", if $\Delta/T \in [0.25; 0.75)$. Notice that the intervals corresponding in-phase and anti-phase synchronization alternate when τ grows. The fact of great importance is that the width of synchronization intervals enlarges with growth of τ . For large values of τ neighboring intervals may even intersect. In this case two or more synchronous solutions exist for one value of time lag τ , and the system becomes *multistable*. Exactly because of this property *phase-flip bifurcation* may occur in the system when in-phase and anti-phase solutions coexist in some parameters region.

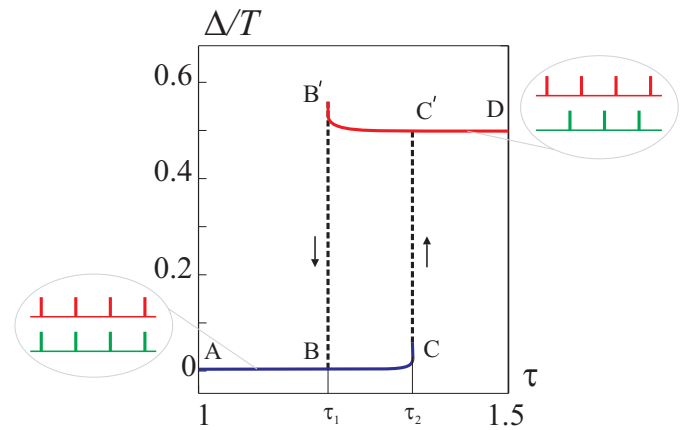


Fig. 2. Phase-flip bifurcation in the system of delay-coupled oscillators. Blue line corresponds to in-phase synchronization brunch, red line corresponds to anti-phase one.

To illustrate this property let us change the lag time from 1 to 1.5 while $\omega_1 = 1$ and $\omega_2 = 1.01$. The behaviour of the system is illustrated in Fig. 2, where

the relative interspike interval Δ/T is plotted versus the lag time τ . For $\tau < \tau_1$ only in-phase synchronization is possible, so we move across the line AB . For $\tau \in [\tau_1; \tau_2]$ both in-phase and anti-phase solutions exist, but the system stays in-phase synchronized, so we are at line BC . For $\tau > \tau_2$ the system switches to anti-phase synchronization, so we jump to line $C'D$, which is phase-flip bifurcation. Now if we will decrease τ from 1.5 back to 1 we will move across line $DC'B'BA$.

Hereby, the phase-flip bifurcation is concerned with the following properties of the system. Firstly, it is multistability or more concretely bistability that takes place in some parameters region. Secondly, it is disappearing of one synchronous mode in the border of multistability area in the result of saddle-node bifurcation and continuation of existence of the other mode. As a result of these two properties the phase flip bifurcation takes place. One of its interesting features is hysteresis behaviour of the system while varying time delay τ .

ACKNOWLEDGMENT

The authors would like to thank the RFBR (grants nos. 08-02-97035, 09-02-00719, 09-02-91061) and the "Dynasty" foundation.

REFERENCES

- [1] A. T. Winfree, *The Geometry of Biological Time* (Springer-Verlag, New York, 1980).
- [2] H. Haken, *Advanced Synergetics* (Springer, Berlin, 1983).
- [3] Y. Kuramoto, *Chemical Oscillations, Waves, and Turbulence* (Springer, Berlin, Heidelberg, New York, 1984).
- [4] A. Pikovsky, M. Rosenblum, and J. Kurths. *Synchronization: a universal concept in nonlinear sciences* (Cambridge University Press, Cambridge, 2001).
- [5] V.I.Nekorkin, M.G.Velarde. *Synergetic phenomena in active lattices*. Berlin, Springer-Verlag, 2002.
- [6] A. Prasad, J. Kurths, S. K. Dana, and R.Ramaswamy. Phase-flip bifurcation induced by time delay. *Phys. Rev. E* 74, 035204, 2006.
- [7] A. Prasad, S. K. Dana, R. Karnatak, J. Kurths, B. Blasius, and R. Ramaswamy. Universal occurrence of the phase-flip bifurcation in time-delay coupled systems. *Chaos* 18, 023111, 2008.

T-point-Hopf bifurcation in electronic circuits

A. Algaba and M. Merino
Facultad de Ciencias,
University of Huelva, Spain
Email: merino@dmate.uhu.es

F. Fernández-Sánchez and A.J. Rodríguez-Luis
Escuela Superior de Ingenieros,
University of Sevilla, Spain
Email: fefesan@us.es

Abstract—We propose a theoretical model to study the T-point-Hopf bifurcation. The phenomena numerically found in a modified van der Pol-Duffing electronic oscillator as well as in Chua's equation strongly agree with the results deduced from the model.

I. INTRODUCTION

In a parameterized three-dimensional system of autonomous differential equations, a T-point is a point of the parameter space where a special kind of codimension-two heteroclinic cycle occurs (see [1] and the references therein). A more degenerate scenario appears when one of the equilibria involved in such a cycle undergoes a Hopf bifurcation. This degeneration, which corresponds to a codimension-three bifurcation, is called T-point-Hopf and has been recently studied for a generic system [2]. However, the presence of \mathbb{Z}_2 -symmetry may lead to the existence of a double T-point-Hopf heteroclinic cycle, which is responsible for the appearance of interesting global behavior that we will study in this paper.

The theoretical model proposed is based on the construction of a Poincaré map. The existence of certain kinds of homoclinic and heteroclinic connections between equilibria and/or periodic orbits is proved and their organization close to the T-point-Hopf bifurcation is described.

II. T-POINT-HOPF BIFURCATION OF THE ORIGIN

In the case of a supercritical Hopf bifurcation of the origin we are going to study a three-parametric family of smooth (in variables and parameters) three-dimensional dynamical systems, for (d_1, d_2, μ) in a neighborhood of the origin, satisfying the following hypotheses:

(H1) Every system of the family is invariant under the change of variables $(x, y, z) \rightarrow (-x, -y, -z)$, i.e., it is \mathbb{Z}_2 -symmetric.

(H2) Every system of the family possesses three stationary points: one of them, Q_1 , situated at the origin of the phase space and the other two, Q_2^+ and Q_2^- , which are mapped onto each other by the symmetry.

(H3) Near Q_1 it is possible to choose coordinates (x, y, z) in such a way that the flow, in a neighborhood of this equilibrium, is generated by the equations

$$\begin{cases} \dot{r} = r(\mu - r^2), \\ \dot{\nu} = \omega, \\ \dot{z} = \lambda z, \end{cases} \quad (1)$$

where (r, ν) are the polar coordinates of (x, y) , ω does not vanish, λ is positive and μ is the principal parameter of the Hopf bifurcation.

Let us call Γ_1 the saddle periodic orbit that emerges, for $\mu > 0$, from the Hopf bifurcation of Q_1 .

(H4) Near Q_2^- it is possible to choose coordinates (X, Y, Z) in such a way that the flow, in a neighborhood of this equilibrium, is generated by the linear equations

$$\begin{cases} \dot{X} = PX - \Omega Y, \\ \dot{Y} = \Omega X + PY, \\ \dot{Z} = -\Lambda Z, \end{cases} \quad (2)$$

where P and Λ are positive numbers and Ω does not vanish.

Note that, using the \mathbb{Z}_2 -symmetry, it is enough to work with one of the symmetrical equilibrium points (for example, Q_2^-) and the conclusions will be valid for the other one (Q_2^+).

In the neighborhoods of Q_1 and Q_2^- we can consider four transversal sections to the flow (see

Figure 1) that can be defined, in the new coordinates, as

$$\begin{aligned}\Sigma_1 &= \{(x, y, z); z = h\}, \\ \Sigma_2 &= \{(X, Y, Z); Z = H\}, \\ \Sigma_3 &= \{(X, Y, Z); Y = 0\}, \\ \Sigma_4 &= \{(x, y, z); y = 0\},\end{aligned}\quad (3)$$

where h and H are small enough positive numbers.

From now on, in this section, we take $\theta = -\omega/\lambda$, $\phi = (\omega/\lambda) \log h$, $\Delta = P/\Lambda$, $\Theta = \Omega/\Lambda$ and $\Phi = (-\Omega/\Lambda) \log H$.

(H5) *There exist two points $(X_0, 0, 0) \in \Sigma_3$, $(x_0, 0, 0) \in \Sigma_4$, with $X_0 > 0$ and $x_0 > 0$, and four numbers $A, B, C, D \in \mathbb{R}$, satisfying $C \neq 0$ and $AD - BC \neq 0$, such that the flow between Σ_3 and Σ_4 , restricted to a neighborhood of $(X_0, 0, 0)$ maps $(X, 0, Z)$ onto $(x, 0, z)$ where*

$$\begin{pmatrix} x - x_0 \\ z \end{pmatrix} = \begin{pmatrix} A & B \\ C & D \end{pmatrix} \begin{pmatrix} X - X_0 \\ Z \end{pmatrix}. \quad (4)$$

(H6) *There exist four numbers $a, b, c, d \in \mathbb{R}$, satisfying $ad - bc \neq 0$, such that the flow between Σ_1 and Σ_2 , restricted to a neighborhood of $(0, 0, h)$, maps (x', y', h) onto (X', Y', H) where*

$$\begin{pmatrix} X' \\ Y' \end{pmatrix} = \begin{pmatrix} d_1 \\ d_2 \end{pmatrix} + \begin{pmatrix} a & b \\ c & d \end{pmatrix} \begin{pmatrix} x' \\ y' \end{pmatrix}. \quad (5)$$

Theorem 1: (see proof in [3]) **(T-point–Hopf of the origin)** Consider a three-parametric family of smooth (in variables and parameters) three-dimensional dynamical systems satisfying hypotheses H1-H6. Then, in a neighborhood of the origin of the space of parameters (d_1, d_2, μ) , the following degeneracies exist:

- 1) A (supercritical) T-point–Hopf bifurcation for $(d_1, d_2, \mu) = (0, 0, 0)$.
- 2) A semi-straight line of T-points between Q_1 and Q_2^- given by $(d_1, d_2) = (0, 0)$ and $\mu \leq 0$.
- 3) An elliptical paraboloid of EPC-points (Equilibrium-Periodic orbit Cycle) between Γ_1 and Q_2^- . The paraboloid is given by

$$\mu = \left\| \begin{pmatrix} a & b \\ c & d \end{pmatrix}^{-1} \begin{pmatrix} d_1 \\ d_2 \end{pmatrix} \right\|_2^2, \quad (6)$$

where $\|\cdot\|_2$ stands for the euclidean norm.

- 4) One cylindrical surface, with logarithmic spiral cross section, of homoclinic connections to Q_1 .

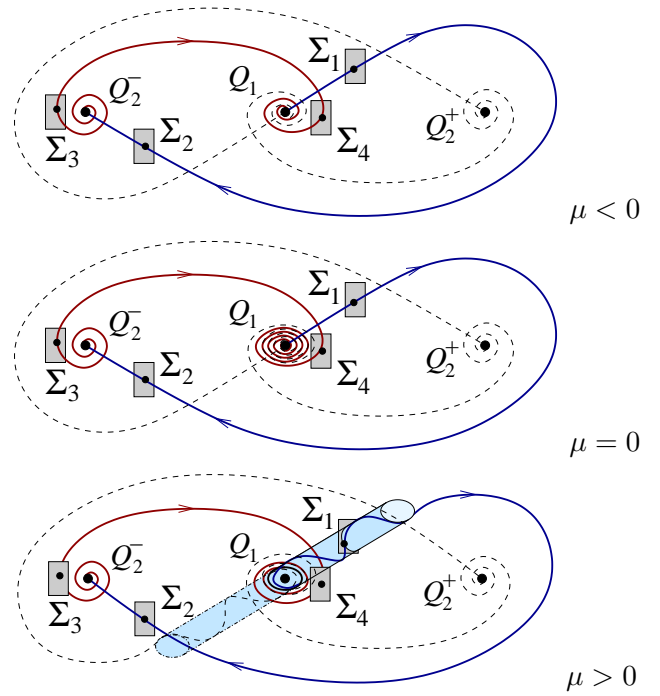


Fig. 1. Different types of heteroclinic cycles depending on the values of μ . The transversal sections used in the construction of the full Poincaré map and the two-dimensional unstable manifold of Γ (for $\mu > 0$) have been also sketched.

The equations of this surface, parameterized by Z and $\mu < 0$, are

$$\begin{pmatrix} d_1 \\ d_2 \end{pmatrix} = \left(X_0 - \frac{D}{C} Z \right) Z^\Delta H^{-\Delta} \begin{pmatrix} \cos(\Theta \log Z + \Phi) \\ \sin(\Theta \log Z + \Phi) \end{pmatrix}.$$

- 5) A logarithmic spiral of Shil'nikov-Hopf bifurcations [4] whose equations, parameterized by Z , are

$$\begin{pmatrix} d_1 \\ d_2 \end{pmatrix} = \left(X_0 - \frac{D}{C} Z \right) Z^\Delta H^{-\Delta} \begin{pmatrix} \cos(\Theta \log Z + \Phi) \\ \sin(\Theta \log Z + \Phi) \end{pmatrix},$$

when $\mu = 0$.

- 6) A solid region of homoclinic connections to Γ_1 whose equations, parameterized by $s \in [0, 2\pi)$, $Z > 0$ and $\mu > 0$, are

$$\begin{pmatrix} d_1 \\ d_2 \end{pmatrix} = - \begin{pmatrix} a & b \\ c & d \end{pmatrix} \begin{pmatrix} \sqrt{\mu} \cos(s) \\ \sqrt{\mu} \sin(s) \end{pmatrix} + \left(X_0 - \frac{D}{C} Z \right) Z^\Delta H^{-\Delta} \begin{pmatrix} \cos(\Theta \log Z + \Phi) \\ \sin(\Theta \log Z + \Phi) \end{pmatrix}.$$

For every point of this region there are also heteroclinic connections between Q_1 and Γ_1 .

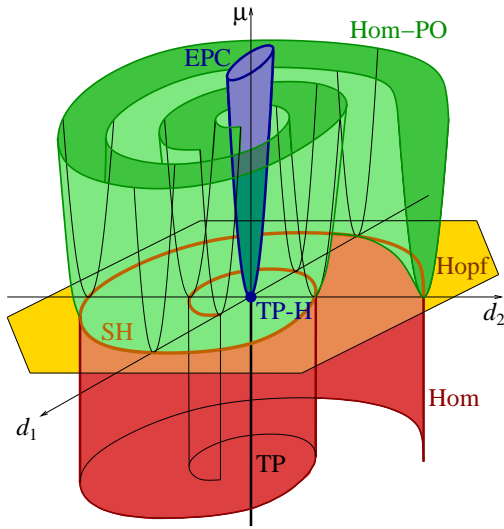


Fig. 2. Location of the different kinds of heteroclinic and homoclinic connections related to Q_1 and Γ in the space of parameters (d_1, d_2, μ) . The following notation is used: T-points (TP), EPC-points (EPC), T-point-Hopf (TP-H), homoclinic connections to Q_1 (Hom), homoclinic connections to Γ (Hom-PO) and Shil'nikov-Hopf points (SH). The plane $\mu = 0$ is the surface of Hopf bifurcations of the equilibrium Q_1 .

- 7) A surface of homoclinic connections to Q_2^- whose equations are

$$\begin{pmatrix} d_1 \\ d_2 \end{pmatrix} = -\hat{r} \left(\tau(\Sigma_4, \Sigma_1); x_0 + \frac{A}{C}z, \mu \right) \begin{pmatrix} a & b \\ c & d \end{pmatrix} \times \begin{pmatrix} \cos(\theta \log z + \phi) \\ \sin(\theta \log z + \phi) \end{pmatrix},$$

where

$$\hat{r}(\tau(\Sigma_4, \Sigma_1); x, \mu) = \begin{cases} xz^{-\frac{\mu}{\lambda}} h^{\frac{\mu}{\lambda}} \sqrt{\frac{\mu}{\mu - x^2 + x^2 z^{-\frac{2\mu}{\lambda}} h^{\frac{2\mu}{\lambda}}}} & \text{if } \mu \neq 0, \\ \frac{x}{\sqrt{1 + \frac{2x^2}{\lambda} \log\left(\frac{h}{z}\right)}} & \text{if } \mu = 0. \end{cases} \quad (7)$$

- 8) A surface of heteroclinic connections between Q_2^- and Q_2^+ whose equations are

$$\begin{pmatrix} d_1 \\ d_2 \end{pmatrix} = \hat{r} \left(\tau(\Sigma_4, \Sigma_1); x_0 - \frac{A}{C}z, \mu \right) \begin{pmatrix} a & b \\ c & d \end{pmatrix} \times \begin{pmatrix} \cos(\theta \log z + \phi) \\ \sin(\theta \log z + \phi) \end{pmatrix},$$

where \hat{r} is given by (7).

Note that, due to the \mathbb{Z}_2 -symmetry, each global connection considered in the theorem has a symmetric one for the same value of the parameters. Moreover, the surfaces given in items 7 and 8 are symmetric, up to first order, with respect to $(d_1, d_2) = (0, 0)$.

III. APPLICATION TO ELECTRONIC CIRCUITS

In this section we will consider two \mathbb{Z}_2 -symmetric circuits. This numerical study have been done with AUTO [5]. The first one is genealogically related to the classical Rayleigh and van der Pol oscillators [6]. After a suitable re-scaling, the corresponding state equations of this circuit are

$$\begin{aligned} \dot{x} &= -\frac{(\nu + \beta)}{r}x + \frac{\beta}{r}y - \frac{a_3}{r}x^3 + \frac{b_3}{r}(y - x)^3, \\ \dot{y} &= \beta x - (\beta + \gamma)y - z - b_3(y - x)^3 - c_3y^3, \\ \dot{z} &= y. \end{aligned}$$

In accordance to other previous works [6], [2] we fix $r = 0.6$, $a_3 = 0.328578$, $b_3 = 0.933578$ and $c_3 = 0$.

First we show the presence of Shil'nikov-Hopf homoclinic bifurcations in the vicinity of the detected T-point-Hopf. A projection of the corresponding curve appears in Fig. 3(a) together with the T-point curve TP. This Shil'nikov-Hopf homoclinic curve spirals around the T-point-Hopf as predicted by our model (see the curve SH in Fig. 2). Moreover the homoclinic orbits we have obtained in the continuation are good to visualize nice approximations to a cycle between a periodic orbit and an equilibrium (see Fig. 3(b)): in the first part of the pulse it approximates the connection between the equilibrium and the periodic orbit and in the second one it is close to the connection between the periodic orbit and the equilibrium.

As a second example, we consider Chua's equation that models a simple electronic circuit exhibiting a wide range of complex dynamical behaviours. Such equation is derived in [7] considering the case of a cubic nonlinearity:

$$\begin{aligned} \dot{x} &= \alpha(y - ax^3 - cx), \\ \dot{y} &= x - y + z, \\ \dot{z} &= -\beta y - \gamma z. \end{aligned} \quad (8)$$

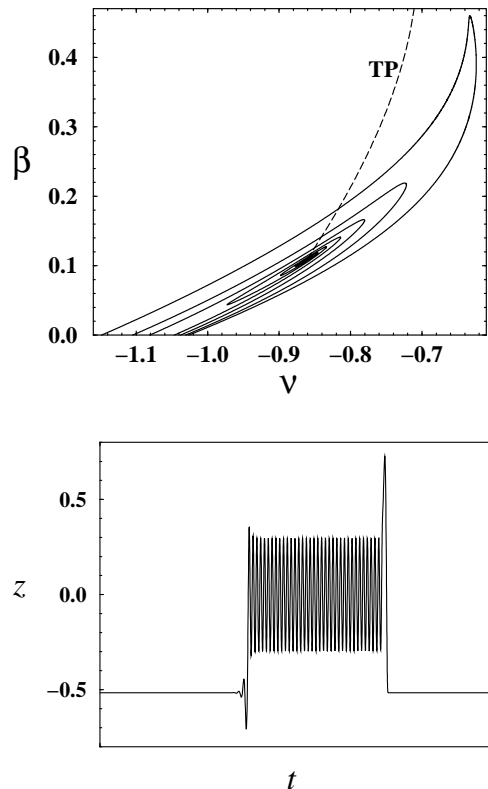


Fig. 3. (a) Projection onto the (ν, β) -plane of the curve of Shil'nikov-Hopf bifurcations in the (ν, β, γ) -parameter space. (b) Temporal profile of a homoclinic orbit of the nontrivial equilibria for $\nu = -0.9$.

A parameter γ is included in this equation in order to take into account small resistive effects in the inductance of the circuit. In this numerical study of Chua's equation, β , c and α are taken as bifurcation parameters and the other two are fixed, namely $a = -1$, $\gamma = 0.3 > 0$, in accordance with previous works (see [3] and the references therein). Two partial bifurcation sets are shown in Fig. 4 on both sides of the T-point-Hopf bifurcation (in this case the Hopf bifurcation is exhibited by non-trivial equilibria [3]).

ACKNOWLEDGMENTS

This work has been partially supported by the *Ministerio de Educación y Ciencia, Plan Nacional I+D+I* co-financed with FEDER funds, in the frame of the project MTM2007-64193 and by the *Consejería de Educación y Ciencia de la Junta de Andalucía* (FOM-276, TIC-0130 and P08-FOM-03770).

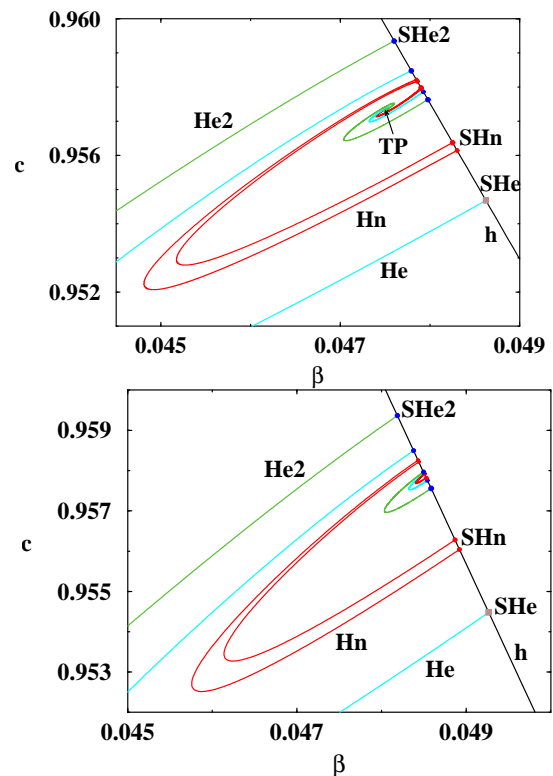


Fig. 4. A partial bifurcation set for $\gamma = 0.3$, $a = -1$ and: (a) $\alpha = -1.64$; (b) $\alpha = -1.7$. The following bifurcations related to the non-trivial equilibria appear: **h** Hopf; **Hn** homoclinic; **He** and **He2** heteroclinic; **SHn**, **SHe** and **SHe2** Shil'nikov-Hopf points of the corresponding homoclinic and heteroclinic curves; **TP** T-point.

REFERENCES

- [1] F. Fernández-Sánchez, E. Freire and A. J. Rodríguez-Luis. “T-points in a \mathbb{Z}_2 -symmetric electronic oscillator. (I) Analysis.” *Nonlinear Dynamics*, vol. 28, pp. 53–69, 2002.
- [2] F. Fernández-Sánchez, E. Freire, and A. J. Rodríguez-Luis. “Analysis of the T-point-Hopf bifurcation.” *Physica D*, vol. 237, 292–305, 2008.
- [3] A. Algaba, F. Fernández-Sánchez, M. Merino and A. J. Rodríguez-Luis. “Analysis of the T-point-Hopf bifurcation with \mathbb{Z}_2 -symmetry.” Application to Chua’s equation. *Internat. J. Bifur. Chaos* (accepted).
- [4] P. Hirschberg and E. Knobloch. “Silnikov-Hopf bifurcation.” *Physica D*, vol. 62, pp. 202–216, 1993.
- [5] E. Doedel, A. R. Champneys, T. Fairgrieve, Y. A. Kuznetsov, B. Sandstede and X. Wang. *AUTO97, Continuation and bifurcation software for ordinary differential equations (with HomCont)*, 1998.
- [6] E. Freire, A. J. Rodríguez-Luis, E. Gamero and E. Ponce. “A case study for homoclinic chaos in an autonomous electronic circuit.” *Physica D*, vol. 62, pp. 230–253, 1993.
- [7] L. Pivka, C.W. Wu and A. Huang. “Lorenz equation and Chua’s equation.” *Internat. J. Bifur. Chaos*, vol. 6, pp. 2443–2489, 1996.

Global bifurcations in a family of coupled systems

Antonio Algaba, Cristóbal García, Manuel Merino and Manuel Reyes
 Department of Mathematics, Facultad de Ciencias,
 Huelva University, Spain
 Email: merino@uhu.es

Abstract—We present a circuit with only one nonlinearity, exhibiting complex dynamics characterized by the presence of several degeneracies of equilibria (triple-fold zero degeneracy and degenerate Takens-Bogdanov) and degenerate global bifurcations.

I. INTRODUCTION

An important problem in the field of electronic devices consists in designing simple electronic systems exhibiting a great variety of dynamical behavior. Among these simple electronic devices, we can cite the Chua's circuit, with only one nonlinearity.

We study the circuit schematically represented in Fig.1, which consists of two simple devices: one of them has two branches and is linear, and the other one is one-dimensional with a nonlinearity $i(V)$, which is modelled by a third-degree polynomial:

$$i(V) = A_0 - A_1 V + A_3 V^3, \quad \text{with } A_0, A_1, A_3 > 0.$$

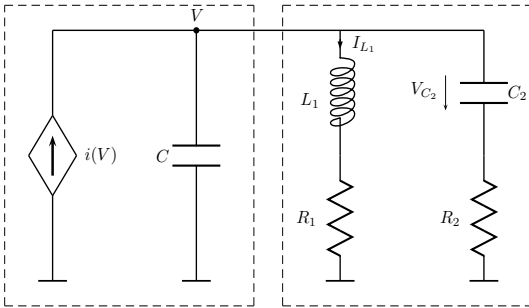


Fig. 1. Electronic circuit.

The equation of the model can be written by:

$$\begin{aligned} \dot{x} &= f(x) - \beta y_1 + r y_2, \\ \dot{y}_1 &= x - \alpha y_1, \\ \dot{y}_2 &= x - y_2, \end{aligned} \quad (1)$$

being $f(x) = -\gamma_0 + \mu x - \frac{\gamma_0}{2} x^3$, $\gamma_0 = \sqrt[3]{2A_0^2 A_3 / (C\omega)}$, $\mu = r(A_1 R_2 - 1)$, $r = \frac{C_2}{C} \geq 0$, $\alpha = \frac{R_1}{L_1 \omega} \geq 0$, $\beta = \frac{1}{C\omega^2 L_1} > 0$ and $\omega = \frac{1}{R_2 C_2}$.

II. LOCAL BIFURCATION ANALYSIS

The system (1) can be embedded in a wider family:

$$\dot{x} = f(x) + \mathbf{c}^T \mathbf{y}, \quad \dot{\mathbf{y}} = \mathbf{b}x + M\mathbf{y}, \quad (2)$$

where $x \in \mathbb{R}$, $\mathbf{y} \in \mathbb{R}^2$, M is a 2×2 matrix and $\mathbf{b}, \mathbf{c} \in \mathbb{R}^2$. This corresponds to a pair of subsystems (one of them linear) linearly interconnected.

Our first goal is to determine how we must design system (2) in order to have an equilibrium point which has a triple-zero eigenvalue. This is a very interesting situation because, as we will see later, we are able to determine parameter regimes where complex dynamics (periodic, quasi-periodic, chaotic, ...) can be predicted.

The starting point consists of determining the equilibria of system (2). The equilibria satisfy $M\mathbf{y} = -\mathbf{b}x$. A first hypothesis, $\det(M) = \Delta \neq 0$, will be assumed in order to assure the presence of an isolated equilibrium (otherwise, the non-existence or the appearance of a straight line of equilibria could arise).

It is easy to show that the equilibrium $(\bar{x}, \bar{\mathbf{y}})$ satisfies

$$f(\bar{x}) = (\mathbf{c}^T M^{-1} \mathbf{b}) \bar{x}, \quad \bar{\mathbf{y}} = -\bar{x} M^{-1} \mathbf{b}.$$

In particular, by intersecting the curve $z = f(x)$ with a straight line passing through the origin with slope $\mathbf{c}^T M^{-1} \mathbf{b}$ the abscissa \bar{x} is obtained. By varying this slope we can have different numbers of equilibria.

Let us denote $a = f'(\bar{x})$. Then, using the Taylor expansion for $f(x)$ around $x = \bar{x}$, and translating the equilibrium $(\bar{x}, \bar{\mathbf{y}})$ to the origin by $\tilde{x} = x - \bar{x}$, $\tilde{\mathbf{y}} = \mathbf{y} - \bar{\mathbf{y}}$, we get

$$\dot{\tilde{x}} = a\tilde{x} + \mathbf{c}^T \tilde{\mathbf{y}} + g(\tilde{x}), \quad \dot{\tilde{\mathbf{y}}} = \mathbf{b}\tilde{x} + M\tilde{\mathbf{y}},$$

where we have dropped the tildes and denoted

$$g(x) = \frac{f''(\bar{x})}{2!} x^2 + \frac{f'''(\bar{x})}{3!} x^3 + \dots$$

The equilibrium $(\bar{x}, \bar{\mathbf{y}})$ in system (2) undergoes a triple-zero degeneracy for the parameter values:

$$\text{TZ} \equiv \begin{cases} a + \tau = 0, \\ \mathbf{c}^T \mathbf{b} - a\tau - \Delta = 0, \\ a - \mathbf{c}^T M^{-1} \mathbf{b} = 0 \end{cases}$$

where $\tau = \text{trace}(M)$.

We obtain, by normal form bifurcation analysis (see [1]), the following result.

Theorem 1: Let assume $f''(\bar{x}) \neq 0$. The system (2) near TZ in the parameter space is C^∞ -locally equivalent up to order 3, to the unfolding:

$$\begin{cases} \dot{x} = y, \\ \dot{y} = z, \\ \dot{z} = \varepsilon_1 + \varepsilon_2 y + \varepsilon_3 z - \frac{1}{2}x^2 + A_1 xy \\ \quad + A_2 xz + B_1 x^2 y + B_2 xz^2, \end{cases} \quad (3)$$

where $\varepsilon_1 = \text{sig}(\mathbf{c}^T M^{-1} \mathbf{b} - a) \Delta^2 (a - \mathbf{c}^T M^{-1} \mathbf{b})^2 + \mathcal{O}(2)$, $\varepsilon_2 = \mathbf{c}^T \mathbf{b} - \Delta - \tau \mathbf{c}^T M^{-1} \mathbf{b} + \mathcal{O}(2)$, $\varepsilon_3 = \tau + \mathbf{c}^T M^{-1} \mathbf{b} + \mathcal{O}(2)$, $A_1 = \tau/\Delta$, $A_2 = -1/\Delta$, $B_1 = -(11f'''(\bar{x})\tau\Delta + 18f''^2(\bar{x})\Delta + 18f''^2(\bar{x})\tau^2)/(54f''^2(\bar{x})\Delta^3)$, $B_2 = (7f'''(\bar{x})\Delta + 18f''^2(\bar{x})\tau)/(72f''^2(\bar{x})\Delta^4)$.

The analysis of local bifurcations of equilibria in system (3) has been considered in [2]. It can be shown that there is a saddle-node bifurcation of the origin at $\varepsilon_1 = 0$, giving rise to two equilibria $(x_\pm, 0, 0)$ where $x_\pm = \pm\sqrt{2\varepsilon_1}$.

There are two further codimension-one local bifurcations, corresponding to Hopf bifurcations of each equilibrium that appear after the saddle-node.

Moreover, the origin of system (3) presents two codimension-two bifurcations:

Takens–Bogdanov: $\varepsilon_1 = \varepsilon_2 = 0$, $\varepsilon_3 > 0$. The singularity is cusp type, and the following bifurcations emerge: Saddle-node bifurcation of the origin, subcritical Hopf bifurcation of equilibrium $(x_-, 0, 0)$ and repulsive homoclinic connections curve of equilibrium $(x_+, 0, 0)$.

Hopf–zero: $\varepsilon_2 > 0$, $A_1 \neq 0$, $A_2 \neq 0$. Generically, from the Hopf–zero point the following bifurcations emerge: Saddle-node bifurcation of the origin, subcritical Hopf bifurcation of equilibrium $(-\sqrt{2\varepsilon_1}, 0, 0)$, supercritical Hopf bifurcation of equilibrium $(\sqrt{2\varepsilon_1}, 0, 0)$, secondary Hopf bifurcation of periodic orbits, and global connections of equilibria (the global connections are unstable for $A_1 A_2 < 0$, and stable for $A_1 A_2 > 0$).

These two-codimension points have the following nonlinear degeneracies out of TZ: Degenerate Takens–Bogdanov and degenerate Hopf–Zero:

$$\text{DTB} \begin{cases} c^t b - a\tau - \Delta = 0, \\ a - c^t M^{-1} b = 0, \\ a\tau + \tau^2 - \Delta = 0, \\ a + \tau \neq 0. \end{cases} \quad \text{DHZ} \begin{cases} a + \tau = 0, \\ c^t b + a^2 = 0, \\ a - c^t M^{-1} b = 0, \\ c^t b - a\tau - \Delta < 0 \end{cases}$$

For a complete detail of the bifurcation set, see [3], [4], respectively.

III. GLOBAL BIFURCATIONS

In this section, we will present some numerical results that correspond to the case of the electronic circuit. Specifically, we take in system (2):

$$\mathbf{b} = (1, 1)^T, \quad \mathbf{c} = (-\beta, r)^T, \quad M = \begin{pmatrix} -\alpha & 0 \\ 0 & -1 \end{pmatrix}.$$

The equilibrium $(\bar{x}, \bar{y}) = (1, 1/\alpha, 1)$ undergoes the following codimension three bifurcations:

$$\begin{aligned} \text{TZ} &\equiv \begin{cases} \alpha_c = \frac{r+1}{r}, \quad \beta_c = \frac{(r+1)^3}{r^2}, \\ \mu_c = \frac{3}{2}\gamma_0 + \frac{2r+1}{r}, \end{cases} \\ \text{DTB} &\equiv \begin{cases} \alpha_c = \left(\frac{r+1}{r}\right)^{1/2}, \quad \beta_c = \frac{(r+1)^2}{r}, \\ \mu_c = (r+1) \left(\frac{r+1}{r}\right)^{1/2} - r + 3, \quad r > 0 \end{cases} \\ \text{DHZ} &\equiv \begin{cases} \alpha_c = \frac{r+1}{r-1}, \quad \beta_c = \frac{r(r+1)^2}{(r-1)^2}, \\ \mu_c = \frac{2r}{r-1} + \frac{3}{2}\gamma_0, \quad r > 1. \end{cases} \end{aligned}$$

The numerical computation which we will present have been performed with AUTO97, see [5], and fixing the values $r = 2$, $\gamma_0 = 2$. Our strategy will be the following one. We will take slices $\alpha = \text{constant}$ of the tridimensional parameter space (α, μ, β) in the neighbourhoods of the codimension-three bifurcations of equilibria analytically detected. Concretely, for the values of r and γ_0 fixed above, a degenerate Takens–Bogdanov bifurcation of homoclinic type DTB takes place at the critical values $\alpha_c \approx 1.22474$, $\mu_c \approx 4.67423$ and $\beta_c = 4.5$. A triple-zero degeneracy TZ occurs when $\alpha_c = 1.5$, $\mu_c = 5.5$ and $\beta_c = 6.75$. Finally, the degenerate Hopf–zero bifurcation takes place at the critical values $\alpha_c = 3$, $\mu_c = 7$ and $\beta_c = 18$.

First, we take two slices $\alpha = \text{constant}$ in both sides of the degenerate Takens–Bogdanov bifurcation of homoclinic type. As it occurs for $\alpha_{\text{DTB}} \approx 1.22474$, we will study the (μ, β) -parameter bifurcation planes for $\alpha = 1$ (see Fig.2) and $\alpha = 1.3$ (see Fig.3).

Notice that the elements which appear have been previously detected in the analytical study. In the first case ($\alpha = 1$), we can see:

- The saddle-node bifurcation SN where the equilibria Eq_\pm emerge (being Eq_+ the equilibrium whose x -component is greater).
- The subcritical Hopf bifurcation h_+ of Eq_+ .
- The homoclinic bifurcation ho_- of Eq_- .

In the second case ($\alpha = 1.3$), the following bifurcations appear:

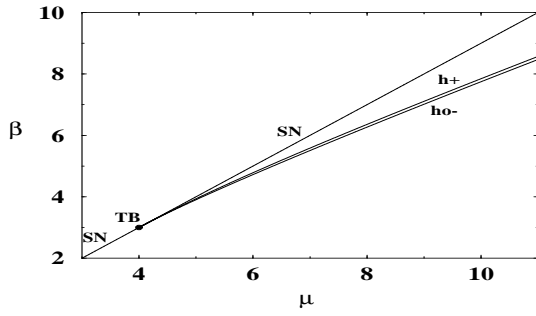


Fig. 2. A partial bifurcation set for system (1) with $\alpha = 1$, $r = 2$, $\gamma_0 = 2$, near the degenerate Takens-Bogdanov point.

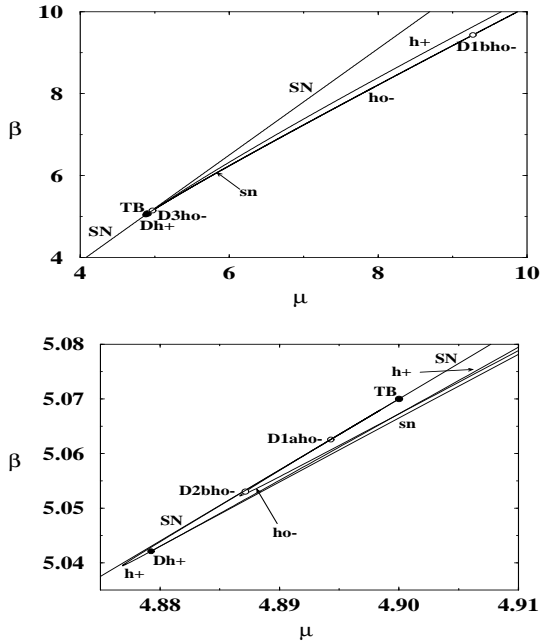


Fig. 3. A partial bifurcation set for system (1) with $\alpha = 1.3$, $r = 2$, $\gamma_0 = 2$, near the degenerate Takens-Bogdanov point. In the lower part, there is a zoom of the Takens-Bogdanov point.

- The saddle-node bifurcation SN where the equilibria Eq_{\pm} emerge.
- The supercritical Hopf bifurcation h_+ of Eq_+ .
- The degenerate Hopf bifurcation Dh_+ . After this point, the Hopf bifurcation h_+ is subcritical.
- The saddle-node bifurcation of periodic orbits sn, arising from Dh_+ .
- The homoclinic bifurcation ho_- of Eq_- .

The curve of principal homoclinic connections ho_- , that emerges from the point TB when Eq_- is a saddle equilibrium, presents for $\alpha = 1.3$ some degeneracies not deduced from the analytical study of local bifurcations. The first one, $D1aho_-$, is caused by the transition of the equilibrium from saddle to saddle-focus, for $\mu \approx 4.89430$, $\beta \approx 5.062574$. Since the double eigenvalues are not determining (an eigenvalue is called *determining*

if it is the eigenvalue closest to the imaginary axis) the homoclinic bifurcation remains tame.

If we denote by $(\rho \pm i\omega, \lambda)$ the eigenvalues of the equilibrium, the second degeneration on ho_- , $D2bho_-$, that occurs for $\mu \approx 4.88714$, $\beta \approx 5.05304$ is produced when $\delta = |\frac{\rho}{\lambda}| = 1$ (resonant eigenvalues). The transition from tame to chaotic homoclinic orbit occurs at this point.

Next, for $\mu \approx 4.96895$, $\beta \approx 5.14656$, a new degeneration $D3ho_-$ appears when $\delta = \frac{1}{2}$ (zero-divergence). The last degeneration we have detected in the parameter range shown in Fig.3, $D1bho_-$, when $\mu \approx 9.27268$, $\beta \approx 9.43127$, is caused by the transition from saddle-focus to saddle of the equilibrium. In this last degeneration is where the curve sn ends, since now the double eigenvalues are determining.

To analyze these codimension-two global bifurcations we continue, in the (α, μ, β) -parameter space, the codimension-two curves of degenerate homoclinic connections. We start from the degenerate points present on ho_- for $\alpha = 1.3$ in the parameter range shown in Fig.3, namely $D1aho_-$, $D1bho_-$, $D2bho_-$ and $D3ho_-$.

In this way, the projection of such curves onto the (α, μ) plane is shown in Fig.4. We can see how several curves emerge from the triple-zero point TZ:

- the locus of homoclinic orbits with a double-real eigenvalue, $D1aho_-$, where the transition of the equilibrium Eq_- from saddle to saddle-focus occurs. Since the double eigenvalues are not determining in the vicinity of the point TZ, the homoclinic bifurcation remains tame and the bifurcation set does not contain bifurcation curves at which limit cycles can bifurcate other than of the primary homoclinic branch. The endpoint of $D1aho_-$ is a new codimension-three point $TD1ho_-$, for $\alpha \approx 1.19775$, $\mu \approx 4.62032$, $\beta \approx 4.33534$, since the eigenvalues are of the form $(-\lambda, -\lambda, \lambda)$ with $\lambda \approx 0.4837$. On the other side of $TD1ho_-$, a curve $D1bho_-$ emerges. Now the double eigenvalues are determining and therefore, the bifurcation set contains an infinite number of bifurcation curves emerging from the codimension-two bifurcation $D1bho_-$. Moreover, a new codimension-three point, $TD3ho_-$, appears on $D1bho_-$, for $\alpha \approx 1.14937$, $\mu \approx 4.71602$, $\beta \approx 4.2506$, when the eigenvalues are of the form $(-\frac{\lambda}{2}, -\frac{\lambda}{2}, \lambda)$ with $\lambda \approx 1.27531$.
- the curve $D2bho_-$ where the equilibrium is a saddle-focus, and the leading stable and unstable eigenvalues are resonant. This curve ends at the

codimension-three point TD1ho₋.

- the curve D3ho₋ where the equilibrium is a saddle-focus and the divergence of the vector field (1) vanishes at the equilibrium. It ends at the codimension-three point TD3ho₋.

We note that the two new organizing centres of codimension three detected: TD1ho₋ (where the equilibrium Eq₋ has the transition focus-node and at the same time $\delta = 1$) and TD3ho₋ (where the equilibrium Eq₋ has the transition focus-node and at the same time $\delta = \frac{1}{2}$) have been neither analytically nor numerically treated in the literature.

The analysis of the codimension-three degenerate Takens-Bogdanov bifurcation DTB shows that from this point emerges a curve of degenerate homoclinic connection (zero trace of the equilibrium). We expect that this degenerate homoclinic connection curve joins the points DTB and TD1ho₋. Then to detect such a homoclinic degeneration we take a value of α between $\alpha_{TD1ho_-} \approx 1.19775$ and $\alpha_{DTB} \approx 1.22474$, namely $\alpha = 1.21$.

For this last value of α , the homoclinic connection ho₋ that emerged attractive from TB changes to repulsive when it crosses the degeneration point D2aho₋, for $\mu \approx 4.64381$, $\beta \approx 4.40857$ (degeneracy predicted by the local analysis of the degenerate Takens-Bogdanov point DTB). From this point now we continue in the three-parameter space the curve D2aho₋, where the equilibrium is saddle type and the stable and unstable leading eigenvalues are resonant. We observe in Fig.4 that D2aho₋ exists between the codimension-three points DTB and TD1ho₋.

Finally we continue in the (α, μ, β) -parameter space, the codimension-two curves of degenerate homoclinic connections ho₊, namely D1aho₊, D2bho₊ and D3ho₊. We start from the degenerate points present on ho₊ for $\alpha = 2.29$

The projection of such curves onto the (α, μ) plane is shown in Fig. 5, where we can see how these curves of degenerate global bifurcations of the homoclinic connections of the equilibria Eq₊ and Eq₋ emerge from the triple-zero point TZ.

ACKNOWLEDGMENT

This work has been partially supported by *Ministerio de Ciencia y Tecnología, Plan Nacional I+D+I* co-financed with FEDER funds, in the frame of the project MTM2007-64193 and by *Consejería de Educación y Ciencia de la Junta de Andalucía* (FQM-276 and EXC/2008).

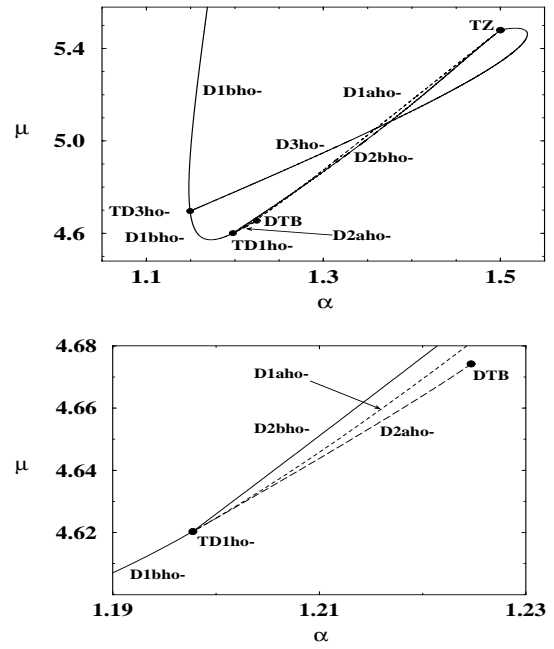


Fig. 4. Projection of loci of degenerate homoclinic orbits onto the (α, μ) plane for $r = 2$, $\gamma_0 = 2$. In the lower part, there is a zoom of the degenerate Takens-Bogdanov point.

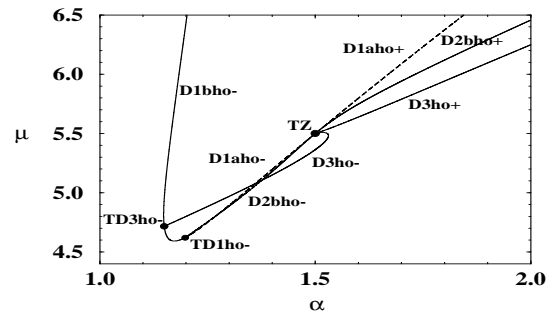


Fig. 5. Projection of loci of degenerate homoclinic orbits onto the (α, μ) plane for $r = 2$, $\gamma_0 = 2$.

REFERENCES

- [1] A. Algaba, E. Freire, E. Gamero and C. García. "An algorithm for computing quasi-homogeneous normal form under equivalence", *Acta Appl. Mathematicae*, vol. 80, pp. 335–359, 2004.
- [2] E. Freire, E. Gamero, A. J. Rodríguez-Luis, A. Algaba. "A note on the triple zero linear degeneracy: Normal forms, dynamical and bifurcation behaviour of an unfolding", *Internat. J. Bifur. Chaos*, vol. 12, pp. 2799–2820, 2002.
- [3] S. N. Chow, C. Li and D. Wang. *Normal Forms and Bifurcations of Planar Vector Fields*. Cambridge: Cambridge University Press, 1994.
- [4] A. Algaba, E. Gamero, C. García and M. Merino. "A degenerate Hopf–saddle–node bifurcation analysis in a family of electronic circuits", *Nonlinear Dynamics*, vol. 48, no. 1–2, pp. 55–76, 2007.
- [5] E. Doedel, A. R. Champneys, T. Fairgrieve, Y. A. Kuznetsov, B. Sandstede and X. Wang. *AUTO97, Continuation and bifurcation software for ordinary differential equations (with HomCont)*, 1998.

Multiobjective Optimization of Echo State Networks for multiple motor pattern learning

André Frank Krause*, Volker Dürr†, Bettina Bläsing* and Thomas Schack*

*Faculty of Sport Science, Dept. Neurocognition & Action email: andre_frank.krause@uni-bielefeld.de

†Faculty of Biology, Dept. for Biological Cybernetics email: volker.duerr@uni-bielefeld.de

all authors: Cognitive Interaction Technology, Center of Excellence

University of Bielefeld, D-33615 Bielefeld, Germany

Abstract—Echo State Networks are a special class of recurrent neural networks, that are well-suited for attractor-based learning of motor patterns. Using structural multi-objective optimization, the trade-off between network size and accuracy can be identified. This allows to choose a feasible model capacity for a follow-up full-weight optimization. It is shown to produce small and efficient networks, that are capable of storing multiple motor patterns in a single net. Especially the smaller networks can interpolate between learned patterns using bifurcation inputs.

I. INTRODUCTION

Neural networks are biological plausible models for pattern generation and learning. A straight-forward way to learn motor patterns is to store them in the dynamics of recurrent neuronal networks. For example, Tani [1] argued that this distributed storage of multiple patterns in a single network gives good generalisation compared to local, modular neural network schemes [2]. In [3] it was shown that it is not only possible to combine previously stored motor patterns to generate new ones, but also to establish an implicit functional hierarchy by using leaky integrator neurons with different time constants in a single network. This network can then generate and learn sequences by use of stored motor patterns and combine them to form new, complex behaviours. Tani [3] uses back-propagation through time (BPTT, [4]), that is computationally complex and rather biologically implausible. Echo State Networks (ESNs, [5]) are a special kind of recurrent neuronal networks. They are very easy and fast to train compared to classic, gradient-based training methods.

The general idea behind ESNs is to have a large, fixed, random reservoir of recurrently and sparsely connected neurons. Only a linear readout layer that taps this reservoir needs to be trained.

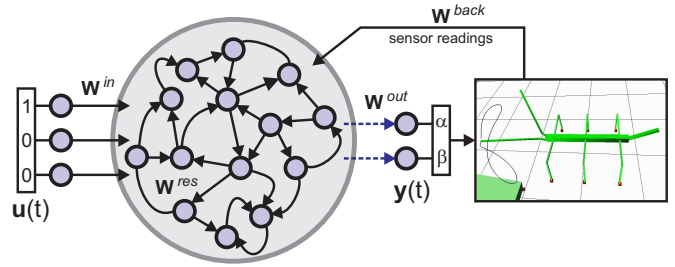


Fig. 1. General structure of an echo state network. Solid arrows indicate fixed, random connections, while dotted arrows are trainable readout connections. The output $[\alpha, \beta]$ sets the joint angles of a bi-articular manipulator, e.g., a bio-inspired active tactile sensor. Joint angles are fed back via the back-projection weight matrix \mathbf{W}^{back} .

Typically, the structural parameters of ESNs, for example the reservoir size and connectivity, are chosen manually by experience and task demands. This may lead to suboptimal and unnecessary large reservoir structures for a given problem. Smaller ESNs may be more robust, show better generalisation, be faster to train and computationally more efficient. Here, multi-objective optimization is used to automatically find good network structures and explore the trade-off between network size and network error.

II. ECHO STATE NETWORK

A basic, discrete-time ESN with a sigmoid activation function was implemented in Matlab©2009b. The purpose of this ESN was to control the joints of a bi-articular manipulator that could serve as a bio-inspired, active tactile sensor. The overall goal was to use the input to the ESN to set the tactile sampling pattern as desired. The state update equations used are:

$$\begin{aligned} \mathbf{y}(n) &= \mathbf{W}^{out} \mathbf{x}(n) \\ \mathbf{x}(n+1) &= \tanh(\mathbf{W}^{res} \mathbf{x}(n) + \mathbf{W}^{in} \mathbf{u}(n+1) + \mathbf{W}^{back} \mathbf{y}(n) + \nu(n)) \end{aligned} \quad (1)$$

where \mathbf{u} , \mathbf{x} and \mathbf{y} are the activation of the input, reservoir and output neurons, respectively. $\nu(n)$ adds a small amount of uniformly distributed noise to the activation values of the reservoir neurons. This tends to stabilize solutions, especially in models that use output feedback for cyclic attractor learning [6]. \mathbf{W}^{in} , \mathbf{W}^{res} , \mathbf{W}^{out} and \mathbf{W}^{back} are the input, reservoir, output and back-projection weight matrices. All matrices are sparse, randomly initialised, and stay fixed, except for \mathbf{W}^{out} . The weights of this linear output layer are learned using offline batch training. During training, the teacher data is forced into the network via the back-projection weights (teacher forcing), and internal reservoir activations are collected (state harvesting). After collecting internal states for all training data, the output weights are directly calculated using ridge regression. Ridge regression uses the Wiener-Hopf solution $\mathbf{W}^{out} = \mathbf{R}^{-1}\mathbf{P}$ and adds a regularization term (Tikhonov regularization):

$$\mathbf{W}^{out} = (\mathbf{R} + \alpha^2 \mathbf{I})^{-1} \mathbf{P} \quad (2)$$

where α is a small number, \mathbf{I} is the identity matrix, $\mathbf{R} = \mathbf{S}'\mathbf{S}$ is the correlation matrix of the reservoir states and $\mathbf{P} = \mathbf{S}'\mathbf{D}$ is the cross-correlation matrix of the states and the desired outputs. Ridge regression leads to more stable solutions and smaller output weights, compared to ESN training using the Moore-Penrose pseudoinverse. A value of $\alpha = 0.08$ was used for all simulations in this paper.

III. MULTI-OBJECTIVE NETWORK STRUCTURE OPTIMIZATION

Multi-objective optimization (MO) is a tool to explore trade-offs between conflicting objectives. In the case of ESN optimization, the size of the reservoir versus the network performance is the main trade-off. In MO, the concept of dominance replaces the concept of a single optimal solution in traditional optimization. A solution dominates another, if strictly one objective value is superior and all other objectives are at least equal to the corresponding objective values of another solution. Following this definition, multiple (possibly infinite) non-dominated solutions can exist, instead of a single optimal solution. The set of non-dominated or pareto-optimal solutions is called the pareto front of the multi-objective problem. The goal of MO is to find a good approximation of the true (best) pareto front, but usually MO algorithms converge to a local (sub-optimal) pareto front due to complexity of the problem and computational constraints.

Usually, the structural parameters of an ESN are chosen manually by experience and task demands. Here, the full set of free network parameters was optimized using MO. The MO was performed with the function 'gamultiobj' from the *Matlab Genetic Algorithm and Direct Search (GADS) Toolbox*, that implements a variant of the 'Elitist Non-dominated Sorting Genetic Algorithm version II' (NSGA-II algorithm, [7]). The network structure was encoded into the genotype as a seven-dimensional vector of floating-point numbers. The first six structural parameters were the sparsity and weight range of the input-, reservoir- and back-projection weights. The seventh parameter was the number of reservoir neurons. The search range of the algorithm was constrained to $[0, 1]$ for the sparsity values, to $[-5, 5]$ for the weight values and to $[1, 100]$ for the reservoir size ($[1, 500]$ for the 4-pattern problem). The optimization was started with a population size of 1000 and converged after around 120 generations. In each iteration of the MO, all genomes were decoded into network structures, the networks were trained and then simulated with random initial activations for 1000 frames per pattern. In order to neglect the initial transient behaviour, the first 50 iterations of network output were rejected. The network output and the training patterns are usually not in-phase. The best match between training pattern and network output was searched by phase-shifting both output time courses by ± 50 frames relative to the training pattern and calculating the mean Manhattan distance across all pairs of data points. The training error was then defined as the smallest distance found in that range. The acceptable error threshold (fig.2) is expressed as the percentage of the amplitude of the training patterns, that is 1.0 units for all patterns. The pareto front for a circular pattern (fig.2a) reveals that even very small networks are capable of learning and generating two sine waves with identical frequency and 90° phase shift. The smallest network found had only 3 reservoir neurons. Including the two output neurons, the overall network size was 5. In comparison, 7 neurons are required for this task when using gradient-based learning methods [8]. Network size increases with the complexity of the motor pattern, and especially when having to store multiple patterns in a single network. Storing 4 patterns in a single network required 166 reservoir neurons to reach an error below 5% (fig.2d).

IV. FULL OPTIMIZATION OF THE NETWORK WEIGHTS

From the pareto front of the two-pattern task, four candidate network structures were selected and opti-

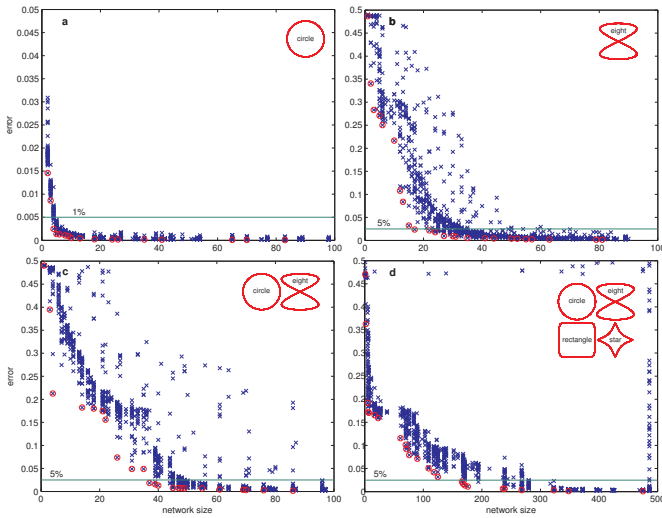


Fig. 2. Minimum reservoir size depends on task complexity. All panels show a set of pareto-optimal solutions (red circles) and the final population (blue crosses). (a) Learning a simple, circular pattern. All networks with 3 or more neurons show an error below 1%. (b) Pareto-front for the figure eight pattern. Learning this pattern requires a notably larger reservoir. Please note the different scaling of the error compared to the easier circle task. Networks with 17 or more neurons have an error below 5%. (c) Storing two motor patterns (circle and figure-eight) as cyclical attractors in a single network requires 37 or more reservoir neurons for errors below 5%. (d) Simultaneous learning of four patterns required 166 neurons.

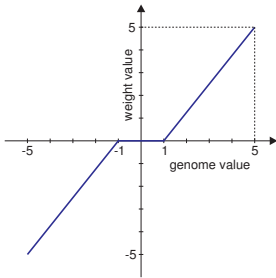


Fig. 3. Threshold function that decodes genome values into weight values, preserving sparse weight coding.

mized further, using a single-objective genetic algorithm. This time, all network weights except the output layer were fully optimized. The output layer was still trained by ridge regression. An initial random population of 200 parents was created from the network structure information of the selected candidate solutions with 4, 14, 26 and 37 reservoir neurons. Network weights were constrained to $[-5, 5]$ and decoded from the genome with a threshold function that preserves sparsity. The threshold function sets a weight to zero, if the genome value is between -1 and 1, see fig.3.

The Genetic Algorithm (GA) options were set to ranked roulette wheel selection, 20 elitist solutions, 80% crossover probability with scattered crossover and self adaptive mutation. Other options were left at their default

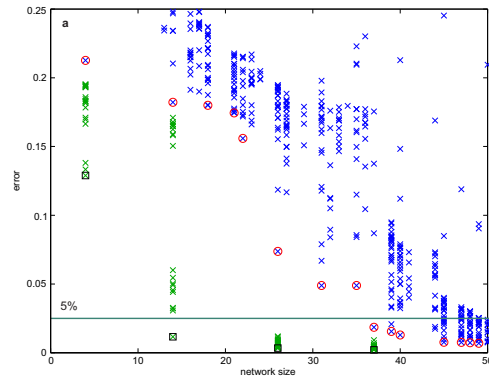


Fig. 4. Subsequent full-weight matrix optimization improves performance. Additional optimization of the four best networks of the two-pattern task with a reservoir size of 4, 14, 26 and 37 neurons. Starting from the best multi-objective solution, 20 GA runs were performed. a) Green crosses indicate the best fitness values of each run. Black squares indicate the overall best solutions that were found.

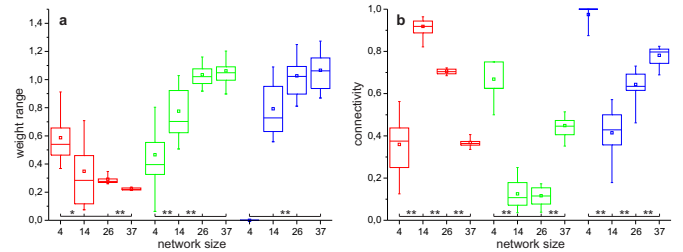


Fig. 5. Optimal weight range and connectivity depends on reservoir size. Network structure after full-weight optimization of the selected networks from fig.4. a) Weight range of all non-zero weights of the reservoir (red), the back-projection weights (green) and the input weights (blue). b) Connectivity (percentage of non-zero weights). Boxplots show 5%, 25%, 50%, 75% and 95% quantiles of $N=20$ datapoints. * $p < 0.05$; ** $p < 0.01$

values (see GADS toolbox, Matlab2009b). The GA-optimization was repeated 20 times for each network size. Fig. 4a shows the improvement in performance compared to the MO structure optimization run. A small network with only 14 reservoir neurons could reproduce the learned patterns with an error of 2.3%. Weight range and connectivity after optimization was analysed with an unpaired Wilcoxon rank sum test. Significant differences in connectivity and weight range were found (fig. 4b) with a clear trend for smaller reservoir weights and less reservoir connectivity with increasing network sizes. Both input- and back-projection weights tend to increase with reservoir size (fig. 4a). Although standard ESNs usually have full connectivity for input- and back-projection weights, evolutionary optimization seems to favor sparse connectivity for smaller networks, when given the choice (fig. 4b).

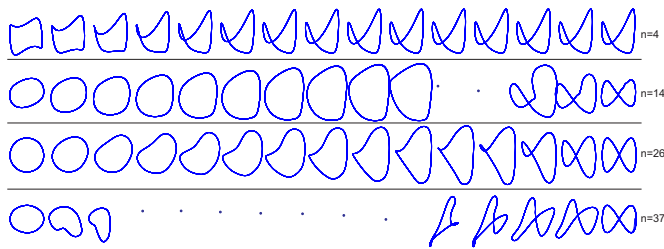


Fig. 6. Dynamic behaviour of selected networks with different reservoir sizes (blue trajectories). Shifting the dynamics of the networks by gradually changing the two input values from 1.0 to 0.0 and from 0.0 to 1.0, respectively, in 15 steps. Changing the input to the network causes a slow morphing between the two learned patterns, allowing the generation of new patterns that were not explicitly trained. Especially the small networks keep stable with no chaotic regions. Larger networks tend to converge to fixed points for input values other than zero or one (blue dots).

V. DYNAMIC NETWORK BEHAVIOUR

Most of the smaller networks show an unexpected behaviour. They are able to interpolate between the learned patterns, generating novel, not explicitly trained outputs. Fig. 6 shows the dynamical responses from the fittest networks of section IV. The first input value was changed gradually in 15 steps from 1.0 to 0.0, while the second input was changed from 0.0 to 1.0. A gradual morphing from the circular to the figure-eight pattern can be observed. It is surprising, that already a small ESN with six reservoir neurons can store two different patterns. Larger networks tend to converge to fixed points for input values other than the trained ones. This interpolation effect might be applied to complex and smooth behaviour generation for neural network controlled robots.

VI. CONCLUSIONS

Using MO, good candidate network structures can be selected as starting points for a followup whole-network optimization and fine-tuning using genetic algorithms. The resulting pareto front helps to identify small and sufficiently efficient networks that are able to store multiple motor patterns in a single network. This distributed storage of motor behaviours as attractor states in a single net is in contrast to earlier, local module based approaches. *"If sequences contain similarities and overlap, however, a conflict arises in such earlier models between generalization and segmentation, induced by this separated modular structure."* [3]. By choosing a feasible model capacity, over-fitting and the risk of unwanted - possibly chaotic - attractor states is reduced. Also, with the right choice of the network

size, an interesting pattern interpolation effect can be evoked. Instead of using a classic genetic algorithm for fine-tuning of the network weights, new, very fast and powerful black box optimisation algorithms [9] [10] could further increase network performance and allow to find even smaller networks for better generalisation. ESNs can be used for direct control tasks (see [11]) and scale well with a high number of training patterns and motor outputs [12]. A more complex simulation, for example of a humanoid robot, will show if direct, attractor-based storage of parameterized motor patterns is flexible enough for complex behaviour generation.

REFERENCES

- [1] J. Tani, M. Itob, and Y. Sugita, "Self-organization of distributedly represented multiple behavior schemata in a mirror system: reviews of robot experiments using rnnpb," *Neural Networks*, vol. 17, pp. 1273 – 1289, 2004.
- [2] M. Haruno, D. M. Wolpert, and M. Kawato, "Mosaic model for sensorimotor learning and control," *Neural Computation*, vol. 13(10), pp. 2201–2220, 2001.
- [3] Y. Yamashita and J. Tani, "Emergence of functional hierarchy in a multiple timescale neural network model: A humanoid robot experiment," *PLoS Computational Biology*, vol. 4 (11), pp. –, 2008.
- [4] P. Werbos, "Backpropagation through time: what it does and how to do it," in *Proceedings of the IEEE*, vol. 78(10), 1990, pp. 1550–1560.
- [5] H. Jäger and H. Haas, "Harnessing nonlinearity: Predicting chaotic systems and saving energy in wireless communication," *Science*, vol. 304, pp. 78 – 80, 2004.
- [6] H. Jäger, M. Lukosevicius, D. Popovici, and U. Siewert, "Optimization and applications of echo state networks with leaky integrator neurons," *Neural Networks*, vol. 20(3), pp. 335–352, 2007.
- [7] K. Deb, A. Pratap, S. Agarwal, and T. Meyarivan, "A fast and elitist multiobjective genetic algorithm: Nsga-ii," *IEEE Transactions on Evolutionary Computation*, vol. 6, No. 2, pp. 182–197, 2002.
- [8] B. A. Pearlmutter, "Learning state space trajectories in recurrent neural networks," *Neural Computation*, vol. 1, pp. 263–269, 1989.
- [9] O. Kramer, "Fast blackbox optimization: Iterated local search and the strategy of powell," in *The 2009 International Conference on Genetic and Evolutionary Methods (GEM'09)*, 2009, in press.
- [10] J. A. Vrugt, B. A. Robinson, and J. M. Hyman, "Self-adaptive multimethod search for global optimization in real-parameter spaces," *Evolutionary Computation, IEEE Transactions on*, vol. 13(2), pp. 243–259, 2008.
- [11] A. F. Krause, B. Bläsing, V. Dürr, and T. Schack, *Human Centered Robot Systems. Cognition, Interaction, Technology*, ser. Cognitive Systems Monographs. Berlin Heidelberg: Springer-Verlag, 2009, vol. 6, ch. Direct Control of an Active Tactile Sensor Using Echo State Networks, pp. 11–21.
- [12] H. Jäger, "Generating exponentially many periodic attractors with linearly growing echo state networks," IUB, technical report 3, 2006.

Parallel Central Pattern Generators for locomotion control in a humanoid robot

Ignazio Aleo, Paolo Arena and Luca Patané

Dipartimento di Ingegneria Elettrica, Elettronica e dei Sistemi (DIEES),
Università degli Studi di Catania,
Italy (email: {ialeo,parena,lpatane}@diees.unict.it)

Abstract—In this paper we investigate a novel algorithm for concurrent control of a multiple-limb robotic structure (i.e. an humanoid robot). The approach is based on the reformulation of the well known Central Pattern Generator (CPG) paradigm by using a set of parallel Recurrent Neural Networks (RNNs) which are synchronized in a well defined sequence of states in order to attain a reliable locomotion control strategy in a humanoid robot. On the contrary of classical algorithms, like pseudo-inverse Jacobian, the proposed RNN approach is at the same time fast, flexible and robust to configuration singularities providing a sub-optimal solution to direct and inverse kinematic problems. Thanks to the modularity nature of this approach, a full body model is proposed: multiple RNN structures control each limb in a humanoid robot model. The whole control system has been tested first in a kinematic and then in a dynamic simulation environment. Finally an experiment with a humanoid robot is also reported.

I. INTRODUCTION

Robotic multi-limb structures are widely used in research as test-bed for biologically relevant models [1] [2]. The control of these kinds of structures is complex and often implies high computational capabilities or pre-programmed motion control. The biological paradigm of the Central Pattern Generator (CPG) can be considered to impose a certain sequence of states on the arms and legs of a robot. In some cases, a redundant configuration can be used, increasing the complexity needed to define a model of the structure and to develop a reliable control algorithm. The robustness against singularities, the capability to face angular constraints in the joint space or other constraints in the operating workspace (e.g. obstacle avoidance) are important aspects that have to be considered [3] [4] [5]. In embedded control platforms, an important performance index that can be, therefore, considered is the computational power. In fact, it constrains the control frequency and therefore the possibility to develop an algorithm on a low MIPS microcontroller unit

(mcu) for real-time applications. The proposed approach is based on the already developed Mean of Multiple Computations (MMC) Recurrent Neural Network (RNN) algorithm which provides a fast, flexible and robust to configuration singularities sub-optimal solution to the discussed problems [6], [7]. In biological movement planning, the weighting of inputs from various limb segments might be biased toward an explicit representation of the whole limb [8] [9] [10]. This representation is also somatotopically distributed, allowing multiple (redundant) representations of the same limb parts. This rule adapts both to cerebral and to cerebellar cortex [11]. Taking inspiration from these considerations, the MMC approach represents a candidate, yet simple model of such an integrated network organization [12]. It provides a framework in which a global, distributed and redundant representation of the limb parameters is encoded, providing a concurrent natural solution to the Inverse Kinematic (IK) and Direct Kinematic (DK) problem iteratively, with the addition of a robust real-time adaptation to external obstacles. From the pure algorithmic point of view the MMC approach provides also a selectable precision-speed trade-off. This paper is organized in four main sections. In Section II the general MMC model is discussed. In Section III control strategy is described. Section IV presents experimental results and finally in Section V results of the proposed model are analyzed and compared with the most common velocity domain algorithms.

II. MODEL DESCRIPTION

Since many years neural networks have been largely used to solve manipulator control problems, in which the set of variables involved in the process are combined in a single pattern [13]. The output values are retrieved by completion of an even partially defined pattern given as input. The MMC is an interesting method introduced in [6], and further exploited in [2], that can be used to

create a model of multi-link, m-dimensional structure by using simple geometrical relations between arcs of the same complete graph. Going deeper into details we can consider as a simple example, a planar manipulator with three Degrees of Freedom (DoF) like that one shown in Fig. 1. The procedure herewith exposed can be fur-

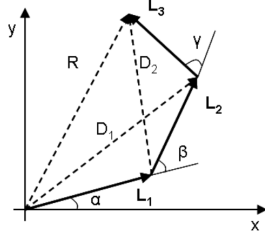


Fig. 1. A planar manipulator consisting of three vector segments: L_1, L_2, L_3 . The joint angles are: α, β and γ . The end-effector position is indicated by the vector R ; D_1 and D_2 are two additional vectors describing the diagonals.

ther extended to more complex structures using simple principles of the graph theory. The modeling phase is important for successive formalization strategies. In fact the proposed control mechanisms are strictly related to the characteristics of the MMC-based model formulated for the redundant manipulator. The main idea followed to construct an MMC-based model is that, looking at the serial manipulator as a geometrical multi-link structure, it is possible to compute each geometric quantity (i.e. vectors $\in \mathbb{R}^2$ in the example) in several ways, using different graph paths, and then average over them. For instance the complete pattern for the planar structure depicted in Fig.1 can be expressed with the vector $\mathbf{P} = (L_1, L_2, L_3, R, D_1, D_2)$.

III. LIMBS MODEL AND CONTROL STRATEGIES

In order to kinematically model both arms and legs, different structures have been considered. As introduced different geometrical structures have been considered to model arms and legs. The modeled geometrical structure for each arm (i.e. left and right) is a three links serial structure with three Degrees of Freedom (DoF) (from $\theta_{arm,1}$ to $\theta_{arm,3}$ for each arm). The geometrical structure used for each leg is a four links serial structure with five (from $\theta_{leg,1}$ to $\theta_{leg,5}$ for each leg) DoF and therefore more than one DoF are computed with the same geometrical quantity (e.g. two relative joints are associated with the same link).

A. Control strategies

The robot control can be easily conceptually divided into high level (behavior) control, and low level (gait and

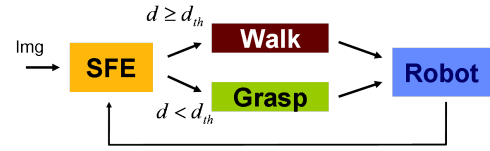


Fig. 2. Simple behavior selection loop implemented through visual processing and robot control. Segmentation and Feature Extraction (SFE) block performs image processing algorithm to detect object distance d . Behavior evaluation is achieved with a binary threshold d_{th} .

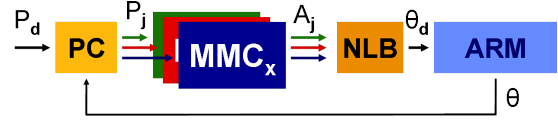


Fig. 3. Control scheme for each arm for a given absolute reference input pattern, \mathbf{P}_d . PC is the Pattern Constructor, MMC_x , MMC_y and MMC_z are the three-dimensional linear computational networks. NLB is the Non-Linear Block and *miniARM* is the manipulator itself (simulator or real robot). P_j are the MMC input pattern while A_j are the outputs. θ_d are the desired angular values and θ are the read joints values.

grasping strategies) control.

1) *Robot behavior*: The robot overall behavior is controlled through simple visual frame-based decision making through direction of walking and grasping. The behavior selection loop is shown in Fig. 2. The Segmentation and Feature Extraction block (SFE) processes image from on-board camera (Img) and it uses distance d for discrimination.

2) *Grasping*: As introduced, two different position controlled MMC with three links have been used to control recognized object grasping. The simplest extension of the two-dimensional positioning of a planar redundant serial manipulator (Fig. 1) introduced in the previous section (deeply described in [6]) is the three-dimensional positioning of the end-effector for the redundant serial manipulator in space (i.e. \mathbb{R}^3). Each vector component of the geometrical links is processed, iteration after iteration by a different linear MMC network and then given as input at the non linear block (NLB), as shown in Fig. 3.

3) *Walking gait*: For the described legs control strategy, the walking gait is obtained using a state dependent reference (from S_1 to S_6) for each leg and a state transition model with transition conditions (as sketched in Fig. 4). Two position and orientation controlled MMCs have been used for convergence toward reference within the state. State dependent offset are introduced in $\theta_{leg,1}$ (off-sagittal plane hip angle) and $\theta_{leg,5}$ (off-sagittal

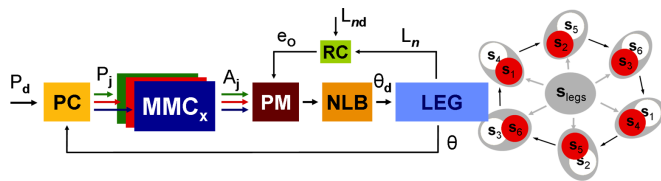


Fig. 4. Algorithm block diagram with relative orientation error feedback (e_O) and absolute position reference (P_d). Reference Comparator (RC) block computes \mathbf{e}_O with respect to desired orientation. \mathbf{L}_n are the last link components while \mathbf{L}_{nd} are the reference components. As shown in the state transition model (on the right), the general state st_{egs} lead toward the nearest walking state (i.e. the one with the minimum overall distance).

plane ankle angle) for balance control. As depicted in Fig. 4, in the algorithm block diagram, the low level control strategy guides the system (i.e. the single leg) towards the desired orientation through a relative error feedback. Therefore the feedback for the orientation error (e_O) is analyzed. The distance between two different leg states can be defined, in the simplest case, as the Euclidian distance between the two end-effector points. Furthermore, overall distance (and therefore the whole system state) can be computed as the mean distance of both legs).

IV. SIMULATION AND EXPERIMENTAL RESULTS

The considered robot has 18 DoF, through revolute joints: three joints for each arm and six joints for each leg. The physical structure can be mapped, as requested for the MMC modeling, into the geometric theoretical model links. Due to the chosen real robot architecture, angular limits are not equal for each joint.

A. Experimental Setup

As described in the previous section, each presented control strategy has been tested both in simulation and on real robot. The proposed algorithms have been implemented both in the PC and in a custom mcu-based board. Respectively a Dual Core Intel Centrino 2.2 GHz host computer with 2GB of RAM and an UC3A AVR32 mcu with 66MHz of maximum clock and only 64KB of RAM were used as comparison platforms (Fig. 5).

As sketched in Fig. 5, in our first implementation the overall robot control can be split in two levels: low level (hardware) control and high level control. The low level control is, in all cases, achieved thanks to a mcu-based board that is used both to acquire information from the distributed sensory system and to control the actuators. Moreover a serial bus is used for low level communication purposes. The high level control and the

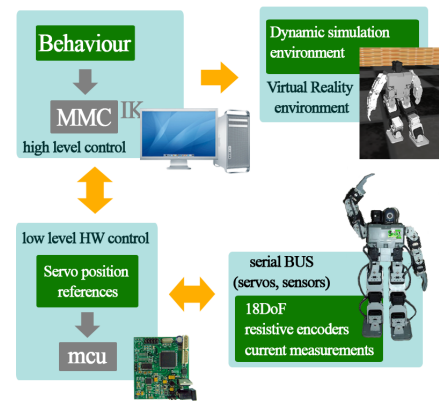


Fig. 5. Hardware configuration of the experimental setup: low level microcontroller AVR32 board, actuators and sensors bus architecture and high level control host computer.

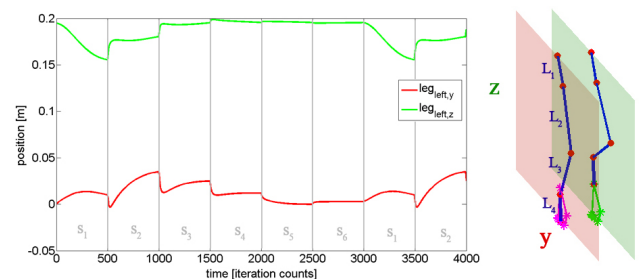


Fig. 6. Left leg end-effector position through different states (on the left). Relevant coordinates (robot sagittal plane) have been plotted with respect to time. Simple sketch of the geometrical structure in which legs are mapped (on the right)

data logging are made through a host PC connected to the board via serial interface (with a USB-to-serial transceiver).

In the second (embedded) version of the control algorithm all the MMC-based calculations are directly executed locally in the mcu-based board while the PC is just used for data logging and for the Virtual Reality (VR) simulation environment.

B. Simulation and Experimental Results

In order to test performance of the designed control structure, trajectories followed in both walking and grasping behaviors have been analyzed. The center point trajectory of the foot-base (i.e. end-effector of leg serial structure) of one leg during sequence in the walking behavior is depicted in Fig. 6. The distance from a known object is estimated based on simple segmented image feature (e.g. area in px^2 or maximum edge of minimum rectangle containing object). After the object area (i.e. camera estimated distance under threshold d_{th})

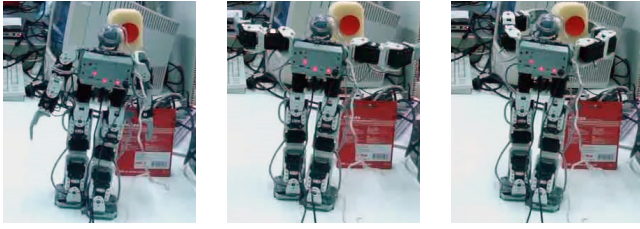


Fig. 7. Multiple snapshots of grasping sequence. End of walking (i.e. $d < d_{th}$) and start of grasping (on the left). MMC iterations are executed in parallel on both arms (center). Grasping sequence ends when both arm position errors go below error tolerance (on the right).

is reached the arms start to converge toward the selected centroid, as shown in Fig. 7.

V. RESULT ANALYSIS

Although the iteration number needed to reach the desired reference strongly depends on the chosen parameters and on the particular given reference, in order to estimate the algorithm performance, multiple comparisons with common algorithms for kinematic inversion, such as pseudo-inverse Jacobian (J^*) and Jacobian transpose (J^t), have been considered. It must be taken into account that in the J^* the joint limit constraints are introduced in the form of an additional task to be completed while in the J^t no joint limitations are considered. Free parameters were chosen to maximize convergence speed keeping a *non-overshoot* condition on end-effector positioning. As it is possible to see in TABLE I the performance in terms of number of iterations needed for convergence (i.e. $\|e_P\| \leq e_t$) are comparable with already known algorithms for the generalized MMC model. TABLE I also gives an idea of time needed for each iteration both in PC and in embedded platforms (MCU).

TABLE I
ALGORITHM PERFORMANCES

Method	Iterations	Time/iterations [s]
$MMC(PC)$	80	$4.1 \cdot 10^{-4}$
$MMC(MCU)$	80	$3.6 \cdot 10^{-3}$
$J^t(PC)$	450	$8.1 \cdot 10^{-3}$
$J^*(PC)$	150	$9.2 \cdot 10^{-3}$

VI. CONCLUSIONS

Forward and inverse kinematic problem solving for redundant serial manipulator is one of the classical problems in industrial robotics. In this field, the most common tasks, such as end-effector position and orientation control, are already well solved from the classic algorithms. In this work a fast, reliable algorithm able to

solve at the same time both position and orientation tasks is proposed. Its implementation on an embedded mcu-based board has been tested and a real robot application has been developed. Furthermore the extension to multi-limb structure (e.g. a humanoid robot) is presented for walking and grasping behavior. The problem is addressed not only in presence of angle limits but also in a dynamically changing environment even in a mcu-based hardware.

ACKNOWLEDGEMENTS

The authors acknowledge the support of the European Commission under the project ICT 216227 - SPARK II "Spatial-temporal patterns for action-oriented perception in roving robots II".

REFERENCES

- [1] B. Siciliano, "Handbook of robotics", Springer 2008.
- [2] U. Steinkuhler, H. Cruse, "A holistic model for an internal representation to control the movement of a manipulator with redundant degrees of freedom", *Biol. Cybernetics* 79, 457-466, 1998.
- [3] K. Ahn and W.K. Chung, "Optimization with joint space reduction and extension induced by kinematic limits for redundant manipulators", in *Proc. 2002 IEEE Int. Conf. Robot Autom.*, Washington, DC, pp. 2412-2417.
- [4] M. Shimizu, H. Kayuka, "Analytical Inverse Kinematic Computation for 7-DOF Redundant Manipulators With Joint Limits and Its Application to Redundancy Resolution", *IEEE transaction on robotics* vol.24, No.5 October 2008.
- [5] B. Tondou, "A closed-form inverse kinematic modelling of a 7R anthropomorphic upper limb based on a joint parametrization", in *Proc. 2006 6th IEEE-RAS Int. Conf. Hum. Robots*, pp. 423-432.
- [6] H. Cruse and U. Steinkuhler, "Solution of the direct and inverse kinematics problems by a common algorithm based on the mean of multiple computations", *Biol. Cybernetics* 69, 345-351 2, 1993.
- [7] P. Arena and L. Patané, "Spatio Temporal Patterns for Action Oriented Perception in Roving Robots", Springer, Series: Cognitive Systems Monographs, vol. 1, 2009.
- [8] G. Bosco and R. E. Poppale, "Proprioception from a spinocerebellar perspective", *Physiol. Rev.* 81: 539-568, 2001.
- [9] M. C. Park, A. Belhaj-Saf, M. Gordon, and P. D. Cheney, "Consistent Features in the Forelimb Representation of Primary Motor Cortex in Rhesus Macaques", *The Journal of Neuroscience*, April 15, 2001, 21(8):2784-2792.
- [10] C. Capaday, C. Ethier, L. Brizzi, A. Sik, C. Van Vreeswijk, D. Gingras, "On the Nature of the Intrinsic Connectivity of the Cat Motor Cortex", *J. Neurophys.* 102: 2131-2141, 2009.
- [11] Kandel, Schwartz and Jessel, "Principles of neural science", McGraw-Hill, 2000.
- [12] H. Cruse, U. Steinkuhler and Ch. Burkamp, "MMC - a recurrent neural network which can be used as manipulable body model", in *From animals to animats 5*, R. Pfeifer, B. Blumberg, J.-A. Meyer, S.W. Wilson (eds.) MIT Press, pp. 381-389, 1998.
- [13] H. Ritter, T. Martinetz and K. Schulten, "Neural Computation and self-organizing maps", Addison-Wesley, New York, 1992.
- [14] EU Project SPARK II, website online at www.spark2.diees.unict.it

Reaction-Diffusion-like systems for event representation and beyond

Jose Antonio Villacorta-Atienza and Valeri A. Makarov and Manuel G. Velarde

Instituto Pluridisciplinar, Universidad Complutense,

Paseo Juan XXIII, 1, Madrid 28040, Spain

Email: joseavillacorta@pluri.ucm.es

Email: vmakarov@mat.ucm.es

Email: mgvelarde@pluri.ucm.es

Abstract—Understanding of how the brain makes an effective compact internal representation (CIR) of time evolving situations in a given landscape is a challenging problem. Before proceeding to such a task we here discuss a model where immobile obstacles are placed in an arena. We show how an internal representation differs from the apparently similar diffusion case.

I. INTRODUCTION

The real world is a continuously changing environment whose complexity often makes useless rigid reactive behaviors. Animals during long evolution developed mechanisms that enable predicting the future and a purpose-based selection of behaviors. Growing experimental evidence suggests that these mechanisms rely on the ability of generating an Internal Representation (IR) of the body and external environment and on the parallel virtual “simulation” of possible alternative. The IR should account both for spatial (static) structure of the environment and for time-dependent changes (moving obstacles). Here we restrict consideration to the former.

The existence of neuroanatomical substrates responsible for the high-level static or time-dependent functions mentioned above has been supported by the finding of *mirror neurons*. These cells respond both when a subject makes a particular action and when there is another individual performing the same action thus leading to mere copying or, more important, planning ahead. Indeed it seems that mirror neurons can react on the intention to perform a purpose-based action.

Recent theoretical research on IR (although the first record goes back to 1943 [1]) elucidated its main advantage: it allows detaching the behavior from direct environmental control by, e.g., inhibition of the motor execution. This enables responses of the organism to features of the world that are not directly present and hence to appropriately plan ahead. Besides, IR can

be evoked mentally (without direct sensory input) to evaluate potential solutions. It is widely believed that IR is a prerequisite of a cognitive behavior [2]. Particularly, the IR concept has been used to control a multisegmented manipulator with redundant degrees of freedom [3]. Specific feed-forward networks and Recurrent Neural Networks (RNNs) have been used as holistic models of geometrical structures like bodies with arms and legs (see, e.g., [4], [5] and references therein). It has been shown that such networks can operate as forward models, inverse models or any mixed combination. Later in a series of papers [5], [6], [7], [8] it has been argued that IR based on RNNs assembled using simple building blocks can implement working memory. Namely, it has been shown that RNNs can store and then reproduce some specific static and time-evolving situations. It has been shown that a network of n neurons can learn and then replicate a sequence of up to n different frames [8]. Another promising application of the IR approach is the construction of sensory-motor maps that implement external anticipation of the sensory information. For example, it has been shown that echo state networks can successively learn forward models for a blind navigation in a square shaped static environment [9]. Toussaint [10] argued that standard sensory-motor maps lack a proper neural representation and proposed the use of neural field models. Then motor activation induce anticipatory shifts of the activity peak in the sensory-motor map, which in turn can be used more naturally for planning and navigation in a maze.

II. SKETCH AN OF IRNN

Let us consider an agent moving in an arena with the objective to reach a target (Fig. 1A). Here just for illustration we consider a static obstacle in the arena. We assume that the target emits or reflects a sensory signal,

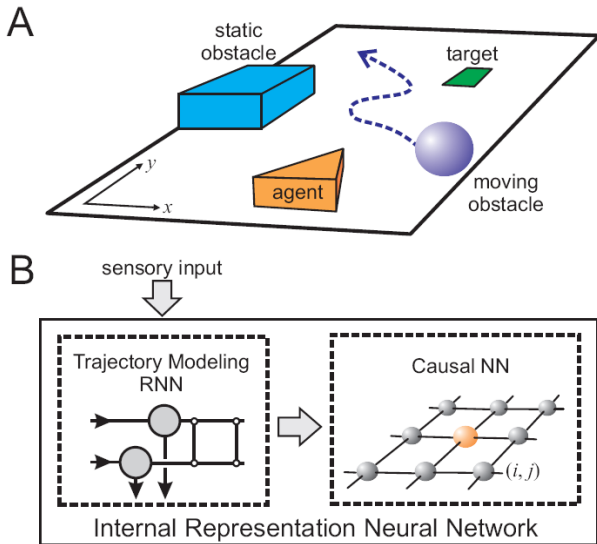


Fig. 1. **A.** Sketch of an arena containing agent, target, and obstacles. The agent perceives all objects in the arena and creates an internal representation of itself and of the environment with the goal of reaching the target avoiding collisions with the obstacles. **B.** General block-scheme architecture of the IRNN consisting of two coupled subnetworks: i) Trajectory Modeling and ii) Causal neural networks. The TM-RNN receives sensory information, simulates trajectories of all objects (except the agent) and maps them into the CNN, which creates the CIR of the static or time-dependent situation.

e.g., sound or light, which is perceived by the agent. We assume that a path to the target can be found.

Figure 1B shows a sketch of the IRNN. It consists of two coupled subnetworks: Trajectory Modeling RNN (TM-RNN) and Causal Neural Network (CNN). The TM-RNN receives a sensory information either directly from the sensory system or from another brain area (e.g., memory). In the latter case, in most general circumstances, the IRNN takes part in completely or partially mental (i.e., without direct observation of the environment) simulations of time-dependent situations. The TM-RNN should be trained by real trajectories. Once the training is deemed finished the network becomes capable of simulating arbitrary trajectories of objects using as an input only their initial conditions.

To create a suitable IR the agent has to synchronize its possible motions with those given by the TM-RNN for the obstacles. This is achieved in the CNN that is a two dimensional ($N \times M$) lattice of locally coupled neurons that geometrically reproduces the arena, i.e., position of a neuron in the lattice described by the pair of indexes (i, j) corresponds to the actual (x, y) -coordinates in the arena (Fig. 1). Such mapping is the simplest but not unique. The assumption of complete sensory

knowledge of the environment suggests the egocentric reference frame for the CNN, i.e., the agent maps itself into the origin of the neuronal lattice (red bigger neuron in Fig. 1B). Such reference frame has been argued to be used by insects [11], although more complex navigational systems have hierarchical organization depending on the context. For instance, honeybees switch between the egocentric and allocentric reference frames depending on whether they are flying along an unknown or a familiar route, respectively [12].

III. MATHEMATICAL MODELING

Let us choose one specific decision making problem: a search for paths to the target (e.g., the shortest or safest).

Then the emergence of a CIR in the IRNN can be viewed as a result of *virtual exploration* of the environment. Conceptually, a number of identical virtual agents start from the agent's initial position and perform a random search in the lattice space until they explore completely the "arena" or some of them reach the target image in the CNN. Then the distribution of the virtual agents in the CNN lattice defines the CIR and the optimal strategy.

For a static case (immobile obstacle) the output of the TM-RNN (Fig. 1B) is time independent, and hence it just maps the immobile objects into the CNN whose dynamics models the process of virtual exploration

$$\dot{r}_{ij} = d \quad r_{ij} - r_{ij} p_{ij} \quad (1)$$

where r_{ij} is the neuron state variable, representing the concentration of virtual agents at the cell (i, j) ; the time derivative is taken with respect to the *mental* (inner) time ; $r_{ij} = r_{i+1,j} + r_{i-1,j} + r_{i,j+1} + r_{i,j-1} - 4r_{ij}$ denotes the discrete Laplace operator describing the local (nearest neighbor) interneuronal coupling, whose strength is controlled by d ; and p_{ij} accounts for the target:

$$p_{ij} = \begin{cases} 1, & \text{if } (i, j) \text{ is occupied by target} \\ 0, & \text{otherwise} \end{cases} \quad (2)$$

Note that a target need not to be a real entity (as an object or place) existing in the environment, instead it is designated by the agent's motivation layer. The target is not an external constraint but an internal emergent property of the brain, whose influence we model by the reactive term in (1). Obstacles are indeed external constraint whose biological identity suggests that they shape the IR through altering states of the neurons corresponding to the obstacle boundaries. We assume

that the obstacles are solid non-penetrable objects, hence a virtual agent reaching an obstacle frontier rebounds and continues exploring the arena.

Stable steady states are the only attractors in the phase space of the dynamical system (1). At $t = 0$ no virtual agent exists, hence we set $r_{ij}(0) = 0$ for all CNN cells except those occupied by the agent, where $r_{ij}(t) = r_a$ for $t > 0$. Then the trajectory in Ψ defined by these initial conditions tends to one of the steady states $r_{ij}^* \in \Psi$, which is the CIR of the given static situation. By unfolding this steady state into the three-dimensional lattice space we get a stationary pattern that can be used to trace curves or paths starting at the agent location and crossing normally the contour lines. We note that r_{ij}^* satisfies the Laplace equation, and consequently the created pattern has no local minima. This ensures that all paths (except a null set) derived from this approach end at the target, and hence we obtain multiple possibilities to reach the target.

The described dynamical process yielding the CIR has certain similarities with the classical diffusion in a 2D reservoir. However, in the classical approach: i) the agent is not explicitly present in the model, while the target is postulated; and ii) the obstacles absorb the diffusing substance (zero boundary conditions). To illustrate the differences we performed two simulations involving the classical and IRNN approaches.

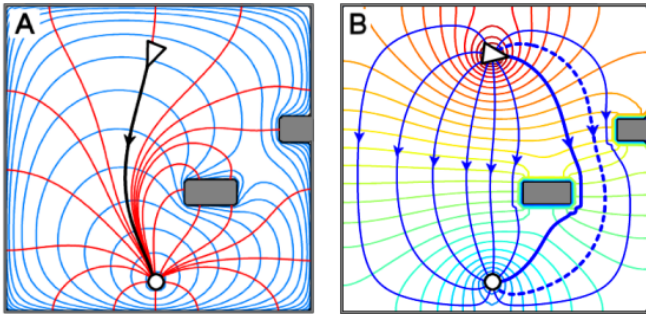


Fig. 2. Moving in a static environment. **A.** Classic 2D diffusion with a constant source at the target position (marked by circle) creates potential field with a single maximum and several saddle points. Then there exists a *unique* path from the agent (triangle) avoiding obstacles (grey rectangles) to the target. **B.** The IRNN approach yields a set of paths starting at the agent position and ending at the target. The agent is free to choose among different possibilities, e.g., by minimizing the path length (solid thick curve) or by rising safety (dashed curve), under additional constraint that it must pass between the two obstacles. Parameter values: (60×60) lattice, $r_a = 1$, $d = 2.5$, $r_{\max} = 10^3$.

Figure 2A shows an example of the potential field and paths to the target obtained using the classical

diffusion with zero boundary conditions at the obstacle and arena frontiers. The target is a source of a “gas” that freely diffuses forming a potential field. Then valid paths are curves radially leaving the target position and perpendicular to the contour lines. As a consequence there exists a unique trajectory connecting the target and location where the agent is supposed to be (Fig. 2A, thick line).

Figure 2B shows the pattern r_{ij}^* (concentration of virtual agents) obtained by the IRNN. We notice that the explicit modeling of the agent leads to multiple curves connecting the agent and the target locations. Thus we achieve a CIR, where the agent has freedom to choose among different possibilities. We also notice that the pattern (Fig. 2B) has smooth transitions between actual obstacles and empty space. This accounts for uncertainty in the obstacle dimensions and positions. Then path planning from the agent to the target can naturally include the level of safety, i.e., selection among different choices can minimize, e.g., the risk of crashing against an obstacle or/and the length of the path. The strategy can also include additional conditions, such as to pass through the gap between two obstacles (dashed curve vs thick solid curve in Fig. 2B), which is impossible in the classical approach.

IV. ABOUT FUTURE WORK

The above discussed IR of static environments cannot be applied directly to time-dependent situations. At present we are working on it. Worth signaling in that IR indeed offers new perspectives for the decision making and it is said to be a prerequisite for a cognitive behavior. A big challenge in the IR research is to understand how the brain makes a compact effective description of complex, time-evolving situations, in such a way that they can later be stored in (presumably static) long term memory and then retrieved on purpose.

CIR is an abstract construction of “what can be done”, i.e., it is not reducible to a search for a best trajectory, since the solution fitness may be subjective or/and goal-dependent. Nevertheless, once the time-dependent problem is solved, one of the straightforward applications of CIRs could be universal path planning. Finally note that the IRNN approach makes it susceptible for biophysical verification.

ACKNOWLEDGEMENTS

The authors acknowledge fruitful discussions with Profs. P. Arena, R. Strauss, H. Cruse and C. Avendaño.

This work has been sponsored by the EU grant SPARK II (FP7-ICT-216227).

REFERENCES

- [1] Craik K (1943) *The nature of explanation*. Cambridge: Cambridge Univ Press
- [2] Cruse H (2003) The evolution of cognition a hypothesis. *Cogn Sci* 27:135-155
- [3] Steinkuhler U, Cruse H (1998) A holistic model for an internal representation to control the movement of a manipulator with redundant degrees of freedom. *Biol Cybern* 79:457-466
- [4] Mohan V, Morasso P (2007) Towards reasoning and coordinating action in the mental space. *Int J Neural Syst* 17:329-341
- [5] Kühn S, Beyn WJ, Cruse H (2007) Modelling memory functions with recurrent neural networks consisting of input compensation units: I. Static situations. *Biol Cybern* 96:455-470
- [6] Kühn S, Cruse H (2007) Modelling memory functions with recurrent neural networks consisting of input compensation units: II. Dynamic situations. *Biol Cybern* 96:471-486
- [7] Cruse H, Hübner D (2008) Selforganizing memory: active learning of landmarks used for navigation. *Biol Cybern* 99:219-236
- [8] Makarov VA, Song Y, Velarde MG, Hübner D, Cruse H (2008) Elements for a general memory structure: properties of recurrent neural networks used to form situation models. *Biol Cybern* 98:371-395
- [9] Svensson H, Morse A, Ziemke T (2009) Representation as internal simulation: A minimalistic robotic model. *Proc CogSci'09*, 2890-2895
- [10] Toussaint M (2006) A sensorimotor map: Modulating lateral interactions for anticipation and planning. *Neural Comput* 18:1132-1155
- [11] Collett TS, Zeil J (1998) Places and landmarks: an arthropod perspective. In *Spatial representation in animals* (ed. S. Healy): 18-53. Oxford: Oxford Univ Press
- [12] Menzel R, Brandt R, Gumbert A, Komischke B, Kunze J (2000) Two spatial memories for honeybee navigation. *Proc R Soc Lond B* 267:961-968

Chunking by Naming: A Nonlinear Recurrent Network for Storing Hierarchical Memory Contents

Holk Cruse and Malte Schilling

Faculty of Biology, University of Bielefeld, D-33501 Bielefeld, Germany

Email: holk.cruse@uni-bielefeld.de

Abstract— We show that learning and retrieval of hierarchically organized information is possible, although this information is not given explicitly and no hierarchical structure can be found in the network. For the simulation, we use a simple, one-layered RNN consisting of IC units and a very simple learning rule based on teacher forcing [3,4], following the ideas presented in [2], which are guided by the observation that children learn superordinate concepts from implicitly given information. Specifically, we show that the agent is able to chunk different sensory inputs to represent the same object in memory, but nevertheless is able to distinguish between the different stimuli if, during learning, a supervisor labels the different stimuli with the same name.

I. INTRODUCTION

How is memory organized? The classical assumptions refer to the observation that items found in the world can be ordered using a hierarchical system. For example, different individual objects with some common properties may be categorized as cows. Together with other objects, e.g. horses, they may be grouped as mammals, or, on a higher level, as animals. Such a tree-like hierarchy has been proposed by early AI to organize objects occurring in the world within a storage of an artificial system [1]. This proposal was paralleled by the suggestion that the architecture of the human memory may follow such a hierarchical structure, too. There are a number of findings in agreement with this view (for an extensive review see [2]), in turn triggering the question how this principle could be realized in terms of neuronal structure, and, of course, followed by the question concerning the mechanisms that allow such a structure to be learned by a neuronal network.

The problem is complicated by the fact that a strict tree-like hierarchy is not sufficient to explain basic observations. Even when focusing on animals only, which, using the evolutionary tree, can be ordered in such a way, humans can use and do use other structures as, for example, grouping all flying animals like birds, bats, and insects together in one category.

This means that hierarchies are not strict but may be variable. To deal with these questions, [2] have proposed a fascinating solution, using a one layered RNN and a specific BP algorithm. In this approach, hierarchies are not explicitly given during learning, but emerge in a self-organized way.

In this article, inspired by the ideas of [2], we will propose a similar solution using an even simpler RNN and a very simple learning rule. The number of learning steps is very small.

II. THE MODEL

A. General Properties of the Model

Following [2], we use a recurrent neural network (RNN) containing 27 units as the memory of an agent. Each object perceived by the agent can be stored as a vector of five properties which represent the individual object (4-legged, surface texture, color, name, plus a further one called Identifier being explained later-on).

In principle, the agent may also be able to record the location where (and, if required) the time when it has observed this object. To maintain a slot for storing this information, but nevertheless keep the network simple, we introduce a specific unit, called Identifier. Note that for each new situation experienced, a new Identifier unit has to be chosen.

Therefore, in our example, each object can be stored by a vector containing 14 components (Identifier, name, and, for each of the three remaining properties (4-legged, surface texture, color) a four-component subvector). This 14-component vector when being stored may be called an episodic memory element.

To investigate the properties of our system, we use a much simpler set of items compared to that used in the work of O'Connor et al. [2]. We have four objects only, two cows, Frieda and Emma, one horse, and a table.

To minimize possible confusion, words that will be given to the system by a supervisor, will in the following be written with capital first letters.

We start with an agent that has no sensory experience and no innate categories. Imagine, for example, that the agent is confronted with a cow equipped with some properties which a human observer may call 4-legged, black-and-white colored, cow-type fur, and which by a supervisor is being named Frieda. Recall that this agent is not able to apply such categories, just experiences sensory input that it will store in its memory representing one specific object.

After having seen and learned the 14-component vector representing cow Frieda, the agent may see another cow, named Emma, according to information given by a supervisor. The sensory input of this new object may look a bit different and is also stored. For example, Emma's color may correspond to what is sometimes called red-colored, and Frieda's black-colored. Similarly the 4-legs of Emma and Frieda may look a bit different, but still more similar than the 4-legs of the horse and of the table. Another object seen, also 4-legged, also with a fur, but brown in this case, is named 'Horse'. The agent may also see an object being named 'Table', colored white, constructed of wood and containing four legs, too.

By learning these objects, the agent is able to build up an episodic memory. But can it also be able to represent some kind of hierarchy, for example by combining the two objects named Frieda and Emma as "cow", or the two cows and the horse as "animal"? As has been stated in [2], children do learn the hierarchical relation not by being explicitly trained that "Frieda is a cow" or "cows and horses are animals", but by being confronted with an object, for example Frieda, that is, instead of being named "Frieda", at another opportunity named "Cow" by a supervisor. Applying this suggestion to the training procedure, here, as did [2], the two objects Frieda and Emma, may, in other training sessions, be called 'Cow' instead of 'Frieda' or 'Emma'. The two cows and the horse may correspondingly be called 'Animals'. Furthermore, the agent may be told that the different surfaces observed in these three objects Frieda, Emma and horse are named 'Fur', although looking different in detail. In addition, in the corresponding way the agent may learn that all the objects are characterized as being '4-Legged'.

To make the structure of the relation between the elements a bit more complex, the somewhat different colors of the two cows are given by the supervisor the category 'Colored', that of the (brown) horse and the (white) table as 'Uni'. Correspondingly, in some training sessions the items Frieda and Emma, but not horse and table, may be replaced by 'Names', here standing for names of individuals. Thus, altogether, we have now 7 higher-level, or superordinate categories (Cow, Animal, 4-Legged, Names, Fur, Colored, Uni).

The structure of this environment is given in Fig. 1. The figure illustrates that there is no strict tree-like hierarchy but that instead various forms of overlap can be found. The properties marked by the gray area characterize one object and may be termed basic-level concepts, the other items situated outside the gray areas are called superordinate concepts. Items that in the training situations are replaced by each other forming different training vectors are connected by dashed arrows.

How can this environmental structure be represented in neuronal terms, i.e. how can the information be learned and how can it be used for retrieval?

B. The Network

To be able to represent the three properties (4-legged, surface texture, color) we reserved four units for each, requiring 12 components in total. As each of the four objects further is characterized by an identifier and a name, altogether we require 20 components for the four objects. In addition we have seven superordinate concepts, each component of which is represented by one neural unit, leading to a network containing 27 units in total.

As lower level units should be able to activate higher level units, but also in turn, higher level units may activate lower level units, we require recurrent connections between all units. Therefore, the RNN consists of 27 units fully recurrently connected.

Using a recurrent network, of course, raises stability problems. Therefore, a fundamental requirement for such a system being functional is that only a limited number of units should be activated after any external input has been provided. Second, if possible, the activity should not grow unlimited. Earlier studies have shown that these requirements can be fulfilled by using RNNs consisting of so called IC units [3,4].

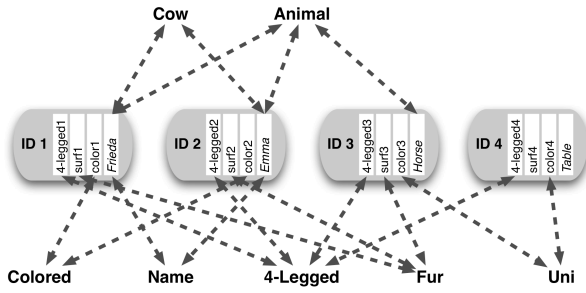


Fig. 1. Illustration of the four objects and how the training vectors are constructed. Basically the four vectors marked in gray represent the four objects. The dashed arrows connect superordinate items with those basic level items that they are replacing to form new training vectors.

An IC unit has the following specific properties [3,4]. As in traditional recurrent networks, a weighted sum of the recurrent inputs is determined:

$$s_i = \sum_j w_{ij} x_j(t)$$

Each unit also has an external input $I_i(t)$. The output of the unit is given by

$$x_i(t+1) = \begin{cases} I_i(t) & \text{if } I_i(t) > 0 \\ s_i(t) & \text{otherwise} \end{cases}$$

Furthermore,

$$x_i(t) = \begin{cases} x_i(t) & \text{if } x_i(t) \geq 0 \\ 0 & \text{otherwise} \end{cases}$$

forming the nonlinear characteristic of a rectifier. For learning, an error value is computed locally

$$\delta_i(t) = I_i(t) - s_i(t)$$

and used to train the weights of unit i according to

$$w_{ij}(t+1) = w_{ij}(t) + \varepsilon \delta_i(t) x_j(t) \quad (1)$$

where $\varepsilon > 0$ is the learning rate.

Learning is performed by providing the input vector and waiting for two iterations per learning step ($\varepsilon = 0.9$). Makarov et al. have shown in [4] that, using this type of RNN and this learning rule, the stable values do not depend on the temporal order of the input vectors given, provided each vector is given often enough.

Results presented in another paper (Cruse and Schilling, submitted [5]) show that in our network training is very fast. If only objects as such have to be

learned, two presentations of each object are sufficient. If all situations depicted in Fig. 1, i.e., 27 items with partly overlapping hierarchies (corresponding to 22 input vectors) should be learned, 15 presentations of each vector are sufficient to reach 97% of final weight values.

Testing the behavior of the trained network revealed that all individual objects and all superordinate concepts could be retrieved without cross talk, while the expected hierarchical relations are illustrated without explicit training and no hierarchical structures being preinstalled. Exploiting this property, it was further possible to simulate bottom-up and top-down priming.

III. RESULTS

Here we concentrate on the following problem. A crucial implicit assumption in our above mentioned and most other such training studies is that the agent shows a property that at first sight appears to be obvious but is not. When the agent is experiencing a specific object, say Frieda, a second time again, it is assumed that the agent recognizes this object as being the same. This faculty is by no means trivial because the object may be seen from a different perspective, a different angle, a different illumination, and therefore the stimuli might physically be quite different. But even if it looked the same, the problem remains. How should one know that it is the same object and not a different one looking similar? How is it possible to recognize the different stimuli as representing the same object? One solution might be that there is a supervisor who gives the same name (e.g., Frieda) to the different stimuli.

In the following we test whether this proposal is sufficient to solve this problem within our framework. To this end, we use the same network and the same learning structure. However, we do not use four different objects for this task, but now the table and three versions, or aspects, of cow Frieda. This means that the components Identifier, 4-legged, surf and color are different for the three cows seen, but they all have the same name Frieda. In other words, we use the training vectors (Identifier1, 4-legged1, surf1, colored1, Frieda), (Identifier2, 4-legged2, surf2, colored2, Frieda), (Identifier3, 4-legged3, surf3, colored3, Frieda) and, as in the earlier experiment, the object table. Superordinate concepts as Cow, Animal, 4-Legged are applied as above, too. Note that the

three different Identifiers may represent different contextual aspects including some measure of time.

After training (30 epochs using 20 training vectors and 27 units) we obtain the following results. If any identifier of the three aspects of Frieda is stimulated, the vector of the four properties of all three aspects plus the name unit (Frieda) are activated, in addition with units Cow and Animal. Stimulation of any other property of the cow vector leads to the corresponding result.

If the neuron representing Frieda is stimulated, correspondingly all the aspects of Frieda including, of course, unit Frieda, are activated. Superordinate vectors might take over activity from basic level units. Units Cow or Animal do not show up (but become activated when using the delayed switching off the input version described by Cruse and Schilling [5]).

When stimulating the unit representing Cow or Animal, the corresponding results have been observed, with unit Frieda being not activated (unless we use the delayed switching off the stimulus version).

Stimulation of a superordinate unit as are 4-Legged, Fur, or Colored, leads to an activation of all aspects of the cow except the local component of the stimulated superordinate unit. Stimulating 4-Legged, in addition, activates the components of object table.

Thus, using our training procedure, different episodic situations can be combined, i.e., chunked in the memory, if a supervisor characterized them with the same name. But nevertheless, the individual episodic memory could be recalled as well.

IV. DISCUSSION

In this article, we simulate a memory system that represents memory elements of different hierarchical levels, eventually termed superordinate concepts, basic-level concepts and subordinate level elements [1], but without explicitly implementing a hierarchical structure into the network. As a main difference to the approach of [2] we use a RNN with specific units which allow for a very simple learning rule. Different to our approach, [2] used supervised learning which requires a separation of input layer and output layer, i.e., the target vector. Instead, we use the same layer for both input and target vector. Therefore, during training there is no mechanism required telling the network which is input and which is target.

O'Connor et al. [2] operate on the level of verbally described features for which appropriate detectors are assumed to be given. However, the framework can also be applied in a more general way. Here we studied two different approaches. For the word units, we, too, apply feature detectors, which might be realized as RNN that represent the individual words (but these networks are not shown here). Beyond that, for the basic-level concepts apart from names, we instead assume a naive system that is only equipped with object recognizers (i.e. the capability of figure-ground separation) and sensors, but no specific feature detectors as, for example, a "fur-detector". Rather we assume neural networks that monitor physical properties like color, shape, tactile stimulation etc. Thereby, the representations can be grounded and thus, in principle, be applied to an autonomous robot.

In our first approach, these properties may vary from object to object, i.e., from, for example, cow Frieda to cow Emma, but are assumed invariant if the same object is seen later again. In the second approach (Sect. III), we realize that the sensory input may even vary for a given object. The results have shown that also in this case chunking is indeed possible. In our approach, the adequate information required for chunking is given by a supervisor. However, other possibilities not studied here could be imagined.

ACKNOWLEDGMENT

We wish to express our thanks to the Exzellenzcluster "Cognitive Interaction Technology" and the EC-IST SPARK II project.

REFERENCES

- [1] A.M. Collins, M.R. Quilian, "Retrieval time from semantic memory", *J. of Verbal Learning and Verbal Behavior*, vol. 8, pp. 240-247, 1969
- [2] C.M. O'Connor, G.S. Cree, K. McRae, "Conceptual hierarchies in a flat attractor network: Dynamics of learning and computations", *Cogn. Science*, vol. 33, pp. 665-708, 2009
- [3] S. Kühn, W.-J. Beyn, H. Cruse, H. "Modelling Memory Functions with Recurrent Neural Networks consisting of Input Compensation Units. I. Static Situations," *Biol. Cybernetics*, vol. 96, pp. 455- 470, 2007
- [4] V.A. Makarov, Y. Song, M.G. Velarde, D. Hübner, H. Cruse, "Elements for a general memory structure: Properties of recurrent neural networks used to form situation models," *Biol. Cybernetics*, vol. 98, pp. 371-395, 2008
- [5] H. Cruse, M. Schilling, "Learning and retrieval of hierarchically organized information in a simple, one-layered RNN", (submitted)

TriBot: a hybrid robot for cognitive algorithm implementation

Paolo Arena, Luca Patané, Massimo Pollino and Cristina Ventura

Dipartimento di Ingegneria Elettrica, Elettronica e dei Sistemi

University of Catania, Italy

parena@diees.unict.it, lpatane@diees.unict.it

Abstract—During the last years considerable attention was focused on finding original robotics structures with new mechanics solutions, to face with complex tasks. An interesting solution consists in realizing hybrid robots. In this paper, the design and realization of a modular hybrid robot, named TriBot, is presented. Its structure is constituted by two wheel-legs modules, an optimal solution for walking in rough terrains and to overcome obstacles. Moreover, a manipulator was added to improve the capabilities of the system that is able to perform various tasks: environment manipulation, object grasping, obstacle climbing and others. All these characteristics make the TriBot a suitable test-bed for many applications in cognitive robotics.

I. INTRODUCTION

Recently, there is a significant interest in the development of robots capable of autonomous operations in complex environments. Critical issues to be solved to succeed in these operations are: terrestrial mobility, reduced power consumption, efficient navigation and adaptive control strategies, robust communication protocols and a suitable payload. Depending on the tasks taken into consideration, the robot should be able to deal with either structured or unstructured environments, where the terrain is not a priori known. The most proper platforms to work in regular terrains are wheeled robots. Wheels, in fact, are relatively simple to control and allow a vehicle to move quickly over flat terrains. On the other side, a major advantage of legs over wheels is their ability to gain discontinuous footholds. This aspect is beneficial on irregular, discontinuous terrains, found in most real-world missions. In addition, to make a robot as much autonomous as possible, power consumption is of notable importance. This aspect is more easily attainable for wheeled robots than for the legged ones. On the other hand, multi-legged robots are more robust, in fact they can continue moving also with the loss of a single leg, while in wheeled vehicles a damaged wheel

could cause the end of mobility. To have advantages of wheeled and legged robots, it is possible to design a hybrid robot combining the simplicity of wheels with the advantages of legs. Examples of wheel-legs robots are Protero, Asguard, RHex and Whegs [1], [2], [3].

Following this research line, in this work, a bio-inspired robot, named TriBot, is proposed. Its mechanical structure joins the advantages both of legs and wheels, exactly as wheel-legs robots previously mentioned but, in addition, it is equipped with a manipulator that allows to add new features to the whole structure. Using this additional module, in fact, the robot is not only able to overcome obstacles otherwise unreachable with the only use of wheel-legs, but it is also possible to grasp and carry light objects or to push a buttons and to do small and precise movements. Moreover, the manipulator can help the robot in the case of loss of balance of the structure. All these features allow to use this robot to test locomotion control strategies, navigation control algorithms using multi-sensor data fusion and algorithms devoted to control multi-link manipulators. Exploiting these basic abilities, the TriBot is an ideal structure for the implementation of cognitive algorithms where the basic behaviors are enhanced with new capabilities learned from the environment constraints, for the implementation of complex action-oriented perception skills.

II. ROBOT DESIGN

In this section, we discuss about the mechanical and electronic characteristics of TriBot, an autonomous mobile hybrid robot.

The mechanical design of the robotic structure and the first prototype are shown in Fig.1. The robot has a modular structure, in particular it consists of two wheel-legs modules and a two-arms manipulator. The two wheel-legs modules are interconnected by a passive joint with a spring that allows only the pitching movement. This joint facilitates the robot during climbing, in fact,

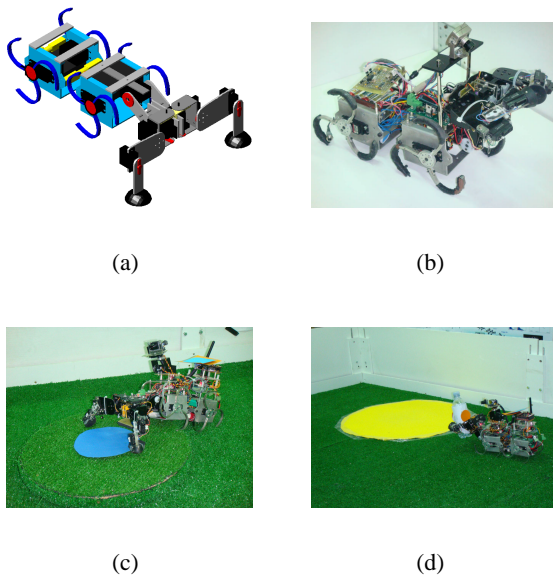


Fig. 1. Robot TriBot. (a) AutoCAD design; (b) Physical realization; (c) Robot TriBot during a climbing action and (d) while is taking an object.

the body flexion easily allows, in a passive way, to adapt the robot posture to obstacles. Each wheel-leg is composed by three spokes that describe a circle of 12cm of diameter and they are 6mm thick. These spokes can be moved in two different directions; if each spoke faces the convex part toward the motion direction, the movement results to be more smooth because the wheel-leg has a quasi-continuous contact with the terrain. Whereas the other configuration is better in overcoming obstacles because there is more grip with the terrain. Moreover, the central part of the robot is connected to a manipulator, that consists of two arms with three degrees of freedom, through an actuated joint. This joint allows the manipulator to move in different configurations. When it is moved down, the arms act as legs. This configuration is useful in rough terrain to increase the robot stability and to improve climbing capabilities. Furthermore, the manipulator adds the possibility to perform small and precise lateral movements otherwise impossible with the only use of wheel-legs. This kind of behavior can be useful when, for instance, the robot has to orient opportunely in order to take correctly an object. Whereas, when the manipulator is moved up, it is possible to use it for manipulation purposes. In this configuration the robot can push obstacles or bottoms, move sliding doors, grasp and carry objects.

III. HARDWARE ARCHITECTURE

The hardware architecture of the robot TriBot follows the modularity of the structure. The hardware structure of TriBot is managed by two microcontroller-based boards connected through a bus in configuration master/slave, that manage motors and sensors distributed on the structure. Furthermore, through a computer, using a RF wireless XBee module, it is possible to acquire data and send commands generated by a high level control algorithm. It is possible, in fact, to read data from the distributed sensory system embedded in the manipulator. In particular, on the manipulator, four distance sensors have been distributed for obstacle detection and a series of micro-switches are used to detect collisions and to grasp objects. Moreover, photo-resistances were added on the low side of the central module. They allow to recognize if the robot is placed on an object of a specific colour that, for the robot, can represent a target to be reached. The sensory system is needed for autonomous navigation and to use the robot as test bed for perceptual algorithms. For these reasons, to implement targeting and homing strategies, a hearing circuit, inspired by phonotaxis in crickets [4], has been also included. The aim is to give the robot the ability to approach sound sources, reproducing the behavior shown by the female cricket to follow a particular sound chirp emitted by a male cricket. Furthermore, one of the most useful and rich senses that guide animal's actions is the visual system. Therefore, the robot is equipped with a wireless camera that can be used for landmark identification, following moving objects and other higher level tasks. All these sensor modalities have been included in the robot in order to make the system able to safely move in unknown environments.

IV. RESULTS

In this section some preliminary results on the TriBot are presented.

First of all a test on the maximum velocity has been done. To measure the maximum speed of the robot an experimental set-up including a tapis-roulant, with a speed control, was used. The result obtained is 46 cm/sec. Experiments to test the climbing capabilities were also performed. Using only wheels, TriBot is able to agilely overcome obstacles up to 8 cm. The robot is not able to overcome a higher obstacle because the spokes are not able to hook the top surface of the obstacle. Therefore, when the obstacle is higher than 8 cm, wheels are not enough to overcome it. At this point, the manipulator can be used, in fact it allows

TABLE I
MAIN CHARACTERISTICS OF THE WHEEL-LEGS ROBOT.

	Asguard	Whlegs	TriBot
Height x Length x Width	44x95x50 cm	12x51 cm	12x36x20 cm (manip. down) 23x28x20 cm (manip. up)
Weight	11.5kg	-	1.95kg
Velocity	2.1 body length/s (200 cm/s)	3 body length/s (153 cm/s)	1.64 body length/s (46 cm/s)
Wheel radius	22 cm	10 cm	6 cm
Maximum obstacle height	1.1 times wheel radius	1.5 times wheel radius	1.8 times wheel radius

to hook the top of the obstacle with its arms. Using this system, TriBot succeeds in overcoming obstacles of about 10cm. Another application of the manipulator is object grasping. Different tests have been accomplished grasping various objects. The maximum payload resulted to be about 300g. Videos of the described experiments are available on the web [5]. TriBot structure and performance can be compared with other hybrid wheel-legs robots among which Whlegs and Asguard. The TriBot has reduced dimensions if compared with most of the wheel-legs robots and comparable performance for locomotion. Table I summarizes the main characteristics of TriBot compared with other two wheel-legs robots: Whlegs and Asguard. The performance, in term of maximum speed, are lower than the other robots, whereas the climbing capability are better thanks to the improvement introduced by the manipulation module that, at the same time, allows to increase the number of basic behaviors that can be performed.

Another interesting parameter that can be used to compare TriBot with other robots is the Energetic Performance. To measure energy efficiency, an increasingly accepted parameter is the “Specific Resistance”, ε , a measure proposed originally by Gabrielli and von Karman [6] in 1950:

$$\varepsilon = P / (mg \cdot v) \quad (1)$$

where m is the robot mass, g is the gravity acceleration, P is its average power consumption at a particular speed. The range of values (i.e. for normal walking, movement at maximum speed on a flat terrain and for obstacle climbing) of the “Specific Resistance” for the robot TriBot compared with other robotic platforms are here reported. Unfortunately for Asguard and Whlegs the

parameter are not published, so the comparison is done with other known robots. RHex robot Specific Resistance ranges between $\varepsilon = 2.5 - 14$ [2], while for Gregor I, an asymmetric hexapod robot inspired by a cockroach, the performance on uneven terrains was $\varepsilon = 42 - 70$ [7]. The robot MiniHex, a bio-inspired mini robot, has a Specific Resistance on even terrain of $\varepsilon = 12.5$ [8]. The results for the Tribot, $\varepsilon = 0.9$, have been obtained during the movement at maximum speed in a flat terrain, while during obstacle climbing using both wheels and manipulator, the value is $\varepsilon = 3.2$. Therefore, the range of TriBot Specific Resistance can be considered more than acceptable.

V. COGNITIVE ALGORITHMS ON THE TRIBOT

As already discussed above, the structure of the Tribot was specifically built to handle with complex environments, to allow the robot to efficiently face with uneven terrains and above all to lead to the emergence of new behaviors through learning in real time to face with new situations, using a network of sensory modalities. To this aim, the basic ability of the robot should be to navigate in changeable conditions. To do this, modern robotic systems use multiple sensors because one knowledge source is often unable to provide all of the information necessary for inspection and manipulation tasks [9]. For these reasons, to implement targeting and homing strategies, different kinds of sensors, such as distance sensors, contact sensors, target sensors, a visual sensor (wireless camera) and a hearing sensor have been added on the robotic structure.

Moreover, walking robots performance can be improved taking inspiration from insect, that can run stably over rough terrains at high enough speeds to challenge the ability of proprioceptive sensing and neural feedback to respond to perturbations within a stride [10]. A network of neurons, implementing the Central Pattern Generator (CPG), is used to control the rhythmic movements typical in many animals. This concept has been found useful in robotics, especially when the control of a locomotion system requires the concurrent activation of many actuators. An example of bio-inspired mini robot controlled using a VLSI chip that implement a CPG through a CNN-based structure is presented in [8] referring to a hexapod robot. The CPG approach could be very efficient in controlling also a hybrid robot like the Tribot; in fact the CPG final aim is to impose suitable phase displacements among the various legs. In this perspective, it could be interesting to synchronize, with a suitable phase displacement, the

locomotion behavior of the front manipulator and the three spoke wheels. In fact, considering the structure of the wheels, the trajectory followed by the robot depends on the synchrony of the touching down of the wheels. In the concave configuration, if the wheels are in phase, the trajectory is a straight line, otherwise a particular curvature will be obtained. Moreover, complex steering strategies could be implemented via the phase synchronization of the front manipulator and the wheel movement. Going up from the basic motion capabilities, a Recurrent Neural Network (RNN) can be used to learn many behaviors, sequence processing tasks, algorithms, realtime learning strategies that are not learnable by traditional machine learning methods. All these features allow to use the robot TriBot to implements more complex skills. Different correlation-based navigation algorithms, based on an unsupervised learning paradigm for spiking neural networks, called Spike Timing Dependent Plasticity (STDP), were implemented on the TriBot, in order to learn and increase its behavioral capabilities. A complete neural architecture, in fact, that allows to control the robot in order to find an object and to perform the basic behaviours available for the robot, has been presented in [11]. A similar spiking neural architecture, that allows the robot to avoid obstacles and to recognize and reach targets, was tested using the robot TriBot. The STDP learning strategy implemented allows the robot to learn high-level sensor features, based on a set of basic reflexes, depending on some low-level sensor inputs. An important features that is being implemented to enhance the potentialities of this strategy is the forgetting capability that allows the robot to cope with environmentally changing conditions. This characteristic is also common in nature: insects can learn to associate specific odors to food but they are also able to modify this association on the basis of the environmental changes. Other kinds of cognitive algorithms can be tested using this robot. Finally, another interesting field of study that can be investigated is the area of collective and cooperative behaviour in swarm of robots. Groups of mobile robots, such as TriBot robots, can, in fact, be developed, in order to have the possibility to study group architectures, resource conflicts, emergence of cooperation.

VI. CONCLUSION

In this paper a hybrid modular mini robot has been presented. Its peculiar characteristics consists in the design of legs: each one is realized with a tri-spoke appendage and actuated by a single motor. The TriBot takes inspiration from the tri-spokes leg used in the Whegs

robot, but, instead of a three pairs of whegs, only two modules have been used and two legs with three degrees of freedom have been included in the frontal part of the robot. This frontal module is used both for locomotion and manipulation purposes. The proposed structure joins the advantages of two typologies of structure (wheeled and legged) joining them to deal with different kinds of scenarios. The manipulator, positioned in the front part of the robot, proved to be useful in overcoming obstacles, moreover it allows the robot to grab objects, to avoid to lose stability during climbing and to complete small and precise movements. The robot presented in this paper has been demonstrated to be an appropriate platform for testing different kinds of control algorithms, such as locomotion control strategies (i.e. Central Pattern Generator), Recurrent Neural Network to control the manipulator, targeting and homing strategies and others.

ACKNOWLEDGMENT

The authors acknowledge the support of the European Commission under the project SPARK II.

REFERENCES

- [1] M. Eich, F. Grimmering, S. Bosse, D. Spenneberg, F. Kirchner; Robotics Lab. Asguard: A Hybrid -Wheel Security and SAR-Robot Using Bio-Inspired Locomotion for Rough Terrain. *IARP/EURON '08*, January 7-8, Benicassim, Spain, 2008.
- [2] U. Saranli, M. Buehler and D. Koditschek. RHex A Simple and Highly Mobile Hexapod Robot. *International Journal of Robotics Research*, 20(7): 616-631, 2001.
- [3] R. T. Schroer, M. J. Boggess, R. J. Bachmann, R. D. Quinn, R. E. Ritzmann. Comparing Cockroach and Whegs Robot Body Motions. *ICRA '04*, New Orleans, 2004.
- [4] L. Alba, P. Arena, S. De Fiore, J. Listan, L. Patané, G. Scordino and B. Webb. Multi-sensory architectures for action-oriented perception. *Proc. of Microtechnologies for the New Millennium (SPIE 07)*, Gran Canaria (SPAIN), May 2007.
- [5] EU Project SPARK II, online at www.spark2.diees.unict.it/TribotI.html
- [6] G. Gabrieli and T. H. von Karman. What price speed?. *Mechanical Engineering*, vol. 72 no. 10, pp. 775-781, 1950.
- [7] P. Arena, L. Fortuna, M. Frasca, L. Patané, M. Pavone. Realization of a CNN-Driven Cockroach-Inspired Robot. *Proc. of ISCAS '06*, Island of Kos, Grecia, 21-24 April 2006.
- [8] P. Arena, L. Fortuna, M. Frasca, L. Patan, M. Pollino. An autonomous mini-hexapod robot controlled through a CNN-based CPG VLSI chip. *Proc. of CNNA*, Istanbul, 2006.
- [9] R. Varadarajan, G. Yuen, M. Bodruzzaman and M. Malkani. Sensory fusion for intelligent navigation of mobile robot. *Proc. of the 30th Southeastern Symposium*, pp. 307-311, 1998.
- [10] J. E. Seipel, P. J. Holmes, R. J. Full, "Dynamics and stability of insect locomotion: a hexapedal model for horizontal plane motions", *Biological Cybernetics*, Volume 91, Issue 2, Pages: 76 - 90, 2004.
- [11] P. Arena, S. De Fiore, L. Patané, M. Pollino, C. Ventura. STDP-based behaviour learning on the Tribot robot. *Proc. of Microtechnologies for the New Millennium (SPIE 09)*, Dresden (GERMANY), 4-6 May 2009, 7365-05.

Comparison of Eyelet Intermittency and Type-I Intermittency with Noise

Alexander E. Hramov, Alexey A. Koronovskii, Maria K. Kurovskaya, Olga I. Moskalenko

Faculty of Nonlinear Processes, Saratov State University,

410012, Astrakhanskaya, 83, Saratov, Russia

Email: alkor@nonlin.sgu.ru

Abstract—In this report we compare the characteristics of two types of the intermittent behavior (type-I intermittency in the presence of noise and eyelet intermittency) supposed hitherto to be the different phenomena. We prove that these effects are very similar to each other. The correctness of our conclusion is proven by the consideration of different sample systems, such as quadratic map, Van der Pol oscillator and Rössler system.

I. INTRODUCTION

Intermittency is well-known to be an ubiquitous phenomenon in nonlinear science. Its arousal and main statistical properties have been studied and characterized already since long time ago, and different types of intermittency have been classified as types I–III [1], on–off intermittency [2], [3], eyelet intermittency [4] and ring intermittency [5].

Despite of some similarity (the presence of two different regimes alternating suddenly with each other in the time series), every type of intermittency is governed by its own certain mechanisms and the characteristics of the intermittent behavior (such as the dependence of the mean length of the laminar phases on the control parameter, the distribution of the lengths of the laminar phases, etc.) of different intermittency types are distinct. There are no doubts that different types of intermittent behavior may take place in a wide spectrum of systems, including cases of practical interest for applications in radio engineering, medical, physiological, and other applied sciences.

This report is devoted to the comparison between characteristics of type-I intermittency in the presence of noise and eyelet intermittency taking place in the vicinity of the phase synchronization boundary. These types of the intermittent behavior seem to be different and determined by the distinct causes. First of them is observed near the saddle-node bifurcation point in the system enforced by the external stochastic signal. The second one takes place in the vicinity of the phase

synchronization boundary in two coupled deterministic chaotic oscillators and it is explained in terms of the synchronization of the unstable periodic orbits embedded into chaotic attractors. Moreover, these types of intermittency are known to be characterized by the different theoretical laws. Nevertheless, we show here that these two types of the intermittent behavior considered hitherto as different phenomena are, in fact, very similar to each other.

II. RELATION BETWEEN TYPE-I INTERMITTENCY WITH NOISE AND EYELET INTERMITTENCY

First, we consider briefly both eyelet intermittency and type-I intermittency in the presence of noise following conceptions accepted generally. The main arguments confirming the similarity of these types of the intermittent behavior are given afterwards.

A. Type-I intermittency with noise

The intermittent behavior of type-I is known to be observed below the saddle-node bifurcation point, with the mean length of laminar phases T being inversely proportional to the square root of the criticality parameter $(\varepsilon_c - \varepsilon)$, i.e.

$$T \sim (\varepsilon_c - \varepsilon)^{-1/2}, \quad (1)$$

where ε is the control parameter and ε_c – its bifurcation value corresponding to the bifurcation point [1]. The influence of noise with the intensity D on the system results in the transformation of the characteristics of intermittency [6], [7], [8], with the intermittent behavior being observed in this case both below and above the saddle-node bifurcation point ε_c . In the supercritical region [8] of the control parameter values (above the point of bifurcation, $\varepsilon > \varepsilon_c$) the mean length T of the laminar phases is given by

$$T = \frac{1}{k\sqrt{\varepsilon - \varepsilon_c}} \exp\left(\frac{4(\varepsilon - \varepsilon_c)^{3/2}}{3D}\right), \quad (2)$$

with Equation (2) being applicable in the region

$$D^{2/3} \ll |\varepsilon - \varepsilon_c| \ll 1 \quad (3)$$

of the control parameter plane [6], [9]. In this region the criticality parameter $(\varepsilon - \varepsilon_c)$ is large enough and, therefore, the approximate equation

$$\ln T \sim D^{-1}(\varepsilon - \varepsilon_c)^{3/2} \quad (4)$$

may be also used (see [7] for detail) instead of (2).

In turn, the distribution $p(\tau)$ of the laminar phase lengths τ is governed by the exponential law

$$p(\tau) = T^{-1} \exp(-\tau/T). \quad (5)$$

Note also, that the theoretical expression (2) is not applicable for the extremely small values of the criticality parameter $(\varepsilon - \varepsilon_c)$ i.e., for $(\varepsilon - \varepsilon_c) \rightarrow +0$, that is caused by the major transformation of the system behavior when the control parameter ε undergoes from the supercritical region to the subcritical one, since the assumptions made in the supercritical region for deriving Eq. (2) stops being correct and, therefore, Eq. (2) becomes inapplicable to the mean length of the laminar phases estimation.

B. Eyelet intermittency

For the chaotic systems in the vicinity of the phase synchronization boundary (if the natural frequencies of oscillator and external signal are detuned slightly) two types of the intermittent behavior and, correspondingly, two critical values are reported to exist [4]. Below the boundary of the phase synchronization regime, the dynamics of the phase difference $\Delta\varphi(t)$ features time intervals of the phase synchronized motion (laminar phases) persistently and intermittently interrupted by sudden phase slips (turbulent phases) during which the value of $|\Delta\varphi(t)|$ jumps up by 2π . For two coupled chaotic systems there are two values of the coupling strength $\sigma_1 < \sigma_2$ being the characteristic points which are considered to separate the different types of dynamics. Below the coupling strength σ_1 the type-I intermittency is observed, with the power law $T \sim (\sigma_1 - \sigma)^{-1/2}$ taking place for the mean length of the laminar phases, whereas above the critical point σ_2 the phase synchronization regime is revealed. For the coupling strength $\sigma \in (\sigma_1; \sigma_2)$ the super-long laminar behavior (so called “eyelet intermittency”) should be detected. For eyelet intermittency (see, e.g. [4]) the dependence of the mean length T of the laminar phases on the criticality parameter is expected to follow the law

$$T \sim \exp(k|\sigma_2 - \sigma|^{-1/2}) \quad (6)$$

or

$$\ln(1/T) = c_0 - c_1|\sigma_2 - \sigma|^{-1/2}, \quad (7)$$

(c_0 , c_1 and k are the constants). The analytical form of the distribution of the laminar phase lengths has not been reported anywhere hitherto for eyelet intermittency.

C. The similarity of the considered types of behavior

Although type-I intermittency with noise and eyelet intermittency seem to be quite different phenomena, they are really close to each other. Indeed, it is well-known that for the periodically forced weakly nonlinear isochronous oscillator (in the case of a small frequency mismatch) the complex amplitude method may be used to find the solution describing the oscillator behavior in the form

$$u(t) = \text{Re } a(t)e^{i\omega t}. \quad (8)$$

For the complex amplitude $a(t)$ one obtains averaged (truncated) equation

$$\dot{a} = -i\nu a + a - |a|^2 a - ik, \quad (9)$$

where ν is the frequency mismatch, and k is the (renormalized) amplitude of the external force. For the small ν and large k the stable solution

$$a(t) = Ae^{i\phi} = \text{const} \quad (10)$$

corresponds to the synchronous regime, with the synchronization destruction corresponding to the local saddle-node bifurcation associated with the global bifurcation of the limit cycle birth. Therefore, below the boundary of the synchronization regime the dynamics of the phase difference

$$\Delta\varphi(t) = \varphi(t) - \omega_e t \quad (11)$$

(where $\varphi(t)$ is the phase of the driven oscillator, ω_e — the frequency of the external harmonic signal) demonstrates time intervals of phase synchronized motion (laminar phases) interrupted by phase slips (turbulent phases). The mean length T of the laminar (synchronous) phases depends on the criticality parameter according to the power law (1) corresponding to the type-I intermittency.

At the same time, the behavior of the periodic and chaotic systems in the vicinity of the onset of the synchronization in many cases is very similar. Thus, both for two coupled chaotic Rössler systems and driven Van der Pol oscillator the same scenarios of the synchronous regime destruction have been revealed [10]. Moreover, under certain conditions the dynamics of chaotic systems may be considered as a random perturbations [7],

including the system behavior near the onset of the synchronous regime. E.g., for two coupled Rössler systems the behavior of the conditional Lyapunov exponent in the vicinity of the onset of the phase synchronization regime is governed by the same laws as in the case of the driven Van der Pol oscillator in the presence of noise [9]. Obviously, one can expect that the intermittent behavior of two coupled chaotic oscillators near the phase synchronization boundary (eyelet intermittency) is close to intermittency of type-I in the presence of noise in the supercritical region.

III. NUMERICAL VERIFICATIONS

To prove the concept of the similarity of intermittencies being the subject of this study we consider several examples of the intermittent behavior classified both as eyelet intermittency (two coupled Rössler systems) and type-I intermittency with noise (quadratic map and driven Van der Pol oscillator).

A. Two coupled Rössler systems

As we have mentioned above, the intermittent behavior of two coupled chaotic oscillators in the vicinity of the phase synchronization boundary is classified traditionally as *eyelet intermittency* [4].

The system under study is represented by a pair of unidirectionally coupled Rössler systems, whose equations read as

$$\begin{aligned}\dot{x}_d &= -\omega_d y_d - z_d, \\ \dot{y}_d &= \omega_d x_d + a y_d, \\ \dot{z}_d &= p + z_d(x_d - c), \\ \dot{x}_r &= -\omega_r y_r - z_r + \sigma(x_d - x_r), \\ \dot{y}_r &= \omega_r x_r + a y_r, \\ \dot{z}_r &= p + z_r(x_r - c),\end{aligned}\tag{12}$$

where (x_d, y_d, z_d) [(x_r, y_r, z_r)] are the Cartesian coordinates of the drive [the response] oscillator, dots stand for temporal derivatives, and σ is a parameter ruling the coupling strength. The other control parameters of Eq. (12) have been set to $a = 0.15$, $p = 0.2$, $c = 10.0$. The ω_r -parameter (representing the natural frequency of the response system) has been selected to be $\omega_r = 0.95$; the analogous parameter for the drive system has been fixed to $\omega_d = 0.93$. For such a choice of the control parameter values, both chaotic attractors of the drive and response systems are phase coherent. The instantaneous phase of the chaotic signals $\varphi(t)$ can be therefore introduced in the traditional way, as the rotation angle $\varphi_{d,r} = \arctan(y_{d,r}/x_{d,r})$ on the projection plane (x, y) of each system.

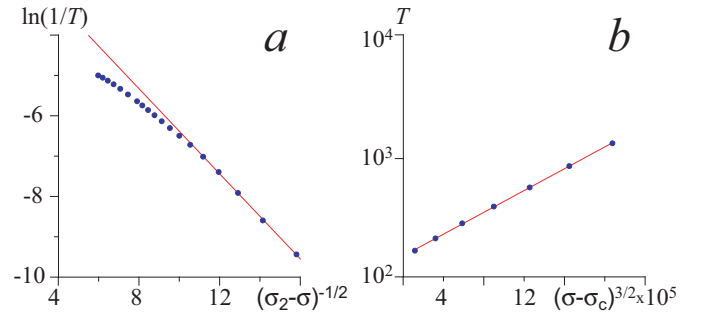


Fig. 1. The points obtained numerically for two unidirectionally coupled Rössler oscillators (12) are shown by symbols “•”. The theoretical laws (7) and (4) are shown by the solid lines. (a) *Eyelet intermittency*: the dependence of $\ln(1/T)$ on the parameter $(\sigma_2 - \sigma)^{-1/2}$. The critical value is $\sigma_2 = 0.042$. (b) *Type-I intermittency with noise*: the dependence of the mean laminar phase length T on the parameter $(\sigma - \sigma_c)^{3/2}$, with the ordinate axis being shown in the logarithmic scale. The critical value is $\sigma_c = 0.0345$

In Fig. 1 one and the same result of the numerical simulation of two coupled Rössler systems (12) is shown in different ways to compare obtained data with the analytical approximations for eyelet intermittency (Fig. 1, a) and type-I intermittency with noise (Fig. 1, b). The dependence of T on $(\sigma_2 - \sigma)$ is shown in the whole range of the coupling parameter strength values (Fig. 1, a) to make evident the deviation of numerically obtained data from law (7) far away from the onset of the phase synchronization. The coupling strength σ plays the role of the control parameter. Note, however, that the critical points σ_c and σ_2 used for the eyelet intermittency and type-I intermittency with noise relations, respectively, do not coincide with each other and their values are different. The critical point $\sigma_2 \approx 0.042$ relates to the onset of the phase synchronization regime in two coupled Rössler systems. The point $\sigma_c \approx 0.0345$ used in (2) and (4) corresponds to the saddle-node bifurcation point if the chaotic dynamics being the analog of noise could be switched off. The value of this point has been found from the dependence of the conditional zero Lyapunov exponent on the coupling strength (see for detail [9]).

One can see, that the intermittent behavior of two coupled Rössler systems may be treated both as eyelet and noised type-I intermittency, with the excellent agreement between numerical data and theoretical curve in both cases.

B. Driven Van der Pol oscillator with noise

The second sample dynamical system to be considered is Van der Pol oscillator

$$\ddot{x} - (\lambda - x^2)\dot{x} + x = A \sin(\omega_e t) + D\xi(t)\tag{13}$$

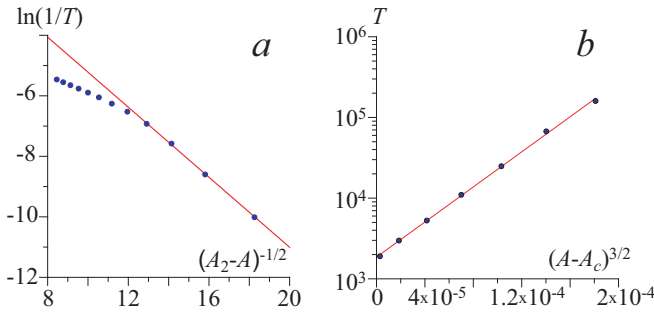


Fig. 2. The points obtained numerically for driven Van der Pol oscillator with the stochastic force (13) are shown by symbols “•”. The theoretical laws (7) and (4) are shown by the solid lines. (a) *Eyelet intermittency*: the dependence of $\ln(1/T)$ on the parameter $(A_2 - A)^{-1/2}$. The critical value is $A_2 = 0.029$. (b) *Type-I intermittency with noise*: the dependence of the mean laminar phase length T on the parameter $(A - A_c)^{3/2}$. The critical value is $A = 0.0238$

driven by the external harmonic signal with the amplitude A and frequency ω_e with the added stochastic term $D\xi(t)$. The values of the control parameters have been selected as $\lambda = 0.1$, $\omega_e = 0.98$. For the selected values of the control parameters and $D = 0$ the dynamics of the driven Van der Pol oscillator becomes synchronized when $A = A_c = 0.0238$ that corresponds to the saddle-node bifurcation. To integrate Eq. (13) the one-step Euler method has been used with time step $h = 5 \times 10^{-4}$, the value of the noise intensity has been fixed as $D = 1$.

On the one hand, as it was discussed above, the intermittent behavior in this case have to be classified as type-I intermittency with noise. The corresponding dependence of the mean length of the laminar phases on the criticality parameter $(A - A_c)$ is shown in Fig. 2, b. If the amplitude A of the external signal exceeds the critical value A_c the exponential law $T \sim \exp(\alpha(A - A_c)^{3/2})$ is expected to be observed. To make this law evident the abscissa in Fig. 2, b has been selected in the $(A - A_c)^{3/2}$ -scale and the ordinate axis T is shown in the logarithmic scale. One can see again the excellent agreement between the numerically calculated data and theoretical prediction (4). The distribution of the lengths of the laminar phases $p(t)$ obtained for $A > A_c$ also confirms the theoretical curve (5), see Fig. 7 in [8].

On the other hand, trying to choose the corresponding values of A_2 for the driven Van der Pol oscillator (13) one can find out that the intermittent behavior of this system also may be identified as eyelet intermittency. Indeed, in Fig. 2, a one can see the very good agreement between the numerically obtained mean lengths T of the laminar phases for the different values of the coupling parameter and theoretical law (7) corresponding to the

eyelet intermittency. Note also, that for the well chosen values of A_2 the dependence $T(A_2 - A)$ in the axes $((A_2 - A)^{-1/2}, \ln(1/T))$ behaves in the same way as the corresponding function $T(\sigma_2 - \sigma)$ in the axes $((\sigma_2 - \sigma)^{-1/2}, \ln(1/T))$ for two coupled Rössler systems (12).

C. Quadratic map with stochastic force & Van der Pol oscillator driven by the chaotic signal

We have also considered the characteristics of the intermittent behavior of the quadratic map with stochastic force and Van der Pol oscillator driven by the chaotic signal. We have found in both cases that the dependencies of the mean length of the laminar phases on the critical parameter may be approximated by both (7) and (4) as well as for two coupled Rössler systems and driven Van der Pol oscillator with noise considered above. It allows us to state about the similarity of the eyelet intermittency and type-I intermittency with noise.

IV. CONCLUSION

Having considered two types of the intermittent behavior, namely eyelet intermittency and type-I intermittency with noise we prove that these effects are the very similar types of the dynamics and may be considered as one and the same type of the system behavior.

ACKNOWLEDGMENT

This work has been supported by Federal special-purpose programme “Scientific and educational personnel of innovation Russia (2009–2013)” and Russian Foundation for Basic Research (projects 08-02-00102 and 09-02-92421).

REFERENCES

- [1] P. Bergé, Y. Pomeau, and C. Vidal, *L'Ordre Dans Le Chaos* (Hermann, Paris, 1988).
- [2] N. Platt, E. A. Spiegel, and C. Tresser, Phys. Rev. Lett. **70**, 279 (1993).
- [3] A. E. Hramov and A. A. Koronovskii, Europhysics Lett. **70**, 169 (2005a).
- [4] A. S. Pikovsky, G. V. Osipov, M. G. Rosenblum, M. Zaks, and J. Kurths, Phys. Rev. Lett. **79**, 47 (1997a).
- [5] A. E. Hramov, A. A. Koronovskii, M. K. Kurovskaya, and S. Boccaletti, Phys. Rev. Lett. **97**, 114101 (2006).
- [6] J. P. Eckmann, L. Thomas, and P. Wittwer, J. Phys. A: Math. Gen. **14**, 3153 (1981).
- [7] W. H. Kye and C. M. Kim, Phys. Rev. E **62**, 6304 (2000).
- [8] A. E. Hramov, A. A. Koronovskii, M. K. Kurovskaya, A. A. Ovchinnikov, and S. Boccaletti, Phys. Rev. E **76**, 026206 (2007a).
- [9] A. E. Hramov, A. A. Koronovskii, and M. K. Kurovskaya, Phys. Rev. E **78**, 036212 (2008).
- [10] A. E. Hramov, A. A. Koronovskii, and M. K. Kurovskaya, Phys. Rev. E **75**, 036205 (2007b).

Bifurcation of a simplified model of the boost converter with solar cell input

Toshimichi Saito and Daisuke Kimura

EE Dept., Hosei University, Tokyo, 184-8584 Japan, tsaito@hosei.ac.jp

Abstract—This paper studies a simple switched dynamical system based on the boost converter. The input is a solar cell that is modeled by a piecewise linear current-controlled voltage source. A variant of peak-current-controlled switching is used in the converter. Applying the mapping procedure, the system dynamics can be analyzed precisely. We have analyzed basic bifurcation phenomena and have clarified that the model can repeat period-doubling and border collision bifurcations alternately. Such phenomena can not occur in the case of dc input.

I. INTRODUCTION

The switched dynamical system (SDS) is characterized by nonlinear switching among several continuous-time sub-dynamics and the switching can cause a variety of bifurcation phenomena [1]-[5]. The SDS relates to many engineering systems including switching power converters. Analysis of the dynamics is important not only as a fundamental study but also for design of desired circuit operation. For example, the analysis has been provided basic information to improve system stability and EMI in power converters [5]-[6].

This paper presents a simple SDS relating to the photovoltaic systems that are important in renewable energy technology [7]-[11]. In the SDS, the input is an equivalent model of a single solar cell [7] and is converted to the output via a boost converter. For simplicity, we introduce a simple model of the solar cell: a current-controlled voltage source (CCVS) having 2-segment piecewise linear (PWL) characteristics. The boost converter is controlled by a switching rule that is a variant of peak-current-controlled switching [6]. Applying a simplification technique in [12] [13], the SDS dynamics can be integrated into analysis of a one dimensional map of the switching phase. The phase map is described explicitly using the exact piecewise solution of the PWL circuit equation. Using the map, we have analyzed the SDS in a parameter subspace. We have clarified that the model can repeat period-doubling and border collision bifurcations alternately in a route to

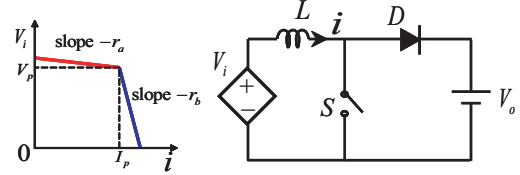


Fig. 1. Circuit model of the boost converter with a solar sell

chaotic behavior. This alternation is impossible in a PWL phase map of the dc-dc converters [12].

Precise analysis of global stability and bifurcation phenomena is very hard without the novel PWL modeling of the solar cell. In existing works, the solar cells are described by exponential forms and the small signal analysis for local stability has been mainstream [9] [10].

II. THE CIRCUIT MODEL

Fig. 1 shows a circuit model of the SDS where the CCVS has two-segment PWL characteristics.

$$V_i(i) = \begin{cases} -r_b(i - I_p) + V_p & \text{for } i > I_p \\ -r_a(i - I_p) + V_p & \text{for } i \leq I_p \end{cases} \quad (1)$$

where $i \geq 0$ and $V_i(i) \geq 0$ are assumed. This CCVS can be regarded as a simplified model of solar cells [7]. Although the solar cells are usually described by a voltage-controlled function, the function is one-to-one and the current-controlled description is convenient to derive circuit equation for inductor current. The constant voltage source V_0 represents the output load derived by simplification in the case where the time constant of the load is much larger than the control clock period [12]. The boost converter has a switch S and a diode D which can be either of the two states.

State 1: S conducting and D blocking

State 2: S blocking and D conducting

The switching rule is defined by :

State 2 \rightarrow State 1: when $i = J_- > 0$.

State 1 \rightarrow State 2: at $t = nT$ and $i > J_-$

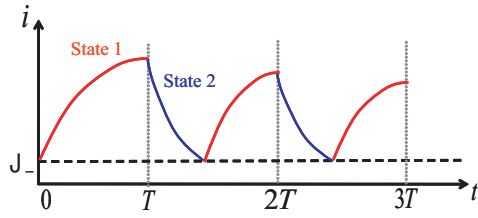


Fig. 2. Switching rule

where T is a clock period and J_- is the lower threshold that controls the valley current as shown in Fig. 2. since J_- is positive, this switching prohibits discontinuous conduction mode where both S and D are blocking. The rule is a variant of the peak-current-control [1] [6] and can cause various phenomena discussed afterward. The circuit dynamics is described by

$$L \frac{di}{dt} = \begin{cases} V_i(i) & \text{for State 1} \\ V_i(i) - V_o & \text{for State 2} \end{cases} \quad (2)$$

where $V_o > V_i(0) = V_p + r_a I_p$ is satisfied in the boost operation. we define the dimensionless variables and parameters:

$$\begin{aligned} \tau = \frac{t}{T}, x = \frac{i}{I_p}, y(x) = \frac{V_i(I_p x)}{V_p}, \alpha = \frac{r_a I_p}{V_p} \\ \beta = \frac{r_b I_p}{V_p}, q = \frac{V_o}{V_p}, \gamma = \frac{TV_p}{LI_p}, X_- = \frac{J_-}{I_p} \end{aligned} \quad (3)$$

Using these, Eq. (2), Eq. (1) and the switching rule are transformed into

$$\frac{dx}{d\tau} = \begin{cases} \gamma y(x) & \text{for State 1} \\ \gamma(y(x) - q) & \text{for State 2} \end{cases} \quad (4)$$

$$y(x) = \begin{cases} -\beta(x-1) + 1 & \text{for } x > 1 \\ -\alpha(x-1) + 1 & \text{for } x \leq 1 \end{cases} \quad (5)$$

SW Rule: State 2 \rightarrow State 1: when $x = X_- > 0$.
State 1 \rightarrow State 2: at $\tau = n$ and $x > X_-$.

The dimensionless 5 parameters can be classified into two categories: (α, β, q) that characterizes "solar cell and load" and (γ, X_-) that characterizes "switching control". Using the exact piecewise solution, we can calculate waveform precisely and typical examples are shown in Fig. 3. As parameters vary, the fundamental periodic orbit with period 1 (Fig. 3 (a)) is changed into a variety of periodic/chaotic orbits.

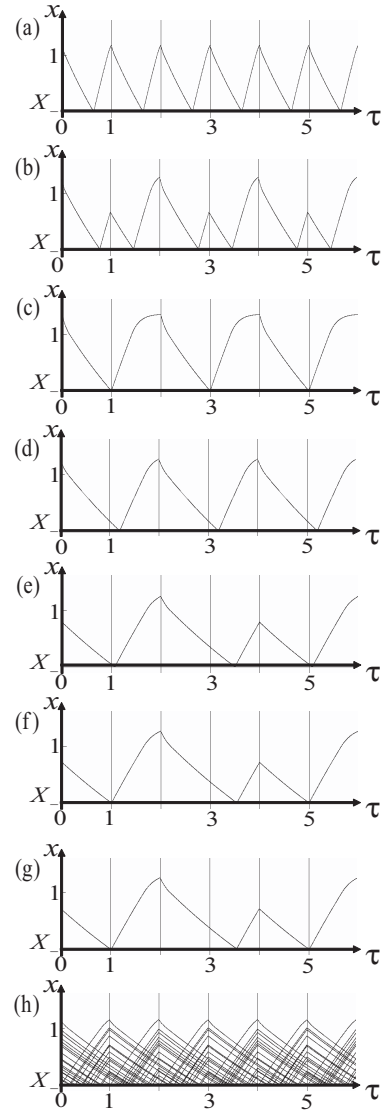


Fig. 3. Typical waveforms for $\alpha = 0.5$, $\beta = 9.0$, $q = 1.6$ and $X_- = 0.7$. (a) $\gamma = 1.0$, (b) $\gamma = 0.85$, (c) $\gamma = 0.6825$ on B_1 , (d) $\gamma = 0.55$, (e) $\gamma = 0.44$, (f) $\gamma = 0.4315105$ on B_2 , (g) $\gamma = 0.4292$, (h) $\gamma = 0.35$.

III. PHASE MAP AND BIFURCATION

In order to analyze bifurcation phenomena, we derive the one-dimensional map. As shown in Fig. 4, let τ_n denote the n -th switching time at the lower threshold X_- . Since τ_n determines τ_{n+1} , we can define a one-dimensional map

$$\tau_{n+1} = F(\tau_n), \quad \tau_n \in \mathbf{R}^+ \quad (6)$$

where \mathbf{R}^+ denotes positive reals. Using the exact piecewise solution, we can describe the map explicitly. Since the normalized clock period is 1, we introduce a phase variable $\theta_n = \tau_n \bmod 1$. Using this, we can define the

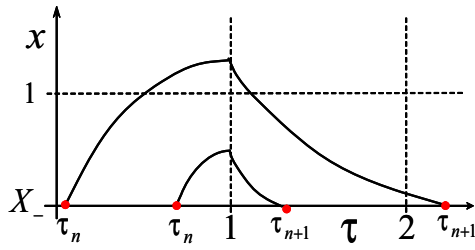


Fig. 4. Definition of return map.

phase map f from unit interval $I \equiv [0, 1)$ to itself:

$$\theta_{n+1} = f(\theta_n) \equiv F(\theta_n) \bmod 1, \quad \text{for } \theta_n \in I \quad (7)$$

As shown in Fig. 5, this phase map consists of convex curves and is different from PWL phase map of the dc-dc converters [12]. Here we give several definitions for periodic behavior. A point p is said to be a k -periodic point if $p = f^k(p)$ and $p \neq f^l(p)$ for $1 \leq l < k$ where $f^l(x_p) = f(f^{l-1}(p))$ and $f^0(p) \equiv p$. A 1-periodic point is referred to as a fixed point. A periodic point p is said to be unstable and stable for initial value if $|Df^k(p)| > 1$ and $|Df^k(p)| < 1$, respectively, where $Df^k(p)$ is the slope of f^k at p .

For simplicity, we focus on bifurcation of fundamental periodic behavior in the 2-dimensional parameter subspace of (X_-, γ) . Let us consider basic bifurcation with typical phase maps in Fig. 5. First, the map has stable fixed point p_1 (Fig. 5 (a)) that corresponds to stable periodic orbit (SPO). As γ decreases, the p_1 becomes unstable and the SPO is changed into the unstable periodic prbot (UPO) through the first period doubling bifurcation set $D_1 = \{\vec{p} \mid Df(p_1) = -1\}$ where $\vec{p} \equiv (\alpha, \beta, \gamma, X_-, q)$. For the SPO and UPO corresponding to p_1 , we have calculated the dimensionless average power:

$$P_A = \frac{1}{N_p} \int_0^{N_p} x(\tau)y(\tau)d\tau \quad (8)$$

where the period $N_p = 1$ for the SPO and UPO. Fig. 6 shows P_A and $|Df(p_1)|$ calculated by exact piecewise solution. We can see that the UPO has larger average power than the SPO and can have the maximum power point for parameter γ . In the parameter space, we have confirmed that the maximum power point (MPP) for γ located near D_1 . This is important information to construct efficient MPP trackers [8]-[11].

As γ exceeds D_1 , the stable 2-periodic points appear (Fig. 3 (b)). It corresponds to the SPO with period 2 in Fig. 3 (b). Since the map does not has peak such as the logistic map, the period-doubling cascade can not occur and the 2-periodic points changed into the

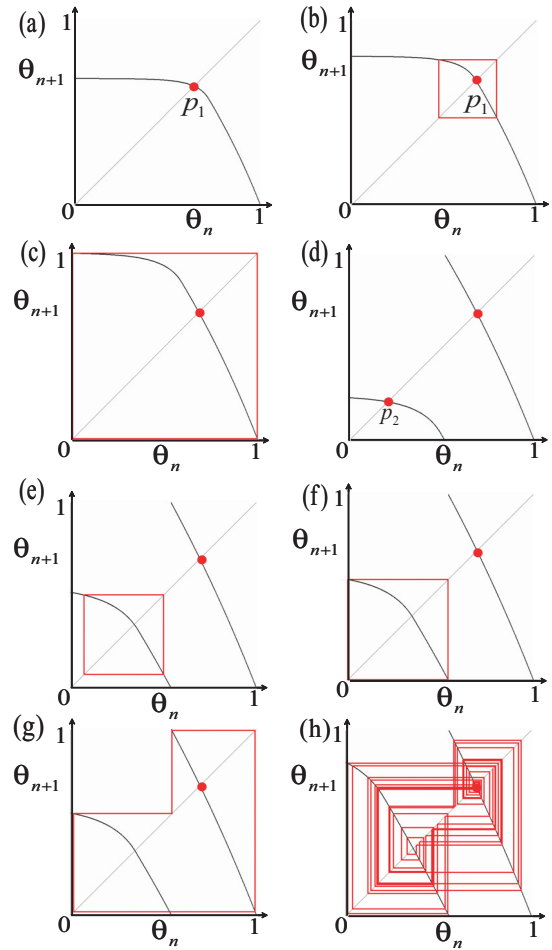


Fig. 5. Typical phase maps for $\alpha = 0.5$, $\beta = 9.0$, $q = 1.6$ and $X_- = 0.7$. (a) Stable fixed point p_1 for $\gamma = 1$, (b) Unstable fixed point p_1 and stable 2-periodic points for $\gamma = 0.85$, (c) 2-periodic points near the first border collision bifurcation set B_1 for $\gamma = 0.6825$, (d) Stable fixed point p_2 for $\gamma = 0.55$, (e) Stable 2-periodic points for $\gamma = 0.44$, (f) Stable 2-periodic points near the second border collision bifurcation set B_2 for $\gamma = 0.4315105$, (g) Stable 3-periodic points for $\gamma = 0.4292$, (h) Chaos for $\gamma = 0.35$.

second stable fixed point p_2 (Fig. 5 (d)) through a border collision bifurcation [2]. The p_2 corresponds to the SPO with period 2 in Fig. 3 (d). Note that the p_2 can not be stable in the PWL phase map of dc-dc converters [12]. At this bifurcation, in the map (Fig. 5 (c)), 0 becomes the 2-periodic point; and in the time domain, the state-dependent switching at threshold X_- collides with the period-2 time-dependent switching at time $\tau = n$, e.g., $x(3 - \epsilon) = X_-$, $x(3) = X_- + \epsilon$, $x(3 + \epsilon) = X_-$ and $\epsilon \rightarrow 0$ in Fig. 3 (c). This is a kind of border-collision bifurcation [2] because the points $(\tau, x) = (2m, X_-)$ are tips of the control signal and the orbit grazes the tips. This first border collision bifurcation set is given by $B_1 = \{\vec{p} \mid F(0) = 2\}$. Then p_2

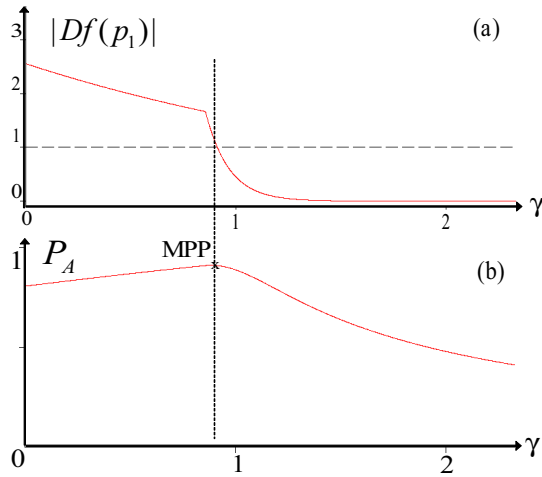


Fig. 6. Stability and the maximum power point for $\alpha = 0.5$, $\beta = 9.0$, $q = 1.6$ and $X_- = 0.7$. (a) Slope magnitude at the fixed point. (b) Average power of the SPO and UPO

becomes unstable and stable 2-periodic points (Fig. 5 (e)) appear through the second period-doubling bifurcation set $D_2 = \{\vec{p} \mid Df(p_2) = -1\}$. After that, the 2-periodic points are changed into stable 3-periodic points (Figs. 5 (g) and 3 (g)) through the second border collision bifurcation set $B_2 = \{\vec{p} \mid 2 < F(0) < 3, F^2(0) = 4\}$. At the B_2 , the state-dependent switching collides with the period-4 time-dependent switching (Figs. 5 (f) and 3 (f)). Note that the second period-doubling is impossible the PWL phase map of dc-dc converters [12] because the p_2 can not be stable. After that the 3-periodic points are changed into various periodic points and into chaos (Figs. 5 (h) and 3 (h)). Using the explicit formula of the map, the bifurcation sets can be calculated precisely. Fig. 7 shows a bifurcation diagram.

IV. CONCLUSIONS

The SDS based on the boost converter with a solar cell input has been studied in this paper. Applying the PWL modeling for the solar cell, we have derived the phase map and have analyzed the basic bifurcation phenomena precisely. Future problems are many, including the following: analysis of the power characteristics, classification and evaluation of various switching rules, and design of practical circuits.

REFERENCES

- [1] S. Banerjee and G. C. Verghese, eds., *Nonlinear Phenomena in Power Electronics: Attractors, Bifurcations, Chaos, and Nonlinear Control*, IEEE Press, 2001.
- [2] C. K. Tse and M. di Bernardo, Complex behavior in switching power converters, *Proc. IEEE*, 90, pp. 768-781, 2002.

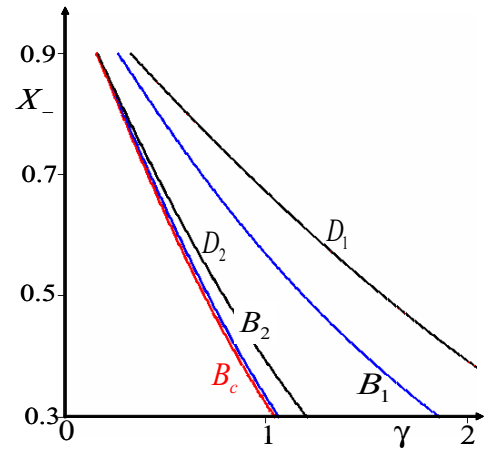


Fig. 7. Bifurcation diagram for $\alpha = 0.5$, $\beta = 9.0$ and $q = 1.6$. D_1 and D_2 : the first and second period doubling bifurcation sets. B_1 and B_2 : the first and second border collision bifurcation sets. B_c : the border to chaos on which Lyapunov exponent is zero.

- [3] S. Banerjee, S. Parui, and A. Gupta, Dynamical Effects of Missed Switching in Current-Mode Controlled dc-dc Converters, *IEEE Trans. Circuits Syst. II*, 51, 12, pp. 649-654, 2004.
- [4] S. Maity, D. Tripathy, T. K. Bhattacharya and S. Banerjee, Bifurcation Analysis of PWM-1 Voltage-Mode-Controlled Buck Converter Using the Exact Discrete Model, *IEEE Trans. Circuits Syst. I*, 54, 5, pp. 1120-1130, 2007.
- [5] Y. H. Lim and D. C. Hamill, Chaos in spacecraft power systems. *Electron. Lett.* 35, 9, pp. 510-511, 1999.
- [6] J. H. B. Deane, P. Ashwin, D. C. Hamill and D. J. Jeffries, Calculation of the periodic spectral components in a chaotic dc-dc converter, *IEEE Trans. Circuits Syst. I*, 46, 11, pp. 1313-1319, 1999.
- [7] P. Maffezzoni and Dario D' Amore, Compact Electrothermal Macromodeling of Photovoltaic Modules, *IEEE Trans. Circuits Syst. II*, 56, 2, pp. 2009.
- [8] H. S.-H. Chung, K. K. Tse, S. Y. Ron Hui, C. M. Mok and M. T. Ho, A Novel Maximum Power Point Tracking Technique for Solar Panels Using a SEPIC or Cuk Converter, *IEEE Trans. Power Electron.*, 18, 3, pp. 717-724, 2003.
- [9] N. Femia, G. Lisi, G. Petrone, G. Spagnuolo and M. Vitelli, Distributed Maximum Power Point Tracking of Photovoltaic Arrays: Novel Approach and System Analysis, *IEEE Trans. Ind. Electron.*, 55, 7, pp. 2610-2621, 2008.
- [10] N. D. Benavides and P. L. Chapman, Modeling the Effect of Voltage Ripple on the Power Output of Photovoltaic Modules. *IEEE Trans. Ind. Electron.*, 55, 7, pp. 2638-2643, 2008.
- [11] D. Sera, R. Teodorescu, J. Hantschel and M. Knoll, Optimized Maximum Power Point Tracker for Fast-Changing Environmental Conditions, *IEEE Trans. Ind. Electron.*, 55, 7, pp. 2629-2637, 2008.
- [12] T. Saito, T. Kabe, Y. Ishikawa, Y. Matsuoka and H. Torikai, Piecewise constant switched dynamical systems in power electronics, *Int'l J. of Bifurcation and Chaos*, 17, 10, pp. 3373-3386, 2007.
- [13] D. Kimura and T. Saito, A Simple Switched Dynamical System based on Photovoltaic Systems, *Proc. of NOLTA*, pp. 487-490, 2009.

Self-Generation of Chaotic Dissipative Soliton Trains in Active Ring Resonators with Ferromagnetic Films

Sergey V. Grishin and Yurii P. Sharaevskii

Faculty of Nonlinear Processes,

Saratov State University,

410012 Astrakhanskaya 83, Saratov, Russia

Email: grishfam@sgu.ru

Abstract—For the first time the passive synchronization of spin-wave self-modulation frequencies with the help of magnetostatic wave signal-to-noise enhancer which was placed in active ring resonator is carried out. Appearance of passive synchronization causes the self-generation of repetition chaotic dissipative soliton trains. The ability to control a soliton-repetition interval by the change of ring gain is shown.

I. INTRODUCTION

It's well known, that in nonlinear dispersive mediums the solitary waves or solitons can be propagated [1]. In the microwave (MW) frequency range such medium is ferromagnetic thin film in which the modulation instability of magnetostatic waves (MSW) is observed, and the envelope soliton trains are formed. In recent years the active ring resonators are used for compensation of MSW linear losses. In this case the joint use of the modulation instability, frequency filtering and mod synchronization causes the self-generation as bright and dark MW magnetic envelope soliton trains in the active ring resonators [2, 3]. The spectra of such signals are line and their spectral components are corresponded to the mod frequencies. Such localized structures generated in the systems with the gain and losses are called the *dissipative solitons* [4]. The principal difference between the dissipative and Schrödinger solitons is a generation of first ones even in the case when a wave propagated through nonlinear dispersive medium is stable [5].

The signal that has a line spectrum can be formed in a one mode generation regime because of the presence of three magnon (3M) decay processes of MSW in a ferromagnetic film. These processes cause the self-modulation of MSW signal generation by the spin waves [5, 6]. In this case the relaxation oscillations are observed in a time domain. The increase of a ring gain stipulates the stochastization

of MW signal spectrum and the break of repetition pulse trains. However the recent experiments showed that the usage of a passive or active resonator in active ring with ferromagnetic film causes the generation of repetition chaotic MW pulse trains [5, 7]. The spectrum of such signal is continuous, the envelope has the quasiperiodic law of change with the spin wave self-modulation frequency and a MW signal is chaotic. The self-generation of repetition chaotic MW pulse trains is connected with the self-synchronization of spin wave self-modulation frequencies, for example, on a weak nonlinearity of a power amplifier.

The goal of this report is an experimental research of a passive synchronization of spin wave self-modulation frequencies with the help of a nonlinear passive element that has a back dynamic characteristic. The nonlinear elements with such response are used in optics for the passive harmonic synchronization of ring modes and generation of ultra-short pulses [4]. In the MW frequency range of such element is a nonlinear MSW transmission line which was called the MSW signal-to-noise enhancer [8].

II. EXPERIMENTAL SETUP

The active ring resonator (see fig. 1) consists of two GaAs power amplifiers 1, 7 and a feedback circuit including a volume resonator 2, two variable attenuators 4, 8, nonlinear magnetostatic surface wave (MSSW) delay line 6 and MSSW signal-to-noise enhancer 10. Each power amplifier has a gain coefficient $K \sim 32$ dB in the frequency band 2-4 GHz. The usage of two power amplifiers in the active ring is necessary for ensuring the MW signal power level higher than the threshold of 3M decay processes at the input of each nonlinear transmission line. The MSSW delay line has two short-circuit microstrip lines with

the width of $w_1 = 70 \mu\text{m}$. The distance between microstrip lines is $d = 3 \text{ mm}$. The yttrium iron garnet (YIG) film is placed under microstrip lines. The MSSW signal-to-noise enhancer consists of a microstrip line that has the meander form with the distance between microstrip lines $l = 6 \text{ mm}$. The microstrip line has the width of $w_2 = 500 \mu\text{m}$ and YIG films are placed over it. All YIG films have the thickness of $t = 40 \mu\text{m}$, saturation magnetization of $4\pi M_0 = 1680 \text{ Gs}$ and a loss parameter of $2\Delta H = 0.69 \text{ Oe}$. The volume resonator has the resonant frequency $f_0 = 2.8 \text{ GHz}$, the losses at resonant frequency $A_0 = -1.8 \text{ dB}$, the loaded Q factor $Q_L = 560$. It's used in the active ring for ensuring the generation in the MSSW signal-to-noise enhancer frequency band. The value of the external bias magnetic field H_0 is set in such a way that 3M decay processes of MSSW are allowed. In the case of the MSSW delay line its central frequency at which the losses have a minimum value coincides with the f_0 at $H_{01} = 415 \text{ Oe}$. In the case of the MSSW signal-to-noise enhancer its central frequency at which the losses have a maximum value coincides with the f_0 at $H_{02} = 270 \text{ Oe}$.

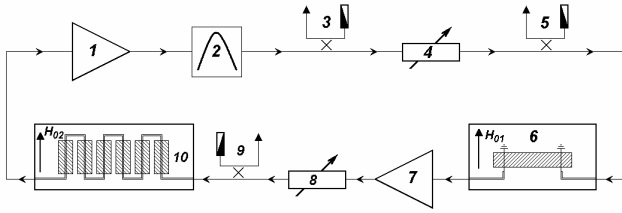


Fig. 1. Schematic diagram of the active ring resonator

The main part of power from the volume resonator output is returned into the active ring, whereas the lesser part via directional decoupler 3 is fed to the inputs of Agilent ESA-L E4408B spectrum analyzer and Agilent Infinium DSO81004B real time oscilloscope. The signal power level at the inputs of the MSSW delay line and the MSSW signal-to-noise enhancer is controlled by the two channels N1912A power meter that is connected to the active ring via directional couplers 5 and 9, respectively.

III. EXPERIMENTAL RESULTS AND DISCUSSIONS

The active ring resonator contains two nonlinear transmission lines with ferromagnetic films: the MSSW delay line and the MSSW signal-to-noise enhancer, as shown in fig. 1. The nonlinearity of both

lines is connected with the 3M decay processes that is the cause of nonlinear MSSW loss appearance. A self-generation of the nonlinear pulse trains is connected with the availability of the nonlinear MSSW delay line in an active ring resonator [5, 6]. It's well known [9], that a presence of high level nonlinear losses in a MSSW delay line stipulates the short MW pulse formation from the rectangular pulses that have a large duration. In this case a pulse front has smaller loss level than a falling edge of the pulse. Also known [10], that a transformation of the MW pulse can be stipulated by the presence of nonlinear losses in a MSSW signal-to-noise enhancer. In this case a pulse front has higher loss level than a falling edge of the pulse. Thus the joint use of a MSSW delay line and a MSSW signal-to-noise enhancer has to stipulate the formation of short MW pulses.

The dynamic response of the MSSW signal-to-noise enhancer is shown in fig. 2 (curve 1). This response has a nonlinear dependence of the output power P_{out} from the input power P_{in} . In this case a MW signal with a small power level ($P_{in} < 0 \text{ dBm}$) has a loss value $A_{sm} \approx -32 \text{ dB}$ and a MW signal with a large power level ($P_{in} > +25 \text{ dBm}$) has a loss value $A_{lg} \approx -16 \text{ dB}$. Thus the small power level spectral components of a complex signal propagating through the MSSW signal-to-noise enhancer will be suppressed stronger than the large power level spectral components. In fig. 2 the dynamic response of the MSSW delay line is also shown (curve 2). In this case a MW signal with a small power level is attenuated on a value smaller than a MW signal with a large power level. Thus the delay line has the dynamic response of a power limiter and the dynamic response of the signal-to-noise enhancer is back to it.

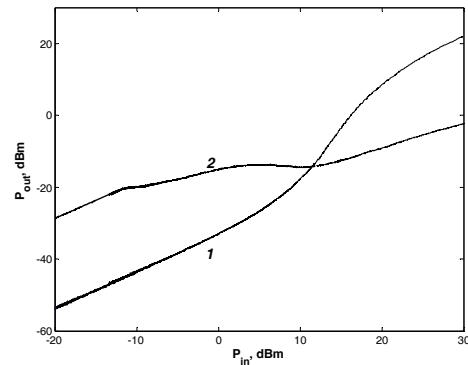


Fig. 2. The dynamics responses of the MSSW signal-to-noise enhancer and the MSSW delay line are measured at f_0

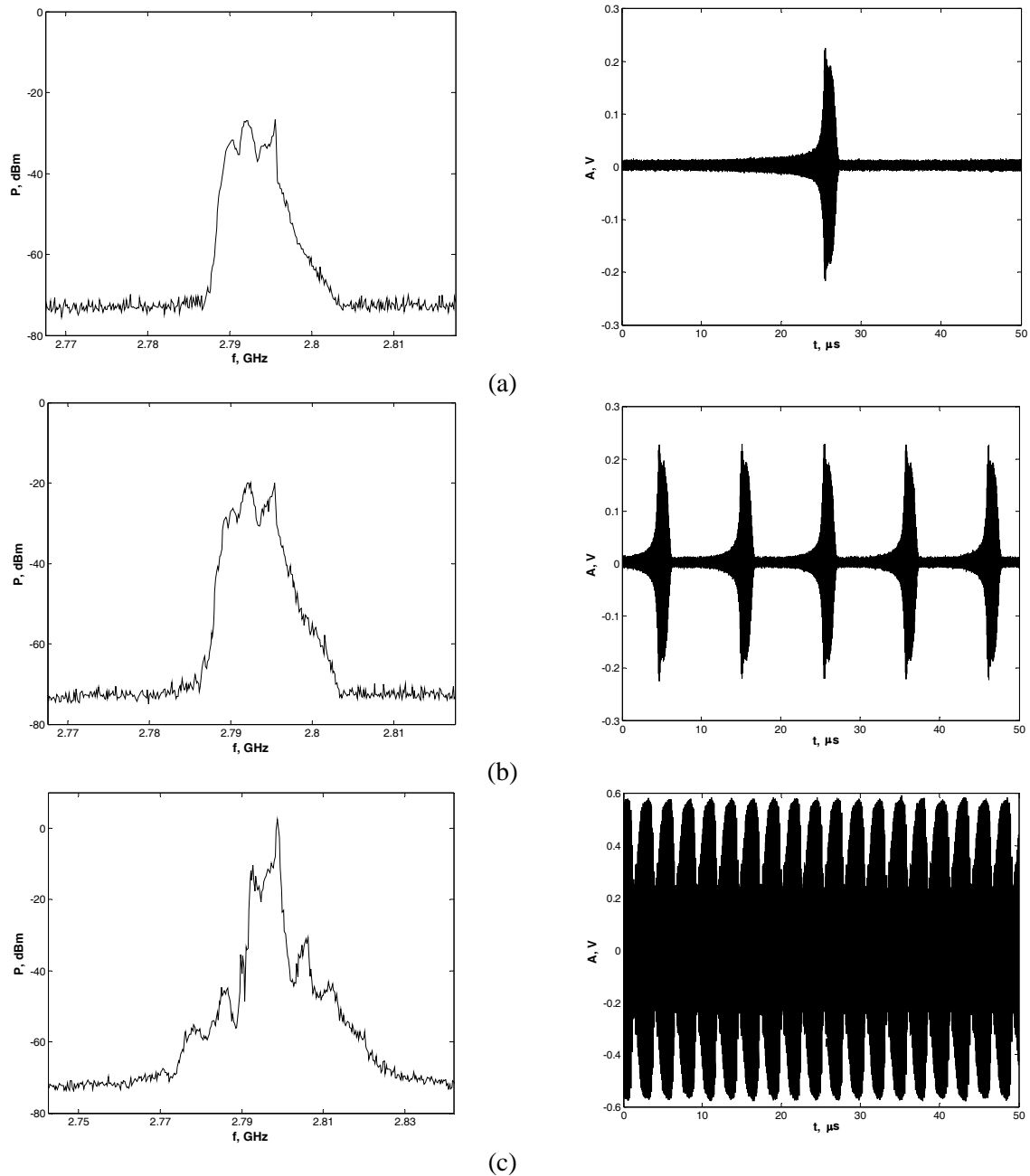


Fig. 3. (Left) Power spectra and (right) time domains of the microwave signal generated in the active ring resonator at $G = 0$ (a), $G = 0.55$ dB (b) and $G = 0.55$ dB, $H_{02}=0$ (c)

The most intriguing results are shown in fig. 3. These results are obtained at various values of a ring gain G . At $G=0$ (see fig. 3a) the power level of a MW signal generated in the active ring is higher than the threshold power level of the 3M decay processes. In this case the MW signal is not a monochromatic signal because the self-modulation of MSSW by the spin waves is appeared. The simultaneous presence in

the active ring the spin wave self-modulation frequencies and the MSSW signal-to-noise enhancer with the back dynamic response cause the formation in a time domain the chaotic MW pulses with the pulse-repetition interval larger than $50 \mu\text{s}$. In this case the spin wave self-modulation frequency has the value below 20 kHz. The further increase of a ring gain stipulates the increase of the integral power level of

the chaotic MW signal at the inputs of the MSSW signal-to-noise enhancer and the MSSW delay line. As shown in fig. 3b, the spin wave self-modulation frequency is increased, and the pulse-repetition interval is decreased with the increase of G . In a time domain the periodic dissipative soliton train is observed. The envelope of such nonlinear pulses has the periodic law of change with the spin wave self-modulation frequency, and the MW signal is chaotic. The soliton duration measured at the half-level of instantaneous amplitude is equal to $\tau_d = 1.3 \mu\text{s}$. This value is larger than a pulse-repetition interval $T_r = 10.4 \mu\text{s}$ on the order of magnitude. As shown in fig. 3a,b the spin wave self-modulation frequency tends to zero (a pulse-repetition interval tends to infinity) with the decrease of G in the active ring resonator with the MSSW signal-to-noise enhancer. In this case the spectrum of a chaotic MW signal tends to the spectrum of a single MW pulse.

The further ring gain increase causes the decrease of pulse-repetition interval and the increase of the spin wave self-modulation frequency. However, as the spectrum width of the chaotic MW signal is larger than the effective frequency band of the MSSW signal-to-noise enhancer the dissipative soliton train is broken.

The appearance of the periodic law of the envelope change is connected with the phase synchronization of the spin wave self-modulation frequencies of the chaotic MW signal. Such synchronization is set through the suppression of the small power level spectral components by the MSSW signal-to-noise enhancer. "The narrowing" of the chaotic MW signal spectrum is well observed from the comparison of the results obtained at the presence (see fig. 3b) and the absence (see fig. 3c) of the external magnetic field of the MSSW signal-to-noise enhancer. The absence of H_0 causes the absence excitation of MSSW in a ferromagnetic film and the absence of the 3M decay processes of MSSW. In this case the signal-to-noise enhancer has not the back dynamic response. The chaotic MW signal spectrum at $H_0 = 0$ (see fig. 3c) is wider than the spectrum obtained at $H_0 \neq 0$ (see fig. 3b) and the periodic dissipative soliton train at $H_0 = 0$ is disappeared.

IV. CONCLUSION

The further research of the passive synchronization of the spin wave self-modulation frequencies in the

active ring resonators with ferromagnetic films should be directed on the study of the ultra-short pulse generation. Such research can be implemented with the help of wideband frequency-selective elements and of the nonlinear MSW transmission lines on the basis of two coupled ferromagnetic films [11].

ACKNOWLEDGMENT

This work was supported by the Russian Foundation of Basic Research (grant # 08-02-00102) and the Federal Agency of Education of the Russian Federation (project # 2.1.1/235).

REFERENCES

- [1] Yuri S. Kivshar and Govind P. Agrawal, *Optical Solitons. From Fibers to Photonic Crystals*. San Diego: Academic Press, 2003.
- [2] B. A. Kalinikos, M. M. Scott, and C. E. Patton, "Self-generation of fundamental dark solitons in magnetic films," *Phys. Rev. Lett.*, vol. 84, no. 20, pp. 4697-4700, May 2000.
- [3] M. M. Scott, B. A. Kalinikos, and C. E. Patton, "Self-generation of bright microwave magnetic envelope soliton trains in ferrite films through frequency filtering," *Appl. Phys. Lett.*, vol. 78, no. 7, pp. 970-972, February 2001.
- [4] N. Akhmediev and A. Ankiewicz (Eds), *Dissipative Solitons*. Berlin: Springer-Verlag, 2005.
- [5] E. N. Beginin, S. V. Grishin, and Yu. P. Sharaevsky, "Generation of a stationary train of chaotic soliton-like microwave pulses in self-oscillating ring systems with a ferromagnetic thin film," *JETP Lett.*, vol. 88, no. 10, pp. 647-650, January 2008.
- [6] V. E. Demidov and N. G. Kovshikov, "Stochastic generation accompanying parametric excitation of spin waves in yttrium iron garnet films," *Tech. Phys. Lett.*, vol. 24, no. 4, pp. 274-276, April 1998.
- [7] S. V. Grishin, B. S. Dmitriev, Yu. D. Zharkov, V. N. Skorokhodov, and Yu. P. Sharaevsky, "Generation of chaotic microwave pulses in a ring system based on a klystron power amplifier and a nonlinear delay line on magnetostatic waves," *Tech. Phys. Lett.*, vol. 36, no. 1, pp. 76-79, January 2010.
- [8] J.D. Adam and S.N. Stitzer, "A Magnetostatic Wave Signal-to-Noise Enhancer," *Appl. Phys. Lett.*, vol. 36, no. 6, pp. 485-487, March 1980.
- [9] V. T. Synogach, Yu. K. Fetisov, C. Mathieu, and C. E. Patton, "Ultrashort microwave pulses generated due to three magnon interactions," *Phys. Rev. Lett.*, vol. 85, no. 10, pp. 2184-2187, September 2000.
- [10] T. Nomoto and Y. Matsushita, "A signal-to-noise enhancer using two MSSW filters and its application to noise reduction in DBS reception," *IEEE Trans. Microwave Theory & Tech.*, vol. 41, no. 8, pp. 1316-1322, August 1993.
- [11] E. N. Beginin, S. V. Grishin, M. A. Morozova, and Yu. P. Sharaevskii, "Wideband chaotic microwave signal generation in a ring system with a nonlinear delay line on coupled ferromagnetic films," *Tech. Phys. Lett.*, vol. 35, no. 9, pp. 853-856, September 2009.

Pages 222 to 225 have been removed due to a canceled paper.

Exponential Transient Oscillations and Their Stabilization in a Bistable Ring of Unidirectionally Coupled Maps

Yo Horikawa and Hiroyuki Kitajima

Faculty of Engineering,
Kagawa University,
2217 Hayashi-cho, Takamatsu, Japan
Email: horikawa@eng.kagawa-u.ac.jp

Abstract— We study properties of traveling waves and oscillations in a bistable ring of unidirectionally coupled maps. A kinematical model of the traveling waves shows that the duration of transient oscillations increases exponentially with the number of elements when coupling is weak. The probability density function of the duration of oscillations generated under random initial conditions has a power law form. Further, oscillations are stabilized through period doubling bifurcations as the strength of coupling increases.

I. INTRODUCTION

In some spatially extended systems, it has been shown that the duration of transient states increases exponentially as system size increases (exponential transients). It was first found in a bistable reaction-diffusion equation, in which the motion of transient kinks (fronts) and kink-antikink pairs (pulses) is exponentially small with domain length and pulse width so that these patterns last exponentially long time until the media reach one of spatially homogeneous steady states [1]. It has also been found in spatiotemporal chaos in a coupled map lattice [2] and a reaction-diffusion model [3], transient cycles in an asymmetric neural network [4], irregular firings in a network of pulse-coupled neurons [5] and transient sequences in a continuous-time Hopfield network [6]. In these systems with exponential transient, systems never reach asymptotically steady states in a practical time when system size is large, and transient states can play important roles in actual systems, e.g. information processing in nervous systems.

Recently, we showed that exponential transient oscillations in a ring of unidirectionally coupled neurons (a ring neural network) and derived its kinematics [7]. Transient oscillations are pulse waves

rotating networks and difference between the speeds of two pulse fronts decreases exponentially with an interval between the fronts. Consequently, it takes exponentially long time until fronts merge and a pulse disappears so that oscillations cease. This kinematics is qualitatively the same as that of the motion of kink patterns in the above-mentioned reaction-diffusion equation [1].

In this study, we consider traveling waves and oscillations in a bistable unidirectional coupled map lattice (CML) of ring structure. It has been pointed out that long-lasting transient oscillations exist in the CML [8]. We show that the CML possess the same properties as those of a ring neural network, which are derived with the same kinematical equation [7]. The duration of pulse waves increases exponentially with pulse width. The distribution of the duration of oscillations occurring from random initial states has a power law tail up to a cut-off, and the mean duration of the oscillations increases exponentially with the total number of elements. Further, oscillations are stabilized as coupling strength increases, in which stable sequences of period two are generated from stable steady states through period doubling bifurcations. This mechanism is similar to that of a ring neural network with inertia [9].

II. A MODEL AND ITS KINEMATICS

We consider the following ring of unidirectionally coupled maps.

$$x_n(t+1) = x_n(t)(1 - x_n^2(t)) + cx_{n-1}(t) \quad (1)$$

$$(1 \leq n \leq N, x_0 = x_N)$$

where t is a discrete time, x_n is the state of the n th

element, $N (\geq 3)$ is the number of elements and $c (> 0)$ is coupling strength. The map is cubic, the elements are linearly connected and the CML is bistable ($x_n = \pm c^{1/2}$, $1 \leq n \leq N$). Until reaching one of the stable steady states, the CML shows transient oscillations, which are traveling waves rotating in the ring.

Figure 1 shows examples of transient oscillations obtained with computer simulation of Eq. (1) with $c = 0.2$ and $N = 20$. Values of initial states ($x_n(0)$) were randomly drawn from Gaussian white noise with mean zero and SD 0.1 ($N(0, 0.1^2)$). The states $x_1(t)$ of the first element are plotted in upper panels, and spatiotemporal patterns in the states of the elements are plotted in lower panels, in which black and white regions correspond to the states of positive and negative signs, respectively. The CML is divided into two blocks in a short time, the fronts (boundaries) of which propagate in the direction of coupling (from bottom to top in the lower panel), which is a traveling relaxational pulse wave (the upper panel). The states of the elements change their signs when pulse fronts pass so that the CML oscillates. Transient oscillations may cease quickly (a) or last a long time (b) depending on initial states.

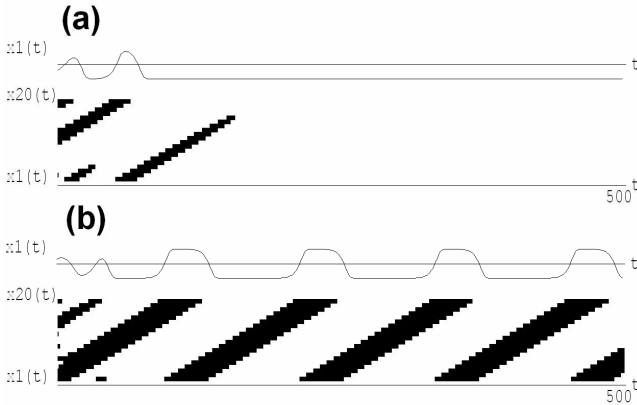


Fig. 1. Examples of transient oscillations in a CML

It is expected that the propagation of pulse waves is described by the same kinematical equation of that in a ring neural network [7]. First, a symmetric pulse wave (a periodic solution of Eq. (1)) of equal pulse width exists. Although it is unstable, it is obtained with computer simulation of Eq. (1) under a symmetric initial condition

$$x_n = c^{1/2} \quad (1 \leq n \leq l_0), \quad x_n = -c^{1/2} \quad (l_0 \leq n \leq N) \quad (2)$$

where $l_0 = l_h \equiv N/2$ for even N . Figure 2 shows the propagation time Δt of a pulse front per element, i.e. the time required for the propagation over one unit

distance (one element) with $c = 0.2$ in Eq. (1). Plotted are a logarithm of $\Delta t(l_h) - \Delta t_\infty$ ($\Delta t_\infty = \Delta t(l_h = 12)$) as a function of pulse width $l_h (= N/2)$ (the number of elements in one pulse), which is approximated as

$$\Delta t(l_h) = \Delta t_\infty + b \exp(-a l_h) \quad (l_h = N/2) \quad (3)$$

where $a \approx 1.515$, $b \approx 28.277$, $\Delta t_\infty \approx 5.952$. The speed of a pulse front depends on the exponential of pulse width. Using $1/\Delta t(l)$ as the speed of a front with the *backward* pulse width l , we obtain a kinematical equation for a change in pulse width l

$$\begin{aligned} dl/dt &= -\beta \{ \exp(-a l) - \exp[-a(N-l)] \} \\ a &= a \approx 1.515, \quad \beta = b / \Delta t_\infty^2 \approx 0.798 \end{aligned} \quad (4)$$

It should be noted that the speed of a front depends on the forward pulse width in a ring neural network. Linearization of Eq. (4) can show that a symmetric pulse wave ($l = N/2$) is unstable, while it is stable in the subspace: $x_{n+N/2} = x_n$ ($1 \leq n \leq N/2$).

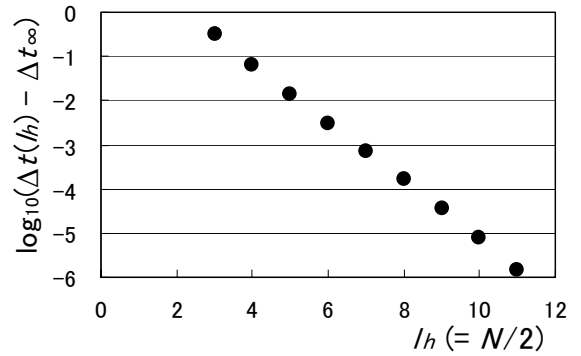


Fig. 2. Propagation time of a pulse front

III. PROPERTIES OF TRANSIENT OSCILLATIONS

First, we consider the duration T of transient oscillations in asymmetric pulse waves, which are generated under the initial condition Eq. (2) with $1 \leq l_0 < N/2$. Equation (4) can be solved and the duration T of transient oscillations (pulse waves) is obtained by $l(T) = 0$ with $l(0) = l_0$ [7]. Since it is rather redundant, we use the equation with $N \rightarrow \infty$ and obtain

$$\begin{aligned} dl/dt &= -\beta \exp(-a l) \\ l(t) &= 1/\alpha \cdot \log[\exp(a l_0) - \alpha \beta t] \quad (l(0) = l_0 < N/2) \\ T(l_0) &= [\exp(a l_0) - 1]/(\alpha \beta) \quad (l(T) = 0) \end{aligned} \quad (5)$$

It can be shown that the duration T in Eq. (5) agrees with that obtained with Eq. (4) for $N \geq 10$. Figure 3 shows a semi-log plot of the duration T of oscillations against initial pulse width l_0 with $c = 0.2$ and $N = 21$. Plotted are the results of computer simulation of Eq. (1) (closed circles) and $T(l_0)$ in Eq. (5) (a solid line). The duration increases exponentially with l_0 , and Eq. (5) agrees with the simulation results.

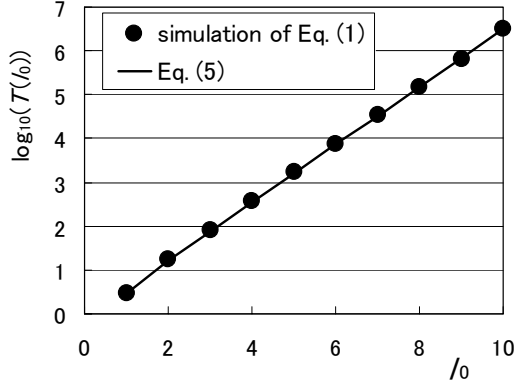


Fig. 3. Duration of transient oscillations with l_0

Next, we consider oscillations generated under random initial conditions. Since random initial states quickly turn into pulse waves as Fig. 1, we can consider initial pulse width l_0 to be distributed uniformly in $(0, N/2)$. The probability density function $h(T)$ of the duration of oscillations is derived with Eq. (5) as

$$\int_0^{l_0} U(0, N/2) dl'_0 = \int_0^T h(T') dT' \quad (6)$$

$$h(T) = \frac{\beta}{\alpha\beta T + 1} \cdot \frac{2}{N} \quad (0 < T < T(N/2))$$

The duration is distributed in a power law form ($\sim 1/T$) up to a cut-off $T(N/2)$, which is given by Eq. (5). It can be shown that the duration is distributed exponentially over the cut-off by using Eq. (4).

Figure 4 shows a log-log plot of the probability density function of the duration, in which a histogram obtained with 10^4 runs of computer simulation of Eq. (1) with $c = 0.2$ and $N = 20$ under random initial conditions: $x_n(0) \sim N(0, 0.1^2)$ (closed circles) and $h(T)$ in Eq. (6) (a solid line) are plotted. They agree with each other in $(10, T(N/2))$, where $T(N/2) \approx 3 \times 10^6$.

The mean and variance of the duration of oscillations occurring from random initial states also increase exponentially with the number of elements. Using Eq. (6), they are given by

$$m(T) = 2[\exp(\alpha N/2) - 1 - \alpha N/2]/(\alpha^2 \beta N)$$

$$\sigma^2(T) = [\exp(\alpha N) - 4\exp(\alpha N/2) + 3 + \alpha N]/(\alpha^3 \beta^2 N) - m(T)^2 \quad (7)$$

$$CV(T) = \sigma(T)/m(T) \approx (\alpha N)^{1/2}/2$$

The coefficient of variation (CV) increases in proportion to the square root of the number of elements. Figure 5 shows the mean duration of oscillations, in which estimates with 10^4 runs of computer simulation of Eq. (1) with $c = 0.2$ and $x_n(0) \sim N(0, 0.1^2)$ (closed circles) and $m(T)$ in Eq. (7) (a solid line) are plotted. Both agree with each other though the simulation results are slightly larger than Eq. (7).

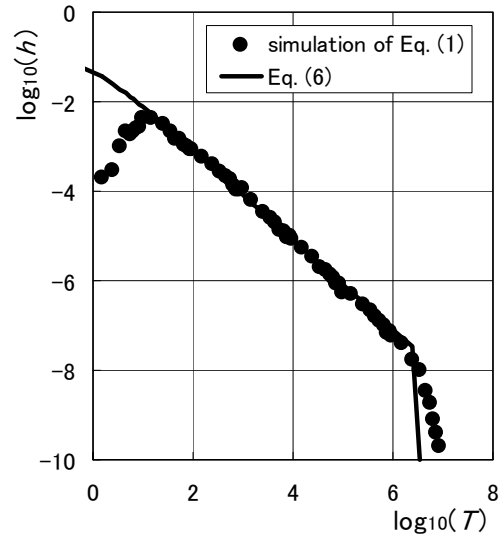


Fig. 4. Histogram of the duration of oscillations

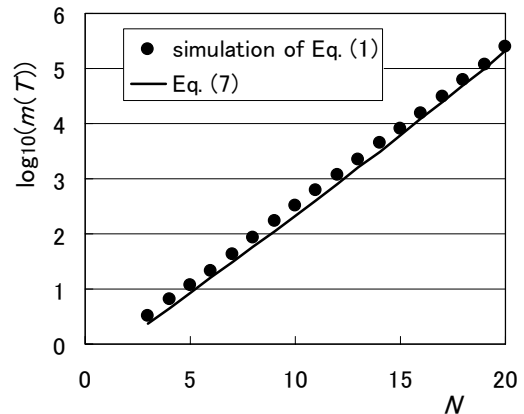


Fig. 5. Mean duration of oscillations

IV. STABILIZATION OF OSCILLATIONS

The exponential dependence of the speed of a pulse front on pulse width comes from the monotonic linear relaxation of x_n to the steady states $\pm c^{1/2}$ occurring alternately in oscillations. It has then been shown that oscillations are stabilized in the presence of inertia, in which changes of x_n are described by second-order differential equations and the approach of x_n to the steady states is oscillatory [9]. It is thus expected that oscillations in the CML are also stabilized when the eigenvalues of Jacobian at the steady states become negative and the approaches to them become oscillatory. Linearizing Eq. (1) at $x_n = c^{1/2}$ leads to

$$\begin{pmatrix} y_1(t+1) \\ y_2(t+1) \\ \vdots \\ y_N(t+1) \end{pmatrix} = \begin{pmatrix} 1-3c & 0 & 0 & 0 & c \\ c & 1-3c & 0 & 0 & 0 \\ & \ddots & \ddots & \ddots & \\ 0 & 0 & 0 & c & 1-3c \end{pmatrix} \begin{pmatrix} y_1(t) \\ y_2(t) \\ \vdots \\ y_N(t) \end{pmatrix} \quad (7)$$

$$y_n(t) = x_n(t) - c^{1/2} \quad (1 \leq n \leq N)$$

$$\lambda = 1 - 3c + c \exp(j2n\pi / N) \quad ((\lambda - 1 + 3c)^N = c^N)$$

where λ is the eigenvalues of the Jacobian matrix, which lie on a circle with center $(1 - 3c, 0)$ and radius c in the complex plane. When the number N of elements is even, the smallest eigenvalue is negative ($\lambda_{\min} < 0$) for $c > 1/4$, the absolute value of it is equal to the largest eigenvalue ($|\lambda_{\min}| = \lambda_{\max}$) at $c = 1/3$, and it is less than -1 ($\lambda_{\min} < -1$) for $c > 0.5$.

In computer simulation of Eq. (1), stabilization of oscillations was observed when $c > 0.5$, in which the period doubling bifurcations of the steady states occur and stable sequences of period two are generated. Figure 6 shows stable oscillations obtained with computer simulation of Eq. (1) with $N = 20$ and $c = 0.52$ (a), $c = 0.60$ (b). Small oscillations at pulse peaks appear (a), and further increases in c cause chaotic wave forms (b).

V. DISCUSSION

It is known that exponentially long transient spatiotemporal chaos exists in the window of period three in the logistic CML [2]. We showed that another mechanism of exponential transients in the CML due to the symmetry of the bistable map. The linear relaxation to the steady states causes exponentially small differences in the speeds of

traveling waves, which makes their duration exponentially long. Effects of asymmetry in the map and spatiotemporal noise are of interest as shown in a ring neural network [10].

Although the properties of transient oscillations were well explained with the kinematical equation of traveling waves, the values of parameters (α, β) were obtained only experimentally. The direct derivation of them from dynamics of Eq. (1) has not been done and is future work.

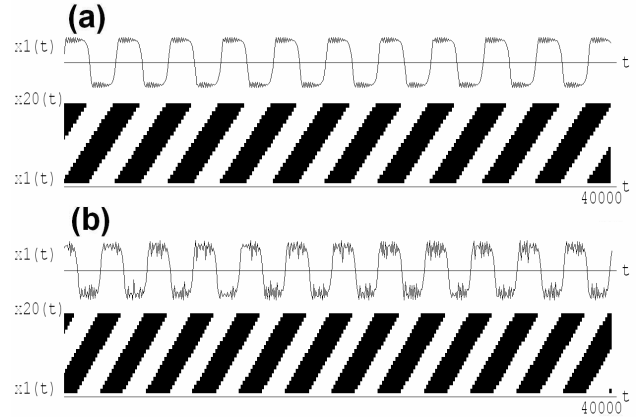


Fig. 6. Stable oscillations with $c = 0.52$ (a), $c = 0.60$

REFERENCES

- [1] K. Kawasaki and T. Ohta, "Kink dynamics in one-dimensional nonlinear systems," *Physica* 116A, pp. 573-593, 1982.
- [2] K. Kaneko, "Supertransients, spatiotemporal intermittency and stability of fully developed spatiotemporal chaos," *Phys. Lett. A*, 149, pp. 105-112, 1990.
- [3] A. Wacker, S. Bose and E. Schöll, "Transient spatiotemporal chaos in a reaction-diffusion model," *Europhys. Lett.*, 31, pp. 257-262, 1995.
- [4] U. Bastolla and G. Parisi, "Relaxation, closing probabilities and transition from oscillatory to chaotic attractors in asymmetric neural networks," *J. Phys. A*, 31, pp. 4583-4602, 1998.
- [5] R. Zillmer, et al., "Desynchronized stable states in diluted neural networks," *Neurocomputing*, 70, pp. 1960-1965, 2007.
- [6] J. Šima and P. Orponen, "Exponential transients in continuous-time Liapunov systems," *Theoret. Comput. Sci.*, 306, pp. 353-372, 2003.
- [7] Y. Horikawa and H. Kitajima, "Duration of transient oscillations in ring networks of unidirectionally coupled neurons," *Physica D*, 238, pp. 216-225, 2009.
- [8] H. Kitajima and Y. Horikawa, "Oscillation in cyclic coupled systems," *Proc. 2007 Int. Symp. on Nonlinear Theory and its Applications (NOLTA 2007)*, pp. 453-456, 2007.
- [9] Y. Horikawa and H. Kitajima, "Bifurcation and stabilization of oscillations in ring neural networks with inertia," *Physica D*, 238, pp. 2409-2418, 2009.
- [10] Y. Horikawa and H. Kitajima, "Effects of noise and variations on the duration of transient oscillations in unidirectionally coupled bistable ring networks," *Phys. Rev. E*, 80, pp. 021934/1-15, 2009.

Bistability and supratransmission in a nonlinear electronic Klein-Gordon network

B. Bodo, S. Morfu[†], P. Marquié and M. Rossé

Laboratoire LE2I UMR Cnrs 5158 Aile des sciences de l'ingénieur BP 47870,
21078 Dijon Cedex.

Email:[†]smorfu@u-bourgogne.fr

Abstract—We propose an electrical transmission lattice exactly ruled by a fifth order Klein-Gordon equation. It is experimentally shown that this medium transmits energy even outside its band-pass via the supratransmission effect. Moreover, a bistable behaviour is also revealed.

I. INTRODUCTION

These past years the development of nonlinear transmission lines has allowed to experimentally investigate the propagation of nonlinear wave in various media, such as the Fitzhugh-Nagumo model [1], the Toda lattice [2] and more recently the Klein-Gordon lattice [3]. Moreover, the properties of these nonlinear circuits inherited from natural systems has allowed to design efficient signal processing tools in real hardware devices via the concept of Cellular Neural Networks [4]. For instance, propagation failure of nerve impulse has been quantified in a Fitzhugh-Nagumo electrical lattice representing a myelinated nerve fiber [5]. Promising image processing applications have been pointed out with this biological system [6]. Stochastic resonance [7], another phenomenon introduced to explain how neurons can detect weak stimuli using noise has also been reported in electronic circuits with potential applications [8], [9]. Lastly, Coherence Resonance [10]— a nonlinear effect allowing to account for the activity of neuron even in absence of stimuli - has been observed in an electronic device [12]. In summary, designing electronic circuits mimicking the behaviour of natural systems is of crucial interest to develop new processing applications. Among these natural systems, those deriving from the nonlinear Schrödinger equation, which has relevance in the field of high speed communication in optical fibers, has recently revealed the possibility to transmit energy when excited outside their bandpass by a sinusoidal driving [13]. In this paper, we report this phenomenon of supratransmission in a real electrical transmission line obeying to the fifth order Klein-Gordon equation.

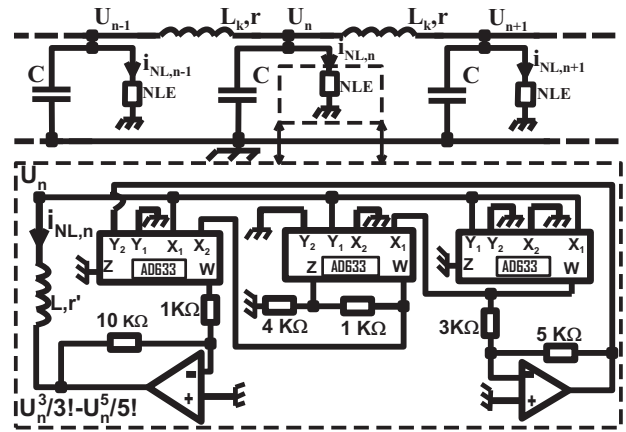


Fig. 1. The Klein-Gordon electrical lattice (Top) and the nonlinear element NLE (inside the broken lines). $C = 100nF$, $L = 0.947mH$ and $L_k = 1.1mH$. r' and r correspond to the series resistors of the self-inductors.

II. THE NONLINEAR LATTICE

A. Equation of the Network

The nonlinear electrical lattice of fig. 1 consists of $N=45$ elementary cells coupled via a lossy inductor with inductance L_k and resistor r . Each elementary cell is realized with a capacitor C in parallel with the nonlinear element NLE represented inside the inset of fig. 1. Applying Kirchoff laws at the nodes of the lattice, the voltage evolution at the n^{th} node $u_n(t)$ is ruled by the following set of differential equations:

$$C \frac{d^2 u_n}{dt^2} + \frac{rC}{L_k} \frac{du_n}{dt} + \frac{r}{L_k} i_{NL,n} + \frac{di_{NL,n}}{dt} = \frac{1}{L_k} (u_{n+1} - 2u_n + u_{n-1}), \quad (1)$$

In eq. (1), $i_{NL,n}$ represents the current through the n^{th} nonlinear element.

As shown inside the inset of fig. 1, this nonlinear circuit

includes three AD633JNZ analog multipliers and two TL081CN operational amplifiers such that the voltage u_n and the nonlinear current $i_{NL,n}$ through the self inductor obey to

$$\frac{di_{NL,n}}{dt} + \frac{r'}{L}i_{NL,n} = \frac{1}{L}f(u_n),$$

with $f(u_n) = u_n - \frac{u_n^3}{3!} + \frac{u_n^5}{5!}$. (2)

In eq. (2), r' denotes the internal resistance of the self inductor L of the nonlinear element.

If we assume that the coupling inductor L_k and the feedback inductor L of the nonlinear element have the same quality factor, then it involves the equality $r/L_k = r'/L$. Substituting eq. (2) into eq. (1) and using the previous equality, the differential equation which rules the voltage at the n^{th} node of the lattice reduces to

$$\frac{d^2u_n}{dt^2} = \frac{1}{L_k C} (u_{n+1} - 2u_n + u_{n-1}) - \frac{r}{L_k} \frac{du_n}{dt} - \frac{1}{LC} f(u_n). \quad (3)$$

Setting the transformation $c_0^2 = 1/L_k C$, $\omega_0^2 = 1/LC$ and $\Gamma = r/L_k$, eq. (3) can be normalized under the following form:

$$\frac{d^2u_n}{dt^2} - c_0^2 (u_{n+1} - 2u_n + u_{n-1}) + \Gamma \frac{du_n}{dt} + \omega_0^2 f(u_n) = 0. \quad (4)$$

According to Eq. (4), our experimental device exactly corresponds to a typical fifth order Klein-Gordon chain with dissipative coefficient Γ , coupling c_0^2 and nonlinearity weight ω_0^2 . When the nonlinearity is $f(u_n) = \sin u_n$, we note that we obtain the well known sine-Gordon equation [11].

In this paper, we focus on the case where one end of the chain (the node 0) is sinusoidally driven with an amplitude A and a frequency f . Therefore, the voltage $u_0(t)$ obeys to

$$u_0(t) = A \cos 2\pi f t. \quad (5)$$

Moreover, we set the value of the self inductors and capacitors to $C = 100nF$, $L = 0.947mH$ and $L_k = 1.1mH$.

B. Dispersion curve of the network

The experimental analysis of the dispersion curve has been carried out by setting the frequency f of the sinusoidal driving. Next, using an oscilloscope, we

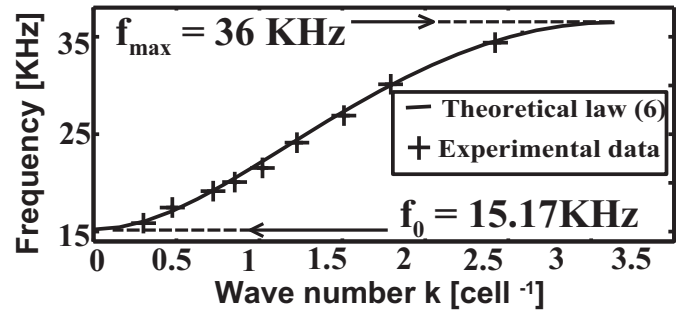


Fig. 2. Experimental and theoretical dispersion curves of the Klein-Gordon chain. The solid line is obtained with the theoretical law (6), while the crosses correspond to the experimental data. Component values: $C = 100nF$, $L = 0.947mH$ and $L_k = 1.1mH$

determine the first node n of the lattice such that the voltage at this node is in phase with the sinusoidal excitation. For the given frequency, the corresponding wave number k is then $k = 2\pi/n$. It provides the experimental data plotted with crosses in fig. 2 which reveal a typical bandpass behaviour with two cut off frequencies $f_0 = 15.17KHz$ (usually called gap) and $f_{max} = 36KHz$. For weak amplitudes of the sinusoidal driving, the linear theory allows to analytically express the dispersion relation of the electrical chain under the form

$$f = \frac{\omega_0}{2\pi} \sqrt{1 + 2 \frac{c_0^2}{\omega_0^2} (1 - \cos k)}. \quad (6)$$

In Fig. 2, the theoretical law (6) confirms the bandpass behaviour of the system since it matches with a perfect agreement the experimental data.

III. BEHAVIOUR OF THE CHAIN IN THE GAP

In this section, we focus on the effect of a sinusoidal excitation whose frequency is chosen below the gap $f_0 = 15.17KHz$. Especially, we analyze the behaviour of the electrical Klein-Gordon lattice versus the amplitude of the sinusoidal driving.

A. Weak amplitude: evanescent wave

In the case where the amplitude is weak, we have recorded in fig 3 the temporal evolution of the voltage at different nodes of the lattice, namely $n = 0$ (initial excitation), $n = 2$, $n = 4$ and $n = 6$. The amplitude of the sinusoidal excitation is very damped when it reaches the 4th node of the lattice and vanishes at the node number 6. As highlighted by Geniet and Leon, who have considered sine-Gordon lattices without dissipative coefficient (that is eq. (4) with $\Gamma = 0$ and $f(u_n) = \sin u_n$), this strong decrease of the amplitude is a specific feature when

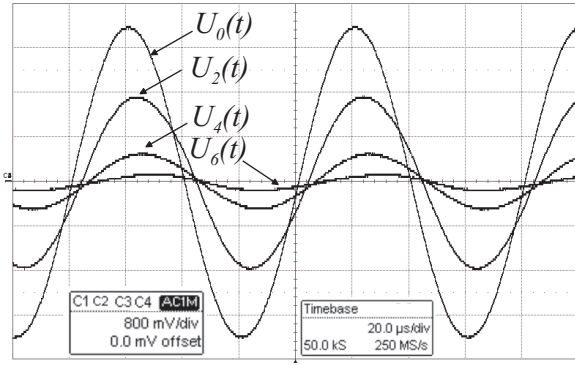


Fig. 3. Temporal evolution of the voltage $U_0(t)$, $U_2(t)$, $U_4(t)$ and $U_6(t)$. The amplitude and the frequency of the sinusoidal driving are respectively set to 2.8V and $f = 12.5\text{KHz}$.

the chain is excited in the Gap [13]. Indeed, they have shown that the decrease of this evanescent wave obeys an exponential law. To verify this exponential decrease of the amplitude, we have plotted the peak amplitude of each node of the network versus node number n in Fig. 4. These experimental data are then compared in fig. 4 to the following law:

$$\max(u_n) = A \exp(-\lambda n), \quad (7)$$

where A corresponds to the amplitude of the sinusoidal driving and $\max(u_n(t))$ represents the peak amplitude reached by the voltage $u_n(t)$. Note that, the exact values of the parameter λ and A are deduced by a least square method between the experimental data and the theoretical law (7). As shown in Fig. 4, with the identified parameters values $\lambda = 0.449 \text{ cell}^{-1}$ and $A = 2.89 \text{ V}$, the agreement between the experimental

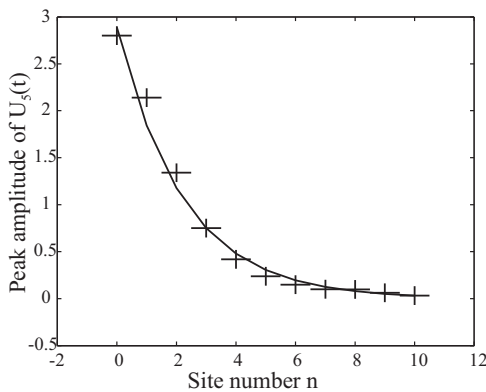


Fig. 4. Exponential decrease of the sinusoidal excitation along the network when the forcing frequency is chosen in the Gap. Crosses: experimental data, solid line: theoretical law (7) obtained with a least square method. The amplitude and the frequency of the sinusoidal driving are respectively set to 2.8V and 12.5KHz.

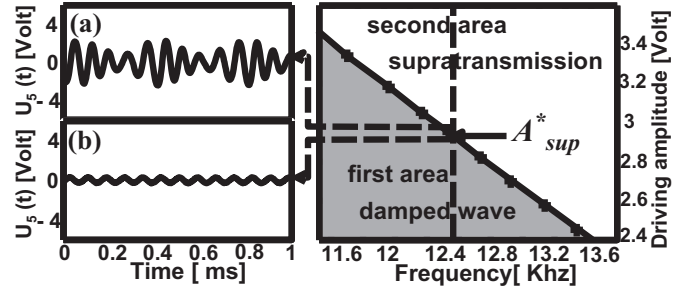


Fig. 5. Bifurcation diagram of the experimental Klein-Gordon lattice (right)- Temporal evolution of $u_5(t)$ for $f = 12.5\text{KHz}$ (left): (a) $A = 2.95 \text{ V} > A_{sup}^*$ and (b) $A = 2.93 \text{ V} < A_{sup}^*$.

data and the theoretical model is the best. Therefore, for weak amplitudes of the sinusoidal driving, our Klein-Gordon electrical lattice behaves in the gap like the sine-Gordon chain considered by Geniet and Leon [13].

B. Amplitude of the Forcing exceeding a critical value: supratransmission

We now consider the case where the amplitude of the forcing exceeds a critical value A_{sup}^* . In the case of the sine-Gordon chain without dissipation, Geniet and Leon have shown that beyond a critical amplitude of forcing the system undergoes a bifurcation and transmits energy by mean of nonlinear mode generation. We propose here to experimentally determine this critical amplitude versus the forcing frequency by observing the temporal evolution of the voltage $u_5(t)$.

As explained in the previous section, below a critical amplitude A_{sup}^* , the sinusoidal excitation is not transmitted in the medium since its amplitude vanishes. Indeed, as shown in Fig. 5.(b), the amplitude at the node $n = 5$ is very damped since we obtain 240mV when the amplitude of the driving is 2.92V and its frequency $f = 12.5\text{KHz}$.

As we increase the amplitude of the driving up to $A = 2.95\text{V}$, the voltage at this node is no more negligible. Indeed, as shown in Fig. 5.(a), the maximum amplitude of the cell number 5 reaches 2.4V instead of 240 mV. It means that when the amplitude is around 2.94V, the medium undergoes a bifurcation and transmits energy by mean of nonlinear mode generation via the effect of supratransmission [13], [14], [15].

Using this methodology, we note for each frequency the amplitude A_{sup}^* for which we obtain a transition from the very damped wave to the nonlinear wave of strong amplitude. It provides the bifurcation diagram at the right of figure 5 where the curve of the critical amplitude A_{sup}^* versus f divides the parameters plane

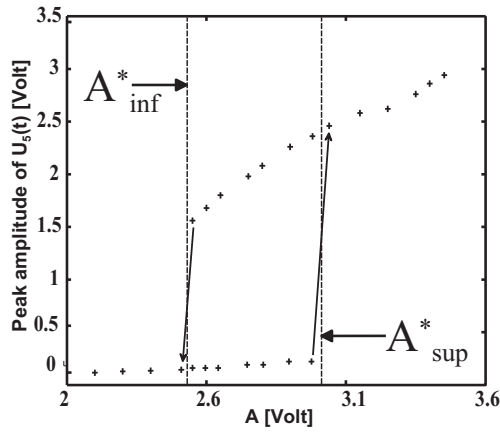


Fig. 6. Bistable behaviour of the system. The frequency of the sinusoidal driving is set to 12.5 KHz. The vertical dotted lines correspond to the two critical amplitudes A_{inf}^* and A_{sup}^* allowing the system to switch from its two states.

in two regions. The first region is located below the critical curve and corresponds to weak amplitude values of the driving which does not allow supratransmission. By contrast, the second part of the diagram provides the range of parameters (A, f) which induces a wave with a large amplitude in the medium and which enables supratransmission.

C. Bistability

Another interesting behaviour often highlighted in nonlinear media sharing this supratransmission effect is bistability [16], [17]. In fact, there exists a second critical value of the driving amplitude A_{inf}^* at which the bifurcation in the reverse direction occurs.

More precisely, starting from the region of fig. 5 which enables supratransmission, the critical amplitude of the driving A_{inf}^* allowing to come back to the first area is lower than the critical amplitude A_{sup}^* introduced in the previous section. The existence of this hysteresis property can be easily shown by plotting the peak amplitude attained by the voltage of the node number 5 versus the amplitude A of the sinusoidal excitation. This experimental curve is represented in fig 6.

It confirms that the critical amplitude A_{sup}^* of the driving for which the transition occurs between weak and strong amplitude waves is greater than the critical amplitude A_{inf}^* that induces the transition in the reverse direction.

IV. CONCLUSION

In this paper, we have presented an electronic lattice whose main advantage is to be exactly ruled by a 5th order Klein-Gordon equation. Therefore, it constitutes a

convenient tool to investigate information transmission in media deriving from the nonlinear Schrödinger equation. Especially, we have experimentally reported the possibility for this pass-band type medium to transmit energy by generating nonlinear modes when it is excited outside its bandpass. Therefore, our work could be of crucial interest in the field of information transmission to understand how the energy of these nonlinear modes can be localized to induce train of solitons [14], [15].

REFERENCES

- [1] J. Nagumo, S. Arimoto, S. Yoshisawa "An active pulse transmission line simulating nerve axon", *Proc IRE* **50**, p206170 (1962).
- [2] H. Nagashima and Y. Amagishi "Experiments on the Toda Lattice using nonlinear transmission line" *J. Phys Soc. Jpn* **45** p680-688 (1978).
- [3] B. Bodo, S. Morfu, P. Marquié and M. Rossé, "A Klein-Gordon electronic network exhibiting the supratransmission effect", *Electron. Lett.* (To appear).
- [4] L.O. Chua and L. Yang, "Cellular Neural Networks: Applications", *IEEE Tans. Circuits and Systems*, **35**, p1273-1290, (1988).
- [5] P. Marquié, J.C. Comte and S. Morfu "Analog simulation of neural information propagation using an electrical FitzHugh Nagumo lattice", *Chaos, Soliton and Fractal*, **19**, p27-30, (2004).
- [6] S. Morfu, P. Marquié, B. Nofiele, and D. Ginjac, "Nonlinear systems for image processing", *Advances in Imaging and Electron. Physics*, **152**, p79-153, (2008).
- [7] L. Gammaitoni, P. Hanggi, P. Jung, and F. Marchesoni, "Stochastic Resonance", *Rev. Mod. Phys.*, **70**, p223-282, (1998).
- [8] F. Chapeau-Blondeau and D. Rousseau, "Injecting noise to improve performance of optimal detector", *Electron. Lett.*, **43**, (16), p897-898, (2007).
- [9] S. Zozor and P.-O. Amblard, "Stochastic Resonance in Locally Optimal Detectors", *IEEE transactions on Signal Processing* **51**, p. 3177-3181, (2003).
- [10] S. Pikovsky, J. Kurths, "Coherence resonance in a noise-driven excitable system" *Phys. Rev. Lett.*, **78**, 775-778, (1997).
- [11] O.M. Braun and Y.S. Kivshar, "The frenkel-Kontorova model, concepts, methods and applications" Springer, Berlin (2004).
- [12] G. Lassere, S. Morfu and P. Marquié "Coherence resonance in Bonhoeffer-Van der Pol circuit", *Electron. Lett.*, **13**, p669-670, (2009).
- [13] F. Geniet and J. Leon, "Energy transmission in the forbidden Band Gap of a Nonlinear Chain", *Phys. Rev. Lett.*, **89**, p134102-1/4, (2002).
- [14] J.E. Macías-Díaz, A. Puri "On the transmission of binary bits in discrete Josephson-junction arrays" *Phys. Lett. A* **372**, p.5004-5010 (2008).
- [15] S. B. Yamgoué, S. Morfu and P. Marquié, "Noise effects on gap wave propagation in a nonlinear discrete LC transmission line" *Phys. Rev. E* **75**, p.036211-1/036211-7 (2007).
- [16] R. Khomeriki and J. Leon "Bistability in the sine-Gordon equation: The ideal switch" *Phys. Rev. E* **71**, p. 056620-1/ 056620-8 (2005).
- [17] J. Macías-Díaz "Bistability of a two-dimensional Klein-Gordon system as a reliable means to transmit monochromatic waves: a numerical approach" *Phys. Rev. E* **78**, p. 056603-1/ 056603-9 (2008).

Memristive effect in the model of superconductive-normal transition

Linda Ponta*, Anna Carbone*, Marco Gilli[†] and Piero Mazzetti*

*Physics Department, Politecnico di Torino,

Corso Duca degli Abruzzi 24, 10129 Torino, Italy

Email: linda.ponta@polito.it, anna.carbone@polito.it, piero.mazzetti@polito.it

[†]Electronic Engineering Department, Politecnico di Torino,

Corso Duca degli Abruzzi 24, 10129 Torino, Italy

Email: marco.gilli@polito.it

Abstract—An array of resistively and capacitively shunted Josephson junctions with nonsinusoidal current-phase relation is considered for modelling the resistive transition in high- T_c superconductors. The emergence of higher harmonics, besides the sinusoid $I_c \sin \phi$, is expected for dominant d -wave symmetry of the Cooper pairs, random distribution of potential drops and dirty grains, or in nonstationary conditions. We show that additional cosine term acts by modulating the global resistance, due to the weak-links whose transition occurs through mixed superconductive-normal states.

I. INTRODUCTION

Arrays of Josephson junctions are under intensive investigation for their potential implementation as superconductor quantum bits and ability to model several fundamental phenomena in disordered superconductive films [1], [2], [3], [4], [5], [6], [7], [8], [9], [10], [11], [12]. In particular, the resistively and capacitively shunted Josephson Junction model (RSJ model) has been adopted to describe the resistive transition in granular superconductors [13], [14], [15], [16], [17]. In the conventional RSJ model, the Josephson current is the simple sinusoid $I_S(\phi) = I_c \sin \phi$, where I_c is the critical current and $\phi = \theta_2 - \theta_1$ the phase difference of the superconductor order parameters $\Delta_1 \exp(i\theta_1)$ and $\Delta_2 \exp(i\theta_2)$ [18].

Sign and magnitude of I_c are affected by the gap function symmetry and relative orientation of the superconductor electrodes. According to the microscopic approach, the current-phase relation can be expressed as:

$$I_S(\phi) \propto \int_{-\infty}^{+\infty} [1 - 2f(E)] \text{Im}[I_E(\phi)] dE, \quad (1)$$

with $f(E)$ the electron energy distribution and $\text{Im}[I_E(\phi)]$ the spectral current, which depend on material, geometry and nonequilibrium conditions. The

current-phase relation (1) can be written as an n -order Fourier series [19], [20]:

$$I_S(\phi) = \sum_{n \geq 1} \left[\tilde{I}_n \sin(n\phi) + \tilde{J}_n \cos(n\phi) \right]. \quad (2)$$

When the sum is restricted to the 1st order, $\tilde{I}_n \sin(n\phi)$ reduces to the familiar sinusoidal Josephson current $I_c \sin \phi$. The term $\tilde{J}_n \cos(n\phi)$ is the quasi-particle-pair-interference current (QPIC). Deviations from the sinusoidal shape have been experimentally observed at temperatures below T_c because, in general, these effects are of the second order. In the vicinity of T_c , they have been theoretically predicted and observed in normal-metal weak-links, as a consequence of the depairing either by proximity effect by supercurrent or in long junctions or in far-from-equilibrium conditions [19]. A disordered polycrystalline superconductor is a nonhomogeneous system with wide variability of the physical and chemical properties of the grains. For current $I \sim I_c$ and voltage $0 < V < V_c$ in the vicinity of the transition, nonequilibrium effects arise in the weak-links making their relevant properties spatially and temporally dependent on the external drive [16], [17], [21], [22], [23], [24], [25], [26], [27]. When a polycrystalline superconductor undergoes the transition, far-from-equilibrium condition, due to the abrupt voltage drops across the grains, may result in the emergence of higher harmonics according to the local voltage values, geometry and material composition of the grains. In the presence of evolution equations which are nonlinear -such as those of Josephson Junctions- intrinsic localized modes (ILM) are obtained as solutions of sine-Gordon equations. These solutions are characterized by being time-dependent and spatially localized as opposed to translationally invariant lattices, in the absence of disorder or defects, where an

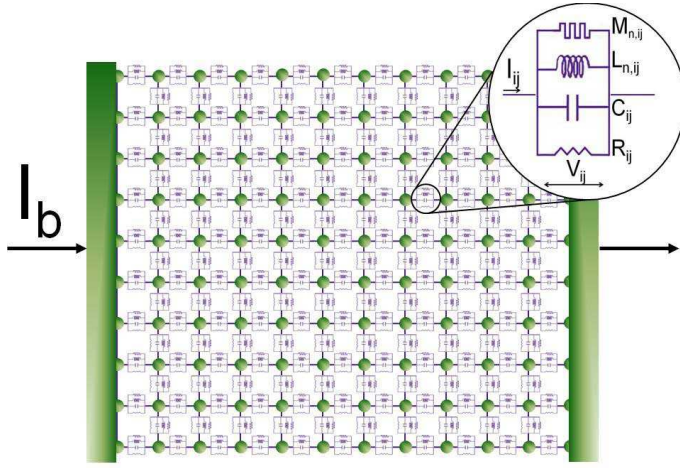


Fig. 1. Two-dimensional Josephson junction array representing a granular superconductor. Circles represent superconducting grains connected by weak-links. The bias current I_b is injected to the left electrode and collected from the right electrode. Equivalent circuit of the weak-link between the grains i and j is shown in the zoom. The linear resistor R_{ij} , the linear capacitor C_{ij} , the nonlinear inductor $L_{n,ij}$ and memristor $M_{n,ij}$ are connected in parallel. The current I_{ij} flows from grain i to grain j . V_{ij} is the voltage drop across the weak-link.

initially localized excitation distributes its energy over the entire system. Deviations from the simple sinusoidal shape in the I-V characteristics of single Josephson junctions and arrays as an effect of the formation of intrinsic localized modes have been reported in [26], [27]. The pair-interference current $\tilde{J}_n \cos(n\phi)$ emerges when the pair-symmetry is broken and it is expected to come into play when the junctions are partly dissipative. This may occur in the mixed state, i.e. in the vicinity of T_c , for current $I \sim I_c$ and voltage $0 < V < V_c$.

In this work, we put forward a model of the superconductive-resistive transition where a network of resistively and capacitively shunted nonsinusoidal Josephson junctions are considered. The network of weak-links, modeled as nonsinusoidal Josephson junctions, should be particularly relevant when the effect of nonequilibrium in the presence of disorder and nonlinearity should be taken into account in the transition of granular superconductors.

II. MODEL

A two-dimensional array of Josephson junctions is sketched in Fig. 1. The bias current I_b is injected to the left electrode and collected from the right electrode. Circles represent superconducting grains connected by weak-links. According to the RSJ model, the current I_{ij}

flowing through each junction is:

$$I_{ij} = C_{ij} \frac{dV_{ij}}{dt} + \frac{V_{ij}}{R} + I_{S,ij}(\phi_{ij}) + \delta I_{L,ij} \quad (3)$$

where C_{ij} and R_{ij} are the shunt capacitance and resistance between grains i and j , $I_{S,ij}(\phi_{ij})$ is the Josephson current, $\delta I_{L,ij}$ is the Langevin fluctuation source. The voltage drop across the junction is given by:

$$V_{ij} = V_i - V_j = \frac{\hbar}{2e} \frac{d\phi_{ij}}{dt}, \quad (4)$$

with ϕ_{ij} the phase difference of the order parameters in the grains i and j . In the usual RSJ model, $I_{S,ij}(\phi_{ij})$ is a simple sinusoid, whereas in the present work the nonsinusoidal form given by Eq. (2) is considered. Therefore, the current I_{ij} flowing through each junction connecting the grains i and j writes as:

$$I_{ij} = C_{ij} \frac{dV_{ij}}{dt} + \frac{V_{ij}}{R_{ij}} + \sum_{n \geq 1} [\tilde{I}_{n,ij} \sin(n\phi_{ij}) + \tilde{J}_{n,ij} \cos(n\phi_{ij})] + \delta I_{L,ij} \quad (5)$$

I_{ij} is given by the sum of the following contributions: the charging current through the shunt capacitance C_{ij} , the Ohmic current through the shunt resistance R_{ij} , the n Josephson current sources $\tilde{I}_{n,ij} \sin(n\phi_{ij})$ and $\tilde{J}_{n,ij} \cos(n\phi_{ij})$ and the Langevin current.

The equivalent circuit of each junction is highlighted in the circle of Fig. 1. It corresponds to a parallel connection of a linear capacitor C_{ij} , a linear resistor R_{ij} , a parallel of n inductors $L_{n,ij}$ (related to the $\tilde{I}_{n,ij} \sin(n\phi_{ij})$ terms) and a parallel of n memristors $M_{n,ij}$ related to the $\tilde{J}_{n,ij} \cos(n\phi_{ij})$ terms (we use the notation memristor after [28]). Eq. (5) can be written more compactly as:

$$I_{ij} = C_{ij} \frac{dV_{ij}}{dt} + \frac{V_{ij}}{R} + \sum_{n \geq 1} I_{c,n,ij} \sin(n\phi_{ij} + \phi_{o,n,ij}) + \delta I_{L,ij}, \quad (6)$$

with:

$$I_{c,n,ij} = \sqrt{\tilde{I}_{n,ij}^2 + \tilde{J}_{n,ij}^2} \quad (7)$$

and:

$$\phi_{o,n,ij} = \arctan\left(\frac{\tilde{J}_{n,ij}}{\tilde{I}_{n,ij}}\right) \quad (8)$$

Josephson junctions are usually classified in terms of the Stewart-McCumber parameter $\beta_c = \tau_{RC}/\tau_J$ with $\tau_{RC} = RC$ and $\tau_J = \phi_0/2\pi I_c R_o$, as overdamped ($\beta_c \ll 1$), general ($\beta_c \simeq 1$) and underdamped ($\beta_c \gg 1$).

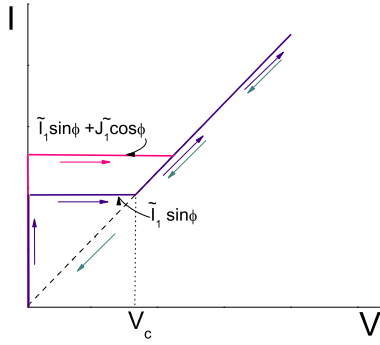


Fig. 2. Josephson junction characteristics of a weak-link with current-phase relation $I_S(\phi) = I_c \sin(\phi)$ (the blue line), $I_S(\phi) = \tilde{I}_1 \sin(\phi) + \tilde{J}_1 \cos(\phi)$ with $\tilde{I}_1 = 1\text{mA}$ and $\tilde{J}_1 = 0.5\text{mA}$ (the pink line). The generalized Stewart-McCumber parameter is $\beta_c^* = 45$.

For the nonsinusoidal junction described by Eq. (6), the generalized Stewart-McCumber parameter can be defined as $\beta_c^* = \tau_{RC}/\tau_J^*$, with $\tau_J^* = \phi_0/(2\pi \sum_n I_{c,n,ij} R_o)$. Eq. (6) can be numerically solved for an arbitrary number n of harmonics. Nonetheless, we restrict our discussion to the following case relevant to the physics of superconductors:

$$I_{S,ij}(\phi_{ij}) = \tilde{I}_{1,ij} \sin(\phi_{ij}) + \tilde{J}_{1,ij} \cos(\phi_{ij}), \quad (9)$$

The scheme of the current-voltage characteristics of an underdamped ($\beta_c^* \gg 1$) Josephson junction obtained by solving Eq.(6) is shown in Fig. 2. In particular, the blue line in Fig. 2 refers to the simple sinusoid, the pink line to $I_{S,ij}(\phi_{ij})$ given by Eq.(9). The intermediate states are characterized by voltage drops in the range $0 < V_{ij} < V_{c,ij}$ and current $I_{ij} = I_{c,n,ij}$. Upon current (voltage) decrease starting from the normal state, the behavior is always resistive, implying that the system reaches the superconductive ground state without exploring the intermediate states.

For overdamped junctions ($\beta_c^* \ll 1$), the intermediate states are characterized by voltage drop and current respectively in the range $0 < V_{ij} < 2V_{c,ij}$ and $I_{c,n,ij} < I_{ij} < I_{c,n,ij}[2V_{c,ij}]$. Upon increasing and decreasing the external drive, the current-voltage behavior is the same, hence no hysteresis is observed.

In the general case ($\beta_c^* \approx 1$), the $I - V$ curve is partly hysteretic. Upon increasing the external drive, the intermediate states are characterized by a voltage drop in the range $0 < V_{ij} < V_{c,ij}$ and current equal to $I_{c,n,ij}$. As the external drive decreases, the backward current lies slightly below the forward current. It is worthy

of remarks that with the nonsinusoidal current phase relation the capacitive effect is reduced in comparison to the simple sinusoidal case.

III. RESULTS AND DISCUSSION

As stated above, the resistive transition is modeled by using a network of weak-links, with Josephson junction characteristics given by Eq. (6). The solution of the network is obtained by a system of Kirchhoff equations that has been already used for the simple sinusoidal Josephson current characteristics in [16]. We have routinely solved the Kirchhoff equations of the networks by using the generalized RSJ model Eq. (6) with weak-links with nonsinusoidal current-phase relation given by Eq. (2) in the temperature range just below T_c . The network is biased by constant current I_b . The superconductor-insulator transition is simulated by solving the system of Kirchhoff equations at varying temperature. The critical currents $\tilde{I}_{n,ij}$ and $\tilde{J}_{n,ij}$ are assumed to vary on temperature according to the linearized equations $\tilde{I}_{n,ij} = \tilde{I}_{o,n,ij} (1 - T/T_c)$ and $\tilde{J}_{n,ij} = \tilde{J}_{o,n,ij} (1 - T/T_c)$, where $\tilde{I}_{o,n,ij}$ and $\tilde{J}_{o,n,ij}$ are the lowest temperature values of $\tilde{I}_{n,ij}$ and $\tilde{J}_{n,ij}$. Hence, the critical current $I_{c,n,ij}$ depends on temperature according to $I_{c,n,ij} = I_{c,o,n,ij} (1 - T/T_c)$, with $I_{c,o,n,ij} = \sqrt{\tilde{I}_{o,n,ij}^2 + \tilde{J}_{o,n,ij}^2}$. In order to take into account the disorder of the array, $\tilde{I}_{n,ij}$ and $\tilde{J}_{n,ij}$ are taken as random variables, distributed according to Gaussian functions with mean values $\tilde{I}_{o,n}$ and $\tilde{J}_{o,n}$ and standard deviations $\Delta\tilde{I}_{o,n} = \Delta\tilde{J}_{o,n}$.

By effect of the temperature increase and consequent reduction of the critical current, the weak-link with the lowest value of the critical current $I_{c,n,ij} = I_{c,min}$ switches to the intermediate state and, then, becomes resistive when $V_{ij} > V_c$. The resistive transition of the first weak-link has the effect to set the value of the voltage drop across the other weak-links in the same layer. The result is the formation of a layer of weak-links either in the resistive or in the intermediate state. As temperature further increases, the critical current $I_{c,n,ij}$ further decreases. More and more weak-links gradually switch from the superconductive to the intermediate state and then to the resistive state. The term $\tilde{J}_{n,ij}$ acts by increasing the critical current value of the weak-link in the intermediate state in the layers undergoing the transition. It is worthy to remark that the increase of critical current is relative to the fraction of normal electrons in the mixed states. The onset of $\tilde{J}_{n,ij} \cos(n\phi_{ij})$ is indeed triggered by the elementary resistive transition of the weak-link with the lowest critical current, since it is related to

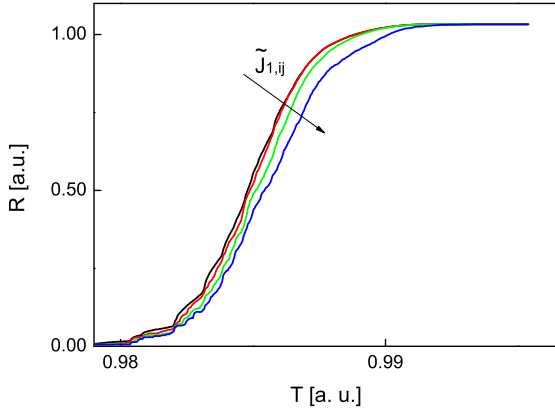


Fig. 3. Resistive transition of a two-dimensional network with current-phase relation of the form $I_{S,ij}(\phi_{ij}) = \tilde{I}_{1,ij} \sin(\phi_{ij}) + \tilde{J}_{1,ij} \cos(\phi_{ij})$. The average value of the critical current $\tilde{I}_{1,ij}$ is 1mA. The curves correspond to different average values of the critical current $\tilde{J}_{1,ij}$, namely $\tilde{J}_{1,ij} = 0\text{mA}$, $\tilde{J}_{1,ij} = 0.5\text{mA}$, $\tilde{J}_{1,ij} = 0.75\text{mA}$ and $\tilde{J}_{1,ij} = 1\text{mA}$. The normal resistance R_o is 1Ω equal for all the junctions.

the partly broken pair-symmetry of the weak-links in the intermediate state. It has no effect on the links in the superconductive state, neither on those in the fully resistive state.

Fig. 3 shows the curves of the resistive transitions obtained with current-phase relation $I_{S,ij}(\phi_{ij}) = \tilde{I}_{1,ij} \sin(\phi_{ij}) + \tilde{J}_{1,ij} \cos(\phi_{ij})$ for a two-dimensional 30×30 network. The curves correspond to different values of the term $\tilde{J}_{1,ij}$. The values of the critical currents are $\tilde{I}_{1,ij} = 1\text{mA}$ and $\tilde{J}_{1,ij}$ ranging from 0 to 1mA. The standard deviation of the critical currents is $\Delta I_{o,n} = 0.5\text{mA}$. Initially, the weak-links are in the superconductive state, thus the network resistance is negligible. As temperature increases, the weak-link with the lowest critical current switches to the intermediate state and then to the resistive state with the consequent onset of the term $\tilde{J}_{n,ij} \cos(n\phi_{ij})$ and redistribution of the currents. One can notice that the curves overlap at the beginning of the transition, whereas become more separated when $T \rightarrow T_c$, implying that the effect of the term $\tilde{J}_{n,ij} \cos(n\phi_{ij})$ is more relevant as the transition approaches its end. The amplification of the $\tilde{J}_{n,ij} \cos(n\phi_{ij})$ effect, as the resistance increases, means that $\tilde{J}_{n,ij}$ acts as modulation of the resistance. The modulation effect due to $\tilde{J}_{n,ij}$ can be noted at the level of each elementary transition step.

IV. CONCLUSIONS

The nonsinusoidal current-phase relation has been considered in the resistively shunted Josephson junction model for describing the superconductive transition. By solving a system of Kirchhoff equations for the array of nonsinusoidal Josephson junctions, it is found that additional cosine and sine terms modify the transition curves by changing resistance and Josephson coupling. The model might be relevant for Cooper pairs with d -wave dominant over s -wave symmetry.

ACKNOWLEDGMENT

We gratefully acknowledge the Istituto Superiore per le Telecomunicazioni M. Boella for financial support.

REFERENCES

- [1] J. Clarke, F. K. Wilhelm, *Nature* **453**, 1031 (2008)
- [2] C. H. Van Der Wal et al., *Science* **290**, 773 (2000)
- [3] H. Hilgenkamp et al., *Nature* **422**, 50 (2003)
- [4] L. N. Bulaevskii, A. E. Koshelev, *Phys. Rev. Lett.* **99**, 057002 (2007)
- [5] V. I. Marconi, *Phys. Rev. Lett.* **98**, 047006 (2007)
- [6] P. Orgiani et al., *Phys. Rev. Lett.* **98**, 036401 (2007)
- [7] R. Fazio, H. van der Zant, *Phys. Rep.* **355**, 235 (2001)
- [8] A. Zazunov, N. Didier, F. W. J. Hekking, *EPL* **83**, 47012 (2008)
- [9] M. V. Fistul et al., *Phys. Rev. Lett.* **100**, 086805 (2008)
- [10] G. Refael et al, *Phys. Rev. B* **75**, 014522 (2007)
- [11] Y. M. Shukrinov, F. Mahfouzi, *Phys. Rev. Lett.* **98**, 157001 (2007)
- [12] I. S. Beloborodov et al., *Rev. Mod. Phys* **79**, 469 (2007)
- [13] S. Chakravarty et al., *Phys. Rev. B* **37**, 3283 (1988)
- [14] D. C. Harris, S. T. Herbert, D. Stroud, J. C. Garland, *Phys. Rev. Lett.* **67**, 3606 (1991)
- [15] W. Yu, D. Stroud, *Phys. Rev. B* **46**, 14005 (1992)
- [16] L. Ponta, A. Carbone, M. Gilli, P. Mazzetti, *Phys. Rev. B* **79**, 134513 (2009)
- [17] A. Carbone, M. Gilli, P. Mazzetti, L. Ponta, arXiv:0912.0367
- [18] B. D. Josephson, *Phys. Lett.* **1**, 251 (1962); V. Ambegaokar, A. Baratoff, *Phys. Rev. Lett.* **10**, 486 (1963)
- [19] A. A. Golubov, M. Yu Kupriyanov, E. Il'ichev, *Rev. Mod. Phys.* **76**, 411 (2004)
- [20] Y. Tanaka, S. Kashiwaya, *Phys. Rev. B* **56**, 892 (1997)
- [21] N. Kopnin (ed) *Theory of Nonequilibrium Superconductivity*, Clarendon Press, Oxford (2001)
- [22] E. V. Bezuglyi, A. S. Vasenko, V. S. Shumeiko, G. Wendin, *Phys. Rev. B* **72**, 014501 (2005)
- [23] A. Brinkman, A. A. Golubov, H. Rogalla, F. K. Wilhelm, M. Y. Kupriyanov, *Phys. Rev. B* **68**, 224513 (2003)
- [24] N. Argaman, *Superlattices and Microstructures* **25**, 861 (1999)
- [25] D. R. Gulevich, et al., *Phys. Rev. B* **80**, 094509 (2009)
- [26] P. Binder, D. Abraimov, A. V. Ustinov, S. Flach, Y. Zolotaryuk, *Phys. Rev. Lett.* **84**, 745 (2000); R. A. Pinto, S. Flach, *EPL* **79**, 66002 (2007)
- [27] M. Schuster, F. Pignatelli, A. V. Ustinov *Phys. Rev. B* **69**, 094507 (2004)
- [28] L. O. Chua, *Proceedings of the IEEE* **91**, 1830 (2003); L. O. Chua, *IEEE Transactions on Circuit Theory* **18**, 507 (1971); D. B. Strukov, G. S. Snider, D. R. Stewart, R. S. Williams, *Nature* **453**, 80 (2008)

Studying Circuit Disturbances of MOS LC-Tank Oscillators based on Order Reduction Techniques

Jan-K. Bremer, Marco Reit, and Wolfgang Mathis
Institute of Theoretical Electrical Engineering
Leibniz University of Hannover, Germany
Email: bremer@tet.uni-hannover.de

Abstract—In this paper an order reduction technique for higher dimensional nonlinear oscillator models based on a center manifold approach is presented and its application to oscillator design will be discussed. Therefore the influences of parasitic elements and other structural extensions of the dynamical behavior of oscillators can be incorporated in oscillator modeling. Using the order reduction technique a generalized second order model will be derived where parameters of the higher order model are included. Moreover by using an Andronov-Hopf bifurcation analysis the reduced system can be studied with respect to stability as well as the oscillator amplitude and frequency. The concept is applied to the design of LC-Tank MOS voltage controlled oscillators (VCOs).

I. INTRODUCTION

Nowadays the design of LC-Tank MOS VCOs, an essential basic circuit block of GHz communication systems, is a rather difficult problem with respect to the very restrictive specifications. Therefore an oscillator design approach based on the linear circuit paradigm, modified by some nonlinear circuit aspects (see e. g. [1], [2]), becomes inefficient, since elaborate circuit simulations are needed to fit the specifications of the oscillator (see [3], [4], [5]). Therefore an alternative design approach based on a complete nonlinear circuit paradigm is needed. The behavior of nonlinear oscillators cannot be discussed using the linearization of the circuit equations since a non-hyperbolic linear system results due to the theorem of Hartman and Grobman (e.g. [6]). We find out that the well-known Barkhausen and Nyquist criteria (e.g. [7]) cannot be interpreted by means of the linear circuit paradigm. Instead it is used to fit the condition of a non-hyperbolic system (see Mandelstam et al. [8] and Mathis [3]). As a conclusion we have to emphasize that nonlinear oscillator models are not only useful for a more precise oscillator modeling and design, but also for a better understanding of the behaviour of oscillators. However, nonlinear oscillator models provide

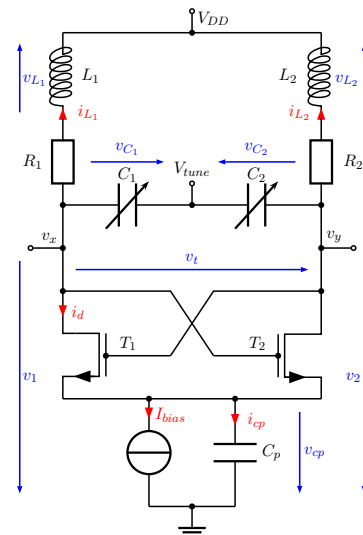


Fig. 1. 5-dimensional circuit model of a LC-Tank VCO.

an opportunity to reduce time-consuming optimizations by circuit simulators.

In contrast to the circuit analysis of oscillators parametrized circuit models are needed for oscillator design where the parameters can be used to adapt an oscillator architecture to the specifications. Since it is known from the Andronov-Hopf theorem that the stationary behavior of regular sinusoidal oscillators takes place on 2-dimensional manifolds many nonlinear oscillator design approaches are based on second order systems. Novel nonlinear design concepts that included the nonlinearity of the varactors and the nonlinearity of the active devices were presented in [9], [10], [11] lately. Due to the parasitic elements of the used inductors and transistors realistic oscillator models have a state-space dimension exceeding two. As a result, a second order differential equation can only be derived if a total capacitance and a total inductance are defined. Usually,

these approximative total elements can only be defined near a certain frequency, but this is not possible for nonlinear elements. In order to optimize selected circuit properties different VCO architectures have been expanded by structural circuit extensions; e.g. filter circuits [12]. Most of these additional circuit elements cannot be considered in the 2-dimensional model approaches. In order to circumvent these difficulties and to study asymmetrical effects, higher dimensional circuit models are needed; see [13].

In the presented approach we use an order reduction technique based on the center manifold approach to extract a second order differential equation for the description of nonlinear oscillators. All steps are performed in a semi-symbolic manner in order to include parameters in the equations to use it for the design of oscillators. The method is applied to the standard LC-Tank VCO architecture, which has been expanded by an additional filter capacitance [12]. The proposed approach allows to study and visualize the influence of circuit asymmetries and structural circuit extensions on the dynamical behavior of oscillators.

II. HIGHER DIMENSIONAL CIRCUIT MODEL

Fig. 1 shows the standard LC-Tank VCO architecture which has been expanded by an additional filter capacitance C_p in order to improve the phase noise behavior of the VCO [12]. The ohmic losses of the circuit are summarized in the resistances R_1 and R_2 . For the sake of simplification, the capacitance of the two MOS varactors [11] is modeled by the constant capacitances C_1 and C_2 , and the bias current is provided by an ideal current source I_{bias} . If we assume that the MOS transistors T_1 and T_2 stay in saturation

$$I_D = K \cdot (V_{GS} - V_{th})^2 \quad \text{with} \quad K = \frac{\mu_n C_{ox}}{2} \frac{W_n}{L_n}, \quad (1)$$

the following circuit equations in a 5-dimensional state space can be derived:

$$\begin{aligned} \frac{dv_{C_p}}{dt} &= \frac{1}{C_p} \cdot [K \cdot (v_2 - v_{C_p} - V_{TH})^2 \\ &\quad + K \cdot (v_1 - v_{C_p} - V_{TH})^2 - I_{bias}] \\ \frac{di_{L_1}}{dt} &= \frac{v_1 - V_{DD} - i_{L_1} \cdot R_1}{L_1} \\ \frac{di_{L_2}}{dt} &= \frac{v_2 - V_{DD} - i_{L_2} \cdot R_2}{L_2} \\ \frac{dv_1}{dt} &= \frac{1}{C_1} \cdot [-K \cdot (v_2 - v_{C_p} - V_{TH})^2 - i_{L_1}] \\ \frac{dv_2}{dt} &= \frac{1}{C_2} \cdot [-K \cdot (v_1 - v_{C_p} - V_{TH})^2 - i_{L_2}] \end{aligned} \quad (2)$$

The transconductance K includes the electron mobility μ_n , whereas W_n und L_n are the width and the length of the channel of the MOS transistors and C_{ox} is the oxide capacitance. Obviously the capacitance C_p cannot be incorporated into a second order model in a direct manner. By using a reduction method based on a center manifold approach, it is possible to obtain a two dimensional system of differential equations of the LC-Tank VCO with filter capacitance, that maintains the dynamics of the 5-dimensional system. The center manifold approach is well-known in mathematics and oscillator analysis and therefore the reader is left to the literature for further details [4], [6], [14], and [15].

III. REDUCTION OF THE LC-TANK VCO EQUATIONS AND THE ANDRONOV-HOPF BIFURCATION

In this section we use the above mentioned reduction approach to the describing equations (2) of the VCO in fig. 1. The specifications of the VCO are based on bluetooth applications with a center frequency of 2.4 GHz and a tuning range from 2.1 GHz to 2.7 GHz. We use a 0.25 μm CMOS process (SGB25V) from the company IHP. The capacitances $C_{1,2}$ are set to 500 fF, which corresponds to the lower limit of the tuning range. For the filter capacitance we choose a suitable value of $C_p = 1$ pF [12], [2]. The parasitic ohmic resistance of the VCO circuit is summarized in $R_{1,2} = 21 \Omega$. The supply voltage is set to 2.5 V. We choose an inductor of $L_{1,2} = 11 \text{ nH}$. The transconductance K is a free parameter that is related to the width W_n of the cross-coupled MOS pair by (1). In order to study the Andronov-Hopf bifurcation the eigenvalues of the linearized system matrix are considered in dependence of K and W_n , respectively. We are interested in a bifurcation parameter μ that does not change the frequency of the VCO. By means of root locus curves it can be shown that K and therefore W_n is a suitable bifurcation parameter. Therefore we use $\mu = \sqrt{K}$ as bifurcation parameter and obtain a system of differential equations in the following form

$$\dot{\mathbf{x}} = \mathbf{F}(\mathbf{x}, K) \quad \text{mit} \quad \mathbf{F}(\mathbf{0}, K) = \mathbf{0}. \quad (3)$$

In the equilibrium point the system can be developed by means of a multidimensional Taylor series

$$\dot{\mathbf{x}} = \mathbf{A}(K) \cdot \mathbf{x} + \mathbf{f}(\mathbf{x}, K) \quad \text{mit} \quad \mathbf{f}(\mathbf{x}, K) = \mathcal{O}(\|\mathbf{x}\|^2), \quad (4)$$

where the Jacobi matrix $\mathbf{A}(\mu)$ for our example VCO is given by $\mathbf{A}(\mu) =$

$$10^9 \cdot \begin{bmatrix} -126.49 \cdot \mu & 0 & 0 & 63.246 \cdot \mu & 63.246 \cdot \mu \\ 0 & -1 & 0 & 90.909 \cdot 10^{-3} & 0 \\ 0 & 0 & -1 & 0 & 90.909 \cdot 10^{-3} \\ 126.49 \cdot \mu & -2 \cdot 10^3 & 0 & 0 & -126.49 \cdot \mu \\ 126.49 \cdot \mu & 0 & -2 \cdot 10^3 & -126.49 \cdot \mu & 0 \end{bmatrix}. \quad (5)$$

The Andronov-Hopf bifurcation point arise at $\mu_b = 7.9057 \cdot 10^{-3}$, where the corresponding W_n can be calculated by $W_n = 2L_n\mu^2/\mu_n C_{ox}$. The remaining nonlinear part is given by $\mathbf{f}(\mathbf{x}, \mu) =$

$$10^{12} \cdot \begin{bmatrix} v_1^2 \cdot \mu^2 - 2 \cdot v_1 \cdot v_{C_p} \cdot \mu^2 + v_2^2 \cdot \mu^2 - 2 \cdot v_2 \cdot v_{C_p} \cdot \mu^2 + 2 \cdot v_{C_p}^2 \cdot \mu^2 \\ 0 \\ 0 \\ -2 \cdot v_{C_p}^2 \cdot \mu^2 + 4 \cdot v_2 \cdot v_{C_p} \cdot \mu^2 - 2 \cdot v_2^2 \cdot \mu^2 \\ -2 \cdot v_{C_p}^2 \cdot \mu^2 + 4 \cdot v_1 \cdot v_{C_p} \cdot \mu^2 - 2 \cdot v_1^2 \cdot \mu^2 \end{bmatrix}. \quad (6)$$

In order to study small derivations from the bifurcation point μ_b we introduce $\mu = \mu_b + \Delta_\mu$ and reformulate the differential equations in the following manner

$$\dot{\mathbf{x}} = \mathbf{A}(\mu_b) \cdot \mathbf{x} + \mathbf{A}(\Delta_\mu) \cdot \mathbf{x} + \mathbf{f}_b(\mathbf{x}, \Delta_\mu). \quad (7)$$

Note, that a center manifold is defined only in the bifurcation point: However the center manifold is embedded into a family of integral manifolds which are parametrized by μ_b near the bifurcation point. From the above mentioned center manifold approach we know that a linear transformation is necessary in order to decompose the system into a stable and a center part

$$\frac{d}{dt} \begin{bmatrix} x_{c1} \\ x_{c2} \end{bmatrix} = 10^9 \cdot \begin{bmatrix} 0 & 13.447 \\ -13.447 & 0 \end{bmatrix} \cdot \begin{bmatrix} x_{c1} \\ x_{c2} \end{bmatrix} + \begin{bmatrix} f_{c1} \\ f_{c2} \end{bmatrix}, \quad (8a)$$

$$\frac{d}{dt} \begin{bmatrix} x_{s1} \\ x_{s2} \\ x_{s3} \end{bmatrix} = 10^9 \cdot \begin{bmatrix} -1 & 13.447 & 0 \\ -13.447 & -1 & 0 \\ 0 & 0 & -1 \end{bmatrix} \cdot \begin{bmatrix} x_{s1} \\ x_{s2} \\ x_{s3} \end{bmatrix} + \begin{bmatrix} f_{s1} \\ f_{s2} \\ f_{s3} \end{bmatrix}, \quad (8b)$$

with $f_{c1,2} = f_{c1,2}(\mathbf{x}_c, \mathbf{x}_s, \Delta_\mu)$ and $f_{s1,2,3} = f_{s1,2,3}(\mathbf{x}_c, \mathbf{x}_s, \Delta_\mu)$. Due to the symmetry of the circuit the non-zero real and the imaginary parts are equal. The center manifold can be represented by

$$\mathbf{x}_s = \mathbf{h}(\mathbf{x}_c, \Delta_\mu). \quad (9)$$

A quadratic polynomial approximation of the center manifold $\mathbf{h}(\mathbf{x}_c, \Delta_\mu)$ is given by

$$\begin{aligned} \phi_i(x_{c1}, x_{c2}, \Delta_\mu) = & a_i \cdot x_{c1}^2 + b_i \cdot x_{c2}^2 + c_i \cdot \Delta_\mu^2 + \\ & + d_i \cdot x_{c1} \cdot x_{c2} + e_i \cdot x_{c1} \cdot \Delta_\mu + f_i \cdot x_{c2} \cdot \Delta_\mu \end{aligned} \quad (10a)$$

where $i = \{1, 2, 3\}$ and the coefficients are: $a_1 = -216.210^{-6}$, $a_2 = 2.21310^{-3}$, $a_3 = -31.4710^{-3}$, $b_1 = 216.210^{-6}$, $b_2 = 4.36910^{-3}$, $b_3 = -31.3810^{-3}$, $d_1 = 4.35310^{-3}$, $d_2 = -541.210^{-6}$ and $d_3 = 62.3310^{-3}$.

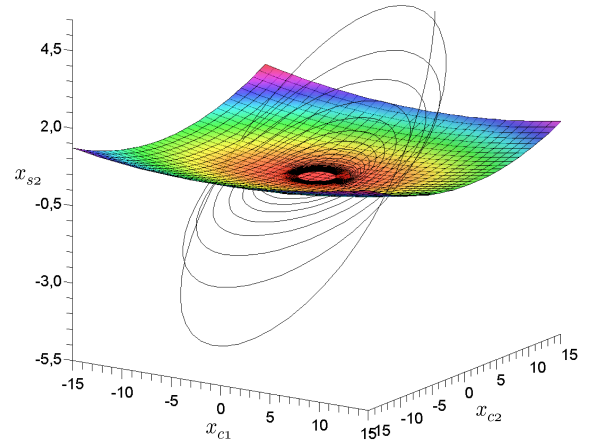


Fig. 2. Transient trajectory in the center manifold (projection into the subspace $\{x_{c1}, x_{c2}, x_{s3}\}$).

It is noticeable that the Δ_μ -dependent coefficients c_i , e_i and f_i with $i = \{1, 2, 3\}$ are zero. The resulting reduced nonlinear system of second order that describes the dynamical behavior near the equilibrium point is of the following form

$$\dot{\mathbf{x}}_c = \mathbf{A}_c \cdot \mathbf{x}_c + \mathbf{f}_c(\mathbf{x}_c, \Delta_\mu, \phi(\mathbf{x}_c, \Delta_\mu)). \quad (11)$$

The dynamic of this system is illustrated in fig. 2.

IV. INFLUENCES OF ASYMMETRIES IN THE CIRCUIT

As a consequence of our circuit modeling we can show that the circuit symmetry of the LC-Tank VCO architecture results in special properties of the associate mathematical models. In order to consider the impact of circuit asymmetry on the LC-Tank VCO architecture we introduce a substantial asymmetry in the circuit in fig. 1 by setting C_1 to 300fF and C_2 to 700fF. In contrast to the quadratic polynomial approximation of the symmetrical model (10a) the coefficients $e_{1,2,3}$ and $f_{1,2,3}$ are not zero anymore for the asymmetrical case. We observe a linear dependency of these coefficients with respect to the variation of the bifurcation parameter Δ_μ . Fig. 3 shows some integral manifolds, projected into the subspace $\{x_{c1}, x_{c2}, x_{s2}\}$, for different parameter values of Δ_μ . In comparison to the center manifold with $\Delta_\mu = 0$ we observe distortions of the integral manifolds. Obviously the dynamics of the system are perturbed; see fig. 3. Fig. 4 shows an integral manifold for the symmetrical VCO case in which a numerically calculated limit cycle is embedded. The integral manifold was calculated by using a 3rd order polynomial approximation for the center manifold. This result illustrates that by

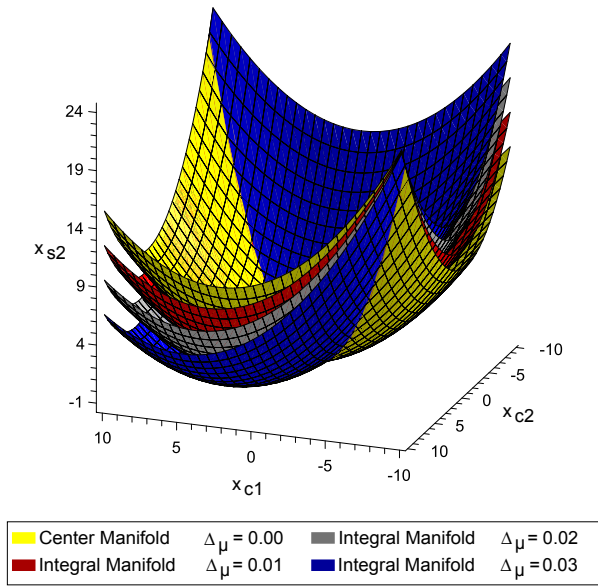


Fig. 3. Integral manifold in dependency of $\Delta\mu$ (projection into the subspace $\{x_{c1}, x_{c2}, x_{s2}\}$).

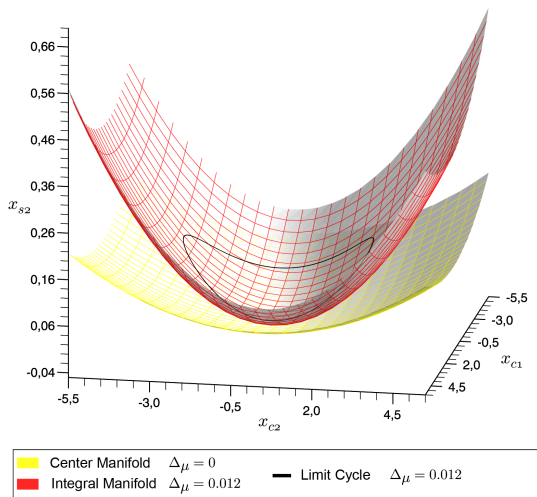


Fig. 4. Limit cycle embedded into the integral manifold for $\Delta\mu = 0.012$ (projection into the subspace $\{x_{c1}, x_{c2}, x_{s2}\}$).

using a more precise VCO model (using a 3rd order or higher center manifold approximation) the dependency of the system dynamics on the bifurcation parameter can be obtained even for a symmetrical designed LC-Tank VCO circuit. Therefore, our approach can be used for a geometrical study of the asymmetries within the VCO and a visualization of the overall VCO dynamics. It can also be used to classify VCO circuits.

V. CONCLUSIONS

In this paper an order reduction technique is realized, that is based on the concept of center manifold. We illustrate this approach by means of a VCO model with a 5-dimensional state space. It was shown that a second order model can be derived which is not only valid near the bifurcation point that is near the oscillatory frequency of the VCO. Furthermore, the dynamics of the circuit can be studied in dependency of structural and parametric disturbances of the circuit. This was illustrated by considering asymmetries within the VCO.

REFERENCES

- [1] Lee, T.: The Design of Cmos Radio-Frequency Integrated Circuits, Cambridge University Press, Cambridge, 2004.
- [2] Hegazi, E.: The Designer's Guide to High-Purity Oscillators, Kluwer Academic Publishers, Boston, 2005.
- [3] Mathis, W.: Nonlinear electronic Circuits - An overview. Proc. 7th MIXDES 2000, Gdynia (Poland), 15.-17. Juni 2000.
- [4] Maggio, G. M., De Feo, O., and Kennedy, M. P.: A general method to predict the amplitude of oscillation in nearly-sinusoidal oscillators, IEEE Trans. Circuits and Systems-I, vol. 51, 8, 1586-95, 2004.
- [5] Prochaska, M., Belski, A. und Mathis, W.: Design and Analysis of Fully Integrated Differential VCOs, Advances in Radio Science, 3, 359-363, 2005.
- [6] Guckenheimer, P. und Holmes, J.: Nonlinear Oscillations, Dynamical Systems, and Bifurcations of Vector Fields, Springer-Verlag, Berlin, 2002.
- [7] Parzen, P.: Design of Crystal and Other Harmonic Oscillators, Wiley, New York, 1983.
- [8] Mandelstam, L., Papalexi, N., Andronov, A.A., Chaikin, S., Witt, A.: Exposé des Recherches Récentes, sur les Oscillations Non Linéaires. Zeitschr. f. Techn. Physik, 4, 81-134, 1935.
- [9] Buonomo, A. und Schiavo, A. L.: Modelling and analysis of differential VCOs: Research Articles, Int. J. Circuit Theory Appl., 32, 117-131, 2004.
- [10] Buonomo, A.: Nonlinear Analysis of Voltage-Controlled Oscillators: A Systematic Approach, Circuits and Systems I: Regular Papers, IEEE Transactions on, 55, 1659-1670, 2008.
- [11] Bremer, J.-K., Zorn, C., Przytarski, J. und Mathis, W.: A nonlinear systematic design flow for LC tank VCOs based on large signal capacitance modeling, in: Proc. IEEE International Symposium on Circuits and Systems ISCAS 2009, pp. 2389-2392, 2009.
- [12] Hegazi, E., Sjolund, H. und Abidi, A.: A filtering technique to lower LC oscillator phase noise, Solid-State Circuits, IEEE Journal of, 36, 1921-1930, 2001.
- [13] Przytarski, J., Bremer, J.-K. und Mathis, W.: Nichtlineare Analyse von LC-TANK VCOs unter Berücksichtigung parasitärer Substrateffekte, Advances in Radio Science, 7, 179-183, 2009.
- [14] Carr, J.: Applications of Centre Manifold Theory, Springer-Verlag, Berlin, 1981.
- [15] Mathis, W., Keidies, C.: Application of Center Manifolds to Oscillator Analysis. Proc. 12th European Conference on Circuit Theory and Design (ECCTD'95), Istanbul, Turkey, 1995.

Author index

Author	Page	Author	Page
Aburatani, Hitoshi	154	Kitajima, Hiroyuki	226
Aihara, Kazuyuki	98, 106	Klinshov, Vladimir	178
Aleo, Ignazio	194	Kohda, Tohru	98, 106
Algaba, Antonio	182, 186	Kolwankar, Kiran M.	138
Arena, Paolo	194, 206	Koronovskii, Alexey A.	50, 70, 174, 210
Asahara, Hiroyuki	118, 122	Kousaka, Takuji	118, 122
Ascoli, Alon	166	Krause, André Frank	190
Benner, Philipp	6	Kurkin, S. A.	50
Bhowmick, Sourav Kumar	26	Kurovskaya, Maria K.	210
Blakely, Jonathan N.	142	Kuzmin, L. V.	42
Bläsing, Bettina	190	Kuznetsov, Alexey	126
Bodo, B.	230	Lindberg, Erik	15
Bremer, Jan-K.	238	Loskutov, Alexander	78
Bumelienė, Skaidra	30	Lunze, Jan	86
Buscarino, Arturo	66, 146	Makarov, Valeri A.	198
Carbone, Anna	234	Marquié, P.	230
Chakraborty, Satyabrata	150	Mathis, Wolfgang	22, 238
Corinto, Fernando	166	Mazzetti, Piero	234
Corron, Ned J.	142	Mchiri, Mohamed	34, 38
Cruse, Holk	202	Merino, Manuel	182, 186
Dana, Syamal Kumar	26, 150	Moradi, Parham	102
Darrat, Ahmed H.	22	Morfu, S.	230
Dmitriev, Alexander	46	Moskalenko, Olga I.	70, 210
Efremova, Elena	46	Mürset, Urs	158
Fernández-Sánchez, F.	182	Mykolaitis, Gytis	30
Fortuna, Luigi	66, 146	Nakada, Kazuki	82
Franco, Carlos Hernández	94	Nakagawa, Masahiro	170
Frasca, Mattia	66, 146	Nekorkin, Vladimir I.	126, 162, 178
García, Cristóbal	186	Nikishov, Artem	46
Gilli, Marco	166, 234	Ning, Bo	130
Grishin, Sergey V.	218	Nishio, Yoshifumi	62, 106, 114, 150
Hasler, Martin	102	Osana, Yuko	134
Hayashi, Hatsuo	82	Ott, Thomas	158
Hori, Yoshihiko	110	Panchuk, Anastasiia	58
Horikawa, Yo	226	Patané, Luca	194, 206
Hou, Jian-Li	130	Philominathan, P.	90
Hramov, Alexander E.	50, 70, 174, 210	Pollino, Massimo	206
Jin'no Kenya	110	Ponta, Linda	234
Jost, Jürgen	138	Rad, Ali Ajdari	102
Kasatkin, Dmitry V.	162	Reibiger, Albrecht	10
Kashchenko, Ilya S.	19	Reit, Marco	238
Kataoka, Hiroshige	114	Ren, Quansheng	130, 138
Kelber, Kristina	94	Reyes, Manuel	186
Khadivi, Alireza	102	Röbenack, Klaus	54
Kimura, Daisuke	214	Rodríguez-Luis, A. J.	182
Kirvaitis, Raimundas	30	Rossé, M.	230
		Roy, Prodyot Kumar	26

Author	Page	Author	Page
Ryabov, Alexei B.	78	Tanaka, Toru	106
Safya, Belghith	34, 38	Tasaki, Kenichi	118
Saito, Toshimichi	214	Tateno, Katsumi	82
Samal, Areejit	138	Trabelsi, Karim	34, 38
Santhiah, M.	90	Une, Takao	98
Schack, Thomas	190	Uwate, Yoko	6, 62
Schild, Axel	86	Velarde, Manuel G.	198
Schilling, Malte	202	Ventura, Chrisina	206
Schwarz, Wolfgang	86	Villacorta-Atienza, Jose A.	198
Sciuto, Gregorio	66	Wabnik, Nils	94
Sharaevskii, Yurii P.	218	Yamagami, Yoshihiro	114
Shurygina, Svetlana A.	70	Yamane, Suguru	154
Slavova, Angela	74	Yamauchi, Masayuki	106, 154
Stahl, Mark T.	142	Yoshii, Kiyonori	82
Stoop, Ruedi	6, 62	Yoshimatsu, Kazuhisa	106
Takamori, Yohei	134	Zakharov, Denis	126
Tamaševičius, Arūnas	30	Zhao, Jianye	130
Tamaševičiūtė, Elena	30		